TECHNISCHE UNIVERSITÄT WIEN

DISSERTATION:

Commissioning of the *q*Bounce-Ramsey-spectrometer and its application to test the neutron's neutrality

Ausgeführt zum Zwecke der Erlangung des akademischen Grades
eines Doktors der technischen Wissenschaften
unter der Leitung von

Univ.Prof. Dipl.-Phys. Dr.rer.nat. Hartmut Abele
E 141 - Atominstitut, TU Wien

unter Mitwirkung von
Dipl.-Phys. Dr.rer.nat. Tobias Jenke
Institut Laue-Langevin, Grenoble

eingereicht an der Technischen Universität Wien
Fakultät für Physik

von

Dipl.-Ing. Joachim Bosina, BSc
Wien

December 12, 2023

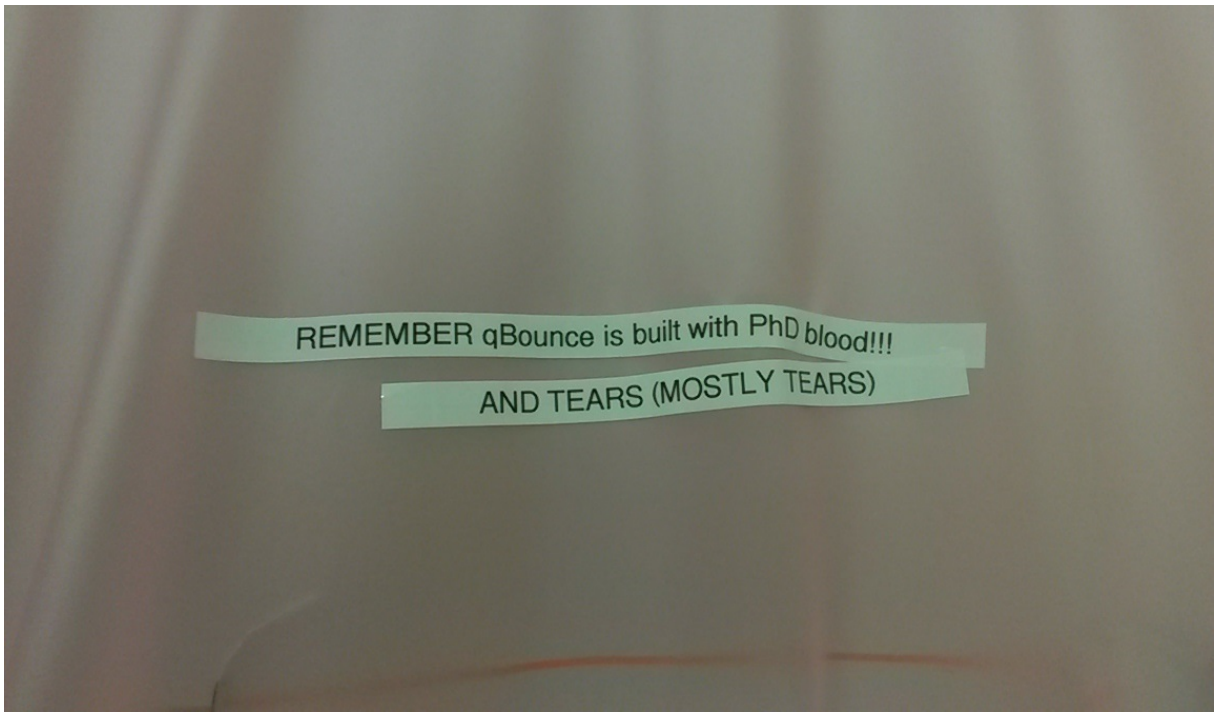

Abstract

Neutral particles form gravitationally bound quantum states above flat impenetrable surfaces. However, in most cases van der Waals forces, couplings between particle's spin and external magnetic fields or other electromagnetic interactions completely superpose this effect. Ultra-cold neutrons are the only ones yet where this phenomenon has been observed. This unique system is well suited to probe gravitation at short distances (µm scale) and test predictions of theories which try to connect quantum mechanics and general relativity. As an example for a possible observable: the electric charge of the neutron is zero within the framework of the Standard Model of particle physics. New theories exploring beyond this Standard Model are not that restrictive. Lower limits from measurements are able to constrain or even rule out such theories and enable to support the development of new theory models.

Since many years the *q*BOUNCE collaboration has developed the technique of Gravitational Resonance Spectroscopy (GRS) in order to study these gravitationally bound quantum states and to test theoretical models probing beyond the Standard Model at the PF2 UCN facility of the Institut Laue-Langevin (ILL) in Grenoble, France. During this thesis, I performed the first successful measurements with the novel Ramsey-type GRS setup (the so-called RAMSEY$^{\mathrm{TR}}$-setup) during its commissioning in 2018. The studied state transitions were $|1\rangle \rightarrow |3\rangle$ and in more detail $|2\rangle \rightarrow |4\rangle$ with their measured frequency values of 462.71(30) Hz and 392.38(26) Hz respectively using a common fit. A preceding Rabi-type measurement additionally observed the previously unexplored transition $|2\rangle \rightarrow |5\rangle$ at 560.0(31) Hz.
This Ramsey-type GRS setup enables to test the electric neutrality of the neutron itself. Contrary to classical deflection experiments, this setup can detect shifts of the gravitational states of ultra-cold neutrons in the presence of strong electric fields which is a novel and complimentary technique. In 2018, a measurement campaign with field strengths up to 7.7(2) MV/m at the transition $|2\rangle \rightarrow |4\rangle$ probed the neutron's electric charge to a value of $2.7(33) \times 10^{-17}\, e$ at the best fitted gravitational acceleration of $g = 9.784(13)\,\mathrm{m/s^2}$ which corresponds to a transition frequency of $\nu_{24} = 392.01(35)$ Hz. Many additional measurements probed the capabilities of different electrode materials (copper, titanium and mirrors) and the utilized large electrode at a dedicated test setup at the Atominstitut (ATI) in Vienna in order to search for the breakthrough voltages of these electrodes. These investigations and other improvements of the last years predict that the sensitivity of the charge measurement can be increased by a factor of 75 with the currently used RAMSEY$^{\mathrm{TR}}$-setup compared to the first measurement of its kind in 2018. A future improved setup can further increase the sensitivity which enables it to outperform the current best limit.

Zusammenfassung

Neutrale Teilchen formen gravitativ gebundene Quantenzustände über undurchdringlichen Flächen. Meistens aber überdecken Van-der-Waals Kräfte, Wechselwirkungen zwischen dem Teilchenspin und externen Magnetfeldern oder andere elektromagnetische Kräfte diesen Effekt komplett. Bis jetzt sind ultrakalte Neutronen die einzigen Teilchen, bei denen dieses Phänomen beobachtet wurde. Dieses einzigartige System ist sehr gut geeignet, um die Gravitation bei sehr kleinen Abständen (µm Skala) zu studieren und Vorhersagen von Theorien, die versuchen Quantenmechanik und die allgemeinen Relativitätstheorie zu verknüpfen, zu testen. Ein Beispiel für einer möglichen Messgröße für solche Tests: Im Rahmen des Standardmodells der Teilchenphysik ist die elektrische Ladung des Neutrons exakt null. Neuartige Theorien, die das Standardmodell zu erweitern versuchen, sind nicht so strikt. Niedrigere Grenzen durch experimentelle Messungen können solche Theorien einschränken oder sogar ausschließen lassen und ermöglichen die Entwicklung neuer theoretischer Modelle zu unterstützen.

Seit vielen Jahren entwickelt die qBOUNCE Kollaboration die Technik der Gravitation-Resonanz- Spektroskopie (GRS), um diese gravitative gebundenen Quantenzustände zu erforschen und theoretische Modelle, die über das Standardmodell hinausgeht, an der ultrakalten Neutronenquelle PF2 des Institut Laue-Langevin (ILL) in Grenoble zu testen. Für diese Dissertation wurden die ersten erfolgreichen Messungen am neuen Ramsey-artigen GRS Aufbau (dem sogenannten RAMSEY$^{\text{TR}}$ Setup) durchgeführt. Die erforschten Zustandsübergänge waren $|1\rangle \rightarrow |3\rangle$ und im Detail $|2\rangle \rightarrow |4\rangle$ mit den gemessenen Frequenzen von 462.71(30) Hz und 392.38(26) Hz, die aus einem gemeinsamen Fit bestimmt wurden. Eine vorangehende Rabi-artige Messung beobachtete zusätzlich den bis dahin unerforschten Übergang $|2\rangle \rightarrow |5\rangle$ bei 560.0(31) Hz.
Dieser Ramsey-artige GRS Aufbau ermöglicht es auch, die elektrische Ladung des Neutrons selbst zu untersuchen. Im Gegensatz zu klassischen Experimenten mittels Ladungsablenkung kann dieser Aufbau Verschiebungen der Gravitationszustände der ultrakalten Neutronen in starken elektrischen Feldern detektieren. Dies ist eine neuartige und komplimentäre Messmethode. 2018 ergab eine Messkampagne am Übergang $|2\rangle \rightarrow |4\rangle$ mit Feldstärken bis zu 7.67 MV/m eine Neutronenladung im Wert von $2.7(33) \times 10^{-17}\, e$ bei einer angepassten Erdbeschleunigung von $g = 9.784(13)\,\text{m/s}^2$, welche einer Übergangsfrequenz von $\nu_{24} = 392.01(35)$ Hz entspricht. Viele zusätzliche Messungen erforschten die Eigenschaften von verschiedenen Elektrodenmaterialen (Kupfer, Titan und Glasspiegel) und der großen Spiegelelektrode, die für die Ladungsmessung verwendet wurde, an einem speziellen Testaufbau am Atominstitut in Wien, um die Durchbruchsspannung für diese Elektroden zu finden. Diese Untersuchungen und andere Verbesserungen der letzten Jahre sagen voraus, dass die Genauigkeit der Ladungsmessung mit dem bestehenden RAMSEY$^{\text{TR}}$ Setup um einen Faktor von bis zu 75 im Vergleich zu der ersten Messung von 2018 verbessert werden kann. Ein zukünftiger weiterentwickelter Aufbau würde eine noch genauere Messung ermöglichen, welches sogar das derzeitige Limit übertreffen kann.

Contents

1. Introduction

This chapter gives an introduction to the neutron's electric charge measurement and an overview of the research with gravitationally bound quantum states. The following chapters describe the theoretical background and the experimental setup before I present the main measurements which I conducted with the help of many students and colleagues during my research.

Measuring the charge of a neutron q_n is an interesting topic for particle physics, even though the well tested *Standard Model of particle physics* (SM) predicts a zero value. In the following, I will present some reasons for this experiment, before I present a historical overview of the most important measurements and attempts to implement new methods to lower the measured limit of the neutron charge. Afterwards, I will introduce other properties of the neutron in order to characterize the test particle used in the measurements in this thesis. At the end I will give an introduction to the gravitational quantum states of *ultra-cold neutrons* (UCN) and its application in *gravitational resonance spectroscopy* (GRS) along with a summary of the research in this field.

1.1. The neutron's electric charge

It is well established, that the neutron does not carry any electric charge ($q_n = 0$). This is contrary to its inner structure which consists of three charged quarks. Two down quarks carry each an electric charge of $-1/3\,e$ and one up quark perfectly compensates this with a charge of $+2/3\,e$. However, electron scattering experiments on neutrons reveal an inhomogeneous charge distribution and a resulting negative charge radius of $\sqrt{\langle r_M^2 \rangle} = 0.864(9)\,\text{fm}$ ($\langle r_M^2 \rangle = -0.1155(17)\,\text{fm}^2$) [21, 197, 319]. In addition, the Standard Model predicts a not yet measured very small value of the neutron's electric dipole moment [2].

The history of physics tells never to take anything for granted. Therefore, everything has to be measured as precise as possible in order to crosscheck it to the theoretical predictions. Any deviations can help us to find good candidates for extensions of the commonly accepted *Standard Model of particle physics* (SM). For this cause: in 1959 Feinberg and Goldhaber insisted to measure the neutron charge in order to confirm the basic charge equality of elementary particles (electrons as leptons vs. protons as hadrons) with a higher accuracy and precision [85]. In his PhD thesis, Christian Siemensen summarized many more good reasons to further lower the limit of the measured absolute value of the neutron charge as he tried it with a newly developed apparatus [280]. One of the major theoretical motivators is the description of the charge quantization within extensions of the Standard Model [91]. Some theories in the field of *Beyond the Standard Model* (BSM) also enable the existence of a finite neutron charge. For example, E. Takasugi and M. Tanaka developed a model with five Higgs bosons (two doublets & one singlet) to describe the spontaneous charge-symmetry-breaking which included very small charges different for neutrons and neutrinos and its predictions still stays within the experimental limits [297]. However, finding a finite neutron charge would have a strong impact on many fields of physics (e.g. the Standard Model, cosmology, neutrino charge, ...). Vice verse, it is important to probe this parameter as precise as possible to confirm the currently accepted theoretical prediction ($q_n = 0\,e$).

There are two ways to measure the electric charge of the neutron: either directly or indirectly. The indirect method uses neutral atoms or molecules which have a tremendous statistical advantage and many different precise methods can be applied (trapping, laser cooling,...). Bressi et al. reached the lowest measured value of $|q_n| < 10^{-21}\,e$ using SF_6 in acoustic resonators as an indirect search method [53]. They also presented a historic summary of indirect and direct methods of how to determine q_n. A big disadvantage of the indirect method is, that it includes the charge equality of particles. Measuring the charge of an atom not only includes the neutron charge q_n but also the charge difference ϵ between electrons and protons which is also expected to be zero. Considering the charge conservation during the beta decay of a free neutron, both values are equal (if the anti-electron neutrino is uncharged). Therefore, direct measurements of the neutron charge with neutrons, which are presented in the next section, are important as complimentary tools to see the full picture.

1.2. Direct neutron charge measurements

Soon after the discovery of the neutron, Philip Ivor Dee presented the first limit of the neutron charge in 1932. He used the interaction of neutrons with the gas within an electric field inside a cloud chamber to estimate an upper limit [70].
With the success of indirect measurement methods the demand arose to lower the limit from the direct methods by orders of magnitudes. This led to the development and improvement of the most common method which is the neutron beam deflection Δx within a very strong homogeneous electric field $\vec{E}$. The limit of q_n is set by not observing a deflection for a given field strength E_z, flight time t (flight distance d / neutron velocity v_n) and total number of counted neutrons (eq. (1.1) is taken from [245]).

$$\Delta x \propto \frac{q_\mathrm{n} E_z}{m_\mathrm{n}} t^2 = \frac{q_\mathrm{n} E_z d^2}{m_\mathrm{n} {v_\mathrm{n}}^2} \tag{1.1}$$

This method could be improved by imprinting a pattern (e.g. grid) into the incoming beam and blocking the outgoing neutron beam for the zero volt measurement with a similar movable pattern. Only with the use of a special neutron optics, the beam pattern is transported with as little as possible aberrations and blurring to the detector. This effort reduces the minimal detectable deflection [34, 36]. Any deflection of neutrons due to an applied electric field would be measured as an increase of the neutron flux. However, the main limitations are the three parameters presented first. In the past, the best measurements used cold neutrons due to their high statistics. The flight path and the field strength were increased to the experimental limits. The following table 1.1 summarizes the best historic measurements and some attempts with different methods:

Table 1.1.: Overview of the neutron charge measurements

Researcher [Publication]	Year	Neutron properties	Length d	E-field E_z	Charge value q_n
P. I. Dee [70]	1932	$<3.3 \times 10^9$ cm/s (fast)	10 cm	50 V/cm	$\lvert q_\mathrm{n}\rvert < 1/700\, e$
Shapiro & Estulin [278]	1956	≈26 meV(thermal)	0.5 m	1.33 MV/m	$\lvert q_\mathrm{n}\rvert < 6 \times 10^{-12}\, e$
Shull [279]	1967	2.4 Å (thermal)	1.5 m	22.5 MV/m	$-1.9(37) \times 10^{-18}\, e$
Kalus & Gähler [94, 95, 105, 106, 152]	1982	10 - 30 Å (cold)	10 m	±5.9 MV/m	$-1.5(14) \times 10^{-20}\, e$
Borisov et al. [43, 245]	1987	<7.8 m/s (UCN)	2 × 0.9 m	±1 MV/m	$-4.3(71) \times 10^{-20}\, e$
Baumann et al. [33, 34, 35, 36, 37, 38]	1988	1.2 - 3 nm (cold)	9 m	±6 MV/m	$-0.4(11) \times 10^{-21}\, e$
Siemensen et al. [245, 280, 281, 282]	2014	≈8 m/s (UCN)	2 × 1.25 m	±1.2 MV/m	$-0.3(35) \times 10^{-20}\, e$

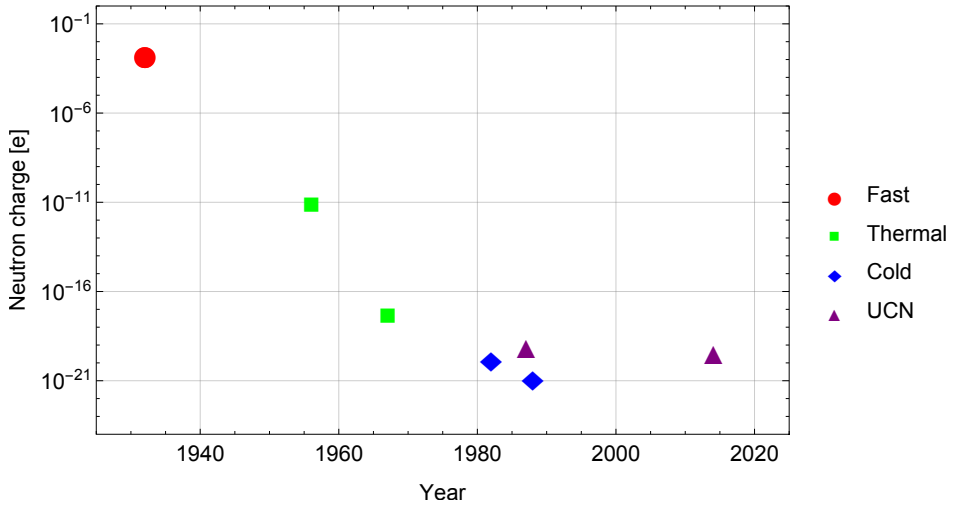

Figure 1.1.: A historic overview of the neutron charge measurements.

Jürgen Baumann, Roland Gähler, Jürgen Kalus, B. Alefeld and Walter Mampe (University of Bayreuth, TU Munich, FZ Jülich and the Institut Laue-Langevin (ILL)) conducted the most precise measurements in a series of experiments between 1980-1988 at the ILL. The theses of Roland Gähler [105] and Jürgen Baumann [33] contain detailed descriptions of these experiments. Their used length of a 10 m setup and an electric field of 6 MV m^{-1} are physically very hard to surpass. They only saw the opportunity

to use a better neutron optic with smaller pattern features and a sharper imaging onto the detector in order to further lower their best limit using cold neutrons. Baumann also provided proof that the maximal possible sensitivity is independent of the used wavelength [33]: On the one hand, using slower neutrons would increase the deflection and on the other hand shifting to the longer wavelength part of the same neutron spectrum decreases the number of counted neutrons and consequently increases the statistical uncertainty. The only possibilities are to shift the complete neutron spectrum to slower energies (moderation without losses) or to store the neutrons for longer periods which is only possible for UCNs. Since the beginning of the *Quantum Bouncer* studies with UCNs, measuring the neutron charge and trying to improve the best value of Baumann et al. has been a major driving force for further developments (e.g. GRS) starting with Frank Rueß who mentioned it the first time in his thesis [258](p.85) in 2000.

At the same time as the previously described measurement campaign, a Soviet researcher group consisting of Yu.V. Borisov, N.V. Borovikova, A.V. Vasiliev, L.A. Grigorieva, S.N. Ivanov, N.T. Kashukeev, V.V. Nesvizhevsky, A.P. Serebrov and P.S. Yaidzhie from the JINR and PNPI investigated the possibility to use UCNs instead of cold neutrons [43]. The advantage is the much longer interaction time of the neutron with the electric field (5-10 times shorter setup but also more than 100 times slower neutrons). On the contrary, the decreased flux (factor 200) reduces the statistical precision. Due to the much slower neutron velocity, gravity starts to be an important phenomenon within the setup. Instead of passing through the electrodes without any wall interaction, UCNs bounce multiple times on the floor of the guides within the electrodes. This leads to a tilt-depending deflection of the beam due to gravity (similar to the expected deflection of a hypothetical neutron charge) which can be used as a systematic test of the horizontal alignment and the rest of the neutron optics. A new feature of using UCNs is the possibility to reflect the neutrons at the end of the electrodes back to the entrance and therefore double the neutron's path length without increasing the setup length. The neutron mirror at the end is curved in order to project the neutron beam pattern from the entrance slit to the detector entrance grating. These additional requirements to the neutron optics drastically increase the systematic influence on the final charge limit (10 times higher than the uncertainty due to the neutron's counting statistic) and need much more attention to correct them. Especially, if there are strong stray fields of the electrodes, these start to slightly move the neutron optics with their electrostatic forces depending on their polarity and mimicking a charge induced beam deflection.

In 2010, Christian Plonka-Spehr et al. (University of Mainz, University of Vienna, ILL) revised the first UCN experiment and its systematic at the PF2/TEST beam of the ILL [245]. They concluded that after significantly reducing the systematic effects, similar setups can reach at novel UCN sources (20 times higher flux as PF2/EDM) the best limit so far measured within 50 days. This triggered new research in this field.
In his PhD thesis, Christian Siemensen built a new apparatus based on the latest investigations together with his group at the University of Mainz [280]. The electrode length and its maximal applied field strength were slightly larger than the Soviet predecessor. To circumvent the horizontal alignment problem, they used a lake of *Fomblin* (a vacuum grease) between the electrodes. In addition, they increased the height of the neutron beam entrance compared to the lower mirror (*Fomblin* lake) in order to reduce the number of bounces to approximately one. With measurements at the PF2/UCN beam in Grenoble, they were able to determine the neutron's charge limit by a factor 2 lower compared to Borisov et al [43]. However, similar to this older UCN experiment, they had also severe systematic challenges and needed large corrections to arrive at the final value. Mainly the liquid *Fomblin* deformed within the very strong electric fields and distorted the measurements. They even tried to freeze it to keep it in shape which resulted in a broken surface randomly reflecting UCNs. The calculated statistical discovery potential of $\sigma_{q_n} \approx 10^{-21}\, e\,\mathrm{d}^{-1}$ is very promising if the systematic effects can be suppressed below this value [282].

There are also some proposals to measure q_n with neutron interferometers and finally further lower the limit compared to the best measurement in 1988 [36]:
V.V. Voronin, L.A. Akselrod, V.N. Zabenkin, I.A. Kuznetsov from the PNPI suggested to apply a strong electric field within the central part of a spin-echo small angle neutron scattering machine (SESANS) [307]. Shifts due to a hypothetical charge would be imprinted in a phase shift of the spin. With incorporating Laue neutron interferometers, the sensitivity could be further improved.
In 2018, Florian M. Piegsa proposed to use a Talbot-Lau interferometer in a pulsed cold neutron beam as the *European Spallation Source* (ESS) in Lund will provide [234]. Compared to normal Laue neutron interferometers, the three needed gratings can be placed much further apart (up to 5 m). This geometry is expected to measure deflections Δx down to 0.5 pm in the ideal case.

The discovery of gravitationally bound quantum states of UCNs [215] and the development of the gravity resonance spectroscopy (GRS) [147] enabled a completely new method to measure q_n. On behalf of the qBOUNCE collaboration, Katharina Dursberger-Rennhofer, Tobias Jenke and Hartmut Abele presented this novel technique using a frequency measurement based on a quantum mechanical effect in 2011 [77]. Compared to the previous experiments it is challenged with the same physical limits of the maximal electrical field but has completely different systematic influences because it does not depend on the alignment of the neutron optics. Instead of measuring the beam deflection, it measures shifts of the transition frequencies between two quantum states with a Ramsey-type spectrometer which is a very sensitive tool by itself [250]. This approach is one of the rare occasions where the neutron's charge can be probed with a Ramsey-type measurement scheme. Normally, a such a scalar quantity would uniformly shift all energy states. This spectrometer type measures only differences between states and therefore it is insensitive to such shifts. However, in the proposed experiment a hypothetical neutron's charge only changes the steepness of the linear potential and consequently shifts every energy state differently (see more in section 2.3). In addition, storing the UCNs can extend the interaction time and the propagation time within the spectrometer up to the lifetime of the neutron itself which would increase the energy resolution many orders of magnitude. Implementing this new approach into the qBOUNCE setup pushed forward many new developments, especially the development of a Ramsey-type GRS setup during the PhD thesis of Tobias Rechberger [254] and the electrode material tests started by Hanno Filter. The final experimental realization and its first measurement are the main topics of this thesis. The following chapters will provide a detailed theoretical description of the method and its experimental realization.

1.3. The neutron as an ideal probe

Discovery

After the discovery of radioactivity inside uranium salts by Henri Becquerel [39, 249], α particles became an important tool in the emerging field of particle physics (e.g. discovery of the atomic nucleus by Ernest Rutherford et al. [259, 260]). More or less systematically bombarding different materials with these particles led to the discovery of an unknown neutral radiation with beryllium as the target. In 1932, James Chadwick was the first who proved that this radiation consists of neutrons [58] which was the discovery of the neutron itself and the starting point for neutron physics.
In 1939, Otto Hahn, Fritz Strassmann, Otto Frisch and Lise Meitner discovered nuclear fission after irradiating uranium with neutrons [108, 190]. This enabled Enrico Fermi and his team to build the first nuclear reactor in 1942 [87]. Since then, nuclear reactors have been the main source of neutrons for science. With the Marietta Blau's and Hertha Wambacher's discovery of nuclear spallation [284], a second method of large scale neutron sources was born [99, 229]. Since then, neutrons have been used in many different fields such as particle physics [3], quantum mechanics [253], solid states physics [198], structural biology [164] or medicine [179, 184].

Basic properties

The neutron n^0 is a baryon consisting of three quarks. The strong nuclear force confines together the two down quarks and one up quark within the neutron. Furthermore, this short-ranged force is responsible for the binding of the neutron with other neutrons and the protons within the nucleus. The binding energy with the rest of the nucleus lowers the mass of each neutron in the order of few MeV/$c_0{}^2$.
The weak interaction induces a beta decay in free neutrons and neutron rich nuclei if the neutron's mass with subtracted mass defect is heavier than the decay products (p^+, e^-, $\bar{\nu}_{e^-}$). The mean lifetime of a free neutron is 878.4(5) s [319]. The correlations within this beta decay (between spins and momenta of all involved particles) are many measurable parameters which are only derived from few parameters in the Standard Model. This overdeterminancy enables to test the Standard Model with multiple and very precise dedicated experiments [4, 207, 309].

Neutrons interact also electromagnetically mainly due to their spin of $\frac{1}{2}\hbar$ [92]. The corresponding magnetic dipole moment μ_n is measured to $-9.662\,365\,1(23) \times 10^{-27}\,\mathrm{J\,T^{-1}}$ [319]. Even though the constituent quarks have an electric charge, the combined electric charge is expected to be zero in the Standard Model (as already described in section 1.1). The current limit of $-2(8) \times 10^{-22}\,e$ for the neutron charge q_n is a

combination of the best values of the direct and indirect measurement methods [36, 53, 319].
The best measurement of neutron's electric dipole moment (nEDM) is $0.0(13) \times 10^{-26}\,e\,\mathrm{cm}$ [2, 319]. The Standard Model predicts $< 10^{-30}\,e\,\mathrm{cm}$ but many new models (BSM) predict higher values. This is connected to the Strong CP problem and the unexplained baryon-antibaryon asymmetry in the universe which motivate new sources of CP violations that also produce contributions to the nEDM [80, 204]. In order to further lower the limits for such models, many new experiments are currently commissioned or planned (e.g. n2edm at PSI [25], PanEDM at ILL [320], TUCAN at TRIUMF [188], nEDM@SNS [177]).
The electric polarizability is measured to $1.18(11) \times 10^{-3}\,\mathrm{fm}^3$ [269, 319]. This is several orders of magnitude smaller than typical values of neutral atoms (e.g. $0.204\,\text{Å}^3$ - $5.2\,\text{Å}^3$ for noble gases) [154, 275]. Due to the low polarizability neutrons do not stick on surfaces as atoms and molecules would do due to van der Waals forces.

Gravitation acts on the mass of neutrons ($1.674\,927\,498\,04(95) \times 10^{-27}\,\mathrm{kg}$ [319]). Therefore, gravity bends the neutron trajectories downwards similar to the projectile motion of a massive object. Lifting a neutron upwards or letting it fall 1 m will need or release 102.5 neV of potential energy. Similar energies are required only within gradient magnetic fields. There, the magnetic dipole moment induces a required energy of 60.3 neV per field gradients of $\Delta 1\,\mathrm{T}$ or 0.06 peV per $\Delta 1\,\mu\mathrm{T}$ respectively. The sign of the energy depends on the alignment of the neutron spin with the external magnetic field. All other electric or magnetic fields have a neglectable low influence on the motion of a neutron compared to gravity, which makes neutrons an ideal probe for local gravitational forces.

Table 1.2.: Overview of the neutron properties

Property	Value	Source
Mass m_n	$939.565\,420\,52(54)\,\mathrm{MeV/c^2} = 1.674\,927\,498\,04(95) \times 10^{-27}\,\mathrm{kg}$	[300, 319]
Lifetime τ_n	$878.4(5)\,\mathrm{s}$	[319]
Magnetic moment μ_n	$-1.913\,042\,73(45)\mu_\mathrm{N} = -9.662\,365\,1(23) \times 10^{-27}\,\mathrm{J\,T^{-1}} = -6.030\,77(23) \times 10^{-8}\,\mathrm{eV\,T^{-1}}$	[300, 319]
Electric charge q_n	$-2(8) \times 10^{-22}\,e$	[319]
Electric dipole moment d_n	$<1.8 \times 10^{-26}\,e\,\mathrm{cm} = 1.8 \times 10^{-13}\,e\,\mathrm{fm}$	[319]
Electric polarizability α_n	$1.18(11) \times 10^{-3}\,\mathrm{fm}^3(cgs) = 1.31(12) \times 10^{-58}\,\mathrm{C\,m^2\,V^{-1}} = 8.19(76) \times 10^{-10}\,e\,\mathrm{fm^2\,V^{-1}}$	[319]

Neutrons themselves are indistinguishable. However, the kinetic energy of each individual neutron can vary a lot. Therefore, most neutron classifications are based on this parameter. One way is to divide neutrons into *fast* and *slow*. Fast neutrons have typical energies in the MeV range comparable to binding energies within the nucleus. Nearly all neutrons have such energies when they are set free during a nuclear reaction (fission, spallation, Be(α,n), ...). Due to scattering with nuclei of matter, neutrons lose nearly all their kinetic energy in a process called *moderation* until they have similar energies as the encountered matter (moderator). These neutrons are *slow* with typical energies around 25 meV or below. Depending on the moderator's temperature, the neutrons can be further classified into *hot* (2000 K), *thermal* (300 K) or *cold* (20 K). If cold neutrons are further decelerated by gravity during an upwards flight and faster ones are eliminated by curved neutron guides, then these neutrons are called *very cold*.
Neutrons interact mainly with the nuclei during the scattering process. Therefore, they are able to deeply penetrate matter before the interaction because they did not interact with the coulomb fields within the atoms. The slower neutrons are, the more important their wave properties become (increasing wavelengths). Instead of single potential wells of the nuclei (approximately 1 fm wide, 50 MeV deep and some Å apart), neutrons experience an averaged potential which is expressed as the *neutron optical potential* V_F. The strength of this potential is positive for most materials and around 50 neV. Neutrons with kinetic energy below this material-depending value cannot enter the corresponding material and they are totally reflected independent of the incident angle. They are called *ultra-cold neutrons* (UCN: see section 1.3). If *cold* or *thermal* neutrons interact with a material surface under an angle, only the transverse momentum is relevant. If the corresponding energy is below the potential V_F, the neutron is totally internally reflected. This effect is used for neutron guides to increase the neutron flux at the experiment. Curvatures in these guides are energy selectors. Slower neutrons have a larger angle of acceptances for the total internal reflection and therefore follow the bending more often. Too fast neutrons are absorbed in the guide's walls.
Overall, there exist many more different classes of neutrons (e.g. *epithermal* between *fast* and *slow*) and the borders between these classes vary a lot in the literature. The main reason is that the neutron energy spectrum depends mainly on the neutron source and the used neutron optics which varies between the different facilities. For this thesis mainly UCNs are used.

In addition to the kinetic energies, neutrons can be classified by their velocity v_n, wavelength λ_B or temperature T. The neutron velocities are mainly used if the timing of them is important (e.g. Time-of-Flight - TOF measurements). The relation between the kinetic energy and the neutron velocity can be calculated classically for slow neutrons (*thermal* $\approx$ 2200 m/s, UCN $<$ 10 m/s, see in the following equation). For fast neutrons, relativistic corrections are important to be included into the calculations.

$$E_{kin} = \frac{m_\mathrm{n} {v_\mathrm{n}}^2}{2} \qquad \Leftrightarrow \qquad v_\mathrm{n} = \sqrt{\frac{2E_{kin}}{m_\mathrm{n}}} \tag{1.2}$$

De Broglie first described the connection between momentum p and consequently the velocity of a particle and its wavelength λ_B [54]. This relation is also valid for neutrons. The neutron wavelength is commonly used in the description of neutron reflection experiments (e.g. crystallography, monochromators, ...) where Bragg's law ($n\lambda_B = 2d\sin(\theta)$) describes this reflection of neutrons on the planes of the crystal structure. The typical wavelengths of thermal neutrons are in the order of a few Å and therefore similar to distances between atoms or wavelengths of X-rays. UCNs have wavelengths above 500 Å which support the assumption that the neutrons only interact with the averaged potential of thousands of nuclei.

$$\lambda_B = \frac{h}{p} \approx \frac{h}{m_\mathrm{n} v_\mathrm{n}} = \frac{h}{\sqrt{2m_\mathrm{n}E_{kin}}} \qquad \Leftrightarrow \qquad v_\mathrm{n} \approx \frac{h}{m_\mathrm{n}\lambda_B} \qquad \Leftrightarrow \qquad E_{kin} = \frac{h^2}{2m_\mathrm{n}{\lambda_B}^2} \tag{1.3}$$

After moderation, the neutron's energies are distributed in a broad spectrum comparable to the thermal motion of the moderator material (water, liquid deuterium, graphite). Therefore, a thermal Maxwell-Boltzmann spectrum can well describe the neutron energy spectrum. This links the neutron energy to the moderator's temperature T:

$$T = \frac{\overline{E_{kin}}}{k_\mathrm{B}} = \frac{m_\mathrm{n}{\overline{v}_\mathrm{n}}^2}{2k_\mathrm{B}} = \frac{h^2}{2m_\mathrm{n}k_\mathrm{B}{\lambda_B}^2} \quad \Leftrightarrow \quad \overline{E_{kin}} = k_\mathrm{B}T \quad \Leftrightarrow \quad \overline{v}_\mathrm{n} = \sqrt{\frac{2k_\mathrm{B}T}{m_\mathrm{n}}} \quad \Leftrightarrow \quad \lambda_B = \frac{h}{\sqrt{2m_\mathrm{n}k_\mathrm{B}T}} \tag{1.4}$$

The basic methods of most neutron sources are nuclear fission, spallation or other nuclear reactions. Most common are research reactors: from small reactors as the 250 kW TRIGA-reactor of the Atominstitut (ATI) in Vienna up to the 58.3 MW high-flux reactor of the Institut Laue-Langevin (ILL) in Grenoble. These reactors have in common that they use fuel elements with medium or high enriched uranium (20 % - 95 % U-235) and water or heavy water to provide cooling and moderation. Cold sources and sometimes UCN sources are also installed next to the core of the largest research reactors. Most research reactors provide a continuous flux of neutrons.
Accelerator-based spallation sources shoot high energetic protons (approx. 1 GeV) on a target (e.g. tungsten or lead) in order to produce neutrons. Due to the accelerator timing (bunches), the neutron production is pulsed. Moderators surrounding the interaction point shape the neutron spectrum. The peak flux is much higher than in nuclear reactors. However, the averaged total fluxes of both source types are comparable. Two of the brightest accelerator-driven sources are the Spallation Neutron Source (SNS) in Oak Ridge, Tennessee, and the currently built European Spallation Source (ESS) in Lund, Sweden.
In laboratories small neutron sources based on nuclear reactions are used. They contain a mixture between radioactive isotopes (plutonium, radium,...) and beryllium, which emits neutrons after irradiation with high energy particles. The flux is relatively low and continuous until all radioactive isotopes are decayed. We used such a source for detector tests in Vienna.

Ultra-cold neutrons

Ultra-cold neutrons are the slowest class of neutrons. Their energies are below the neutron optical potential V_F of the wall material (e.g. Al 54 neV [24], Si 50 neV [24], Ni-58 335 neV [100]). Therefore, they are reflected under any angle. This reduces the losses within neutron guides as long as the wall has a very high neutron optical potential and is free from absorbing materials (e.g. organic residue, water, ...). This also enables to store UCNs in material bottles up to their lifetime. Even though the flux of UCNs is orders of magnitude lower than the flux of thermal or cold neutrons, the interaction time is much longer. This makes them a very promising probe for many fundamental properties of the neutrons themselves. For example, the best measurements of the neutron lifetime [102] or the neutron's electric dipole moment [2] are performed with stored UCNs. Due to the low velocity of these neutrons (around 10 m/s), they are

also very suitable to study gravity, which has a strong influence on their motion.
Robert Golub [100] and Albert Steyerl [292] summarized many aspects of physics with UCNs in their books which provide good sources for more information.

First detection of the UCN

Already in the 1950ies, Ya B. Zeldovich proposed the possibility to store cold neutrons into material bottles [321]. He also estimated the number of UCNs which are trapped in these bottles. In 1969, two groups independently observed the UCNs for the first time. Albert Steyerl used a TOF spectrometer in a vertical neutron guide at the FRM in Garching (Germany) to measure neutrons with velocities down to 5 m/s [290]. In Dubna (Soviet Union), F. L. Shapiro together with V. I. Lushchikov, Y. N. Pokotilovskii and A. V. Strelkov used a strongly curved neutron guide where only UCNs could follow the curvature. Each detected neutron at the end demonstrated the unique properties of the UCNs [181].

Production of UCNs for the PF2 instrument

We performed nearly all neutron measurements of this thesis, similar to all other measurements of the *q*BOUNCE collaboration, at the PF2, an UCN facility at the ILL in Grenoble with the support of its team, especially the instrument responsible Peter Geltenbort and the technician Thomas Brenner and in the recent years also Tobias Jenke and Stephanie Roccia as part of this collaboration. In the following paragraph, I will shortly describe the production of the UCNs at this instrument.
The high-flux reactor of the ILL uses only one fuel element with high enriched uranium. During a reactor cycle (beam time) of around 50 days, this fuel element produces a constant power of up to 58.3 MW, depending on the actual length of the cycle, and a neutron flux of $1.5 \times 10^{15}\,\mathrm{n/s/cm^2}$ (see [1]). Heavy water surrounding the fuel element cools the reactor core and moderates the neutrons to thermal energies (around 25 meV). Within a small cold source in the heavy water tank, liquid deuterium ($\approx$20 K) further moderates the neutrons down to cold neutrons ($<$2 meV). A vertical neutron guide (TGV) transports these cold neutrons 18 m upwards to the first floor of the reactor hall (Niveau D). Due to the curvature of the guide, only neutrons slower than 50 m/s are reflected on the guide's walls. Additionally, gravity decelerates the neutrons by $m_\mathrm{n} g z = 1.5\,\mu\mathrm{eV}$ during the flight through the TGV. At the top, they become very cold neutrons with energies below 13 µeV and their flux is already significantly reduced due to the velocity cut-off. The so-called *Steyerl neutron turbine* of the PF2 is situated at the end of the vertical beam guide. This turbine consists of a wheel with 1.7 m diameter and rotates 250 times per minute in the neutron flight direction (22.3 m/s at the tips). One fraction of the beam is guided beside the turbine wheel towards the PF2/VCN chamber. The rest hits the turbine blades. Via doppler-shifting bounces, their velocity is reduced into the UCN regime. At the position with the highest UCN density of $2.6 \times 10^4\,\mathrm{cm^{-1}\,s^{-2}}$ (see [2]), a switcher guides them towards three different beam lines (PF2/MAM, PF2/UCN or PF2/EDM) which use the high continuous UCN flux in a time shared mode. An additional port delivers a continuous flux (around a factor 10 weaker) to the PF2/TEST beam site. In 1986, Albert Steyerl and his coworkers from the TU Munich and the ILL built the turbine [294] as an improved version of the neutron turbine at the FRM [291]. Since then, the so-called PF2 turbine has been well maintained and has provided many experiments with the worldwide highest continuous UCN flux.

There also exist different methods to produce UCNs. One possibility is to use very cold converters where coherent scattering further decelerates neutrons to UCNs by exciting phonons within the cooled medium. Opposite to moderation, there is only a negligible neutron acceleration due to phonon absorption due to the low numbers of phonons at the used temperatures. Due to the design of many sources, they are often used in pulsed mode because they need an accumulation time before they can release UCNs with a high enough density. The most commonly used converters are solid deuterium (e.g. PSI [18, 19, 22, 174]) or superfluid helium-4 (e.g. Sun [235, 322], Sun2 and SuperSun [60, 71] at the ILL).

[1] www.ill.eu/reactor-and-safety/high-flux-reactor/technical-characteristics (8.10.2023)
[2] www.ill.eu/users/instruments/instruments-list/pf2/technical-details (8.10.2023)

1.4. Gravitationally bound quantum states of UCNs

Particles above an impenetrable surface are confined by gravity in vertical direction. A classical object (e.g. a ball) would bounce on the surface. The maximal possible height of a particle above only depends on the total energy (kinetic and potential) of the object which also allows lying on the surface with zero energy. However, very small particles obey the rules of quantum mechanics and only behave as classical particles at higher energies. Quantum mechanics predicts that the particle's kinetic energy will form quantized states similar to a particle in a box. Consequently, the described system has a minimal non-zero kinetic energy and the corresponding heights are quantized[3]. Already shortly after the publication of the Schrödinger equation in 1926 [272], physicists calculated these states (as particles in uniform fields [52, 158]) and called this particular problem the *Quantum Bouncer*. This became a textbook example for physics students to understand quantum mechanics by calculating it as an analogue of the inclined plane known from the classical mechanics lectures. Therefore, it can be found multiple times in the literature including many different theoretical extensions and methods [57, 73, 74, 75, 97, 98, 103, 171, 172, 261, 316, 317].

In 1978, V. I. Luschikov and A. I. Frank first theoretically described a possible realization of the quantum bouncer with UCNs as particles [180]. They calculated the first two energy states of this system (1.4 peV and 2.45 peV). They also proposed to prepare the first gravitational state by guiding the neutron beam through a 20 µm wide slit between a flat surface and an absorber. This technique is still used for all experiments (as for the measurements of this thesis). Their ideas of manipulating the gravitational states with magnetic fields are not yet realized or published similar to their considerations of storing these states.

The first studied particles were cold atoms (cesium, rubidium) bouncing on surfaces (laser-pumped dielectric surfaces or magnetic mirrors) after they were released from a magneto-optical trap (MOT) [17, 256, 308]. Due to their height (around 3 mm) and the corresponding high quantum numbers, the motion of the atoms was in the classical limit. The losses after each reflection were between 27 % and 39 % which enabled to study up to 10 bounces [258](p.9-11).

First observation of a Quantum Bouncer with UCNs

Between 1999 and 2002, a collaboration between members of the ILL (V. V. Nesvizhevsky et al.), the University of Heidelberg (H. Abele et al.) and the institutes PNPI (St. Petersburg, Russia) & JINR (Moscow, Russia) conducted and evaluated the first experiments proving the existence of gravitationally bound quantum states of UCNs. They used an absorber (a glass plate with an acid roughened surface coated with titanium-gadolinium-zirconium alloy) positioned above very flat glass plates. The gap size could be adjusted with piezoelectric motors down to 1 µm. These stages varied the slit width between zero and 50 µm in 2 µm steps, and for measurements up to 160 µm in 10 µm steps. A He-3 counter tube detector and also spatial-resolving, uranium-coated CR-39 film detectors recorded in total three identical runs. These measurements showed a strong deviation from classical expectations. Below 14 µm (height of the lowest gravitational state), no neutron was able to pass through the slit, even though the size of a neutron is expected to be around 1 fm. At a gap size above 50 µm, the measured neutron rate converged to the classically expected theoretical curve.

Two diploma theses, which were conducted by members of the experimental team under the supervision of Hartmut Abele, present the experiments in detail: Frank Rueß completed the first diploma thesis in this field [258]. After a theoretical description (quantum bouncer, classical vs. quantum density function), his work focused mainly on the experimental setup and the data evaluations of the detectors (He-3 and CR-39 analysis) including a comparison to the theoretical predictions. Alexander Westphal's diploma thesis [312] additionally depicted many theoretical considerations: the surface roughness, the neutron optical potential, a classical absorber wave guide description, a quantum analogue, the two mirror solution and a full description of the first setup. His suggested measurement with a reversed geometry (absorber below a mirror) confirmed again that the interplay between gravity and quantum mechanics realized the observed quantum bouncer [314]. Additionally, Martin Klein started the detector developments for the following experiments with his PhD thesis [161].

[3] The corresponding height of the bound state is defined by equating the eigenenergy with the linearized Newtonian potential ($E_i = m_n g z_i$) [110]

Different aspects of the experiment were published in various articles [211, 213, 214, 215, 218, 219, 306, 314]. In addition, some articles also present limits on fifth forces in the µm range [6, 29, 222, 313]. This discovery also triggered some discussions in the scientific community if the results could be mimicked by other effects [109, 217, 304].

Other approaches

Soon after the first experiments, the collaboration divided itself into two groups. The first group formed around Hartmut Abele from the University of Heidelberg. In the following years, it transformed into the *q*BOUNCE collaboration which aimed to measure the *quantum Bouncing Ball* (qBB) and to induce state transitions with mechanical oscillations which is now known as *Gravitational Resonance Spectroscopy* (GRS). The next section will describe the experiments and published theses of this group in detail which are also the foundation of this thesis.
The second group formed the GRANIT collaboration (ILL, LPSC and LMA together with many other institutes). The contributing scientists were Valery V. Nesvizhevsky, M. Kreuz, P. Schmidt-Wellenburg, T. Soldner, Guillaume Pignol, Konstantin V. Protasov, D. Rebreyend, F. Vezzu, L. Pinard, Stefan Baeßler, A.V. Strelkov and A.Yu. Voronin and many more. I will summarize their works in the following paragraphs.

The GRANIT collaboration started with many theoretical considerations of the setup and its application to set limits on hypothetical models [15, 20, 26, 30, 50, 82, 83, 191, 221, 240] before they built a new spectrometer at the ILL. Their main aims were to improve the state preparation (including the possibility to polarize), store the quantum states and manipulate these states with spatially varying magnetic fields [168, 239]. The spectrometer was located at the SUN-1 UCN source at level C (H172A). A special clean room equipped with magnetic coils and vibration dampers shielded the experiment against external disturbances. Different to the first experiments with gravitationally bound quantum states, the GRANIT spectrometer used a 20 µm step as a state preparation. This should suppress the first state and populate more higher states. Driving state transitions downwards (e.g. $|4\rangle \rightarrow |1\rangle$) would enable to measure transmitting neutrons through the conventional absorber region before the detector which was either a He-3 counter tube or a position sensitive detector positioned further away to measure the free fall of the UCNs. Guillaume Pignol summarized all theoretical aspects of the spectrometer including systematic effects on the storage time or expected limits for fifth forces (*New physics*) in his PhD thesis [237].
In 2008, Valery V. Nesvizhevsky and other members of the GRANIT collaboration proposed for thermal or cold neutrons the existence of *centrifugal states* within the whispering gallery wave along the walls of a strongly curved neutron guide, which have a very similar theoretical description as the quantum bouncer [220]. In the following year, they were able to experimentally observe these states [212, 223, 224].
In the first years, the main focus was on the detector development and the optimization of the neutron extraction from the superfluid He-4 UCN source [28, 216, 268]. This also included a full analysis of the incoming neutron spectrum and the performance of the UCN source [257]. In the beginning, the extraction system heated up the source too much and consequently reduced the produced UCN flux by more than one order of magnitude. In addition, the source only worked in a pulsed mode due to this reheating during the extraction. In parallel to this developments, the main spectrometer was built and commissioned [27, 238]. Measurements until 2021 showed that the GRANIT spectrometer is capable of suppressing lower quantum states with steps or higher ones with absorbers [63]. Position sensitive detectors were able to determine $z_0 = 5.9(3)$ µm. More results are expected to be published soon. Overall, many techniques first tested in the GRANIT spectrometer are very promising to be implemented and further developed in the *q*BOUNCE experimental setups: e.g. step state suppression, magnetic field induced GRS or newly developed online detectors with spatial resolutions around 2 µm [47, 62, 64].

A Japanese collaboration also measured the spatial distribution of the quantum states at the PF2/UCN beam line at the ILL [121, 153, 156, 263]. Similar to other experiments, they used a 200 mm long mirror to guide the UCNs to the detector with a shifted absorber above. The gap size was 100 µm which enabled also higher states to pass through the setup. At the end of the mirror, a magnification rod (6 mm diameter) widened the neutron beam. A B-10 coated CCD pixel detector (24 µm × 24 µm) recorded the spatial distribution of the neutron wave function with a resolution of 3.35(9) µm of the initial gravitational states. This experiment showed that the gravitational quantum states of UCNs are an interesting testing ground for detector developments. Some years later, this Japanese group started to develop new emulsion detectors with resolutions of only 100 nm for similar purposes [117, 206, 209].

1.5. The *q*BOUNCE experiments

From the first experiments onward, Hartmut Abele was involved in gravitational state measurements. In the following years, his diploma students and he pursued to realize the *quantum Bouncing Ball* (qBB) which is the measurement of the neutron's density function after dropping downwards a small step (e.g. 30 µm). This also required new detector developments to reach a spatial resolution below 2 µm and a sufficiently lowered background noise. In 2008, the diploma student Tobias Jenke [138] prepared a first qBB setup. He, already as a PhD student [139], the diploma student David Stadler [287] and Hartmut Abele made their initial attempts to measure the qBB in 2008 and 2009. However, the group around Hartmut Abele and Tobias Jenke only succeeded with the observation of a qBB in 2014. This measurement is the main part of Martin Thalhammer's PhD thesis [299]. I will present a detailed summary of these developments in the following section.
In 2009, the now so-called *q*BOUNCE group moved from the *Physik Institut* of the University of Heidelberg to the TU Munich and one year later to the Atominstitut (ATI) of the TU Wien.
Tobias Jenke became the first PhD student in 2009 [139] and also later the first post-doc of the *q*BOUNCE-group in 2011. He stayed in this position until 2016. After a short intermission, he became one of the instrument responsibles of the PF2 and has been supporting the *q*BOUNCE-measurements as a member of the collaboration since then. During his PhD thesis, he and his colleagues developed and measured state transitions between gravitationally bound quantum states for the first time which were induced by mechanically oscillating mirrors below [147]. The *q*BOUNCE collaboration named this technique *Gravitational Resonance Spectroscopy* (GRS). The first setup is called GRS$^{\text{TJ}}$-setup[4]. It consisted of only one region (oscillating mirror with an absorber on top) which did the state preparation, transition and analysis at once.
Until 2012, the next PhD student Gunther Cronenberg [65] realized a Rabi-type GRS setup together with the other members of the *q*BOUNCE collaboration [66]. This so-called RABI$^{\text{GC}}$-setup consisted already of three regions in order to separate the three needed tasks. This required also the construction of a new and bigger vacuum chamber and the development of a mirror alignment system. After this experiment, Hanno Filter, another already involved PhD student, started the investigations for the optimal electrode material of a future neutron's electric charge measurement setup.
The origins of the currently used Ramsey-type GRS setup go back to 2010, after the successful measurements of the GRS$^{\text{TJ}}$-setup [10]. The *q*BOUNCE collaboration started the developments for this setup already beside the other running measurement campaigns. The main construction and assembly phase started with the PhD thesis of Tobias Rechberger in 2014 [254]. Therefore, this is called RAMSEY$^{\text{TR}}$-setup. In the following years, the *q*BOUNCE group designed and developed this Ramsey-type GRS setup consisting of five regions. This required upgrades in nearly all aspects of the setup.
In 2018, I was able to commission the RAMSEY$^{\text{TR}}$-setup with its first successful GRS measurement during the time of this thesis. In addition, I probed the electric charge of the neutron with this setup. Afterwards, Jakob Micko further increased the sensitivity up to a factor 42 better than the preceding RABI$^{\text{GC}}$-setup [194].
In the last section of this chapter, I will mention all student theses (written in German or English) which were needed to realize these GRS experiments and all articles associated with their results.
All *q*BOUNCE experiments so far have been assembled for neutron measurements at the UCN facility PF2, an instrument of the ILL, with the support of its technician Thomas Brenner and the beam responsibles Peter Geltenbort, Christian Plonka-Spehr, Sergei Ivanov, Tobias Jenke and Stephanie Roccia.

1.5.1. The quantum Bouncing Ball

After the first measurements of the gravitational quantum states described by the master students Frank Rueß [258] and Alexander Westphal [312], the main aim changed to measure the *quantum Bouncing Ball* (qBB). Figure 1.2 displays more details of such experiments. The first achievement was the development of boron-coated CR-39 film detectors (see more in section 3.2.4) started by Martin Klein [161]. Sophie Nahrwold summarized the first measurements of these detectors at the ILL in 2004 and their evaluation in her master thesis [210]. The spatial resolution was determined to be 1.4 µm. In addition, she reevaluated the experiments from 2002 in order to relatively determine Earth's gravitational acceleration g. Following

[4] In the following, I will name all setups after the responsible PhD student because their theses contain the most information about the corresponding experiment and they were the main person responsible during the measurements. However, all members of the *q*BOUNCE collaboration at the time contributed to the success of these measurement campaigns

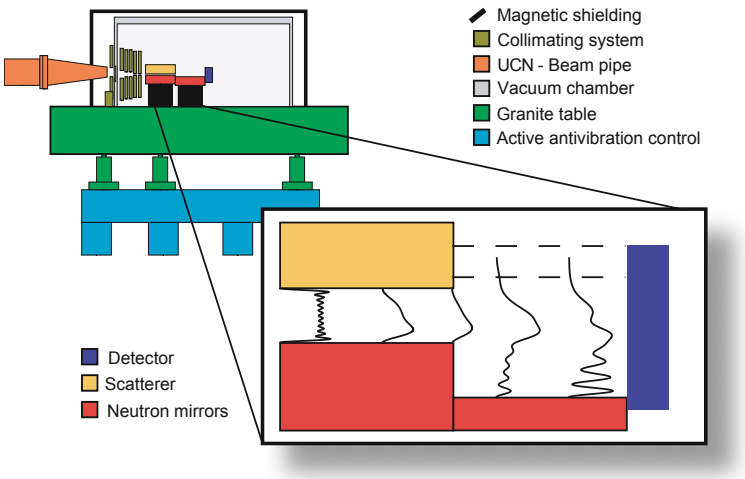

Figure 1.2.: The qBB of 2008-2009. The UCNs enter from the left. The collimating system (aperture) in combination with the absorber gap restricts the horizontal velocity in flight direction. The scatterer (absorber) suppresses higher states. The step downwards between the neutron mirrors of region I and region II (red) transforms the lower states to an infinite sum of higher states. The mean of the free propagating quantum mechanical wave function resembles the motion of a classical bouncing ball (a downward and upward motion). However, at the lowest point quantum mechanic predicts an interference of the neutrons wave function with itself as depicted as the last density distribution. This figure is taken from [148].

her example, Claude Krantz evaluated the measurements of 2005 for his master thesis [166]. There he presented a complete theoretical description of the setup (from the aperture, through the wave guide including steps and the free evolution afterwards until the detector). With these tools and the spatially resolved measurements, he concluded that the UCNs formed bound states when they moved through an absorber. This was a different method compared to the *transmission* method of the first measurements between 1999 and 2002.
With a new funding of the DFG[5] (project number: 66291586) and a grant of the cluster of excellence *Origin and Structure of the Universe* at the TU Munich, Hartmut Abele and his diploma students Tobias Jenke and David Stadler built a new setup and used it to measure during three beam times in 2008 (TEST-1463, 3-14-237 and 3-14-245). This was also the official start of the *q*BOUNCE collaboration which was first denoted as Q-BOUNCE or QuBounce. Tobias Jenke prepared this qBB experiment for his diploma thesis [138] and continued with the measurements and its evaluation as a PhD student [139]. For his thesis [287], David Stadler developed and tested the new counter tube detectors (see more in section 3.2.1). In addition, he improved and described many experimental parts (new basement, leveling, vibration damping, B-field shielding, ...).
In the following year, Hanno Filter described the properties of the CR-39 from the production to the read-out in detail in his project thesis [88] and Kevin Mitsch further improved the evaluation of these spatially resolving detectors in his bachelor thesis [199]. Additional measurements of the qBB were performed during the beam time 3-14-253 in 2009. Under the supervision of Prof. Helmut Leeb, Rafael Reiter, Bernhard Schlederer and David Seppi started also to simulate the quantum bouncing ball as 2-dimensional videos during their joined bachelor's thesis [255]. Tobias Jenke displayed all these developments for a qBB setup and its measurements in his PhD thesis [139] and together with the other members of the *q*BOUNCE collaboration in multiple articles [7, 12, 13, 148]. However, the experimental improvements and detector developments were not enough to really observe a quantum bouncing ball without doubt, especially when the wave packet was reflected on the mirror surface and interfered with itself. Due to the fast developments of the GRS at the same time, further measurements of the qBB were postponed for some years.

In 2014, the *q*BOUNCE collaboration with Martin Thalhammer as the responsible PhD student started a new attempt to measure a qBB with the already commissioned RABI^{GC}-setup [299] during the measurement campaign 3-14-331 (171-14/1 & 172-14/2, qBB^{MT}-setup). The experimental team consisted of

[5] *Deutsche Forschungsgemeinschaft* (German Research Foundation): www.dfg.de (23.10.2023)

himself, Tobias Jenke as the post-doc, the new PhD student Tobias Rechberger, the master student Jörg Herzinger [115] and the bachelor's students Tamara Putz and Martin Stöger. They succeeded with multiple measurements at different heights (20 µm & 30 µm) and different distances (41 mm, 51 mm, 54 mm, 61 mm and 67 mm). Up to now, the results are only partially published in a Moriond's proceeding [146].

In recent years, a Japanese group developed emulsion film detectors with a resolution around 100 nm as already presented [117, 206, 209]. Between 2019 and 2021, measurements of a qBB within *q*BOUNCINO (a revived version of the RABI^{GC}-setup, see more in section 3.10) with the help of the PF2 team and the *q*BOUNCE group were a perfect opportunity to show the capabilities of these detectors. The first results showed a clear characteristic of a quantum bouncing ball with only a few observed neutrons (below 3000 n which is a factor 3 smaller than usually needed for CR-39 detectors). The results will be published soon. In addition, the bachelor students Raphael Neubacher [226] and Alexander Ernst [81], and the project student Johannes Schilberg [265] reworked the 3-D video rendering of the qBB based on the works of Martin Thalhammer [299]. They also observed new details in their simulations: a small fraction of the neutron density can be found in much higher regions (> 150 µm) after a step height of only 50 µm which would be imp

1.5.2. Gra

The basic ide
oscillating th
mirror only t
or $|2\rangle \rightarrow |x\rangle$ l
which suppre
difference bet
a frequency o
spends above
broadened arc
The exact sha
wave approxi
measured tra
models. Simil
by these mod
effects) [5].

GRS^{TJ}-setup

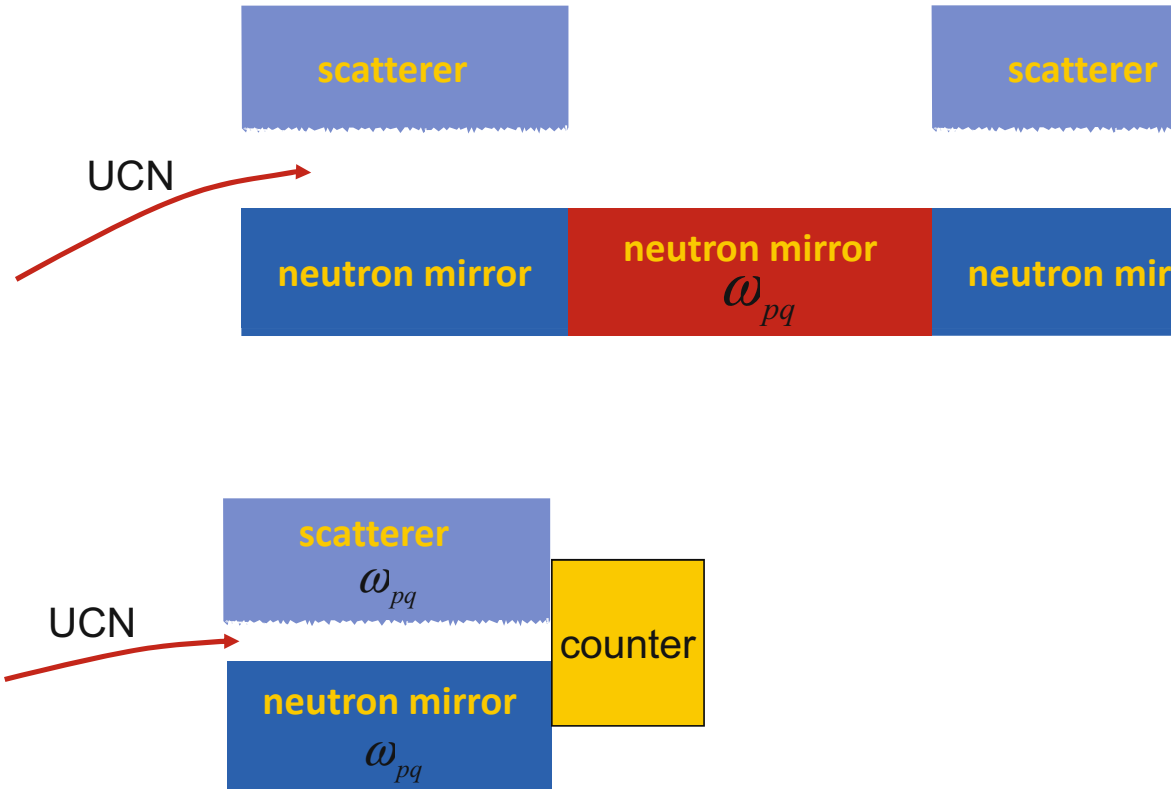

Figure 1.3.: The GRS^{TJ}-setup: It consists only of one region which fulfills all tasks: state preparation, transition and analysis. Taken from [139]

Tobias Jenke realized the first GRS setup as his PhD thesis [139]. This so-called GRS^{TJ}-setup consisted only of one region with an absorber on top as depicted in figure 1.3. This scatterer above the mirror suppressed incoming higher states and continuously damped excited states generated by the mirror oscillation of this region. In addition, the small gap between these two glass plates (mirror & absorber) squeezed the wave function together and increased the state's energies. This shifted the transition fre-

quencies upwards. The first observed transition was $|1\rangle \rightarrow |3\rangle$ at a frequency of 705(6) Hz, a gap size of 25.5 µm and a mirror length of 150 mm during the beam time 3-14-253 (April 2009). This measurement was repeated with a shorter mirror (100 mm) and a wider gap size (27.1 µm) during a specially assigned beam time (TEST-1692) in July of the same year. Due to the increased gap size, the transition frequency decreased to 592(11) Hz. In total, the statistical significance improved from 3.5 sigma to 4.9 which enabled to claim this as a discovery [147].
The finding of the transition resonances also trigger new experimental developments. After Heiko Saul had already helped the measurements as a project student, he developed and implemented a second generation of detectors based on the designs of David Stadler during his master thesis [264] (see more in section 3.2.1). This also included detector tests at the PF2 in Grenoble (TEST-1812).
The necessity to measure very accurately the frequency and the amplitude of the mirrors induced a second major development. Two bachelor students, Matthias Fink [90] and Roman Zimmermann [323], started to measure the mirror's surface oscillations with a newly bought laser interferometer (see more in section 3.6.2). The master student Tobias Lins [178] successfully implemented this system into the GRS^{TJ}-setup during the next large measurement campaign in the end of 2010 (3-14-283).
Tobias Jenke, Tobias Lins, Heiko Saul, Mario Adam, the new PhD Gunther Cronenberg and Hartmut Abele conducted the experiments during the beam time 3-14-283. In addition to the previously described improvement, they used a bigger newly built vacuum chamber (the so-called *q*BOUNCINO chamber, see more in section 3.4.1) which also was the starting point where the GRS^{TJ}-setup slowly transformed into the RABI^{GC}-setup. They still used only one 150 mm long region with an approximately 26 µm wide absorber slit. Compared to the first measurements, a broader frequencies range was probed. This enabled to not only observe the transition $|1\rangle \rightarrow |3\rangle$ (539(3) Hz) but also $|2\rangle \rightarrow |4\rangle$ (679(15) Hz) and the three level system $|1\rangle \leftrightarrow |2\rangle \leftrightarrow |3\rangle$ ($\nu_{12} = 258(2)$ Hz & $\nu_{23} = 280(3)$ Hz). These results were used to derive limits on the hypothetical chameleon fields [145].
In 2011, the measurements with the GRS^{TJ}-setup were repeated during the beam time DIR-94 but this time with polarized neutrons. This enabled to set limits on axions and similar particles [143].
The results were additionally published in the following articles [8, 9, 13, 76, 140, 141, 146]. This research acquired additional funding by the FWF[6] to pursue further experiments as a joint project (I 529) with the DFG as part of the *SPP 1491* (167716080, 168288055), a priority project (*Schwerpunktprogramm*) with Hartmut Abele and Stefan Paul as the spokespersons in the beginning. In general, the measurements with the GRS^{TJ}-setup were a success and proved that GRS can set limits to hypothetical *fifth forces* which could alter gravity in the µm scale. However, the state squeezing due to the absorber limited the precision reachable for this setup. In principle, the energy shifts could be calculated but the exact absorber gap height experienced by the neutrons was uncertain. The roughness of this upper glass plate was around 1 µm and the neutron wave function could be limited by either the dips, the averaged height or the valleys in between. This vagueness could only be resolved by separating the state preparations with absorbers and the state transitions with oscillating mirrors. This idea was the starting point for the next generation *q*BOUNCE experiment.

RABI^{GC}-setup

As Gunther Cronenberg's PhD thesis [65], the *q*BOUNCE collaboration assembled the RABI^{GC}-setup after the successes of the first GRS measurements. In contrast to the preceding GRS^{TJ}-setup, it had three separated regions and was consequently the first full Rabi-like GRS setup. This simplified its theoretical treatment (no state squeezing or damping). However, the alignment of these long mirror surfaces had to be better than 1 µm, which needed a completely new additional sensing system. The project student Stefan Lüftenegger [183] started this development by investigating the oscillating behavior of a two region setup. For the three region setup, the *q*BOUNCE group built a new gantry which moved capacitive sensors above the mirrors to measure their alignments and the piezoelectric stages below the mirrors corrected their position to minimize the steps between the mirror's surfaces (see more in section 3.5).

Beside the development of this mirror alignment system, many other parts of the setup were upgraded to increase their performance. The bachelor student Jakob Fellinger replaced parts of the experimental substructure to improve the possibilities to align the setup horizontally including a LabView implementation [86]. The bachelor student Benedikt Holzmann [118] and the master student Martin Thalhammer [298] further improved the detector and its electronics in order to reduce its background even more [144].

[6] The *Fonds zur Förderung der wissenschaftlichen Forschung* (Austrian Science Fund) is a state-owned funding organization for research in Austria - www.fwf.ac.at (30.10.2023)

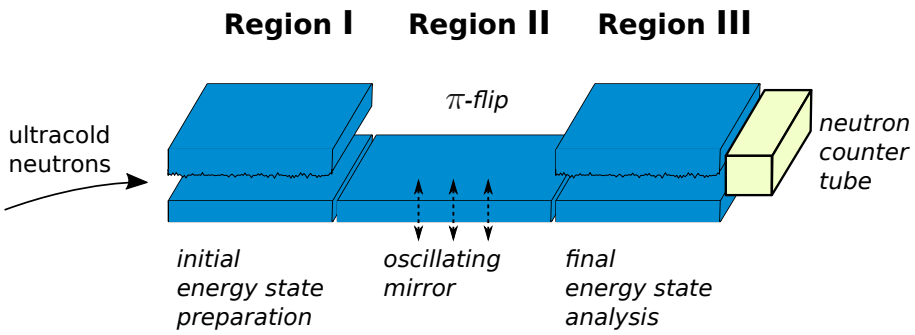

Figure 1.4.: The RABI^{GC}-setup: It consists of three regions with different lengths (150 mm, 200 mm, 150 mm). Each region has a different task. The first prepares the states, the second drives transitions with mechanical oscillations and the last analyses the states. Therefore, the first and the last region have an absorber on top to suppress higher states. This 3-region spectrometer type is called *Rabi-like* due to its inventor Isidor Isaac Rabi [248]. The figure is taken from [254](p.24).

The bachelor student Sebastian Keerl calculated and measured the vacuum pressure of the new chamber and of single components (pumps and flanges) [157]. The bachelor student David Jelem verified the measured frequencies and amplitudes with an additional accelerometer [137]. The project student Markus Spanring [285] calibrated a new logic box. And the master student Thomas Bittner completely redesigned the aperture and the connection between the beam guides and the vacuum chamber [42].

The main measurement with the RABI^{GC}-setup took place in the beam time 3-14-305 (167-12/2 & 168-12/3) in autumn 2012. The experimenter were the post-doc Tobias Jenke, the PhD students Gunther Cronenberg and Hanno Filter, the master student Martin Thalhammer, who had also the opportunity to test the upgraded detectors [298], and the project student Jason Jung who described the setup in his thesis [150]. In the following years, Gunther Cronenberg analyzed the recorded data and presented them in his PhD thesis [65]. The measured state transition were $|1\rangle \rightarrow |3\rangle$ at 464.1(12) Hz and for the first time also $|1\rangle \rightarrow |4\rangle$ at 648.8(16) Hz without a squeezing due to an upper absorber. This observation enabled him to calculate a gravitational acceleration of $g = 9.844(36)\,\mathrm{m/s^2}$ at the location of the experiment which was comparable to the classical measured local value around $g = 9.805\,\mathrm{m/s^2}$ [311]. In addition, he displayed the measurement of the polarized detector foil [65](p.73-77) taken during the beam time TEST-2034. These measurements were also used to set limits on the hypothetical symmetron field [66, 141, 142] and chameleon fields [68]. These *New physics* searches were funded by the FWF in cooperation with its French analogue ANR as a joint project (I 862).
Some years later, Alex J. Schimmoller, Gerard McCaul, Denys I. Bondar from the Tulane University (New Orleans, US) in collaboration with Hartmut Abele used these GRS results to derive limits for a decoherence-free entropic gravity model as the Ramsey-GRS data were not fully evaluated yet [266].

During the commissioning phase of the large RAMSEY^{TR}-setup, a Rabi-like GRS configuration was assembled twice. The first time unsuccessfully in 2017 due to problems with the mirror alignment. Jakob Micko documented this campaign in his master thesis [193]. I started the second attempt in the beginning of the GRS measurements of this thesis (3-14-358-III, 182-18/1). I will present the results of this so-called RABI-GRS-18 measurements in section 4.4.

RAMSEY^{TR}-setup

The idea of building a Ramsey-type GRS setup started to form with the first GRS measurement which was further developed by Hartmut Abele, Tobias Jenke, Helmut Leeb and Jörg Schmiedmayer [10]. Therefore, the RABI^{GC}-setup was always planned to be the intermediate step before implementing a full-scale Ramsey-like setup.
Already in 2011, Katharina Durstberger-Rennhofer, Tobias Jenke and Hartmut Abele declared the test of the neutron's neutrality to be the first application of the to-be-built Ramsey-like GRS setup [77]. The FWF funded this idea with two grants (I 531 in cooperation with the DFG and I862-N20) which helped

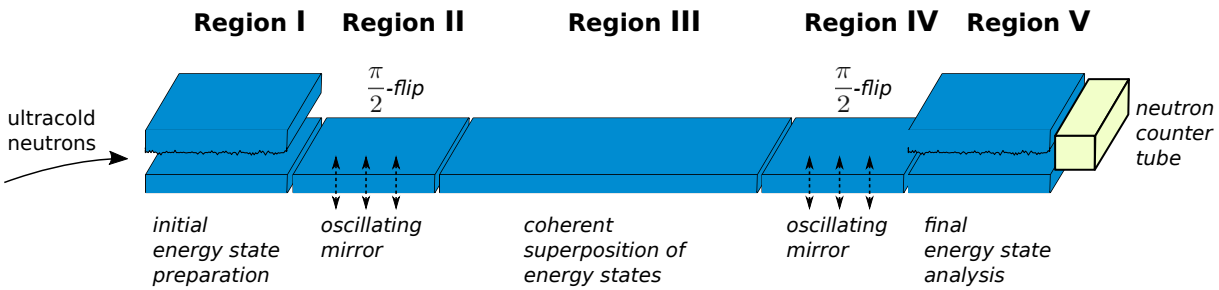

Figure 1.5.: The RAMSEY^{TR}-setup: Compared to Rabi-like GRS setups, this Ramsey-type spectrometer has five different regions. The middle region of the Rabi-like setup is split in three parts. Instead of driving a complete transition from the lower initial state to the excited final state in region II only, this is done in two steps: one in region II and the other in region IV. The wave function propagates as a fifty-fifty coherent superposition through region III without disturbances. Norman Foster Ramsey Jr. realized that this method is more sensitive and he successfully proved it during the measurement of the magnetic moments within molecular beams [250]. The figure is taken from [254](p.25).

also to develop the needed upgrades of the GRS experiments. In preparation of this measurement, Hanno Filter started to test different electrode materials in order to reach as high as possible electric fields. Over the years, many students were helping him with this research: Lukas Schrangl - project thesis [271], Michael Iro - bachelor's thesis [122], Markus Spanring - bachelor's thesis [286], Martin Mock - bachelor's thesis [200], Jakob Micko - project thesis [192] and Florian Honz - project thesis [119] who was also the student when I took over this development. I summarize their works in section 3.3.1 in more detail.

Similar to the RABI^{GC}-setup, the new Ramsey-type GRS setup needed an even bigger vacuum chamber (more than twice the length of the *q*BOUNCINO chamber). Consequently many other subsystem required upgrades which was also a chance to improve them with the experience of the previous measurement campaigns of the *q*BOUNCE collaboration. Since 2014 until the assembly and the start of the commissioning (2017), the PhD student Tobias Rechberger[7] was one of the prime movers of these developments [254]. The support for him to realize this so-called RAMSEY^{TR}-setup came from the *q*BOUNCE group, the workshops at the ATI, the PF2-team and many students at different academic levels. I will summarize their contributions in the following paragraphs.

The preparatory works already started before and during the qBB^{MT}-setup measurements in 2014. The master student Jörg Herzinger [115] reorganized the complete LabView measurement control including its hardware. Instead of needing multiple PCs to control organically-grown independent subsystems in order to operate the full experiment, the new measurement control needed only one small server. In addition, it used a common structure for all devices to keep them synchronized and their data similarly organized. It was still modular enough to handle any additional device which was not foreseen at that time.
Another focus were the detectors (CR-39 films and the counter tubes) in order to improve their performance and reliability. Therefore, Alexander Leopold characterized a new PVD machine, which should coat CR-39 detectors at the ATI, as his project thesis [176]. Further investigations enabled Hanno Filter to produce well-functioning detector patches, which were used for the state selector measurements of the RAMSEY^{TR}-setup, at the end of 2016 as part of his PhD thesis [89]. Also the counter tube detectors were renewed. As part of his PhD thesis [299], Martin Thalhammer with the help of the bachelor student Paul Heistracher [113] built a new detector generation with fully integrated environmental sensors. Nadine Freistetter tested these detectors at a PuBe neutron source (ATI) and designed a detector sensor read-out card for her bachelor's thesis [93]. The bachelor student Nikolaus Huber finally integrated the detector and its sensors into the main LabView program [120]. One detector had a much higher noise level than its twin. Anselm Balthasar equalized it to the lower level during his bachelor thesis under the supervision of Martin Thalhammer and me [32].
Heinz-Georg Stangl characterized the new vacuum chamber and its pumping behavior for his bachelor's thesis [288] and Alexander Gruber constructed and programmed a full automation of the vacuum circuits

[7] He was funded as part of the doctoral school *DkPI*, a project funded by the FWF (W 1252). The *DkPI* also supported Hanno Filter, Martin Thalhammer and me during the PhD.

for his bachelor's thesis [104]. During her project thesis [189], Sabrina Mayr characterized the new leveling system of the granite which is situated within the vacuum chamber of the RAMSEY^{TR}-setup instead of being the floor of the chamber as in the previous setups. Due to the new position on the granite and the different mirror surface height, the bachelor student David Rath [252] constructed and calibrated a new aperture which was partly made of Bittner's old aperture.
Two master students helped with the final technical implementation. Manuel Heiß set up a new laser interferometer and studied the interplay with the oscillating regions [114]. These mechanical oscillations disturbed the optics of the new laser interferometer and required the integration of a second external interferometer into the setup. Patrick Schmidt optimized the new and larger mirror alignment system for five mirrors beside the characterization of multiple other smaller parts of the setup [267]. He was also involved in the preparations of the beam site in Grenoble.
The master student Gregor Wautischer [310] studied the more fundamental question of the working principle of the absorbers within a cooperation between the *q*BOUNCE collaboration and Larisa Chizhova, Stefan Rotter and Joachim Burgdörfler from the Institute for theoretical physics (TU Wien). In 2012 (3-14-314), Wautischer and the experimenters of the *q*BOUNCE collaboration conducted special measurements with a two absorber setup to test quantum transport theory including the systematic effects of mirror steps and drifts. These results were then compared to Monte Carlo simulations [61].

The assembly of the RAMSEY^{TR}-setup at the PF2/UCN beam site started at the end of 2016 after the completion of a several-month-long necessary earthquake safety reinforcement of the platform bearing the vacuum chamber. The complete installation including adjustments took nearly two beam times of the proposal 3-14-358 (I-180-16/3 & II-181-17/1). Detailed descriptions can be found in the following theses of involved students: Tobias Rechberger [254] (PhD thesis, complete setup characterization), Jakob Micko [193] (master thesis, theory and Rabi setup), Rudolf Golubich [101] (project thesis, velocity spectrum), Peter Salajka [262] (project thesis, magnetic fields) and Nico Einsidler [79] (bachelor's thesis, vibration studies). I joined the experimental team in winter 2017 for the second beam time which ended with a completely assembled setup but a failed attempt to observe a Ramsey-like GRS transition.
Until the next beam times in 2018, together with the following students which were mainly under my supervision, we tried to optimize the setup in order to successfully commission the RAMSEY^{TR}-setup and to prepare it for future measurements: Alice Jardel [136] (ILL stagiaire supervised by Tobias Jenke, mirror oscillation sensing), Paul Feichtinger [84] (bachelor's thesis, mirror surface alignment), Anselm Balthasar [32] (bachelor's thesis, detector noise reduction), Florian Honz [119] (project thesis, electric field tests), Christoph Mühlmann [208] (project thesis, electrode simulations) and Mathias Winder [318] (project thesis, B-field coils design and characterization).

The final successful commissioning of RAMSEY^{TR}-setup with UCNs and the test of the neutron's neutrality happened during three reactor cycles in 2018 which are the main topics of this thesis. The first cycle (3-14-358-III, 182-18/1) was dedicated to reassemble the mirror regions and to test the complete setup. At the end of this beam time, we successfully measured with a Rabi-like GRS setup (RABI-GRS-18). During the second cycle (3-14-358-IV, 183-18/2), we completed the commissioning with the first Ramsey-like GRS measurements ever performed (RAMSEY-GRS-18). The third cycle (3-14-384, 184-18/3) was used to test the neutrality of the neutron by applying an additional electric field within the RAMSEY^{TR}-setup (Rams$\vec{E}$y).
Many students supported me during these measurement times in Grenoble: Daniel Schuh [274] (project thesis, detector sensors), Lukas Achatz [14] (master thesis, CR-39 evaluation), Magdalena Pieler and Valentin Czamler [236] (project thesis, *q*BOUNCINO, 3-14-385), Elisabeth Kreuzgruber [169] (project thesis, electric field setup), Vito Pecile [233] (project thesis, mirror alignment), and Carina Killian [159] (project thesis, mirror alignment). In addition, Jakob Micko started his PhD in the beginning of the last cycle and he helped me during this cycle in order to take over the experiment afterwards for his measurements starting in 2019. During the data evaluation, the bachelor student Robin Havlik [112] analyzed the detector sensors.
The measurement chapter of this thesis contains a more detailed description of all measurements done during these beam times and also displays their results (see chapter 4). In addition, I published a description of the neutron's charge measurement in [46].

Based on the works of Elisabeth Kreuzgruber and her predecessors, three pairs of bachelor students did extensive tests with the large Rams$\vec{E}$y electrode used for the neutron's charge measurements and its surrounding setup in the ATI's laboratories in Vienna: Anika Gassner [96] and Julius Piso [241], Jasmin Juroszek [151] and Nicole Pruggmayer [247], Paul Klieber [162] and Luca Neubacher [225]. A detailed description of the used setup and their measurements can be found in section 3.3.

Similarly, all other sections of the theory chapter (ch. 2) and the setup chapter (ch. 3) contain references to previous works of students which they are based on or include more information.

In 2019, Jakob Micko succeeded me with the research using the RAMSEY^{TR}-setup. During his measurements, he successfully demonstrated the possible sensitivity of this setup [194, 195, 196]. For the completeness of the display of all *q*BOUNCE student theses, I will list the students supervised by Jakob Micko or René Sedmik here: Blerta Zeka (bachelor's thesis), Richard Bergmayer [40] (project thesis, magnetic field measurements), Carina Killian [160] (master thesis, neutron spectrum), Nikolaus Sattler (bachelor's thesis, CR-39 evaluation), Veronika Kraus [167] (bachelor's thesis, mirror oscillations), Stefan Ballok [31] (project thesis, beam guides and shielding), Andrej Brandalik [48] (bachelor's thesis, beam divergence), Hugo Wetter [315] (master thesis, spin polarization), Julius Schnee [270] (bachelor's thesis, aperture) and Christoph Grüner (project student, power supply of B-field coils). In addition, the master student Heinz-George Stangl developed a new mirror alignment system [289] which Mathias Kaplan [155] and Janik Trauner [302] implemented in the *q*BOUNCINO setup during a measurement campaign in 2021. These recent measurement campaigns were supported by the FWF (P 33279).

During all these years, the theoreticians of the *q*BOUNCE collaboration have been studying to apply various *Dark Matter* or *Dark Energy* models to the *q*BOUNCE experiments and to derive limits from the measurement results:
Andrei N. Ivanov (1945 - 2021) together with Roman Höllwieser, Markus Wellenzohn, Tobias Jenke and Hartmut Abele investigated the *chameleon fields* model and its possible influences on GRS measurements [126, 127, 129, 129, 130, 131, 132, 133]. This topic overlapped with researches in the field of space-time torsion in General Relativity and the formulation of the Einstein-Cartan gravity. Therefore, Andrei N. Ivanov, Mario Pitschmann and Markus Wellenzohn explored also the implications of these theories [8, 124, 125, 128, 129, 130, 131, 132, 133]. These studies are also one of the main reasons for future polarized measurements with the RAMSEY^{TR}-setup.
In the last years, Andrei N. Ivanov, Markus Wellenzohn and Hartmut Abele also evaluated Lorenz invariance tests with *q*BOUNCE [134] and probes for beyond-Riemann gravity [135].

Beside Andrei N. Ivanov, Mario Pitschmann became the second main theoretician of the *q*BOUNCE collaboration. Together with Philippe Brax from Paris-Saclay (France), he calculated the exact solution between two mirrors of the *symmetron dark energy model* [51, 242, 243]. The currently best limits are from the RABI^{GC}-setup [66, 142]. The advantage of *q*BOUNCE compared to atom interferometers are the larger distances between the mirrors and the experimental stuff above. An interesting uncertainty occurs in such *dark matter model* evaluations. It is not known if these hypothetical fields couple with the neutron density as a particle (1 fm) or its gravitational wave function (>10 µm). An other effect, the finite size of the mirror below, was studied by Daniel Schuh as his project thesis supervised by Mario Pitschmann [273].
Since 2021, the FWF has funded a small theory group for Mario Pitschmann (P 34240). The post-doc Christian Käding, the PhD student Hauke Fischer and the master student Caroline Voith [305] joined him. They, together with Philippe Brax, started to investigate the *dilaton model* and its possible implications and limitations [49, 170].

In addition, the theoretical description of GRS has been studied and expanded: Giovanni Manfredi and Omar Morandi from the University of Strasbourg and Lazar Firedland from the Universtiy of Jerusalem together with Tobias Jenke and Hartmut Abele investigated the applications of chirped frequencies in order to excite multiple states in one oscillating region [185]. Mario Pitschmann and Hartmut Abele calculated the theoretical framework of two differently vibrating mirrors below and above the neutron beam [244]. The Bachelor student Maximilian Jugl expanded the multi-state calculations based on works of Hartmut Abele which are usable for driving multiple transitions in a sequence (e.g. in a UCN storage bottle) [149]. And Martin Suda and Manfred Faber together with the *q*BOUNCE collaboration described the gravitationally bound quantum states with Wigner functions [295].

2. Theory

The first section of this chapter describes the gravitationally bound states of UCNs (the *quantum bouncer*). Furthermore, the effects of variations and uncertainties of the natural constants (Planck's constant h, neutron's mass m_n) and field strengths (gravitational acceleration g) are illustrated. The second part explains the *gravitational resonance spectroscopy* (GRS) of these states for Rabi and Ramsey-type setups. The last section summarizes the influence of the hypothetical electric charge of neutrons on the quantum bouncer and the theoretical description of electric charge measurement. The derived theory functions for Rabi and Ramsey-type setups are compared with the actual measurement in chapter 4. Further small calculations for measurements and their corrections (aperture, detector, capacitive sensors, ...) are situated in the corresponding section within the setup chapter 3.

2.1. Gravitationally bound quantum states

The following time-dependent Schrödinger equation describes the motion of a particle (e.g. neutrons) in an arbitrary potential $\vec{V}(\vec{r},t)$:

$$\left(-\frac{\hbar^2}{2m_i}\Delta + \vec{V}(\vec{r},t)\right)\Psi(\vec{r},t) = \mathrm{i}\hbar\frac{\partial}{\partial t}\Psi(\vec{r},t) \tag{2.1}$$

Note that the particle mass is either denoted as m_i for the inertial mass or m_g for the gravitational mass. This distinction is important for studies of the Weak Equivalence Principle (WEP).

For potentials V with only a z dependency (height), the time evolution can be separated. Similarly, the x and y propagation can be expressed as plane waves (in the horizontal plane). The wave function fully separates as following:

$$\Psi(\vec{r},t) = \psi(z)\mathrm{e}^{\mathrm{i}(k_x x + k_y y - \omega t)} \tag{2.2}$$

Detailed calculations can be found in [312](p.47), [138](p.21), [287](p.17), [255], [178](p.17). The derived time-independent Schrödinger equation in z-direction is:

$$\left(-\frac{\hbar^2}{2m_i}\frac{\partial^2}{\partial z^2} + V(z)\right)\psi(z) = E\psi(z) \tag{2.3}$$

The potential $V(z)$ can be chosen in any manner. In the qBOUNCE experiments, neutrons experience mainly the influence of the gravitational field of the Earth. This can be described with the Newtonian gravitational potential V_g (using G as the gravitational constant and the mass of the Earth $M_\oplus$):

$$V_g(r) = -G\frac{M_\oplus m_g}{r} \tag{2.4}$$

This potential V_g has a radial dependence. For small distances this can be linearized: r is separated into the Earth's radius $R_\oplus$ (distance from Earth's center to the mirror surface) and the height above the mirror surface z with $z \ll R_\oplus$. The potential V_g is Taylor expanded at the position of the neutron ($r = R_\oplus + z$):

$$V_g(R_\oplus + z) \approx V_g(R_\oplus) + V_g{}'(R_\oplus)(R_\oplus + z - R_\oplus) \approx -G\frac{M_\oplus m_g}{R_\oplus} + g m_g z \tag{2.5}$$

The constant term is only a global offset to the potential and is neglected. Therefore, the used linearized potential is (with $g = G\frac{M_\oplus}{{R_\oplus}^2}$):

$$V_g(z) \approx g m_g z \tag{2.6}$$

This calculation can also be found in [166](p.10, 15-16) or [138](p.19). Additional influences due to Earth's rotation, tides, Coriolis forces and other gravitational effects are either included into an effective gravitational acceleration g or neglected [65](p.42-44) (see more in section 2.1.3).

The Schrödinger equation (2.3) for neutral particles with mass m in the linearized Newtonian gravitational potential is:

$$\left(-\frac{\hbar^2}{2m_i}\frac{\partial^2}{\partial z^2} + m_g g z\right)\psi(z) = E\psi(z) \tag{2.7}$$

In order to search for *New Physics*, every plausible field can be added (if the additional field has only a height dependence, then it can be added in eq. (2.7), otherwise in eq. (2.1), e.g. if it is time depending). Comparing the resulting solution with the purely gravitational results is a good test for the legitimacy of the introduced model. A good example for such an extension is the introduction of a hypothetical neutron charge q_n. Section 2.3 discusses all the implications in the theory and the measurements.

2.1.1. Solving the Schrödinger equation

For solving the equation (2.3) we need first to specify the boundary conditions. A flat surface at $z = 0$ is described with a Heaviside step function $\Theta(-z)$ times the neutron optical potential V_F. This potential is for most materials in the order of 100 neV and therefore 10^5 times bigger than the expected gravitational energy levels which will be calculated in the next subsection. For simplicity the potential is set to infinity. This is equivalent to the fact that the UCN cannot penetrate the surface[1]. The neutron's wave function has to vanish within the material similar as at an infinite distance. These are the needed boundary conditions:

$$\psi(z \leqslant 0) = \psi(z \to \infty) = 0 \tag{2.8}$$

The next step is a substitution for the height and the energy in order to receive a dimensionless differential equation[2] with an arbitrary linear potential $V(z) = V_z z$:

$$\tilde{z} = z/z_0 \qquad \& \qquad z_0 = \sqrt[3]{\frac{\hbar^2}{2m_i V_z}} \tag{2.9}$$

$$\tilde{E} = E/E_0 \qquad \& \qquad E_0 = V_z z_0 = \sqrt[3]{\frac{\hbar^2 {V_z}^2}{2m_i}} \tag{2.10}$$

At first, equation (2.3) is divided by E_0 and a short calculation results in the following dimensionless equation:

$$\left(\frac{\mathrm{d}^2}{\mathrm{d}\tilde{z}^2} - \left(\tilde{z} - \tilde{E}\right)\right)\psi(\tilde{z}) = 0 \tag{2.11}$$

A further coordinate shift $\left(\sigma = \tilde{z} - \tilde{E} = \sqrt[3]{2m_i V_z/\hbar^2}\,[z - E/V_z] := (z - z_n)/z_0\right)$ [244](p.2) transforms the Schrödinger equation into to the Airy differential equation (2.12) (or Stokes Equation). This transformation could also be done directly without any steps in between by using directly σ as substitution [244](p.2):

$$\frac{\mathrm{d}^2 y}{\mathrm{d}x^2} - xy = 0 \tag{2.12}$$

$$\frac{\mathrm{d}^2\psi(\sigma)}{\mathrm{d}\sigma^2} - \sigma\psi(\sigma) = 0 \tag{2.13}$$

[1] For finite potentials the wave function would enter the material and exponentially decrease with the penetration depth. Recently, Jakob Micko calculated the expected energy shifts for his PhD thesis [194](p.13-14 & 105-106) as did already others before: e.g. [312](p.47-57). This small effect nearly cancels out if only differences between two close states are measured.

[2] In early works z_0 was also named R. ζ and ϵ were used for $\tilde{z}$ and $\tilde{E}$ [166, 210, 295, 312]

The solutions of the Airy differential equation (2.13) are the two Airy functions $\mathrm{Ai}(\sigma)$ and $\mathrm{Bi}(\sigma)$ [3]. A detailed derived solution can be found in [193](p.32-35):

$$\mathrm{Ai}(\sigma) = \frac{1}{\pi}\int_0^\infty \cos\left(\frac{t^3}{3} + \sigma t\right) \mathrm{d}t \tag{2.14}$$

$$\mathrm{Bi}(\sigma) = \frac{1}{\pi}\int_0^\infty \left[\exp\left(-\frac{t^3}{3} + \sigma t\right) + \sin\left(\frac{t^3}{3} + \sigma t\right)\right] \mathrm{d}t \tag{2.15}$$

Only the Airy function $\mathrm{Ai}(\sigma)$ can fulfill both boundary conditions (2.8). It converges to zero as the argument of $\mathrm{Ai}(\sigma)$ tends to infinity. The function $\mathrm{Bi}(\sigma)$ diverges in the limit of infinity which makes it impossible to normalize the resulting solution (as depicted in fig. 2.1).

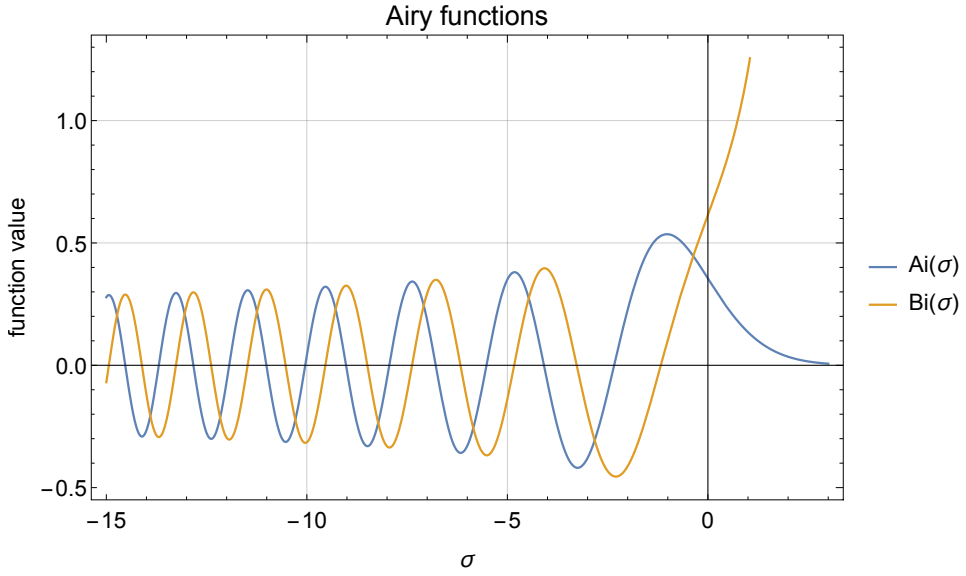

Figure 2.1.: Airy functions

In the different case of a neutron between two mirrors with a distance of L, both Airy functions are needed in order to fulfill both boundary conditions ($\psi(z \leqslant 0) = \psi(z \geqslant L) = 0$). Details of the calculations can be found in [312](p.66), [166](p.39-43), [138](p.26-28), [287](p.23-26), [178](p.19-22), [310](p.7-8), [65](p.70-71), [244](p.3).

The product of the Airy function $\mathrm{Ai}(\sigma)$ and a normalization constant C_n represents the resulting wave function $\varphi_n(z)$:

$$\varphi_n(z) = C_n \mathrm{Ai}(\sigma) = C_n \mathrm{Ai}\left(\frac{z}{z_0} + \mathrm{AiZ}(n)\right) \tag{2.16}$$

The rules for overlapping Airy functions ([65](p.70), [194](p.101-104), [244](p.9)) determine the normalization constant[4] with $\mathrm{Ai}'(\sigma) = \frac{\partial}{\partial\sigma}\mathrm{Ai}\,(\sigma)$:

$$|\varphi_n(z)|^2 = {C_n}^2 \int_0^\infty \mathrm{Ai}^2\left(\frac{z}{z_0} + \mathrm{AiZ}(n)\right) \mathrm{d}z = 1 \tag{2.17}$$

$$1/{C_n}^2 = \infty \mathrm{Ai}^2(\infty) - \mathrm{AiZ}(n)\mathrm{Ai}^2(\mathrm{AiZ}(n)) - z_0\mathrm{Ai}'^2(\infty) + z_0\mathrm{Ai}'^2(\mathrm{AiZ}(n))$$

$$C_n = 1/\sqrt{z_0\mathrm{Ai}'^2(\mathrm{AiZ}(n))} = (-1)^{n+1}/\sqrt{z_0}\mathrm{Ai}'(\mathrm{AiZ}(n)) \tag{2.18}$$

The complete solution of the time-independent Schrödinger equation (2.3) for a particle above a non penetrable surface is an ordered sum of the Airy function $\mathrm{Ai}(\sigma)$ shifted by the values of its zero points

[3] It is also possible to solve the differential equation with the related Hankel functions [255](p.7-9).

[4] There are two commonly used possibilities of normalization (depending on the resolving of the square root): Either only positive values are considered which leads to wave functions with a similar slope close to the mirror. The second method uses alternating signs which also alternates the slope sign but gives the same behavior in the limit to infinity (used in this thesis). This also affects the definition of the matrix element V_{fi}, especially the sign pattern.

AiZ(n) from the first to infinity:

$$\psi(z) = \sum_{n=1}^{\infty} b_n \varphi_n(z) = \sum_{n=1}^{\infty} b_n \frac{(-1)^{n+1} \mathrm{Ai}\left(\frac{z}{z_0} + \mathrm{AiZ}(n)\right)}{\sqrt{z_0}\mathrm{Ai}'(\mathrm{AiZ}(n))} \tag{2.19}$$

b_n are the occupation numbers of the linear combination of states n. These energy levels are always counted from *1* upwards. However, this is different to other systems (e.g. harmonic oscillator) which are named ground state, 1st excited state, 2nd excited state ,.... which start counting with *0*. In some works this nomenclature is used [160, 193, 258] but mainly the counting starts with *1* as in this work and many others [65, 90, 138, 139, 166, 178, 194, 244, 254, 255, 264, 267, 273, 287, 295, 312].

The corresponding energy levels are:

$$E_n = -E_0 \mathrm{AiZ}(n) \tag{2.20}$$

The energy levels can either be calculated accurately with eq. (2.20) or also be approximated via the formula (2.21). For higher states both methods converge [210](p.4). The basis of this approximation is the Wentzel-Kramers-Brillouin (WKB) method [166](p.13), [312](p.71-74), [258](p.4-6):

$$E_n = E_0 \left(\frac{3\pi}{2}\left(n - \frac{1}{4}\right)\right)^{\frac{2}{3}} \tag{2.21}$$

As visible in figure 2.2, these energy levels are not equidistant in contrast to the harmonic oscillator.

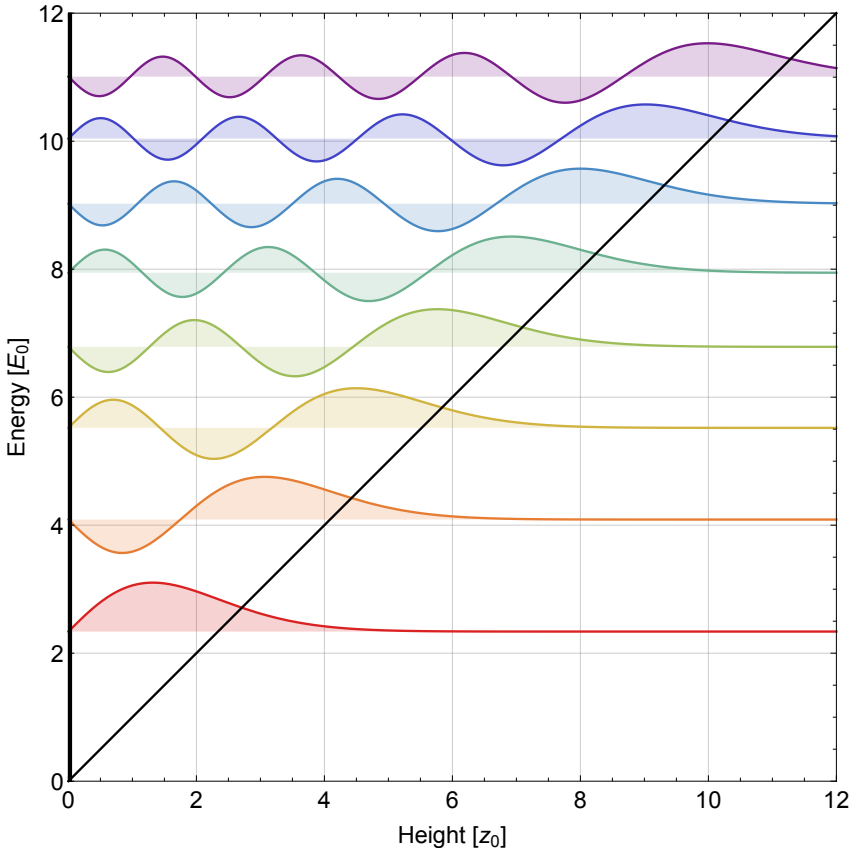

Figure 2.2.: Solution of the Schrödinger equation (2.3) in units of z_0 and E_0

All energy differences between two arbitrary states are unique numbers. Therefore, a given energy can only address one transition between two specific states. The corresponding transition frequencies can be calculated as follows:

$$\nu_{fi} = (E_f - E_i)/h = -E_0/h\,(\mathrm{AiZ}(f) - \mathrm{AiZ}(i)) \tag{2.22}$$

In this calculation, spatial wave functions represent the solution [226]. It is also possible to Fourier transform them into the momentum space [81] or to join both together as Wigner functions in phase space. Detailed calculation can be found in [295].

2.1.2. Solution for a neutron above a mirror

Within qBOUNCE only gravity plays a significant role. Therefore, only the gravitational potential V_g (2.6) is considered. To solve the corresponding Schrödinger equation (2.7) the following factors are needed:

$$z_0 = \sqrt[3]{\frac{\hbar^2}{2m_i m_g g}} = \sqrt[3]{\frac{\hbar^2}{2{m_\mathrm{n}}^2 g}} \qquad \Rightarrow \qquad z_0\,(g_0) = 5.868\,627\,466(4)\,\mu\mathrm{m} \tag{2.23}$$

$$E_0 = m_g g z_0 = \sqrt[3]{\frac{\hbar^2 {m_g}^2 g^2}{2m_i}} = \sqrt[3]{\frac{\hbar^2 m_\mathrm{n} g^2}{2}} \qquad \Rightarrow \qquad E_0\,(g_0) = 0.601\,648\,502(8)\,\mathrm{peV} \tag{2.24}$$

$$\sigma = \tilde{z} - \tilde{E} = \frac{z}{z_0} - \frac{E}{E_0} = \sqrt[3]{\frac{2m_i m_g g}{\hbar^2}}\left(z - \frac{E}{m_g g}\right) = \sqrt[3]{\frac{{m_\mathrm{n}}^2 g}{\hbar^2}}\left(z - \frac{E}{m_\mathrm{n} g}\right) \tag{2.25}$$

This thesis always utilizes the new exact definition of the reduced Plank's constant $\hbar$ (SI 2019 [41]). Assuming the weak equivalent principle, the value of the neutron mass m_n (CODATA 2018 [300]) is utilized for the inertial mass m_i and the gravitational mass m_g. In this section, the local gravitational acceleration value is $g_0 = 9.806\,65\,\mathrm{m/s^2}$ (standard gravity on Earth). This value is exactly defined and therefore the errors in (2.23) and (2.24) are only induced by the measurement of the neutron mass m_n. This choice of parameter's values can be compared worldwide and will not change significantly over time. For the real measurements the local gravitational acceleration g strongly depends on the location and its measurement. This will be the main source of error. However, measuring the energy states is also an independent method to determine g and therefore this constant will be a free fitting parameter in the evaluation of the measurements. Subsection 2.1.3 discusses in more detail the influence of these parameters on the energy levels and transition frequencies.
Using this choice of constants, the first energy states are displayed below. In the following examples, the transition frequencies between these states (tab. 2.1)[5], their wave function and their density distribution (fig. 2.3) are displayed:

1. 1.406 718 822(10) peV
2. 2.459 508 661(17) peV
3. 3.321 436 552(23) peV
4. 4.083 212 758(29) peV
5. 4.779 576 075(34) peV
6. 5.428 464 372(38) peV
7. 6.040 655 855(43) peV

Table 2.1.: Transition frequencies with standard parameters [Hz]

$i\backslash f$	2	3	4	5	6	7	8
1	254.5634	462.9767	647.1733	815.5532	972.4537	1120.4810	1261.3546
2		208.4132	392.6099	560.9898	717.8903	865.9175	1006.7911
3			184.1967	352.5766	509.4771	657.5043	798.3779
4				168.3799	325.2804	473.3076	614.1812
5					156.9005	304.9277	445.8013
6						148.0272	288.9008
7							140.8736

[5] A table including transitions up to state 15 can be seen in [194](p.19)

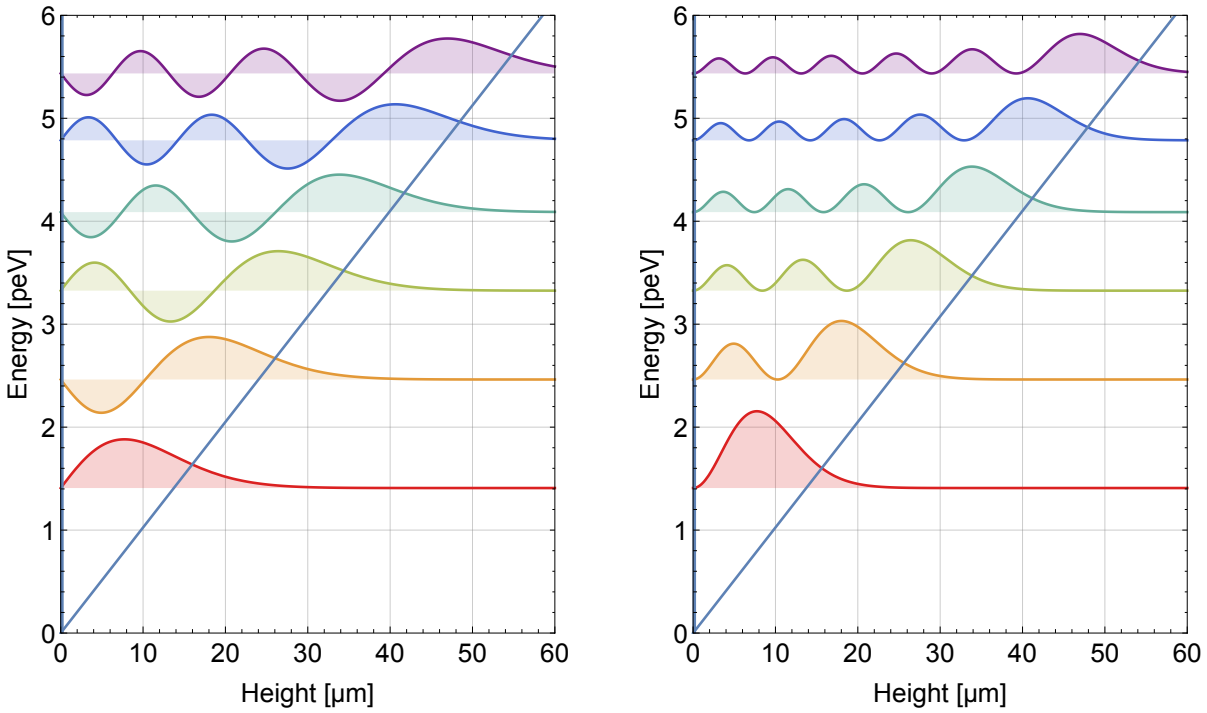

(a) Wave function as solution of eq. (2.7)

(b) Density distribution of the neutron above the mirror surface

Figure 2.3.: Quantum bouncer in Earth's gravity

2.1.3. Dependency of the transition frequency on its parameters

In the simple model of a linearized Newtonian gravitational potential (eq. (2.7)), the bound states as solutions of the quantum bouncer only depend on the neutron mass m_n, the Planck's constant h and the local acceleration of gravity g. All parameters and their uncertainties have a direct influence on the measurable transition frequency and its error (as seen in eq. (2.28)). In the following subsections, I will discuss the influence on the quantum bouncer for each parameter. The impact of Planck's constant and the neutron mass are very small. On the contrary, the gravitational acceleration g can strongly vary and therefore also significantly change the transition frequencies. Vice versa, measurements of the transition frequency (GRS) enable to determine g at the site of the experiment. The following equations display the general dependencies of the uncertainties due to the three underlying parameters:

$$\sigma_{z_0} = \frac{z_0}{3}\sqrt{4\left(\frac{\sigma_\hbar}{\hbar}\right)^2 + \left(\frac{\sigma_{m_i}}{m_i}\right)^2 + \left(\frac{\sigma_{m_g}}{m_g}\right)^2 + \left(\frac{\sigma_g}{g}\right)^2} = \frac{z_0}{3}\sqrt{4\left(\frac{\sigma_\hbar}{\hbar}\right)^2 + 4\left(\frac{\sigma_{m_\mathrm{n}}}{m_\mathrm{n}}\right)^2 + \left(\frac{\sigma_g}{g}\right)^2} \tag{2.26}$$

$$\sigma_{E_0} = \frac{E_0}{3}\sqrt{4\left(\frac{\sigma_\hbar}{\hbar}\right)^2 + \left(\frac{\sigma^2_{m_i}}{m_i}\right)^2 + 4\left(\frac{\sigma^2_{m_g}}{m_g}\right)^2 + 4\left(\frac{\sigma_g}{g}\right)^2} = \frac{E_0}{3}\sqrt{4\left(\frac{\sigma_\hbar}{\hbar}\right)^2 + \left(\frac{\sigma_{m_\mathrm{n}}}{m_\mathrm{n}}\right)^2 + 4\left(\frac{\sigma_g}{g}\right)^2} \tag{2.27}$$

$$\sigma_{\nu_{fi}} = \frac{\nu_{fi}}{3}\sqrt{\left(\frac{\sigma_\hbar}{\hbar}\right)^2 + \left(\frac{\sigma_{m_i}}{m_i}\right)^2 + 4\left(\frac{\sigma_{m_g}}{m_g}\right)^2 + 4\left(\frac{\sigma_g}{g}\right)^2} = \frac{\nu_{fi}}{3}\sqrt{\left(\frac{\sigma_\hbar}{\hbar}\right)^2 + \left(\frac{\sigma_{m_\mathrm{n}}}{m_\mathrm{n}}\right)^2 + 4\left(\frac{\sigma_g}{g}\right)^2} \tag{2.28}$$

Planck's constant h

In May 2019, the International System of Units received a major revision [41, 56]. Beside the already fixed speed of light c_0, also the Planck's constant h, the elementary charge e, the Boltzmann constant k_B and the Avogadro constant N_A have been defined by exact values since then. The new fixed value of Planck's constant is $6.626\,070\,15 \times 10^{-34}\,\mathrm{J\,s}$ (CODATA 2018 [300], SI 2019 [41]). This value is always used in this thesis and the complete data evaluation (with the software package *Mathematica*).

Before the exact definition of h, different values were in use as displayed in the following list:

- CODATA 2010 [203]: $6.626\,069\,57(29) \times 10^{-34}\,\mathrm{J\,s}$ (used in [65, 139])
- CODATA 2014 [201]: $6.626\,070\,040(81) \times 10^{-34}\,\mathrm{J\,s}$ (used by *Mathematica 11.1*)
- CODATA 2017 [202]: $6.626\,070\,150(69) \times 10^{-34}\,\mathrm{J\,s}$ (used by *Mathematica 11.3*)
- Old *q*BOUNCE crude value: $6.626\,06 \times 10^{-34}\,\mathrm{J\,s}$ (used for fast evaluations)

Using these outdated values leads to small shifts and introduction of an error:

$$z_{01} - z_{02} = z_{01}\left(1 - \sqrt[3]{\frac{\hbar_2^2}{\hbar_1^2}}\right) \qquad \sigma_{z_0} = \frac{2z_0}{3\hbar}\sigma_\hbar \tag{2.29}$$

$$E_{01} - E_{02} = E_{01}\left(1 - \sqrt[3]{\frac{\hbar_2^2}{\hbar_1^2}}\right) \qquad \sigma_{E_0} = \frac{2E_0}{3\hbar}\sigma_\hbar \tag{2.30}$$

$$\nu_{fi_1} - \nu_{fi_2} = \nu_{fi_1}\left(1 - \sqrt[3]{\frac{\hbar_1}{\hbar_2}}\right) \qquad \sigma_{\nu_{fi}} = \frac{\nu_{fi}}{3\hbar}\sigma_\hbar \tag{2.31}$$

Using the crude value induces a relative shift of 1.021×10^{-6} in z_0 and E_0 and relative shift of the transition frequency of 5.106×10^{-7}. The relative shift in frequency for the outdated CODATA 2010 is 1.46×10^{-8}. In the measured frequency range (100 - 1000 Hz) the maximum shift of each of these outdated values is below 1 mHz (e.g. for $|1\rangle \to |3\rangle$: 0.236 mHz and 6.75 µHz respectively), which is four orders of magnitudes below the best transition frequency measurement of Gunther Cronenberg [65](p.50) and therefore negligible.
The additional error if using the old *Mathematica 11.3* value (CODATA 2017) instead of the new exact SI value is $\frac{1}{2}\frac{\sigma_{z_0}}{z_0} = \frac{1}{2}\frac{\sigma_{E_0}}{E_0} = \frac{\sigma_{\nu_{fi}}}{\nu_{fi}} = \frac{\sigma_\hbar}{3\hbar} \approx 3.4711 \times 10^{-9}$. The corresponding error in the frequency is a few µHz (e.g. $\sigma_{\nu_{13}} = 1.607\,\mu\mathrm{Hz}$). Similar to the shift, the current GRS methods cannot detect this induced error.

Neutron mass m_n

The determination of neutron mass has been subject to many experiments since the discovery of the neutron [59, 230]. The currently accepted value of the neutron mass is $m_\mathrm{n} = 1.674\,927\,498\,04(95) \times 10^{-27}\,\mathrm{kg}$ (CODATA 2018 [300]). This value will be used for the complete analysis. Previous works and evaluations used outdated values (current values at the time):

- CODATA 2010 [203]: $1.674\,927\,351(74) \times 10^{-27}\,\mathrm{kg}$ (used in [65](p.79))
- CODATA 2014 [201]: $1.674\,927\,471(21) \times 10^{-27}\,\mathrm{kg}$ (used by *Mathematica 11.1-11.3*)

Each time the value of the neutron mass has been updated, z_0, E_0 and the transition frequencies ν_{fi} shift slightly. Additionally, the error corresponding to the measured neutron mass changes (mainly decreased over the years).

$$z_{01} - z_{02} = z_{01}\left(1 - \sqrt[3]{\frac{m_{\mathrm{n}1}^2}{m_{\mathrm{n}2}^2}}\right) \qquad \sigma_{z_0} = \frac{z_0}{3}\sqrt{\left(\frac{\sigma_{m_i}}{m_i}\right)^2 + \left(\frac{\sigma_{m_g}}{m_g}\right)^2} = \frac{2z_0}{3m_\mathrm{n}}\sigma_{m_\mathrm{n}} \tag{2.32}$$

$$E_{01} - E_{02} = E_0\left(1 - \sqrt[3]{\frac{m_{\mathrm{n}2}}{m_{\mathrm{n}1}}}\right) \qquad \sigma_{E_0} = \frac{E_0}{3}\sqrt{\left(\frac{\sigma^2_{m_i}}{m_i}\right)^2 + 4\left(\frac{\sigma^2_{m_g}}{m_g}\right)^2} = \frac{E_0}{3m_\mathrm{n}}\sigma_{m_\mathrm{n}} \tag{2.33}$$

$$\nu_{fi_1} - \nu_{fi_2} = \nu_{fi_1}\left(1 - \sqrt[3]{\frac{m_{\mathrm{n}2}}{m_{\mathrm{n}1}}}\right) \qquad \sigma_{\nu_{fi}} = \frac{\nu_{fi}}{3}\sqrt{\left(\frac{\sigma_{m_i}}{m_i}\right)^2 + 4\left(\frac{\sigma_{m_g}}{m_g}\right)^2} = \frac{\nu_{fi}}{3m_\mathrm{n}}\sigma_{m_\mathrm{n}} \tag{2.34}$$

The neutron mass measurements from the CODATA 2010 or CODATA 2014 compared to the current best value of CODATA 2018 shifts the transition frequency by a factor of 2.9263×10^{-8} and 5.3813×10^{-9} respectively (e.g. $\nu_{13_{2018}} - \nu_{13_{2010}} = 13.55\,\mu\mathrm{Hz}$ and $\nu_{13_{2018}} - \nu_{13_{2014}} = 2.491\,\mu\mathrm{Hz}$).

The corresponding relative errors to the CODATA values ($\frac{\sigma_{z_0}}{2z_0} = \frac{\sigma_{E_0}}{E_0} = \frac{\sigma_{\nu_{fi}}}{\nu_{fi}}$) from 2010 to 2018 are 1.4727×10^{-8}, 4.179×10^{-9} and 1.8906×10^{-10} which correspond to errors in the transition frequency in the µHz regime (e.g. $\nu_{13} = 6.818\,\mu\mathrm{Hz}$, 1.935 µHz or 87.532 nHz). Any future more precise and accurate

measurements of the neutron mass will further reduce this error. Similar to the Planck's constant, changes of the neutron mass can be neglected. However, in future analyses the neutron mass and its error have to be changed to keep up with the commonly accepted value.

Earth gravitational acceleration g

In comparison to the Planck's constant and the neutron mass, the gravitational acceleration g is not a universal fundamental constant which is either defined or can be measured to a high precision. It has strong spatial dependence. In first order, g depends on the mass and size of the planets, on which surface the experiment takes place:

$$g = G \cdot M/R^2 \tag{2.35}$$

Our solar system provides places with a variety of different gravitational accelerations which also varies the experimental parameters of the quantum bouncing ball (see table 2.2). Specially low gravity regions provide an advantage (e.g. at a future Moon base). The size of the wave functions increases which results in larger absorber gaps (approximately twice on the Moon compared to Earth) and in smaller relative errors due to the easier adjustment process. This can result in better state preparation. Also the transition frequencies decrease by more than a factor of three. The current setup can provide for lower frequencies higher maximum amplitudes (less stored energy). This can either be used to drive higher harmonics of a transition or address transitions to higher states which in general have better contrasts.

Table 2.2.: Gravitational acceleration on the surface of planets/dwarf planets/moon

Planet	Mass M	Radius R	g	z_0	E_0	$2 \to 4$	$1 \to 3$	$1 \to 4$
Mercury	3.301×10^{23} kg	2440(1) km	$3.70\,\mathrm{m\,s^{-2}}$	8.12 µm	0.314 peV	210 Hz	240 Hz	340 Hz
Venus	4.867×10^{24} kg	6050(1) km	$8.87\,\mathrm{m\,s^{-2}}$	6.07 µm	0.563 peV	370 Hz	430 Hz	610 Hz
Earth	5.97×10^{24} kg	6371 km	$9.82\,\mathrm{m\,s^{-2}}$	5.866 µm	0.602 peV	393 Hz	463 Hz	648 Hz
Mars	6.417×10^{23} kg	3390 km	$3.73\,\mathrm{m\,s^{-2}}$	8.101 µm	0.316 peV	206 Hz	243 Hz	340 Hz
Pluto	1.309×10^{22} kg	1189.9 km	$0.617\,\mathrm{m\,s^{-2}}$	14.76 µm	0.0952 peV	62.1 Hz	73.2 Hz	102.4 Hz
Moon	7.346×10^{22} kg	1737.4 km	$1.624\,\mathrm{m\,s^{-2}}$	10.686 µm	0.1814 peV	118.4 Hz	139.6 Hz	195.2 Hz

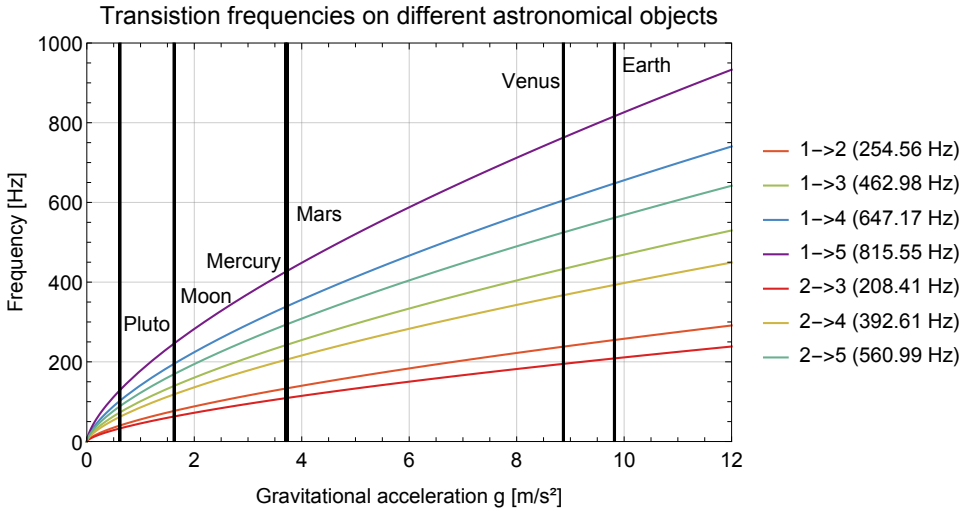

Figure 2.4.: Variation of the transition frequencies on the surfaces of different astronomical objects

Even on Earth g varies significantly. The main contribution to the spatial variation is the Earth's rotation. Depending on the latitude $\phi_\oplus$, it induces a centrifugal force which counteracts gravity. Additionally, the Earth is not a perfect sphere. Due to rotation, it is more an oblate spheroid. The equatorial semi axis $a_\oplus$ is bigger than the polar semi axis $b_\oplus$ ($a_\oplus = 6378.137\,\mathrm{km}$ vs. $b_\oplus = 6356.752\,\mathrm{km}$ [228](p.38-40)). The larger distance to the center of mass of the Earth further reduces g closer to the equator similar to the centrifugal force. Therefore, the local gravitational acceleration on the equator is $g_e = 9.780\,325\,335\,9\,\mathrm{m/s^2}$

and at the poles it is $g_p = 9.832\,184\,937\,8\,\mathrm{m/s^2}$ [228]. This corresponds to a variation of 0.5 % globally. Additionally, the height z (compared to the sea level) has an influence on g. Above the Earth's surface this can be corrected with the following formula:

$$g_z = g\left(\frac{R_\oplus}{R_\oplus + z}\right)^2 \tag{2.36}$$

Approaching the Earth's center g has not a simple linear dependence due to the non homogeneous density of the Earth.

In order to calculate g on any place on Earth (e.g. Grenoble), there are different approaches. The most simple one is to use the standard acceleration due to gravity $g_0 = 9.806\,65\,\mathrm{m/s^2}$ from 1901. This fixed value approximately represents g at a latitude $\phi_\oplus$ of 45° and sea level. This value is used in the theory section of this thesis due to its universality.
A quite precise calculation is recommended by the *World Geodetic System 1984* (WGS84) [228] which includes the effects of Earth's rotation and can also be combined with a height correction due to modeling the Earth as an ellipsoid:

$$g[\phi_\oplus] = g_e\left[\frac{1 + \left(\frac{b_\oplus g_p - a_\oplus g_e}{a_\oplus g_e}\right)\sin^2\phi_\oplus}{\sqrt{1-(1-(b_\oplus/a_\oplus)^2)\sin^2\phi_\oplus}}\right] \tag{2.37}$$

Mass density variations are not only responsible for the complicated dependency of g underneath the surface but also along the Earth's surface. To account for these variances, satellites globally measure Earth's gravity field. On the bases of the WGS84 geometrical form of the Earth, spherical harmonic coefficients take into account the local variations of g. The *Earth Gravitational Model* (EGM) is the result of these measurements and approximations which additionally implements a longitudinal dependence and also includes local measurements. At the moment, there exist four generations of this model (EGM84 [228], EGM96 [175], EGM2008 [232], EGM2020) with more and more orders of harmonic coefficients (therefore higher resolution). The current versions of *Mathematica* (11.3) use the map EGM96 via the function *GeogravityModelData* in order to calculate g for any given position (incl. height) on Earth. EGM2008 includes the results of the satellite mission GRACE and would be even more precise.
However, these global maps cannot resolve the local composition of the Earth's crust close to the experiment. Tidal forces of moon and sun or movement of large masses close to the experiment can have an influence on g as time-depending variation [89](p.66-67). Falling corner cubes or atom interferometers can determine this local time-depending g with an absolute measurement and a relative accuracy of 10^{-9} [186].
All measurements with the current and past setups of qBOUNCE have been carried out at the ILL in Grenoble. As seen in table 2.3 all previously described methods to calculate g can be used for planning the experiments at any place on Earth (e.g. Grenoble). In addition, there exists an old measurement of $g = 9.805\,07(2)\,\mathrm{m/s^2}$ with a precision spring balance [311, 324, 325] at the PF2/VCN cabin (10 m away from the PF2/UCN platform). All previous qBOUNCE measurements used its rounded value $g = 9.805\,\mathrm{m/s^2}$ [6]. In 2021, a new measurement with a falling corner cube directly next to the vacuum chamber on the PF2/UCN platform confirms this value with a higher precision at $g_{2021} = 9.804\,916\,47(10)\,\mathrm{m/s^2}$ [194, 301]. In the evaluation of the measurements in this thesis, g is a fit parameter and is determined via the resonance frequency and therefore via the rate measurements.
A very interesting systematic test in the future will be to measure with a GRS-setup at different UCN sources in different locations (e.g. SUN@ILL [235], PSI [22], ESS [163], TRIUMF [187], LANL [123]). This will enable us to cross check the theory, specially the influence of g. Especially the UCN source at the Los Alamos National Lab (LANL) and the St. Petersburg Nuclear Physics Institute (PNPI) in Gatchina are suitable candidates. Due to the large difference in g compared to Grenoble, the transition frequency shifts almost 0.5 Hz, which is already detectable with the current RAMSEY$^{\mathrm{TR}}$-setup. An utopian test would be to use an UCN source on a ship. An experiment similar to the qBOUNCE-setup could continuously measure the influence in the range between g_e and g_p (as seen in fig. 2.5). Even more possibilities offer a nuclear submarine as a platform of the source which could also probe variation in the vertical direction. These globalized tests would measure the gravitational potential of the Earth with a pure quantum mechanical setup and are complementary to classical tests.

[6] Exceptions: Claude Krantz used g_0 [166](p.13) and Gunther Cronenberg utilized the full measurement value [65](p.79).

Table 2.3.: Gravitational acceleration g on Earth

g	method	place	g [m s^{-2}]	z_0 [µm]	E_0 [peV]	$2 \to 4$ [Hz]	$1 \to 3$ [Hz]	$1 \to 4$ [Hz]
g_{planet}	Eq. 2.35	Earth (sphere)	9.820(1)	5.866	0.602	393	463	648
g_0	3rd CGPM(1901)	$\phi = 45°$	9.806 65	5.868 63	0.601 649	392.610	462.977	647.173
g_e	WGS 1984	Equator	9.780 325 335 9	5.873 89	0.600 571	391.907	462.148	646.015
g_p	WGS 1984	Poles	9.832 184 937 8	5.863 54	0.602 692	393.291	463.780	648.296
g_{WGS84}	WGS 1984	Grenoble ($z = 219$)	9.8057	5.868 82	0.601 609	392.584	462.947	647.131
g_{WGS84}	WGS 1984	Grenoble ($z = 0$)	9.806 37	5.868 68	0.601 637	392.602	462.968	647.161
g_{EGM96}	*Mathematica 11.3*	Grenoble	9.806 13	5.868 73	0.601 627	392.596	462.960	647.150
g_{EGM96}	*Mathematica 11.3*	Grenoble (+12 m)	9.806 09	5.868 74	0.601 626	392.595	462.959	647.149
g_{EGM96}	*Mathematica 11.3*	Villigen (PSI)	9.807 73	5.868 41	0.601 693	392.639	463.011	647.221
g_{EGM96}	*Mathematica 11.3*	Vienna(ATI)	9.809 10	5.868 14	0.601 749	392.675	463.054	647.281
g_{EGM96}	*Mathematica 11.3*	Munich (FRM2)	9.808 07	5.868 34	0.601 706	392.648	463.021	647.236
g_{EGM96}	*Mathematica 11.3*	Lund (ESS)	9.815 66	5.866 83	0.602 017	392.850	463.260	647.570
g_{EGM96}	*Mathematica 11.3*	Gatchina (PNPI)	9.818 51	5.866 26	0.602 133	392.926	463.350	647.695
g_{EGM96}	*Mathematica 11.3*	Dubna (JINR)	9.816 36	5.866 69	0.602 046	392.869	463.282	647.601
g_{EGM96}	*Mathematica 11.3*	Vancouver (TRIUMF)[303]	9.809 92	5.867 97	0.601 783	392.697	463.080	647.318
g_{EGM96}	*Mathematica 11.3*	Los Alamos (LANL)	9.791 43	5.871 67	0.601 026	392.204	462.498	646.504
g_{PF2}	Spring balance	PF2/VCN @ ILL	9.805 07(2)	5.868 94	0.601 584	392.568	462.927	647.104
$g_{qBOUNCE}$	qBOUNCE	Grenoble (ILL)	9.805	5.868 95	0.601 58	392.566	462.925	647.101

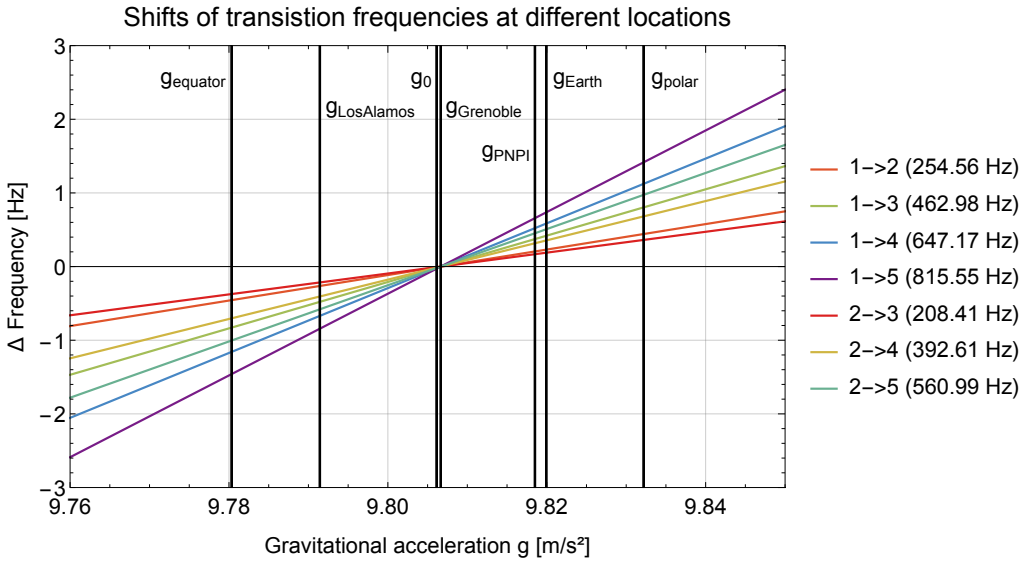

Figure 2.5.: Variation of the transition frequencies on the surfaces of the Earth

The influence of g on the quantum bouncing ball and the GRS is seen together with its induced error in the following examples:

$$z_0 = \sqrt[3]{\frac{\hbar}{2{m_\mathrm{n}}^2 g}} \propto g^{-\frac{1}{3}} \qquad \sigma_{z_0} = \frac{z_0}{3g}\sigma_g \propto g^{-\frac{4}{3}} \tag{2.38}$$

$$E_0 = m_\mathrm{n} g z_0 = \sqrt[3]{\frac{\hbar m_\mathrm{n} g^2}{2}} \propto g^{\frac{2}{3}} \qquad \sigma_{E_0} = \frac{2E_0}{3g}\sigma_g \propto g^{-\frac{1}{3}} \tag{2.39}$$

$$\nu_{fi} = \frac{E_0}{h}\left(\mathrm{AiZ}(f) - \mathrm{AiZ}(i)\right) \propto g^{\frac{2}{3}} \qquad \sigma_{\nu_{fi}} = \frac{2\nu_{fi}}{3g}\sigma_g \propto g^{-\frac{1}{3}} \tag{2.40}$$

The choice of g_0 in the theory section does not induce any error and establishes comparable results. For the theoretical predictions of the transition frequencies in real experiments, g is the main source of the error because either a close by measurement of g or an interpolated value of a global method (e.g. EGM96) has to be used. For the measurement at PF2/VCN the absolute error in z_0 is 3.99 pm and for E_0 it is 0.818 feV. Translated in the transition frequency, it is a relative error of 1.36×10^{-6} (e.g. $\nu_{13} = 0.6$ mHz), which is not measurable at the moment. This is also the case for the generally used rounded value (e.g. $\nu_{13} = 15.7$ mHz).

GRS setups measure transition frequencies and therefore the characteristic energy scale E_0. The main source of error in these measurements are statistical errors of the count rates. These results can determine the local gravitational acceleration g:

$$g_{z_0} = \frac{\hbar}{2{m_\mathrm{n}}^2 {z_0}^3} \qquad \sigma_{g_{z_0}} = \frac{\hbar}{2}\sqrt{\frac{4\sigma_{m_\mathrm{n}}^2}{{m_\mathrm{n}}^6 {z_0}^6} + \frac{9\sigma_{z_0}^2}{{m_\mathrm{n}}^4 {z_0}^8}} \approx \frac{3\hbar}{2{m_\mathrm{n}}^2}\frac{\sigma_{z_0}}{{z_0}^4} = 3\frac{\sigma_{z_0}}{z_0} g_{z_0} \tag{2.41}$$

$$g_{E_0} = \sqrt{\frac{2{E_0}^3}{\hbar m_\mathrm{n}}} \qquad \sigma_{g_{E_0}} = \sqrt{\frac{2}{\hbar}}\sqrt{\frac{{E_0}^3}{4{m_\mathrm{n}}^3}\sigma_{m_\mathrm{n}}^2 + \frac{9E_0}{4m_\mathrm{n}}\sigma_{E_0}^2} \approx \frac{3}{2}\sqrt{\frac{2E_0}{\hbar m_\mathrm{n}}}\sigma_{E_0} = \frac{3}{2}\frac{\sigma_{E_0}}{E_0} g_{E_0} \tag{2.42}$$

$$g_{\nu_{fi}} = 2h\sqrt{\frac{{\nu_{fi}}^3}{m_\mathrm{n}\left(\mathrm{AiZ}(f) - \mathrm{AiZ}(i)\right)^3}} \tag{2.43}$$

$$\sigma_{g_{\nu_{fi}}} = 2h\sqrt{\frac{\pi\left(\frac{{\nu_{fi}}^3}{4{m_\mathrm{n}}^3}\sigma_{m_\mathrm{n}}^2 + \frac{9\nu_{fi}}{4m_\mathrm{n}}\sigma_{\nu_{fi}}^2\right)}{\left(\mathrm{AiZ}(f) - \mathrm{AiZ}(i)\right)^3}} \approx 3h\sqrt{\frac{\pi\nu_{fi}}{m_\mathrm{n}\left(\mathrm{AiZ}(f) - \mathrm{AiZ}(i)\right)^3}}\sigma_{\nu_{fi}} = \frac{3}{2}\frac{\sigma_{\nu_{fi}}}{\nu_{fi}} g_{\nu_{fi}} \tag{2.44}$$

If g is known locally to an uncertainty of 1 percent or 1 per mill, the frequency can be calculated with an error of 3.1 Hz or 0.31 Hz (for transition $1 \to 3$). Vice versa, a measurement at a level of Hz or mHz determines g at the experimental site with a relative precision of 3.2×10^{-3} or 3.2×10^{-6} respectively.

2.2. Gravitational Resonance Spectroscopy (GRS)

The main method of all qBOUNCE-GRS experiments to induce state transitions is to mechanically oscillate the boundary condition (mirror)[7]. In principle, this time-dependent oscillation could be an arbitrary function $f(t)$ which is either periodic or non periodic. Due to the fact that any arbitrary function can be expressed as a sum of sine and cosine[8], we could restrict this function in the following calculation to $f(t) = a_x \sin(\omega t + \phi)$ (as in [65, 193, 254, 264, 267]). However, this thesis will utilize an arbitrary excitation to profit from the more general form (similar calculation can be found in [139](p.56-60), [160](p.12-14, 56-59), [194](p.18-25)). At the end, the applied sinusoidal excitation will be inserted. The calculations are in the spatial space representation. Similarly, this can be also done in momentum space or in a more general bra-ket notation which I will display at certain points.

The calculation of GRS starts with the time-depending Schrödinger equation consisting of the *Quantum Bouncer* part (eq. (2.7)) and an additional time-depending potential representing the applied mechanical oscillation $f(t)$. With a transformation into the oscillating frame this equation can be rewritten into a non-oscillating Hamiltonian $\hat{H}_0$ and a perturbation. The solution of the steady-state case (eq. (2.16)) can be used as an ansatz with time-depending state population coefficients b_i. Multiplying a second wave function ψ_f to this initial ansatz from the left and integrating over the spatial coordinate simplifies the solution via defining the matrix element V_{fi}. A further separation of the searched coefficients leads to a simple matrix equation to describe the time evolution of the state population completely. Only for a two level system with a rotating wave approximation this can be solved analytically as an eigenvalue problem. Otherwise, a numerical calculation is necessary to describe the system. From these solutions the transition probability and the transmission of a bound state through a Rabi or Ramsey-type system are calculated. The transmission curves of the lowest states close to the measured frequencies are the bases for the fitting routine. This approximation of the data points determines the transition frequency and therefore the local gravity g and the hypothetical neutron charge q_n. Note, the calculations of GRS in this thesis are independent of the choice of the linear potential V_z and therefore able to compute the results of a purely Newtonian setting or a neutron charge measurement (e.g. $V_z = V_g$ or $V_z = V_g + V_{\vec{E}}$).

In the following sections, I will describe these calculations in detail as a consistent derivation of the needed theoretical curves. All this is based on the work of previous students and members of the qBOUNCE collaboration which also contains similar calculations [65, 139, 160, 193, 194, 196, 244, 254, 264, 267][9]. I will depict similarities and differences to these theses and publications throughout this section.

[7] A very different approach is to use oscillating magnetic gradient fields to excite the quantum states as the GRANIT-collaboration aimed to realize (see more in section 1.4).

[8] Some functions (e.g. rectangular function) need an infinite sum to represent it completely. A calculable finite sum would only be an approximation of the represented function.

[9] The calculations in the thesis [254] use the most different approach to all others in order to have more similarities to the calculations of Norman F. Ramsey [250].

2.2.1. Calculations of GRS transitions

The time-dependent Schrödinger equation with an oscillating boundary condition is written as the following (with V_F as the neutron optical potential of the material and $f(t)$ as an arbitrary time-depending disturbance):

$$\left(-\frac{\hbar^2}{2m_i}\frac{\partial^2}{\partial z^2}+V_z+V_F\Theta\left(f(t)-z\right)\right)\Psi\left(z,t\right))=\mathrm{i}\hbar\frac{\partial}{\partial t}\Psi\left(z,t\right) \tag{2.45}$$

A transformation ($\tilde{z}=z-f(t)$ and $\tilde{t}=t$) from the laboratory frame into an oscillating frame will separate the potential in multiple parts:

$$\begin{aligned}\left(-\frac{\hbar^2}{2m_i}\frac{\partial^2}{\partial \tilde{z}^2}+V_z\tilde{z}+V_F\Theta\left(-\tilde{z}\right)+V_z f(\tilde{t})+\mathrm{i}\hbar\frac{\partial}{\partial\tilde{t}}f(\tilde{t})\frac{\partial}{\partial\tilde{z}}\right)\tilde{\Psi}\left(\tilde{z},\tilde{t}\right)&=\mathrm{i}\hbar\frac{\partial}{\partial\tilde{t}}\tilde{\Psi}\left(\tilde{z},\tilde{t}\right)\\ \left(\hat{H}_0+V_z f(\tilde{t})+\mathrm{i}\hbar\dot{f}(\tilde{t})\frac{\partial}{\partial\tilde{z}}\right)\tilde{\Psi}\left(\tilde{z},\tilde{t}\right)&=\mathrm{i}\hbar\frac{\partial}{\partial\tilde{t}}\tilde{\Psi}\left(\tilde{z},\tilde{t}\right)\end{aligned} \tag{2.46}$$

As seen in the time-independent Schrödinger equation (eq. (2.7)), the first terms are identified as the Hamiltonian of the initially unperturbed system $\hat{H}_0$. The already calculated eigenstates E_i and wave functions $\tilde{\psi}_i(\tilde{z})$ (eq. (2.16)) describe a neutron above a single steady state mirror which can be interpreted as the initial condition. This solution is the main part for an ansatz to solve the time-depending system. Additionally, a time propagation of the unperturbed system $\mathrm{e}^{\mathrm{i}\frac{E_i}{\hbar}\tilde{t}}$ and a time-depending state population of the eigenstates $b_i\left(\tilde{t}\right)$ represent the time evolution[10]:

$$\tilde{\Psi}\left(\tilde{z},\tilde{t}\right)=\sum_{i=1}^{\infty}b_i\left(\tilde{t}\right)\mathrm{e}^{-\mathrm{i}\frac{E_i}{\hbar}\tilde{t}}\tilde{\psi}_i(\tilde{z}) \tag{2.47}$$

The inserted ansatz (2.47) in the time-dependent Schrödinger equation (2.46):

$$\hat{H}_0\sum_{i=1}^{\infty}b_i(\tilde{t})\mathrm{e}^{-\mathrm{i}\frac{E_i}{\hbar}\tilde{t}}\tilde{\psi}_i(\tilde{z})+\left(V_z f(\tilde{t})+\mathrm{i}\hbar\dot{f}(\tilde{t})\frac{\partial}{\partial\tilde{z}}\right)\sum_{i=1}^{\infty}b_i(\tilde{t})\mathrm{e}^{-\mathrm{i}\frac{E_i}{\hbar}\tilde{t}}\tilde{\psi}_i(\tilde{z})=\mathrm{i}\hbar\frac{\partial}{\partial\tilde{t}}\sum_{i=1}^{\infty}b_i(\tilde{t})\mathrm{e}^{-\mathrm{i}\frac{E_i}{\hbar}\tilde{t}}\tilde{\psi}_i(\tilde{z}) \tag{2.48}$$

After rearranging the terms, calculating the time derivative and inserting the solution of the time-independent Schrödinger equation (2.7), the unperturbed terms cancel:

$$\sum_{i=1}^{\infty}b_i(\tilde{t})\mathrm{e}^{-\mathrm{i}\frac{E_i}{\hbar}\tilde{t}}\left(V_z f(\tilde{t})+\mathrm{i}\hbar\dot{f}(\tilde{t})\frac{\partial}{\partial\tilde{z}}\right)\tilde{\psi}_i(\tilde{z})=\mathrm{i}\hbar\sum_{i=1}^{\infty}\dot{b}_i(\tilde{t})\mathrm{e}^{-\mathrm{i}\frac{E_i}{\hbar}\tilde{t}}\tilde{\psi}_i(\tilde{z}) \tag{2.49}$$

We multiply a second unperturbed wave function $\tilde{\psi}_f(\tilde{z})$ from the left and integrate over $\tilde{z}$. This corresponds to the projection of the perturbed initial state i onto a final state f:

$$\int_0^{\infty}\tilde{\psi}_f(\tilde{z})\sum_{i=1}^{\infty}b_i(\tilde{t})\mathrm{e}^{-\mathrm{i}\frac{E_i}{\hbar}\tilde{t}}\left(V_z f(\tilde{t})+\mathrm{i}\hbar\dot{f}(\tilde{t})\frac{\partial}{\partial\tilde{z}}\right)\tilde{\psi}_i(\tilde{z})\,\mathrm{d}\tilde{z}=\int_0^{\infty}\tilde{\psi}_f(\tilde{z})\mathrm{i}\hbar\sum_{i=1}^{\infty}\dot{b}_i(\tilde{t})\mathrm{e}^{-\mathrm{i}\frac{E_i}{\hbar}\tilde{t}}\tilde{\psi}_i(\tilde{z})\,\mathrm{d}\tilde{z} \tag{2.50}$$

Rearranging the terms (moving out all height-independent terms from the integral) gives the following equation:

$$\begin{aligned}\sum_{i=1}^{\infty}b_i(\tilde{t})\mathrm{e}^{-\mathrm{i}\frac{E_i}{\hbar}\tilde{t}}\left(V_z f(\tilde{t})\int_0^{\infty}\tilde{\psi}_f(\tilde{z})\tilde{\psi}_i(\tilde{z})\,\mathrm{d}\tilde{z}+\mathrm{i}\hbar\dot{f}(\tilde{t})\int_0^{\infty}\tilde{\psi}_f(\tilde{z})\frac{\partial}{\partial\tilde{z}}\tilde{\psi}_i(\tilde{z})\,\mathrm{d}\tilde{z}\right)&\\ =\mathrm{i}\hbar\sum_{i=1}^{\infty}\dot{b}_i(\tilde{t})\mathrm{e}^{-\mathrm{i}\frac{E_i}{\hbar}\tilde{t}}\int_0^{\infty}\tilde{\psi}_f(\tilde{z})\tilde{\psi}_i(\tilde{z})\,\mathrm{d}\tilde{z}&\end{aligned} \tag{2.51}$$

[10] Very similar transformations to the oscillating frame and calculations with this ansatz can be found in [139](p.57-58), [267](p.10-13), [193](p.7-9), [254](p.31-33), [160](p.13,56)

Introduction of the Matrix element V_{fi}

The matrix element V_{fi} for the overlap integral simplifies eq. (2.51) as it can be calculated analytically[11]:

$$V_{fi} = \int_0^\infty \tilde{\psi}_f^*(\tilde{z}) \frac{\partial}{\partial \tilde{z}} \tilde{\psi}_i(\tilde{z})\, \mathrm{d}\tilde{z} = \langle f | \frac{\partial}{\partial \tilde{z}} | i \rangle \tag{2.52}$$

Inserting the definition of the stationary wave function (eq. 2.16) into the integral leads to:

$$V_{fi} = \frac{(-1)^{f+i}}{z_0 \mathrm{Ai}'(\mathrm{AiZ}(f))\,\mathrm{Ai}'(\mathrm{AiZ}(i))} \int_0^\infty \mathrm{Ai}\left(\frac{\tilde{z}}{z_0} + \mathrm{AiZ}(f)\right) \frac{\partial}{\partial \tilde{z}} \mathrm{Ai}\left(\frac{\tilde{z}}{z_0} + \mathrm{AiZ}(i)\right) \mathrm{d}\tilde{z} \tag{2.53}$$

Analytical expressions exist already for the integral of Airy functions [16]. The calculations of M. Pitschmann [244](p.13-15), G. Cronenberg's thesis [65](p.72) or J. Micko's PhD thesis [194](p.101-104) provide a more general solution for $\int_0^\infty \mathrm{Ai}(\sigma) \frac{\partial}{\partial \sigma} \mathrm{Ai}(\sigma - \lambda)\, \mathrm{d}\sigma$:

$$\begin{aligned}\int_{\sigma_A}^{\sigma_B} F(\sigma) \frac{\partial}{\partial \sigma} G(\sigma - \lambda)\, \mathrm{d}\sigma =& \frac{1}{\lambda^2} F'(\sigma_B) G(\sigma_B - \lambda) - \frac{1}{\lambda^2} F'(\sigma_B) G(\sigma_B) + \frac{1}{\lambda} F'(\sigma_B) G'(\sigma_B - \lambda) \\ & - \frac{1}{\lambda^2} F'(\sigma_A) G(\sigma_A - \lambda) + \frac{1}{\lambda^2} F'(\sigma_A) G(\sigma_A) - \frac{1}{\lambda} F'(\sigma_A) G'(\sigma_A - \lambda)\end{aligned} \tag{2.54}$$

The arbitrary linear combination of Airy functions F and G are simplified with the pure function Ai. The argument σ and its shift λ are adjusted for the calculation of the matrix element V_{fi} too:

$$\sigma = \frac{\tilde{z}}{z_0} + \mathrm{AiZ}(f) \qquad\qquad \lambda = \mathrm{AiZ}(f) - \mathrm{AiZ}(i) \tag{2.55}$$

The boundaries σ_A and σ_B are substituted with $\mathrm{AiZ}(f)$ ($\tilde{z} = 0$) and ∞ in order to solve the case of a neutron above a single mirror surface. In addition, the properties of the Airy function Ai simplify the result ($\mathrm{Ai}(\infty) = 0$ and $\mathrm{Ai}(\mathrm{AiZ}(n)) = 0$):

$$\begin{aligned}\int_{\mathrm{AiZ}(f)}^\infty \mathrm{Ai}(\sigma) \frac{\partial}{\partial \sigma} \mathrm{Ai}(\sigma - \lambda)\, \mathrm{d}\sigma =& \frac{1}{\lambda^2} \mathrm{Ai}'(\infty) \mathrm{Ai}(\infty - \lambda) - \frac{1}{\lambda^2} \mathrm{Ai}'(\infty) \mathrm{Ai}(\infty) + \frac{1}{\lambda} \mathrm{Ai}'(\infty) \mathrm{Ai}'(\infty - \lambda) \\ & - \frac{1}{\lambda^2} \mathrm{Ai}'(\mathrm{AiZ}(f)) \mathrm{Ai}(\mathrm{AiZ}(f) - \lambda) + \frac{1}{\lambda^2} \mathrm{Ai}'(\mathrm{AiZ}(f)) \mathrm{Ai}(\mathrm{AiZ}(f)) \\ & - \frac{1}{\lambda} \mathrm{Ai}'(\mathrm{AiZ}(f)) \mathrm{Ai}'(\mathrm{AiZ}(f) - \lambda)\end{aligned}$$

$$\int_{\mathrm{AiZ}(f)}^\infty \mathrm{Ai}(\sigma) \frac{\partial}{\partial \sigma} \mathrm{Ai}(\sigma - \lambda)\, \mathrm{d}\sigma = -\frac{1}{\mathrm{AiZ}(f) - \mathrm{AiZ}(i)} \mathrm{Ai}'(\mathrm{AiZ}(f)) \mathrm{Ai}'(\mathrm{AiZ}(i)) \tag{2.56}$$

Inserting the solution of the Airy function integral (eq. (2.56)) into the equation (2.53) results in a simple analytical expression for the matrix element:

$$V_{fi} = -\frac{(-1)^{f+i}}{z_0 \left[\mathrm{AiZ}(f) - \mathrm{AiZ}(i)\right]} \tag{2.57}$$

For the standard parameters (h, m_n, g_0) the values of the matrix elements can be seen in the following table. In general, the matrix elements are antisymmetric $V_{fi} = -V_{if}$ [12]:

[11] Using the analytical form is much faster as any numerical integration especially with the software *Mathematica*.

[12] Depending on the definition of the normalization of the wave function (2.16) the signs of the matrix elements are either alternating (as in this thesis and with opposite sign in [193](p.9), [254](p.129), [160](p.13)) or in a triangle form with the low triangle consisting of only negative values.

Table 2.4.: Values of the matrix element V_{fi} [m^{-1}]

$f \backslash i$	1	2	3	4	5	6	7
1	0	-97378.84	53542.86	-38303.64	30395.43	-25491.28	22123.62
2	97378.84	0	-118942.03	63139.25	-44188.14	34530.48	-28627.55
3	-53542.86	118942.03	0	-134579.50	70308.40	-48655.96	37701.80
4	38303.64	-63139.25	134579.50	0	-147221.22	76208.39	-52374.17
5	-30395.43	44188.14	-70308.40	147221.22	0	-157992.46	81294.98
6	25491.28	-34530.48	48655.96	-76208.39	157992.46	0	-167463.06
7	-22123.62	28627.55	-37701.80	52374.17	-81294.98	167463.06	0

Inserting the introduced definition of the matrix element V_{fi} simplifies the equation of GRS (2.51). Additionally, the orthogonality of the wave function ($\int_0^\infty \tilde{\psi}_f(\tilde{z})\tilde{\psi}_i(\tilde{z})\,\mathrm{d}\tilde{z} = \delta_{fi}$ or in more general $\langle f|i\rangle = \delta_{fi}$) simplifies the expression further:

$$\sum_{i=1}^{\infty} b_i(\tilde{t})\mathrm{e}^{-\mathrm{i}\frac{E_i}{\hbar}\tilde{t}}\left[V_z f(\tilde{t})\delta_{fi} + \mathrm{i}\hbar\dot{f}(\tilde{t})V_{fi}\right] = \mathrm{i}\hbar\sum_{i=1}^{\infty}\dot{b}_i(\tilde{t})\mathrm{e}^{-\mathrm{i}\frac{E_i}{\hbar}\tilde{t}}\delta_{fi} \tag{2.58}$$

After resolving the Kronecker delta δ_{fi} and multiplying with $\mathrm{e}^{\mathrm{i}\frac{E_f}{\hbar}\tilde{t}}$, this can be rewritten with defining the resonance angular frequency $\omega_{fi} = \frac{E_f - E_i}{\hbar}$. Note: I always apply the *final-initial* order to the indices of the matrix element V_{fi} and the transition angular frequency ω_{fi} [13]:

$$V_z f(\tilde{t})b_f(\tilde{t}) + \mathrm{i}\hbar\dot{f}(\tilde{t})\sum_{i=1}^{\infty} b_i(\tilde{t})\mathrm{e}^{\mathrm{i}\omega_{fi}\tilde{t}}V_{fi} = \mathrm{i}\hbar\dot{b}_f(\tilde{t}) \tag{2.59}$$

Transformation of the state population coefficient from b_i to c_i

The transformation $b_f(\tilde{t}) = c_f(\tilde{t}) \times u(\tilde{t})$ (separating an arbitrary function $u(\tilde{t})$) eliminates the term consisting of the linear potential V_z within the equation [193](p.9-11), [160](p.13-14,57), [194](p.18):

$$V_z f(\tilde{t})u(\tilde{t})c_f(\tilde{t}) + \mathrm{i}\hbar\dot{f}(\tilde{t})u(\tilde{t})\sum_{i=1}^{\infty} c_i(\tilde{t})\mathrm{e}^{\mathrm{i}\omega_{fi}\tilde{t}}V_{fi} = \mathrm{i}\hbar\left[\dot{c}_f(\tilde{t})u(\tilde{t}) + c_f(\tilde{t})\dot{u}(\tilde{t})\right] \tag{2.60}$$

Demanding $V_z f(\tilde{t})u(\tilde{t}) = \mathrm{i}\hbar\dot{u}(\tilde{t})$ cancels two terms and the arbitrary function $u(\tilde{t})$ can be eliminated. The differential equation simplifies as the following:

$$\dot{f}(\tilde{t})\sum_{i=1}^{\infty}\mathrm{e}^{\mathrm{i}\omega_{fi}\tilde{t}}V_{fi}\,c_i(\tilde{t}) = \dot{c}_f(\tilde{t}) \tag{2.61}$$

A sinusoidal oscillation $f(\tilde{t}) = a_x\sin\left(\omega\tilde{t}+\phi\right)$ determines the arbitrary function to:

$$u(\tilde{t}) = \mathrm{e}^{\frac{\mathrm{i}V_z}{\hbar\omega}a_x\cos\left(\omega\tilde{t}+\phi\right)} \tag{2.62}$$

$$a_x\omega\cos\left(\omega\tilde{t}+\phi\right)\sum_{i=1}^{\infty}\mathrm{e}^{\mathrm{i}\omega_{fi}\tilde{t}}V_{fi}\,c_i(\tilde{t}) = \dot{c}_f(\tilde{t}) \tag{2.63}$$

For the measurements, the mechanical oscillation strength a_v is more commonly used than the mechanical oscillation amplitude a_x. Therefore, I will use from here on only a_v. Both are connected via the angular frequency $a_v = a_x\omega$. The product with the matrix element V_{fi} is sometimes called *Rabi frequency* (in this thesis denoted as a_vV_{fi}).

Rotating wave approximation

The cosine of the periodic perturbation can be rewritten in terms of an exponential function:

$$a_v\frac{1}{2}\left[\mathrm{e}^{\mathrm{i}\left(\omega\tilde{t}+\phi\right)} + \mathrm{e}^{-\mathrm{i}\left(\omega\tilde{t}+\phi\right)}\right]\sum_{i=1}^{\infty}\mathrm{e}^{\mathrm{i}\omega_{fi}\tilde{t}}V_{fi}\,c_i(\tilde{t}) = \dot{c}_f(\tilde{t})$$

[13] A changed ordering leads to different signs due to the opposite definitions as in [193](p.11)

Introducing the detuned angular frequency $\Delta\omega = \omega - \omega_{fi}$ gives the final formula[14]:

$$\frac{a_v}{2}\sum_{i=1}^{\infty}\left[\mathrm{e}^{\mathrm{i}\left((\omega+\omega_{fi})\tilde{t}+\phi\right)} + \mathrm{e}^{-\mathrm{i}\left(\Delta\omega\tilde{t}+\phi\right)}\right] V_{fi}\, c_i(\tilde{t}) = \dot{c}_f\left(\tilde{t}\right) \tag{2.64}$$

This rewritten cosine can be interpreted by two counter rotating waves with half the amplitude each. At resonance ($\omega = \omega_{fi}$), one term is $\mathrm{e}^{-\mathrm{i}\Delta\omega\tilde{t}} = 1$ and the other term is strongly suppressed by the fast oscillating exponential factor $\mathrm{e}^{\mathrm{i}2\omega_{fi}\tilde{t}}$. In the rotating wave approximation this term, where the two frequencies add up, is neglected. The error made by this approximation is called *Bloch-Siegert shift* [72, 251]. The approximated resulting equation is the so-called *Rabi equation* [248]:

$$\frac{a_v}{2}\sum_{i=1}^{\infty}\mathrm{e}^{-\mathrm{i}\left(\Delta\omega\tilde{t}+\phi\right)} V_{fi}\, c_i(\tilde{t}) = \dot{c}_f\left(\tilde{t}\right) \tag{2.65}$$

Matrix form

This Rabi equation can also be interpreted as vector equation with the form:

$$\dot{\vec{c}} = U\vec{c} \tag{2.66}$$

We call the matrix U *Rabi matrix* because it describes the change of the state population due to an applied Rabi pulse. The dimension of this square matrix U corresponds to the included energy states in the calculation. The most simple calculation uses only the final and the initial state and therefore only a dimension of 2. In this configuration the equation (2.65) can be solved analytically. For higher dimensions only numerically methods can calculate the transition probabilities. For state transitions which are well separated from neighboring transitions and their oscillation amplitudes a_x are small (no multiple transitions), the 2-level approach is sufficient. In this thesis I use this approach successfully for the transitions $|2\rangle \rightarrow |4\rangle$, $|1\rangle \rightarrow |3\rangle$ and $|2\rangle \rightarrow |5\rangle$. Only for measurements of the lowest transitions with high oscillation strengths ($|1\rangle \rightarrow |2\rangle$, $|2\rangle \rightarrow |3\rangle$, ..) this approach fails completely.

2-Level solution of the Rabi equation

The most general analytic solution from the Rabi equation (2.61) in matrix form and only two dimensions is stated in the following[15]:

$$\dot{\vec{c}} = \begin{pmatrix}\dot{c}_i\left(\tilde{t}\right)\\ \dot{c}_f\left(\tilde{t}\right)\end{pmatrix} = \begin{pmatrix}0 & -\dot{f}(\tilde{t})\mathrm{e}^{-\mathrm{i}\omega_{fi}\tilde{t}}V_{fi}\\ \dot{f}(\tilde{t})\mathrm{e}^{\mathrm{i}\omega_{fi}\tilde{t}}V_{fi} & 0\end{pmatrix}\begin{pmatrix}c_i\left(\tilde{t}\right)\\ c_f\left(\tilde{t}\right)\end{pmatrix} = U\vec{c} \tag{2.67}$$

Within qBOUNCE the analytic solution in two dimensions (initial and final state) and in matrix form is derived from equation (2.63) (sinusoidal oscillation):

$$\begin{pmatrix}\dot{c}_i\left(\tilde{t}\right)\\ \dot{c}_f\left(\tilde{t}\right)\end{pmatrix} = \begin{pmatrix}0 & -a_v\cos(\omega\tilde{t}+\phi)\mathrm{e}^{-\mathrm{i}\omega_{fi}\tilde{t}}V_{fi}\\ a_v\cos(\omega\tilde{t}+\phi)\mathrm{e}^{\mathrm{i}\omega_{fi}\tilde{t}}V_{fi} & 0\end{pmatrix}\begin{pmatrix}c_i\left(\tilde{t}\right)\\ c_f\left(\tilde{t}\right)\end{pmatrix} \tag{2.68}$$

Using the rotating wave approximation (eq. (2.65)) this simplifies to:

$$\begin{pmatrix}\dot{c}_i\left(\tilde{t}\right)\\ \dot{c}_f\left(\tilde{t}\right)\end{pmatrix} = \begin{pmatrix}0 & -\frac{1}{2}a_v\mathrm{e}^{\mathrm{i}\left(\Delta\omega\tilde{t}+\phi\right)}V_{fi}\\ \frac{1}{2}a_v\mathrm{e}^{-\mathrm{i}\left(\Delta\omega\tilde{t}+\phi\right)}V_{fi} & 0\end{pmatrix}\begin{pmatrix}c_i\left(\tilde{t}\right)\\ c_f\left(\tilde{t}\right)\end{pmatrix} \tag{2.69}$$

A further coordinate shift of the state population coefficient $c_i\left(\tilde{t}\right)$ to $d_i\left(\tilde{t}\right)$ leads to a time-independent matrix U [16]. This choice of transformation also includes the phase of the perturbation. It is also possible

[14] Take care the order of the transition state can change the sign of the introduction of the detuned angular frequency $\Delta\omega$. In this thesis the order *final-initial* is chosen as in [193](p.11), [160](p.14), [194](p.18), other works use the reversed order (see [139](p.59), [65](p.14)). Additionally, the order used in this thesis provides that an applied frequency above the resonance frequency represents a positive detuning.

[15] Note that the different sign comes from inverting the state order of the matrix element V_{fi} and/or the definition of the detuned angular frequency $\Delta\omega$ if you compare it to other works [139](p.59-60), [264](p.16-17), [267](p.13-14), [193](p.11-12), [160](p.14,57-59), [194](p.19-20).

[16] Jakob Micko describes in his PhD thesis an elegant short cut to the following steps [194](p.19-20)

to exclude the phase from the transformation in order to preserve it within the calculations. This will be discussed in subsection 2.2.1:

$$c_i\left(\tilde{t}\right) = \mathrm{e}^{\frac{\mathrm{i}}{2}\left(\Delta\omega\tilde{t}+\phi\right)} d_i\left(\tilde{t}\right) \qquad c_f\left(\tilde{t}\right) = \mathrm{e}^{-\frac{\mathrm{i}}{2}\left(\Delta\omega\tilde{t}+\phi\right)} d_f\left(\tilde{t}\right) \tag{2.70}$$

$$\begin{pmatrix} \dot{d}_i\left(\tilde{t}\right) \\ \dot{d}_f\left(\tilde{t}\right) \end{pmatrix} = \begin{pmatrix} -\frac{\mathrm{i}}{2}\Delta\omega & -\frac{1}{2}a_v V_{fi} \\ \frac{1}{2}a_v V_{fi} & \frac{\mathrm{i}}{2}\Delta\omega \end{pmatrix} \begin{pmatrix} d_i\left(\tilde{t}\right) \\ d_f\left(\tilde{t}\right) \end{pmatrix} \tag{2.71}$$

To solve this homogeneous linear differential equation (2.71) an exponential ansatz is a good choice [139](p.11):

$$\begin{pmatrix} d_i\left(\tilde{t}\right) \\ d_f\left(\tilde{t}\right) \end{pmatrix} = \mathrm{e}^{\frac{\mathrm{i}\Lambda}{2}\tilde{t}} \begin{pmatrix} d_i(0) \\ d_f(0) \end{pmatrix} \tag{2.72}$$

This ansatz inserted into the differential equation (2.71) gives:

$$\begin{pmatrix} \dot{d}_i\left(\tilde{t}\right) \\ \dot{d}_f\left(\tilde{t}\right) \end{pmatrix} = \frac{\mathrm{i}\Lambda}{2}\mathrm{e}^{\frac{\mathrm{i}\Lambda}{2}\tilde{t}} \begin{pmatrix} d_i(0) \\ d_f(0) \end{pmatrix} = \frac{\mathrm{i}}{2}\mathrm{e}^{\frac{\mathrm{i}\Lambda}{2}\tilde{t}} \begin{pmatrix} -\Delta\omega & \mathrm{i}a_v V_{fi} \\ -\mathrm{i}a_v V_{fi} & \Delta\omega \end{pmatrix} \begin{pmatrix} d_i(0) \\ d_f(0) \end{pmatrix} \tag{2.73}$$

This results in the following eigenvalue equation:

$$\Lambda\vec{v}_\Lambda = \begin{pmatrix} -\Delta\omega & \mathrm{i}a_v V_{fi} \\ -\mathrm{i}a_v V_{fi} & \Delta\omega \end{pmatrix} \vec{v}_\Lambda \tag{2.74}$$

With the characteristic polynomial (from the determinant of the matrix) the two eigenvalues are calculated:

$$\left| \begin{pmatrix} -\Delta\omega-\Lambda & \mathrm{i}a_v V_{fi} \\ -\mathrm{i}a_v V_{fi} & \Delta\omega-\Lambda \end{pmatrix} \right| = \Lambda^2 - \left[\left(a_v V_{fi}\right)^2 + \Delta\omega^2 \right] = \Lambda^2 - {\Omega_R}^2 = \left(\Lambda-\Omega_R\right)\left(\Lambda+\Omega_R\right) \tag{2.75}$$

This polynomial determines the eigenvalues to $\Lambda = \pm\Omega_R = \pm\sqrt{\left(a_v V_{fi}\right)^2 + \Delta\omega^2}$. The introduced Ω_R is called *Rabi frequency* or *generalized Rabi frequency*. The corresponding eigenvectors are:

$$\vec{v}_{\Lambda+} = \begin{pmatrix} \mathrm{i}a_v V_{fi} \\ \Delta\omega+\Omega_R \end{pmatrix} = \begin{pmatrix} \mathrm{i}\left(\Omega_R-\Delta\omega\right) \\ a_v V_{fi} \end{pmatrix} \qquad \vec{v}_{\Lambda-} = \begin{pmatrix} \mathrm{i}a_v V_{fi} \\ \Delta\omega-\Omega_R \end{pmatrix} \tag{2.76}$$

The general solution of the differential equation (2.71) is the sum of the eigenvectors of the matrix including the time propagation (exponential ansatz eq. (2.72)) and the arbitrary parameters α and β:

$$\begin{pmatrix} d_i\left(\tilde{t}\right) \\ d_f\left(\tilde{t}\right) \end{pmatrix} = \alpha\mathrm{e}^{\mathrm{i}\frac{\Omega_R}{2}\tilde{t}}\vec{v}_{\Lambda+} + \beta\mathrm{e}^{-\mathrm{i}\frac{\Omega_R}{2}\tilde{t}}\vec{v}_{\Lambda-} = \begin{pmatrix} \mathrm{i}\left(\Omega_R-\Delta\omega\right)\mathrm{e}^{\mathrm{i}\frac{\Omega_R}{2}\tilde{t}} & \mathrm{i}a_v V_{fi}\mathrm{e}^{-\mathrm{i}\frac{\Omega_R}{2}\tilde{t}} \\ a_v V_{fi}\mathrm{e}^{\mathrm{i}\frac{\Omega_R}{2}\tilde{t}} & \left(\Delta\omega-\Omega_R\right)\mathrm{e}^{-\mathrm{i}\frac{\Omega_R}{2}\tilde{t}} \end{pmatrix} \begin{pmatrix} \alpha \\ \beta \end{pmatrix} \tag{2.77}$$

To calculate these arbitrary parameters, we set $\tilde{t} = 0$ in order to express them with the initial conditions of the population coefficients $\vec{d}(0)$:

$$\begin{pmatrix} d_i(0) \\ d_f(0) \end{pmatrix} = \alpha \begin{pmatrix} \mathrm{i}\left(\Omega_R-\Delta\omega\right) \\ a_v V_{fi} \end{pmatrix} + \beta \begin{pmatrix} \mathrm{i}a_v V_{fi} \\ \Delta\omega-\Omega_R \end{pmatrix} = \begin{pmatrix} \mathrm{i}\left(\Omega_R-\Delta\omega\right) & \mathrm{i}a_v V_{fi} \\ a_v V_{fi} & \Delta\omega-\Omega_R \end{pmatrix} \begin{pmatrix} \alpha \\ \beta \end{pmatrix} \tag{2.78}$$

Multiplying from the left the complex conjugate transpose matrix resolves the equation:

$$\begin{pmatrix} -\mathrm{i}\left(\Omega_R-\Delta\omega\right) & a_v V_{fi} \\ -\mathrm{i}a_v V_{fi} & \Delta\omega-\Omega_R \end{pmatrix} \begin{pmatrix} d_i(0) \\ d_f(0) \end{pmatrix} = \begin{pmatrix} -\mathrm{i}\left(\Omega_R-\Delta\omega\right) & a_v V_{fi} \\ -\mathrm{i}a_v V_{fi} & \Delta\omega-\Omega_R \end{pmatrix} \begin{pmatrix} \mathrm{i}\left(\Omega_R-\Delta\omega\right) & \mathrm{i}a_v V_{fi} \\ a_v V_{fi} & \Delta\omega-\Omega_R \end{pmatrix} \begin{pmatrix} \alpha \\ \beta \end{pmatrix}$$
$$\frac{1}{2\Omega_R\left(\Omega_R-\Delta\omega\right)} \begin{pmatrix} -\mathrm{i}\left(\Omega_R-\Delta\omega\right) & a_v V_{fi} \\ -\mathrm{i}a_v V_{fi} & \Delta\omega-\Omega_R \end{pmatrix} \begin{pmatrix} d_i(0) \\ d_f(0) \end{pmatrix} = \begin{pmatrix} \alpha \\ \beta \end{pmatrix} \tag{2.79}$$

Inserting this fixation of the parameter α and β with the initial conditions into equation (2.77) leads to the final form:

$$\begin{pmatrix} d_i\left(\tilde{t}\right) \\ d_f\left(\tilde{t}\right) \end{pmatrix} = \begin{pmatrix} \cos\left(\frac{\Omega_R}{2}\tilde{t}\right) - \mathrm{i}\frac{\Delta\omega}{\Omega_R}\sin\left(\frac{\Omega_R}{2}\tilde{t}\right) & -\frac{a_v V_{fi}}{\Omega_R}\sin\left(\frac{\Omega_R}{2}\tilde{t}\right) \\ \frac{a_v V_{fi}}{\Omega_R}\sin\left(\frac{\Omega_R}{2}\tilde{t}\right) & \cos\left(\frac{\Omega_R}{2}\tilde{t}\right) + \mathrm{i}\frac{\Delta\omega}{\Omega_R}\sin\left(\frac{\Omega_R}{2}\tilde{t}\right) \end{pmatrix} \begin{pmatrix} d_i(0) \\ d_f(0) \end{pmatrix} \tag{2.80}$$

This result is similar to [193](p.12 eq. 26) except a different sign in the off diagonal due to the use of the reversed matrix element. Taking also a reversed order in the definition of the detuned angular frequency into account, the signs within the imaginary part of the diagonal elements change too (as in [65](p.14, eq 2.14)).
This equation can also be expressed similar to the general matrix differential equation eq. (2.66). The used *Rabi matrix* describes the influence of a Rabi pulse on the state population coefficients $\vec{d}\left(\tilde{t}\right)$:

$$\vec{d}\left(\tilde{t}\right) = U\left(\tilde{t},0\right)\vec{d}(0) \tag{2.81}$$

Rabi Transformation Calculation

A different approach of diagonalizing the matrix is the so-called *Rabi method* which Jakob Micko used in his master thesis [193](p.11-12). He introduces the following variables for a coordinate shift to emphasize the mathematical structure (circular) of the solution:

$$r\cos\Omega := \frac{\Delta\omega}{2} \qquad r\sin\Omega := \frac{1}{2}a_v V_{fi} \qquad r := \sqrt{\left(\frac{\Delta\omega}{2}\right)^2 + \left(\frac{1}{2}a_v V_{fi}\right)^2} = \frac{\Omega_R}{2} \tag{2.82}$$

Using the ansatz $d_i\left(\tilde{t}\right) = \mathrm{e}^{\Lambda\tilde{t}} d_i\left(\tilde{t}\right)$ the differential equation transforms to a simple matrix equation. Calculating the roots of the characteristic polynomial determines the eigenvalues to $\pm\mathrm{i}\frac{\Omega_R}{2}$. The corresponding eigenvectors are:

$$v_{ir} = \begin{pmatrix} -\sin\frac{\Omega}{2} \\ \mathrm{i}\cos\frac{\Omega}{2} \end{pmatrix} \qquad v_{-ir} = \begin{pmatrix} \cos\frac{\Omega}{2} \\ \mathrm{i}\sin\frac{\Omega}{2} \end{pmatrix} \tag{2.83}$$

Using the same evaluation as for eq. (2.80) leads to the following solution:

$$\begin{pmatrix} d_i\left(\tilde{t}\right) \\ d_f\left(\tilde{t}\right) \end{pmatrix} = \begin{pmatrix} \cos\left(\frac{\Omega_R}{2}\tilde{t}\right) - \mathrm{i}\sin\left(\frac{\Omega_R}{2}\tilde{t}\right)\cos\Omega & -\sin\Omega\sin\left(\frac{\Omega_R}{2}\tilde{t}\right) \\ \sin\Omega\sin\left(\frac{\Omega_R}{2}\tilde{t}\right) & \cos\left(\frac{\Omega_R}{2}\tilde{t}\right) + \mathrm{i}\sin\left(\frac{\Omega_R}{2}\tilde{t}\right)\cos\Omega \end{pmatrix} \begin{pmatrix} d_i(0) \\ d_f(0) \end{pmatrix} \tag{2.84}$$

Undoing the Rabi transformation (2.82) leads to the previous expression (2.80) of the Rabi matrix U.

2-Level solution including the phase information

A third option to solve the differential equation (2.69) is to use a different coordinate shift of the state population coefficient $c_i\left(\tilde{t}\right)$ to $\tilde{d}_i\left(\tilde{t}\right)$ which leads to a time-independent matrix too. In comparison to the transformation (2.70), the initial phase between the applied oscillation and the wave function is not included in the transformation:

$$c_i\left(\tilde{t}\right) = \mathrm{e}^{\frac{\mathrm{i}}{2}\Delta\omega\tilde{t}}\tilde{d}_i\left(\tilde{t}\right) \qquad c_f\left(\tilde{t}\right) = \mathrm{e}^{-\frac{\mathrm{i}}{2}\Delta\omega\tilde{t}}\tilde{d}_f\left(\tilde{t}\right) \tag{2.85}$$

$$\begin{pmatrix} \dot{\tilde{d}}_i\left(\tilde{t}\right) \\ \dot{\tilde{d}}_f\left(\tilde{t}\right) \end{pmatrix} = \begin{pmatrix} -\frac{\mathrm{i}}{2}\Delta\omega & -\frac{1}{2}a_v V_{fi}\mathrm{e}^{\mathrm{i}\phi} \\ \frac{1}{2}a_v V_{fi}\mathrm{e}^{-\mathrm{i}\phi} & \frac{\mathrm{i}}{2}\Delta\omega \end{pmatrix} \begin{pmatrix} \tilde{d}_i\left(\tilde{t}\right) \\ \tilde{d}_f\left(\tilde{t}\right) \end{pmatrix} \tag{2.86}$$

Again the exponential ansatz $\vec{\tilde{d}}\left(\tilde{t}\right) = \mathrm{e}^{\frac{\mathrm{i}\Lambda}{2}\tilde{t}}\vec{\tilde{d}}(0)$ resolves this homogeneous linear differential equation (2.86) into an eigenvalue problem of a matrix. The characteristic polynomial determines the eigenvalues to $\Lambda = \pm\Omega_R = \pm\sqrt{\left(a_v V_{fi}\right)^2 + \Delta\omega^2}$. They are the same as for the phase-less calculation. The corresponding eigenvectors include the phase information:

$$\vec{v}_{\Lambda+} = \begin{pmatrix} \mathrm{i}a_v V_{fi}\mathrm{e}^{\mathrm{i}\phi} \\ \Delta\omega + \Omega_R \end{pmatrix} = \begin{pmatrix} \mathrm{i}\left(\Omega_R - \Delta\omega\right) \\ a_v V_{fi}\mathrm{e}^{-\mathrm{i}\phi} \end{pmatrix} \qquad \vec{v}_{\Lambda-} = \begin{pmatrix} \mathrm{i}a_v V_{fi}\mathrm{e}^{\mathrm{i}\phi} \\ \Delta\omega - \Omega_R \end{pmatrix} \tag{2.87}$$

General solution of the differential equation is the sum of the eigenvectors of the matrix including the time propagation (exponential ansatz) and the initial conditions:

$$\begin{pmatrix} \tilde{d}_i\left(\tilde{t}\right) \\ \tilde{d}_f\left(\tilde{t}\right) \end{pmatrix} = \begin{pmatrix} \cos\left(\frac{\Omega_R\tilde{t}}{2}\right) - \mathrm{i}\frac{\Delta\omega}{\Omega_R}\sin\left(\frac{\Omega_R\tilde{t}}{2}\right) & -\frac{a_v V_{fi}}{\Omega_R}\mathrm{e}^{\mathrm{i}\phi}\sin\left(\frac{\Omega_R\tilde{t}}{2}\right) \\ \frac{a_v V_{fi}}{\Omega_R}\mathrm{e}^{-\mathrm{i}\phi}\sin\left(\frac{\Omega_R\tilde{t}}{2}\right) & \cos\left(\frac{\Omega_R\tilde{t}}{2}\right) + \mathrm{i}\frac{\Delta\omega}{\Omega_R}\sin\left(\frac{\Omega_R\tilde{t}}{2}\right) \end{pmatrix} \begin{pmatrix} \tilde{d}_i(0) \\ \tilde{d}_f(0) \end{pmatrix} \tag{2.88}$$

This result is quite similar to equation (2.80) except additional phase terms in the off diagonal.

Generalizing the two level solution

As described in the previous subsections, transforming the differential equation (2.69) leads to an eigenvalue problem of a time-independent matrix, which is easily solvable. There are different possibilities of the transformations (with and without phase) which are summarized in the following:

$$c_i\left(\tilde{t}\right) = \mathrm{e}^{\frac{\mathrm{i}}{2}\left(\Delta\omega\tilde{t}+\phi\right)} d_i\left(\tilde{t}\right) = \mathrm{e}^{\frac{\mathrm{i}}{2}\Delta\omega\tilde{t}} \tilde{d}_i\left(\tilde{t}\right) \qquad c_f\left(\tilde{t}\right) = \mathrm{e}^{-\frac{\mathrm{i}}{2}\left(\Delta\omega\tilde{t}+\phi\right)} d_f\left(\tilde{t}\right) = \mathrm{e}^{-\frac{\mathrm{i}}{2}\Delta\omega\tilde{t}} \tilde{d}_f\left(\tilde{t}\right) \tag{2.89}$$

$$\mathrm{e}^{-\frac{\mathrm{i}}{2}\left(\Delta\omega\tilde{t}+\phi\right)} c_i\left(\tilde{t}\right) = d_i\left(\tilde{t}\right) = \mathrm{e}^{-\frac{\mathrm{i}}{2}\phi} \tilde{d}_i\left(\tilde{t}\right) \qquad \mathrm{e}^{\frac{\mathrm{i}}{2}\left(\Delta\omega\tilde{t}+\phi\right)} c_f\left(\tilde{t}\right) = d_f\left(\tilde{t}\right) = \mathrm{e}^{\frac{\mathrm{i}}{2}\phi} \tilde{d}_f\left(\tilde{t}\right) \tag{2.90}$$

$$\mathrm{e}^{-\frac{\mathrm{i}}{2}\Delta\omega\tilde{t}} c_i\left(\tilde{t}\right) = \mathrm{e}^{\frac{\mathrm{i}}{2}\phi} d_i\left(\tilde{t}\right) = \tilde{d}_i\left(\tilde{t}\right) \qquad \mathrm{e}^{\frac{\mathrm{i}}{2}\Delta\omega\tilde{t}} c_f\left(\tilde{t}\right) = \mathrm{e}^{-\frac{\mathrm{i}}{2}\phi} d_f\left(\tilde{t}\right) = \tilde{d}_f\left(\tilde{t}\right) \tag{2.91}$$

The solutions with and without the phase (eq. (2.88) and eq. (2.80)) can be transformed into each other. Reversing the transformation completely leads for both solutions to the same time-dependent matrix including the initial phase information and describing the effect of the oscillation:

$$\begin{pmatrix} c_i\left(\tilde{t}\right) \\ c_f\left(\tilde{t}\right) \end{pmatrix} = \begin{pmatrix} \left[\cos\left(\frac{\Omega_R}{2}\tilde{t}\right) - \mathrm{i}\frac{\Delta\omega}{\Omega_R}\sin\left(\frac{\Omega_R}{2}\tilde{t}\right)\right] \mathrm{e}^{\frac{\mathrm{i}}{2}\Delta\omega\tilde{t}} & -\frac{a_v V_{fi}}{\Omega_R}\sin\left(\frac{\Omega_R}{2}\tilde{t}\right) \mathrm{e}^{\mathrm{i}\left(\frac{\Delta\omega\tilde{t}}{2}+\phi\right)} \\ \frac{a_v V_{fi}}{\Omega_R}\sin\left(\frac{\Omega_R}{2}\tilde{t}\right) \mathrm{e}^{-\mathrm{i}\left(\frac{\Delta\omega\tilde{t}}{2}+\phi\right)} & \left[\cos\left(\frac{\Omega_R}{2}\tilde{t}\right) + \mathrm{i}\frac{\Delta\omega}{\Omega_R}\sin\left(\frac{\Omega_R}{2}\tilde{t}\right)\right] \mathrm{e}^{-\frac{\mathrm{i}}{2}\Delta\omega\tilde{t}} \end{pmatrix} \begin{pmatrix} c_i(0) \\ c_f(0) \end{pmatrix} \tag{2.92}$$

Time generalization: A further generalization of the solution eq. (2.92) is the generalization of the initial time $U\left(\tilde{t},0\right) \rightarrow U\left(\tilde{t}+\Delta\tilde{t},\tilde{t}\right)$. This is important for further calculations especially for the expansion of the Rabi solution [248] to a Ramsey setup [250]:

$$\vec{\tilde{d}}\left(\tilde{t}+\Delta\tilde{t}\right) = U\left(\tilde{t}+\Delta\tilde{t},\tilde{t}\right)\vec{\tilde{d}}\left(\tilde{t}\right) \qquad U\left(\tilde{t}+\Delta\tilde{t},\tilde{t}\right) = U\left(\tilde{t}+\Delta\tilde{t},0\right)U^{-1}\left(\tilde{t},0\right) \tag{2.93}$$

The Rabi matrix is in all its transformations a unitary matrix which simplifies the calculation of the inverse matrix $U^{-1} = U^{\dagger}$. The Rabi pulse at a later time is calculated in the following for the case of the transformed solution including all time terms (eq. (2.92)):

$$\begin{aligned} U\left(\tilde{t}+\Delta\tilde{t},\tilde{t}\right) = & \\ & \begin{pmatrix} \left[\cos\left(\frac{\Omega_R\left(\tilde{t}+\Delta\tilde{t}\right)}{2}\right) - \mathrm{i}\frac{\Delta\omega}{\Omega_R}\sin\left(\frac{\Omega_R\left(\tilde{t}+\Delta\tilde{t}\right)}{2}\right)\right] \mathrm{e}^{\frac{\mathrm{i}\Delta\omega}{2}\left(\tilde{t}+\Delta\tilde{t}\right)} & -\frac{a_v V_{fi}}{\Omega_R}\sin\left(\frac{\Omega_R\left(\tilde{t}+\Delta\tilde{t}\right)}{2}\right) \mathrm{e}^{\mathrm{i}\left(\frac{\Delta\omega\left(\tilde{t}+\Delta\tilde{t}\right)}{2}+\phi\right)} \\ \frac{a_v V_{fi}}{\Omega_R}\sin\left(\frac{\Omega_R\left(\tilde{t}+\Delta\tilde{t}\right)}{2}\right) \mathrm{e}^{-\mathrm{i}\left(\frac{\Delta\omega\left(\tilde{t}+\Delta\tilde{t}\right)}{2}+\phi\right)} & \left[\cos\left(\frac{\Omega_R\left(\tilde{t}+\Delta\tilde{t}\right)}{2}\right) + \mathrm{i}\frac{\Delta\omega}{\Omega_R}\sin\left(\frac{\Omega_R\left(\tilde{t}+\Delta\tilde{t}\right)}{2}\right)\right] \mathrm{e}^{-\frac{\mathrm{i}\Delta\omega}{2}\left(\tilde{t}+\Delta\tilde{t}\right)} \end{pmatrix} \\ & \cdot \begin{pmatrix} \left[\cos\left(\frac{\Omega_R}{2}\tilde{t}\right) + \mathrm{i}\frac{\Delta\omega}{\Omega_R}\sin\left(\frac{\Omega_R}{2}\tilde{t}\right)\right] \mathrm{e}^{-\frac{\mathrm{i}\Delta\omega}{2}\tilde{t}} & \frac{a_v V_{fi}}{\Omega_R}\sin\left(\frac{\Omega_R}{2}\tilde{t}\right) \mathrm{e}^{\mathrm{i}\left(\frac{\Delta\omega\tilde{t}}{2}+\phi\right)} \\ -\frac{a_v V_{fi}}{\Omega_R}\sin\left(\frac{\Omega_R}{2}\tilde{t}\right) \mathrm{e}^{-\mathrm{i}\left(\frac{\Delta\omega\tilde{t}}{2}+\phi\right)} & \left[\cos\left(\frac{\Omega_R}{2}\tilde{t}\right) - \mathrm{i}\frac{\Delta\omega}{\Omega_R}\sin\left(\frac{\Omega_R}{2}\tilde{t}\right)\right] \mathrm{e}^{\frac{\mathrm{i}}{2}\Delta\omega\tilde{t}} \end{pmatrix} \end{aligned}$$

The Rabi matrix for a shifted time is similar to the original matrix starting at $\tilde{t} = 0$ (eq. (2.88)) except additional terms for the time propagation. Take care, the shifted time has to be used if the time transformation is reversed[17]:

$$U\left(\tilde{t}+\Delta\tilde{t},\tilde{t}\right) = \begin{pmatrix} \left[\cos\left(\frac{\Omega_R\Delta\tilde{t}}{2}\right) - \mathrm{i}\frac{\Delta\omega}{\Omega_R}\sin\left(\frac{\Omega_R\Delta\tilde{t}}{2}\right)\right] \mathrm{e}^{\frac{\mathrm{i}\Delta\omega\Delta\tilde{t}}{2}} & -\frac{a_v V_{fi}}{\Omega_R}\sin\left(\frac{\Omega_R\Delta\tilde{t}}{2}\right) \mathrm{e}^{\mathrm{i}\Delta\omega\left(\tilde{t}+\frac{\Delta\tilde{t}}{2}\right)}\mathrm{e}^{\mathrm{i}\phi} \\ \frac{a_v V_{fi}}{\Omega_R}\sin\left(\frac{\Omega_R\Delta\tilde{t}}{2}\right) \mathrm{e}^{-\mathrm{i}\Delta\omega\left(\tilde{t}+\frac{\Delta\tilde{t}}{2}\right)}\mathrm{e}^{-\mathrm{i}\phi} & \left[\cos\left(\frac{\Omega_R\Delta\tilde{t}}{2}\right) + \mathrm{i}\frac{\Delta\omega}{\Omega_R}\sin\left(\frac{\Omega_R\Delta\tilde{t}}{2}\right)\right] \mathrm{e}^{\frac{-\mathrm{i}\Delta\omega\Delta\tilde{t}}{2}} \end{pmatrix} \tag{2.94}$$

Reversing the potential independence Reversing the first state population coefficient transformation (eq. (2.60)) leads to:

$$b_f(\tilde{t}) = c_f(\tilde{t}) \times \mathrm{e}^{\frac{\mathrm{i}V_z}{\hbar\omega}a_x\cos\left(\omega\tilde{t}+\phi\right)} \qquad c_f(\tilde{t}) = b_f(\tilde{t}) \times \mathrm{e}^{-\frac{\mathrm{i}V_z}{\hbar\omega}a_x\cos\left(\omega\tilde{t}+\phi\right)} \tag{2.95}$$

$$\begin{aligned} \begin{pmatrix} b_i\left(\tilde{t}\right) \\ b_f\left(\tilde{t}\right) \end{pmatrix} = & \mathrm{e}^{\frac{\mathrm{i}V_z}{\hbar\omega}a_x\left[\cos\left(\omega\tilde{t}+\phi\right)-\cos\phi\right]} \\ & \cdot \begin{pmatrix} \left[\cos\left(\frac{\Omega_R}{2}\tilde{t}\right) - \mathrm{i}\frac{\Delta\omega}{\Omega_R}\sin\left(\frac{\Omega_R}{2}\tilde{t}\right)\right] \mathrm{e}^{\frac{\mathrm{i}}{2}\Delta\omega\tilde{t}} & -\frac{a_v V_{fi}}{\Omega_R}\sin\left(\frac{\Omega_R}{2}\tilde{t}\right) \mathrm{e}^{\mathrm{i}\left(\frac{\Delta\omega\tilde{t}}{2}+\phi\right)} \\ \frac{a_v V_{fi}}{\Omega_R}\sin\left(\frac{\Omega_R}{2}\tilde{t}\right) \mathrm{e}^{-\mathrm{i}\left(\frac{\Delta\omega\tilde{t}}{2}+\phi\right)} & \left[\cos\left(\frac{\Omega_R}{2}\tilde{t}\right) + \mathrm{i}\frac{\Delta\omega}{\Omega_R}\sin\left(\frac{\Omega_R}{2}\tilde{t}\right)\right] \mathrm{e}^{-\frac{\mathrm{i}}{2}\Delta\omega\tilde{t}} \end{pmatrix} \begin{pmatrix} b_i(0) \\ b_f(0) \end{pmatrix} \end{aligned} \tag{2.96}$$

[17] A similar result is obtained in [254](p.36-37).

Complete wave function: Setting the found coefficient relations into the used ansatz (eq. (2.47)) for only two states reveals the full wave function:

$$\tilde{\Psi}\left(\tilde{z},\tilde{t}\right) = b_i\left(\tilde{t}\right)\mathrm{e}^{-\mathrm{i}\frac{E_i}{\hbar}\tilde{t}}\tilde{\psi}_i(\tilde{z}) + b_f\left(\tilde{t}\right)\mathrm{e}^{-\mathrm{i}\frac{E_f}{\hbar}\tilde{t}}\tilde{\psi}_f(\tilde{z}) \tag{2.97}$$

$$\begin{aligned}\tilde{\Psi}\left(\tilde{z},\tilde{t}\right) &= \mathrm{e}^{\frac{\mathrm{i}V_z}{\hbar\omega}a_x\left[\cos\left(\omega\tilde{t}+\phi\right)-\cos\phi\right]} \\ &\cdot\left[\left(\left[\cos\left(\frac{\Omega_R}{2}\tilde{t}\right)-\mathrm{i}\frac{\Delta\omega}{\Omega_R}\sin\left(\frac{\Omega_R}{2}\tilde{t}\right)\right]b_i(0)-\frac{a_vV_{fi}}{\Omega_R}\sin\left(\frac{\Omega_R}{2}\tilde{t}\right)\mathrm{e}^{\mathrm{i}\phi}b_f(0)\right)\mathrm{e}^{\frac{\mathrm{i}}{2}\Delta\omega\tilde{t}-\mathrm{i}\frac{E_i}{\hbar}\tilde{t}}\tilde{\psi}_i(\tilde{z})\right. \\ &\left.+\left(\frac{a_vV_{fi}}{\Omega_R}\sin\left(\frac{\Omega_R}{2}\tilde{t}\right)\mathrm{e}^{-\mathrm{i}\phi}b_i(0)+\left[\cos\left(\frac{\Omega_R}{2}\tilde{t}\right)+\mathrm{i}\frac{\Delta\omega}{\Omega_R}\sin\left(\frac{\Omega_R}{2}\tilde{t}\right)\right]b_f(0)\right)\mathrm{e}^{-\mathrm{i}\frac{\Delta\omega\tilde{t}}{2}-\mathrm{i}\frac{E_f}{\hbar}\tilde{t}}\tilde{\psi}_f(\tilde{z})\right]\end{aligned} \tag{2.98}$$

Similar final solutions can be found in [193](p.12), [267](p.14). This solution can also be expressed with the Rabi matrix elements U_{mn}:

$$\begin{aligned}\tilde{\Psi}\left(\tilde{z},\tilde{t}\right) &= \mathrm{e}^{\frac{\mathrm{i}V_z}{\hbar\omega}a_x\left[\cos\left(\omega\tilde{t}+\phi\right)-\cos\phi\right]} \\ &\cdot\left[\left(U_{11}b_i(0)+U_{12}\mathrm{e}^{\mathrm{i}\phi}b_f(0)\right)\mathrm{e}^{\frac{\mathrm{i}}{2}\Delta\omega\tilde{t}-\mathrm{i}\frac{E_i}{\hbar}\tilde{t}}\tilde{\psi}_i(\tilde{z})+\left(U_{21}\mathrm{e}^{-\mathrm{i}\phi}b_i(0)+U_{22}b_f(0)\right)\mathrm{e}^{-\mathrm{i}\frac{\Delta\omega\tilde{t}}{2}-\mathrm{i}\frac{E_f}{\hbar}\tilde{t}}\tilde{\psi}_f(\tilde{z})\right]\end{aligned} \tag{2.99}$$

Transmission and state transition probability

The state occupation probability after a Rabi pulse is $\langle\Psi|\Psi\rangle$. In spatial coordinates this calculates to:

$$\langle\Psi|\Psi\rangle = \int_0^\infty \tilde{\Psi}^\star\left(\tilde{z},\tilde{t}\right)\tilde{\Psi}\left(\tilde{z},\tilde{t}\right)\mathrm{d}\tilde{z} = \left|\vec{b}^T(0)\tilde{U}^\dagger\tilde{U}\vec{b}(0)\right| = 1 \tag{2.100}$$

The measured state population after a Rabi pulse only depends on the initial conditions and the two level Rabi solution matrix U including the phase (eq. (2.88)). All other reversed transformations (eq. (2.95) and eq. (2.70)) cancel out. In the following discussion of state transmission and transition probability, I will use the simple Rabi solutions (eq. (2.88)) for the evolution of the state population. All state populations ($\vec{b}$, $\vec{c}$, $\vec{d}$ and $\vec{\tilde{d}}$) are initially equal but have different values at later times. However, the transformations fix the relations between different used state population coefficients. For the following calculations I will use the originally introduced coefficient $\vec{b}\left(\tilde{t}\right)$ (see eq. (2.19)).

Simple case: If only the initial state is populated and the final state is initially empty ($b_i(0)^2 = 1 \;\&\; b_f(0)^2 = 0$), everything is easier to calculate. In general this is true, if the initial state can pass the selector regions and the final state is blocked (e.g. $|1\rangle \rightarrow |5\rangle$). This simplifies the calculation to:

$$\begin{aligned}\begin{pmatrix}b_i\left(\tilde{t}\right)\\ b_f\left(\tilde{t}\right)\end{pmatrix} &= \begin{pmatrix}\cos\left(\frac{\Omega_R\tilde{t}}{2}\right)-\mathrm{i}\frac{\Delta\omega}{\Omega_R}\sin\left(\frac{\Omega_R\tilde{t}}{2}\right) & -\frac{a_vV_{fi}}{\Omega_R}\sin\left(\frac{\Omega_R\tilde{t}}{2}\right)\mathrm{e}^{\mathrm{i}\phi}\\ \frac{a_vV_{fi}}{\Omega_R}\sin\left(\frac{\Omega_R\tilde{t}}{2}\right)\mathrm{e}^{-\mathrm{i}\phi} & \cos\left(\frac{\Omega_R\tilde{t}}{2}\right)+\mathrm{i}\frac{\Delta\omega}{\Omega_R}\sin\left(\frac{\Omega_R\tilde{t}}{2}\right)\end{pmatrix}\begin{pmatrix}1\\0\end{pmatrix} \\ &= \begin{pmatrix}\cos\left(\frac{\Omega_R\tilde{t}}{2}\right)-\mathrm{i}\frac{\Delta\omega}{\Omega_R}\sin\left(\frac{\Omega_R\tilde{t}}{2}\right)\\ \frac{a_vV_{fi}}{\Omega_R}\sin\left(\frac{\Omega_R\tilde{t}}{2}\right)\mathrm{e}^{-\mathrm{i}\phi}\end{pmatrix}\end{aligned} \tag{2.101}$$

Probability of a flip (a state transition) P is implemented in the *Mathematica* data analysis as the function $Prabi[\omega, i, f, a_v, \tilde{t}, g]$ [18]:

$$P_{fi}\left(\tilde{t}\right) = |b_f\left(\tilde{t}\right)|^2 = \left|\frac{a_vV_{fi}}{\Omega_R}\sin\left(\frac{\Omega_R\tilde{t}}{2}\right)\mathrm{e}^{-\mathrm{i}\phi}\right|^2 = \left(\frac{a_vV_{fi}}{\Omega_R}\right)^2\sin^2\left(\frac{\Omega_R\tilde{t}}{2}\right) \tag{2.102}$$

[18] The result can be compared to previous works [139](p.60, eq.3.29), [264](p.17, eq.2.12), [254](p.35, eq.4.30), [196](p.123 eq.2).

In order to completely flip the state from the initial (lower) state to the final (higher) state, the following conditions have to be fulfilled at resonance ($\Delta\omega = 0$) depending on the mirror length l_{II} and the neutron velocity v_n ($\tilde{t} = l_{II}/v_\mathrm{n}$) [254](p.35-36):

$$P_{fi}\left(\tilde{t}\right) = 1 = \left(\frac{a_v V_{fi}}{\Omega_R}\right)^2 \sin^2\left(\frac{\Omega_R \tilde{t}}{2}\right) = \frac{\left(a_v V_{fi}\right)^2}{{a_v V_{fi}}^2 + {\Delta\omega}^2} \sin^2\left(\frac{\sqrt{\left(a_v V_{fi}\right)^2 + {\Delta\omega^2}}\tilde{t}}{2}\right) = \sin^2\left(\frac{a_v V_{fi}\tilde{t}}{2}\right)$$

$$\frac{a_v V_{fi} l_{II}}{2 v_\mathrm{n}} = \frac{a_v V_{fi}\tilde{t}}{2} = \frac{2n+1}{2}\pi \quad \rightarrow \quad a_v = \frac{\pi}{V_{fi}\tilde{t}} = \frac{\pi v_\mathrm{n}}{V_{fi} l_{II}} \tag{2.103}$$

Interestingly, there is a simple linear relation between the resonance frequency ν_{fi} and its optimal oscillation strength a_v for a π-flip. The connecting factor is $\frac{\pi v_\mathrm{n} h}{l_{II} m_\mathrm{n} g}$ which can be derived by inserting the definitions of the matrix element V_{fi} and the resonance frequency into their ratio. Normally, Rabi transitions are displayed and measured with a constant oscillation strength a_v in order to have a symmetric function around the resonance. For measurements of multiple transitions it would make more sense to adapt the oscillation strength a_v according to the frequency correlation. This would distort the shape of each transition but each one would have the highest possible contrast which increases the statistical significance of the measurement.

The calculation of the transmission of the initial state T is quite similar to the transition probability P. The detector measures only the transmission of the lower initial state because the higher final state has in the most cases (state 4 or higher) a nearly zero transmission through the final selector region (similar results [65](p.14, eq. 2.15), [193](p.12 eq. 30)):

$$T_{fi}\left(\tilde{t}\right) = \left|b_i\left(\tilde{t}\right)\right|^2 = \left(\frac{a_v V_{fi}}{\Omega_R}\right)^2 \cos^2\left(\frac{\Omega_R \tilde{t}}{2}\right) + \left(\frac{\Delta\omega}{\Omega_R}\right)^2 = 1 - P_{fi}\left(\tilde{t}\right) \tag{2.104}$$

General case: In the general case both states are partly occupied. This is more complicated and only necessary if both states can pass the first absorber. All transitions to the 4th state or higher can be treated as initial pure lower states. For the transitions $|1\rangle \rightarrow |2\rangle$, $|1\rangle \rightarrow |3\rangle$ and $|2\rangle \rightarrow |3\rangle$ this more complicated calculation should be considered:

$$\begin{pmatrix} b_i\left(\tilde{t}\right) \\ b_f\left(\tilde{t}\right) \end{pmatrix} = \begin{pmatrix} b_i(0)\cos\left(\frac{\Omega_R\tilde{t}}{2}\right) - b_f(0)\frac{a_v V_{fi}}{\Omega_R}\sin\left(\frac{\Omega_R\tilde{t}}{2}\right)\mathrm{e}^{\mathrm{i}\phi} - \mathrm{i}b_i(0)\frac{\Delta\omega}{\Omega_R}\sin\left(\frac{\Omega_R\tilde{t}}{2}\right) \\ b_i(0)\frac{a_v V_{fi}}{\Omega_R}\sin\left(\frac{\Omega_R\tilde{t}}{2}\right)\mathrm{e}^{-\mathrm{i}\phi} + b_f(0)\cos\left(\frac{\Omega_R\tilde{t}}{2}\right) + \mathrm{i}b_f(0)\frac{\Delta\omega}{\Omega_R}\sin\left(\frac{\Omega_R\tilde{t}}{2}\right) \end{pmatrix} \tag{2.105}$$

The probability of a flip with both states initially populated corresponds now to the more complex form, which takes also into account transitions from the final state to the initial state:

$$\begin{aligned} P_{fi}\left(\tilde{t}\right) = \left|b_f\left(\tilde{t}\right)\right|^2 &= b_f^2(0) + \sin^2\left(\frac{\Omega_R\tilde{t}}{2}\right)\left(\frac{a_v V_{fi}}{\Omega_R}\right)^2\left[b_i^2(0) - b_f^2(0)\right] \\ &+ 2b_i(0)b_f(0)\frac{a_v V_{fi}}{\Omega_R}\sin\left(\frac{\Omega_R\tilde{t}}{2}\right)\left[\cos\left(\frac{\Omega_R\tilde{t}}{2}\right)\cos(\phi) - \frac{\Delta\omega}{\Omega_R}\sin\left(\frac{\Omega_R\tilde{t}}{2}\right)\sin(\phi)\right] \end{aligned}$$

The initial phase ϕ cannot be determined. An integration over all possible settings of it reflects the situation of the measurement[19]:

$$\frac{1}{2\pi}\int_0^{2\pi} P_{fi}\left(\tilde{t}\right)\mathrm{d}\phi = b_f^2(0) + \sin^2\left(\frac{\Omega_R\tilde{t}}{2}\right)\left(\frac{a_v V_{fi}}{\Omega_R}\right)^2\left[b_i^2(0) - b_f^2(0)\right] \tag{2.106}$$

Probability of the transmission of the lower state (initial) is in general not the value that is measured by the detector. The higher final state will also have a probability to pass the final absorber as it has passed the first one. This can be interpreted as a background in the order of $b_f^2(0)$ and a reduced contrast of the transitions ($c_{fi} \approx b_i^2(0) - b_f^2(0)$). However, it is stronger suppressed as the lower initial state:

$$\begin{aligned} T_{fi}\left(\tilde{t}\right) = \left|b_i\left(\tilde{t}\right)\right|^2 &= b_i^2(0) + \left(\frac{a_v V_{fi}}{\Omega_R}\right)^2\sin^2\left(\frac{\Omega_R\tilde{t}}{2}\right)\left[b_f^2(0) - b_i^2(0)\right] \\ &- 2b_i(0)b_f(0)\frac{a_v V_{fi}}{\Omega_R}\sin\left(\frac{\Omega_R\tilde{t}}{2}\right)\left[\cos\left(\frac{\Omega_R\tilde{t}}{2}\right)\cos\phi + \frac{\Delta\omega}{\Omega_R}\sin\left(\frac{\Omega_R\tilde{t}}{2}\right)\sin\phi\right] \end{aligned}$$

[19] If the phase is not included in the calculation from the beginning, then the phase term will not vanish because this calculation path sets the initial phase ϕ to zero. Similar approaches can be found in [65](p.14, eq.2.17), [267](p.16, eq 2.35).

Again it is necessary to integrate over the initial phase ϕ in order to gain a reasonable solution. The result is equivalent to [65](p.14, eq. 2.16) or [194](p.21 eq. 2.28):

$$\frac{1}{2\pi}\int_0^{2\pi} T_{fi}\left(\tilde{t}\right)\mathrm{d}\phi = b_i^2(0) + \left(\frac{a_v V_{fi}}{\Omega_R}\right)^2 \sin^2\left(\frac{\Omega_R \tilde{t}}{2}\right)\left[b_f^2(0) - b_i^2(0)\right] \tag{2.107}$$

Multi 2-level Theory

Within GRS multiple transitions can be addressed. Especially, if the second or even the third state are populated[20], these transitions can overlap in frequency space[21]. There are multiple approaches to deal with these overlapping transitions. The most simple one is the multi 2-level approach. All transitions are taken as independent and they are acting on different neutrons. These approaches are further divided in two different groups: the contrast based ones and the state based ones. Both are described in more detail below. All multi 2-level approaches only work for well separated transitions. If a state has more than one possibility for a transition at a given frequency, this kind of description fails, especially at higher amplitudes. There a so-called state hopping can occur (e.g. $|1\rangle \to |7\rangle \to |16\rangle$ around 1116 Hz). A very special region is at low frequencies (<300 Hz). There are all neighboring transitions sharing a common addressed state which makes the ladder even easier (e.g. $|1\rangle \to |2\rangle \to |3\rangle$ around 225 Hz). An analytic generalization for more states is limited. Tobias Jenke showed that 3-level calculations are possible if one transition is neglected (e.g. $|1\rangle \to |3\rangle$ in the last example) [139](p.63-65). A more general approach are true multilevel calculations. Only they can take state hopping into account. Their disadvantage is their need for computational power. All general multilevel approaches have in common that they do not have analytical solutions and can only be calculated numerically.

In the most simple case of state based approaches, only a population of the first three states is allowed and their populations add up to one in the beginning ($b_3 = 1 - b_1 - b_2$). Higher states are not able to reach the detector as the third state. Here is the combination of all relevant transitions effecting the transmission up to 600 Hz:

$$T_{Fit}[\omega, b_1, b_2, a_v, t] := 1 - (b_1 + 2b_2 - 1)P_{23} - b_2 P_{24} - (2b_1 + b_2 - 1)P_{13} - b_2 P_{25} \tag{2.108}$$

More sophisticated state based models take into account all involved states, a common background rate and the transition probability of all accounted states through the second absorber. The strength of such model is to describe multiple transitions of similar states with only fewer parameters (e.g. 300 Hz to 1000 Hz: 9 states involved and 14 possible transitions for only low states populated in the beginning).

On the contrary, contrasted based models are advantageous if only few transitions are taken into account. Here the transition probability is scaled with an individual contrast parameter. An example is the used model of Gunther Cronenberg for his measured GRS with the RABI^{GC}-setup [65](p.14-15, eq 2.19; p.47, eq 4.2):

$$T_{Fit}[\omega, a_v] := 1 - c_{13}P_{13} - c_{14}P_{14} \tag{2.109}$$

Here the contrasts c_{if} are together with g the fit parameters during the data evaluation. He didn't take into account a strongly populated second state and its transitions in the same frequency region ($|2\rangle \to |4\rangle$ & $|2\rangle \to |5\rangle$). This can potentially induce a shift in the transition frequency.
For the RABI-GRS-18, RAMSEY-GRS-18 and the Rams$\vec{E}$y measurements, these additional transitions are taken into account accordingly to the measured transitions[22]. If the neighboring transitions are not measured (mainly during the Ramsey-type measurements), a fixed contrast is presumed (values from RABI-GRS-18). This thesis and the included analysis use a contrast-based multi 2-level model:

$$T_{Fit}[\omega, a_v] := 1 - c_{12}P_{12} - c_{13}P_{13} - c_{14}P_{14} - c_{23}P_{23} - c_{24}P_{24} - c_{25}P_{25} \tag{2.110}$$

[20] The mixing depends on the state selector in region I and is experimentally always observed (see more in [194](p.14-16)).
[21] At a typical interaction time τ of around 17 ms, the transition width b of the neighboring transitions $|2\rangle \to |3\rangle$ (208.41 Hz) and $|1\rangle \to |2\rangle$ (254.56 Hz) is around 23 Hz for both transitions which is close to half of their distance to each other.
[22] All multi-state considerations can be applied to Rabi and Ramsey-type GRS similarly.

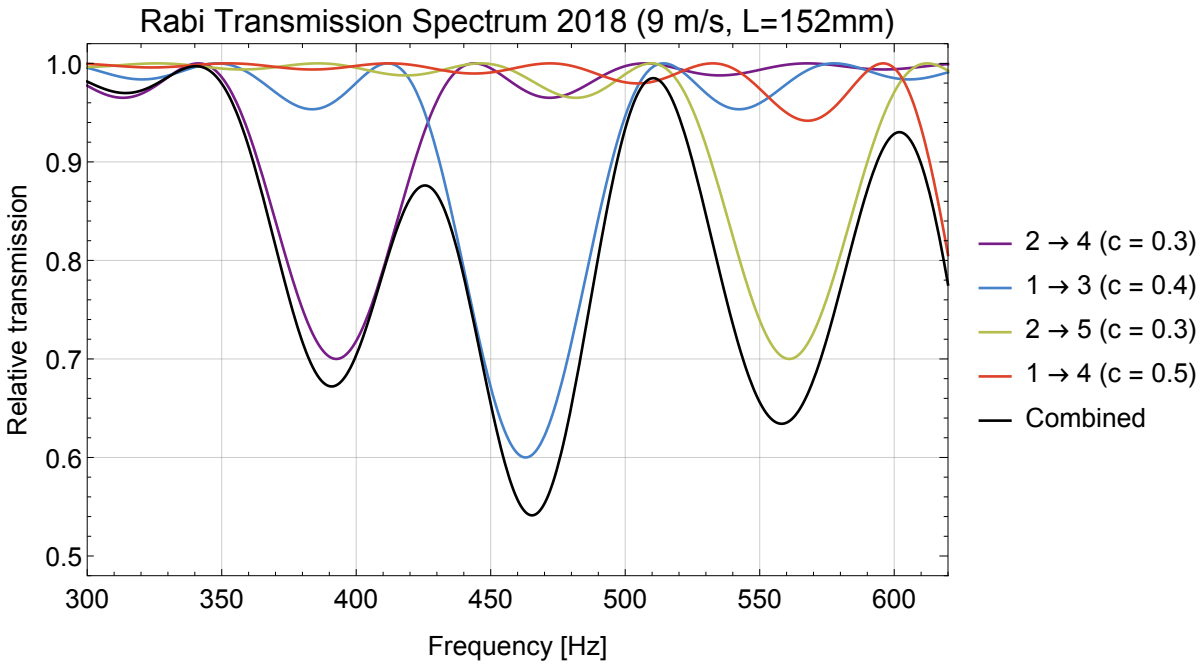

Figure 2.6.: Single Rabi transmission with constant optimal oscillation strength a_v (colored) versus the combined multi 2-level theory function with adapted amplitude (black). The contrast increases for all transitions due to the side bands of the other transitions. Caution, the center of the peaks shifts slightly due to the neighboring transitions (spectator shift).

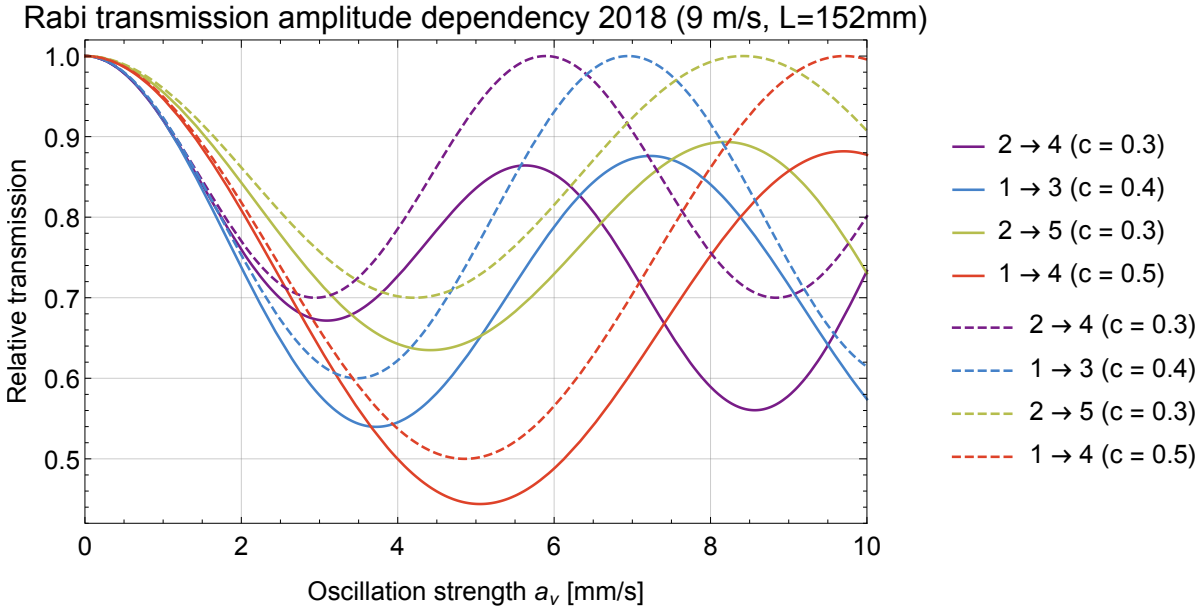

Figure 2.7.: Single Rabi transmissions at their corresponding resonance frequency and varied oscillation strength a_v. The dashed lines represent the theoretical curves of single transitions. The continuous lines are based on the multi 2-level theory function where the side bands of neighboring transition are taken into account. This increases the maximal transmission drop and shifts it to higher amplitude strength. However, there is no full revival of the wave function anymore.

2.2.2. Rabi to Ramsey spectroscopy

The 2-Level solution from a Rabi excitation (eq. 2.80) can also be described as (see [194](p.21-22), [196], [264](p.18-19)):

$$\vec{b}\left(\tilde{t}\right) = U\left(\tilde{t},0\right)\vec{b}(0) \tag{2.111}$$

Ramsey transitions can be written similarly as two consecutive Rabi transitions $U\left(\tilde{t}_f,\tilde{t}_i\right)$ with a free time evolution $M(t_p)$ in between [250]. Eq. (2.92) describes the first Rabi pulse $U(\tau_{II},0)$ in region II including the phase ϕ_{II}. The 2nd Rabi pulse $U(\tau_{II}+t_p+\tau_{IV},\tau_{II}+t_p)$ needs the time shifted equation (2.94) as a template. In the oscillating frame, the free time evolution $M(\tau_{II}+t_p,\tau_{II})$ is an identity matrix[23]. The interaction times τ_{II} and τ_{IV} are the travel times of neutrons through region II and region IV respectively. Within the RAMSEY$^{\text{TR}}$-setup their lengths are equal and the neutron velocity stays constant. Therefore, they are equal ($\tau \approx 152\,\text{mm}/9\,\text{m}\,\text{s}^{-1} = 16.9\,\text{ms}$). The propagation time t_p corresponds to the flight time through region III ($t_p \approx 340\,\text{mm}/9\,\text{m}\,\text{s}^{-1} = 37.8\,\text{ms}$):

$$\vec{b}\left(\tau_{II}+t_p+\tau_{IV}\right) = U(\tau_{II}+t_p+\tau_{IV},\tau_{II}+t_p)\,M(\tau_{II}+t_p,\tau_{II})\,U(\tau_{II},0)\,\vec{b}(0) \tag{2.112}$$

With this evolution of the state occupations the Ramsey transition probability is calculated in the following (Note that eventhough region II and region IV have the same length, they can oscillate at different frequencies ω and different oscillation strengths a_v which also changes the detuned angular frequency $\Delta\omega$, the *Rabi frequency* $a_v V_{fi}$ and the *general Rabi frequency* Ω_R accordingly). Similar calculations can be found in [267](p.14-16), [254](p.36-41), [194](p.21-22), [196]. The most general time depending state occupation is depicted in the following:

$$\begin{aligned}
&b_i(\tau_{II}+t_p+\tau_{IV}) = \\
&= \left[\cos\left(\frac{\tau_{IV}\Omega_{RIV}}{2}\right) - \mathrm{i}\frac{\Delta\omega_{IV}}{\Omega_{RIV}}\sin\left(\frac{\tau_{IV}\Omega_{RIV}}{2}\right)\right]\left[\cos\left(\frac{\Omega_{RII}}{2}\tau_{II}\right) - \mathrm{i}\frac{\Delta\omega_{II}}{\Omega_{RII}}\sin\left(\frac{\Omega_{RII}}{2}\tau_{II}\right)\right]\mathrm{e}^{\frac{\mathrm{i}\Delta\omega_{IV}\tau_{IV}}{2}}\mathrm{e}^{\frac{\mathrm{i}\Delta\omega_{II}\tau_{II}}{2}}b_i(0) \\
&\quad - \left[\cos\left(\frac{\tau_{IV}\Omega_{RIV}}{2}\right) - \mathrm{i}\frac{\Delta\omega_{IV}}{\Omega_{RIV}}\sin\left(\frac{\tau_{IV}\Omega_{RIV}}{2}\right)\right]\frac{(a_vV_{fi})_{II}}{\Omega_{RII}}\sin\left(\frac{\Omega_{RII}}{2}\tau_{II}\right)\mathrm{e}^{\frac{\mathrm{i}\Delta\omega_{IV}\tau_{IV}}{2}}\mathrm{e}^{\frac{\mathrm{i}\Delta\omega_{II}\tau_{II}}{2}}\mathrm{e}^{\mathrm{i}\phi_{II}}b_f(0) \\
&\quad - \frac{(a_vV_{fi})_{IV}}{\Omega_{RIV}}\sin\left(\frac{\tau_{IV}\Omega_{RIV}}{2}\right)\frac{(a_vV_{fi})_{II}}{\Omega_{RII}}\sin\left(\frac{\Omega_{RII}}{2}\tau_{II}\right)\mathrm{e}^{\mathrm{i}\Delta\omega_{IV}\left(\tau_{II}+t_p+\frac{\tau_{IV}}{2}\right)}\mathrm{e}^{-\frac{\mathrm{i}\Delta\omega_{II}\tau_{II}}{2}}\mathrm{e}^{\mathrm{i}\Delta\phi}b_i(0) \\
&\quad - \frac{(a_vV_{fi})_{IV}}{\Omega_{RIV}}\sin\left(\frac{\tau_{IV}\Omega_{RIV}}{2}\right)\left[\cos\left(\frac{\Omega_{RII}}{2}\tau_{II}\right) + \mathrm{i}\frac{\Delta\omega_{II}}{\Omega_{RII}}\sin\left(\frac{\Omega_{RII}}{2}\tau_{II}\right)\right]\mathrm{e}^{\mathrm{i}\Delta\omega_{IV}\left(\tau_{II}+t_p+\frac{\tau_{IV}}{2}\right)}\mathrm{e}^{-\frac{\mathrm{i}\Delta\omega_{II}\tau_{II}}{2}}\mathrm{e}^{\mathrm{i}\phi_{IV}}b_f(0)
\end{aligned} \tag{2.113}$$

$$\begin{aligned}
&b_f(\tau_{II}+t_p+\tau_{IV}) = \\
&= \frac{(a_vV_{fi})_{IV}}{\Omega_{RIV}}\sin\left(\frac{\tau_{IV}\Omega_{RIV}}{2}\right)\mathrm{e}^{-\mathrm{i}\phi_{IV}}\left[\cos\left(\frac{\Omega_{RII}}{2}\tau_{II}\right) - \mathrm{i}\frac{\Delta\omega_{II}}{\Omega_{RII}}\sin\left(\frac{\Omega_{RII}}{2}\tau_{II}\right)\right]\mathrm{e}^{-\mathrm{i}\Delta\omega_{IV}\left(\tau_{II}+t_p+\frac{\tau_{IV}}{2}\right)}\mathrm{e}^{\frac{\mathrm{i}\Delta\omega_{II}\tau_{II}}{2}}b_i(0) \\
&\quad - \frac{(a_vV_{fi})_{IV}}{\Omega_{RIV}}\sin\left(\frac{\tau_{IV}\Omega_{RIV}}{2}\right)\frac{(a_vV_{fi})_{II}}{\Omega_{RII}}\sin\left(\frac{\Omega_{RII}}{2}\tau_{II}\right)\mathrm{e}^{-\mathrm{i}\Delta\omega_{IV}\left(\tau_{II}+t_p+\frac{\tau_{IV}}{2}\right)}\mathrm{e}^{\frac{\mathrm{i}\Delta\omega_{II}\tau_{II}}{2}}\mathrm{e}^{-\mathrm{i}\Delta\phi}b_f(0) \\
&\quad + \left[\cos\left(\frac{\tau_{IV}\Omega_{RIV}}{2}\right) + \mathrm{i}\frac{\Delta\omega_{IV}}{\Omega_{RIV}}\sin\left(\frac{\tau_{IV}\Omega_{RIV}}{2}\right)\right]\frac{(a_vV_{fi})_{II}}{\Omega_{RII}}\sin\left(\frac{\Omega_{RII}}{2}\tau_{II}\right)\mathrm{e}^{-\frac{\mathrm{i}\Delta\omega_{IV}\tau_{IV}}{2}}\mathrm{e}^{-\frac{\mathrm{i}\Delta\omega_{II}\tau_{II}}{2}}\mathrm{e}^{-\mathrm{i}\phi_{II}}b_i(0) \\
&\quad + \left[\cos\left(\frac{\tau_{IV}\Omega_{RIV}}{2}\right) + \mathrm{i}\frac{\Delta\omega_{IV}}{\Omega_{RIV}}\sin\left(\frac{\tau_{IV}\Omega_{RIV}}{2}\right)\right]\left[\cos\left(\frac{\Omega_{RII}}{2}\tau_{II}\right) + \mathrm{i}\frac{\Delta\omega_{II}}{\Omega_{RII}}\sin\left(\frac{\Omega_{RII}}{2}\tau_{II}\right)\right]\mathrm{e}^{-\frac{\mathrm{i}\Delta\omega_{IV}\tau_{IV}}{2}}\mathrm{e}^{-\frac{\mathrm{i}\Delta\omega_{II}\tau_{II}}{2}}b_f(0)
\end{aligned} \tag{2.114}$$

[23] This is the result of describing $M(\tau_{II}+t_p,\tau_{II})$ as a Rabi pulse $U(\tau_{II}+t_p,\tau_{II})$ with no oscillation ($a_v = \omega = 0$, $\Omega_R = \Delta\omega = -\omega_{fi}$).

A first simplification is to set the same interaction time as previously described ($\tau_{II} = \tau_{IV} = \tau$):

$$\begin{aligned}
b_i(2\tau + t_p) = &\left[\cos\left(\frac{\Omega_{RIV}}{2}\tau\right) - \mathrm{i}\frac{\Delta\omega_{IV}}{\Omega_{RIV}}\sin\left(\frac{\Omega_{RIV}}{2}\tau\right)\right]\left[\cos\left(\frac{\Omega_{RII}}{2}\tau\right) - \mathrm{i}\frac{\Delta\omega_{II}}{\Omega_{RII}}\sin\left(\frac{\Omega_{RII}}{2}\tau\right)\right]\mathrm{e}^{\frac{\mathrm{i}(\Delta\omega_{IV}+\Delta\omega_{II})\tau}{2}}b_i(0)\\
&- \left[\cos\left(\frac{\Omega_{RIV}}{2}\tau\right) - \mathrm{i}\frac{\Delta\omega_{IV}}{\Omega_{RIV}}\sin\left(\frac{\Omega_{RIV}}{2}\tau\right)\right]\frac{(a_vV_{fi})_{II}}{\Omega_{RII}}\sin\left(\frac{\Omega_{RII}}{2}\tau\right)\mathrm{e}^{\frac{\mathrm{i}(\Delta\omega_{IV}+\Delta\omega_{II})\tau}{2}}\mathrm{e}^{\mathrm{i}\phi_{II}}b_f(0)\\
&- \frac{(a_vV_{fi})_{IV}}{\Omega_{RIV}}\sin\left(\frac{\Omega_{RIV}}{2}\tau\right)\frac{(a_vV_{fi})_{II}}{\Omega_{RII}}\sin\left(\frac{\Omega_{RII}}{2}\tau\right)\mathrm{e}^{\mathrm{i}\Delta\omega_{IV}\left(t_p+\frac{3\tau}{2}\right)}\mathrm{e}^{-\frac{\mathrm{i}\Delta\omega_{II}\tau}{2}}\mathrm{e}^{\mathrm{i}\Delta\phi}b_i(0)\\
&- \frac{(a_vV_{fi})_{IV}}{\Omega_{RIV}}\sin\left(\frac{\Omega_{RIV}}{2}\tau\right)\left[\cos\left(\frac{\Omega_{RII}}{2}\tau\right) + \mathrm{i}\frac{\Delta\omega_{II}}{\Omega_{RII}}\sin\left(\frac{\Omega_{RII}}{2}\tau\right)\right]\mathrm{e}^{\mathrm{i}\Delta\omega_{IV}\left(t_p+\frac{3\tau}{2}\right)}\mathrm{e}^{-\frac{\mathrm{i}\Delta\omega_{II}\tau}{2}}\mathrm{e}^{\mathrm{i}\phi_{IV}}b_f(0)
\end{aligned} \tag{2.115}$$

$$\begin{aligned}
b_f(2\tau + t_p) = &\frac{(a_vV_{fi})_{IV}}{\Omega_{RIV}}\sin\left(\frac{\Omega_R\tau_{IV}}{2}\right)\mathrm{e}^{-\mathrm{i}\phi_{IV}}\left[\cos\left(\frac{\Omega_{RII}}{2}\tau\right) - \mathrm{i}\frac{\Delta\omega_{II}}{\Omega_{RII}}\sin\left(\frac{\Omega_{RII}}{2}\tau\right)\right]\mathrm{e}^{-\mathrm{i}\Delta\omega_{IV}\left(t_p+\frac{3\tau}{2}\right)}\mathrm{e}^{\frac{\mathrm{i}\Delta\omega_{II}\tau}{2}}b_i(0)\\
&- \frac{(a_vV_{fi})_{IV}}{\Omega_{RIV}}\sin\left(\frac{\Omega_R\tau_{IV}}{2}\right)\frac{(a_vV_{fi})_{II}}{\Omega_{RII}}\sin\left(\frac{\Omega_{RII}}{2}\tau\right)\mathrm{e}^{-\mathrm{i}\Delta\omega_{IV}\left(t_p+\frac{3\tau}{2}\right)}\mathrm{e}^{\frac{\mathrm{i}\Delta\omega_{II}\tau}{2}}\mathrm{e}^{-\mathrm{i}\Delta\phi}b_f(0)\\
&+ \left[\cos\left(\frac{\Omega_R\tau_{IV}}{2}\right) + \mathrm{i}\frac{\Delta\omega_{IV}}{\Omega_{RIV}}\sin\left(\frac{\Omega_R\tau_{IV}}{2}\right)\right]\frac{(a_vV_{fi})_{II}}{\Omega_{RII}}\sin\left(\frac{\Omega_{RII}}{2}\tau\right)\mathrm{e}^{-\frac{\mathrm{i}(\Delta\omega_{IV}+\Delta\omega_{II})\tau}{2}}\mathrm{e}^{-\mathrm{i}\phi_{II}}b_i(0)\\
&+ \left[\cos\left(\frac{\Omega_R\tau_{IV}}{2}\right) + \mathrm{i}\frac{\Delta\omega_{IV}}{\Omega_{RIV}}\sin\left(\frac{\Omega_R\tau_{IV}}{2}\right)\right]\left[\cos\left(\frac{\Omega_{RII}}{2}\tau\right) + \mathrm{i}\frac{\Delta\omega_{II}}{\Omega_{RII}}\sin\left(\frac{\Omega_{RII}}{2}\tau\right)\right]\mathrm{e}^{-\frac{\mathrm{i}(\Delta\omega_{IV}+\Delta\omega_{II})\tau}{2}}b_f(0)
\end{aligned} \tag{2.116}$$

For transition to 4th state or any higher state the initial occupation of the higher state (final state) can be set to zero ($b_{>3}(0) = 0 = b_f(0) \rightarrow b_i(0) = 1$) because these states cannot pass through the absorbers. For the transition $|1\rangle \rightarrow |3\rangle$ this can be also used as an approximation (Note that only the phase difference $\Delta\phi$ between the regions is important from this approximation onward):

$$\begin{aligned}
b_i(2\tau + t_p) = &\left[\cos\left(\frac{\Omega_{RIV}}{2}\tau\right) - \mathrm{i}\frac{\Delta\omega_{IV}}{\Omega_{RIV}}\sin\left(\frac{\Omega_{RIV}}{2}\tau\right)\right]\left[\cos\left(\frac{\Omega_{RII}}{2}\tau\right) - \mathrm{i}\frac{\Delta\omega_{II}}{\Omega_{RII}}\sin\left(\frac{\Omega_{RII}}{2}\tau\right)\right]\mathrm{e}^{\frac{\mathrm{i}(\Delta\omega_{IV}+\Delta\omega_{II})\tau}{2}}b_i(0)\\
&- \frac{(a_vV_{fi})_{IV}}{\Omega_{RIV}}\sin\left(\frac{\Omega_{RIV}}{2}\tau\right)\frac{(a_vV_{fi})_{II}}{\Omega_{RII}}\sin\left(\frac{\Omega_{RII}}{2}\tau\right)\mathrm{e}^{\mathrm{i}\Delta\omega_{IV}\left(t_p+\frac{3\tau}{2}\right)}\mathrm{e}^{-\frac{\mathrm{i}\Delta\omega_{II}\tau}{2}}\mathrm{e}^{\mathrm{i}\Delta\phi}b_i(0)
\end{aligned} \tag{2.117}$$

$$\begin{aligned}
b_f(2\tau + t_p) = &\frac{(a_vV_{fi})_{IV}}{\Omega_{RIV}}\sin\left(\frac{\Omega_R\tau_{IV}}{2}\right)\left[\cos\left(\frac{\Omega_{RII}}{2}\tau\right) - \mathrm{i}\frac{\Delta\omega_{II}}{\Omega_{RII}}\sin\left(\frac{\Omega_{RII}}{2}\tau\right)\right]\mathrm{e}^{-\mathrm{i}\Delta\omega_{IV}\left(t_p+\frac{3\tau}{2}\right)}\mathrm{e}^{\frac{\mathrm{i}\Delta\omega_{II}\tau}{2}}\mathrm{e}^{-\mathrm{i}\phi_{IV}}b_i(0)\\
&+ \left[\cos\left(\frac{\Omega_R\tau_{IV}}{2}\right) + \mathrm{i}\frac{\Delta\omega_{IV}}{\Omega_{RIV}}\sin\left(\frac{\Omega_R\tau_{IV}}{2}\right)\right]\frac{(a_vV_{fi})_{II}}{\Omega_{RII}}\sin\left(\frac{\Omega_{RII}}{2}\tau\right)\mathrm{e}^{-\frac{\mathrm{i}(\Delta\omega_{IV}+\Delta\omega_{II})\tau}{2}}\mathrm{e}^{-\mathrm{i}\phi_{II}}b_i(0)
\end{aligned} \tag{2.118}$$

The set frequencies are commonly the same during all measurements because they come from the same source ($\Delta\omega_{II} = \Delta\omega_{IV} = \Delta\omega$). In general, this is not the case for the oscillation strength ($a_{vII} \neq a_{vIV} \neq a_v$). Due to the different mechanical response of the regions, the variation is normally in the permille regime:

$$\begin{aligned}
b_i(2\tau + t_p) = &\left[\cos\left(\frac{\Omega_{RIV}}{2}\tau\right) - \mathrm{i}\frac{\Delta\omega}{\Omega_{RIV}}\sin\left(\frac{\Omega_{RIV}}{2}\tau\right)\right]\left[\cos\left(\frac{\Omega_{RII}}{2}\tau\right) - \mathrm{i}\frac{\Delta\omega}{\Omega_{RII}}\sin\left(\frac{\Omega_{RII}}{2}\tau\right)\right]\mathrm{e}^{\mathrm{i}\Delta\omega\tau}b_i(0)\\
&- \frac{(a_vV_{fi})_{IV}}{\Omega_{RIV}}\sin\left(\frac{\Omega_{RIV}}{2}\tau\right)\frac{(a_vV_{fi})_{II}}{\Omega_{RII}}\sin\left(\frac{\Omega_{RII}}{2}\tau\right)\mathrm{e}^{\mathrm{i}\Delta\omega(t_p+\tau)}\mathrm{e}^{\mathrm{i}\Delta\phi}b_i(0)
\end{aligned} \tag{2.119}$$

$$\begin{aligned}
b_f(2\tau + t_p) = &\frac{(a_vV_{fi})_{IV}}{\Omega_{RIV}}\sin\left(\frac{\Omega_R\tau_{IV}}{2}\right)\left[\cos\left(\frac{\Omega_{RII}}{2}\tau\right) - \mathrm{i}\frac{\Delta\omega}{\Omega_{RII}}\sin\left(\frac{\Omega_{RII}}{2}\tau\right)\right]\mathrm{e}^{-\mathrm{i}\Delta\omega(t_p+\tau)}\mathrm{e}^{-\mathrm{i}\phi_{IV}}b_i(0)\\
&+ \left[\cos\left(\frac{\Omega_R\tau_{IV}}{2}\right) + \mathrm{i}\frac{\Delta\omega}{\Omega_{RIV}}\sin\left(\frac{\Omega_R\tau_{IV}}{2}\right)\right]\frac{(a_vV_{fi})_{II}}{\Omega_{RII}}\sin\left(\frac{\Omega_{RII}}{2}\tau\right)\mathrm{e}^{-\mathrm{i}\Delta\omega\tau}\mathrm{e}^{-\mathrm{i}\phi_{II}}b_i(0)
\end{aligned} \tag{2.120}$$

In ideal case even the oscillation amplitudes are the same ($a_{vII} = a_{vIV} = a_v$) and therefore also the general Rabi frequencies are equal ($\Omega_{RII} = \Omega_{RIV} = \Omega_R$). If both amplitudes are only similar (e.g. adjusted to each other as well as possible), the mean amplitude strength would be a good approximation ($(a_{vII} + a_{vIV})/2 = a_v$):

$$b_i(2\tau+t_p) = \left[1-\sin^2\left(\frac{\Omega_R\tau}{2}\right)\left[1+\left(\frac{\Delta\omega}{\Omega_R}\right)^2+\left(\frac{a_v V_{fi}}{\Omega_R}\right)^2\cos(\Delta\omega t_p+\Delta\phi)\right]\right.$$
$$\left.-\,\mathrm{i}\left[\left(\frac{a_v V_{fi}}{\Omega_R}\right)^2\sin^2\left(\frac{\Omega_R\tau}{2}\right)\sin(\Delta\omega t_p+\Delta\phi)+2\frac{\Delta\omega}{\Omega_R}\cos\left(\frac{\Omega_R\tau}{2}\right)\sin\left(\frac{\Omega_R\tau}{2}\right)\right]\right]\mathrm{e}^{\mathrm{i}\Delta\omega\tau}b_i(0) \tag{2.121}$$

$$b_f(2\tau+t_p) = 2\frac{a_v V_{fi}}{\Omega_R}\sin\left(\frac{\Omega_R\tau}{2}\right)b_i(0)\left[\cos\left(\frac{\Delta\omega t_p+\Delta\phi}{2}\right)+\mathrm{i}\sin\left(\frac{\Delta\omega t_p+\Delta\phi}{2}\right)\right]$$
$$\cdot\left[\cos\left(\frac{\Omega_R\tau}{2}\right)\cos\left(\frac{\Delta\omega t_p+\Delta\phi}{2}\right)-\frac{\Delta\omega}{\Omega_R}\sin\left(\frac{\Omega_R\tau}{2}\right)\sin\left(\frac{\Delta\omega t_p+\Delta\phi}{2}\right)\right]\mathrm{e}^{-\mathrm{i}\Delta\omega(t_p+\tau)}\mathrm{e}^{-\mathrm{i}\phi_{IV}} \tag{2.122}$$

The neutron transmission T is the absolute square of the lower initial state population (similar to Rabi-type GRS-setups). It can also be derived from the state transition probability P_{fi} between the two states:

$$T = |b_i(2\tau+t_p)|^2 = 1-P_{fi} \tag{2.123}$$

The state transition probability P_{fi} is easier to calculate:

$$P_{fi} = 4\frac{(a_v V_{fi})^2}{{\Omega_R}^2}\sin^2\left(\frac{\Omega_R\tau}{2}\right)\left[\cos\left(\frac{\Omega_R\tau}{2}\right)\cos\left(\frac{\Delta\omega t_p+\Delta\phi}{2}\right)-\frac{\Delta\omega}{\Omega_R}\sin\left(\frac{\Omega_R\tau}{2}\right)\sin\left(\frac{\Delta\omega t_p+\Delta\phi}{2}\right)\right]^2 \tag{2.124}$$

In the case of no phase difference ($\Delta\phi = 0$) this simplifies to the formula for the so-called *Simple Ramsey Model* (similar equations can be seen in [254](p.39, eq. 4.46), [194](p.22, eq.2.33), [196](p.123, eq. 4)). This is implemented in the *Mathematica* *q*BOUNCE-*support* package together with the solution including the phase. More general solutions are not yet implemented in this analysis:

$$P(a_v,\Delta\omega,\tau,t_p) = 4\left(\frac{a_v V_{fi}}{\Omega_R}\right)^2\sin^2\left(\frac{\Omega_R\tau}{2}\right)\left[\cos\left(\frac{\Omega_R\tau}{2}\right)\cos\left(\frac{\Delta\omega t_p}{2}\right)-\frac{\Delta\omega}{\Omega_R}\sin\left(\frac{\Omega_R\tau}{2}\right)\sin\left(\frac{\Delta\omega t_p}{2}\right)\right]^2 \tag{2.125}$$

In resonance ($\Delta\omega = 0$) everything simplifies ($\Omega_R = a_v V_{fi}$) to:

$$P(a_v,0,\tau,t_p) = 4\sin^2\left(\frac{a_v V_{fi}\tau}{2}\right)\left[\cos\left(\frac{a_v V_{fi}\tau}{2}\right)1-0\right]^2 = 4\sin^2\left(\frac{a_v V_{fi}\tau}{2}\right)\cos^2\left(\frac{a_v V_{fi}\tau}{2}\right) = \sin^2(a_v V_{fi}\tau)$$

The amplitude needed for a full state transition is half the amplitude of a Rabi-type GRS (2.103) with the same length l_{II} of one interaction region (region II)[24]:

$$a_v V_{fi}\tau = a_v V_{fi}\frac{l_{II}}{v_\mathrm{n}} = \frac{2n+1}{2}\pi \quad\rightarrow\quad a_v = \frac{\pi}{2V_{fi}\tau} = \frac{\pi v_\mathrm{n}}{2V_{fi}l_{II}} \tag{2.126}$$

[24]Similar calculations can be found in [267](p.17) and [194](p.23).

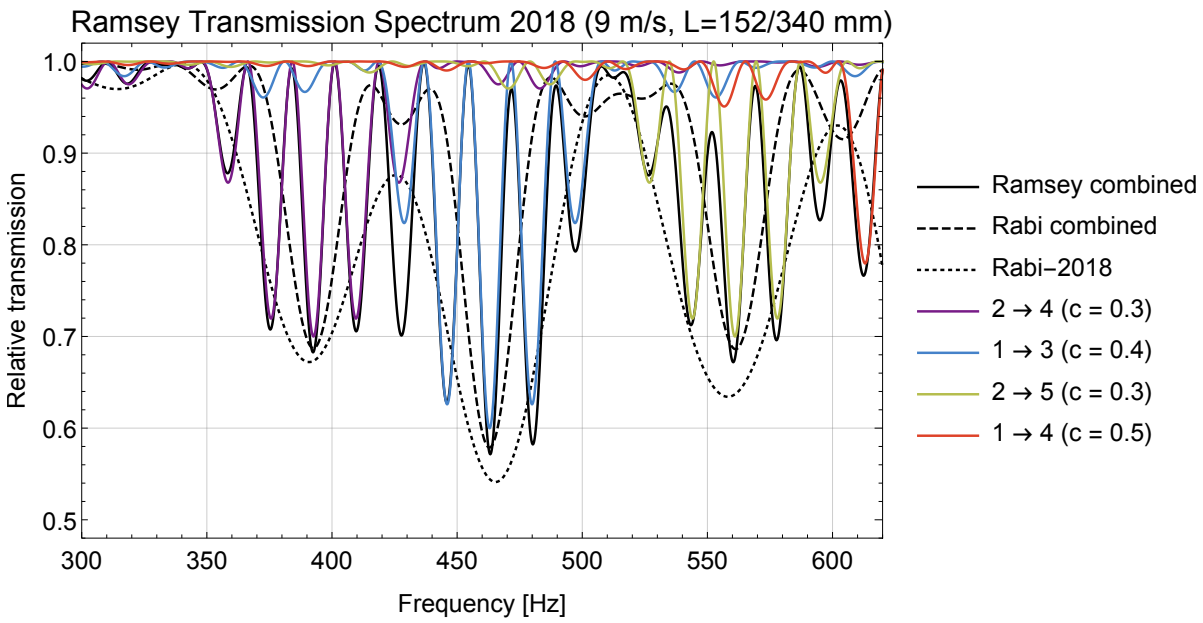

Figure 2.8.: A Ramsey transmission spectrum for a single velocity ($v_n = 9\,\mathrm{m/s}$) and mirror lengths of $l_{II} = 152\,\mathrm{mm}$ and $l_{III} = 340\,\mathrm{mm}$. The single 2-level transitions (colored) have a fixed oscillation strength a_v according to the flip condition (eq. (2.126)). The combined multi 2-level theory function (black) uses a frequency dependent oscillation strength a_v in order to deploy a full contrast for all transitions. The state transitions of the multilevel regime ($\nu < 300\,\mathrm{Hz}$) are not taken into account. For comparison two corresponding Rabi transmission curves are additionally displayed. The dashed line represents a Rabi-type GRS with the same interaction length ($2l_{II}$) and oscillation strength a_v as the displayed Ramsey-type GRS. The dotted line represents the RABI-GRS-18 setup which has only one interaction region and applies twice the oscillation strength a_v. The Rabi peaks are broader than the Ramsey transition and therefore less sensitive.

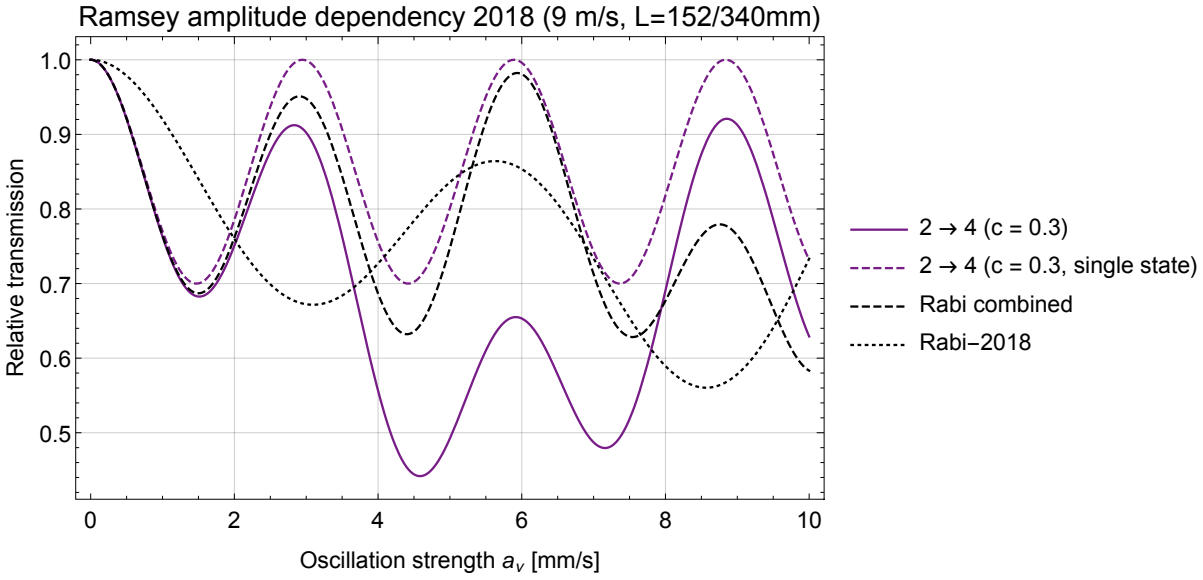

Figure 2.9.: A single state transition has a sine like dependency of the oscillation strength a_v (dashed colored line). Multi-state effects disturb this pattern (continuous line). The count rates are expected to never reach the zero rate r_0 again. The contrast increases for strong excitation to much higher values. In comparison to a Rabi setup with a similar interaction time τ, the multi-state effects are stronger for Ramsey-type setups. The RABI-GRS-18 with only one interaction region needs twice the amplitude to reach a full state transition.

Approximation of the Rabi and Ramsey curves

The transition and transmission probabilities for both Rabi and Ramsey type GRS setups are expressed with analytical functions. Close to the resonance frequencies these functions can be further simplified (e.g. via a Taylor expansion around the resonance frequency). The resulting simplifications can either be used for quick analyses of measured transitions or for estimations of the experiment's sensitivity[25].

For Rabi setups the Taylor expansions of the transition and transmission probabilities (eq. (2.102) and eq. (2.104)) read as the following:

$$P_{Rabi}\left(a_v, \Delta\omega, \tau\right) \approx \sin^2\left(\frac{a_v V_{fi}\tau}{2}\right) + \left[\frac{\tau\cos\left(\frac{a_v V_{fi}\tau}{2}\right)\sin\left(\frac{a_v V_{fi}\tau}{2}\right)}{2a_v V_{fi}} - \frac{\sin^2\left(\frac{a_v V_{fi}\tau}{2}\right)}{\left(a_v V_{fi}\right)^2}\right]\Delta\omega^2 + \mathcal{O}\left(\Delta\omega^4\right)$$

$$T_{Rabi}\left(a_v, \Delta\omega, \tau\right) \approx 1 - \sin^2\left(\frac{a_v V_{fi}\tau}{2}\right) + \left[-\frac{\tau\cos\left(\frac{a_v V_{fi}\tau}{2}\right)\sin\left(\frac{a_v V_{fi}\tau}{2}\right)}{2a_v V_{fi}} + \frac{\sin^2\left(\frac{a_v V_{fi}\tau}{2}\right)}{\left(a_v V_{fi}\right)^2}\right]\Delta\omega^2 + \mathcal{O}\left(\Delta\omega^4\right)$$

At the optimal oscillation strength (eq. (2.103)) it further simplifies to these power series:

$$P_{Rabi}\left(\frac{\pi}{V_{fi}\tau}, \Delta\omega, \tau\right) \approx 1 - \frac{\tau^2}{\pi^2}\Delta\omega^2 + \frac{(16-\pi^2)\tau^4}{16\pi^4}\Delta\omega^4 - \frac{(32-3\pi^2)\tau^6}{32\pi^6}\Delta\omega^6 + \mathcal{O}\left(\Delta\omega^8\right) \tag{2.127}$$

$$T_{Rabi}\left(\frac{\pi}{V_{fi}\tau}, \Delta\omega, \tau\right) \approx \frac{\tau^2}{\pi^2}\Delta\omega^2 - \frac{(16-\pi^2)\tau^4}{16\pi^4}\Delta\omega^4 + \frac{(32-3\pi^2)\tau^6}{32\pi^6}\Delta\omega^6 + \mathcal{O}\left(\Delta\omega^8\right) \tag{2.128}$$

The expanded Taylor series of the transition and transmission probabilities can be expressed with a cosine by comparing to its Taylor expanded coefficients ($\cos(x) \approx 1 - \frac{x^2}{2} \quad \rightarrow \quad \frac{1}{2}(1-\cos(x)) \approx \frac{x^2}{4}$ & $\frac{1}{2}(1+\cos(x)) \approx 1 - \frac{x^2}{4}$):

$$P_{Rabi}\left(\frac{\pi}{V_{fi}\tau}, \Delta\omega, \tau, t_p\right) \approx \frac{1}{2}\left[1 + \cos\left(\frac{2\tau}{\pi}\Delta\omega\right)\right] \tag{2.129}$$

$$T_{Rabi}\left(\frac{\pi}{V_{fi}\tau}, \Delta\omega, \tau, t_p\right) \approx \frac{1}{2}\left[1 - \cos\left(\frac{2\tau}{\pi}\Delta\omega\right)\right] \tag{2.130}$$

Similar for Ramsey-type setups, both the theory function for a two level state transition P (eq. (2.125)) and the transmission T of a lower state (eq. (2.123)) can be Taylor expanded:

$$P = \sin^2(a_v V_{fi}\tau) - \sin(a_v V_{fi}\tau)\left[\frac{t_p}{a_v V_{fi}} - \frac{[\tau + t_p]}{a_v V_{fi}}\cos(a_v V_{fi}\tau) + \left[\frac{1}{a_v V_{fi}} + \frac{{t_p}^2}{4}\right]\sin(a_v V_{fi}\tau)\right]\Delta\omega^2 + \mathcal{O}\left(\Delta\omega^4\right) \tag{2.131}$$

$$T = \cos^2(a_v V_{fi}\tau) + \sin(a_v V_{fi}\tau)\left[\frac{t_p}{a_v V_{fi}} - \frac{[\tau + t_p]}{a_v V_{fi}}\cos(a_v V_{fi}\tau) + \left[\frac{1}{a_v V_{fi}} + \frac{{t_p}^2}{4}\right]\sin(a_v V_{fi}\tau)\right]\Delta\omega^2 + \mathcal{O}\left(\Delta\omega^4\right) \tag{2.132}$$

At the optimal oscillation strength (eq. (2.126), $a_v = \frac{\pi}{2V_{fi}\tau}$) this reads as the following[26]:

$$P = 1 - \frac{1}{4}\left(\frac{4\tau}{\pi} + t_p\right)^2\Delta\omega^2 - \left(\frac{(-16+\pi^2)\tau^4}{\pi^4} + \frac{2(-6+\pi)\tau^3 t_p}{\pi^3} - \frac{2\tau^2 {t_p}^2}{\pi^2} - \frac{\tau {t_p}^3}{3\pi} - \frac{{t_p}^4}{48}\right)\Delta\omega^4 + \mathcal{O}\left(\Delta\omega^6\right) \tag{2.133}$$

$$T = \frac{1}{4}\left(\frac{4\tau}{\pi} + t_p\right)^2\Delta\omega^2 + \left(\frac{(-16+\pi^2)\tau^4}{\pi^4} + \frac{2(-6+\pi)\tau^3 t_p}{\pi^3} - \frac{2\tau^2 {t_p}^2}{\pi^2} - \frac{\tau {t_p}^3}{3\pi} - \frac{{t_p}^4}{48}\right)\Delta\omega^4 + \mathcal{O}\left(\Delta\omega^6\right) \tag{2.134}$$

Everything expressed in a cosine reveals that Ramsey-type setups can narrow down the central transition peak by increasing the free propagation time t_p which is by a factor $\frac{\pi}{2}$ more effective than increasing the interaction time τ by the same amount:

$$P = P_{Ramsey}\left(\frac{\pi}{2V_{fi}\tau}, \Delta\omega, \tau, t_p\right) \approx \frac{1}{2}\left[1 + \cos\left(\left(\frac{4\tau}{\pi} + t_p\right)\Delta\omega\right)\right] \tag{2.135}$$

$$T = T_{Ramsey}\left(\frac{\pi}{2V_{fi}\tau}, \Delta\omega, \tau, t_p\right) \approx \frac{1}{2}\left[1 - \cos\left(\left(\frac{4\tau}{\pi} + t_p\right)\Delta\omega\right)\right] \tag{2.136}$$

[25] Furthermore, an envelope of the Ramsey function can be calculated using a corresponding Rabi theory function [194, 196].
[26] Note for $t_p = 0$ the result is equal to an approximated Rabi flip with a 2τ long interaction time (eq. (2.128))

Slope determination at the inflection points

Shifts in the resonance frequency ν_{fi} due to additional forces (e.g. a hypothetical electric charge q_{n} within an external electric field) affect the measured transmission in the flanks the most due to the steepness of the theoretical curve in these regions. The slope of the transmission curve is the first derivation of itself. This can be calculated directly with the full Ramsey curve (eq. (2.123)) or with the approximation (eq. (2.136)) both for the transition and the transmission probabilities (the derivation of the full curve is not displayed because of its length):

$$\frac{\partial}{\partial\Delta\omega}P\left(\frac{\pi}{2V_{fi}\tau},\Delta\omega,\tau,t_p\right)\approx\frac{\left(\frac{4\tau}{\pi}+t_p\right)}{2}\sin\left(\left(\frac{4\tau}{\pi}+t_p\right)\Delta\omega\right) \tag{2.137}$$

$$\frac{\partial}{\partial\Delta\omega}T\left(\frac{\pi}{2V_{fi}\tau},\Delta\omega,\tau,t_p\right)\approx-\frac{\left(\frac{4\tau}{\pi}+t_p\right)}{2}\sin\left(\left(\frac{4\tau}{\pi}+t_p\right)\Delta\omega\right) \tag{2.138}$$

The maximal slope is at the inflection points at $\pm\Delta\omega_m$ and therefore the points with the highest sensitivity of shifts of the transition frequency:

$$\frac{\partial^2}{\partial\Delta\omega^2}P\left(\frac{\pi}{2V_{fi}\tau},\Delta\omega,\tau,t_p\right)=\frac{\partial^2}{\partial\Delta\omega^2}T\left(\frac{\pi}{2V_{fi}\tau},\Delta\omega,\tau,t_p\right)=0$$

$$\Delta\omega_m\approx\pm\frac{\pi}{2\left(\frac{4\tau}{\pi}+t_p\right)}\qquad\qquad\Delta\nu_m\approx\pm\frac{1}{4\left(\frac{4\tau}{\pi}+t_p\right)} \tag{2.139}$$

The width b of the main transition peak is expressed by the distance between the two inflection points[27]:

$$b=2|\Delta\nu_m|=\frac{1}{\pi}|\Delta\omega_m|=\frac{1}{2\left(\frac{4\tau}{\pi}+t_p\right)} \tag{2.140}$$

The slope in these points is approximated:

$$\frac{\partial}{\partial\Delta\omega}P\left(\frac{\pi}{2V_{fi}\tau},\pm\frac{\pi}{2\left(\frac{4\tau}{\pi}+t_p\right)},\tau,t_p\right)\approx\frac{1}{2}\left(\frac{4\tau}{\pi}+t_p\right)\sin\left(\pm\frac{\pi}{2}\right)=\pm\frac{1}{2}\left(\frac{4\tau}{\pi}+t_p\right) \tag{2.141}$$

$$\frac{\partial}{\partial\Delta\omega}T\left(\frac{\pi}{2V_{fi}\tau},\pm\frac{\pi}{2\left(\frac{4\tau}{\pi}+t_p\right)},\tau,t_p\right)\approx-\frac{1}{2}\left(\frac{4\tau}{\pi}+t_p\right)\sin\left(\pm\frac{\pi}{2}\right)=\mp\frac{1}{2}\left(\frac{4\tau}{\pi}+t_p\right) \tag{2.142}$$

For further evaluations this slope can either be determined from this theoretical approximation or from a measurement. However, the slope cannot be measured directly, only as a difference of two quasi symmetrical measurements around the inflection point ($\Delta\omega_m\pm\delta_m$) via the difference quotient:

$$\frac{\partial T}{\partial\Delta\omega}=\frac{T\left(\frac{\pi}{2V_{fi}\tau},\Delta\omega_m+\delta_m,\tau,t_p\right)-T\left(\frac{\pi}{2V_{fi}\tau},\Delta\omega_m-\delta_m,\tau,t_p\right)}{2\delta_m} \tag{2.143}$$

If both slopes are measured in a 4 point measurement this enlarges the calculation by taking the absolute mean of both:

$$\begin{aligned}\frac{\partial T}{\partial\Delta\omega}=\frac{1}{4\delta_m}\Bigg[&-T\left(\frac{\pi}{2V_{fi}\tau},-\Delta\omega_m+\delta_m,\tau,t_p\right)+T\left(\frac{\pi}{2V_{fi}\tau},-\Delta\omega_m-\delta_m,\tau,t_p\right)\\&+T\left(\frac{\pi}{2V_{fi}\tau},\Delta\omega_m+\delta_m,\tau,t_p\right)-T\left(\frac{\pi}{2V_{fi}\tau},\Delta\omega_m-\delta_m,\tau,t_p\right)\Bigg]\end{aligned} \tag{2.144}$$

As shown later in the section 2.3.2, the sensitivity of the measurement is proportional to the width b of central resonance peak and consequently the slope in the inflection points. This enables to compare the sensitivity of Rabi-type and Ramsey-type GRS measurements (with $l_{II}=152\,\mathrm{mm}$ and $l_{III}=340\,\mathrm{mm}$):

$$\frac{b_{Rabi}}{b_{Ramsey}}=\frac{\frac{1}{2\left(\frac{2\tau}{\pi}\right)}}{\frac{1}{2\left(\frac{4\tau}{\pi}+t_p\right)}}=2+\frac{\pi t_p}{2\tau}=2+\frac{\pi}{2}\frac{l_{III}}{l_{II}}\approx5.5 \tag{2.145}$$

[27] A different definition is given in [196].

2.2.3. Velocity spreading

The interaction time τ and the propagation time t_p are the main parameters for the previously described calculations of Rabi and Ramsey-type GRS. However, the setup does not directly determine these parameters. The only fixed values are the mirror lengths of each region within the setup (see section 3.1.5, $\tau = l_{II}/v_\mathrm{n}$ and $t_p = l_{III}/v_\mathrm{n}$). The neutron velocity v_n depends on the source (section 1.3), the beam guides (section 3.1.2) and the aperture alignment (section 3.1.3). The UCN source always emits neutrons in a broad velocity interval which can be approximated with a Maxwell-Boltzmann distribution of ideal gases (see more at the end of this section, eq. (2.148)). The beam guides disturb the spectrum with a velocity depending transmission[28]. The aperture limits the velocity interval to its set boundaries (e.g. 5-13 m/s for the measurements in 2018). It would be possible to reduce the neutron velocity interval but this will also decrease the neutron count rate[29]. Using a velocity interval results in a spread of the interaction and propagation times τ & t_p. At the resonance frequency ν_{fi}, the optimal oscillation strength a_v can only be adapted to the mean neutron velocity $\overline{v}_\mathrm{n}$. Therefore, most neutrons are either to fast or to slow and they do not experience a complete state transition which is measured as a reduced transition contrast c_{fi}. The shape of the spectral transmission curve depends on the timing and therefore on the neutron velocity. The side minima and maxima are different for each neutron due to their different velocities. Broad velocity distributions have a strong washing out of these extreme values[30]. In order to account for this experimental fact, the GRS transmission/transition curves have to be convoluted with the measured and approximated velocity distribution $f(v_\mathrm{n})$ [267](p.18-20), [193](p.13-14):

$$P = \int_{v_{min}}^{v_{max}} P(a_v, \nu, \tau(v_\mathrm{n})) \cdot f(v_\mathrm{n})\,\mathrm{d}v_\mathrm{n} \tag{2.146}$$

In order to reduce the calculation time, the convolution can also be expressed as a sum. The velocity distribution $f(v_\mathrm{n})$ is split into equidistant sampling points $v_{\mathrm{n}i}$. The transmission/transition probability $T\&P$ is calculated for each point. Summarizing the results weighted with $f(v_{\mathrm{n}i})$, the probability of the sample point within the velocity distribution, approximates the convolution. The smaller the sampling point distance is set, the smaller is the deviation to the correct integral convolution. However, the calculation time is directly proportional to the chosen number of sampling points. The evaluation of all measurements in this thesis uses a sampling interval of 0.01 m/s.

$$P = \sum_{i=1}^{n} P(a_v, \nu, \tau(v_{\mathrm{n}i})) \cdot f(v_{\mathrm{n}i}) \tag{2.147}$$

The velocity distribution itself has to be measured either with a TOF measurement within the beam guides or by sweeping through different aperture settings (see more in section 4.3.1). There are no accurate theoretical descriptions of the neutron transport from the reactor core[31] through the UCN source to the experiment yet. A fit tries to describe the measured data points with a Maxwell-Boltzmann like velocity distribution as it is common to describe ideal gases:

$$f(v_\mathrm{n}) = n\sqrt{\frac{2}{\pi}}\frac{(v_\mathrm{n}-v_0)^2}{a^3}\mathrm{e}^{-\frac{(v_\mathrm{n}-v_0)^2}{2a^2}} \tag{2.148}$$

This function includes a scaling parameter n to adjust the distribution to the integrated count rate of the measurement, a velocity cutoff v_0 to account for the strong absorption of the thin aluminum entrance windows (54 neV corresponding to 3.24 m/s) and the Maxwell-Boltzmann factor a which can be associated with a neutron temperature $a = \sqrt{k_\mathrm{B}T/m_\mathrm{n}}$. In general, UCNs can be described with temperatures around and below 4 mK [174]. This corresponds to a Maxwell-Boltzmann factor a of 5.7 m/s.

Any aperture measurement can only measure a velocity interval. Therefore, the measured count rates have to be fitted with the integrated Maxwell-Boltzmann distribution $F(v_\mathrm{n})$ which has the following

[28] There are hints and good reasons that also the aligned mirror setup of the GRS has a state and velocity depending transmission. For faster neutrons higher states have a higher transmission through the absorber regions and the losses due to the beam divergence are stronger for slower neutrons. Long GRS-setups like the RAMSEY$^{\mathrm{TR}}$-setup favor faster neutrons and therefore a smaller contrast is observed

[29] A decrease of the upper velocity limit can increase the contrast. Therefore, the highest statistical significance of a measurement is a trade-off between contrast and count rate.

[30] For Ramsey-type GRS setups this helps to separate transitions in close neighborhood.

[31] Thermal neutrons are described as an ideal gas with the temperature of the surrounding moderator within the reactor core.

analytical form:

$$F(v_\mathrm{n}) = \frac{n}{a\sqrt{2\pi}}\left(\frac{2(v_{min}-v_0)}{\mathrm{e}^{\frac{(v_{min}-v_0)^2}{2a^2}}} - \frac{2(v_{max}-v_0)}{\mathrm{e}^{\frac{(v_{max}-v_0)^2}{2a^2}}} - a\sqrt{2\pi}\,\mathrm{erf}\left[\frac{-v_{max}+v_0}{\sqrt{2}a}\right] + a\sqrt{2\pi}\,\mathrm{erf}\left[\frac{-v_{min}+v_0}{\sqrt{2}a}\right]\right) \tag{2.149}$$

In order to generalize the Maxwell-Distribution $f(v_\mathrm{n})$ the second power in the linear and in the exponential term can also be set to arbitrary numbers c and b:

$$f(v_\mathrm{n}) = n\sqrt{\frac{2}{\pi}}\frac{(v_\mathrm{n}-v_0)^c}{a^3}\mathrm{e}^{-\frac{(v_\mathrm{n}-v_0)^b}{2a^2}}\Theta(v_\mathrm{n}-v_0) \tag{2.150}$$

The generalized integrated form is denoted as the following:

$$F(v_\mathrm{n}) = \Re\left[\frac{1}{\sqrt{\pi}b}2^{\frac{1}{b}+\frac{1}{2}+\frac{c}{b}}a^{\frac{2}{b}-3+\frac{2c}{b}}n\left(-\Gamma\left[\frac{1+c}{b},\frac{(v_{max}-v_0)^b}{2a^2}\right]\Theta\left(v_{max}-v_0\right)\right.\right.$$
$$\left.\left.+\Gamma\left[\frac{1+c}{b},\frac{(v_{min}-v_0)^b}{2a^2}\right]\Theta\left(v_{min}-v_0\right)\right)\right] \tag{2.151}$$

In the past, the velocity measurements were compared with different versions of this distribution: a general integral form for the aperture measurements of the GRS$^{\mathrm{TJ}}$-setup [139](p.44&77) [310](p.68), a general differential form for the TOF measurement of the RAMSEY$^{\mathrm{TR}}$-setup in 2016 [254](p.109) and a general differential form with equal exponents ($b = c$) for a similar TOF measurement in 2019 [160](p.26). This thesis uses the simple form eq. (2.148). A detailed comparison between the past measurements and the velocity measurement of this thesis is presented in section 4.3.1. Additionally, the difference between the simple and the generalized form of the Maxwell-Boltzmann distribution is also discussed there.

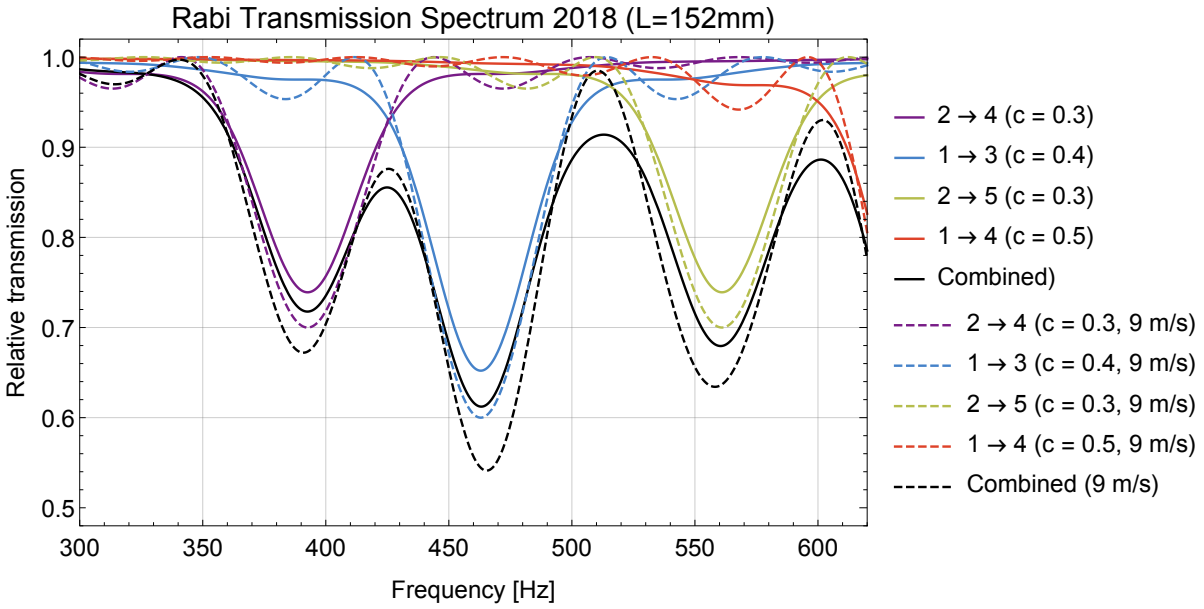

Figure 2.10.: Single Rabi transitions with constant optimal oscillation strength a_v (colored) and the multi 2-level theory function with adapted oscillation strength (black). The continuous lines represent velocity spread transmission adapted to the velocity spectrum of 2018. The dashed lines depend only on the single velocity of 9 m/s. The velocity spreading reduces the contrast, broadens slightly the transition peaks and washes out the side band (which decreases the spectator shift). In real measurements, the changed contrast due to the different models is hidden in the fit parameters. Therefore, the fitted curves with and without velocity broading are closer together.

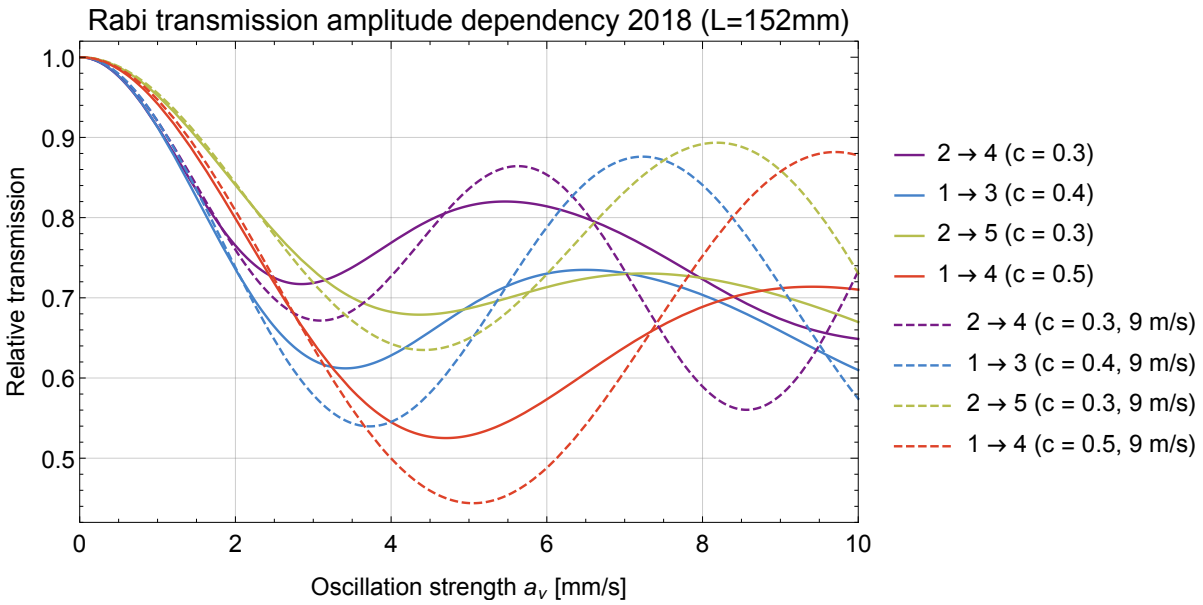

Figure 2.11.: Transmission of Rabi transitions at their resonance frequency. The continuous lines represent velocity spread transmission adapted to the velocity spectrum of 2018. The dashed lines depend only on the single velocity of 9 m/s. The velocity spreading reduces the contrast and further grinds down the revival of the function.

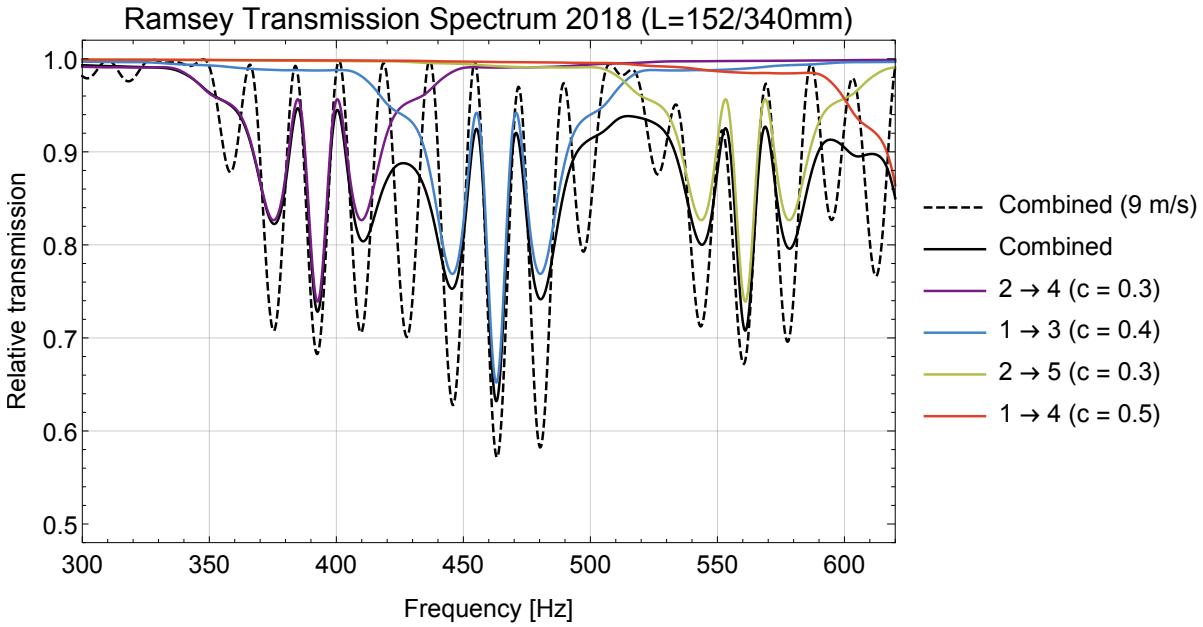

Figure 2.12.: Velocity spread Ramsey transmission spectrum: As a comparison the dashed line represents the transmission curve of a UCN with the velocity v_n of 9 m/s. The velocity spreading washes out the side peaks and makes it possible to separate the single transitions.

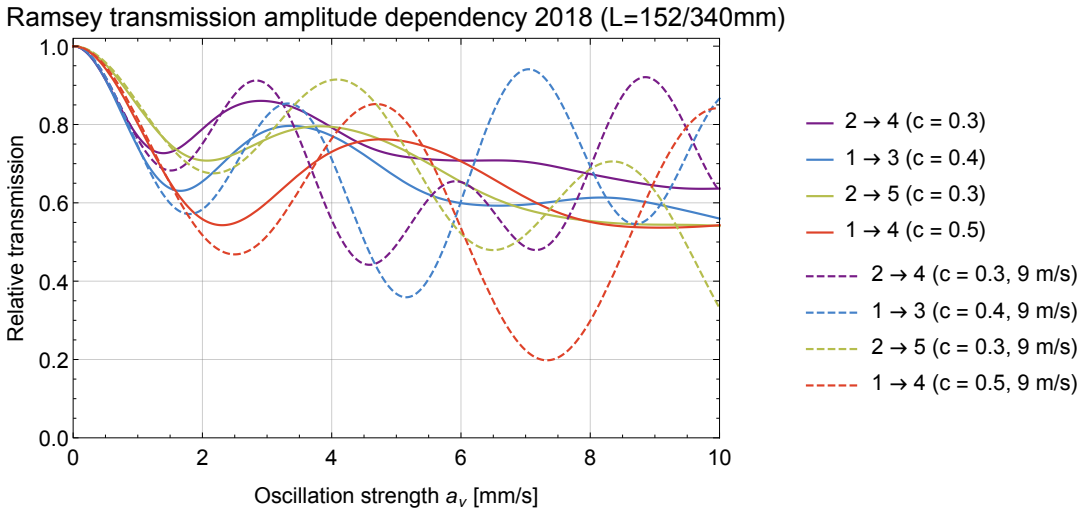

Figure 2.13.: Amplitude dependency of the Ramsey transmission: the velocity spreading (continuous lines) washes out nearly completely the revival of the count rate compared to the transmission curve of a UCN with the velocity v_n of 9 m/s (dashed lines). For high amplitudes the count rate loss is independent of the oscillation strength.

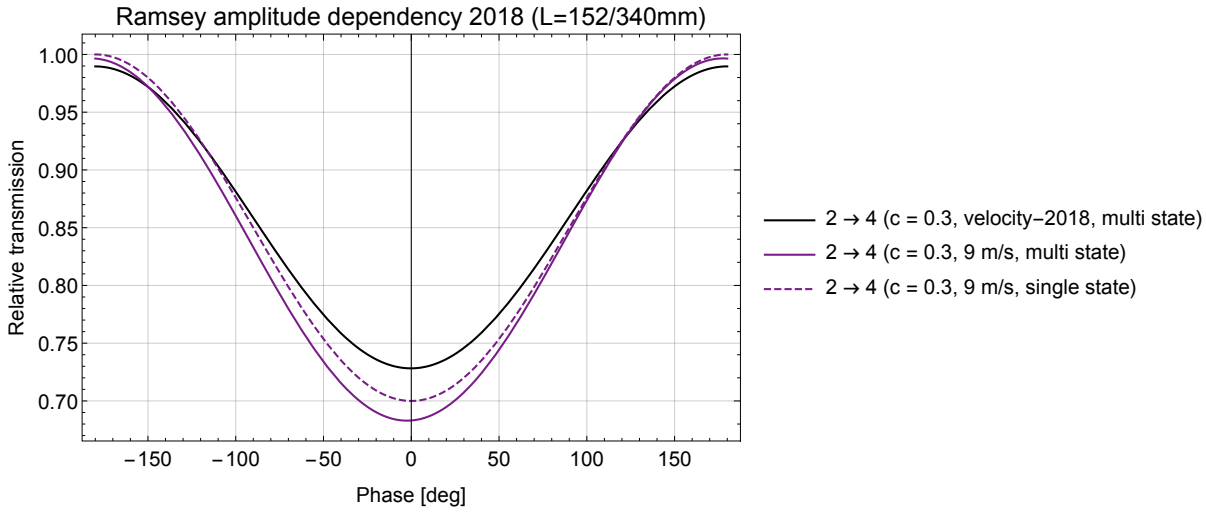

Figure 2.14.: Phase sweep of the Ramsey transmission: multi-state effects increase the contrast and velocity spreading decreases it. The velocity interval also decreases slightly the maximal reachable rate at the complete opposite oscillation.

2.2.4. Notation comparison for GRS calculations

In order to be able to better compare the calculations of this thesis with previous works, I present here a short summary of the different nomenclatures used in the past. The use of glossaries within LaTeX enables to quickly adapt the naming to any desired convention.

Table 2.5.: Notation comparison of Rabi/Ramsey calculation in reverse chronological order

This thesis	Micko 2023 [194]	Killian 2020 [160]	Pitschmann 2019 [244]	Moriond19 2019 [196]	Rechberger 2018 [254]	Micko 2018 [193]	Schmidt 2017 [267]	Cronenberg 2016 [65]	Jenke 2011 [139]
i	n	n	k	-	k	n	m	j	m
i (2 state)	p	i	-	0	n	0	p	i	p
f	m	m	m	-	m	m	n	i	n
f (2 state)	q	j	-	1	m	1	q	j	q
ν	ν	ν	-	ν	ν	f	f	f	ν
ν_{fi}	ν_{mn}	ν_{mn}	-	ν_1	ν_{mn}	-	-	f_{ij}	ν_{mn}
ω_{fi}	ω_{mn}	ω_{mn}	-	ω_{10}	ω_{mk}	ω_{mn}	ω_{mn}	$2\pi f_{ij}$	ω_{mn}
$\Delta\omega$	δ	$\omega - \omega_{ji}$	-	$\omega - \omega_{10}$	$\Delta\omega$ or ϵ	$\tilde{\omega}$	$-\delta_{nm}$ or δ	$\delta\omega$	δ_{nm}
$\omega - \omega_{fi}$	$\omega - \omega_{qp}$	$\omega - \omega_{ji}$	-	$\omega - \omega_{10}$	$\omega_{mn} - \omega$	$\omega - \omega_{10}$	$\omega_{nm} - \omega$	$2\pi(f - f_{ij})$	$\omega_{nm} - \omega$
a_x	a	a	a	a	a or a_x	a	A	A_x	A
a_v	$a\omega$	$a\omega$	-	$a\omega$	$a\omega$ or a_ν	$a\omega$	ωA or A_ν	A_ν	u_v
V_{fi}	V_{mn}	V_{mn}	-	V_{10}	V_{mk} or Q_{mn}	V_{mn}	Q_{nm}	$\langle i\vert\partial_z\vert j\rangle$	Q_{nm}
$a_v V_{fi}$	$a\omega V_{pq}$	$a\omega V_{ji}$	-	$a\omega V_{10}$	Ω_R	$a\omega V_{mn}$	T_{nm} or T	Ω_R	T_{nm}
Ω_R	Ω_R	R	-	Ω_R	Ω	$r/2$	Ω	Ω_{RS}	Ω
Θ	Θ	Θ	-	-	Θ	Θ	Θ	Θ	Θ
V_F	V_0	V_0	-	-	V	V_0	V	V_F	V
ϕ	ϕ	ϕ	-	-	ϕ	ϕ	ϕ	θ	ϕ_{mn}
t	t	t	t_0	-	$\tilde{t}$	t	t	t	t
z	z	z	z_0	-	$\tilde{z}$	z	z	z	z
$\Psi(z,t)$	$\psi(z,t)$	$\psi(z,t)$	$\psi(z_0,t_0)$	-	$\tilde{\psi}(\tilde{z},\tilde{t})$	$\psi(z,t)$	$\psi_z(z,t)$	$\vert\Psi\rangle$	$\Psi_z(z,t)$
$\tilde{t}$	$\bar{t}$	$\tilde{t}$ and t	$\tilde{t}$	t	t	$\tilde{t}$	t	t	t
$\tilde{z}$	$\bar{z}$	$\tilde{z}$ and z	$\tilde{z}$	-	z	$\tilde{z}$	$\bar{z}$	z	$\tilde{z}$
$z - f(t)$	$z - f(t)$	$z - f(t)$	$z_0 - a\sin(\omega t_0)$	-	$\tilde{z} - a\sin(\omega\tilde{t})$	$z - a\sin(\omega t + \phi)$	$z - A\sin(\omega t)$	-	$z - A\sin(\omega t)$
$\tilde{\Psi}(\tilde{z},\tilde{t})$	ψ	-	$\tilde{\psi}(\tilde{z},\tilde{t})$	-	$\psi(z,t)$	$\psi(\tilde{z},\tilde{t})$	$\bar{\psi}(\bar{z},t)$	$\vert\Psi\rangle$	$\Psi(\tilde{z},t)$
$\tilde{\psi}_i(\tilde{z})$	ψ_n	$\psi_n(\tilde{z})$	$\psi_k^{(0)}(z)$	-	$\psi_k^{(0)}(z)$	$\psi_n(\tilde{z})$	$\vert m\rangle$	$\vert\psi_j\rangle$ or $\vert i\rangle$	$\vert m\rangle$
$b_i(\tilde{t})$	$\bar{C}_n(t)$	$C_n(t)$	$a_k(t)$	$C(t)$	$a_k(t)$	$C_n(\tilde{t})$	$C_m(t)$	$c_i(t)$	$b_m(t)$
$c_i(\tilde{t})$	$C_n(t)$	$\tilde{C}_n(\tilde{t})$ & $C_i(t)$	-	-	-	$\tilde{C}_n(\tilde{t})$	$\tilde{C}_m(t)$	-	$c_p(t)$
$d_i(\tilde{t})$	-	$C_i'(t)$	-	-	b_n	$C_0'(t)$	$B_q(t)$	-	-
$\hat{H}_0$	$\hat{H}$	-	-	-	$\hat{H}_0$	-	$\bar{H}_0$	-	$\tilde{H}_0$
t_p	T	T	-	T	T	-	T	-	-
τ	τ	τ	-	τ	τ	$\tilde{t}$	τ	t or τ	τ
P	-	$\vert C_j(t)\vert^2$	-	P	P_m	$P(\psi_1)$	-	-	-
T	$P(\vert p\rangle\rightarrow\vert p\rangle)$	$\vert C_i(t)\vert^2$	-	-	P_n	$P(\psi_0)$	$P_p = \vert C_p\vert^2$	P_i	-

2.3. Neutron's electric charge measurements with GRS

The main goal of this thesis is to search for the electric charge of the neutron q_n within the qBOUNCE experiment. In 2011, Katharina Durstberger-Rennhofer, Tobias Jenke and Hartmut Abele presented a method to do this with a Ramsey-type GRS setup [77]. In contrast to all previously conducted neutron's charge measurements which are based on classical deflection experiments in strong electric fields (see more in section 1.2), the new approach sets limits by searching for shifts in the transition frequency of gravitationally bound quantum states due to the presence of very high electric fields. This is a rare case where it is possible to measure scalars with a Ramsey spectroscopy technique.
In the following section, I will describe theoretically this new quantum mechanical measurement technique based on the previously mentioned work. The details of the realization within the RAMSEY$^{\mathrm{TR}}$-setup and the electrode breakthrough determination at the electrode test setup are summarized in the setup section 3.3. The conducted measurement of 2018 also called Rams$\vec{E}$y is displayed in section 4.6.

As mentioned in the introduction to the gravitationally bound states, any additional potential can be added to the final Schrödinger equation (2.7) in order to test an underlying hypotheses. In the case of the charge measurement, we assume a hypothetical non-zero electric charge of the neutron q_n and apply a strong electric field $\vec{E}$ parallel ($+E_z$) or antiparallel ($-E_z = |\vec{E}|_z$) to gravity. This assumption introduces an additional electric potential $V_{\vec{E}}$:

$$V_{\vec{E}}(z) = \pm q_\mathrm{n} E_z z \tag{2.152}$$

Both potentials joined together result in the following Schrödinger equation which is the basis for the Rams$\vec{E}$y experiment to determine the electric charge of the neutron:

$$\left(-\frac{\hbar^2}{2m_i}\frac{\partial^2}{\partial z^2} + \left(m_g g \pm q_\mathrm{n} E_z\right) z\right)\psi(z) = E\psi(z) \tag{2.153}$$

Similar to the purely gravitational quantum bouncer (see section 2.1.1), the equation (2.153) can be transformed with the following substitution:

$$z_0 = \sqrt[3]{\frac{\hbar^2}{2m_i\left(m_g g + q_\mathrm{n} E_z\right)}} = \sqrt[3]{\frac{\hbar^2}{2m_\mathrm{n}\left(m_\mathrm{n} g_0 + q_\mathrm{n} E_z\right)}} \tag{2.154}$$

$$E_0 = \left(m_g g + q_\mathrm{n} E_z\right) z_0 = \sqrt[3]{\frac{\hbar^2\left(m_\mathrm{n} g_0 + q_\mathrm{n} E_z\right)^2}{2m_\mathrm{n}}} \tag{2.155}$$

$$\sigma = \tilde{z} - \tilde{E} = \frac{z}{z_0} - \frac{E}{E_0} = \sqrt[3]{\frac{2m_\mathrm{n}\left(m_\mathrm{n} g_0 + q_\mathrm{n} E_z\right)}{\hbar^2}}\left(z - \frac{E}{\left(m_\mathrm{n} g_0 + q_\mathrm{n} E_z\right)}\right) \tag{2.156}$$

The resulting dimensionless Airy equation is the same as (2.13). Therefore, the further calculations of the wave functions are the same too.

Figure 2.15 visualizes the effect of the additional electric field $\vec{E}$ and a hypothetical charge of the neutron q_n which is exaggerated in order to maximize the visibility of the influences. The shape of the potential is the same but the slope changes similar to a change of the local gravitational acceleration g. The energy states are shifted differently.

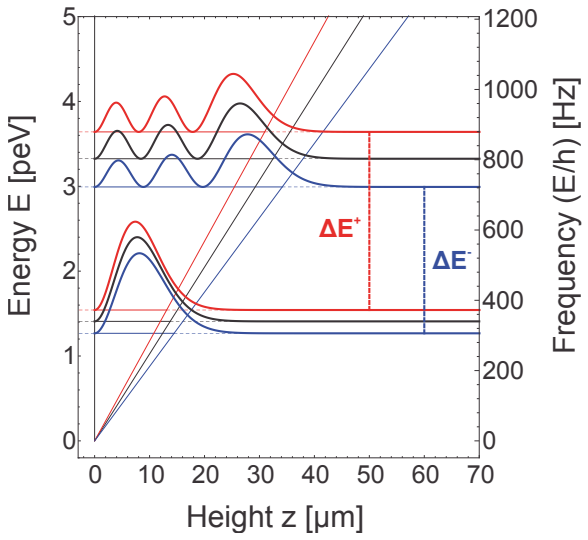

Figure 2.15.: Change of the energy states due to a hypothetical neutron charge q_n of $5 \times 10^{-16}\,e$ and an electric field $\vec{E}$ of 6 MV/m [77]

2.3.1. Electric charge measurements

Shifts of the energy states are not directly measurable. However, GRS measures the transition frequencies ν_{fi} which are sensitive to the difference of two energy states. Changes of these frequencies due to an applied electric field enable us to measure the electric charge q_n directly [77]. The difference of the transition frequency with the electric field and the purely gravitational case is:

$$\begin{aligned}\Delta_{\nu_{fi}} = {\nu_{fi}}^{\vec{E}} - {\nu_{fi}}^{g} &= \left(\sqrt[3]{\frac{\hbar^2\left(m_\mathrm{n}g + q_\mathrm{n}E_z\right)^2}{2m_\mathrm{n}}} - \sqrt[3]{\frac{\hbar^2 m_\mathrm{n} g^2}{2}}\right)\frac{1}{h}\left(\mathrm{AiZ}(f) - \mathrm{AiZ}(i)\right) \\ &= -{\nu_{fi}}^{g}\left(1 - \sqrt[3]{\left(1 + \frac{q_\mathrm{n}E_z}{m_\mathrm{n}g}\right)^2}\right) \approx {\nu_{fi}}^{g}\frac{2q_\mathrm{n}E_z}{3m_\mathrm{n}g} + \mathcal{O}\left(\left(\frac{q_\mathrm{n}E_z}{m_\mathrm{n}g}\right)^3\right)\end{aligned} \tag{2.157}$$

The simplification with a Taylor expansion in eq. (2.157) is legitimated due to the small size of the term $\frac{q_\mathrm{n}E_z}{m_\mathrm{n}g}$ ($= 9.75 \times 10^{12}\,e^{-1}q_\mathrm{n}$ for $E_z = 1\,\mathrm{MV/m}$; using the current best value of q_n, the total magnitude is 4×10^{-9}), especially because the next order is cubic.

The corresponding error of the shift depends on the statistical precision of the transition frequency measurements:

$$\sigma_{\Delta_{\nu_{fi}}} = \sqrt{\sigma^2_{{\nu_{fi}}^{g}} + \sigma^2_{{\nu_{fi}}^{\vec{E}}}} \tag{2.158}$$

To enhance the effect of a hypothetical neutron charge a reversal of the electric field $\vec{E}$ doubles the measurable shift:

$$\begin{aligned}\Delta_{\nu_{fi}} = {\nu_{fi}}^{+\vec{E}} - {\nu_{fi}}^{-\vec{E}} &= \left(\sqrt[3]{\frac{\hbar^2\left(m_\mathrm{n}g + q_\mathrm{n}E_z\right)^2}{2m_\mathrm{n}}} - \sqrt[3]{\frac{\hbar^2\left(m_\mathrm{n}g - q_\mathrm{n}E_z\right)^2}{2m_\mathrm{n}}}\right)\frac{1}{h}\left(\mathrm{AiZ}(f) - \mathrm{AiZ}(i)\right) \\ &= {\nu_{fi}}^{g}\left(\sqrt[3]{\left(1 + \frac{q_\mathrm{n}E_z}{m_\mathrm{n}g}\right)^2} - \sqrt[3]{\left(1 - \frac{q_\mathrm{n}E_z}{m_\mathrm{n}g}\right)^2}\right) \approx {\nu_{fi}}^{g}\frac{4q_\mathrm{n}E_z}{3m_\mathrm{n}g} + \mathcal{O}\left(\left(\frac{q_\mathrm{n}E_z}{m_\mathrm{n}g}\right)^3\right)\end{aligned} \tag{2.159}$$

The error of the bipolar measured shift is:

$$\sigma_{\Delta_{\nu_{fi}}} = \sqrt{\sigma^2_{{\nu_{fi}}^{+\vec{E}}} + \sigma^2_{{\nu_{fi}}^{-\vec{E}}}} \tag{2.160}$$

Expressing the equations (2.157) and (2.159) in the terms of the hypothetical neutron charge q_n:

$$q_\mathrm{n} \approx -\frac{\Delta_{\nu_{fi}}}{{\nu_{fi}}^g}\frac{3m_\mathrm{n}g}{2E_z} = -\left(1-\frac{{\nu_{fi}}^{\vec{E}}}{{\nu_{fi}}^g}\right)\frac{3m_\mathrm{n}g}{2E_z} \qquad or \qquad q_\mathrm{n} \approx \frac{\Delta_{\nu_{fi}}}{{\nu_{fi}}^g}\frac{3m_\mathrm{n}g}{4E_z} = \left(\frac{{\nu_{fi}}^{+\vec{E}}-{\nu_{fi}}^{-\vec{E}}}{{\nu_{fi}}^g}\right)\frac{3m_\mathrm{n}g}{4E_z} \tag{2.161}$$

Multiple measurements at different electric field strengths or transition frequencies can be combined:

$$q_\mathrm{n} = \frac{1}{n}\sum_j^n \frac{\Delta_{{\nu_{fi}}_j}}{{\nu_{fi}}^g{}_j}\frac{3m_\mathrm{n}g}{2E_{zj}} \tag{2.162}$$

However, the best measurements (highest shift $\Delta_{\nu_{fi}}$, smallest probable charge q_n) should have an as high as possible field $\vec{E}$, a high frequency transition ν_{fi} and should be bipolar ($\pm E_z$). More information on the technical limitations of these three parameters are in the sections 3.3.2 (electrode design), 3.1.6 (mechanical oscillations) and 3.3.5 (bipolarity).

Error calculation and the derived limit of the neutron charge

The following calculation expresses the error for a single neutron charge measurement:

$$\sigma_{q_\mathrm{n}} = q_\mathrm{n}\sqrt{\frac{{\sigma^2}_{{\nu_{fi}}^{\vec{E}}}}{{\Delta_{\nu_{fi}}}^2} + \frac{{\nu_{fi}}^{\vec{E}^2}}{{\nu_{fi}}^{g2}}\frac{{\sigma^2}_{{\nu_{fi}}^g}}{{\Delta_{\nu_{fi}}}^2} + \frac{{\sigma^2}_{m_\mathrm{n}}}{{m_\mathrm{n}}^2} + \frac{\sigma_g^2}{g^2} + \frac{{\sigma^2}_{E_z}}{{E_z}^2}} \tag{2.163}$$

The contributions of the error of the neutron mass m_n, local gravity g and the electric field strength E_z are below 1 % of the hypothetical charge q_n and will be neglected for the further calculations (more information of the error dependencies are found in section 2.1.3).

Only the errors of the transition frequencies can contribute strongly to the error of the charge (further approximation ${\nu_{fi}}^{\vec{E}^2}/{\nu_{fi}}^{g2} \approx 1$):

$$\sigma_{q_\mathrm{n}} \approx q_\mathrm{n}\sqrt{\frac{{\sigma^2}_{{\nu_{fi}}^g}}{\left({\nu_{fi}}^g-{\nu_{fi}}^{\vec{E}}\right)^2} + \frac{{\nu_{fi}}^{\vec{E}^2}}{{\nu_{fi}}^{g2}}\frac{{\sigma^2}_{{\nu_{fi}}^{\vec{E}}}}{\left({\nu_{fi}}^g-{\nu_{fi}}^{\vec{E}}\right)^2}} \approx q_\mathrm{n}\frac{\sqrt{{\sigma^2}_{{\nu_{fi}}^g}+{\sigma^2}_{{\nu_{fi}}^{\vec{E}}}}}{\left({\nu_{fi}}^g-{\nu_{fi}}^{\vec{E}}\right)} = q_\mathrm{n}\frac{\sigma_{\Delta_{\nu_{fi}}}}{\Delta_{\nu_{fi}}} \approx \frac{\sigma_{\Delta_{\nu_{fi}}}}{{\nu_{fi}}^g}\frac{3m_\mathrm{n}g}{2E_z} \tag{2.164}$$

Similar calculations with similar results can be obtained for the bipolar measurements:

$$\sigma_{q_\mathrm{n}} = q_\mathrm{n}\sqrt{\frac{{\sigma^2}_{{\nu_{fi}}^{+\vec{E}}}}{{\Delta_{\nu_{fi}}}^2} + \frac{{\sigma^2}_{{\nu_{fi}}^{-\vec{E}}}}{{\Delta_{\nu_{fi}}}^2} + \frac{{\sigma^2}_{{\nu_{fi}}^g}}{{\nu_{fi}}^{g2}} + \frac{{\sigma^2}_{m_\mathrm{n}}}{{m_\mathrm{n}}^2} + \frac{\sigma_g^2}{g^2} + \frac{{\sigma^2}_{E_z}}{{E_z}^2}} \approx q_\mathrm{n}\frac{\sqrt{{\sigma^2}_{{\nu_{fi}}^{+\vec{E}}}+{\sigma^2}_{{\nu_{fi}}^{-\vec{E}}}}}{\left({\nu_{fi}}^{+\vec{E}}-{\nu_{fi}}^{-\vec{E}}\right)} = q_\mathrm{n}\frac{\sigma_{\Delta_{\nu_{fi}}}}{\Delta_{\nu_{fi}}} \approx \frac{\sigma_{\Delta_{\nu_{fi}}}}{{\nu_{fi}}^g}\frac{3m_\mathrm{n}g}{4E_z} \tag{2.165}$$

As seen in eq. (2.161), (2.164) and (2.165) a non zero electric charge induces a shift of the measured transition frequency which should be significantly larger than the frequency error. For a very small or vanishing neutron charge, the measurement uncertainties of the transition frequencies will mainly contribute to the measured charge value and its error. Even though the calculated charge value should be (close to) zero. Therefore, the precision of the transition frequency sets limits to the neutron charge measurement. If the errors are purely statistically and normal distributed, the difference between two transition frequency measurements is normally distributed around zero with a variance as the sum of the measurement variances ($\sigma^2_{\Delta_{\nu_{fi}}} = {\sigma^2}_{{\nu_{fi}}^g} + {\sigma^2}_{{\nu_{fi}}^{\vec{E}}}$ or bipolar $\sigma^2_{\Delta_{\nu_{fi}}} = {\sigma^2}_{{\nu_{fi}}^{+\vec{E}}} + {\sigma^2}_{{\nu_{fi}}^{-\vec{E}}}$). To exclude a hypothetical charge within an interval with 95 % confidence level, the limit is twice the statistical error of the shift:

$$|q_{\mathrm{n}limit}| \leqslant \frac{\sqrt{{\sigma^2}_{{\nu_{fi}}^g}+{\sigma^2}_{{\nu_{fi}}^{\vec{E}}}}}{{\nu_{fi}}^g}\frac{3m_\mathrm{n}g}{E_z} \qquad or \qquad |q_{\mathrm{n}limit}| \leqslant \frac{\sqrt{{\sigma^2}_{{\nu_{fi}}^{+\vec{E}}}+{\sigma^2}_{{\nu_{fi}}^{-\vec{E}}}}}{{\nu_{fi}}^g}\frac{3m_\mathrm{n}g}{2E_z} \tag{2.166}$$

Assuming the statistical errors to be ${\sigma_{\nu_{fi}}}^g = {\sigma_{\nu_{fi}}}^{+\vec{E}} = {\sigma_{\nu_{fi}}}^{-\vec{E}} = 10^{-3}\nu_{fi}$, an electric field $E_z = 8.4\,\mathrm{MV\,m^{-1}}$ and the transition $|2\rangle \rightarrow |4\rangle$, the charge limit will be $5.2 \times 10^{-17}\,e$ or $2.6 \times 10^{-17}\,e$ if measured bipolar.

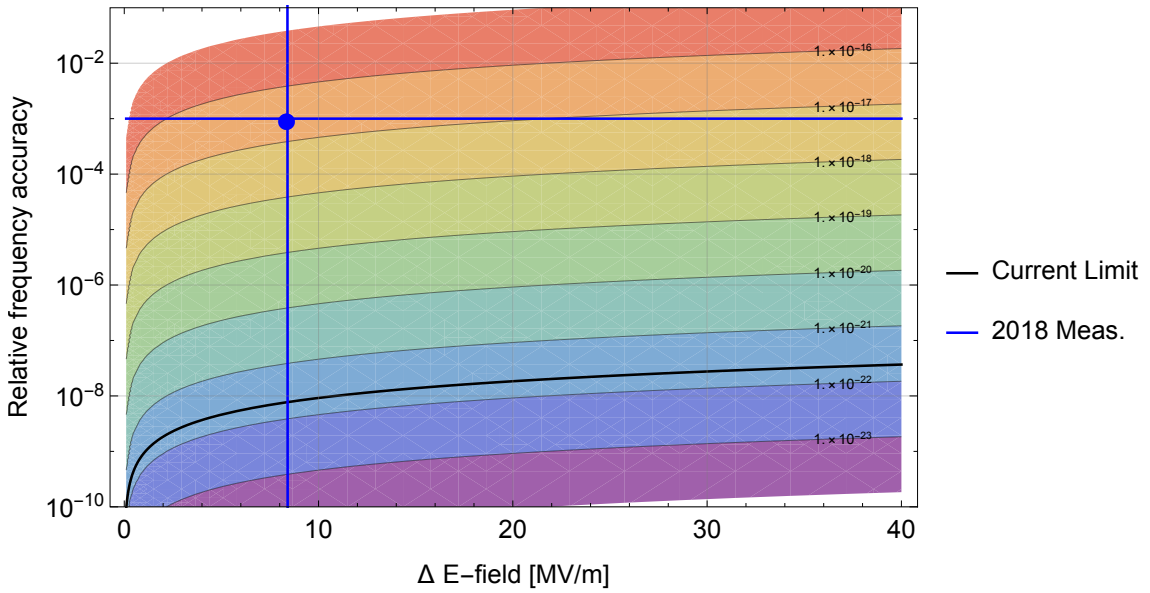

Figure 2.16.: Needed electric field strength and relative frequency precision for a certain charge limit. Blue lines are the expected experimental parameters.

The statistical error $\sigma_{\Delta_{\nu_{fi}}}$ depends on the statistical significance of the transition frequency measurement and therefore mainly on the number of counted neutrons. The exact relation between the counted neutrons and the error of ν_{fi} are expressed by the so called *sensitivity*. Together with a mean neutron count rate this sensitivity can be expressed as a discovery potential per day.
The measurement scheme (2-point measurement as suggested in [77] or 4-point measurement used for this thesis) can statistically optimize the usage of the measurement time and therefore increase the sensitivity. The end of the following section describes in detail the sensitivity of the Ramsey-GRS and its application to the electric charge measurement.

2.3.2. Dependencies on parameters and the sensitivity

In this subsection I will describe the relation between an applied electric field $\vec{E}$ and the neutron charge q_n in an extended model (eq. (2.153)). Similar to the measurements of g, the neutron charge can be determined within the statistical errors of the neutron rate measurements and the stability of the electrical field which will be elaborated in the second part of this subsection.

Electric field strength $\vec{E}$ and neutron charge q_n

During the measurement of the neutron charge q_n, an applied electric field $\vec{E}$ is responsible for the strength of the possible shift $\Delta_{\nu_{fi}}$ in the transition frequency from the zero field measurement (see eq. (2.157)):

$$\Delta_{\nu_{fi}} \approx \nu_{fi}{}^{g} \frac{2q_\mathrm{n}E_z}{3m_\mathrm{n}g} \tag{2.167}$$

The current best measured value of the neutron charge is $q_\mathrm{n} = 2(8) \times 10^{-22}\, e$ [319]. Using eq. (2.167) the expected shift for the used transition $2 \to 4$ is $\Delta\nu_{24} \approx 3(12)\,\mu\mathrm{Hz}$ in an electric field of 6 MV/m (the uncertainty is similar to the error of the neutron mass measurement).
Using a different transition can increase the frequency shift. Preferable are transitions from the first state to an as high as possible state due to the better contrast and higher increase (e.g. for $\Delta_{\nu_{17}}$ by a factor of 2.85 compared to $\Delta_{\nu_{24}}$). The finally chosen transition depends on the mechanical properties of the GRS setup: the transition frequency has to be far away from mechanical resonance frequencies and the reachable amplitude strength has to be high enough for a complete state transition (see more in subsection 3.1.6). A second important influence on the shift is the strength of the electric field E_z which is linear. The higher the field strength is, the stronger the shift will be. The technical reasons for a

limitation of the maximal electric field are discussed in section 3.3. Measuring bipolar also immediately doubles the frequency shift. Figure 2.17 visualizes the expected frequency shift due to the neutron charge depending on the used and possible electric fields (in this thesis $\approx 8\,\mathrm{MV\,m^{-1}}$), a possible field increase, bipolar measurement and the transition frequency ($|2\rangle \rightarrow |4\rangle$, $|1\rangle \rightarrow |7\rangle$).

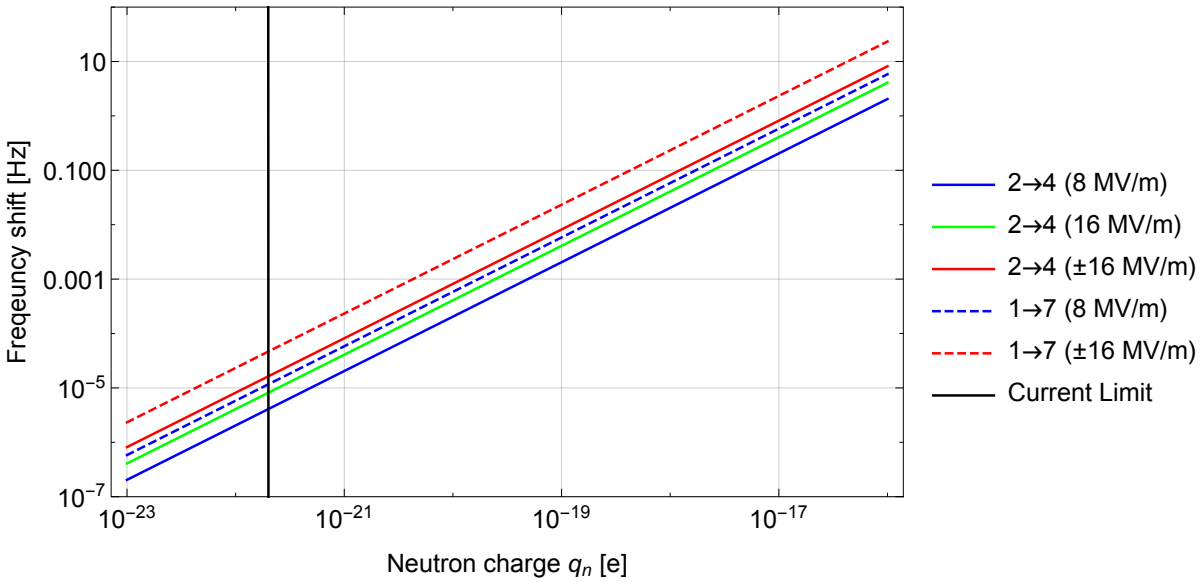

Figure 2.17.: Frequency shift due to a hypothetical neutron charge for different electric field strengths and transitions

Opposite to eq. (2.158), where the variance of the shift is expressed as the sum of the variances of the single frequency determinations, the error of the transition frequency shift can also be expressed as the following:

$$\sigma_{\Delta_{\nu_{fi}}} = \Delta_{\nu_{fi}} \sqrt{\left(\frac{\sigma_{\nu_{fi}g}}{\nu_{fi}g}\right)^2 + \left(\frac{\sigma_{q_\mathrm{n}}}{q_\mathrm{n}}\right)^2 + \left(\frac{\sigma_{E_z}}{E_z}\right)^2 + \left(\frac{\sigma_{m_\mathrm{n}}}{m_\mathrm{n}}\right)^2 + \left(\frac{\sigma_g}{g}\right)^2} \tag{2.168}$$

These relative measurement errors have different orders of magnitude. The error of the frequency measurement depends on the measurement time and therefore on the counted neutrons. The relation is derived in the next subsection. For the RAMSEY$^{\mathrm{TR}}$-setup a 10^{-3} precision can be expected. The error of the charge is the goal of the measurement and therefore it has to be determined by the other errors involved (see subsection 2.3.1). The error of the electric field is in the order of 1 % with corrections in the order of 10 %. The following paragraphs describe this large contribution in more detail. The error due to the neutron mass is negligible (see subsection 2.1.3.2) similar to the local gravitational acceleration g if it is measured classically (see subsection 2.1.3.3). If it is taken directly from the GRS measurement it has a similar uncertainty as the transition frequency.

The electric field E_z consists of two measured values: the set voltage U and the measured distance between the electrodes d:

$$E_z = U/d \tag{2.169}$$

$$\sigma_{E_z} = \sqrt{\frac{1}{d^2}\sigma_U^2 + \frac{U^2}{d^4}\sigma_d^2} \tag{2.170}$$

Therefore, the error of the electric field measurements σ_{E_z} depends on two uncertainties σ_U and σ_d (eq. (2.170)).
The main uncertainty σ_U of the applied voltage U is the dark resistance of the electrode [241](p.28-29) which can induce a correction of over 10 %. Better determination of this resistance via dark current measurements or the increase of the dark resistance by introducing better electronic components (e.g. HV diodes [247]) can reduce the contribution down to the uncertainty of the power supply ($\approx 3\,\mathrm{V}$, see subsection 3.3.5) [151](p.39-40).

The distance d ($100 - 200\,\mu m$) is measured with an accuracy of few µm which is a relative error on the percent level (see subsection 3.3.6). There are two methods to determine the distance d. Either via an absolute measurement with Linear Gauges and spacers (see section 3.7.1) or with a relative capacities measurement which also measures the relative alignment. Both measurements can complement each other [96]. However, the absolute measurement needs a strict protocol and does not provide an opportunity to review the adjustment. The relative measurement is based on the alignment of the electrode as a plate capacitor with the dimensions $a_E \times b_E$ [169](p.5-6). In 2022, the expansion to the 4th order was necessary to describe the measurements accurate enough [162](p.9-10):

$$C = \frac{\epsilon_0 a_E b_E}{d}\left(1 + \frac{{a_E}^2\alpha^2}{12d^2} + \frac{{b_E}^2\beta^2}{12d^2} + \frac{{a_E}^4\alpha^4}{80d^4} + \frac{{b_E}^4\beta^4}{80d^4} + \frac{{a_E}^2\alpha^2{b_E}^2\beta^2}{24d^4} + \mathcal{O}\left(\alpha^6\right) + \mathcal{O}\left(\beta^6\right)\right) + C_P \tag{2.171}$$

In principle, the accuracy of the alignment parameters (distance d, pitch angle α and roll angle β) increases with the number and variety of the measurement points. The correction of the parasitic capacitance C_P is in the order of 10 %. It can be measured either directly with an open cable measurement or more precisely with enough data points during the alignment [96, 151, 162, 169, 225].

Sensitivity of the electric charge measurement

For the electric charge measurement, the measured shift (eq. (2.167)) can be expressed with a movement of the measured rate on the slope of the resonance peak. The end of the section 2.2.2 already presented an approximation of the theoretical predicted transition curves and how to calculate the steepness of the slope at the infliction points which are the basis for the following calculations.

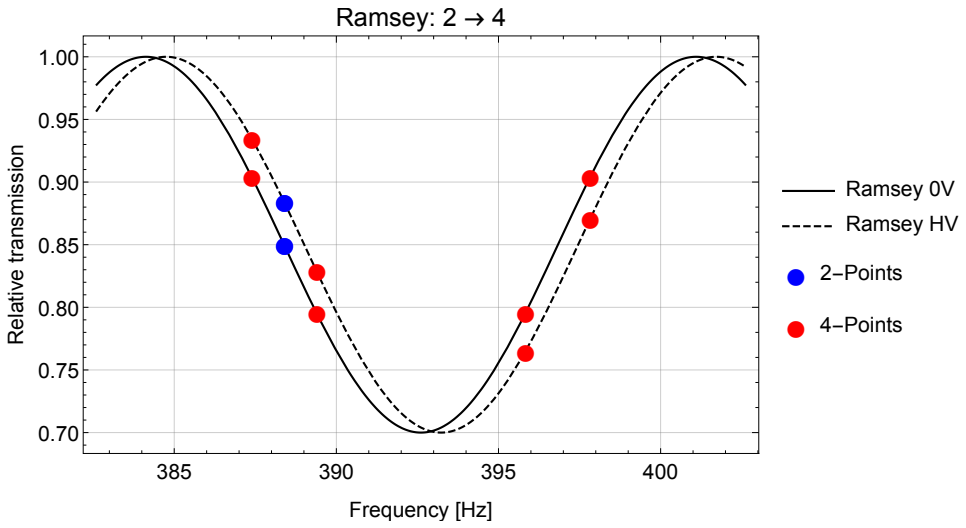

Figure 2.18.: Possible working points of the charge measurement. The shift due to a hypothetical charge is highly exaggerated for a better visibility.

In contrast to the original intentions (2 point measurement, [77]), the inflection points are not directly measured. Instead, two points around these particular points are measured for the determination of the slope (4 point measurement) as depicted in figure 2.18. Therefore, the mean of the two surrounding measured points is used for the determination of the inflection points:

$$\Delta_{\nu_{fi}} = \frac{T_+ - T_{0V}}{\frac{\partial T}{\partial \nu}|_{\Delta\nu_m}} = \frac{T_+ - T_{0V}}{2\pi\frac{\partial T}{\partial \Delta\omega}|_{\Delta\omega_m}} = \frac{T_+\left(\frac{\pi}{2V_{fi}\tau}, \Delta\omega_m + \delta_m\right) + T_+\left(\frac{\pi}{2V_{fi}\tau}, \Delta\omega_m - \delta_m\right) - T_{0V}\left(\frac{\pi}{2V_{fi}\tau}, \Delta\omega_m + \delta_m\right) - T_{0V}\left(\frac{\pi}{2V_{fi}\tau}, \Delta\omega_m - \delta_m\right)}{4\pi\frac{\partial T}{\partial \Delta\omega}} \tag{2.172}$$

The theoretical approximated slope can also be replaced with real measurements (see eq. (2.143)):

$$\Delta_{\nu_{fi}} = \frac{\delta_m}{\pi} \frac{T_+\left(\frac{\pi}{2V_{fi}\tau}, \Delta\omega_m + \delta_m\right) + T_+\left(\frac{\pi}{2V_{fi}\tau}, \Delta\omega_m - \delta_m\right) - T_{0V}\left(\frac{\pi}{2V_{fi}\tau}, \Delta\omega_m + \delta_m\right) - T_{0V}\left(\frac{\pi}{2V_{fi}\tau}, \Delta\omega_m - \delta_m\right)}{T_+\left(\frac{\pi}{2V_{fi}\tau}, \Delta\omega_m + \delta_m\right) - T_+\left(\frac{\pi}{2V_{fi}\tau}, \Delta\omega_m - \delta_m\right) + T_{0V}\left(\frac{\pi}{2V_{fi}\tau}, \Delta\omega_m + \delta_m\right) - T_{0V}\left(\frac{\pi}{2V_{fi}\tau}, \Delta\omega_m - \delta_m\right)} \tag{2.173}$$

This shift is measured on both sides of the transition peak. The results are averaged. Additionally, this can be applied for different voltage settings. In the ideal case for a bipolar measurement, the measurements with zero voltage cancel out and the shift doubles.

The sensitivity of the charge measurement is the error of the measured neutron charge. As shown in eq. (2.164), the error of the charge q_n mainly depends on the error of the shift $\Delta_{\nu_{fi}}$. The errors of all other parameters (transition frequency ν_{fi}, neutron mass m_n, gravitational acceleration g or electric field strength E_z) only contribute on the percent level or less (see more in section 2.1.3):

$$\sigma_{q_\mathrm{n}} \approx q_\mathrm{n} \frac{\sigma_{\Delta_{\nu_{fi}}}}{\Delta_{\nu_{fi}}} = \frac{\sigma_{\Delta_{\nu_{fi}}}}{{\nu_{fi}}^g} \frac{3 m_\mathrm{n} g}{2 E_z} \tag{2.174}$$

As a first approximation, the error of the slope is neglected as this can be measured to a higher precision in advance without an applied electric field:

$$\sigma_{\Delta_{\nu_{fi}}} = \frac{1}{2\pi} \sqrt{\frac{1}{\left(\frac{\partial T}{\partial \Delta\omega}\right)^2}\sigma_{T_+}^2 + \frac{1}{\left(\frac{\partial T}{\partial \Delta\omega}\right)^2}\sigma_{T_{0V}}^2 + \frac{\left[T_+ - T_{0V}\right]^2}{\left(\frac{\partial T}{\partial \Delta\omega}\right)^4}\sigma_{\frac{\partial T}{\partial \Delta\omega}}^2} \approx \frac{\sqrt{\sigma_{T_+}^2 + \sigma_{T_{0V}}^2}}{2\pi \frac{\partial T}{\partial \Delta\omega}} \tag{2.175}$$

The transmission probability T is the measured neutrons N divided by the measurement time t rescaled with the zero rate r_0. Its error mainly depends on the uncertainty of the counted neutrons ($\sigma_N = \sqrt{N}$). Additionally, the uncertainty of the zero rate measurement can also contribute if the number of detected neutrons is similar between both measurements:

$$T = \frac{N}{t}\frac{1}{r_0} \qquad \sigma_T = \sqrt{T^2\frac{\sigma_N^2}{N^2} + T^2\frac{\sigma_{r_0}^2}{{r_0}^2}} = \sqrt{\frac{T^2}{N} + T^2\frac{\sigma_{r_0}^2}{{r_0}^2}} \approx \frac{T}{\sqrt{N}} \tag{2.176}$$

In the picture of the cosine approximation, the measured rates at the inflection points are exactly between the zero rate r_0 and the reduced rate at the transition frequency (for measurements with and without an applied electric field). This rate r_{fi} is ideally zero. In reality background from other states and velocity smearing increases this transition rate r_{fi}. The difference between the zero rate r_0 and transition rate r_{fi} relative to the zero rate r_0 is the so called contrast:

$$T_+ \approx T_{0V} = \frac{N}{t}\frac{1}{r_0} \approx \frac{r_0 + r_{fi}}{2}\frac{1}{r_0} \qquad \sigma_{T_+} \approx \sigma_{T_{0V}} \approx \frac{r_0 + r_{fi}}{2}\frac{1}{r_0}\frac{1}{\sqrt{N}} \tag{2.177}$$

Of course, this simplification only holds if both measurements at different voltage settings counted an equal amount of neutrons N with the same zero rate r_0 in a similar time t.

This result is further inserted into the frequency shift error $\sigma_{\Delta_{\nu_{fi}}}$. Additionally, the contrast has to be taken into account also in the slope of the theory function (eq. (2.142)):

$$\sigma_{\Delta_{\nu_{fi}}} \approx \frac{\sqrt{2}\frac{r_0+r_{fi}}{2}\frac{1}{r_0}\frac{1}{\sqrt{N}}}{\frac{r_0-r_{fi}}{r_0}2\pi\frac{\partial T}{\partial\Delta\omega}} \approx \frac{\sqrt{2}\frac{r_0+r_{fi}}{2}\frac{1}{r_0}\frac{1}{\sqrt{N}}}{\frac{r_0-r_{fi}}{r_0}(4\tau + \pi t_p)} = \frac{1}{\sqrt{2N}}\frac{r_0 + r_{fi}}{r_0 - r_{fi}}\frac{1}{(4\tau + \pi t_p)} \tag{2.178}$$

This approximation for a two point measurement gives the sensitivity of the neutron charge. Introducing the number of measured points n generalizes the formula to different measurement schemes (e.g. 2 point measurement $n = 2$, 4 point measurement $n = 8$: two measurement points for each flange and voltage setting):

$$\sigma_{q_\mathrm{n}} \approx \frac{1}{\sqrt{nN}}\frac{r_0 + r_{fi}}{r_0 - r_{fi}}\frac{1}{(4\tau + \pi t_p)}\frac{1}{{\nu_{fi}}^g}\frac{3 m_\mathrm{n} g}{2 E_z} \tag{2.179}$$

The expected values of the setup used for the charge measurement are: $N = 400$ neutrons for each measurement point, a zero rate r_0 of 20 mcps, a transition rate r_{fi} of 14 mcps which corresponds to a contrast of $c_{42} = 30\,\%$, a *Mambo factor* of 0.4 (see more in section 3.1.1), an interaction time τ of 17 ms ($= 152\,\mathrm{mm}/9\,\mathrm{m\,s^{-1}}$), a propagation time t_p of 38 ms ($= 340\,\mathrm{mm}/9\,\mathrm{m\,s^{-1}}$), the transition $|2\rangle \rightarrow |4\rangle$ and an electric field strength E_z of $8\,\mathrm{MV\,m^{-1}}$. This gives a projected sensitivity of $5.3 \times 10^{-17}\,e$ for a simple two point measurement. A full four point measurement needs four measurements per voltage setting which increases the counted neutrons by a factor 4 and decreases the sensitivity to $2.6 \times 10^{-17}\,e$.
Per day the sensitivity with this setting will be $6.1 \times 10^{-17}\,e\,\mathrm{d}^{-0.5}$ independent of the measurement scheme because it depends only on the number of totally counted neutrons nN. This corresponds to a measured precision of the frequency of $1.26\,\mathrm{Hz\,d}^{-0.5}$ due to eq. (2.178) which only depends on the counted neutrons nN, GRS contrast c_{42}, mirror length l_{II} and neutron velocity v_n (which are related to the interaction time τ and the propagation time t_p).
However, the zero rate r_0 and the transition rate at resonance r_{fi} can change significantly between different voltage settings[32] due to changes of the reactor power level[33]. Therefore, for each measurement set (voltage setting) the zero rate r_0 and the transition rate r_{fi} are determined additionally with at least one measurement point. These values are also important for systematic checks and stability of the system because the value of the contrast is not expected to change due to a power level change. These additional measurement points have to be accounted for with at least one third of the measurement time. This reduces the total counted neutrons per day during a charge measurement and its sensitivity.
Also the error of the contrast could be accounted within the sensitivity calculation which reduces the sensitivity slightly. However, the real data evaluation uses the full Ramsey-GRS equations (eq. (2.124)) to determine the neutron charge and therefore a very detailed sensitivity calculation based on approximations is not necessary (see more in section 2.3.3).
The reduced sensitivity is $7.5 \times 10^{-17}\,e\,\mathrm{d}^{-0.5}$ corresponding to a limit of the frequency shift of $1.54\,\mathrm{Hz\,d}^{-0.5}$.
The measurements in 2018 planned to collect at least 400 neutrons per measurement point. This resulted in an expected sensitivity of $2.6 \times 10^{-17}\,e$ with a precision of 0.54 Hz. This would take 8.2 days with the expected zero rate of 20 mcps.

Since 2018, the RAMSEY$^{\mathrm{TR}}$-setup improved a lot [194]. The zero rate r_0 increased to 30 mcps and the contrast to over 60 %. The stability of all components allows to measure more than 50 days during one cycle. This increased statistical precision improves the frequency precision to $0.57\,\mathrm{Hz\,d}^{-0.5}$ (which is comparable to the planned sensitivity of all measurements in 2018) and 81 mHz over a complete reactor cycle. The possible sensitivity with the current available electric field strength in 2018 ($8\,\mathrm{MV\,m^{-1}}$) is $3.9 \times 10^{-18}\,e$. A change to the now available transition $|1\rangle \rightarrow |7\rangle$ further improves the sensitivity to $1.4 \times 10^{-18}\,e$. Also an easy to implement bipolar measurement scheme changes it to $6.9 \times 10^{-19}\,e$ and a potential doubling of the electric field strength to $3.5 \times 10^{-19}\,e$. Compared to the measurements in 2018, the immediate possible improvements of the electric charge measurement enable a better sensitivity up to factor 75. This is still a factor 430 away from the best neutron charge measurement of Baumann et al. [36].

Two long term projects can close this gap. First, eliminating the losses of the neutron divergence can increase the count rates up to a factor of 10. This so-called *HL-Ramsey*[34] can reach a precision of 25 mHz and sensitivity of $1.1 \times 10^{-19}\,e$ within one cycle. Second, a long-term project is to implement a storage Ramsey-type GRS-setup. This will eliminate the velocity dependency, consequently the corresponding contrast losses and the *Mambo factor* because it can better adapt to the PF2 switching cycle. Storing neutrons increases the propagation time t_p between 10 s and 100 s if the expected technical difficulties to preserve the quantum states are solved [237](p.75-88). On the other hand, the neutron rate decreases to a not yet known value (e.g. due to the used pulsed mode in a continuous beam). In a pessimistic case, each storage cycle measures only one neutron and has a complete length of 200 s. The achievable sensitivity in this case would be $3.2 \times 10^{-21}\,e$ or $3.2 \times 10^{-22}\,e$ for a shorter or longer storage time in one complete reactor cycle. The very optimistic scenario of 15 neutrons per cycle improves it to $8.2 \times 10^{-22}\,e$ and $8.2 \times 10^{-23}\,e$ respectively, which would be lower than the current limit.

[32] Each voltage setting is measured as one consecutive set of measurement points because changing the value of the high voltage is done slowly (0.5 V/s) and therefore it is very time consuming.
[33] In 2018, the reactor power decreased from the zero volt measurement to the high voltage measurements to only around 70 % of the reactors previous power due to a malfunction.
[34] *HL* stands for high luminosity

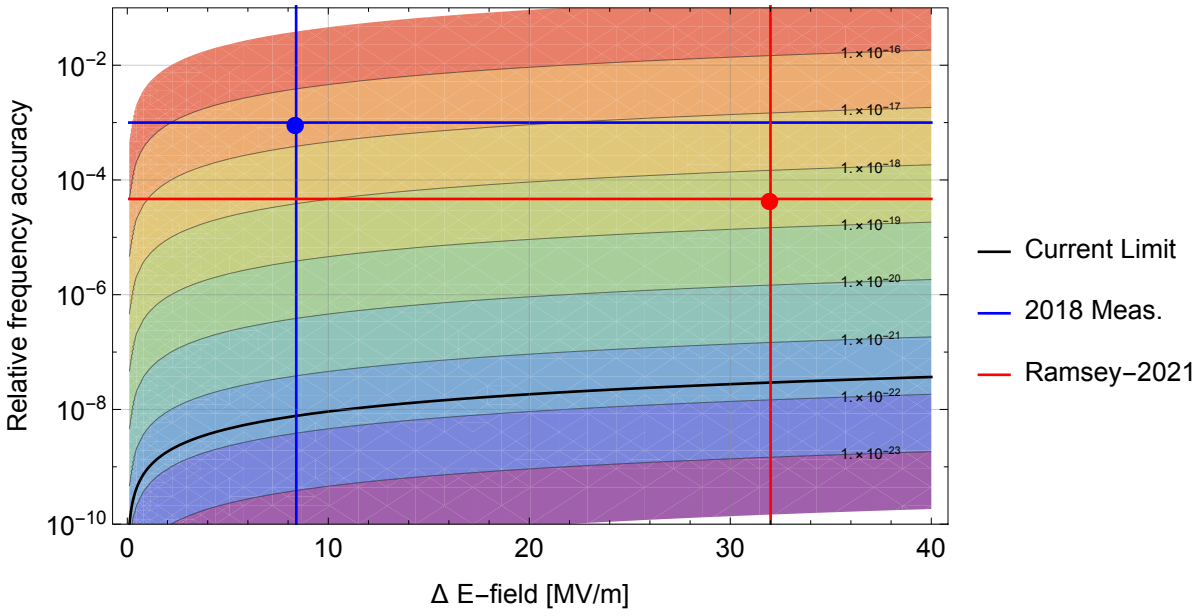

Figure 2.19.: Needed electric field strength and relative frequency precision: Red straight lines are the currently possible values within the RAMSEY^{TR}-setup. Jakob Micko reached already this level of precision [194].

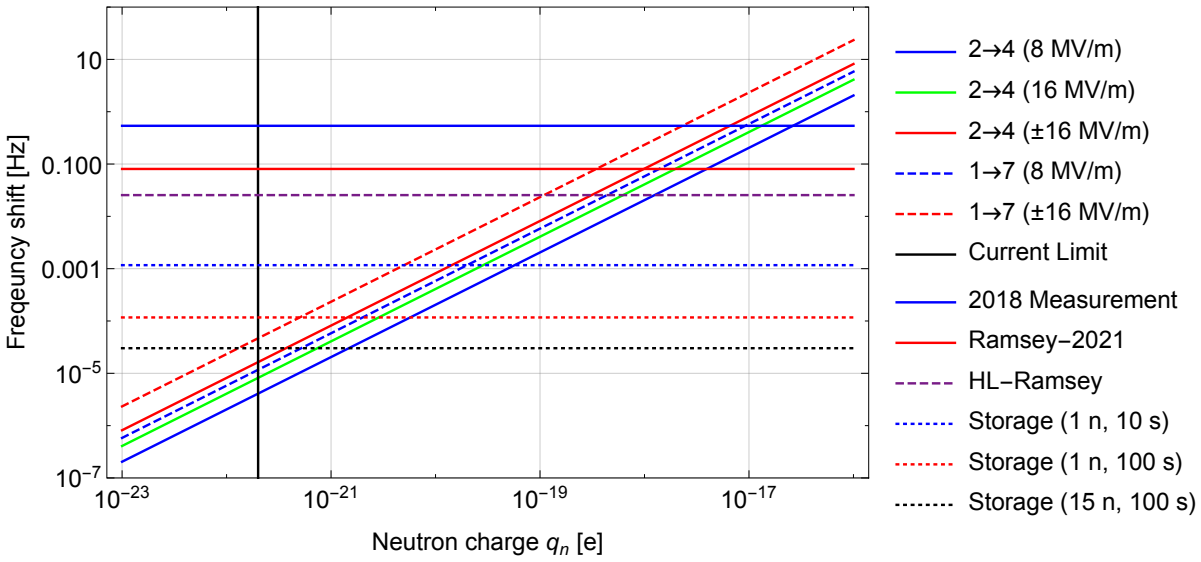

Figure 2.20.: Sensitivity of different setups compared to frequency shifts due to a hypothetical neutron charge for different electric field strengths and transitions

2.3.3. Charge measurement

In order to measure the electric charge of a neutron, a Ramsey transition is studied in detail. Ideally, this transition should have a very high frequency which is mainly limited by the mechanical response of the PI-tables (piezoelectric stages, see section 3.1.6). As the measurement took place soon after the successful commissioning of the RAMSEY^{TR}-setup the only studied state transition was $|2\rangle \rightarrow |4\rangle$. Therefore, this was used for the charge measurement. The second ingredient is a different setting for the applied high voltage. Each setting needs enough data points to determine the transition frequency ν_{fi} independent of other voltage settings. For this thesis multiple measurement points were taken for the zero voltage measurement and five points for 1000 V and 1750 V respectively (see section 4.6). In the ideal case, bipolar settings with maximal reachable electric field strength would result in the highest achievable sensitivity (see details in section 2.3.2).

The main data evaluation method is to fit all measured data points together with the input parameters: frequency ν, amplitude strength a_v, measured and corrected neutron count rate normalized by the zero rate r_0 to a relative transmission and the electric field strength E_z. The phase information was not used because all frequency measurements were adjusted to the same zero phase difference and an investigation showed that statistically a deviation cannot be determined. The underlying Ramsey theory fit function (eq. (2.125)) uses the characteristic parameter for the additional electric charge potential (eq. (2.156)). The fit parameters are the contrast c_{fi}, the local gravitational acceleration g and the searched hypothetical neutron charge q_n. The charge q_n and g have similar effects on the theoretical curve (they shift the resonance frequency ν_{fi}). Therefore, g has to be fixed before the charge q_n is fitted. The fixed value of g can either be the calculated value for Grenoble (see table 2.3) or the fitted value of the zero field measurement[35]. The second method has the advantage that all unknown systematic effects are equal for all measurements (with electric fields and without) and therefore can be ignored. In this thesis this approach is used to determine the final limit of the electric charge of the neutron. To visualize the parameter space, pairs of g and q_n are used to fit the corresponding contrast c_{fi}. The calculated map of the χ^2 surrounding displays the most likely values of the neutron charge q_n depending on the local gravitational acceleration g.

A different approach is to calculate the transition frequency ν_{fi} and therefore local gravity g for each voltage setting independently. The charge can be determined by the dependency of the transition frequency ν_{fi} on the electric field strength $\vec{E}$. A hypothetical charge would generate the following behavior:

$$\nu_{fi}{}^{\vec{E}} = \nu_{fi}{}^{g} \sqrt[3]{\left(1 + \frac{q_\mathrm{n} E_z}{m_\mathrm{n} g}\right)^2} \approx \nu_{fi}{}^{g} + \nu_{fi}{}^{g} \frac{2 q_\mathrm{n} E_z}{3 m_\mathrm{n} g} \tag{2.180}$$

A simple linear regression ($y = kx + d$) would determine the charge as $q_\mathrm{n} \approx 3 k m_\mathrm{n} g/(2d)$. As a limit for the charge serves the tripled error of this fitted value. This evaluation will also be displayed in the measurement as an additional graphical information (see section 4.6).

[35] For this analysis the simple purely gravitational theory is used for the fitting routine (eq. (2.7)).

3. Description of the *q*BOUNCE setup

The following chapter describes all the necessary elements to run a *q*BOUNCE experiment, in particular the RAMSEY^{TR}-setup. This state-of-the-art GRS setup has been situated at the PF2/UCN beam port at the ILL in Grenoble since autumn 2016 [254].

Figure 3.1 displays a schematic view of the RAMSEY^{TR}-setup. In each section a highlighted version of this figure depicts the described parts. A more realistic view is the rendering in figure 3.2 as for every part a 3D-model exists in the CAD software *Inventor* from Autodesk[1].

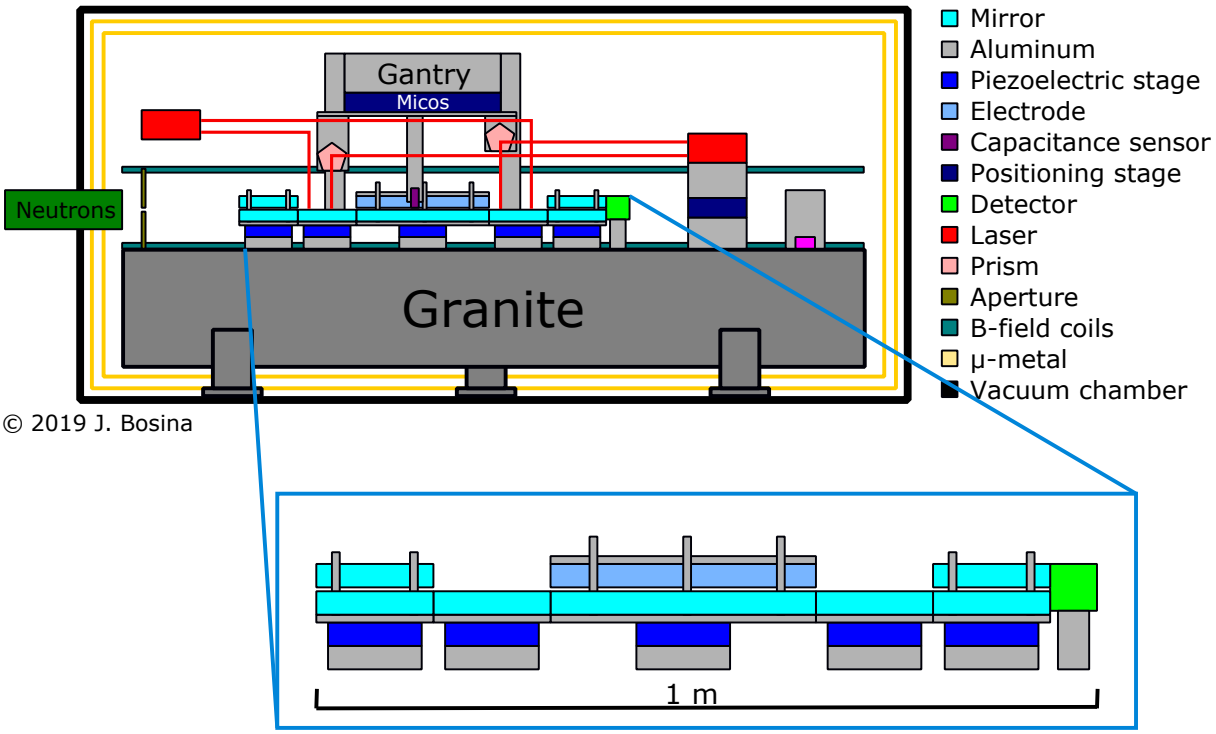

Figure 3.1.: A schematic view of the RAMSEY^{TR}-setup

The first section 3.1 describes the neutron guiding system from the beam line to the mirror regions. The second section 3.2 covers all different detector types used for the neutron detection. Section 3.3 explains the electrode test setup which is situated at the ATI in Vienna. For the neutron charge measurement the essential parts were brought to Grenoble and integrated temporarily into the RAMSEY^{TR}-setup. In section 3.4, I explain the tools and workflows for sustaining vacuum condition within the experiment. Section 3.5 specifies the components needed to align the mirror surfaces. The devices to induce and monitor the mirror oscillations are depicted in section 3.6. Section 3.7 comprises all auxiliary systems which are needed for various purposes. I describe the data acquisition infrastructure in section 3.8. Preparations for future measurements with polarized neutrons can be found in section 3.9. The final section 3.10 presents the new *q*BOUNCINO test platform [236]. This is a modular small scale *q*BOUNCE-setup consisting of spare or old experimental parts for systematical tests of future components (detectors, guiding systems,...).

More detailed information on specific subjects can be found in the quoted specialized theses of all the previous students, in particular the thesis of Tobias Rechberger who built the RAMSEY^{TR}-setup during his PhD thesis [254]. For future students, additional information can be found in [1, 45].

[1] Autodesk, 111 McInnis Parkway San Rafael, 94903 California, U.S., www.autodesk.com (13.11.2023)

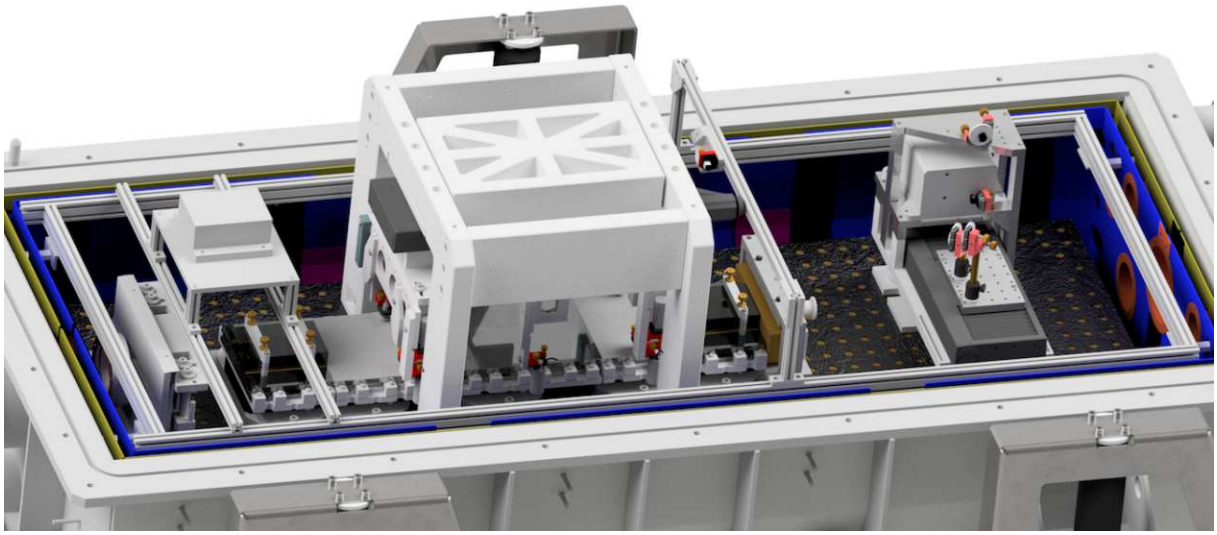

Figure 3.2.: A rendered view of the RAMSEY^{TR}-setup [254](p.91)

3.1. Neutron guiding system

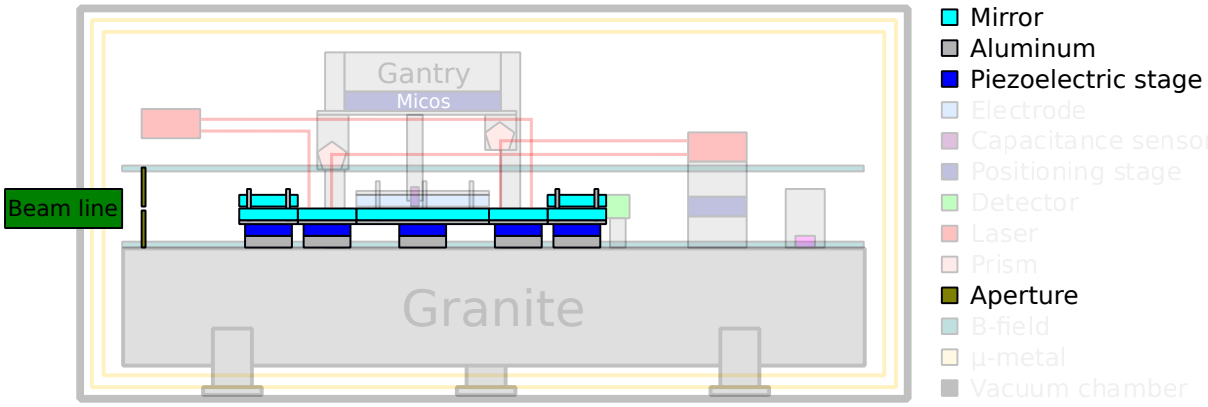

Figure 3.3.: A schematic view of the neutron guiding system within the RAMSEY^{TR}-setup

As displayed in figure 3.3, this section will describe all parts necessary to guide the neutrons from the PF2 turbine to the detector including their physical requirements and their technical realization:

- The PF2 switcher for sharing the neutron beam (not visible in fig. 3.3)
- The beam line consisting of the beam guides, shutters and the monitor detector
- The aperture as the velocity selector
- The neutron mirrors as guides within the setup and also state selectors

3.1.1. PF2 switcher

As described in subsection 1.3, the PF2 turbine produces UCNs and delivers them to five different beam sites: The PF2/VCN receives the neutrons bypassing the turbine as very cold neutrons. The PF2/TEST beam is connected to a port behind the turbine and receives only a small amount of the produced UCNs. Both beams are completely independent. The other three beam sites have to share one port of the turbine which is situated at the position with the highest produced UCN flux. These three ports are called PF2/MAMBO, PF2/UCN and PF2/EDM. *q*BOUNCE is situated at the PF2/UCN beam port.
For distributing the neutron beam between the three beam ports a switcher guides the neutrons to only one beam tube at the time. The so-called *turbine control* operates the switcher and handles the needs for neutron flux of the experiments attached to these ports. Due to the non-continuous flux, a special time structure is imprinted on the measurement.

Turbine control timing

NOMAD[2] based control computers (since 2017) deliver the *request* set from the three beam ports to the turbine control. When the switcher reaches the requesting position, the turbine control gives *permission* to this chosen beam. At this moment the 10 s long so-called *filling* time window starts. During this time, the neutron beam flux is rising. At the end, the actual measurement can start at a stable rate [298](p.47). The measurement time itself is 190 s long and is coordinated with the other users of the PF2. A *veto* set from the start of the *permission* (incl. adjusting of the switcher - *filling*) until the end of measurement (200 s later) denies every request of other beam lines. Otherwise, these requests would force the switcher to move to another beam port during the measurement window. There is always a time before and after the measurement window of 10 s and 12 s respectively without commands in order to provide the switcher with enough time to move without disturbance[3]. As mentioned previously, the time window before the measurement is called *filling*, the time afterwards *emptying*. Together with the measurement window we call these three time windows a *cycle* [115](p.12-13). Between cycles, when another beam line receives the neutron beam, there is the background window.
During measurements, the NOMAD software continuously requests the beam and handles the cycles in a for-loop. Additional TTL-signals from the control PC operate the detectors and the pneumatic shutter [298](p.45-47). These signals are also recorded via the main LabView program and are needed to automatically change measurements during *emptying* if a desired neutron count is reached via the *measurement queue*. During data analysis, the measurement cycles are reconstructed with the recorded TTL-signals. Comparing the obtained cycle number with the AFG (section 3.6.1) and the detector (section 3.2.1), allows to distinguish between zero rate measurements and measurements with oscillating mirrors.

Sharing the beam leads to dead time. To take this into account during the planning of measurements we use the duty cycle or also called MAMBO-*factor*. This is the ratio of measurement time (life time) to real time. If only one experiment is running, the maximum MAMBO-*factor* is ≈89 % with no time for background measurements. At the PF2/MAMBO beam line Gravitrap, a large storage experiment for measuring the neutron lifetime, is situated [277]. Its huge tank needs to be filled only few times every hour so the experiment needs only 10-20 % of the total time. During the last reactor cycles, the PF2/EDM beam line hosted mainly experiments which needed a continuous flux with a similar cycle timing as we have (e.g. measuring the scattering cross section of solid deuterium [78]). The MAMBO-*factor* decreases down to only 40 % when all experiments are running simultaneously. This increases the needed time to count the same amount of neutrons and should always be considered in planning measurements, especially with CR-39 detectors.

[2] a sequencer for instrument control developed by the ILL, www.ill.eu/redirects/tools/glossary/N#nomad (11.12.2022)
[3] From 1.10.2018 onward this was changed to 12 s and 15 s respectively in order to leave the switcher even more time to move.

3.1.2. Beam line

Beam line elements

Due to strong absorption of UCNs in air, only evacuated beam guides can transport a sufficient amount of these very slow neutrons to the experiment (Calculations of pressure-dependent neutron transmission can be found in section 3.4). Hence, the beam line mainly consists of these evacuated beam guides. Additional coatings and choice of materials decrease the loss due to absorption in the walls and enhance the wall reflections within these guides. Further losses can occur in the junctions between the guides due to gaps and misalignments.

Polished stainless steel tubes and coated glass tubes are commonly used as neutron guides due to their smooth surfaces. The advantages of coatings are the used materials (high neutron optical potential e.g. Ni-58) and the possible layer structure which increases the reflectivity even for higher neutron velocities and larger angles. The main disadvantage of the coated glass tubes is their brittleness. Therefore, glass tubes have thicker walls (5 mm to 6 mm instead of $\approx$ 1 mm at steel tubes). Additional spacers made of aluminum foil or Teflon rings between the glass tubes prevent spalling of the edges. Especially at the presence of pressure gradients (e.g. evacuation, venting), implosion of the glass tubes is a severe hazard. Slow changes reduce the mechanical stress. An additional analog pressure gauge close to the vent valve helps to control the pressure gradients during manual venting. Utilized outer diameters for glass tubes are 90 mm and for metal tubes 70 mm and 81 mm.

Wilson flanges connect the tubes with minimal spacing (= losses). Additional small side flanges on the Wilson flange allow to connect pressure gauges, pipes to the vacuum pumps or monitor detectors. These neutron detectors are always situated below the flange in order to catch all neutrons falling through the gap between the beam tubes and an opening at the bottom of the spacers between them. The detector's count rate is proportional to the delivered neutrons. This monitor rate normalizes the detector count rate and accounts for changes in the reactor power level, cold source conversion efficiency or the PF2 turbine performance. A larger flange diameter (KF25 instead of KF16) and better material (stainless steel instead of aluminum) increases the efficiency of the monitor detector by increasing the solid angle of entering neutrons. A larger guided fall distance to the detector accelerates neutrons and increases their transmission through the foil at the detector window (especially for very slow neutrons).

Thin aluminum foils (Al97Mg3) at the beginning and at the end of the beam tubes enclose the vacuum within this part of the beam line and separate it from the neutron source and the experiment. During venting of the experimental vacuum chamber, these foils have to withstand a mechanical stress of 1 bar. This leads to a strong concavity of the foil towards the vacuum (in the direction of the neutron source). The mechanical integrity of these windows is very important. Tools must be handled very carefully near these neutrons windows. Even touching should be avoided in order to prevent their rupture. A second measure is always to evacuate the volumes starting from the source (PF2-turbine) and venting from the experiment (main vacuum chamber first) in order to prevent a flopping of the foils due to a different pressure gradient.

Shutters and switchers are often inserted in the beam line. Shutters can block the beam for background measurements or for safety reasons (e.g. for works at the experiment). There are two types of shutters. Some are modified vacuum gate valves, the others are switchers with only two ports. The gate valve inserts a rectangular beam tube piece (e.g. 100 mm $\times$ 50 mm at the PF2/UCN beam port) in the open position and completely separates the vacuum into two parts in the closed position. They also act as a mechanical shielding during a foil failure and instant venting of one side. This is a very important safety feature to protect the neutron source and its vacuum, especially as the source (PF2 turbine) is part of the reactor safety. A switcher normally consists of a rotatable cylinder made of neutron-absorbing materials. The inserted beam tube is either straight or bent. A vacuum housing encloses the cylinder and has two or more ports for connecting beam tubes. An electric motor or pneumatic mechanics turn the beam tube from the outside to the desired positions. As a drawback the needed vacuum-tight mechanical feedthrough always leaks a little bit, especially during movements, and the mechanical connection loosens slowly over time. The resulting misalignment reduces the transmission. Additionally, the neutron tightness narrows the mechanical tolerances. The advantage is the availability of a three port switcher [116]. A good alignment during the operation is crucial. During the open position, there should be a maximal transmission and during the closed position the beam should be blocked completely in order to be able to measure the background.

Shutter transmission function

The rotatable shutter can be considered as two cylinders (one is the beam guide, the other is the rotating shutter reel). The beam guide is aligned around the $x-$axis (neutron flight direction) and has a diameter of $r_b \approx 40\,\text{mm}$. The shutter reel's axis is vertical (z-direction). Its radius r_s is most likely around 65 mm:

$$y^2 + z^2 = {r_b}^2 \qquad\qquad x^2 + y^2 = {r_s}^2 \tag{3.1}$$

Intersecting both cylinders leads to the following two curves which represent the first and second intersection between the beam guide and the shutter with $t \in [-r_b, r_b]$:

$$f_1(t) = \begin{pmatrix} -\sqrt{-{r_b}^2 + {r_s}^2 + t^2} \\ \pm\sqrt{{r_b}^2 - t^2} \\ t \end{pmatrix} \qquad\qquad f_2(t) = \begin{pmatrix} \sqrt{-{r_b}^2 + {r_s}^2 + t^2} \\ \pm\sqrt{{r_b}^2 - t^2} \\ t \end{pmatrix} \tag{3.2}$$

If the shutter reel and the guide are aligned, the intersection represents the edges of both. To display the edges of the rotated shutter, the intersection curve is rotated around the z-axis:

$$\tilde{f}_1(t,\phi) = \begin{pmatrix} -\sqrt{-{r_b}^2 + {r_s}^2 + t^2}\cos\phi \pm \sqrt{{r_b}^2 - t^2}\sin\phi \\ \pm\sqrt{{r_b}^2 - t^2}\cos\phi + \sqrt{-{r_b}^2 + {r_s}^2 + t^2}\sin\phi \\ t \end{pmatrix} \tag{3.3}$$

$$\tilde{f}_2(t,\phi) = \begin{pmatrix} \sqrt{-{r_b}^2 + {r_s}^2 + t^2}\cos\phi \pm \sqrt{{r_b}^2 - t^2}\sin\phi \\ \pm\sqrt{{r_b}^2 - t^2}\cos\phi - \sqrt{-{r_b}^2 + {r_s}^2 + t^2}\sin\phi \\ t \end{pmatrix} \tag{3.4}$$

The projection of the rotated intersection curve to yz-plane is basis for all further calculations:

$$y_1 = \pm\sqrt{{r_b}^2 - z^2}\cos\phi + \sqrt{-{r_b}^2 + {r_s}^2 + z^2}\sin\phi \qquad \forall z \in [-r_b, r_b] \tag{3.5}$$

$$y_2 = \pm\sqrt{{r_b}^2 - z^2}\cos\phi - \sqrt{-{r_b}^2 + {r_s}^2 + z^2}\sin\phi \qquad \forall z \in [-r_b, r_b] \tag{3.6}$$

There are two simple geometric concepts to describe the count rate reduction due to a rotation of the shutter reel.
The so-called *absorber approach* assumes that any neutron hitting the reel will be absorbed. Only particles which can go in a straight line through the half open shutter are able to pass. For a parallel beam this will be the intersecting area between both rotated shutter edges. Physically, this is expected to be realized for thermal neutron beams or a parallel light beam.
The second approach is the so-called *guide approach* which is probably more suitable for UCNs. These neutrons are only absorbed at the outside walls of the reel when they enter and leave the shutter. Inside they are guided by the beam tube of the shutter without losses. Mathematically this is realized by reducing the flux once or twice by the ratio of the intersection area of the rotated reel and the beam tube to the full beam tube.
Divergent beams are more complex and probably cannot be described with these simple calculations. In this case, they need a full Monte Carlo treatment to understand the transfer function. A measurement can reveal if simple geometric considerations are in first order enough to describe the behavior of the shutter rotation (see section 4.3.3). In the following both approaches are described in more details.

For the *absorber approach* the intersection points between both rotated edges of the shutter in the yz-projections (as seen in figure 3.4 as red points) are:

$$\vec{r}_i^{\,(a)} = \begin{pmatrix} 0 \\ \pm\sqrt{{r_b}^2 - \frac{{r_s}^2}{2}\left[1 - \cos(2\phi)\right]} \end{pmatrix} \tag{3.7}$$

The maximal angle for neutrons to pass is (including an approximation for realistic values of r_s and r_b):

$$\phi_{max}^{(a)} = \pm\frac{1}{2}\arccos\left(\frac{{r_s}^2 - 2{r_b}^2}{{r_s}^2}\right) \approx \pm 37.98° \tag{3.8}$$

The full transmission function can be calculated by numerical integrating from the $y-$axis crossing to the $z-$axis (where the intersection points are). The resulting area is divided by a quarter of the beam guide circle to result into the relative transmission:

$$\int_{y(z=0)}^{0} z(y)\,\mathrm{d}y = \int_{-r_b\cos\phi+\sqrt{-{r_b}^2+{r_s}^2}\sin\phi}^{0} z_1(y_1)\,\mathrm{d}y$$
$$= \int_{-r_b\cos\phi+\sqrt{-{r_b}^2+{r_s}^2}\sin\phi}^{0} \sqrt{{r_b}^2 - \frac{{r_s}^2}{2} + \left(\frac{{r_s}^2}{2} - y^2\right)\cos(2\phi) + \sqrt{y^2\left({r_s}^2 - y^2\right)\sin^2(2\phi)}}\,\mathrm{d}y \tag{3.9}$$

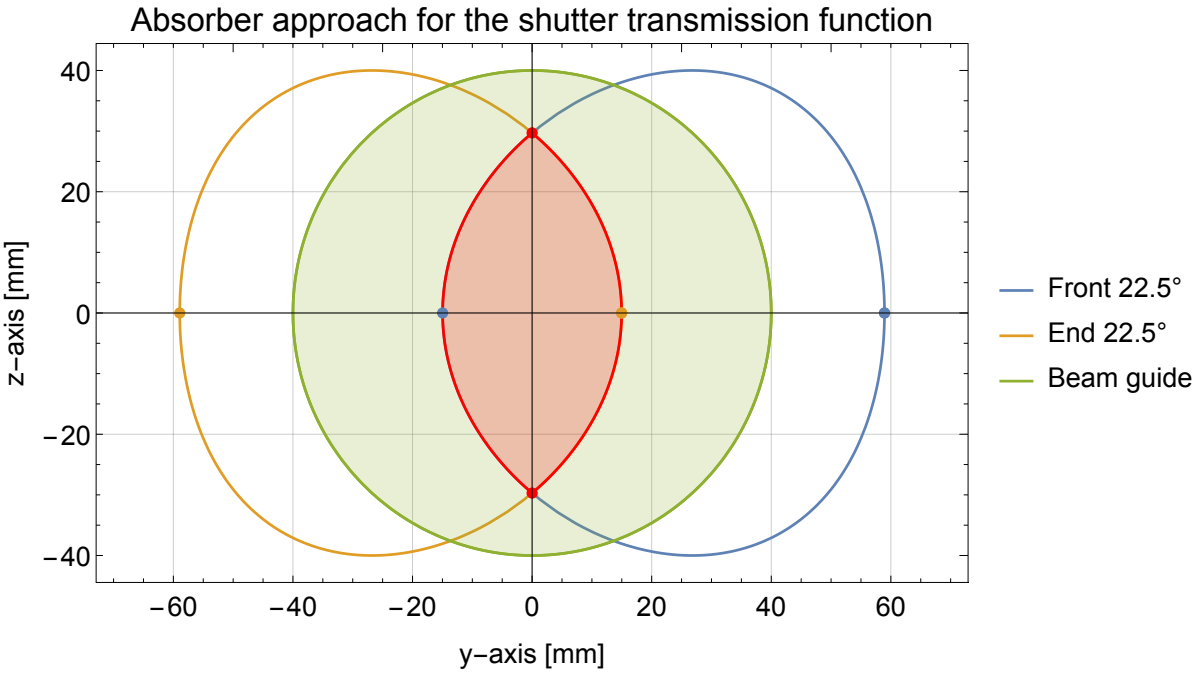

Figure 3.4.: In the *absorber approach* particles are only able to pass the shutter in the red area. The red points represents the calculated intersection points (eq. (3.7)).

The second approach only reduces the transmission by the blockage of the entry. In principle, there are two options: The first is to count this loss only once at the entrance, the second is to count it twice (entrance and exit).
This is done by calculating the area enclosed by one rotated projection and the beam guide yz-projection as seen in figure 3.5. The intersection points of both used curves are:

$$\vec{r}_i^{\,(b)} = \frac{1}{2\sqrt{1+\cos\phi}}\begin{pmatrix} \mathrm{sgn}\phi\sqrt{{r_s}^2 - {r_s}^2\cos(2\phi)} \\ \pm\sqrt{4{r_b}^2 - {r_s}^2 + 4{r_b}^2\cos\phi + {r_s}^2\cos(2\phi)} \end{pmatrix} \tag{3.10}$$

The maximal angle for neutrons to pass is larger compared to the *absorber approach* (including an approximation for realistic values of r_s and r_b):

$$\phi_{max}^{(b)} = \pm 2\arccos\left(\pm\frac{\sqrt{{r_s}^2 - {r_b}^2}}{r_s}\right) \approx \pm 75.96° \tag{3.11}$$

The transmission function is again calculated with an integral. This time the upper boundary is also angle dependent. Above this intersection point between the curves the area is integrated over the complete neutron guide area to its end. To calculate the relative transmission the resulting area is divided by half of the beam guide cross section:

$$\int_{y(z=0)}^{r_y^{(b)}} z(y)\,\mathrm{d}y + \int_{r_y^{(b)}}^{r_b} \sqrt{{r_b}^2 - y^2}\,\mathrm{d}y = \int_{-r_b\cos\phi+\sqrt{-{r_b}^2+{r_s}^2}\sin\phi}^{\sqrt{{r_s}^2-{r_s}^2\cos(2\phi)}} z_1(y_1)\,\mathrm{d}y$$
$$+ \frac{1}{4}\left[\pi{r_b}^2 - 2{r_b}^2\arctan\left(\frac{r_s\sqrt{1-\cos\phi}}{\sqrt{2{r_b}^2 - {r_s}^2\left[1-\cos\phi\right]}r_b}\right) - r_s\sqrt{\left[1-\cos\phi\right]\left(2{r_b}^2 - {r_s}^2\left[1-\cos\phi\right]\right)}\right] \tag{3.12}$$

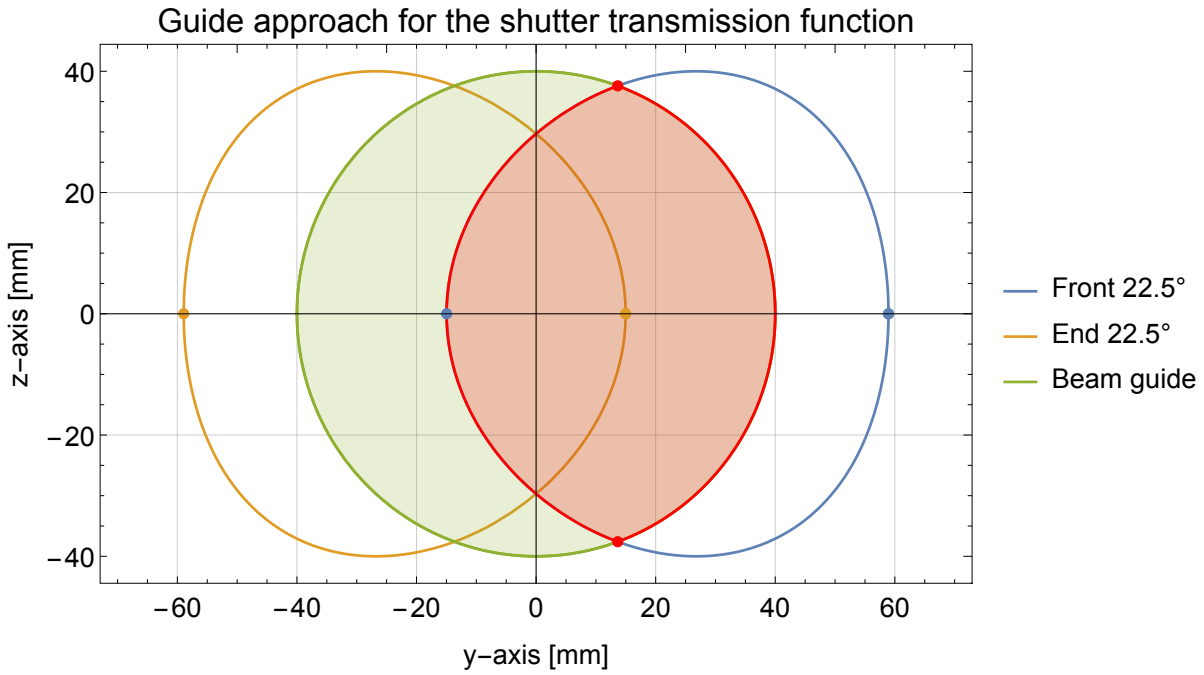

Figure 3.5.: In the *guide approach* particles are able to enter the shutter reel in the full red area. The transmission is only reduced by neutrons which hits the shutter reel (green area) instead of entering. Inside the shutter reel the neutrons are guided completely through it. The red points represents the calculated intersection points (eq. (3.10)).

Beam line configuration at PF2/UCN

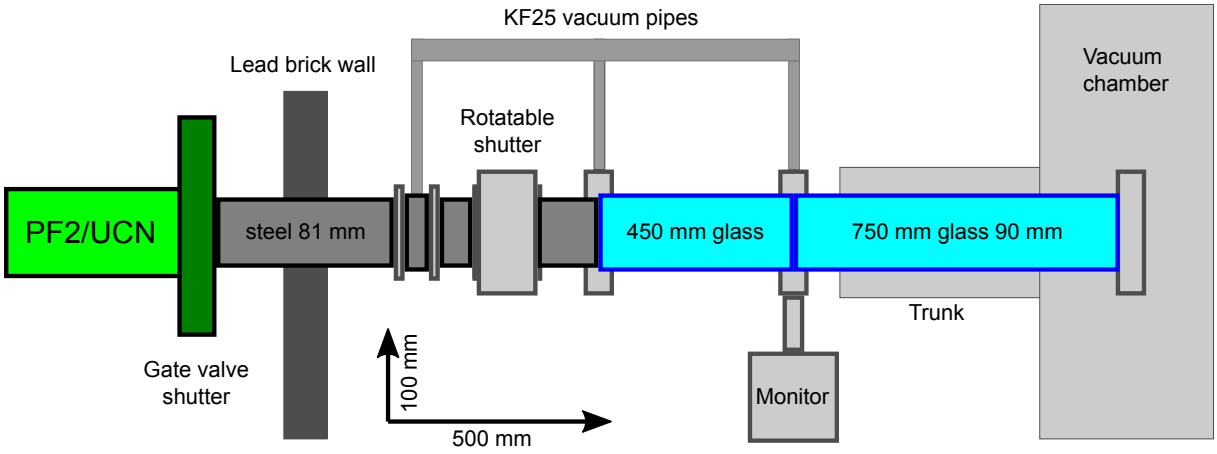

Figure 3.6.: A schematic view of the beam line (2016-2019)

Neutron guides: You can find a first description of the beam line installed in autumn 2016 in [254](p.77-80). All tubes have an inner diameter of 80 mm which is 10 mm larger than in the quite similar beam line of the previous RABI^{GC}-setup [150](p.7-8) in order to increase the neutron flux.
The first guides are made of stainless steel. After the rotatable shutter, they are made of glass (450 mm and 750 mm). Thorsten Laue with his company Movatec[4] coated these glass tubes with nickel-molybdenum layers [101](p.3), which have a higher transmission than the previously used steel ones [69].
The last beam guide ends already inside the vacuum chamber. A trunk-like adjustable bellow encloses it by additionally extending and sealing the main vacuum chamber. At the end of this beam guide, a flat

[4]Movatec GmbH, Erfurter Straße 23, 85386 Eching, Germany

end cap with a neutron window separates the vacuums from the beam line and the chamber.
A different shape of the end cap and the last beam pipe could increase the count rate within the setup. These possibilities have to be simulated and measured before implementation. Probably a continuous transition between circular and rectangular shape could increase the count rate. Also, a complete rectangular beam line could change the flux. At the moment only the guides from the turbine as far as the first shutter are rectangular. Afterwards, they change into a circular shape. This step-like transition is probably the reason for changes within the velocity spectrum.

Position	Type	Length	Diameter
I	steel	≈460 mm	81 mm
II	steel	≈140 mm	81 mm
III	shutter	140 mm	81 mm
IV	steel	140 mm	81 mm
V	glass	450 mm	90 mm
VI	glass	750 mm	90 mm
All	-	2080 mm	-

Table 3.1.: Beam tube lengths

Shutters: As seen in figure 3.6, there are two shutters: one gate valve and one pneumatic rotatable shutter. The gate valve or turbine shutter is always open during the measurements and closed only when there are works on the experimental platform, especially when the vacuum chamber is vented and opened. Here, the shutter protects the turbine from debris during a neutron window rupture or students from neutron irradiation.
The pneumatic shutter has three operation states: *open*, *closed* and *auto*. During normal rate measurements, it is set to *auto* (at CR-39 measurements it is always open to increase the total number of incoming neutrons). The signal from the switcher controller operates this shutter automatically. It opens when the switcher starts to move to the PF2/UCN-position (start of the *filling* window, *permission* of the beam) and closes after the measurement window. It is open during the complete *veto* time and closed during the background window. Otherwise, either the complete beam or, if the switcher moves to different beam port, stray neutrons would increase the background rate significantly. During works on the platform, this shutter is also closed for safety reasons. The acoustic sound of the pneumatic mechanics enables to hear the measurement *cycles* and to check if it is working properly.

Beam monitor: The monitor detector is situated underneath the last Wilson flange, before the vacuum chamber. A pile of boron plastic shields it from any stray neutrons from the reactor pool or the PF2 turbine. An additional oscilloscope within the *detector-fridge* (metal housing of the detector electronics) displays the neutron counts, which is important to check if the shutters are open. The flange itself strongly influences the count rate of the monitor detector. Problems with the designs led to multiple replacements in the past years. To change this flange, the aperture within the chamber has to be removed and the screws of the bellow sealing the last beam tube have to be loosened in order to move this pipe into the chamber and have space to exchange the flange.
In 2014, the monitor flange was a steel tube T pipe but only for guides with a diameter of 70 mm. Due to the large opening angle and the used material, the count rate was around 400 cps. The new RAMSEY^{TR}-setup had a new Wilson flange in order to fit around the glass tubes. It was made of aluminum with only a small diameter for the monitor port. After a very low monitor rate, this port was widened and a KF25 steel pipe was glued in. This flange was used during all beam times of the proposal 3-14-358 (cycles 180-16/3 to 183-18/2). In 2017, the count rate was between 60 cps and 70 cps. In 2018, it decreased to 20 to 30 cps at full reactor power due to detector efficiency decrease (The He-3 in the sealed detector gas has slowly diffused out of detector). At the end of August 2018 before the cycle 184-18/3 (3-14-384), the Wilson flange and the monitor detector were replaced. The new flange was made completely of aluminum and had a KF16 port for the monitor. Its properties were worse than those of the original flange. Therefore, another aluminum flange was built in 2019 with a screwed-in stainless steel KF25 port.

Neutron window At the end of the beam line, there is a 100 µm thin AlMg3[5] window inside the end cap [254](p.78-80), [264](p.21), [42](p.31-35). It separates the beam tube's vacuum from the main chamber (see more in section 3.4). The size of the window is 80 mm × 20 mm with round edges (⌀ 20 mm). It is large enough to let through all neutrons which can also pass the aperture and enter the first mirror region. All other neutrons, which would only contribute to the background, hit the end cap. This cap itself is made of aluminum which is coated with NiMo inside. This coating reflects neutrons and increases the counted neutrons in the monitor detector by over 50 % [160](p.30).
In 2018, we measured the beam profile right after the end cap and before the aperture (approximately 16 mm apart) with two CR-39 detectors (ID T35 and ID 016). Lukas Achatz displays the measurements in his diploma thesis [14](p.33-35). These CR-39 measurements prove that the end cap is not transparent for neutrons. The measured vertical beam divergence is almost 14° (see details in section A.4.2).
The beam tube bearing inside the vacuum chamber adjusts the height of the neutron window relative to the aperture slit. This adjustment was carried out during the assembly of the beam line in the cycle 180-16/3.

Works on the beam line: Tobias Rechberger [254], Jakob Micko [193], Peter Salajka [262] and Rudolf Golubich [101] assembled and adjusted all main components of the beam line in November 2016 during the cycle 180-16/3 (3-14-358-I). During the following cycles (181-183, 3-14-358-II-IV), the beam line stayed untouched.
End of August 2018 the beam monitor and the attached Wilson flange were exchanged. During this work, small glass shards were found above this gap of the beam tubes. Movements of these shards above the gap could have been the reason for sudden changes in the monitor count rate during the cycle 183-18/2 (3-14-358-IV).
In 2019, the beam line was altered due to extensive renovation of the PF2 turbine. The biggest changes were repairs and better alignment of the large gate valve shutter. During the disassembly of the beam line, further damages on the edges of the glass tubes appeared, especially after removing the end cap in June 2019. Thomas Brenner built a new end cap which consists mainly of a neutron window. Jakob Micko, Carina Killian and I mounted it on the last beam tube after carefully vacuum cleaning it from the glass shards lying in the glass beam tube [160](p.6-7). The change resulted in a monitor rate drop of 30.6 % due to less reflection backwards from the end cap [160](p.30).
At end of 2019, Stefan Ballok, Veronika Kraus and Jakob Micko exchanged the complete beam line [31](p.21-29). Now there are only steel beam tubes and no rotatable shutter. The replacement of the glass tube increased the mechanical stability significantly [48](p.7).
In order to further improve the transmission of the beam line, a detailed study of the neutron transport within the current design is needed. A major drawback of the current setup is the strong divergence and the flat end cap. Probably a smooth transformation from the circular beam profile towards a rectangular one, comparable to the neutron window, could increase the neutron flux entering the experiment. Further investigations have to be conducted if the rate of the ground state increases too.

3.1.3. Aperture

The aperture is situated between the beam tube end cap and the beginning of region I. Two large horizontal blades made out of boron steel restrict the neutron beam in the vertical direction. In order to receive the highest transmission, the aperture has to be as close as possible to the end cap and the beam from the entrance window should fill the complete aperture slit. This was tested during the cycle 182-18/1 (2018) with CR-39 [14](p.33-36).

The distance d between region I and the aperture together with the relative aperture blade heights compared to the mirror surface height (Δh) act as a velocity selector (as shown in figure 3.7). The basic principle is that only certain trajectories are possible. Classical mechanics describes this as projectile motion in x and z direction:

[5] Before 2012 48 µm thin pure aluminum foils were used. Their disadvantage is a higher boron content and less resistance to mechanical stress. The thicker AlMg3 foils withstand multiple pressure changes of few bars as long the foil is not damaged by any sharp object or edge [42].

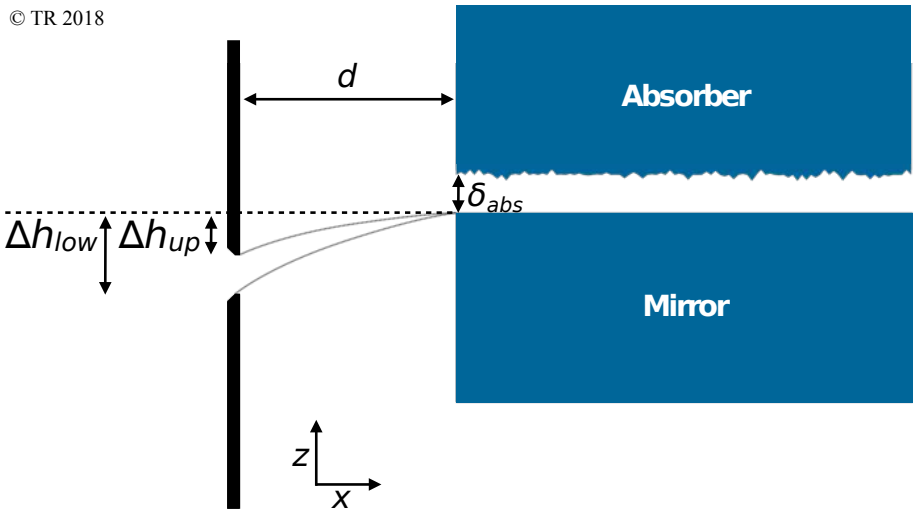

Figure 3.7.: A schematic view of the velocity selection [254](p.83)

$$r(t) = \begin{pmatrix} x(t) \\ z(t) \end{pmatrix} = \begin{pmatrix} v_0 t \cos\beta \\ v_0 t \sin\beta - \frac{g}{2}t^2 \end{pmatrix} \tag{3.13}$$

$$v_{\mathrm{n}}(t) = \begin{pmatrix} v_0 \cos\beta \\ v_0 \sin\beta - gt \end{pmatrix} \tag{3.14}$$

At the beginning of region I after the neutron flight time t_f from the aperture there should be the peak of the trajectory parabola:

$$r(t_f) = \begin{pmatrix} d \\ \Delta h \end{pmatrix} = \begin{pmatrix} v_0 t_f \cos\beta \\ v_0 t_f \sin\beta - \frac{g}{2}{t_f}^2 \end{pmatrix} \tag{3.15}$$

$$v_{\mathrm{n}}(t_f) = \begin{pmatrix} v_x \\ 0 \end{pmatrix} = \begin{pmatrix} v_0 \cos\beta \\ v_0 \sin\beta - g t_f \end{pmatrix} \tag{3.16}$$

A short calculation leads to:

$$\begin{aligned} t_f &= \frac{v_0 \sin\beta}{g} \\ d &= v_0 t_f \cos\beta = \frac{v_0^2 \sin\beta\cos\beta}{g} \\ \Delta h &= v_0 t_f \sin\beta - \frac{g}{2}{t_f}^2 = \frac{v_0^2 \sin^2\beta}{2g} \\ v_0^2 &= \frac{dg}{\sin\beta\cos\beta} = \frac{2g\Delta h}{\sin^2\beta} \\ \frac{d}{\cos\beta} &= \frac{2\Delta h}{\sin\beta} \quad \rightarrow \quad \frac{2\Delta h}{d} = \tan\beta \\ v_x^2 &= v_0^2 \cos^2\beta = \frac{gd^2}{2\Delta h} \end{aligned}$$

The resulting velocity selection relation is:

$$v_x = d\sqrt{\frac{g}{2\Delta h}} \tag{3.17}$$

Similar calculations can be found in [42](p.14-15 incl. error calculation p.25-30), [252](p.5-6), [258](p.39-40), [287](p.29-30), [193](p.19-22), [270](p.35-37).

A more detailed calculation including the finite slit height δ_{abs} of the first region can be found in [310](p.7-10), [65](p.17-21), [193](p.36-38):

$$v_{x_{max}} = \sqrt{\frac{g}{2}} \frac{d}{\sqrt{\Delta h_{up} + \delta_{abs}} - \sqrt{\delta_{abs}}} \tag{3.18}$$

$$v_{x_{min}} = \sqrt{\frac{g}{2}} \frac{d}{\sqrt{\Delta h_{low} + \delta_{abs}} + \sqrt{\delta_{abs}}} \tag{3.19}$$

Additionally to the restriction of the velocity in vertical direction and along the beam path, the third component is also restricted via the distance between the beam tube and the detector Δx ($\approx 1\,\mathrm{m}$) and the width of the detector window Δy (100 mm) [310](p.9):

$$v_{y_{max}} = \frac{\Delta y}{\Delta x} v_{x_{max}} \tag{3.20}$$

Originally, the aperture consisted of an aperture for the velocity selection and multiple collimator plates to filter out stray neutrons [312](p.27-28), [178](p.26), [42](p.7-8,12-13).

Thomas Bittner [42] designed and built the main parts of the currently used aperture (2.5 mm boron steel blades, adjustment mechanism) for the Rabi beam times (2012-RABI^{GC}-setup). Additionally, he designed a special housing for the aperture which was flanged between the beam tube and the qBOUNCINO-vacuum chamber (see more in subsection 3.4.1). This was a major improvement, especially for the count rate with an expected increase of 10 % [42](p.16-17). Before, these parts were separated by neutron windows and an air gap. There, the old aperture was situated. The advantage of aperture in air was that the slit position could be easily adjusted without breaking the vacuum[6] and the chamber was mechanically decoupled from the beam tube and therefore isolated from possibly harmful vibrations [287](p.27-28). However, the air gap (≈10 mm [287](p.27)) and the second neutron window decreased the count rate.

Within the new RAMSEY^{TR}-setup vacuum chamber, the aperture's housing became obsolete and a new aperture-design was necessary [254](p.81-84). David Rath [252] recycled Bittner's aperture and constructed the current aperture during the Ramsey preparations in 2015-2016. The main changes are the new position on the granite (before it was in a separated housing which led to systematic errors due to movements of the flange), the new frame (in order to reach the new set mirror surface height of 105 mm) and a new nonius scale on the screws to more easily adjust the blades (down to $25 \pm 5\,\mu\mathrm{m}$) [252](p.3-5). Additionally, many small changes in the mechanics during the construction, assembly and testing improved the usability and accuracy of the aperture adjustment. Rath also took great care that all parts were clean and non magnetic.

For Rabi-type measurements [65] and especially measurements of the quantum bouncing ball [299] the velocity spread must be very small in order not to wash out the effects. On the other hand, the Ramsey-method is less influenced by a broader velocity spread. Especially, the main peak is unchanged (only the contrast is slightly decreased, see more in section 2.2.3). The position of the side minima and maxima depends strongly on the neutron's velocity. Therefore, broader velocity spectra will wash out these peaks. This also separates better peak patterns from different transitions. A compilation of the set velocity distribution in previous experiments can be seen in table 3.2.

For all Rabi and Ramsey-type measurements in this thesis (3-14-358 & 3-14-384: 2016-2018), the selected neutron velocity was 5 to 13 m/s at the heights 99.7 mm and 104.2 mm of the lower and upper blade respectively and a distance d of 164 mm. This nearly covers the complete neutron spectrum [254](p.107-110).
Future tests with even broader velocity spectra and a complete Ramsey-setup can determine the optimal velocity selection. A higher acceptance will increase the count rate but can also reduce the contrast[7]. Tests with a completely open aperture in front of the Ramsey setup (this means using the complete spectrum) could even prove that the aperture is obsolete. In this case, the setup could be moved towards the beam guide and the count rate increases due to a higher solid angle of the beam in the detector.

[6] In the RAMSEY^{TR}-setup the time between stopping a measurement, adjusting the aperture (incl. venting, opening, closing and evacuation of the chamber) and starting of the next measurement takes approximately 1 hour. With a well trained staff times around 45 minutes are possible.

[7] Neutrons with high velocities have a short interaction time in the state selectors. Classically speaking they only bounce a few times and therefore their probability to scatter out of the setup from the rough upper mirror is very low.

v_x	year	experiment	source
6 to 7 m/s	2005	qBB	[166](p.20)
6.5(7) m/s	2008	qBB	[287](p.30)
5.5 to 7.2 m/s	2009	GRS^{TJ}-setup	[139](p.45)
5 to 7 m/s	2010	qBB	[178](p.26) [139](p.17)
5.74 to 9.52 m/s	2010	GRS^{TJ}-setup	[139](p.82)
5.6 to 9.5 m/s	2012	RABI^{GC}-setup	[65](p.20)
5.77 to 7.9 m/s	2014	qBB^{MT}-setup	[299]
5 to 13 m/s	2016-2018	RAMSEY^{TR}-setup	[254](p.107-110)
4 to 14 m/s	2020	RAMSEY^{TR}-setup	[48](p.8) [194](p.83-84)

Table 3.2.: Velocity selection of different *q*BOUNCE experiments

For experiments with polarized neutrons the velocity must be below 7.5 m/s due to the soft iron coating of the detector foil which can only absorb neutrons spin depending underneath this velocity limit [65](p.73-77). This will reduce the count rate probably disproportionally due to the velocity-dependent beam divergence. On the contrary, it will probably increase the contrast. Slower neutrons interact more often with the absorber of the state selectors and higher states are better suppressed.

With a height gauge[8] we measure the slit height directly on the blades compared to a well placed and cleaned gauge block[9]. Additionally, we determined the height on two metal pieces (brass & aluminum) attached to either the lower or the upper blade on both sides. This is more convenient or sometimes the only option if the aperture slit is very narrow. Occasionally, this measurement has to be repeated in order to exclude drifts. Additionally, the magnetization can be checked, even though during construction every steel part was measured and when it exceeded the limit of $\mu_r = 1.05$, it was annealed at 800 °C for 2.5 hours [252](p.14).

During the assembly of a *q*BOUNCE setup, the velocity spectrum is determined by varying the slit height and measuring the count rate after the first region (see subsection 4.3.1). There are two possibilities: either measuring an integral spectrum by opening the aperture at first completely and then closing one blade stepwise or measuring a differential spectrum by narrowing the slit down to a velocity interval of only 1 m/s and then sweeping through the complete spectrum by adjusting both blades simultaneously. The measurement of the setup can be found in section 4.3.1.

In the future, an electronically adjustable aperture could shorten the time between two measurements of the velocity spectrum by adjusting and measuring the blades accurately in the vacuum. In order to find the optimal setting, systematic tests of the relation between velocity spectrum and count rate or contrast would profit from this automation. For normal measurements (Rabi, Ramsey, qBB) this is not needed as they only use one setting. A simple realization consists of four non magnetic motors on the spindles and a laser system (or a comparable method) which is able to measure absolute distances of dm with an accuracy of around 20 µm. Julius Schnee did a first detailed study of the requirements [270](p.6-14).

The aperture and the slit of the first region are not the only components which influence the velocity within the setup. Both together extremely narrow down the used phase space[10]. All other neutrons are absorbed or reflected back into the beam tube and therefore are lost. Steps within the beam guides due to different beam tube shapes and diameters disable certain bouncing neutron trajectories which would fit through the aperture slit into the first region gap. Different transmission of single beam line components reduces selectively the intensity of only a velocity interval. Both possibilities further reduce the available phase space. This could be the source of non Maxwell-Boltzmann distributed velocity spectra within the RAMSEY^{TR}-setup [138](p.92-95). For future measurements this must be studied in more detail.
Additionally positioned mirrors can reflect parts of the phase space into the used part. This would increase the total count rate. A first step would be parabolically shaped vertical mirror walls before and after the aperture which reflect strong horizontally diverging neutrons back into the setup with a focus on the detector. Vertical focusing is much more difficult but would increase the percentage of the used neutrons tremendously.

[8] We use the digital height gauge double column *HDM-A* from Mitutoyo (192-663-10). It has a measurement range of 300 mm, resolution and repeatability of 0.02 mm, and an accuracy of ±0.02 mm.
[9] In 2018, we used a ceramic gauge block with a measured height of 100.0002 mm (tolerance class 0) from Mitotoyo.
[10] The end cap entrance window should be large enough not to cut into the used beam.

3.1.4. Neutron shielding

An UCN beam always has a strong divergence because all surfaces in the beam tube and in the experiment setup reflect UCNs at any angle. If no measures are taken, a fraction of the beam will propagate around the aperture, reflect on any surface (e.g. vacuum chamber walls) and still hit the detector from all possible angles. This neutron signal strongly contributes to the background during a measurement (with an absence during the background window). In order to suppress this contribution, all possible neutron paths have to be blocked by absorbing materials except for the desired one through the aperture slit into the first region, through the mirror path until the end of the last region and then directly into the detector.
At two points strong shielding is implemented to suppress stray UCNs: a so-called *boron castle* around the aperture and a tight shielding cover around the detectors [139](p.67). There are high requirements for the chosen material. Beside high neutron absorption (e.g. high boron-10 content) it should be vacuum tight and non magnetic.
Also, stray neutrons from the reactor, the vertical beam guide (TGV) or the PF2 turbine can enter the setup. At the RAMSEY^{TR}-setup this is a main concern for the monitor detector background. For *q*BOUNCINO the main source is the neighboring PF2/VCN beam [236](p.29-30). These sources are shielded already outside the vacuum chambers with many white bricks or black sheets of borated plastic. A complete cover is preferable, also more and thicker shielding increases the efficiency. In 2019, Stefan Ballok realized with the help of Veronika Kraus and Jakob Micko a tight shielding as close as possible around the monitor detector to have a nearly full coverage [31](p.17-20).

Boron castle

The so-called *boron castle*, a box around the aperture (see sec. 3.1.3), provides good collimation of the neutron beam. Only neutrons, which pass through the aperture and into the gap between mirror and absorber of the first region, can pass this shielding structure. All other neutrons are absorbed or reflected in the walls of this castle.
Beside covering the end cap and the aperture, another constraint on this castle is that it should only touch the granite or some clamps or screws attached. Therefore, it has to be below 210 mm tall due to the ITEM frame of the external SIOS laser interferometer which should be completely mechanically decoupled from the granite.
Jakob Micko [193](p.17-18) and I built the boron plastic design during the reactor cycle 181-17/1 (3-14-358-II) in January 2017. It is made of boron plastic sheets (5 mm thickness, content of 50 % B_4C) and four aluminum frame rods (ITEM, 20 mm width) for stability[11].
The castle consists of five parts: A front panel, a joint outer wall, a top cover and two L-shaped inner walls.
The front panel on the reactor siteof the castle has a gate-like opening for the beam tube. It stands on the edge of the granite and surrounds the beam tube before the end cap. The other three walls are joined together by two item rods in the corners to the joint outer wall. The side walls are close to the aperture to prevent neutrons circumventing it. The detector sided wall stands very close to the first region. A small rectangular exit window enables neutrons to enter the slit between the mirror and the absorber of the first region. The two L-shaped inner walls stand closer around the aperture within the box in order to define the horizontal divergence of the beam further. The top cover consisting of a single sheet only lies on top of the castle in a height of 200 mm above the granite surface. If the window of the castle is blocked, no neutron can reach the detector. Additional small boron pieces cover slits at the gate around the neutron guide and between the front panel and the outer side walls.
A boron plastic plate before the exit window completely blocks the beam. This setting provides a good test of the boron castle shielding performance. In 2017, the measured reduction factor was over 642 already with only an aluminum sheet covered with a double layer of Kapton tape [254](p.115-116).

The used boron plastic sheets are good absorbers and non magnetic but have poor vacuum properties. Before the usage of these sheets in the vacuum chamber, they have to be extensively cleaned. They tend to have a thick layer of dirt on all surfaces. Cleaning sergeants as Isopropanol are suitable. Cleaning can be stopped when the used tissues are not brown any more and become black due to dissolving of the upper most layers of the plastic itself. Even after the cleaning the plastic itself is not vacuum safe but at the time the only available option. During the beam times in 2018, outgassing of the material did not

[11] The sheets fit perfectly in the ITEM profile after applying some pressure. These joints are very stable.

reduce the count rate nor influenced the pressure within the chamber.
Better materials would be neutron absorbing metals. They are much easier to clean and are vacuum safe. Possible options are boron steel, gold coated copper, gadolinium painted aluminum and BorAlu.
Boron steel is already used in the aperture. It can be magnetized during the machining which is not wanted inside the *q*BOUNCE-experiment. Glowing of the pieces can be necessary in order to reduce magnetization. A second disadvantage is the low boron content of 1.8 %.
A copper castle can be easily manufactured and then be electrochemically coated with 20 µm gold on the complete surface of approximately 1 m^2. This 0.4 kg of gold is currently worth more than €10 000.
A castle made of aluminum painted with epoxy raisin is vacuum compatible too. Adding gadolinium oxide to the raisin increases neutron absorption to a desired level. It is critical that the raisin is mixed well with the gadolinium powder. Additionally, it must be distributed flawlessly over the large surfaces of the castle [246, 293], [100](p.160).
BorAlu or *Boral*, a mixture of up to 10 % boron or B_4C up to 30 % within an aluminum alloy, is the best option to replace the boron plastic. It is vacuum compatible, non magnetic and no coating of any kind is needed. Due to the boron content the hardness of *Boral* increases significantly. For cutting and drilling diamond saws or abrasive-jet machining are recommended. Even though steel drills easily scratch such alloy sheets, the deterioration can be much higher than it would be expected from aluminum. A disadvantage is the availability. Only a few companies produce this alloy (e.g. Böhler-Bleche, SD-H). In 2019, we received cutting scraps from a much larger order at Böhler-Bleche[12]. With these sheets the workshops at the ATI designed and built a new boron castle made out of *BorAlu* which replaced the old one afterwards. Niels Geerits also compared *Boral* with boron plastic sheets in a TOF-setup within the ATI-white beam facility and found no difference in the absorption factor.

Detector shielding

The counter tube detector was also shielded in a similar way to the aperture. One layer of boron plastic sheets enclosed the detector completely within the detector holder and left only a small slit open for the entrance window. Additionally, broad Kapton tape wrapped around everything held the pieces of the shielding together. Small wiggles of the tape at the front made it quite difficult to place the detector as close as possible without touching to the end of a region. Additional Mylar sheets defined the entrance slit opening to 100 mm.
At the end of 2019, Stefan Ballok replaced the boron plastic shielding with new *Boral* plates with the help of Veronika Kraus and Jakob Micko [31](p.30-34). This is more vacuum compatible and makes the positioning of the detector easier. In addition, they placed vacuum compatible Mylar sheets around the detector between the shielding in order to electrically insulate the detector from its holder.

3.1.5. Neutron mirrors

Neutron mirrors are the most important parts of the *q*BOUNCE-setup [254](p.84-87). The gravitational quantum states of the UCN occur above their smooth surfaces. Additional rough glass plates clamped above these mirrors are called *absorbers*, *scatters* or *state selectors*. They filter out higher bound quantum states. Piezoelectric tables from PI (so-called *PI-tables*) and mechanical coarse adjustments align these mirrors with an accuracy below 1 µm, which is necessary for guiding the neutrons without state transition to the detector. One pack of a coarse adjustment, a PI-table, a base plate and a mirror is called *region*. The following subsections and an overview in figure 3.8 provide more details about these components.

[12] voestalpine BÖHLER Bleche GmbH & Co KG, Böhler-Gasse 1, 8680 Mürzzuschlag, Austria, www.bohler-bleche.com (13.11.2023)

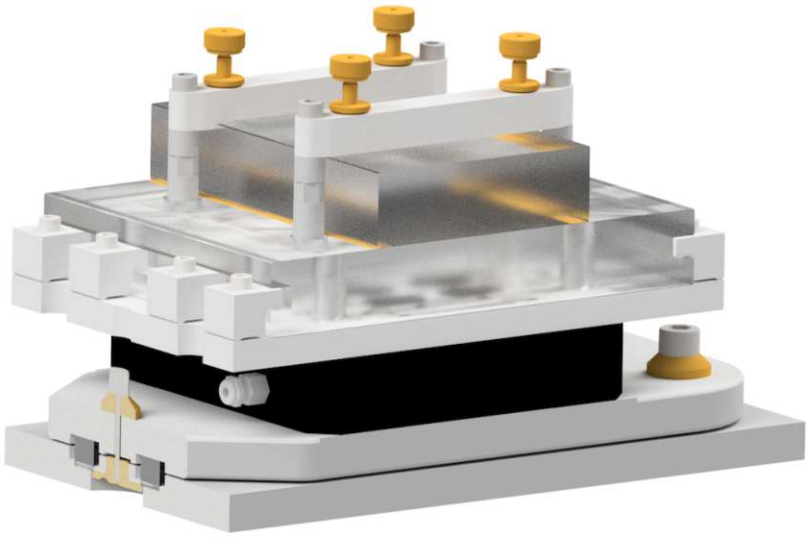

Figure 3.8.: A rendering of a complete state selection region including a coarse adjustment (lowest two plates), a PI-table (black), a base plate with clamps, a lower mirror and an absorber with bearings (on top) [254](p.85).

Mirror glass plates

The manufacturer of the glass plates which are used as mirrors and absorbers is the German company Präzisionsoptik Gera GmbH (POG)[13]. A unique mirror ID is assigned to each glass plate which is written on its side face. These IDs should consist of three digits. The first digit denotes the purchaser (chronological), the second the specific order itself, and the third digit assigns, consecutively numbered, the glass plate within that order. Additionally, POG assigns a type number to all types of mirrors. All ID-labeled glass plates are listed in a database in order to keep track of the order, usage, location and current state of them.

Glass composition: All glass plates are made of borosilicate glass, mainly N-BK7 from Schott[14] (until 2016 and some large mirrors in 2018) or S-BSL 7, an equivalent glass from Ohara[15] (2017-2019). Chemists commonly use borosilicate glass due to its high chemical resistance and low thermal expansion. A small index of refraction and smooth and flat mechanical preparation of even large surfaces make it also ideal for optical usage. The high content of around 10 % boron oxide is an important advantage for the usage as a neutron mirror. All neutrons entering the glass plate will be absorbed.

Glass plates' specifications: All glass plates have a thickness of 30 mm in order to reduce bending. A calculation of the bending due to weight if only supported on two opposing corners can be found in [139](p.23-24). Even for the largest mirrors this is below 1.3 µm and for the smaller mirrors 0.2 µm. Smaller thickness would significantly increase bending (For the smaller mirrors a reduction to half the thickness would result in a bending still below 1 µm). Thinner mirrors would lead to less energy stored in the oscillations. Therefore, piezoelectric stages could oscillate them to higher amplitudes and the laser interferometer (mainly the optics) would pick up less of this oscillation.
Due to the polishing of the glass plates, the real thickness varies a little. The mechanical coarse adjustment underneath the piezoelectric stage compensates for this in order to reach the assigned mirror height of 105.00 mm at the mid range of the piezoelectric stage.
Since 2012, there has been a U-notch along the middle of two opposite side faces of the mirror. Until 2014 the size (width and depth) was 5.5 mm with an accuracy of ±1 mm. Since then, it has been 10 mm. Aluminum clamps fix the mirror via this notch to the 10 mm thick aluminum base plates. This has always been done by a torque wrench to apply evenly 0.5 N m.

[13] POG, Gewerbepark Keplerstraße 35, 07549 Gera, Germany, www.pog.eu (12.11.2023)
[14] Schott AG, Hattenbergstrasse 10, 55122 Mainz, Germany
[15] Ohara Inc., 1-15-30, Oyama, Chuo-ku, Sagamihara-shi, Kanagawa, 252-5286, Japan

The specification by POG of the glass plates are:

- Dimension tolerance ±0.2 mm / parallelism < 5”
- Spalling at the edges up to 1 mm are acceptable
- All edges have protective chamfer <0.5 mm
- Both sides polished (grade of polishing P3)
- Flatness both sides 3/0,5(0,2) in every ⌀ 60 mm gliding
- Surface both sides 5/3x0,16 in every ⌀ 60 mm gliding

The side without U-notch is ground down additionally in order to remove the protective chamfer. A possible length reduction is up to 1 mm. This process is very delicate and can lead to spalling of glass from these edges. This defect makes these glass plates unusable for neutron guiding because the mirrors are joined together on this face. In the future, an additional U-notch on this faces enables to laser cut away the chamfer which should result in cleaner edges.

Coating: All mirrors and a few absorbers have a reflective aluminum layer with a SiO_2 protection layer on top of it. The thicknesses are 120 nm and 180 nm respectively with a homogeneity of ±10 %. The main reason for the coating is to reflect the laser beams of the interferometer (HeNe-laser at 633 nm). These interferometers from SIOS measure the mirror oscillations (see section 3.6.2). For the adjustment of the mirror height, the capacitive sensing system also needs the mirror coating as a conductor (see section 3.5.3). For accurate measurements the coating has to be bonded and electrically connected with the sensing system.

Mirror types: For the modern RAMSEY^{TR}-setup six different glass plate types are needed: two *absorber mirrors*, two *oscillation mirrors*, either a *Ramsey mirror* or an *electrode mirror*, two *absorbers* and one *reference mirror*. All mirrors are coated. The *absorbers* have a rough surface instead. All mirrors except the *reference mirror* have a width of 200 mm. They form the neutron path. The *reference mirror* and the *absorbers* have a width of only 100 mm. The lengths of the *absorber mirror*, the *oscillation mirror* and the *absorber* are 152 mm (in order to be slightly longer than the piezoelectric stage). The lengths of the *Ramsey mirror*, the *electrode mirror* and the *reference mirror* are 340 mm (maximum length which POG can produce). *Absorber mirrors* and *electrode mirrors* have additional four or six drill holes with a diameter of 15 mm respectively. These holes are 58.5 mm away from the center line and provide space for the bearings of the *absorbers* or the electrode.
With time and usage the mirrors slowly deteriorate due to mishandling and cleaning. Therefore, they are exchanged with completely new ones at every new Ramsey assembly or after accidents. Since 2022, POG can refurbish the used mirrors by polishing the scratched mirror surfaces again. The following configurations have been used (in the order of the neutron's path, denoted with their mirror IDs):

- Ramsey-2017: #603 + #709, #703, #707, #704, #705 +#306
- RABI-GRS-18: #802 + #805, #702, #801 +#804
- RAMSEY-GRS-18: #802 + #805, #702, #811, #701, #801 +#804
- Rams$\vec{E}$y: #802 + #805, #702, #831, #701, #801 +#804

The *reference mirror* #339 was used until the end of cycle 182-18/1 in spring 2018. Then it was exchanged with the mirror #821 because this one had a measured mirror surface.

Roughness and flatness: The first calculations of the influence of flatness and roughness of the neutron mirrors are to be found in the master thesis of Westphal [312] (p.11 ff) in 2000. They measured a roughness of 22.0(1) Å at the XSAS of Ben K. Saidane at ILL [312](p.17). Repeated measurements by S-DH[16] in 2008 resulted in 1.5(1) nm [287](p.33). This is more than by a factor 20 smaller than the neutron wavelength and therefore negligible.

POG produces all glass plates with the flatness specification of *3/0,5(0,2)* within any circular area with a 60 mm diameter. This means that within this area only half a Newton ring is visible with a maximal

[16] S-DH GmbH, Sputter-Duennschichttechnik Heidelberg, Hans-Bunte-Straße 8-10, 69123 Heidelberg, Germany, www.s-dh.de (20.6.2021)

deviation of 20 % of a ring. A helium-neon laser with a wavelength of 633 nm produces the interference pattern. Therefore, the surface has to have a curvature greater than $r = 2844$ m. This can be calculated with the following formula: $r = \frac{4h^2+s^2}{8h}$ [84](p.6). Short mirrors are expected to have an absolute flatness below 0.8 µm. In 2008, SD-H measured a collection of mirrors and found a maximal flatness below 0.5 µm [287](p.33) at a maximal measurement length of 130 mm. The 340 mm long mirrors can exceed these values. Therefore, in 2017 and 2018 SD-H measured a set of mirrors (the *electrode mirrors* #811 and #812 [233](p.10-15), the *reference mirror* #821 and the Llyode mirrors [89] which were also used for the Rams$\vec{E}$y electrode). The maximum deviations were 2.5 µm for the full 330 mm measurement range. This was far more than originally expected[17]. As seen in table 3.3, the deviations vary a lot between the different mirrors, which is expected because POG polishes the mirror until the specifications are reached and some are even better by chance. Additionally, during the tests SD-H measured different mirror surfaces depending on where they lie upon (granite or soft foam). Therefore, complete regions with fully mounted mirrors should be tested in order to see the real surfaces and be able to verify the measurements of the CapSens system.
Flatness plays an important role in the systematics mainly because it can influence the mirror alignment system. Subsection 3.5.4 provides more about this topic.

Mirror	Date	Length	Max. height	Curvature	Sign
Old mirror: long	23.07.2010	130 mm	0.4 - 0.5 µm	5.3 - 4.2 km	+
Old mirror: short	23.07.2010	90 mm	0.1 - 0.12 µm	10 - 8.4 km	-
#502 (Llyode mirror): long	26.10.2017	330 mm	0.4 - 0.75 µm	34 - 18.2 km	+
#502 (Llyode mirror): short	26.10.2017	90 mm	0.1 - 0.2 µm	5.1 - 10.1 km	-
#501 (Rams$\vec{E}$y electrode): long	26.10.2017	330 mm	1.9 - 2.5 µm	7.2 - 5.4 km	+
#501 (Rams$\vec{E}$y electrode): short	26.10.2017	90 mm	0.1 µm	10 km	-
#811 (electrode mirror): long	08.02.2018	330 mm	(-0.6) - 0.2 µm	1000 - 23 km	+/-
#811 (electrode mirror): short	08.02.2018	190 mm	0 - 0.3 µm	1000 - 15 km	+
#821 (reference mirror): long	20.03.2018	330 mm	1.0 - 1.4 µm	13.6 - 9.7 km	-
#821 (reference mirror): short	20.03.2018	90 mm	0 - 0.15 µm	1000 - 6.8 km	-
#822 (reference mirror): long	20.03.2018	330 mm	1.8 - 2.1 µm	7.6 - 6.5 km	-
#822 (reference mirror): short	20.03.2018	90 mm	0.12 - 0.25 µm	8.4 - 4.1 km	-
POG-specifications	-	60 mm	633 nm/4 = 158 nm	2.844 km	+/-
POG-specifications	-	100 mm	<0.44 µm	>2.844 km	+/-
POG-specifications	-	152 mm	<1.02 µm	>2.844 km	+/-
POG-specifications	-	340 mm	<5.08 µm	>2.844 km	+/-

Table 3.3.: Summary of flatness measurements S-DH

Absorbers

Absorbers or *scatters* are glass plates with rough surfaces to prepare the neutrons in the ground state. These names stand synonymously for the *Absorbing Reflecting Mirror System* (ARMS) or also called *state selector* which are used for beam preparation and analyzation. One ARMS consists of a lower *absorber mirror* and an upper rough *absorber* glass plate which scatters out all higher energy states. A small slit between these two pieces provides a path for the neutrons [254](p.87). This gap is ensured by brass thickness gauges (30 µm) and pressure from four fine thread screws within the bearings [193](p.22-23). These vacuum safe brass screws have a pitch of only 0.15 mm and they are produced by Radiant Dyes[18]. Once adjusted to a gap of approximately 22 µm this state selector will be used for many beam times[19]. An alternative would be to use piezoelectric stages instead of the screws which were already implemented in the first setup [258](p.31-33). An ideal actuator for this alignment is the PI-*N-472* motor which is similar to the used PI-*N-470.12V* (see section 3.3.6) [225]. A different approach with a fixed mirror to a coarse adjustment as lower stage and a piezo driven upper stage (*absorber*) was realized 2014 [310](p.19-22). A motorization has the advantage of varying the gap size during measurements and therefore the suppression of higher states. The resulting change of the transmission contrast c_{fi} is an important systematic check of a GRS setup.

[17] A fix laser interferometer can recognize this by shifting the mirror below on the flat granite surface. In 2010 Matthias Fink used such a setup to measure the imperfect parallelism between the surfaces of the glass plate [90](p.12-13). This is also visible with the capacitive sensors system [84](p.26-28).
[18] Radiant Dyes Laser & Accessories GmbH, Friedrichstraße 58, 42929 Wermelskirchen, Germany
[19] This was lower than for the Ramsey-2017 (region I: 25.0(1) µm, region V: 26.0(1) µm) [193](p.22) in order to suppress higher states more with the disadvantage of a reduced count rate.

The bearings, also called *absorber clamps*, are connected to the mirror base plate via the holes of the absorber mirror. The distance of the bearing posts is $c = 84\,\text{mm}$ on a total length of $L = 152\,\text{mm}$. The distance between the absorber end and the posts is $a = 34\,\text{mm} = \frac{L-c}{2}$. This spacing of the bearing corresponds to Bessel points which ensure the smallest deformation. Below this glass sandwich is a normal region substructure (coarse adjustment and piezoelectric stage).
Rainer Stadler from the glass workshop of the Physikalische Institut Heidelberg produces the rough surfaces. At least since 2012 [310](p.24), he has used a 600 corundum paste for all absorbers [267](p.39). In order to test different roughnesses, there are some exceptions: two absorbers in 2017 (#805-#806) and two absorbers in 2019 (#835-#836). These were polished with a 500 corundum paste. Additionally, there are two absorbers (#833-#834) which were polished with a 320 paste in 2019. In general, he is able to use pastes with the following corundum grain sizes: F600, F500, F400, F320.
A *SE-1700* surface structure gauge from Innovatest[20] can quantify the roughness of the absorber [122], [150](p.13-16), [310](p.24-43), [267](p.39-49), [119](p.15-18). It senses a 4 mm long line. Multiple measurements on different positions and orientations on the surface enhance the accuracy of the result.
Before using the absorber plates (#804-#806), I measured their roughness. Table 3.4 compares the results to previously measured absorbers.

Mirror	Device	Date	R_a	R_z	Source
#306	SE-1700	2013	0.35(32) - 0.40(34) µm	3.36(51) - 4.03(84) µm	[150](p.16)
#307	SE-1700	2013	0.36(29) - 0.40(32) µm	3.09(40) - 3.96(81) µm	[150](p.16)
#402	SE-1700	2015	0.368(24) µm	4.021(770) µm	[310](p.46), [267](p.49)
#410	SE-1700	2015	0.361(12) µm	3.908(406) µm	[310](p.46), [267](p.49)
#708	SE-1700	2016	0.453(23) µm	3.628(402) µm	[267](p.49)
#709	SE-1700	2016	0.464(39) µm	3.574(533) µm	[267](p.49)
#804	SE-1700	2018	0.35 - 0.43 µm	2.91 - 3.48 µm	this work
#805	SE-1700	2018	0.41 - 0.47 µm	2.88 - 3.58 µm	this work
#806	SE-1700	2018	0.38 - 0.49 µm	2.78 - 4.14 µm	this work

Table 3.4.: Measured roughness of absorber glass plates

Region supplies

Region supplies are all aluminum parts which are necessary to mount the mirrors (base plate and clamps) and the piezoelectric stages (coarse adjustment). All plates are specially treated to have a flat and as smooth as possible surface. This is necessary for the alignment between the different parts of one region. The coarse adjustments consist of two aluminum plates with up to six elastomer compression springs. Normally, only four springs are mounted in order to be able to adjust the height without excessive force. These springs are *E1556/16x16 (70 shore A)* produced by Meussburger[21] [114](p.18), [167](p.33-36). After adjustment, the fixed mirror drifts for multiple hours until it reaches a new stable position [310](p.58-61).
The springs influence the notch frequencies of the PI-tables between the mirrors and the coarse adjustment. Close to these frequencies mirrors cannot oscillate properly (purely vertical). State transitions in close vicinity are not addressable as for the transition $|1\rangle \rightarrow |4\rangle$ during the beam times in 2017 and 2018. In autumn 2019, Veronika Kraus described these phenomena theoretically and measured the notch frequencies for different tensions of the springs [167]. Different arrangement of the springs and different tensions and therefore a different spring constant can change the mechanical resonance for more than 50 Hz. This is enough to enable gravitational state transitions at similar frequencies. A second result was that not centered mirrors can increase the resonance behavior but the corresponding frequency changes only slightly. Concluding these tests, the coarse adjustment was adapted in order to separate the height adjustment from the tension adjustment via the introduction of an additional tension adjustment screw on top of the elastomer springs.

[20] INNOVATEST Europe BV, Borgharenweg 140, 6222 AA Maastricht, Netherlands, www.innovatest-europe.com (26.11.2022)
[21] Meusburger Georg GmbH & Co KG, Kesselstraße 42, A-6960 Wolfurt

3.1.6. PI-tables

Five piezoelectric positioning stages called *PI-tables* are needed to build the RAMSEY^{TR}-setup. The German company Physik Instrumente (PI)[22] manufactured all stages. All tables can adjust the height and the tilts pitch and roll. We use three different models *PI-558*, *PI-518* and *PI-528*. Their height adjustment ranges are 50 µm, 100 µm and 200 µm respectively [227](p.5).
Depending on the setup, a different number of PI-tables is needed. The Ramsey-type setup needs five and the Rabi configuration only three (200-100-50 [150](p.13), [65](p.27-28)). For an optimal use of the adjustment ranges the middle stage has the smallest range and the outermost ones have the largest (Ramsey: 200-100-50-100-200). In this configuration the complete mirror alignment is able to tilt.
Each stage additionally needs a controller (*E-712.3CDA*), a long extension cable ($\geqslant$3 m), a vacuum feedthrough and a vacuum cable which is directly attached to the stage. The first region needs an additional vacuum safe extender cable in order to be placed the furthest away from the feedthrough at the back of the vacuum chamber.
As part of one region, the PI-tables are mounted between the coarse adjustment and the mirror base plate. Their cables are always on the PF2/MAMBO side.
Before using a PI-table, all their axes have to be calibrated [227](p.7-8). Therefore, the PI software (*PI Nanopositioning*) shocks the table and measures the ringing down of the piezos. These scans reveal resonances/notches at different frequencies. We manually select two frequencies which are later suppressed by the controller [114](p.20). State transitions close to these notches cannot be addressed by the piezoelectric stages.
The PI-tables can either be operated in an open loop or they can be fixed with a servo to a set value. In this mode, the controller tries to keep this value as precise as possible. In 2014, the measured standard deviation of the set position was 0.032 µm [310](p.62-63). Figure 4.7 in section 4.2.4 displays the stability during the measurements in 2018. If a PI-table is wrongly calibrated and the servos are turned on, the PI-tables can start to vibrate very strongly. You will hear it as a loud sound even through the vacuum, the vacuum chamber and down the platform. Therefore, it is recommended to be careful when calibrating the system and to be able to reach the turn-off button in order to prevent damage of the system. The same cautiousness is necessary during the tests of new frequencies.
The PI-tables can also be stabilized in the offset mode with the LabView-PID regulation [227]. This is for the vibrating mode which uses an offset on the offset to apply the sinusoidal signal from the AFG [114](p.25-26).
The PI-tables can only be used continuously below a certain power consumption which limits the amplitude depending on the frequency. At higher values, the tables overheat and the controllers shut them down for some minutes. This effect was first seen at a power consumption above 59 W in 2010 [178](p.70-74). Additionally, the mechanical amplitude saturates above this limit. After the discovery of the effect, all table controllers received a new and stronger amplifier [65](p.30-31). In 2018, similar effects occurred at a power consumption above 80 W. This limits the reachable amplitude in particular for higher frequencies (see fig. 4.5 in section 4.2.3). An advantage of the RAMSEY^{TR}-setup is that it only needs half the amplitude strength of a Rabi-setup and therefore can fully excite even higher transitions.
In principle, it is also possible to measure the mirror oscillation with the built-in capacitive sensors which was demonstrated with a sample rate up to 50 kHz in 2012 [65](p.31-32).

[22] Physik Instrumente (PI) GmbH & Co. KG, Auf der Roemerstrasse 1, 76228 Karlsruhe, Germany, www.physikinstrumente.de (13.11.2023)

3.2. Neutron detectors

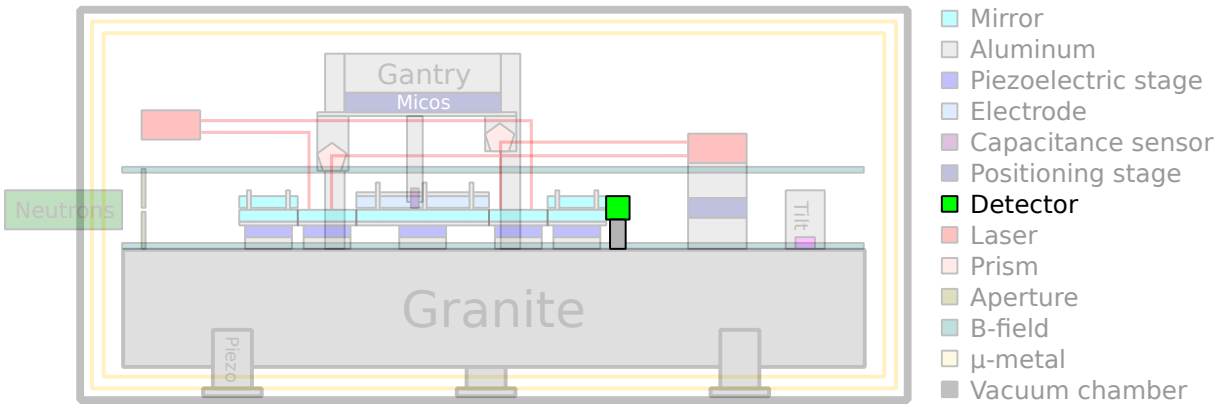

Figure 3.9.: A schematic view of the detector position within the RAMSEY^{TR}-setup

Neutrons are commonly detected indirectly via nuclear reactions which produce charged particles. The resulting particles are easily detected with standard particle detection systems. The kinetic energy of the neutron is much smaller (<1 µeV) compared to the released energy of the nuclear reaction (few MeV) and can be neglected. The products share the totally released energy and the total momentum is approximately zero. Only if there are two end products, their momentum is equally distributed and both reaction constituents will separate in opposite directions. The released energy will be split as kinetic energy inverse to ratio of masses.
Suitable nuclear reactions need a high neutron-absorption cross section. Possible nuclear reactions are a nuclear fission in U-235 ($\sigma_f = 586\,\mathrm{b}$), a (n,p$^+$)-reaction in He-3 ($\sigma_{\mathrm{n,p^+}} = 5330\,\mathrm{b}$) and a (n,$\alpha$)-reaction in B-10 ($\sigma_{\mathrm{n},\alpha} = 3840\,\mathrm{b}$)[23]:

$$^3\mathrm{He} + \mathrm{n} \rightarrow \mathrm{T} + \mathrm{p}^+ + E(764\,\mathrm{keV}) \tag{3.21}$$

$$\mathrm{n} + {}^{10}\mathrm{B} \rightarrow {}^{7}\mathrm{Li} + \alpha + E(2.789\,\mathrm{MeV})(6\,\%) \tag{3.22}$$

$$\mathrm{n} + {}^{10}\mathrm{B} \rightarrow {}^{7}\mathrm{Li}^* + \alpha \rightarrow {}^{7}\mathrm{Li} + \alpha + \gamma(0.48\,\mathrm{MeV}) + E(2.31\,\mathrm{MeV})(94\,\%) \tag{3.23}$$

Uranium and boron are solid and used as coating to convert neutrons into charged particles. For track detectors these *converters* are coated directly on films (e.g. photo emulsion) or CR-39. This enables a very good spatial resolution with no timing resolution[24]. In gas counter tubes these nuclides are coated on the inside of the entrance window so that one of the charged particles can ionize the gas and trigger the detector. The number of ionized atoms depends on the incident energy, track length, gas composition, temperature and gas pressure. Due to an applied voltage all ions drift as current to the electrodes and induce a signal (ion chamber). With higher voltages and special geometries (cylindrical shape) the electrons are accelerated enough to further ionize the gas. The signal is therefore amplified but still proportional to the energy of the incident particle (proportional counter tube). A further increase of the voltage will saturate the amplification. Every incoming charged particle will fully ionize the gas within the detector volume and no energy dependents can be observed anymore (Geiger-Müller counter). Gas counter tube detectors have a good timing resolution but no spatial resolution. Only special detector geometries enable to record spatial information. A simple method is to have an array of small gas detectors in order to achieve a spatial fragmentation of the detector area. The blind spots between the detector pixels are a disadvantage. A more sophisticated method are Cascade detectors [161]. With different layers these detectors achieve a gas amplification and a spacial resolution.
Gaseous target materials as He-3 can be used directly within a gas detector. Therefore, all the released energy can be detected except when the neutron capture occurs too close to the wall and one particle exits the detector. The energy deposition is different to the previously described detectors, where only one of the two particles can enter the detector volume, the other one will end up within the detector window[25]. This is clearly visible in the spectra. If the full energy is deposited, then only one peak at

[23] All cross sections are at a thermal neutron velocity of 2200 m s^{-1}. They are taken from Karslruher Nuclid Chart (Auflage 8, 2012).
[24] The readout is done after the radiation via chemical enhancing or fixating and a microscope.
[25] Due to momentum conservation they will fly back to back, splitting the total energy with the inverse ratio of masses (see

this energy will be visible, otherwise two or more peaks will be visible in the spectrum corresponding to each possible particle. A disadvantage of having the detection material within the gas is the problem of leakage, especially for helium. Over time, the detector efficiency will decrease due to this loss and change of the gas mixture.

In *q*BOUNCE experiments at two positions detectors are needed: one within the beam tube to monitor the incoming neutron flux and the other one after the last mirror parallel to its edge [254](p.88). The so-called *monitor detector* is a He-3 gas counter tube and will be described in detail in subsection 3.2.2. As the main detector at the end of the setup, we use two different detector types: For rate measurements (e.g. GRS) we use a proportional counter tube with a B-10 coated entrance window (see more in the following subsection 3.2.1). In order to visualize the probability density of the neutron's wave function (measurements of the quantum bouncing ball (e.g. qBB^{MT}-setup) or the efficiency of the state selectors), the detector needs a very high spatial resolution (in the order of 1 µm). B-10 coated CR-39 track detectors achieve these goals (see more in subsection 3.2.4). An overview of all used detectors can be found in [144].

In principle, a second detector within the chamber can measure the divergence of the neutron beam. This was done during CR-39 measurements with the counter tube in 2018. The lost neutrons due to divergence could also be used as a *monitor beam*: A detector capturing neutrons going through the setup and bypassing only the last absorber region gives similar information to a zero rate measurement. During frequency measurements, this *monitor beam* can detect misalignments due to the mirror oscillation which could not be seen with resting mirrors. Additionally, this would make zero rate measurements obsolete and expand the usable time for frequency measurements by simultaneously enabling both rate measurements.

3.2.1. Detector: proportional counter tube

The main detector for rate measurements within all *q*BOUNCE setups is a proportional gas counter tube with a boron coated entrance window. Detailed information can be found in [31, 32, 93, 113, 120, 264, 298]. The detector itself consists of a front panel with an entrance window, a main part with the counter tube wire at the front and the detector sensors at the back, a back panel, a surrounding neutron shielding and a holder. Additionally, each detector needs specialized electronics for the readout and the voltage supply, and a gas supply.
The front panel and the main part are made of brass[26]. Together, they seal a cylindrically shaped tube (30 mm diameter, 225 mm length, [32](p.11)) around a thin tungsten-gold wire (15 µm [264](p.46)). This is the active detector volume. Teflon and polyethylene isolate the wire from the grounded housing. The wall of this tube is polished and coated with a 30 µm layer of pure copper to reduce the background of α-emissions within the housing material [113](p.4). The filling gas itself is 90 % argon and 10 % CO_2. Argon is responsible for the gas amplification and CO_2 quenches the discharge again by absorbing the UV photons induced from the local discharge [287](p.54+60). The gas is constantly exchanged to ensure a constant gas mixture.
The entrance window in the front plane is more than 100 mm wide (normally reduced with absorbing material) and 3 mm high at the center of the detector's height[27]. A thin AlMg3 foil closes the window gas tightly[28]. UCNs mainly pass through the foil. On the gas tube side of the foil behind the entrance window a 3 mm × 110 mm enriched boron coating absorbs most of the neutrons[29].
High voltage (700 V) between the grounded tube and the tungsten wire produces a strong electric field around the wire. The charged particle from the neutron induced reaction will ionize numerous argon atoms proportionally to the energy of the particle. The free electrons will ionize further atoms close to the positively charged wire. This gas amplification increases the signal proportionally depending on the gas mixture, pressure, temperature and voltage[30]. These parameters need to be stable and controlled constantly (see evaluations in section A.3.2). The produced ions drift slowly, compared to the electrons,

energies and ranges of B-10 in [298](p.19)). In rare cases when both are emitted nearly parallel to the foil none will enter the detector [32](p.9).

[26] Brass contains less radioactive impurities than aluminum [287](p.63), [111].

[27] The detector is 60 mm high. Therefore, the slit center is at the upper edge of a mirror, if the detector and the mirror are attached to the same base (e.g. metal plate) [287](p.55).

[28] The thickness is 48 µm [287](p.56) or 60 µm [264](p.44-45). AlMg3 has better mechanical properties and a smaller boron content than pure aluminum foils and therefore a higher transmission [23].

[29] The boron coating is always inside the gas tube because the ions cannot pass through the aluminum foil [287](p.56-60). Calculation of the efficiency of the boron coating thickness can be found in [264](p.30-33). The optimal thickness for velocity of 6.5 m/s is 221 nm and reaches an efficiency of over 90 % [298](p.19).

[30] A detailed calculation of the amplification can be found in [264](p.33-37), [298](p.59-63).

to the walls and induce a current. Therefore, the geometry of the active volume defines the shape of the signal pulse [298](p.22).
The back panel seals off an air filled volume between the main detector brass and itself, except for a DN25KF flange opening. An attached DN25KF vacuum hose connects this volume to the ambient air. The electronics positioned within the detector cannot withstand the surrounding vacuum conditions. There are a *CR-110* charge-sensitive preamplifier from Cremat[31], which picks up capacitively the signal from the wire and further increases the signal [298](p.23,35-39) [113](p.5), a temperature sensor, a Honeywell[32] *ASDX Series* silicon pressure sensor [120](p.10) [93](p.20-21) and a MFS-3A flux gate magnetic field sensor [32](p.13).
A long DN25KF vacuum hose[33] connected to the back panel flange guides two vinyl gas pipes (for flushing the gas tube), a SHV cable for the voltage supply, a BNC cable (preamplified detector signal) and a D-Sub-9 cable (for the detector sensor signals (I^2C) and power supply of the preamplifier) to the outside of the vacuum chamber (via an inverse flange). Further, an electrically insulated metal tube (*Anaconda*) guides them to the so-called *detector-fridge*. This metal box shields the detector electronics from potentially harmful electromagnetic radiation from other experiments which would increase the background[34]. The detector electronics are placed in a NIM grate and consist of a high voltage supply (*NHQ 203M* from iseg[35]), an amplifier (Ortec[36] *570 Amplifier*, [298](p.23)), logic cards, *Quad-ADC* (itech instruments[37]), and a detector sensor card. An additional oscilloscope directly visualizes the signals. Neutron counts of the monitor detector are displayed immediately due to the high rate if the shutters are open. The logic cards prepare (invert) some of the PF2 turbine signals which control the gates of the *quadADC*. This device actually measures and counts the signals including their strength (1024 channels) and arrival time with timestamp resolution of 0.5 µs [113](p.5). It communicates via Ethernet with the program InterWinner from itech instruments. It can handle up to four detectors simultaneously or up to two detectors (Gas counter tube and monitor detector) with two measurement windows each (measurement and background) selected by the gates. The main LabView program operates InterWinner which stores the detector spectra [298](p.41-42). Calculations of the expected spectra are in [264](p.37-38) and information of the complete signal acquisition in [264](p.39-43). A program called *decode* which was developed by Martin Thalhammer carries out the final analysis of the data and spectra [298](p.42-44). This program can also filter out bursts (multiple events within a relative time difference below 100 µs). Nikolaus Huber further integrated InterWinner and *decode* into the main LabView program by operating them remotely [120].

The detector sensor card reads out the two detector sensors of the detector. Additionally, it can also amplify the raw signal and operate up to three flow sensors via I^2C. Nadine Freistetter [93](p.23,34-36) designed them and assembled one which was used in 2017 for the RAMSEY^{TR}-setup and 2018 for *q*BOUNCINO. In 2017, Anselm Balthasar [32] finalized the second card which has been used in the main setup since 2018. Nikolaus Huber implemented the software for the I^2C communication between the sensors, the card and the main LabView program [120]. These cards also transmit the signals from the magnetic field sensor to a RS232 socket in the front panel which can be connected to a suitable read-out electronic.

A gas bottle provides the detector gas. A throttling valve on top of the bottle reduces the pressure from over 100 bar to a small overpressure of around 30 mbar above air pressure. Two small valves before (at the inlet pipe) and after the detector (at the end of the outlet pipe) are responsible for the fine tuning of the overpressure and the gas flow. Close to them two Honeywell *Zephyr*^{TM} digital airflow sensors with a range of $\pm 50\,\mathrm{cm^3\,s^{-1}}$ are located (See [93](p.15,21-23)). All three valves are adjusted with great care at the beginning of the beam time in order to achieve a small overpressure and a low gas flow of 10 sccm (around 1 bubble each second) [113](p.9), [274](p.14-15). Too strong transients could lead to a rupture of the detector entrance window foil (during measurement already 1 bar of air pressure strains

[31] Cremat Inc, 950 Watertown St, Suite 3, West Newton, MA 02465, United States, www.cremat.com (25.5.2021)
[32] Honeywell International Inc, 300 South Tryon Street, Charlotte, NC, United States, www.honeywell.com (25.5.2021)
[33] For long setups (Ramsey type) a 1 m DN25KF flexible hose is sufficient. For state selector or aperture measurements with only one or two regions a 2 m hose is needed. Either the short hose is exchanged or a second one is pieced on. During the threading, it is important to not forget the gaskets. For simplicity DN40KF flanges can also be used to fasten up the process.
[34] The ground of the detector and its electronic itself is galvanically decoupled from the shielding which is again decoupled from the common ground in order to shield off noise of the ground induced by neighboring experiments [298](p.27-34).
[35] iseg, Bautzner Landstraße 23, 01454 Radeberg, Germany
[36] Advanced Measurement Technology, 801 South Illinois Avenue, Oak Ridge, TE 37830, United States, www.ortec-online.com (25.5.2021)
[37] Itech Instruments SAS, 497 AvenueDenis Papin, F-13340 Rognac, France

the foil towards the surrounding vacuum and a repair would take days). A stable gas mixture within the gas tube is provided after some days. The pressure of the bottle is checked on a daily basis in order to recognize if the gas bottle is empty (always remember: seeing is without touching the valve!). The decreasing pressure in the bottle can also be seen in the decrease of the pressure difference between the detector and the surroundings. Daniel Schuh first analyzed this by subtracting the air pressure measured at the airport of Grenoble from the measured values in order to cancel all disturbances of the changing air pressure due to weather [274](p.8-14). Robin Havlik further developed this analysis [112]. If the vacuum chamber is open, additionally the Pfeiffer *PCR 280* pressure gauge attached to the chamber can be used as a barometer which follows the underpressure within the reactor hall better than corrected values from many kilometers away.
The air tightness of the detector can be checked with increasing the pressure to 1.6 bar with the detector in air and closing all valves. The slowly decreasing pressure enables calculating a leakage rate. The P-Detector has a final rate of $3.158 \times 10^{-6}\,\mathrm{s}^{-1}$ [93](p.17-18) and the M-detector of $2.183 \times 10^{-6}\,\mathrm{s}^{-1}$ [32](p.21-22).
The temperature sensor built into the detector will measure the vacuum conditions within the chamber as Daniel Schuh describes [274](p.15-18). During the evacuation process, the detector slowly heats up some degrees due to the missing convection cooling. The temperatures quickly normalize to ambient condition during venting.

A specialty are the polarized detectors (see more about polarized measurements in section 3.9). For this, the outside of the aluminum foil is coated with 150 nm soft iron [113](p.6) which absorbs mainly one spin component if an external B-field magnetizes the foil. One such window was already characterized by Gunther Cronenberg [65] and used [139](p.89-92). The coils for the magnetization have 200 windings made with a 0.5 mm copper wire. A yoke around the detector guides the stray magnetic field around it. A current of 0.25 A normally produces a magnetic field of 1 mT. While reversing the polarity, the 6 folded field is needed [267](p.36).
Due to the soft iron the neutron velocity is limited to maximum 8 m/s, otherwise the effect of spin-dependent absorption vanishes. This limit reduces the count rate to more than the expected 50 %.
For measuring the magnetic field applied, an *MFS-3A* flux gate is also built into the detector [32](p.13,16). See more about the sensor in section 3.9.2.

Detector generation overview [32](p.5): Originally, the first used detectors came from Alexander V. Strelkov and were filled with He-3 [258](p.33-35), [166](p.22-23).
David Stadler started the development of the detectors optimized for *q*BOUNCE in 2008 [287](p.53-71). The main challenge has been to reduce the background of the detector. Possible sources can be found in [264](p.38-39,44) and [32](p.9-10). From the start, the chosen design was a gas counter tube with a boron coated window.
Heiko Saul developed the second generation of detectors [118, 264] in 2010 and Martin Thalhammer improved these detectors during his master thesis in 2012 [298]. During his PhD thesis [299], he built the third generation using the gained experience from the previous generations with the help of many students [32, 93, 113, 120].
Normally, two to three detectors are built per generation. Either the material is varied or twins are built for their own backup. Despite their similar building process the background of identical twins can differ a lot.

The improvement of each generation can be best visualized in the background rate. The best detector of the first generation reached 5 mcps [287](p.68-70). Heiko Saul's improvements in the geometry reduced the background of the second generation to 1.7 mcps at ideal conditions [264](p.50-53). With the improvements of Martin Thalhammer the second generation reached 0.65(2) mcps [298](p.58-59). The third generation reached, under ideal conditions, 0.41(4) mcps [113] (P-detector) and 0.49(5) mcps [32](p.28-29) (M-detector). In Grenoble, within the reactor hall, a 50 % increased background is expected due to higher surrounding noise.

1st Generation David Stadler built three detector prototypes [287](p.63-64). The first twin types had a crude design with a 0.5 mm wire electrode and a full 4π, 5 mm thick B_4C plastic neutron shielding. The difference between the detectors was the material. The first was made of aluminum and the second of the less radioactive impure brass[38]. The third detector was already an improved version again made of

[38] They are called *Aurelie* and *Margarethe*. The second aluminum detector is called *Angela*.

aluminum with a more optimized geometry. David Stadler tested the twins at the PF2/TEST beam in 2008 (TEST-1463). Compared to a gold foil measurement the efficiency was only 35(7) % (probably due to the converter foil properties). The background for the twins was around 5 mcps with a similar background of neutrons. The brass detector was used for all further measurements due to its low background [139](p.38).

2nd Generation Heiko Saul implemented the cylindrical shape of the gas tube for a more homogeneous field and reduced the boron coating size to 110 mm × 3 mm in order to reduce the background of intrinsic radionuclids or fast stray neutrons respectively [264](p.44-47). Based on the experiences from the first generation experiences the second generation is made of brass. Additionally, the wire size decreased from 25 µm to 15 µm to enhance the gas amplification. The length of the wire is 19 cm. Due to the isolation around the wire fixations and field inhomogeneities at the edges, only 15 cm of the wire are suitable for particle detection. Additionally, the redesigned gas inlet and outlet into the active volume reduces the effects on the field homogeneity. One of the detectors also received a 30 µm pure copper coating in the inside of the active volume. To distinguish both detectors they received the names *Manfred* and *Marie Curie*[39].
The first tests with the detectors were done during the beam times TEST-1812 at PF2/TEST, 3-14-283 at PF2/UCN and in Vienna at the Atominstitut (ATI) [264](p.47-56). The brass detector was used for the real experiments. Data acquisition was accomplished by a multi-channel analyzer (MCA) and also a Sampling-ADC (SADC) developed at the TU Munich for a better time resolution. Heiko Saul also programmed a ROOT based readout software for the SADC [264](p.57-68). This brought the advantage of simultaneous measurements of the background and neutron rates. The new method was used from 2010 onward [139](p.66-69). In 2011, Benedikt Holzmann compared the new SADC-electronics with the conventional MCA using three detectors during the beam time DIR-94 [118]. Especially the better time resolution helped to exclude interfering signals from neighboring experiments.
During the beam time 3-14-305, the copper coated detector *Marie Curie* measured the rates of the RABI^{GC}-setup [298](p.17-18,55).
Martin Thalhammer [298] improved the readout of the detectors significantly and improved the shielding against electromagnetic disturbances. A major change was a new housing around the detectors with an integrated *VV50-3* preamplifier from the workshops of the *Physikalisches Institut* (PI) Heidelberg[40] and a complete electromagnetic shielding. A double layer Faraday cage decouples the electronics from the surrounding and the common ground (detector housing, shielded cables, *Anaconda*, *detector fridge*,..). For a better readout he implemented the *quadADC* from itech instruments with the commercial InterWinner software to have a more reliable and mature system than the SADC. The final efficiency during tests and beam times in 2012 was 77 % and a background of only 0.65(2) mcps [298](p.58-59).

3rd Generation: M & P Martin Thalhammer built two identical detectors as the third generation. They are named *P* and *M*[41] [299]. Paul Heistracher characterized them with a PuBe neutron source at the ATI during his Bachelor's thesis [113]. Additionally, he calibrated the three new implemented flow sensors.
The major change to previous generations was the integration of the preamplifer and the detector sensors within the detector housing itself. A *CR-110* charge-sensitive preamplifier on a *CR-150-R2 evaluation board* from Cremat was introduced. The shift to a commercial preamplifier was necessary because the workshops of the University of Heidelberg no longer produced the *VV50-3* preamplifiers.
Nadine Freistetter conducted the first comparable performance test including a comparison of a 220 nm and a 500 nm B-10 foil (P and M-detector respectively) [93](p.25-31). The P-detector was approved for operation and has been used since 2016 in the RAMSEY^{TR}-setup with a background of 0.41(4) mcps [113] and 0.47(4) mcps [93] in ideal conditions. The M-detector had a 17 times bigger background than the P-detector. However, it was adapted for the polarization measurement and therefore equipped with the polarizing foil and shipped to Grenoble as a spare detector.
After the beam time 181-17/1 in 2017, all needed parts including the electronics were transported back from Grenoble to Vienna in order to repair the M-detector. Under the supervision and a lot of help from Martin Thalhammer [299], Anselm Balthasar targeted these problems during his Bachelor's thesis

[39] *Manfred* consists only of brass (German: *Messing*). *Marie Curie* has the additional copper coating (Cu).
[40] University of Heidelberg, Im Neuenheimer Feld 226, 69120 Heidelberg, Germany, www.physi.uni-heidelberg.de (26.11.2022)
[41] Originally, they were named *Paul* and *Martin* as remark for the builders Paul Heistracher and Martin Thalhammer. Due to the bad initial performance of the M-detector the full names were dropped and only the initials remained.

[32]. From the beginning small tips on the inner coating made of copper crystals were the suspected cause of the high background count rate. Therefore, we disassembled the complete detector and tried to remove as many of these small tips as possible with polish paste. Due to the hardness of these tips, this procedure only polished the surroundings. The solution was to cover up everything with Kapton tape for protection and gently remove the tips with a small screwdriver. In the end, we polished everything with fine paste and cleaned it in the ultrasonic bath (water, acetone, isopropanol, water). Martin Thalhammer exchanged the wire and the sealing gasket rings.
After the completed reassembly, the detector was calibrated with neutrons. In Vienna, a small PuBe neutron source or the TRIGA reactor are available for this task. The neutrons produce a spectrum of charged particles which can be displayed after three stages of amplification and the *quadADC* in 1024 channels. The amplification has to be tuned in order to separate the low energy electronic noise from events corresponding to the gas ionization of alpha particles or lithium nuclei inside the ROI.
This was done with the PuBe source and afterwards the background count rate was measured in the UG2 detector lab. In addition, Anselm Balthasar conducted tests of the environment sensors and a leakage test of the detector, analyzed the measurements and compared them to Nadine Freistetter's old measurements. In the end, the detector performance was improved by a factor of 16 to a background rate of 0.49(5) mcps [32](p.28-29).
Furthermore, he completed the second detector sensor card. The complete M-detector setup was brought back to Grenoble for the *q*BOUNCINO measurements. Magdalena Pieler and Valentin Czamler successfully used this equipment parallel to the RAMSEY^{TR}-setup [236]. However, the background was 2.8(2) mcps due to stray neutrons and probably the not shielded cables and detector electronics.
In 2021, the M-detector conducted the first polarized measurements within the RAMSEY^{TR}-setup [194], [270](p.21-26).

3.2.2. Monitor detector

The used detectors originate from the Russian scientist Alexander V. Strelkov. Therefore, they are also called *Strelkov detectors* or originally *Dunya detectors* [78]. The PF2 owns 5 numbered detectors. We always borrow one of them to use it as our monitor detector which is built into the beam line (see more in section 3.1.2) [31](p.15-17). These detectors are gas counter tubes. In contrast to the main detector, they use He-3 for the neutron detection within a large sealed detector volume. This difference is directly visible in the spectrum (see figure A.34). Neutrons are absorbed within the monitor detector and nearly all the energy is deposited there by both reaction products [258](p.33-35), [31](p.12-14). Contrary to this, only one of the charged particles deposits its fraction of the total energy within the main detector.
The monitor detector does not need a constant detector gas flow. Over the years helium slowly diffuses out of the detector and its efficiency decreases. To restore the original efficiency the detector gas has to be exchanged completely. Originally, this was done from time to time by the constructor Alexander V. Strelkov when he was at the ILL. Since his retirement, the PF2-team, in particular Thomas Brenner, has continued to do this procedure.
The detector itself has a thin aluminum entrance foil with a diameter of 70 mm and it can be flanged on a corresponding beam tube, which makes it a multi-purpose detector. In comparison to the main gas counter tube, this one can handle much higher count rates but it has also a 10 times higher background. Stray neutrons (e.g. from the reactor and the PF2-turbine entering through holes within the detector shielding) can increase this background. Misalignment of the rotatable shutter can be the main internal source of background. During the cycle 183-18/2 (3-14-358-IV), the shutter overshot the closing position by 30° [42] and therefore it opened again slightly. This resulted in a measured background noise above 1 cps. Both background contributions are detected as a neutron signal in the background window. A well aligned shutter and a complete thick neutron shielding can reduce the background down below 10 mcps comparable to the electronic noise (the measurements are displayed in section A.4.5).
Originally, the monitor detectors had a built-in preamplifier and we used an amplifier and a high voltage supply (1400 V) within the *detector fridge* for the operation, similar to the other detector. In 2019, the detector workshop at the ILL exchanged the electronics. The preamplifier is now an external box which is wired as closely as possible to the detector and the signal almost does not need any further amplification.
Number #5 of the PF2 owned detectors was mounted during the assembly of the RAMSEY^{TR}-setup until the beam time 183-18/2 in 2018. During this beam time, the monitor rate was rather low (a comparison

[42] A slightly loose screw at the limiter was the reason for the limiter to slowly move by the constant stress of the pneumatic switching.

can be found in table 3.5) and changes up to 50 % of the measured rate were observed (probably due to glass shards at the gap in the beam tube). At the beginning of the beam time 184-18/3, Tobias Jenke compared the available *Dunya detectors* (#2 newly filled, #4 spare, #5 monitor until then) at the PF2/EDM beam line. The best detector was the newly filled #2 *Dunya detector* (1 cycle, cascade detector: #2 1200 cts, #4 750 cts, #5 450 cts) and we built it into the beam line as the new monitor detector. The old one showed a strong electric noise and was brought to the workshop for repairs.

Setup (Beamtime)	Year	Detector	Rate	Background	Source
RABI^{GC}-setup(3-14-305)	2012		435-470 cps	0.16 cps	[298](p.11), [65](p.39)
RAMSEY^{TR}-setup(182-18/1, 3-14-358-III)	2018	5	18.0 cps @ 49.5 MW	0.12 cps	this work
RAMSEY^{TR}-setup(182-18/1, 3-14-358-III)	2018	5	23.7 cps @ 58 MW	0.14 cps	this work
RAMSEY^{TR}-setup (183-18/2, 3-14-358-IV)	2018	5	20 cps @ 52.5 MW	0.06 cps	this work
RAMSEY^{TR}-setup (184-18/3, 3-14-384)	2018	2	117 cps @ 51.5 MW	0.15 cps	this work
RAMSEY^{TR}-setup (184-18/3, 3-14-384)	2018	2	82.8 cps @ 34.5 MW	0.04 cps	this work

Table 3.5.: Comparison of monitor detector performances

3.2.3. Detector corrections

The neutron background, electronic noises, reactor power level variations, the cold source temperature and other factors influence the measured count rate r_D of the main detector. To extract the real neutron count rate r_{D_c} various corrections have to be considered (see also [65](p.39)).

The monitor correction accounts for source fluctuations (reactor power level, cold source performance,..). The average monitor rate $\langle r_M \rangle$ (average over a complete measurement set) divided by the currently measured monitor rate r_M rescales the detector count rate r_D. This is only possible if the monitor rate is stable and only influenced by source fluctuations. During the RAMSEY-GRS-18 measurements in spring 2018, the count rate jumped up to 50 % probably due to glass shards in the beam guides. Therefore, the correction was neglected for these measurements. Ideally the monitor rate r_M should be as high as possible in order to reduce its relative statistical error σ_{r_M}, which also decreases the influence on the detector rate error $\sigma_{r_{D_c}}$:

$$r_{D_c} = \frac{\langle r_M \rangle}{r_M} \cdot r_D \qquad \sigma_{r_{D_c}} = \sqrt{\left(\frac{\langle r_M \rangle}{r_M}\right)^2 \sigma_{r_D}^2 + \left(\frac{r_D \cdot \langle r_M \rangle}{{r_M}^2}\right)^2 \sigma_{r_M}^2 + \left(\frac{r_D}{r_M}\right)^2 \sigma_{\langle r_M \rangle}^2} \tag{3.24}$$

The background correction erases with high probability all counts in the detector with a none UCN origin. Mainly the electronic noise of the detector itself induces these stochastic noise counts. Thermal neutrons from the reactor are an additional source. Faraday cages and neutron shielding around the detector and its electronics reduce the noise level as low as possible (≈0.6 mcps). Due to the low signal rate r_D (10-20 mcps) the subtraction of the averaged[43] background rate $\langle r_B \rangle$ is the biggest correction of the neutron count rate.

$$r_{D_c} = r_D - \langle r_B \rangle \qquad \sigma_{r_{D_c}} = \sqrt{\sigma_{r_D}^2 + \sigma_{\langle r_B \rangle}^2} \tag{3.25}$$

Both corrections joined together give the complete detector rate correction. This also includes that the monitor rates have to be corrected by the average background rate $\langle r_{MB} \rangle$ of the monitor:

$$r_{D_c} = \frac{\langle r_M \rangle - \langle r_{MB} \rangle}{r_M - \langle r_{MB} \rangle} \cdot (r_D - \langle r_B \rangle) \tag{3.26}$$

$$\begin{aligned} \sigma_{r_{D_c}}^2 = &\left(\frac{r_M - \langle r_{MB} \rangle}{r_M - \langle r_{MB} \rangle}\right)^2 \left(\sigma_{r_D}^2 + \sigma_{\langle r_B \rangle}^2\right) + \left(\frac{\langle r_M \rangle - \langle r_{MB} \rangle}{(r_M - \langle r_{MB} \rangle)^2} \cdot (r_D - \langle r_B \rangle)\right)^2 \sigma_{r_M}^2 \\ &+ \left(\frac{\langle r_M \rangle - r_M}{(r_M - \langle r_{MB} \rangle)^2} \cdot (r_D - \langle r_B \rangle)\right)^2 \sigma_{\langle r_{MB} \rangle}^2 + \left(\frac{r_D - \langle r_B \rangle}{r_M - \langle r_{MB} \rangle}\right)^2 \sigma_{\langle r_M \rangle}^2 \end{aligned} \tag{3.27}$$

[43] a long average time is necessary to collect enough counts because during one rate measurement only few background counts are detected.

If the shutter before the monitor beam is not completely closed during the background measurement window, stray neutrons will increase the background rate $\langle r_{MB} \rangle$ significantly (up to a factor 10 and more). Therefore, this correction has to be neglected during such malfunctions:

$$r_{D_c} = \frac{\langle r_M \rangle}{r_M} \cdot (r_D - \langle r_B \rangle) \tag{3.28}$$

$$\sigma_{r_{D_c}} = \sqrt{\left(\frac{\langle r_M \rangle}{r_M}\right)^2 \left(\sigma^2_{r_D} + \sigma^2_{\langle r_B \rangle}\right) + \left(\frac{\langle r_M \rangle}{{r_M}^2} \cdot (r_D - \langle r_B \rangle)\right)^2 \sigma^2_{r_M} + \left(\frac{r_D - \langle r_B \rangle}{r_M}\right)^2 \sigma^2_{\langle r_M \rangle}} \tag{3.29}$$

The corrected detector rates give comparable measurement points within a measurement set. However, they are unsimilar to measurements of different reactor cycles or setups due to different reactor power levels and zero rates. Therefore, all corrected detector rates are divided by the corrected average zero rate of their measurement set. The resulting value is the relative transmission with an accordingly rescaled error (including the error of the zero rate). All measurements in this thesis are given in this representation.

3.2.4. CR-39 detectors

The CR-39 image plates are the detectors with the best spatial resolution in the experimental setup. They are similar to photographic plates and therefore these detectors do not store any time information. They are made of allyl diglycol carbonate, generally known as *Columbia Resin #39* (CR-39) and are produced by *Intercast*[44] [88]. This material is mainly used for glasses but also suitable as particle detector. The dimensions of these plastic detectors are 1.5 mm × 15 mm × 120 mm [88](2.4 p.18), [258](p.35-37), [210](p.17), [166](p.24-30).
These small plates are additionally coated with copper and enriched boron (170 nm to 220 nm)[45]. The thickness of the boron determines the detector efficiency and the spatial resolution with opposite dependencies ([161](p.76-80), [138](p.80-81)). This detector design is a key technology of studying the quantum bouncing ball and was developed for this purpose. The original and similar approach with an uranium-235 coating was used for the first measurements of the gravitationally bound states in 1999 [258], [312](p.93-100). Later, this was dropped due to worse spatial resolution (higher kinetic energy of the fission products and consequently longer tracks) compared to the boron coated ones.
The measurement principle is similar to the gas counter tube. The boron layer absorbs the incoming neutrons and the boron nucleus splits into an α particle and a Li-7 nucleus back-to-back. One of them enters the CR-39 itself and damages the polymer structure on its flight path. After removing the coating with acid, lye (sodium hydroxide) etches the CR-39. Damaged areas are dissolved faster than the bulk [88](p.21-26). After some hours, the tracks become visible under a microscope as µm-sized holes. All neutron tracks are counted by scanning and photographing the area of interest. The evaluation is done mainly with *Mathematica*[46] scripts: First to distinguish between neutron tracks and other surface defects and second to fit a theory to the visible pattern in order to calculate the state occupation.
In order to keep track of all used plates, each of them has an assigned number and a database keeps all important information on the plate properties (coating, use, etching, microscope scans).
A first alternative approach with online detectors failed due to worse spatial resolution. One tested detector candidate was a combination of a CASCADE-detector and a taper in 2008 [138](p.83-91). In the recent years, a Japanese collaboration developed a new emulsion based detector with an even higher resolution [205]. First test with UCNs were preformed within the *q*BOUNCINO-chamber at the PF2 in 2019 [206] and 2021. Their techniques of etching a reference grid on to the detectors and using a 3D scanning microscope could also improve the CR-39 readout methods.
More details about CR-39 can be found in [89](p.138-164), [139](p.24-36), [166, 199, 210, 299], [287](p.73-81) and information about properties of the materials in [88].

[44] Intercast Europe Srl, Via G Natta 10/A Parma, 43100 Italy, www.intercast.it (9.11.2022)
[45] 220 nm are the optimized values for a velocity spectrum of 5 m/s to 7 m/s at the PF2 [287], [264](p.32), [139](p.26). Smaller values reduce the efficiency and are only used if the coating is incomplete.
[46] A software from Wolfram Research

Coating

The coating process is quite tricky because boron is heated up to very high temperatures to be able to reach the surface for coating and CR-39 is mainly plastic. Under heat stress it will deform and bend, which complicates the read-out process ([161](p.91-95)). To reduce the thermal stress the coating of boron is done very slowly and an additional 50 nm copper intermediate layer fastens up the thermalization of the surface during the boron coating [287](p.76-77). Other materials, like chromium, cannot provide this feature and the surface will crack into multiple small islands during coating. Every crack reduces the active surface and therefore the efficiency of the detector. Similarly, the thickness of the intermediate coating (e.g. copper) decreases the penetration depth of the detected particles. The second purpose of this coating is to be able to etch the complete coating with acids from the CR-39 [139](p.25). In the project thesis of Alexander Leopold [176] you can find more information about the PVD production of the detectors.
The first UF_4 coated detectors were developed at the Khlopin Radium Institute (KRI), St. Petersburg [258](p.84). In 2004, Martin Klein produced for the first time boron coated detectors in Heidelberg ([161], [210](p.33-39), [138](p.82), [88]) and later Dominik Sailer manufactured more detectors in Munich [139](p.25). Since 2014, a Pfeiffer[47] *Classic 500L* PVD machine in the basement of the ATI has been available for coatings. Alexander Leopold first described the machine and the process of the coating in his project thesis [176]. He first achieved to produce titanium coatings on wavers to comparatively measure the layer thickness via the machine itself and $x-$rays. Ultimately, he was able to coat three CR-39 detectors and tested them at the beam line D of the TRIGA reactor in Vienna (ATI). In the end of 2016, Hanno Filter produced, after many trials, a batch of excellent detectors there [89](p.142-144). This batch was used in 2017 and 2018. With him leaving the institute, most of the knowledge of the production was lost and it will take years to be able to have detectors with similar, trustworthy quality produced.

Irradiation

We use the detectors for two different purposes, either to measure the beam profile or to determine the state population. Visualizing the shape of the neutron beam, after it left the beam guide, enables studying the divergence of the beam and the properties of the end cap. During these tests, the detectors were placed upwards and were only lighted for one PF2-cycle (190 s).
The studies of the density distribution of the neutrons within or after the setup (e.g. in order to measure the state population after a state selector or visualize the quantum bouncing ball) are more tricky. For this purpose, the counter tube measures the rate of the tested setup first. Afterwards, a CR-39 detector is horizontally glued to a special aluminum block (*CR-39 holder*)[48]. Small engravings on the block help to align the center of the CR-39 with the height of the mirrors (105 mm). This holder replaces the counter tube and is positioned very close to the edge of the last mirror so that the CR-39 detector is not touching it.
To calculate the number of collected neutrons, the irradiation time is multiplied by the previously measured rate. Additionally, the *MAMBO-factor* (0.4-0.9) and the detector efficiency difference (40 %) are multiplied. Otherwise, the collected neutrons will be overestimated which already led to some underexposed and therefore wasted detectors. For the complete detector at least 3000 neutrons are necessary to be even able to find a track of neutrons (This is normally reached after 26 h at a rate of 200 mcps). The track of neutron impacts after a state selector is only 30 µm wide and 100 mm long. Around 450 pictures taken with the microscope cover this track. Therefore, one picture captures only 6-8 neutrons, which are quite hard to find, especially when the surface is not really clean. Capturing 10000 neutrons is much better. First the track is found more easily, second the statistical error is much smaller if the resulting pattern is analyzed for the state distribution.
Two measures are taken to reduce the background of the neutron radiation before and after the measurement: they are transported to and from the reactor hall short before or after irradiation and are additionally shielded with borated plastic blocks. To increase the counted neutrons the shutter stays open during irradiation also to benefit from the stray neutrons from the switcher. Especially if the switcher does not move at all, the full beam can enter the setup also during the transition times (*filling + cleaning*).

[47] Pfeiffer Vacuum GmbH, Berliner Strasse 43, 35614 Asslar, Germany, www.pfeiffer-vacuum.com (13.11.2023)
[48] Originally in 2008-2009 the detectors were fixed with screws on a holder but due the mechanical stress this method was dropped [139](p26-27,34).

Etching

The etching process needs some basic experience in chemistry [210](p.40-41), [139](p.27), [14](p.15). There also exist protocols as guidance. In 2018, Daniel Schuh updated the existing one [274](p.5). Additionally, it is important to keep record of all steps taken by writing them in a special chemistry laboratory journal. First, the detectors are cleaned from any super glue residues with acetone in an ultrasonic bath. Second, pure water washes away all remaining acetone on the detector which could lead to potentially problematic reactions in the next steps. Afterwards, sulfuric acid and hydrogen peroxide etch away the coating (mainly the copper underneath the boron) in an ultra sonic bath. This process is repeated until the complete coating is removed. If the coating has many cracks, it will dissolve very quickly. Residue of the coating could slow down the next step in that area and therefore reduce the number of visible neutron holes. The most important step during the chemistry process is etching the CR-39 itself with lye in a temperature-controlled heat bath. Here the lye's concentration (20 %), the temperature (42 °C) and the time (5 h) define the etching speed. The more the detector is etched the more neutron impacts are visible but also the size of these holes increases. This decreases the spatial resolution [287](p.36-41). To stop the process the detectors are moved into hydrochloric acid with a concentration of 25 %. To normalize the pH value the detector is moved further to lower and lower concentrated acids until it is in pure water. A tricky part is to dry the detector without having too many stains on the surface.
If new batches of CR-39 are used and especially if the manufacturer has changed, the etching time and the temperature should be confirmed with a sequential etching. For this highly irradiated detectors are preferable (e.g. from beam divergence measurements). The etching itself is paused with acids already after few hours and the detector scanned with a microscope. In order to always find the same spot, marking it with a scalpel helps. After scanning, the etching is repeated for an hour. The etching time should be timed as precise as possible. In the end, an optimal etching time can be determined as a trade off between spatial resolution and neutron detection efficiency. This was done in 2008 [287](p.36-41) and repeated in 2018 [14](p.26-33) with similar results. A similar technique can also be used to gain more information of the detectors by tracking the neutron hole position at different etching times and being able to better localize the impact (direction of the inclination).

Microscopy

We use an optical microscope *BX41* from Olympus[49] to visualize the neutron impact holes with a 50 times amplification [139](p.27-28). A camera on top of the optics photographs the detector with a picture size of 1376 × 1032 pixel corresponding to 288 µm × 216 µm (The shorter length is along the scanning path in order to have a broader picture of the track taken with more pictures)[89](p.148-149). A stage from Märzhäuser[50] can move in all directions [139](p.27-28)[51]. The program *Cell^D* controls the microscope and all attached components [199].
Before scanning the CR-39 detectors, the microscope has to stand on a stable table and it should be cleaned and adjusted [139](p.28-29), [14](p.16-17), [155](p.10-12). The calibration of the x and y stages is done with two calibration glass plates. The first one has various sized marks which calibrate the length of the pictures and the movement of the stages. It is important that two consecutive pictures are touching each other (without overlap or gap in between). The second plate has a long straight line similar to a neutron track. This should be scanned before and after a detector scan to be able to measure the jitter of the x-stage and later eliminate it from the data. Additionally, a dark picture should be taken to eliminate artifacts due to the optics.
Via a joystick the detector can be inspected and the track searched. For automatized scans the program is able to move the x and y axes. The operator has to adjust the z axis, therefore the focal plane, manually before a picture is taken (this is important if the detector has a strong bending). If the track is found, the detector should be aligned in order to picture it with only moving one axis. If it is not found or a larger pattern is searched, it is preferable to scan larger rectangles with multiple pictures. In this case it is important to see how the program meanders over the detector which is needed later for the analysis. A pit fall is scanning the correct side of the detector. Scratching (best before the exposure little above the mirror) or marking the detector on the coated side is helpful. Experienced operators also see the face by defects due to the removed coating.
In principle, the program already makes a pattern recognition and stores the pictures and its position.

[49] Olympus Europe SE & Co. KG, Amsinckstraße 63, 20097 Hamburg, Germany
[50] Märzhäuser Wetzlar GmbH & Co. KG, In der Murch, 35579 Wetzlar, Germany
[51] Take care of the connecting piece of the vertical motor. Over time it loosens and the motor skids.

A disadvantage of the current setup is the old firewire interface which is very problematic for newer types of Windows (Windows 7 or higher) and can crash the system during long scans.
In the future, real 3-dimensional scans would help to better distinguish between neutron holes and dirt on the surface. It would also eliminate the human bias of focusing each picture individually [89](p.171). Additionally, the direction of the entering particle can be reconstructed with very high accuracy, which increases the spatial resolution [283]. Similarly, multiple scans with different etching times could increase the resolution. Also overlapping pictures and track matching in these areas can eliminate influences of small jittering of the transitional stages.

Evaluation

The evaluation of the scanned detectors consists of two steps. First the neutron hits have to be detected, distinguished from other surface defects and their position calculated relative to each other over multiple pictures. The second step is to correct defects of the pattern (rotation, bending, stage jitter,..) in order to create a histogram over the complete width of the detector and then to be able to fit a suitable state distribution.
For the first evaluation step there are three possibilities: a C++ code used at the beginning from CERN [258](p.62-71), the search routine of the program itself and a machine learning algorithm in *Mathematica* created by Hanno Filter. The Olympus software *Cell^D* finds possible impacts via a threshold. Various properties (area, shape, ...) are selection criteria for neutron impacts and their discrimination. Automatically the software searches for hits in each taken picture and stores them in a spreadsheet together with the position of the stages [139](p.29-32). From 2009 [199] until the bouncing ball measurement of Martin Thalhammer [299] in 2014 this process was optimized. Especially Tamara Putz and Martin Stöger worked on this for their Bachelor thesis during the beam time 3-14-331 (172-14/2). However, they never finished their thesis.
The third possibility was developed by Hanno Filter for his Lloyd neutron interferometer measurements [89](p.149-161). In the beginning, it adjusts all pictures to a common gray level. Only an area interval of joined pixels above a gray level threshold is used to find possible neutron hits. A small picture around these candidates is fed into a machine learning algorithm which is trained by a fixed set of manually classified events. The algorithm assigns each hit to a class (e.g. neutron, inclined neutron, double, faint, candidate, dust, crack,...). Afterwards, only handpicked classes are used for further analysis. Classes with a random distribution are excluded, which reduces the background of dust and cracks and enhances the statistical significance of the searched pattern. Lukas Achatz used this method to analyze the state selectors of the 2018 beam times which were used for all neutron measurements in this thesis [14](p.18-21). All methods have never been compared and the *Mathematica* routine has never been optimized to an optimal spatial resolution (Using a gray level weighted center or geometric center, calculate inclined trajectories,..). Therefore, comparing results like the spatial resolution is difficult (a calculation of the resolution can be found in [258](p.71-72), [210](p.41-42) 1.4 µm, [166](p.28), [287](p.79-80) 2 µm, [199] 1-2 µm).

For the second part of the analysis, we use a special *Mathematica* notebook [199] originally written by Tobias Jenke [139](p.32-34) and further developed by Martin Thalhammer [299] for the quantum bouncing ball measurements (qBB^{MT}-setup). It was further used by Tobias Rechberger and Lukas Achatz [14](p.21-25) for the Ramsey state selector measurements. The first steps of this notebook are to rotate the neutron track horizontally, to exclude certain areas (e.g. the edges or areas with high background) and to mirror everything if it is upside down. Further, it is possible to unbend the neutron track if it is strongly curved due to deformed CR-39 detectors [287](p.76-79). This is only possible if enough neutrons are detected. Afterwards, all detected neutrons are plotted in a histogram (neutron height vs counts). A fit routine searches for the state occupation. Additionally, the state selector gap and the spatial resolution are calculated.

Table 3.6.: List of all important CR-39 detector measurements

ID	Experiment	Details	Result
TM5, TI12	qBB-2008	step wise etching	[287](p.37-39)
HA07, HB01, HB08, HB12	qBB 2009	0-8 cm	[199]
HA01	qBB-2009	Region I	[199], [139](p.45-48)
HB04	qBB-2009	48(1) µmx30 mm step	[199], [139](p.49-51)
L09	RABI^{GC}-setup-2012	Region I	[65](p.25-27), [298](p.14-16)
077, 088, 100	Coating tests-2014		[176](p.26-29)
008, 011, 043, 049	qBB^{MT}-setup	CR-39-test	[299]
010, 012, 015, 020, 026, 030, 040, 050, 087	qBB^{MT}-setup	qBB	[89](p.161-162) [299]
019, 041, 044	qBB^{MT}-setup	Divergence	[299]
005, 012, 026, 028, 042	qBB^{MT}-setup	Velocity spectrum	[299]
L01, 098	Llyode interferometer		[89](p.133-134)
T37	Ramsey-2017	Region I (603+709)	[254](p.111-113)
122	Ramsey-2017	Region I (706+708)	[254]
L06	Ramsey-2017	Region V 5-13 m/s	[254](p.112-113)
036	Ramsey-2017	Region V 5.7-9.5 m/s	[254]
129	Ramsey-2017	Region I + Region V	[254](p.112-113)
E03, T35, 016, 103	RAMSEY-GRS-18	Beam divergence	[14](p.26-36), section 4.3.2
003, 116, 128	RAMSEY-GRS-18	Region I (802+805)	[14](p.36-48)
L11, 102	RAMSEY-GRS-18	Region V (801+804)	[14](p.48-52)
062, 070	RAMSEY-GRS-18	Region I + Region V	[14](p.52-60)

3.3. E-Field Test Setup

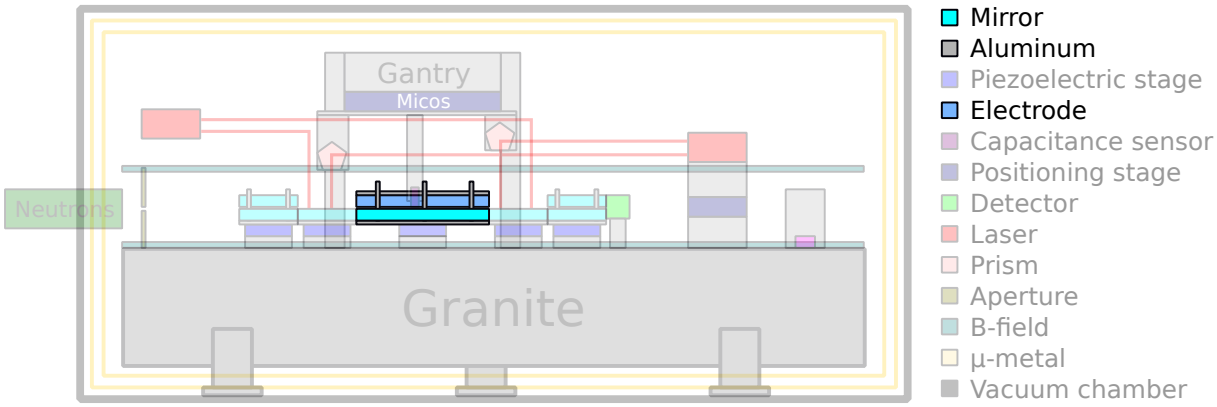

Figure 3.10.: A schematic view of the electrode position within the RAMSEY^{TR}-setup

For the neutron's electric charge measurement, a suitable electrode is necessary to provide an as high as possible stable electric field in region III. Since the first proposal of Durstberger-Rennhofer [77], various materials and configurations have been tested for an optimal setup. This work resulted in the *E-Field Test Setup* which is situated in Vienna and was used in Grenoble during the charge measurements of this thesis (Rams$\vec{E}$y, section 4.6).
The following subsections give an overview of the conducted experiments and tested materials. Further, I will present the test setup, the finally used electrode, the data acquisition and the alignment process.

3.3.1. Overview of all electrode tests

In 2012, Hanno Filter started the search for the optimal electrode to measure the neutron's electric charge. The first tests consisted of aluminum plates (100 mm × 70 mm × 30 mm with 650 µm plastic spacers, a *CEAN N1470* voltage supply and SHV cabeling, within the *q*BOUNCINO chamber) [157](p.12), [271]. First results were that sparks occurred close to the edges of the spacers and spark conditioning was observed. Lukas Schrangl also programmed a first controller to automate the tests as part of his project thesis [271]. Markus Spanring [286] further repeated the measurements with the aluminum blocks and plastic spacers of Schrangl within the *q*BOUNCINO chamber. He used a different power supply (*LNC 6000-5 ngeg* from

Heinzinger[52]) which can provide 6 kV and 5 mA, which is enough current also during breakdown events. He also implemented a LabView program for the operation of the device and used two DAC for the communication (*NI-DAQ 621x OEM* and a *NI PCIe 63xx card*).
Michael Iro [122] tested the maximum possible field with two sets of iron spheres (very small surface effects). He already implemented FuG HV supply and the small vacuum setup of the test setup including the pumps and the pressure gauges. The distance was adjusted via linear gauges and micrometer screws. The highest field was 240(33) kV/m with destruction of the surface at $1.6(2) \times 10^{-7}$ mbar.
In order to search the optimal electrode more systematically, Hanno Filter designed and built the *electrode test setup* together with Andrzej Pelczar of the ATI electronic workshop. It is situated at the Atominstitut (ATI) in Vienna. With this setup Hanno Filter and his students measured different types of small electrodes until 2018: Jakob Micko (copper - glass spacer - copper [192] 4.5 MV/m), Florian Honz (titanium - glass spacer - titanium [119] 19 MV/m). Jakob Micko additionally conducted tests with plastic spacers and concluded that they were impractical for the use in high electric fields. Their complex behavior led to strong currents through the electrodes due to a low parasitic resistance. Therefore, all previous measurements using plastic spacers [271, 286] should not be considered. Florian Honz also described the setup and conducted many measurements of the surface roughness of different electrode materials with the *SE-1700* surface structure gauge (see more about the device in subsection 3.1.5).
Additionally, Martin Mock prepared the possibility with an automatized precision valve to adjust the vacuum pressure to a defined value by inflating different gases [200]. This is useful to study the behavior of electrodes at different pressures or to apply gas conditioning.
Christoph Mühlmann [208] simulated the electrodes with the finite element program *CST Studio Suite*[53], which allows to calculate field distribution, charging behavior and capacitance calculations. *COMSOL Multiphysics*[54] could also provide such simulations but needs much more efforts for the mesh settings in order to run a simulation.
In summer 2018, the final electrode (Rams$\vec{E}$y) was built and transported together with all other parts to the ILL. During the cycle 184-18/3 the setup, except for the vacuum chamber, was part of the RAMSEY^{TR}-setup in Grenoble. Elisabeth Kreuzgruber analyzed the alignment and the performance of the electrode during the neutron electric charge measurement [169] (see results in section 4.6).
After successful measurements at the ILL, the setup parts went back to Vienna during winter 2019. In order to test the final limit of the large Rams$\vec{E}$y electrode, Andrzej Pelczar and the Bachelor students Anika Gassner [96] and Julius Piso [241] repaired all damages from the beam time and successfully rebuilt the setup in Vienna including the *q*BOUNCINO vacuum chamber. Due to time pressure (the vacuum chamber had to be sent back for measurements in Grenoble) and a nonlinear behavior of the dark current, the final breakthrough did not occur. In 2020, Nicole Pruggmayer [247] and Jasmin Juroszek [151] improved the setup and measured with it up to a maximal field strength of 10.8 MV/m (final destructive breakthrough). Preceding these measurements in 2019 and 2020, they also measured with the small copper electrodes separated by glass spacers [241, 247]. This has always been a test to find out if the complete setup works properly. The observed maximal fields were >10 MV/m (only few reversible breakthroughs observed) and 7.6 MV/m (above occurred a very high spark rate) respectively.
In 2021, Luca Neubacher [225] and Paul Klieber [162] implemented stick slip motors from PI in order to automate the alignment procedure. They measured small titanium electrodes (breakthrough at 4.1 MV/m [225]) and small mirrors without spacers (breakthrough at 11.4 MV/m [162]).

3.3.2. Electrode properties

There are two kinds of electrodes: many small ones for testing different materials and configurations and one large electrode, the so-called Rams$\vec{E}$y-electrode. This was used for the charge measurement. Therefore, it needs to fit as region III in the current RAMSEY^{TR}-setup and has to provide a stable and as high as possible electric field. Its dimensions are limited to a length of 340 mm and a width of 100 mm for the upper electrode in order to leave space for the passing capacitive sensors. With *CST Studio Suite* we simulated all possible electrode geometries including the surrounding electric network [208](p.17-18).

[52]Heinzinger electronic GmbH, Anton-Jakob-Strasse 4, 83026 Rosenheim, Germany, www.heinzinger.de (10.7.2021)
[53]Dassault Systèmes, 10 rue Marcel Dassault, 78140 Vélizy-Villacoublay, France
[54]COMSOL AB, Tegnérgatan 23, 111 40 Stockholm, Sweden, www.comsol.de (9.11.2022)

Electrode material and design

Three possible materials are used for different electrodes: BK7-glass mirrors, copper and titanium.
Coated glass mirrors are already built into the qBOUNCE-setup. Due to their flatness and the material, they are ideal neutron guides. The aluminum coating, which is used for the capacitive sensor system (see more section 3.5.3) and to reflect the lasers of the SIOS-interferometers (subsection 3.6.2), also acts as an electrode with a very smooth surface. In contrast, the surface of full metal is too rough even after special treatments (lapping and etching). A full evaluation of the roughness of different materials after diverse polishing techniques can be found in the work of Florian Honz [119](p.19-33). Especially titanium has an additional disadvantage of not being a neutron guide. Its negative neutron optical potential enables the neutrons to enter the material where they have a high absorption probability.
A major advantage of these full metal electrodes is that they can be trained. This means that sparks or breakthroughs between the electrodes can flatten the surfaces by burning away small tips or dust particles. Breakthroughs at mirror electrodes will irreversibly destroy the coating due to the lack of heat transport away from the impact. Afterwards, the electrode acts more as a random discharge than as a capacitor. Irreversible damage of the surface can also occur at full metal electrodes at very high voltages, but mechanical surface treatment could erase such imperfections.
The material itself also has a major impact on the performance of an electrode. Refractory metals like titanium deform or sputter less than soft metals like copper during a discharge. Tungsten or molybdenum would have even better properties than titanium but they are more expensive. You can find more information on the material choice in [173].
Beside geometric considerations (e.g. Rogowski profile), contacting of the electrode is an important issue in the design process. Full metal electrodes are easily contacted from the side or the top. Mirrors are commonly contacted by scrapping off the protective layer via a scalpel and gluing a wire with silver conductive varnish. Such contacts can only be placed outside the gap between the electrodes. Either the mirrors are shifted, which is done for small test electrodes, or only the larger electrode can be contacted this way. The smaller one (which in the case of the Rams$\vec{E}$y setup is the upper electrode) needs a more sophisticated way. A hole in the lower electrode could be used or a second coating of this mirror could solve this problem by elongating the conductive layer on the side face. POG initially coats all mirrors only on one side with no further options. Therefore, the used mirror electrode was coated with titanium on all faces at the TU Wien. Ideally the side faces are covered with Kapton tape except for a large patch where the contact is placed. The Rams$\vec{E}$y electrode is coated only for a few millimeters from the main surfaces. Above, there is a gap of 10 mm due to the Kapton tape and above there is a coating connected to the ground already before the U-notch. This makes it quite hard to attach the wire without shortening the high voltage to the ground.
A combination between different types of electrodes is also possible (e.g. a coated mirror as neutron guide at the bottom and a titanium full metal electrode on top which is trained in advance).

A further important design element is the method of achieving a uniform spacing. There are two main possibilities. Either using spacers with a specific height or an adjustment system which can provide a material free gap. Spacers are easy to handle and provide an alignment with similar errors to the thickness of themselves. Two types of spacer materials were tested: plastic and glass. Plastic spacers at first gave results with very high breakdown voltages. This is due to a specific behavior of plastic within very high electric fields. These spacers store the energy of the electric field in geometric changes of the polymer itself and therefore their thickness, which makes them useless for their task [192](p.16-22), [231]. Glass spacers do not have this effect. Additionally, glass spacers in certain thicknesses (170(5) µm) are commonly used in microscopy and available in high precision. Due to the spacers' dielectric properties as an isolating material they change the electric field within the electrode and therefore increase the capacity. In addition, sparks often occur at the edges of the spacers which could lead to destruction of the electrode surface similarly if they struck through the vacuum gap. On the contrary, sparks through spacers could protect the surface, especially for coated glass electrodes due to the better heat distribution.
Spacer-free adjustment systems should have higher breakdown voltages. Spacers can be used as the starting point of the adjustment. We observed the alignment with linear gauges and measurements of the capacitance. The simplest adjustment system consists of fine threaded screws connecting the electrode to the bearing. They can only be adjusted manually in air. More sophisticated are piezoelectric driven motor stages as first tested by Paul Klieber [162] and Luca Neubacher [225]. They can be adjusted remotely even in vacuum similar to mirrors. Alignments and variation of the distance could be easily done between measurements. Similar ideas were already discussed for the state selectors.

3.3.3. Test electrodes

BK7-mirrors

The small BK7-electrodes are quadratic mirrors from POG with an edge length of 50 mm, a thickness of 20 mm and a central U-notch of 10 mm [119](p.12-13,56). We have 10 numbered small mirrors of this kind. Hanno Filter coated them up to number # 8 and used them for tests with 170(1) µm glass spacers. Some of them (#6 & #7) are not fully coated in order to place the spacers in the non-coated areas to simulate tests without spacers [119](p.12-13). At the first tests with fully coated mirrors most sparks struck at the edge of the spacers and often destroyed the electrode's surface. Some breakthroughs appeared through the spacers which baked the thin glass onto the mirror and kept the coating intact.
These small mirrors and similar electrodes have a simulated capacitance of 130 pF [208](p.15-16).
Hanno Filter conducted tests with pairs: #2+#3, #4+#5, #6+#7. He reached a maximal field between 10.6 MV/m and 24 MV/m. #1 and #8 are coated but were never used. Niels Geerits coated #9 and #10 in May 2021 [162](p.22-24). Luca Neubacher and Paul Klieber measured spacerless with them. They determined a breakthrough voltage of 1250(3) kV/109.5(5) µm ≈ 11.42(6) MV/m [162].

Small copper electrodes

These four full metal copper electrodes are an exact copy of the small mirrors [119](p.13-14). The only difference are two M6 screw holes on the side face for contacting. In autumn 2017, they were also lapped, which improved the surface roughness to $R_a = 0.07(1)$ µm and $R_z = 0.7(2)$ µm with a strong directional waviness up to $W_t = 0.24$ µm [119](p.33)).
In 2019, Anika Gassner and Julius Piso used a pair to successfully test the electrode test setup in particular the amperemeter after the damages done to it during the use in Grenoble 2018 [241]. The test ended at 1750 kV/171(1) µm ≈ 10 MV/m due to a hardware limit in the high voltage supply with slightly higher spark rate than for the titanium electrodes.
In 2020, Nicole Pruggmayer [247] and Jasmin Juroszek similarly used the same electrodes and reached a final limit of 1300 kV/171(1) µm ≈ 7.6 MV/m. This lower value occurred either due to aging of the assembly or the upgrades of the setup.
Compared to the simulated capacitance of 130 pF [208](p.15-16), Julius Piso measured 105 pF [241](p.7-8) including spacers. Nicole Pruggmayer measured with spacers and the digital multimeter a capacitance of around 215 pF (with already subtracted parasitic capacitance of the cables) [247](p.30-31). A different area size of the spacer within the electrode gap explains this difference.

Large copper electrodes

The large copper electrodes have a similar base to the small mirrors or copper electrodes. An attached 70 mm wide and 10 mm thick plate enlarges the electrode surface. Additionally, the edges have a rounding radius of 2 mm. At a distance of 50 µm and 170 µm these electrodes have a calculated capacitance of 868 pF and 255 pF respectively [208](p.15-16). The 3-D simulated values of 793 pF and 241 pF are smaller because they take the rounded edges into account [208](p.43-44). Jakob Micko used these electrodes during his project thesis and he measured a capacitance of 325(11) pF at 170 µm [192](p.24). The higher capacitance can be explained by the additional capacitance of the holders and between the assembly and the vacuum chamber.
Using the glass spacer the maximum stable field without sparks was 4.5 MV/m (770 V at a distance of 171(1) µm) [192](p.26-28).

Titanium-electrodes

The ATI-workshop cut these four titanium electrodes out of a single titanium rod. They have the same geometry as the small copper electrodes [119](p.14). Therefore, they have no round edges. Together with the copper ones, the titanium electrodes were lapped in autumn 2017. In order to improve the surface even more, electropolishing could flatten the tips further down.
Florian Honz tested a pair of the electrodes [119](p.37-44). He observed a spark conditioning due to a decrease of breakthroughs over time. Most of these occurred at the 173 µm glass spacers. Up to 3300 V all sparks caused reversible damages. At 3400 V a final breakthrough irreversibly destroyed the surface.

Therefore, the maximum acceptable applied electric field was 19 MV/m.
In 2021, Paul Klieber and Luca Neubacher used the remaining two titanium electrodes in a new automatized electrode alignment setup [225](p.60-66). The advantage of this configuration is the spacer-less measurement. However, the final breakthrough was already at 800 V and a distance of 183.2(2) µm. The last stable electric field strength was 4.09(2) MV/m.

3.3.4. Rams$\vec{E}$y electrode

The lower electrode is a coated BK7 mirror in order to guide the neutrons. As already mentioned (subsection 3.1.5), the coating is aluminum with a protection layer of silicon oxide to reflect the laser and for the capacitive sensing system. Titanium with its negative scattering length would have absorbed the UCN. The dimensions of this mirror are 340 mm × 200 mm × 30 mm similar to a normal region III mirror. Additionally, the electrode mirror has six holes for the bearings of the upper electrode (See fig. 3.11). The spacing of the holes in neutron flight direction is optimized to minimize the bending of the upper electrode[55]. The lateral distance is the same as for the absorber bearings which is constrained between the beam width and the capacitive sensors' tracks. Additionally, a new aluminum base plate holds the mirror, which is similar to the original region III base plate except additional clearance holes for the upper electrode bearing.

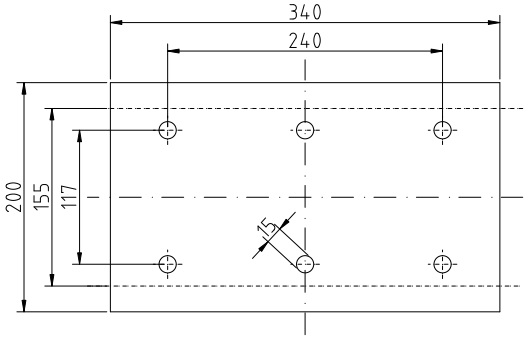

Figure 3.11.: Dimensions of the electrode mirror [mm] [208](p.9 Fig. 5)

Four electrode mirrors were produced by POG. One of the first two (#812) was accidentally destroyed during surface measurement. The other one (#811) was used for the normal Ramsey measurements (RAMSEY-GRS-18) and suffered some small surface damages. For the charge measurement (Rams$\vec{E}$y) this mirror was replaced with the unused mirror #831 which was ordered after the accident.
The upper electrode was originally planned to be a titanium full metal block but the blank was not ordered together with the one for the small titanium electrodes due to money considerations and later due to a tight time frame. During the summer of 2018 after two beam times, the electrode design was quickly adapted. A mirror from the Llyode interferometer [89] was designated for the electrode. S-DH cut rounder edges instead of the lower chamfer. At the TU Wien the mirror side and the side faces were coated again with a layer of titanium where a Kapton tape left a small band below the u-notch free of coating. Ivica Garlic designed a mounting system with three bearings and three micrometer screws for adjustment. It was planned to attach them directly into the mirror, which was not possible. Instead S-DH glued a 10 mm aluminum plate on to the top of the mirror where now the adjustment screws are attached. Due to this plate the bearings are too short and have to be extended by two M6 nuts at each column. A description can also be found in [169](p.12-13), [96](p.11-12) and [151](p.15-17).
Due to cold weather during the transport back to Vienna the glass of the upper electrode was ripped apart by the thermal stress of the different materials. As described in the Bachelor's thesis of Anika Gassner [96](p.12-13), we superglued it back together.
In principle, all setup parts within *q*BOUNCE are on the same ground, therefore also the mirror base plate, the electrode bearing, the aluminum plate and the titanium coating on the side faces of the upper electrode. The large electrode mirror is not connected to the common ground, instead it is attached to

[55] Similar to a 2 point support of a bending beam (Bessel or Airy points), the bending due to support on three points can be calculated analytically.

the ammeter measurement circuit. Any breakthrough of the electrode setup should not directly hit the ground, otherwise sensible systems like the capacitive sensors could be harmed[56]. The upper electrode is always attached to the HV power supply.
The capacitance C of the electrode (total area $A = a_E b_E = 340\,\text{mm} \times 100\,\text{mm}$) calculated with the simple formula for a parallel plate capacitor at a distance $d = 170\,\mu\text{m}$ is 1.77 nF [208](p.13):

$$C = \epsilon_0 \frac{A}{d}$$

The simulated capacitance between two mirrors embedded within region II and region IV is 1.836 nF [208](p.35). The real setup is expected to have an even larger capacitance due to the coating on the edges and the bearing plate on top of the upper electrode.
Simulation also shows that the field between these two mirrors is extremely homogeneous and only on the edges there are small disturbances, as it decreases from a quite constant value to zero especially in the vicinity of neighboring mirrors. [208](p.18-23). In reality, the waviness of the mirror surface (max. 3 µm) also wraps the field inside slightly.

Possible safety measures

Short circuits have to be prevented at any cost because they can irreversibly destroy the mirror electrodes [208](p.10). On the other hand, an as high as possible electric field improves the setup's sensitivity.
One way would be to measure the small rise in dark current before the breakthrough but this would need a much more sensitive ammeter and fast switching. Another way is to use a predetermined breaking point. This is a second electrode pair placed parallel to the large electrode in the Ramsey setup. This additional capacitor could be as small as the test setup. The housing should be separated from the huge vacuum chamber in order to be able to replace it without breaking the vacuum of the experiment chamber. In addition, it should have a smaller spacing than the main electrode in order to function as breaking point and limiter of the high voltage. Still, small dust or solvent residues can produce tiny tips on the mirror which can lead to a lower short cut voltage in the large electrode setup than this limiter. This uncertainty is quite hard to handle.
A second important protection would be a housing of the upper electrode. This would limit the stray fields of the electrode which could disturb the capacitive sensing system and increase the total capacitance of the electrode (see more at Mühlmann [208](p.10,13-15)).

3.3.5. Electrode data acquisition

In order to apply voltage to the electrodes and measure the current running through them (charging, dark current, sparks,...), the electrode test setup was built. It consists of a high voltage power supply, a limiter resistor, a vacuum chamber to house the electrode, a clamping resistor network, an ammeter and an ADC readout card. Additionally, a multimeter enables to characterize each component. In the following section I will describe each component starting with the auxiliary multimeter. Similar descriptions can be found in [192](p.13-14), [119](p.9-12), [96](p.7-11), [241](p.6-7), [151](p.11-12), [247](p.6-13), [162](p.16-17), [225](p.14-15). The setup during the neutron charge measurement can be found in the project thesis of Elisabeth Kreuzgruber [169](p.11-17).

Multimeter - Fluke 8846a

The *Fluke* corporation[57] manufactured our *Fluke 8846a* 6.5 digit precision multimeter. It is able to measure voltages (100 nV-1000 V, DC&AC), currents (100 pA-10 A, DC&AC), resistances (10 µΩ-1 GΩ), capacitance (1 pF-0.1 F) and diodes. The main usage is to measure the capacitance of the electrodes before and after the high voltage tests. This function evolved to an integral part of the alignment process (see section 3.3.6). Julius Piso [241] and Nicole Pruggmayer [247] additionally used it to characterize the electrode test setup after Piso programmed a remote LabView connection. Together with a power supply the current measurement mode of the multimeter enables to measure current-voltage characteristics of each single component (resistors, diodes,...). The following theses contain more information: [169](p.18), [96](p.13), [241], [151](p.18), [247](p.10), [162](p.24-25), [225](p.18).

[56] During the measurements, they were additionally turned off in order to protect them.
[57] Fluke Corporation, 6920 Seaway Boulevard, Everett, WA 98203, United States, www.fluke.com (12.11.2022)

High Voltage power supply - FuG

We have used a FuG[58] *HCP 35-35000* power supply since 2013 [122](p.8). It can provide up to 35 kV and 1 mA. The adjustment resolution of the voltage is denoted as 10^{-4} of the full range (± 3.5 V) as the current setting (0.1 µA) [169](p.12). The actual setting resolution is smaller (0.39 V) hinting at a 16-bit resolution. The even smaller resolution of the internal voltage measurement shows that the set voltage has a standard deviation of 0.022 V [241](p.17-18).
The voltage range is limited either via the LabView software or a hardware adjustment screw. During the neutron charge measurements in 2018 and the copper electrode testing in 2019 [241], the hardware limit was at 1790 V. Before and after, the limit was much higher in order not to interfere with the measurements.
The applied voltage increases instantly reach ($\leqslant$1 ms) the preset values but decreases in the voltage settings need multiple seconds to internally discharge [241](p.7). The power supply can also reverse polarity and is remotely controlled via Ethernet. For safety reasons an emergency stop button has to be installed in the grid connections.

Limiter resistor and cables

All cables in air were replaced in autumn 2018 with cables which are certified up to 40 kV.
A 20 GΩ resistor limits the current, especially after a discharge, and plays a major role in the time characteristic of the electrode charging. It consists of four 5 GΩ resistors within a protective glass tube (touching would reduce the resistance). The glass tube can also be filled with dry nitrogen in order to eliminate the effect of changing humidity on the resistance. Since 2019, the outside of the glass tubes has been covered in a network of grounded copper tape to prevent a build-up of surface charges [241](p.8-9). Nadine Pruggmayer measured the most accurate resistance value of 19.98(1) GΩ with the FuG power supply and the *Fluke 8846a* multimeter by extracting the resistance from the voltage-current diagram.

Vacuum chambers for electrodes

The electrodes are tested within a vacuum chamber first in order to have similar conditions to those during a normal measurement with UCNs and second because vacuum is a much better isolation than air. Within four different chambers we conducted tests (more details about the chambers are in subsection 3.4.1). The small test chamber in ATI housed nearly all tests with small electrodes (except Cu-Cu 2019 [241]). The Rams$\vec{E}$y electrode is too large for this chamber. For the neutron measurement it was within the big vacuum chamber of the RAMSEY^{TR}-setup. For the breakdown voltage test in Vienna afterwards, we used the *q*BOUNCINO twin chambers: the aluminum one in 2019 [96] and both (steel then aluminum) in 2020 [151]. The wiring within the chamber is done with copper wires with Kapton lacqeur kept with maximum distance to the surrounding chamber.

Clamping resistor network

This network consists of multiple diodes and resistors within a glass tube. An adhesive copper tape on the outer glass surface grounds it in order to minimize possible electrostatic charging. It has two major purposes:
First, it is a voltage divider with a 1 GΩ resistor serial to two parallel 100 MΩ resistors. One of them is the internal resistor of the ammeter. This leads to a divider ratio between the ammeter and the total voltage of 1:21 (a theoretical description can be found in [241](p.3-4)).
Secondly, the network is equipped with a safety feature for the ammeter [241](p.9-11). Its internal operation amplifier only tolerates ± 15 V. Therefore, the maximum voltage applied to the network should be below 300 V. Two strands of HV diodes parallel to the resistors provide this feature. Originally, the strand in forward direction was equipped with 20 HV diodes (probably more) and the reverse strand with only 6 standard Si diodes. Symmetric strands would have enabled a measurement in both directions, which was not necessary for the electrode tests done in Vienna [119, 192]. In the summer of 2018, I disassembled the working setup and sent it to Grenoble, where only the external wiring and the plastic end caps should be replaced. During these simple works, the network was severely damaged without any

[58] FuG Elektronik GmbH, Am Eschengrund 11, 83135 Schechen, Germany, www.FuG-elektronik.de (27.4.2021)

documentation of the status before. Only the reverse diode strand stayed attached to the measurement circuit and made a current flow through the network impossible. Some HV diodes were lost due to carelessness (now only 18 remained). Additionally, the new end caps were glued with epoxy raisin to the glass tubes to seal them. Luckily, Jakob Micko and I were able to open them with some force and restored some functions of the network for the neutron charge measurement. We reattached the resistor strand on both ends (directly to the ammeter) in order to have a current flow. The reverse strand was kept and connected to the return path of the ammeter (it should have been connected to the ground). The attachment of the HV diode strand and the second 100 MΩ were still missing during the measurements. In case of electrode breakdown, the discharge current could destroy the ammeter. A detailed plan of the connections during the neutron charge measurement can be found in the thesis of Elisabeth Kreuzgruber [169](p.15-17). In spring 2019, Julius Piso was able to restore the full functionality of the network with the help of constructor Andrzej Pelczar [241]. He renewed the missing glass tube grounding, reattached the left over HV diodes to a strand of the network, soldered in the missing resistor and restored the correct wiring to the ammeter and the ground (a BNC cable for each line). At this time the diodes had a limiting voltage of 285 V and −4 V in the forward and the reverse strand respectively, each at the maximum current of 1 mA. This corresponds to a maximal voltage of 12.95 V and −0.18 V at the ammeter input. In autumn 2020, Nicole Pruggmayer remeasured the properties of the isolated network parts and additionally added 8 HV *B074Y9DXDB Ecowsera* diodes[59] in the reverse strand (2 CLG, 20 kV, 20 mA) [247].

Ammeter

The ammeter is the center piece of the electrode test setup [169](p.13-14), [241](p.11-12). It measures charging, discharging and dark currents of the electrode. It is situated on a large copper plate which is the central grounding spot. All components (glass tubes, vacuum chamber, FuG HV-supply, power grid, ...) have a ground connection with it for safety reasons. The input signal comes as a BNC cable from the clamping resistor network (more precisely from between the two resistors within).
A special so-called *Andrew connector* connects the signal cable with the so-called *AIN* BNC socket for the signal input and the *Ret Ain* isolated Banana socket. The ammeter mirrors the normal signal from the *AIN* input to the return output *Ret Ain*. In this configuration, the shielding is not grounded instead it floats with the signal and the differential voltage between them is as low as possible. This strongly suppresses leakage currents between the core (signal) and the shielding of the BNC cable. A low pass filter within the *Andrew connector* reduces possible induced noise. In 2018, the connector was forgotten during the "improvement" in the workshop of the ILL. Luckily, we found it still lying there after one month which enabled measuring with a much lower noise. In 2020, the ATI electronic workshop built an encased version of the connector to have more stable connections.
The ammeter needs an external power supply of 18 V DC and around 0.18 A which is connected via the left multipole connector (4 pols). The right multipol connector (5 pol) transports the raw signal (*AOU*) and an offset signal (*Offset*). On the front panel there is a knob in order to adjust the offset (to zero).
There is also a banana socket on the front panel for the ground. At the moment it is internally connected to the casing and therefore to the common ground. During the construction of the ammeter, it was intended to isolate the internal ground from the common ground and to be able to choose a voltage offset between both grounds via this connector.
In principle, the ammeter measures voltages and needs a calibration in order to calculate the current through the setup. Only for low voltages on the clamping resistor network the current measurements can be linearly determined. At higher voltages the safety diodes introduce a nonlinear behavior of the setup. Julius Piso measured this transfer function factor via voltage measurements to 20.70(98) nA V^{-1}. He was limited by the uncertainties of the resistance values and the diode characteristics, the comparably low resistance of the voltage probes and their influence on the measurements. Therefore, he was not able to fully reconstruct the nonlinear characteristic of the setup [241](p.20-28).
In 2020, Nicole Pruggmayer characterized each component of the setup separately [247]. She used the FuG or a newly bought *Hameg 4040* power supply (see section 3.9.5) and the *Fluke 8846A* multimeter to measure fully automatized the current-voltage characteristic in a wide range with multiple gauges. This was very helpful, especially for the understanding of the low current regime of the diode behavior.

[59] Tesla Ham Electronics

DAQ

The multi-strand output signal cable is split after a certain length into two BNC-cables. They are connected to a NI *BNC 2090A* at channel *AI0* and *AI1*. Additionally, a 50 Ω terminator is on one socket. Via a special National Instruments cable the signals are guided to a *PCI 6259* card. A 16-Bit ADC within digitizes all signals. Commonly not only the two signals of the ammeter are recorded but also the terminated channel and one open channel. The terminated channel measures the accuracy of the ADC of around 0.3(4) mV and the open port the possible pick up noise [241](p.12).

3.3.6. Electrode alignment

A simple approach to align the electrodes parallel, is to use spacers. Glass or plastic are possible spacer materials. Plastic spacers are available in multiple thickness but can change their thickness due to polarization within high electric fields or pressure. Glass spacers are quite stable. Due to usage in microscopy, certain thicknesses are available in high quality and large quantities (e.g. 170(5) µm). With a Mitutoyo *MDC-25PJ* micrometer screw gauge two or four spacers can be selected with identical thickness, accuracy and resolution of ±1 µm. The spacers can also stay within the electrode gap during the test. This will change the capacitance. At the edges of the spacers sparks often occur and therefore it is better to remove them [119](p.44).
Removing the spacers and keeping the alignment needs a special bearing system with fine thread screws. Three linear gauges (see section 3.7.1) on the corners of the upper electrodes measure the alignment during movement. Combinations of two different gauge values are translated into the height and the tilt measurements [169](p.19). Additionally, the *Fluke 8846A* multimeter measures the capacitance. Until 2019, we did this manually by writing down only important capacitance measurements [96, 169, 241]. In 2020, Julius Piso implemented to remotely operate the multimeter [151](p.18). This increased the resolution by a factor of 10 and the values are measured continuously parallel to the linear gauges. This reduced the number of students needed to only one and enabled also a live analysis within LabView[60]. The number of data points increased significantly and were easier to handle because they were already in a suitable digital format [151](p.18-20). A further improvement was the replacement of the fine thread screws with PI-*N-470.12V* piezoelectric stages[61] [162](p.18-22), [225](p.18-34) in 2021. This setup enabled to completely automatize the alignment process and increased the number of data points to a level where the fourth order effects were measurable and the precision of the measurement could be extracted from the data points.
By measuring height (distance d) and tilt (pitch α and roll β) variations separately, it is also possible to fit the alignment and the electrode distance without measuring an absolute height from spacers. Elisabeth Kreuzgruber describes the methods with the following underlying formula [169](p.5-7) which was extended to the forth order by Klieber [162](p.9-10) and Neubacher [225](p.11):

$$C = \frac{\epsilon_0 A}{d}\left[1 + \frac{{a_E}^2\alpha^2}{12d^2} + \frac{{a_E}^4\alpha^4}{80d^4} + \frac{{b_E}^2\beta^2}{12d^2} + \frac{{b_E}^4\beta^4}{80d^4} + \frac{{a_E}^2\alpha^2{b_E}^2\beta^2}{24d^4} + \mathcal{O}(\alpha^6) + \mathcal{O}(\beta^6)\right] \tag{3.30}$$

The fit routine calculates the offset between the relative linear gauge measurement and the absolute capacitance values. With only a few measurement points before the charge measurement (2018), it was not possible to extract any parasitic capacities. Anika Gassner and Julius Piso conducted further measurements in Vienna afterwards and succeeded also in measuring a parallel parasitic capacity [96]. An absolute measurement with spacers and linear gauges agrees at the µm level with the technique using relative linear gauge measurements and the recorded capacitance[62]. With the automatized measurement readout, Jasmin Juroszek was able to include also data points which vary in multiple parameters [151](p.7). Therefore, she extended the *Mathematica* tools from Elisabeth Kreuzgruber [169] and Anika Gassner [96] to

[60] Before this one student had to turn the fine threaded screws to change the alignment to a different setting. The second student had to operate the LabView program by manually taking measurements at each setting and writing all preliminary values in an excel spreadsheet for a fast analysis for further alignment steps.

[61] These piezoelectric actuators use a stick-slip motion to move around 20 nm per step. Each motor can lift up to 22 N and interlock itself with a force up to 100 N during resting or power loss. The total traveling range is 7 mm. An additional feedback system (linear gauges - section 3.7.1, capacitive sensors - section 3.5.3, SIOS laser interferometers - section 3.6.2, ...) measures the exact motion of the motors. The similar PI-*N-472* actuators have a build-in measurement system to determine their position. They are ideal candidates for the absorber plates alignment too (3.1.5).

[62] Anika Gassner used a parallel translation for the height measurement and the determination of the parasitic capacitance. She used the roll and pitch variations only for the measurement of the parallel alignment.

include various variable fitting routines[63]. With the full automation Paul Klieber [162](p.10-12) and Luca Neubacher [225](p.35-59) showed that a joined analysis of the tilt angles or all degrees of freedom together can similarly describe the alignment but reduces the number of needed fit routines. Ideally only one fit routine can determine the offset of the distance d, both tilt angles (α & β), the parasitic capacitance, the measurement error and one electrode length (a_E or b_E) which needs a dataset with large variation in each spatial degree of freedom.
Figure 3.12 displays the improvements made of the alignment processes and its usability. On the one hand, the number of data points increased with each development step by a factor of 10 and on the other hand the operation of the process simplified from needing multiple students to fully automatized. This was only possible due to the efforts and cooperation between the involved students: Elisabeth Kreuzgruber [169], Anika Gassner [96], Julius Piso [241], Jasmin Juroszek [151], Nicole Prugmayer [247], Paul Klieber [162] and Luca Neubacher [225].

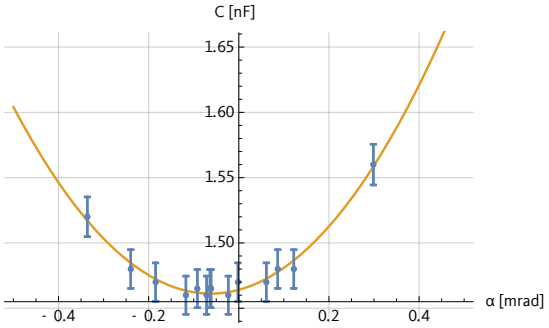

(a) 2018: First alignment of the Rams$\vec{E}$y electrode during the charge measurement at the ILL at a height of 228.2(58) µm [169](p.22, fig.4.1)

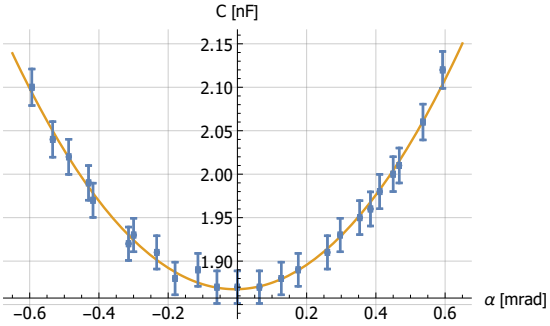

(b) 2019: Rams$\vec{E}$y electrode tests in Vienna with more data points at a height of 170(1) µm [96](p.39, fig.B.2)

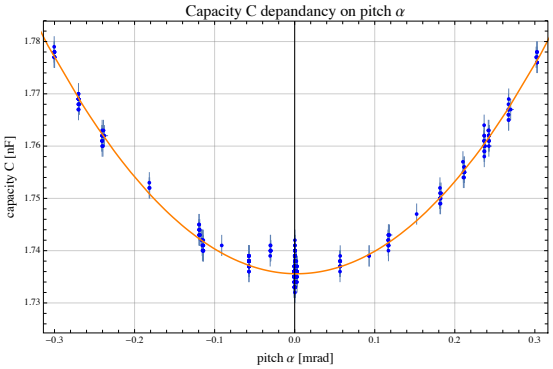

(c) 2020-2021: final Rams$\vec{E}$y electrode tests in Vienna with a fully automatized data acquisition at a height of 186(4) µm [151](p.22, fig.4.1)

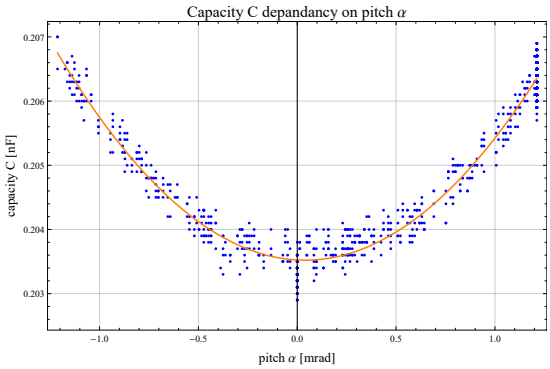

(d) 2021-2022: small mirror electrodes tests with a fully automatized alignment at a height of 107(1) µm [162](p.37, fig.4.1.a)

Figure 3.12.: Electrode alignment: Improvements of the process over the years [96, 151, 162, 169, 225, 241, 247]

3.3.7. Charging curve of the electrodes

Calculations of the charging behavior can be found in [192](p.9-12). The applied voltage models are either steps or trapezes [119](p.36-37), [96](p.25). The measured current can be used to determine the capacitance. Calculations can be found in the project thesis of Jakob Micko [192](p.15-12) and more detailed by Elisabeth Kreuzgruber in her thesis [169](p.8-10). Julius Piso also further expanded this formulation with a *dark resistor*. This effective resistor is parallel to the capacitance of the electrode and enables a constant so-called *dark current* proportional to the applied voltage running through the electrode. A low dark resistance lowers the effective potential applied to the electrode as it divides the voltage with the other resistors (limiter resistor and clamping resistor network) [241](p.28-29).

[63] With this notebook it is possible to extract the height also with parabola fits to angle variation or its minimum.

3.4. Vacuum system

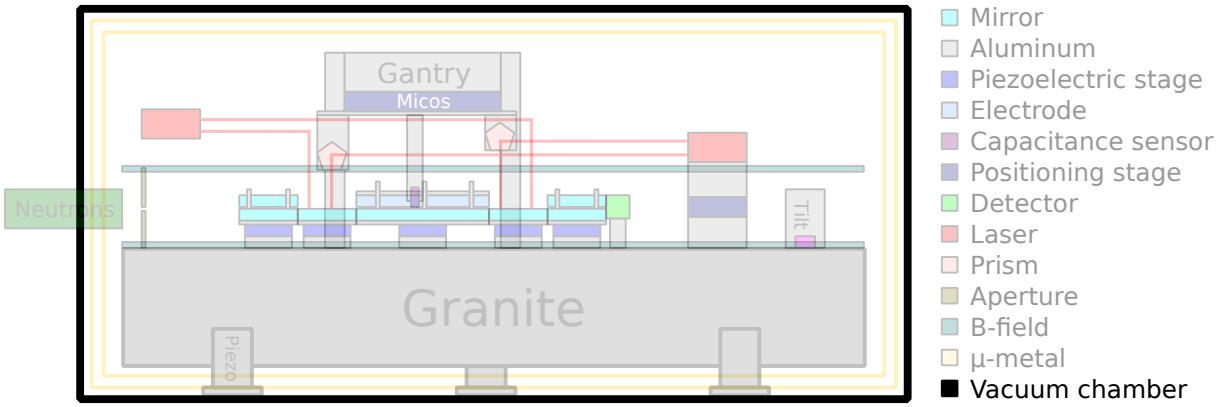

Figure 3.13.: A schematic view of the vacuum chamber within the RAMSEY^{TR}-setup

Physics with UCNs always needs a vacuum environment to reduce the absorption losses in air (mainly nitrogen, humidity and argon). For beam experiments also scattering losses are important (mainly nitrogen, oxygen and hydrogen). Air has a total microscopic cross section $\sigma_{air} = 2648\,\text{b}$ for neutrons with a velocity of 8 m/s and a humidity of 50 % at 300 K [64]. The velocity-dependent total cross section and the pressure within the vacuum chamber determine the transmission of the UCN through the approximately 1.5 m long path from the entrance window to the detector, as figure 3.14 displays.

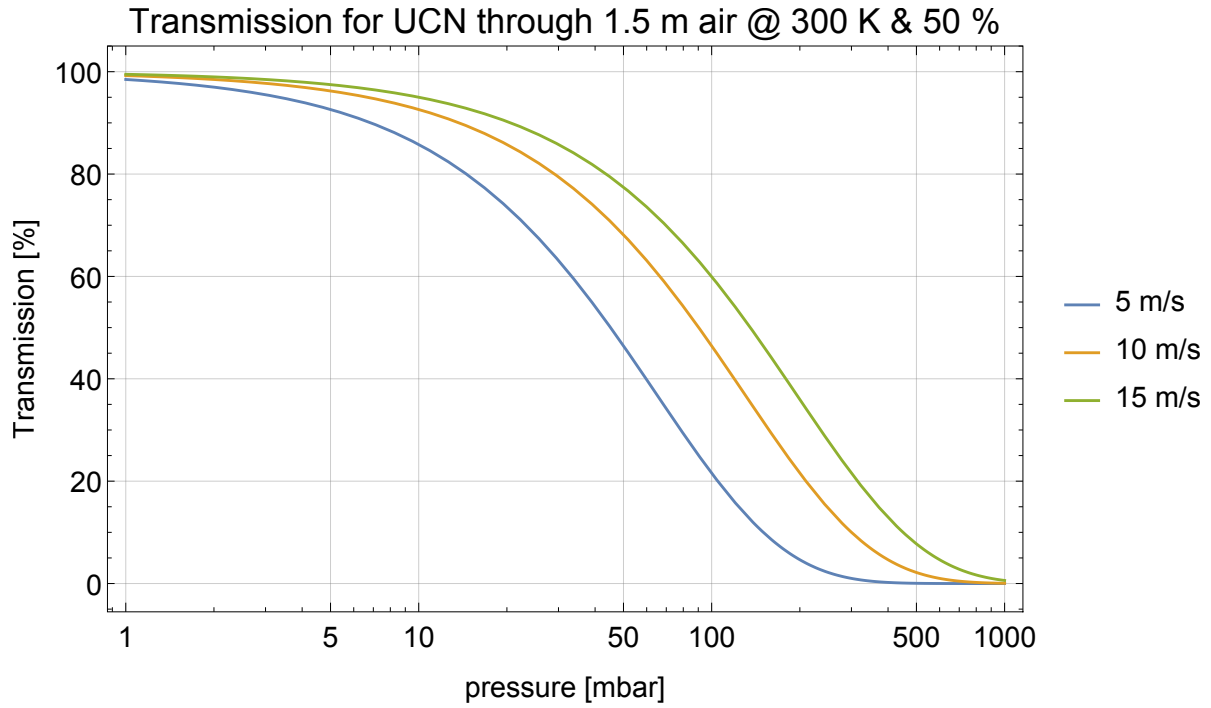

Figure 3.14.: Transmission of UCNs through the setup depending on the vacuum pressure at a 50 % relative humidity.

The air pressure must be below 5 mbar to have a transmission above 90 %. In other words, the mean free path of the neutrons has to be much longer than the experiment. Similar calculation can be found

[64] This number is calculated by extrapolating the velocity-dependent total cross section of air. For cold neutrons or slower ones the cross sections have an ideal $\frac{1}{v}$ dependence. Take care, this is normally not the case for thermal neutrons. The standard air composition of 78.08 % N_2 (N-14), 20.95 % O_2 (O-16) and 0.93 % Ar-40 was used. Humidity and its temperature dependence was additionally integrated. The cross section data is part of the library *ENDF/B-VII.1* (www.nndc.bnl.gov/sigma/index.jsp). It covers values for neutrons with energies from 10 µeV up to 100 MeV.

in [150](p.8-9), [42](p.17 & 46), [44](p.42).
In June 2019, Carina Killian, Jakob Micko and I measured the pressure-dependent absorption during evacuation and venting of the vacuum chamber. The evaluation can be found in Killian's master thesis [160]. Her finding suggests that around 1 mbar the losses are negligible, as predicted. For a more precise value the analysis has to be redone with a focus on the low pressure regime. For searches of hypothetical particles and forces, the vacuum should be as low as possible [49, 170]. Similarly, applying high electric fields needs a very high vacuum as it is the best insulator [173].

The vacuum within the *q*BOUNCE experiment is divided into two parts (beam tube and chamber) which are separated only by a thin aluminum foil on the end of the beam guides. This section will focus on the main vacuum chamber and all necessary parts to provide a low vacuum pressure. Section 3.1.2 contains more information about the beam tube geometry.
Furthermore, the vacuum system has to be cleaned as well as possible to reduce the oil contamination to a minimum. Similarly, non vacuum compatible materials (e.g. plastic, greased motors) are avoided. These can evaporate during the evacuation and condensate on the mirror surface, which leads to a slow count rate loss, as happened in 2012 [65](p.45-46), 2017 [254](p.112-115) and 2019 [194](p.84).

3.4.1. Vacuum chambers

The vacuum chamber contains all important systems of the setup (e.g. aperture, regions, detector, leveling systems). Since the beginning of *q*BOUNCE, the setup has grown by increased components and complexity and therefore demanded a bigger chamber. The RAMSEY^{TR}-setup already uses the third chamber generation.
Studying the pump down processes of each chamber enables us to calculate the minimum pressure and to compare them. Jasmin Juroszek first implemented such an analysis for the three chambers at the electrode test setup [151](p.8-10).

The first generation could only house a quantum bouncing ball setup or a single region GRS. David Stadler and Tobias Jenke used it between 2008 and 2010 for their measurements (GRS^{TJ}-setup). The size of the chamber was smaller than the granite block which acted as the floor (600 mm × 1000 mm).

Gunther Cronenberg designed the second generation of vacuum chambers for his RABI^{GC}-setup [65](p.40-41). These chambers have the same ground area as the granite surface in order to house three complete regions. They are two nearly identical vacuum chambers. The first was made out of stainless steel (1.4571) in 2010 by Hortischoner Werkzeugbau[65]. Unfortunately, this is magnetic and therefore the nearly identical second chamber was made out of aluminum (AlCu4MgSi(A) (2017A) T451). The only difference between the chambers except for the material is their wall thickness. It was increased from 25 mm to 40 mm. Both chambers are not welded together, instead they are glued with *Aradite AW116*. The inner dimensions are 905 mm × 530 mm × 480 mm. The weight of the aluminum chamber is 385 kg [96](p.9). Both chambers have an entrance flange with a neutron window on one face (a small long slit). Almost all other standard flanges for the feedthroughs are on the opposite face. Thomas Bittner constructed an aperture housing with a large circular neutron window. This vacuum chamber extension adjustably connects a 70 mm beam tube with the chamber [42]. The aluminum chamber was the main *q*BOUNCE chamber between 2010 and 2014 including the RABI^{GC}-setup in 2012 [150] and the qBB^{MT}-setup of Martin Thalhammer in 2014 [299]. In 2018, this chamber became the main part of the new *q*BOUNCINO setup (See more in section 3.10 and [236]). The chamber fits perfectly at the PF2/TEST beam or the PF2/EDM site and was also used to measure the Rams$\vec{E}$y electrode in Vienna 2019 [96] and 2020. The steel chamber remained in the storage until 2020. Then Jasmin Juroszek and Nicole Pruggmayer refurbished it (new gaskets and flanges, extensive cleaning,...) [151](p.13-15). Still, it had a strong leakage and only reached $2.3(1) \times 10^{-4}$ mbar [151](p.15) compared to the aluminum one with a limit of 5.1×10^{-6} mbar after 120 h in 2012 [157](p.21) and a leakage rate of $1.6(5) \times 10^{-4}$ mbar L s^{-1} [42](p.36-37). Fully equipped within the RABI^{GC}-setup it reached only a pressure of 1×10^{-4} mbar [65](p.41) and with a *ATP 100* turbo pump 1.47×10^{-4} mbar in 2018 after nine days [236](p.31-32). Nearly empty and using a Pfeiffer *TMU 521* turbo pump much lower pressures were achieved again with final 2.4×10^{-5} mbar at the electrode test setup in 2019 [96](p.16-18) and $1.6(1) \times 10^{-5}$ mbar with an additional roughing pump in 2020 [151](p.15).

The RAMSEY^{TR}-setup has the biggest and newest chamber. Tobias Rechberger and Horvath Miklos

[65] Hortischoner Werkzeugbau GmbH, Industriestraße 1, 7312 Hortischon, Austria

designed it and Pfeiffer Vacuum[66] built it in 2015 [254](p.66-70). Heinz-Georg Stangel gave a detailed description of the new chamber and characterized its behavior [288]. Contrary to the previous generations, it contains two layers of the µ-metal shielding and a complete large granite block (700 mm × 1900 mm) with its leveling system below (before the shielding surrounded the chamber and the granite was the floor of the chamber). This reduces the requirements on the material (especially its magnetism) and therefore around one tonne of V2A(1.4301) steel was used. The chamber uses all possible space of the PF2/UCN-platform, which makes it difficult to access it from all sides (The PF2/EDM side can only be reached via the boulder route *la dura dura*). Large flanges on the reactor-sided face are used by the vacuum pumps and the one in the middle has a trunk-like extension to bear the beam tube (ISO-K 200 with a vibration-isolation). The face on the detector side hosts most flanges for all the feedthroughs of the installed devices within the chamber and also the venting valve[67].
On each side face there are two additional flanges. During the charge measurement, the high voltage cables to power the Rams$\vec{E}$y electrode used the flanges on the PF2/MAMBO side for their feedthroughs. Three adjustable bearings carry the approximately 2500 kg setup (chamber, granite, shielding, "experimental stuff",...) [254](p.70-71). Three piezo stages within the chamber automatically fine adjust the surface further[68] (their performance is displayed in section 4.2.2). Due to earthquake safety, the bearings are additionally fixed to the base plate of the platform (as seen in [254](p.64, fig 7.3)).
The top cover has a weight of approximately 600 kg (including the loosely fixed µ-metal shielding) and has to be lifted by either the hall crane or a bully hanging on the hall crane. Another small crane was built to open the chamber similar to the one which was used for the older chambers (e.g. *q*BOUNCINO). Due to earthquake safety restrictions, this crane was never commissioned. During 2016 and 2018, it was only used to securely park the top cover on it to be able to work underneath, even though it was still hanging on the huge hall crane. Thomas Brenner, the PF2 technician, or an available reactor technician had to lift the top cover. In 2019, the crane was disassembled and stored because Jakob Micko was allowed to use the hall crane. In order to close the top cover more easily, two metal rods (*Hot Dog warmers*) with different heights help to align the cover during lowering. This is very important because the two layers of µ-metal fit very tight in each other. In 2017, Thomas Brenner replaced the smaller ones with longer versions to make this process even easier. It is very important to see if the top cover is not blocked somewhere during the lowering process[69].
Initially the empty chamber reached a vacuum of 2.9×10^{-6} mbar after 18 hours [288]. During the fully equipped measurement runs (RAMSEY-GRS-18), a minimal pressure of 2.9×10^{-5} mbar was reached (see evaluation in section 4.2.1).

Additionally, the electrode test setup has its own small vacuum chamber. It consists of a CF-160 pipe with two side ports. A turbo pump closes the back of the pipe and a CF-160 flange with a small window the front. The two side ports have each an additional T or X pipe attached. The outermost flanges are used for the high voltage feedthroughs. Due to the small volume and the CF flanges, the minimal pressure can reach comparable low values: $2.3(1) \times 10^{-7}$ mbar in 2020 [151](p.26).

3.4.2. Vacuum circuits

RAMSEY^{TR}-setup: This setup is the most advanced vacuum setup within *q*BOUNCE [288](p.5-6,11), [254](p.68-70). All valves are automatized in order to evacuate the chamber without human interaction. Beside a normal bypass of the turbo pump a second bypass exists which allows a slow evacuation through an adjustable needle valve. To decrease the evacuation time of the large chamber volume, the turbo pump is directly connected via DN 160 CF Series *110 HV* gate valve from VAT Vakuumventile AG[70] to the vacuum chamber. The main pipe from the chamber via the bypass to the roughing pump has a dimension of ISO-K 63 to reach prevacuum conditions faster [104].

[66] Pfeiffer Vacuum Technology AG, Berliner Strasse 43, 35614 Asslar, Germany, www.pfeiffer-vacuum.com(12.7.2021)
[67] It is important to open or close the two venting valves at the end of the chamber in order to vent or to evacuate it. During venting, always open slowly the small metal valve first and then the large black one. Never overturn them because this will break them.
[68] This coarse alignment brings the piezos in range. This has to be done when the chamber is evacuated. During the evacuation process, the granite surface moves in average 200 µrad which is more than the range.
[69] It could happen that this blockade gets loose suddenly and one guiding rod sticks between the magnetic shielding. If a panic stricken student lifts it up too fast, the top cover will rotate until it hits the opposite guiding rod. The resulting shock wave knocks out the turbo pump attached to the chamber. Consequently, the emergency breaks of the pump will stop its rotation with a siren-like sound.
[70] VAT Vakuumventile AG, "Product Datasheet, 11044-CE24", www.vatvalve.com/products/product?id=11044-CE24 (8.2.2021).

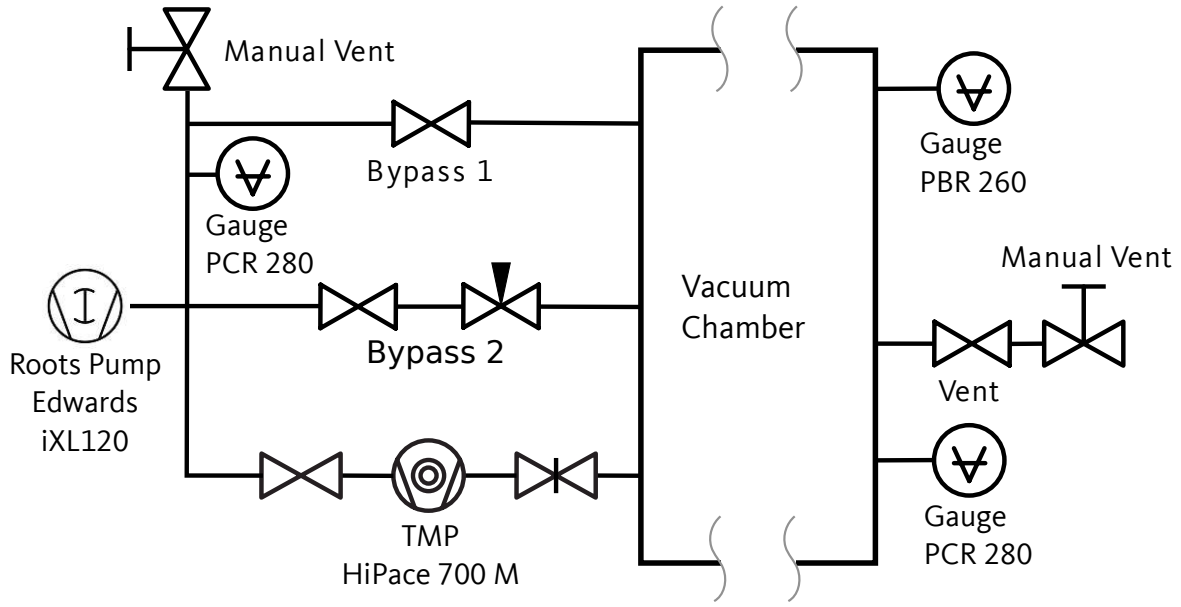

Figure 3.15.: Vacuum circuit of the RAMSEY^{TR}-setup [254](p.69)

Beam tube: The vacuum circuit is very simple. All valves are manual ones. Only for works at the beam line it will be vented, otherwise the beam tube will stay at vacuum conditions all the time during the reactor cycle. Between cycles, it has to be vented only if the PF2 turbine has to be vented for maintenance.

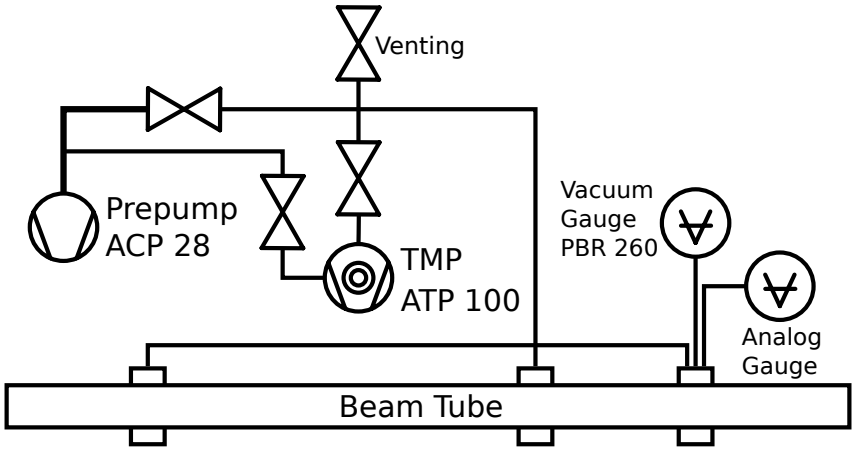

Figure 3.16.: Vacuum circuit of the beam tube at the PF2/UCN platform during the experiments with the RAMSEY^{TR}-setup

***q*BOUNCINO:** This setup at the PF2/TEST beam has two separated vacua similar to the main experiment. Each is a complete three valve circuit. It has only manual valves which are used regularly during testing. This takes a lot of responsibility for the operators. Full automation with a *vacuum box* and pneumatic valves would be an improvement if the setup is used more regularly.

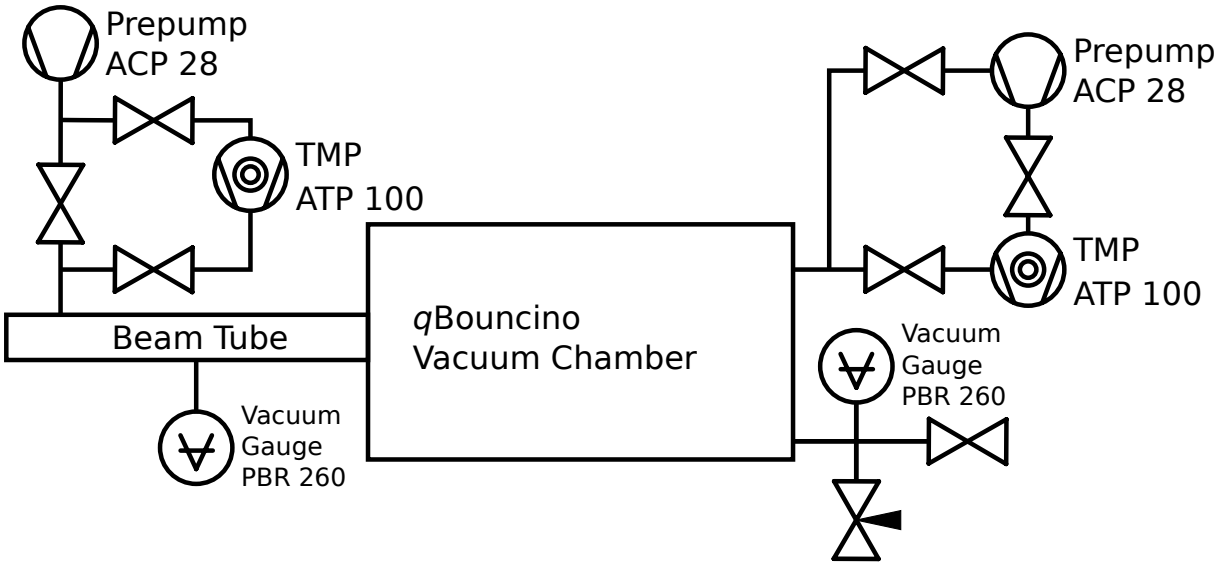

Figure 3.17.: Vacuum circuit of the *q*BOUNCINO [236](p.20)

Electrode test setup: This setup is quite simple with a vacuum pump, a pressure gauge within the prevacuum circuit, a manual valve to separate it from the high vacuum, a turbo pump which has a venting valve and is directly connected to a small vacuum chamber. This high vacuum chamber is basically a CF-160 pipe with two side ports. On the left side a CF-40 T pipe connects it to a high vacuum pressure sensor and the feedthrough of the lower electrode. The right side has multiple ports. One hosts the high voltage feedthrough for the upper electrode. The chamber has only CF flanges, which makes it suitable to host pressures down to 10^{-8} mbar. Their size only allows to place small electrodes into the chamber. A CF-KF adapter and a long KF-40 corrugated hose connects the small chamber to the *q*BOUNCINO chamber if a larger chamber is needed (e.g. for testing the Rams$\vec{E}$y electrode). The following theses provide more information: [122](p.7), [119](p.8), [200](p.7-8), [96](p.7-10), [151](p.12-13). A specialty of the electrode test setup is the possibility to integrate a precision valve with stepper motor *ZSS 42-200-1/2 GPL 42.2* [200](p.8-9). With this valve gases with very low partial pressure can be filled into the chamber. These gases (helium, argon, nitrogen,..) can be used for gas conditioning of the electrode.

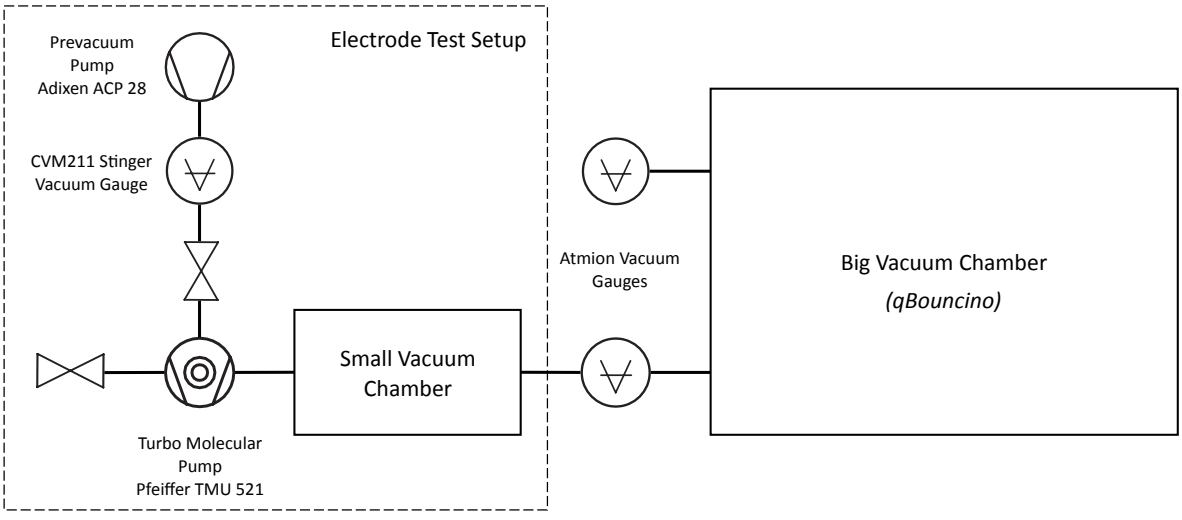

Figure 3.18.: Vacuum circuit of the electrode test setup [96](p.8)

3.4.3. Vacuum pumps

Three different types of turbo molecular pumps and four different roughing pumps are used for the different setups. A mayor requirement of all pumps is that they are oil free in order not to contaminate the vacuum chamber, which could lead to a slow decrease in the neutron count rate due to absorption on the mirrors.

The RAMSEY^{TR}-setup uses a *HiPac 700 M* turbo pump from Pfeiffer Vacuum. Its pumping rate is 685 L/s (N_2). The normal rotation speed is 820 Hz[71]. The operation current varies between around 0.34 A at standby, 0.5 A at normal operations and up to 7.5 A at the start of pumping. The pump should only start up below 8 mbar. Then it takes approximately 5 minutes to reach the maximum rotational speed [104](p.7).
An Edwards[72] *iXL120* is an oil-free roughing pump of the setup (pumping rate 110 m^3/h or 30.5 L/s). It was built in 2013 and first used in the qBB^{MT}-setup in 2014 [115](p.47). It needs water for cooling[73]. A valve on top of the pump enables to seal the prevacuum circuit from a turned off and vented prepump.

Beam tubes at PF2 and *q*BOUNCINO use the available Alcatel[74] *ATP 100* turbo pumps and Adixen *ACP 28* roughing pumps from PF2 [236](p.19-21), [150](p.10). This turbo pump reaches 27084 rpm (451 Hz), currents up to 1.31 A and a pumping rate of 100 L/s (N_2). The Adixen roughing pump has a pumping rate of 28 m^3/h (7.8 L/s).

The electrode test setup in Vienna consists of a Pfeiffer *TMU 521* turbo pump (*TC 600* motor controller, *DCU 300* process controller, 521 L/s, 833 Hz, a similar one was used in the RABI^{GC}-setup [157]) and a fixed Adixen *ACP 28* roughing pump. Additionally, an Edwards *XDS35i* pump can accelerate the evacuation process (pumping rate 40 m^3/h) [151](p.12). See more in the theses of Anika Gassner [96] (p.7-8) and Florian Honz [119].

3.4.4. Vacuum sensors

In Grenoble, there are two kinds of pressure sensors from Pfeiffer. *PCR 280*[75] for pressures between 5×10^{-5} mbar up to normal air pressure (1.5 bar) and *PBR 260*[76] for low pressures down to 5×10^{-10} mbar. Only the *PCR 280* sensors can also measure the air pressure similar to a barometer and are mainly used within the prevacuum circuits. The *PBR 280* sensors are already out of range above 200 mbar [288](p.7). Therefore, they are used only within the high vacuum (e.g. vacuum chamber and beam tube). Up to three *TPG 362 DualGauges* connect up to six sensors with the PCs (four for the RAMSEY^{TR}-setup and two for *q*BOUNCINO). A direct comparison between both sensors can be found in [274](p.25-27). Within the RAMSEY^{TR}-setup two *PCR 280* sensors (prevacuum circuit, main vacuum chamber PF2/MAMBO) and two *PBR 260* (beam tube, main vacuum chamber PF2/EDM) gauges are built in.

In Vienna, we use two Vacom[77] *Atmion* sensors to measure the pressure inside the chambers from 1 bar down to 1×10^{-10} mbar [122](p.8) and a *CVM 211 Stinger* pressure gauge from InstruTech[78] for the prevacuum circuit (from 1333 mbar down to 1.3×10^{-4} mbar) [119](p.8), [200](p.7), [151](p.12-13). A *MVC-3* controller connects the prevacuum sensor and one *Atmion* to the PC.

At some critical positions like the beam tube, we also use analog pressure gauges in order to see the pressure gradient directly. A too high gradient would lead to high mechanical stress which could implode the glass tubes and severely harm the operator of the valve.

[71] Pfeiffer Vacuum GmbH, *HiPace 700 M* with *TM 700*, static.pfeiffer-vacuum.com/productPdfs/PMP04982.en.pdf (8.2.2021).
[72] Edwards Vacuum Inc, 15 Marshall Road, Eastbourne BN22 9BA, United Kingdom
[73] Check this always before the beam times because during shut downs the cooling water supply is normally turned off.
[74] Alcatel Adixen Vacuum Products or Pfeiffer Vacuum SAS, since 2011 part of Pfeiffer Vacuum GmbH, 98 avenue de Brogny, 74009 Annecy, France
[75] Pfeiffer Vacuum GmbH, *PCR 280*, www.pfeiffervacuum.com/productPdfs/PTR26856.en.pdf (8.2.2021).
[76] Pfeiffer Vacuum GmbH, *PBR 260*, Pirani/Bayard-Alpert", www.pfeiffer-vacuum.com/productPdfs/PTR27002.en.pdf (8.2.2021).
[77] VACOM Vakuum Komponenten & Messtechnik GmbH, In den Brückenäckern 3, 07751 Großlöbichau, Germany
[78] InstruTech, 1475 S. Fordham Street, Longmont, CO 80503, United States

3.4.5. Vacuum box

The simplest vacuum setup connects the prepump, the turbo pump and the vacuum chamber together in this order. To evacuate the chamber first the prepump has to start up and when a pressure of around 1 mbar is reached, the turbo pump can be started up too. At higher pressures the turbo pump cannot reach full speed and due to vibration it can be damaged severely.
To speed up this process a valve between the pumps enables a continuous operation of the roughing pump (which they are made for) even when the chamber is open. During the evacuation, slow opening of the valve conserves the pumps. This kind of setup is realized at the electron test setup in Vienna (see figure 3.18).
To be able to run also the turbo continuously (starting up and ramping it down could take hours) two additional valves are needed. One before and one after the turbo pump and the third in an additional direct connection between the prepump and the chamber also called *Bypass*. At the start of the evacuation the valves around the turbo pump are closed and the bypass opened to directly evacuate the chamber with the roughing pump. At low pressures the bypass is closed and the others are opened (starting from behind the turbo) to lower the pressure at a faster pace. During the venting, all valves attached to the chamber are closed and only the valve between the pumps stays open. An additional venting valve could be opened to vent the chamber faster. An additional advantage is that the pipe diameter can be increased to evacuate the air faster and there is also less friction due to the turbo pump rotor within the airflow. This scheme was used for the *q*BOUNCINO-setup (see figure 3.17), the beam tube (see figure 3.16) and earlier *q*BOUNCE-setups [157](p.9). Furthermore, using a bypass with a small gas dosage valve called *bypass*[2] can slow down the evacuation speed and therefore reduce the mechanical stress gradient, which is necessary for sensitive experiments [104](p.5) (realized within the RAMSEY^{TR}-setup as seen in figure 3.15).
In order to reduce human errors by opening and closing valves in the wrong order and also account for vacuum breaks and failures of the sensor, pneumatic valves could be used together with an automatized vacuum electronic box. Jörg Herzinger built the first prototype of an automation together with the electronic workshop (ATI) and implemented it in 2014 in the qBB^{MT}-setup [115](p.14-16,47-50). He proved that this accelerated the evacuation process.
Alexander Gruber implemented a similar box for the newly built RAMSEY^{TR}-setup in 2015 [254](p.68-69). His bachelor's thesis gives a good overview of it [104]. This box controls the turbo pump and all five pneumatic valves from VAT vacuum valves. It also receives the data of the vacuum sensors. It contains a valve battery from Festo[79] to convert the electric signals into compressed air levels and a programmable logic controller (PLC) which is a *Siemens LOGO!24RCE*[80] with the two expension modules *DM 24R*. Everything is packed into a box which is mounted within the rack. Controlled by buttons, the box can bring the setup into a standby mode (turn on the turbo pump at a low vacuum pressure), evacuate or vent the chamber by operating the valves (with supplied compressed air 4 bar to 8 bar). Even failures of the pressure sensors or vacuum breaks are accounted for by encapsulating the turbo pump and shutting it down, if necessary. During normal operation, the evacuation process starts by pressing the button *high vacuum*. For around 5 min the bypass is opened until the pressure reaches 0.5 mbar. At this moment, the evacuation is automatically switched to the turbo pump, which results in a pressure rise of up to 2.5 mbar in the prevacuum circuit and a drastic decrease within the vacuum chamber itself. If there are problems with the roughing pump or the valve on top of it, the pressure rises above 3 mbar and the box switches back to the bypass. Some oscillations between these modes can occur until it stays at the turbo pump.
Typical pumping curves can be found in figure 3.19 and in [274](p.21-24). The turbo pump usually starts after 620 s and a pressure of 3×10^{-3} mbar is reached after 1400 s depending on the duration of air exposure of the chamber before.

[79] Festo SE & Co. KG, Ruiter Straße 82, 73734 Esslingen, Germany, www.festo.com (20.7.2021)
[80] Siemens AG, Werner-von-Siemens-Straße 1, 80333 München, Germany, https://new.siemens.com/de/de/produkte/automatisierung/systeme/industrie/sps/logo.html (20.7.2021)

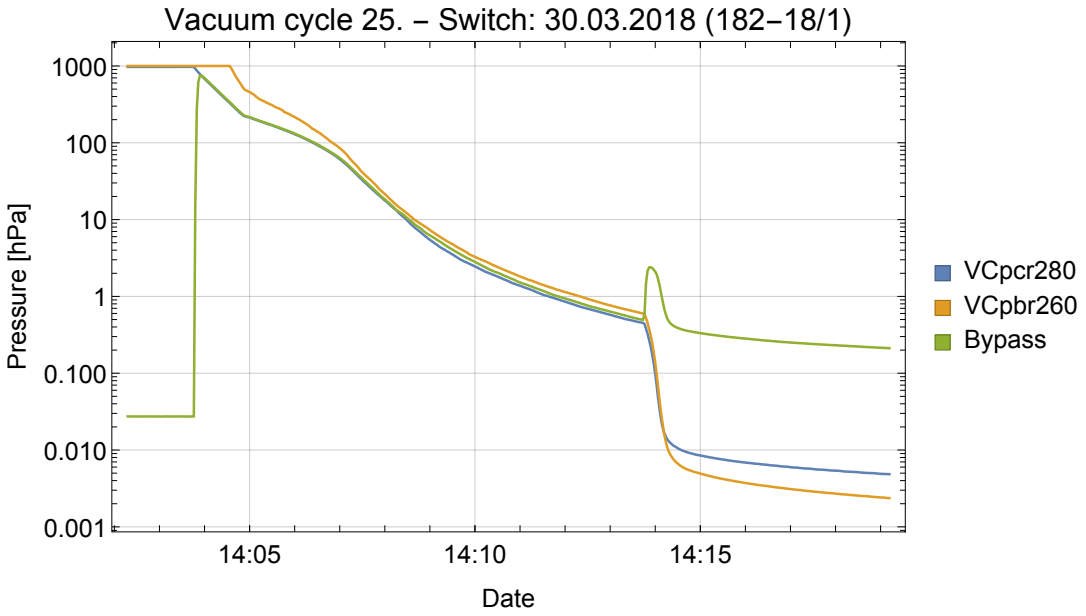

Figure 3.19.: A typical evacuation curve: at the beginning, the pressure in the prevacuum circuit (bypass, green) rises to the same pressure as within the main chamber (blue) and together they decrease during the evacuation process. The Pfeiffer sensor *PBR260* (orange) only starts to react to the pressure drop when the other sensors are below 300 mbar due to its inaccuracy at high pressures. Below 0.5 mbar the bypass valve closes and the turbo pump starts to evacuate the main chamber. There, the pressure drops drastically. In the prevacuum cycle the pressure rises quickly until the prevacuum pump slowly removes the rest gases. At low pressures the sensor *PBR260* more accurately measures the vacuum pressure.

3.5. Alignment

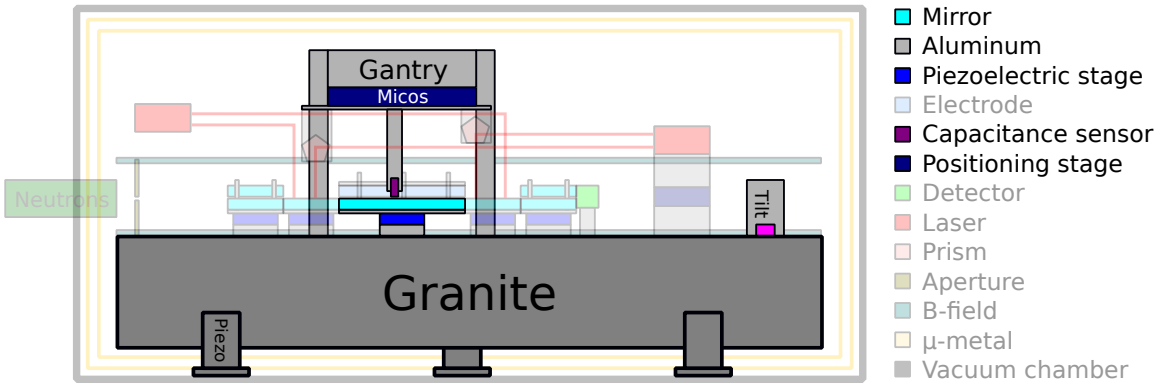

Figure 3.20.: A schematic view of the components within the RAMSEY^{TR}-setup which are needed for the alignment.

The horizontal alignment of the granite surface, which is the absolute reference for the mirror surfaces, and the stepless alignment between the mirrors are crucial sources of systematic errors. Unwanted steps can induce state transitions which mainly reduce the total count rate [150](p.16-25), [267](p.51-53). A more theoretical discussion can be found in [310](p.55-65) including measurements of the step height uncertainty. The horizontal alignment is important, otherwise the direction of the Earth's gravity acting on the states is changed ($g' = g\cos\alpha \approx g\left(1+\alpha^2/2\right)$) and therefore the transition frequencies [65](p.28-30), [254](p.98-101), [194](p.67-68)[81]. The small gaps between the mirrors (40 µm) can be neglected because the neutron's fall time is to short for a measurable height change.

[81] In order to see a change in the order of $\Delta g = 10^{-5}$ the tilt has to be approximately 4.5 mrad which corresponds to 0.26° or an height difference of 2.2 mm over the total length of the experiment (2 m).

3.5.1. Granite and leveling

A granite block is the basis of a good precision measurement setup [254](p.72-73) [296]. The RAMSEY^{TR}-setup has two granite blocks from Fischer-Aschaffenburg[82] with a surface area of 1900 mm × 700 mm and a thickness of 220 mm [267](p.27) and a weight of approx. 840 kg [189](p.4). Each stone has 773 M6 threads with a spacing of 40 mm drilled in the surface to mount all components. The surface itself is very flat. The maximum deviation of the complete surface is less than 2 µm for these large granite blocks. This enables referencing all components via gauge blocks on the granite (e.g. measure the mirror surface height of all regions even with distances up to 1 m).
Both of these granite blocks are used. One within the vacuum chamber is the basis of the experiment, the second is situated next to the PF2/UCN platform for testing components. The old setups (from GRS^{TJ}-setup to qBB^{MT}-setup) used three different granite blocks with a size of 1000 mm × 600 mm × 160 mm [139](p.34). The main difference between these blocks is the M6 thread array suitable as the floor of different smaller vacuum chambers (e.g. *q*BOUNCINO chamber).
Within the RAMSEY^{TR}-setup the granite itself lies on three *PSt 150/20/80 VS25* piezo elements from Piezomechanik[83] [189](p.9). The range of 95 µm enables a maximal roll angle of ±264 µrad and a pitch angle of ±79 µrad with the distances of 0.36 m and 1.2 m respectively. The input signal of the DAC is ±3 V. The amplifier *SVR 150* increases it to the range of −30 V to 150 V and applies it to the piezo elements. The noise level of the amplifier induces small movements in the piezoelectric crystals of 0.16 nm or max. 36 nrad, which is comparable to the resolution of the ADC of the tilt sensor but much smaller than the resolution of the tilt sensor itself and therefore is negligible.
With a goniometer or tile sensor at the end of the granite a LabView program via a PID-adjustment levels the granite surface below 0.1 µrad relatively. The absolute leveling depends on the calibration of the sensor.
To bring the piezoelectric elements into their range, there is a coarse adjustment built into the three bearings of the vacuum chamber itself which can compensate misalignments up to ±3° [254](p.70-72). For adjusting the chamber, the earthquake safety bolts fixing the adjustment have to be loosened first. A coarse adjustment down to an accuracy of 10 µrad is possible. It is preferable to adjust the chamber as precise as possible to the zero points of the piezoelectric elements in the middle of their range. Additionally, adjusting it with vacuum inside the chamber is preferable because the difference between this condition and the one vented with air is nearly 200 µrad.
The current leveling system was set up during the project thesis of Sabrina Mayr [189]. Similar systems were already implemented in previous setups [287](p.41-46), [139](p.34-36), [86], [115](p.31-46).

Tilt sensor

The tilt sensor model *755* with the electronic model *83162A* from Tech-Sys Instruments[84] is situated in the detector-Mambo corner of the large granite [115](p.13,33). It can only be operated in air, therefore it is covered with a vacuum tube to protect it from the surrounding vacuum. A hose guides the cables to the ADC of the *Jörg's box* (details about it are in subsection 3.8.1). It can measure two axes with a gain of 0.1 µrad/mV and a range of ±800 µrad. The resolution is 0.1 µrad in the *High gain* setting. In the *Low gain* setting all values are by a factor 10 higher. Additionally, it measures the temperature.
Even though, the sensor measures its relative tilting very accurately (0.3 µrad [115](p.37)), the absolute value depends on the calibration. This is done either by comparing it with other more precise tilt sensors or by rotating it around its central axis which is fixed by a screw hole. In 2018, we rotated only with approximately 90° angles. In 2019, Jakob Micko designed a new table for the sensor with only three legs and rotated the sensor under random angles. With this method he measured an offset circle. Its fitted center coordinates are the offset values. These resulting values were used as goals for the active leveling routine. Section 4.2.2 presents the calibration and the evaluation of this sensor during the GRS measurements.

[82] Johann Fischer Aschaffenburg Präzisionswerk GmbH & Co. KG, Ruhlandstrasse 72-78, 63741 Aschaffenburg, Germany, www.jfa.de (13.11.2023)
[83] Piezomechanik, Dr. Lutz Pickelmann GmbH, Berg am Laim Str. 64, 81673 Munchen, Germany, www.piezomechanik.com (25.6.2021)
[84] Jewell Instruments, 850 Perimeter Road, NH 03103 Manchester, United Kingdom, www.jewellinstruments.com (13.11.2023)

3.5.2. Gantry

The *gantry* (originally called *Gerüst*) is a structure around the mirrors in order to move different sensors above them. Therefore, it consists of three parts: a massive table like aluminum frame, a positioning stage and a hanging movable aluminum platform for the sensors. These sensors are up to three magnetic field sensors (see more in section 3.9.2), up to 16 capacitive sensors (section 3.5.3 - CapSens) and two large pentaprisms for the SIOS laser interferometer (section 3.6.2). For the laser system additionally a small pentaprism is attached to a long rod on the front of the table frame.

The first gantry was built for the RABI^{GC}-setup with only one large pentaprism and place for six capacitive sensors on one beam. The 300 mm moving range of the position stage was too short for the new RAMSEY^{TR}-setup and the complete gantry had to be redesigned [267](p.28-29).
The table like frame was completely exchanged in order to use the larger space of the Ramsey vacuum chamber and cope with the 15 mm higher mirror surface. The table like frame has now a height of 503 mm which is already the maximum for fitting into the Ramsey vacuum chamber[85]. Its width is limited by the magnetic coils on the edge of the granite and the mirrors within the four legs. Its length is 480 mm and actually around 15 mm too short to fully use the range of the positioning stage.
Instead of one beam to hold the sensors, the new gantry has three which are based on the old design and are fixed to a long plate. Each outer beam holds a pentaprism and two capacitive sensors[86]. The middle beam at the moment has no pentaprism attached. Originally, it had place for six capacitive sensors (two above the mirrors and four above the reference mirror). As a result of the Bachelor's thesis of Paul Feichtinger [84], the two holders above the central mirror were exchanged at the beginning of the beam 182-18/1 in 2018. Now each can hold three sensors instead of one. Since then, the region III mirror can also act as a reference mirror for the CapSens system. At the same time, we also exchanged the positioning stage. It is always necessary that the stage can move its full range without any collisions (During the referencing and after the start up, it will move the complete range automatically from one limit switch to the other). Due to a slightly different design it was not possible to reduce its range enough by changing the position of the limit switch. Therefore, one holder was replaced with one from the old gantry and a piece had to be cut off on both holders in order to avoid collisions. Afterwards, there were still four but rearranged sensor positions above the reference mirror.

The positioning stage is a *HPS-170* miCos[87] table with a range of 300 mm. A shorter version with a range of only 150 mm moves two deflection mirrors of the internal laser interferometer (section 3.6.2). Both are operated together with the same controller. The first generation of miCos tables was from Corvus Eco and they were called *kurz* and *lang*. The system was bought in 2010 for the GRS^{TJ}-setup [178] and further used in the RABI^{GC}-setup and RAMSEY^{TR}-setup until 2017. Both setups had problems with a slow count rate loss during evacuation due to oil contamination of the mirrors [65](p.45-46), [254](p.112-115). As a possible source, we replaced these stages with a vacuum tight version of them (*HPS-170 VSS43 MLS HV*) in winter 2018 before the beam time 182-18/1. A *SMC-Hydra CM* two axes motion controller operates the new stages called *Steve* (*long2017*) and *Bucky* (*short2017*). A drawback of all miCos stages is the stray magnetic field of their motor (up to 4 mT on the surface). This magnetic field is the strongest source of magnetic gradients within the magnetic shielding (see the measurements in section 4.2.5). In 2019, a small µ-metal-shielding around the drive unit was able to reduce the stray field by a factor of 10 [40](p.7-8).

A disadvantage of the new gantry is its load. The approximate 35 kg platform is not as balanced around the center as the old gantry. This probably increases vertical movements and tilts of the moving stage. Additionally, the table transmits very well vibrations from the granite to the sensors. This is critical for the optics. Damping in the legs or a better design of the optic bearings could reduce this effect. A small flaw is the clearance for the laser hitting the front pentaprism which should be 30 mm wider in order not to block the beam at the beginning of the $y-$range.

[85] Actually some screws of the µ-metal shielding have to fit into the recess of the table plate, otherwise the chamber top cover will not close entirely.
[86] One pentaprism was newly bought, the outer one is the old one still in its original holder.
[87] PI miCos GmbH, Freiburger Straße 30, 79427 Eschbach, Germany

3.5.3. Capacitive sensor system - CapSens

The cylindrically shaped *D-510 PISeca* capacitive sensors have a diameter of 20 mm and an active sensor diameter of 8.4 mm [84](p.2-3). The miCos stage moves them approximately 150 µm above the mirrors due to their used range of 250 µm (a second possible range is 750 µm). Via an attached triaxial cable the controller can measure the distance between the sensor and the mirror surface. This works properly only if the coating is connected to the ground of the controller, otherwise a large offset will disable the measurement. The precision is below 10 nm and the linearity is 0.1 % within the nominal range of 100 µm. The RABI^{GC}-setup used 6 *old* capacitive sensors (*D-510.101* with a PI *E517* controller [65](p.29-30)) in order to fill the six possible positions of its gantry. For the RAMSEY^{TR}-setup ten *new* sensors (originally 10 positions) with longer wires were bought with a new PI *E712K225* controller. PI manufactured all 16 different sensors and the two controllers. In principle, they are interchangeable except for small deviations due to different calibration. Therefore, they are normally used at the assigned positions of their controller. In order to fit together the correct sensors, cables and feedthroughs, they are all labeled with numbers from *73* to *82* (*new*, *E712*) and *75-80* (*old*, *E517*).
To check the linearity of the sensors they are compared with the movement of the piezoelectric stage underneath [84](p.5-6), [254](p.101-102). Additionally, linear gauges (see section 3.7.1) and the SIOS laser interferometer (section 3.6.2) can be used for comparison. Some of the *new* sensors have much worse linearity than the *old* ones because of their cable length (maximal length possible to produce) and possible damages due to cable ties.
In 2018, both sensor systems were used simultaneously to operate enough sensors. Since 2019, only the new controller with partial old sensors has been operated, because it is not possible to link the old controller with the other controllers of PI. This is needed to synchronize them and avoid inducing oscillations between sensors and piezoelectric elements.

The sensors are fixed to special holders from Radiant Dyes[88] which are normally used to mount mirrors. There exist three sets due to their different ordering: eight holders from 2012, three holders from 2017/18 and five holders form 2022 (*RDI-HS-L3-3010(10H7)*). All so-called *CapSens holders* should be vacuum tight and non magnetic. It is crucial that the sensors are aligned parallel to the mirrors as precise as possible, otherwise the non linearity will increase [84](p.5-6). This is done with the fine thread screws of the holders. The height can also be adjusted and fixed with them. In general, the center of the range is the optimal height for the operation.

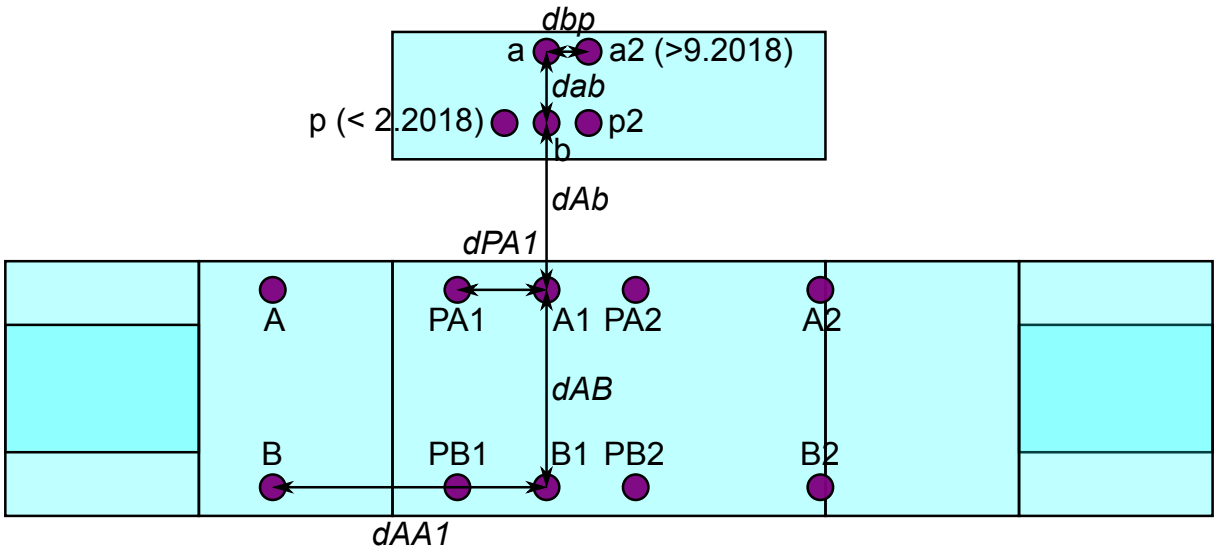

Figure 3.21.: Capacitive sensor position within the RAMSEY^{TR}-setup

As displayed in figure 3.21 or in [267](p.55-56), [84](p.2-3) the general naming rules for the sensor position are: All capital lettered sensors are above the Ramsey mirrors to measure their position and alignment. *A* stands for PF2/EDM side, *B* for PF2/MAMBO. The distance between both sensor lines is $dAB = 155$ mm. The gap between is slightly larger than the width of the absorbers and their bearings.

[88] Radiant Dyes Laser & Accessoires GmbH, Friedrichstraße 58, 42929 Wermelskirchen, Germany, www.radiant-dyes.com (13.11.2023)

During placing the absorbers, a smooth passing has to be ensured. A and B are in the front (reactor side) and are able to scan mirrors I to III. $A1$ and $B1$ are in the middle and only probe mirror III. $A2$ and $B2$ are in the back (detector side) and measure mirrors III to V. The three rows are equidistant with a spacing of $\frac{1}{2}dAA2 = dAA1 = 215\,\text{mm}$. The new pitch sensors in region III are called P + side (A/B) + 1 or 2 depending if they are before or after the middle sensors. The distance of the sensors from the central line is $dPA1 = 70\,\text{mm}$. The small letters are the sensors on the reference mirror. a is on the PF2/EDM side and b on the PF2/MAMBO side. The pitch sensor p is before sensor b. $p2$ and $a2$ are after b and a respectively.
The coordinates of all sensors are in relation to b, whereas the x direction is parallel to the neutron beam and z vertical upwards:

$$A = \begin{pmatrix} -\frac{1}{2}dAA2 \\ -dAb + \Delta AA1 \\ ZA \end{pmatrix} \qquad B = \begin{pmatrix} -\frac{1}{2}dAA2 \\ -dBb + \Delta AA1 \\ ZB \end{pmatrix} \tag{3.31}$$

$$A1 = \begin{pmatrix} 0 \\ -dAb \\ ZA1 \end{pmatrix} \qquad B1 = \begin{pmatrix} 0 \\ -dBb \\ ZB1 \end{pmatrix} \tag{3.32}$$

$$A2 = \begin{pmatrix} \frac{1}{2}dAA2 \\ -dAb + \Delta AA2 \\ ZA2 \end{pmatrix} \qquad B2 = \begin{pmatrix} \frac{1}{2}dAA2 \\ -dBb + \Delta AA2 \\ ZB2 \end{pmatrix} \tag{3.33}$$

$$PA1 = \begin{pmatrix} -dPA1 \\ -dAb \\ ZPA1 \end{pmatrix} \qquad PB1 = \begin{pmatrix} -dPA1 \\ -dBb \\ ZPB1 \end{pmatrix} \tag{3.34}$$

$$PA2 = \begin{pmatrix} dPA1 \\ -dAb + \Delta AA2 \\ ZPA2 \end{pmatrix} \qquad PB2 = \begin{pmatrix} dPA1 \\ -dBb + \Delta AA2 \\ ZPB2 \end{pmatrix} \tag{3.35}$$

$$dAb = 131\,\text{mm} \quad , \quad dAB = 155\,\text{mm} \quad , \quad dBb = dAb + dAB = 286\,\text{mm}$$

$$dPA1 = 70\,\text{mm} \quad , \quad dAA2 = 430\,\text{mm} \quad , \quad \Delta AA1 \approx 4.2\,\text{mm} \quad , \quad \Delta AA2 \approx 4.5\,\text{mm}$$

dAB and $dAA2$ are fixed values due to the shape of the gantry. $\Delta AA1$ and $\Delta AA2$ are variable due to the slotted holes for the connection between the crossbar with a pair of sensors and the base plate of the movable platform. During the miCos table exchange, all beams were aligned in order to be able to neglect this offset (before beam time 182-18/1). In addition, the distance dAb has five possibilities with a spacing of 5 mm (116 mm to 136 mm). This is also true for the distance dab because the reference sensors mount for $p2$-b-p and $a2$-a respectively can be mounted on five different positions independently. Due to other restrictions (sensor size, reference mirror position,...) the position is quite designated. Position 1 of the b aluminum holder and 5 for the a holder were used throughout the entire year 2018. This resulted in a distance dAb of 116 mm and dAb of 56 mm. In contrast, the distance of the pitch sensors is fixed due to the holder shape to $dbp = 33\,\text{mm}$.
The reference sensor positions relative to b are:

$$a = \begin{pmatrix} 0 \\ dab \\ Za \end{pmatrix}, \; b = \begin{pmatrix} 0 \\ 0 \\ Zb \end{pmatrix}, \; p = \begin{pmatrix} dbp \\ 0 \\ Zp \end{pmatrix}, \; p2 = \begin{pmatrix} -dbp \\ 0 \\ Zp2 \end{pmatrix}, \; a2 = \begin{pmatrix} -dbp \\ dab \\ Za2 \end{pmatrix}$$

$$dab = 56\,\text{mm} \quad , \quad dbp = 33\,\text{mm}$$

Until 2017, we had only 8 sensor holders. During the beam time 181-17/1, we used sensors A, B, $A2$, $B2$, a, p, b, $A1$, ($B1$) - (LabView order, 25.9.2016 - 1.2018), whereas $A1$ was installed on 20.2.2017 after troubles with the step control.
Paul Feichtinger studied these problems of the mirror alignment during his Bachelor's thesis [84]. As a result, four new positions have been available due to the replacement of the middle sensor holders ($A1$+$B1$) since spring 2018. These positions are used for pitch sensors for the middle region ($PA1$, $PB1$, $PA2$, $PB2$). They have a more than twice as large distance from the middle axis ($B1$-$A1$-b-a) than the reference pitch sensor p and therefore they are more sensitive to the pitch angle of the gantry (mainly the error of the sensors propagates less with the height correction). At the ends of the miCos ranges, one side of the new pitch sensors will leave region III. Still, the large region III mirror can be used as reference mirror if two opposing pitch sensors are used.

We bought three new holders to fill the required positions. For the beam times in 2018, we had 11 operable sensors available. This also induced a significant change of the LabView program in 2018. All sensor positions were implemented in the following order: *A*, *B*, *A1*, *B1*, *A2*, *B2*, *a*, *p*, *b*, *PA1*, *PB1*, *PA2*, *PB2*, *p2*, *a2*. Both controllers can be used simultaneously and different correction options are available. The sensor-position assignment is implemented in the initialization of the *pi_E712_kap_sens_2018.vi* and needs adaptations after a sensor exchange. In spring 2018, the exchange of the position stage (miCos) resulted in the loss of the *p* position and the gain of the *a2* position [159](p.5-7).
The capacitive sensors can only measure the height (z-axis) with an accuracy of 0.1 %. The miCos table moves the sensors over the mirrors in $x-$direction to an accuracy of 2 µm. A misalignment between the miCos table and the $x-$axis is ignored, therefore it defines the $x-$axis. There should be no significant movement in the $y-$axis. On µm scale the table does not move smoothly over its rails. It rotates in all directions and moves away from the ideal position. Only translation of the sliding carriage in the $z-$axis and rotations around the $x-$ and $y-$axis (roll and pitch) change the measurements of the capacitive sensors, even though the mirror underneath is perfectly flat. Three sensors in an orthogonal triangle are necessary for a simple correction by assuming that the moving structure of the CapSens is stiff. This is the purpose of the reference sensors: *b* corrects the height, the difference between *a* and *b* the roll angle, and similarly the difference between *b* and a pitch sensor (*p* or *p2*) the pitch angle. *a2* can be either used as control or to correct the other sensors with two other reference sensors. This works for every triplet of sensors as long as they are on the same mirror, are not in a line and have enough spacing (as it is possible for the sensors on the large region III). See more about the correction algorithm in section 3.5.4.

Sensor assignment: The RABI-GRS-18 setup used the following sensor assignments with only new sensors: *A-74*, *B-76*, *a-75*, *b-73* and *p2-78*. The longer RAMSEY-GRS-18 setup further used *A1-79*, *B1-77* and *PB1-81* and sensors from the old shorter setup with the new holders at the end: *A2-76*, *B2-77* and *PA2-75*. The high voltage cables of the electrodes on the PF2/MAMBO side made it necessary within the Rams$\vec{E}$y-setup to remove *B1* and *PB1* during the beam time 184-18/3. These sensors were relocated to *PA1-77* and *a2-81* [233](p.4-5).

3.5.4. Step control

The step control uses the position and the corrected measured values of the capacitive sensors to calculate the position of the mirror surfaces relatively to the reference mirror surface [254](p.102-106). In a second step, step heights and the needed position adjustments for all regions are calculated. Setting these values and repeating the measurement leads to an iterative reduction of all step heights [267](p.56-69). This algorithm increases in complexity for each added region.
The correction of the CapSens values due to the movements of miCos is described in the following subsections or within [84](p.7-11). The resulting measured lines representing the mirror surfaces were always expected to be flat lines if the corrections were correct. In reality, this is only partially true because the mirror surface waviness is larger than the measurement accuracy and the moving parts of the gantry could be deforming during the motion. These effects result in parabolic or even higher oscillating curves [267](p.62-64). Instead of linear fits, higher polynomial fits can better account for this oscillating behavior and are used to extrapolate the sensor data for calculating the step height. In 2017, a static CapSens system measuring a mirror on different positions proved the origin due to the mirror waviness [84](p.26-28). The sensor correction algorithm amplifies this problem because it transfers the reference mirror surface on to the measured surfaces of each mirror. This mapping is scaled by a factor up to 6.5 with the ratio between the distance of the corrected sensor to coordinate center and the one of the angle correcting reference sensors. Due to this, the corrected values can shift some µm and the calculated steps one order of magnitude smaller. A surface measurement of the reference mirror can correct this effect [233]. Many systematic tests, during and after the beam time 181-17/1 conducted by Tobias Rechberger [254](p.101-106), Paul Feichtinger [84] and myself, also identified other effects: Poor grounding is only problematic if the mirror surface is not grounded at all, which leads to a large offset. Beside dust, especially below the reference sensors, also sensors moving on or off a mirror surface can induce artifacts [84](p.28-30). In principle, tilting the piezo tables underneath can determine the position of the sensors [84](p.12). Similarly with changing the piezoelectric stage height the linearity can be determined (In the optimal case even referenced with linear gauges or the SIOS laser interferometer) [254](p.101-102)[89].

[89] This can either be achieved with a LabView script or directly with the software *MicroMove* from PI.

An ultimate test of the step control via capacitive sensors are measurements with linear gauges (see sub section 3.7.1). After many difficulties during the beam time 181-17/1, the mirror alignment was finally done manually with the linear gauges. In 2018, this method was used from the start on. Later Carina Killian [159] compared the steps calculated by one CapSens measurement with linear gauge measurements taken at different occasions (for the alignment and control measurements before the disassembly). She also exploited different extrapolation of the data (linear, quadratic, cubic) with an inconclusive result.

CapSens Correction

The most simple correction is done via similar triangles using three reference sensors. This is a good approximation of a complete description of the rotations and translations of the gantry as shown in the next subsection.
In the beginning, the first measurement of a sensor is subtracted from all following measurements to eliminate the different heights of the sensors above the mirrors. The next step is the height correction of the vertical gantry movement (horizontal movements are neglected). The measured vertical distance to the mirror of the central reference sensor r_h is subtracted from all other sensors:

$$ZX' = ZX - Zr_h \tag{3.36}$$

$$\Delta ZX' = \sqrt{\Delta ZX^2 + \Delta Zr_h^2} \tag{3.37}$$

To correct the two tilts (roll and pitch) of the gantry around two horizontal axes (x and y) we use similar triangles, one between two reference sensors and the other including the corrected sensor, as can be seen in figure 3.22.

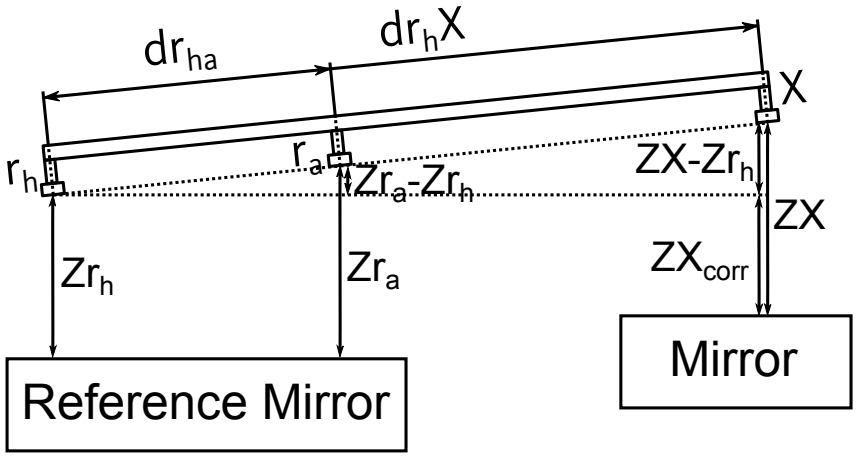

Figure 3.22.: Capacitive sensor angle correction [267](p.60)

Pitch correction of tilt angle α:

$$ZX'' = ZX' - \frac{dX_x}{dr_x}(Zr'_p - Zr'_h)$$

$$\Delta ZX'' = \sqrt{\Delta ZX'^2 + \left(\frac{Zr'_p - Zr'_h}{dr_x}\right)^2 \Delta dX_x^2 + \left(\frac{dX_x}{dr_x^2}(Zr'_p - Zr'_h)\right)^2 \Delta dr_x^2 + \left(\frac{dX_x}{dr_x}\right)^2 \Delta Zr_p'^2 + \left(\frac{dX_x}{dr_x}\right)^2 \Delta Zr_h'^2}$$

Roll correction of tilt angle β:

$$ZX''' = ZX'' - \frac{dX_y}{dr_y}(Zr''_r - Zr''_h)$$

$$\Delta ZX''' = \sqrt{\Delta ZX''^2 + \left(\frac{Zr''_r - Zr''_h}{dr_y}\right)^2 \Delta dX_y^2 + \left(\frac{dX_y}{dr_y^2}(Zr''_r - Zr''_h)\right)^2 \Delta dr_y^2 + \left(\frac{dX_y}{dr_y}\right)^2 \Delta Zr_r''^2 + \left(\frac{dX_y}{dr_y}\right)^2 \Delta Zr_h''^2}$$

All corrections done consequently:

$$ZX_{corr} = ZX - Zr_h - \frac{dX_x}{dr_x}(Zr_p - Zr_h) - \frac{dX_y}{dr_y}(Zr_r - Zr_h) \tag{3.38}$$

$$\Delta ZX^2_{corr} = \Delta ZX^2 + \left(1 + \left(\frac{dX_x}{dr_x}\right)^2 + \left(\frac{dX_y}{dr_y}\right)^2\right)\Delta Zr_h^2 \tag{3.39}$$

$$+ \left(\frac{Zr_p - Zr_h}{dr_x}\right)^2 \Delta dX_x^2 + \left(\frac{dX_x}{dr_x^2}(Zr_p - Zr_h)\right)^2 \Delta dr_x^2 + \left(\frac{dX_x}{dr_x}\right)^2 \Delta Zr_p^2 \tag{3.40}$$

$$+ \left(\frac{Zr_r - Zr_h}{dr_y}\right)^2 \Delta dX_y^2 + \left(\frac{dX_y}{dr_y^2}(Zr_r - Zr_h)\right)^2 \Delta dr_y^2 + \left(\frac{dX_y}{dr_y}\right)^2 \Delta Zr_r^2 \tag{3.41}$$

The resulting correction is independent of the ordering of the tilt corrections. Further, all reference sensors are corrected to zero ($Zr_{h\,corr} = Zr_{p_{corr}} = Zr_{r\,corr} = 0$). Note that the corresponding errors are not zero. The errors of the distances between the sensors are assumed as 0.1 mm. This corresponds to a relative error between 4.7×10^{-4} and 0.3 % and therefore is low enough not to conduct more detailed measurements.

Summarized correction for *b* zero (pitch *p2*): The following list displays the standard corrections used in 2018.

$$ZX_{corr} = ZX - Zb - \frac{dX_x}{dbp}(Zp2' - Zb') - \frac{dX_y}{dab}(Za'' - Zb'') \tag{3.42}$$

$$ZX_{corr} = ZX - Zb - \frac{dX_x}{dbp}(Zp2 - Zb) - \frac{dX_y}{dab}(Za - Zb) \tag{3.43}$$

$$ZA_{corr} = (ZA - Zb) + \frac{\frac{1}{2}dAA2}{dbp}(Zp2 - Zb) + \frac{dbA}{dab}(Za - Zb) \tag{3.44}$$

$$ZB_{corr} = (ZB - Zb) + \frac{\frac{1}{2}dAA2}{dbp}(Zp2 - Zb) + \frac{dbB}{dab}(Za - Zb) \tag{3.45}$$

$$ZPA1_{corr} = (ZPA1 - Zb) + \frac{dPA1}{dbp}(Zp2 - Zb) + \frac{dbA}{dab}(Za - Zb) \tag{3.46}$$

$$ZPB1_{corr} = (ZPB1 - Zb) + \frac{dPA1}{dbp}(Zp2 - Zb) + \frac{dbB}{dab}(Za - Zb) \tag{3.47}$$

$$ZA1_{corr} = (ZA1 - Zb) + \frac{dbA}{dab}(Za - Zb) \tag{3.48}$$

$$ZB1_{corr} = (ZB1 - Zb) + \frac{dbB}{dab}(Za - Zb) \tag{3.49}$$

$$ZPA2_{corr} = (ZPA2 - Zb) - \frac{dPA1}{dbp}(Zp2 - Zb) + \frac{dbA}{dab}(Za - Zb) \tag{3.50}$$

$$ZPB2_{corr} = (ZPB2 - Zb) - \frac{dPA1}{dbp}(Zp2 - Zb) + \frac{dbB}{dab}(Za - Zb) \tag{3.51}$$

$$ZA2_{corr} = (ZA2 - Zb) - \frac{\frac{1}{2}dAA2}{dbp}(Zp2 - Zb) + \frac{dbA}{dab}(Za - Zb) \tag{3.52}$$

$$ZB2_{corr} = (ZB2 - Zb) - \frac{\frac{1}{2}dAA2}{dbp}(Zp2 - Zb) + \frac{dbB}{dab}(Za - Zb) \tag{3.53}$$

$$Za_{corr} = Za - Zb + \frac{0}{dbp}(Zp2 - Zb) - \frac{dab}{dab}(Za - Zb) = 0 \tag{3.54}$$

$$Zb_{corr} = 0 \tag{3.55}$$

$$Zp_{corr} = Zp - Zb + \frac{dbp}{dbp}(Zp2 - Zb) - \frac{0}{dab}(Za - Zb) = Zp + Zp2 - 2Zb \tag{3.56}$$

$$Zp2_{corr} = Zp2 - Zb\frac{dbp}{dbp}(Zp2 - Zb) - \frac{0}{dab}(Za - Zb) = 0 \tag{3.57}$$

$$Za2_{corr} = Za2 - Zb - \frac{dbp}{dbp}(Zp2 - Zb) - \frac{dab}{dab}(Za - Zb) = Za2 - Za - Zp2 + Zb \tag{3.58}$$

General corrections of gantry movements

Most generally we have to correct the movement of the gantry in three translations (x, y and z) directions and three rotations: roll angle β (x-axis), pitch angle α (y-axis) and the yaw angle γ (z-axis) with r, s, t as the sign representing the direction of the rotation. We will apply the rotation in the order z-x-y (other orders can also be used). $\vec{X}_s$ is the real sensor position including the movement of the gantry and $\vec{X}_{corr}$ a corrected position assuming the movement was ideally in x-direction. x_{corr} and y_{corr} are the coordinates of the sensor in the chosen coordinate system (see equation 3.35). Then the measured z_{corr}-profile represents the surface of the mirrors without a vertical movement of the sensor. $\vec{b}$ is the position of coordinate center including the translational movement of the gantry which for the most common correction is the position of sensor b:

$$\vec{X}_{corr} = \begin{pmatrix} \cos\alpha & 0 & s\cdot\sin\alpha \\ 0 & 1 & 0 \\ -s\cdot\sin\alpha & 0 & \cos\alpha \end{pmatrix} \begin{pmatrix} 1 & 0 & 0 \\ 0 & \cos\beta & -r\cdot\sin\beta \\ 0 & r\cdot\sin\beta & \cos\beta \end{pmatrix} \begin{pmatrix} \cos\gamma & -t\cdot\sin\gamma & 0 \\ t\cdot\sin\gamma & \cos\gamma & 0 \\ 0 & 0 & 1 \end{pmatrix} \left(\vec{X}_s - \vec{b}\right) \tag{3.59}$$

Equation (3.60) is simplified with the small angle approximation of the trigonometric functions (β, α, γ are « 1). All angles are expected to be even smaller than 1 mrad:

$$\begin{pmatrix} x_{corr} \\ y_{corr} \\ z_{corr} \end{pmatrix} = \begin{pmatrix} 1+rst\cdot\beta\alpha\gamma & rs\cdot\beta\alpha - t\cdot\gamma & s\cdot\alpha \\ t\cdot\gamma & 1 & -r\cdot\beta \\ -s\cdot\alpha + rt\cdot\beta\gamma & st\cdot\alpha\gamma + r\cdot\beta & 1 \end{pmatrix} \begin{pmatrix} x_s - b_x \\ y_s - b_y \\ z_s - b_z \end{pmatrix} \tag{3.60}$$

We can only use the first order and drop all terms with products of rotation angles due to their small magnitude:

$$\begin{pmatrix} x_{corr} \\ y_{corr} \\ z_{corr} \end{pmatrix} = \begin{pmatrix} x_s - b_x - t\cdot\gamma(y_s - b_y) + s\cdot\alpha(z_s - b_z) \\ t\cdot\gamma(x_s - b_x) + y_s - b_y - r\cdot\beta(z_s - b_z) \\ -s\cdot\alpha(x_s - b_x) + r\cdot\beta(y_s - b_y) + (z_s - b_z) \end{pmatrix} \tag{3.61}$$

x_s and y_s is in the order of 100 mm and dominating, which leads to a further reduction of negligible terms:

$$\begin{pmatrix} x_{corr} \\ y_{corr} \\ z_{corr} \end{pmatrix} = \begin{pmatrix} x_s \\ y_s \\ -s\cdot\alpha x_s + r\cdot\beta y_s + (z_s - b_z) \end{pmatrix} \tag{3.62}$$

The resulting correction does not depend on the yaw angle γ, the translations in x and y direction (b_x, b_y) and the order of the applied rotations. It is the same result as the simple correction (see equation 3.41). For mirror surfaces aligned parallel to the xy plane the yaw angle γ and the horizontal translations (x and y) have no influence on the height measurement at all.

3.6. Oscillations

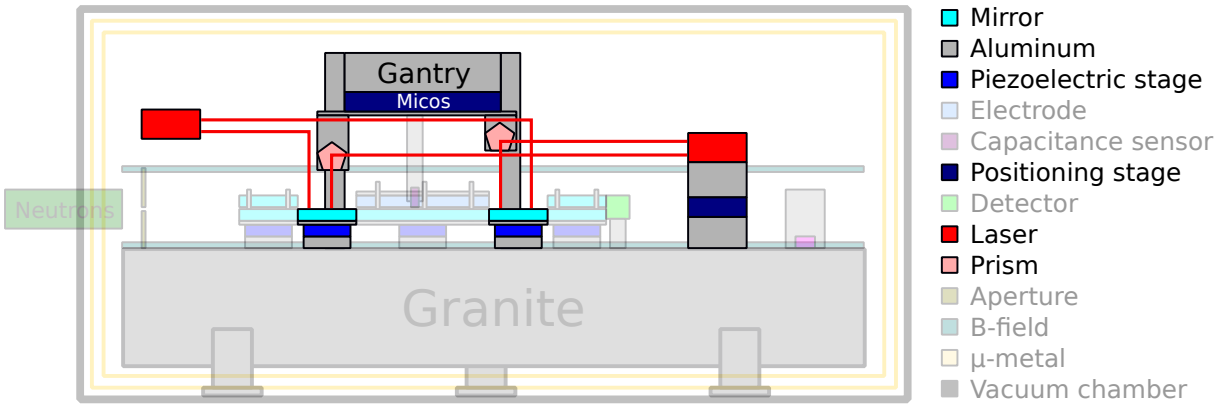

Figure 3.23.: A schematic view of the components within the RAMSEY^{TR}-setup which are needed to induce and measure the mirror oscillations.

The following section describes the induction and measurement of the mirror surface oscillations which can drive state transitions as the most essential part of every GRS setup [254](p.89-98).
The AFG produces oscillating signals and their basic properties (frequency, amplitude, relative phases and waveform). The piezoelectric stage translates this electronic signal into a mechanical motion of the attached mirror (see more in section 3.1.6). The mechanical amplitude of the mirror surface depends on the frequency and amplitude of the input signal and the mechanical response of the complete region (coarse adjustment, piezoelectric stage, mirror). Close to mechanical resonance frequencies of the region, it is not possible to apply a stable controllable mirror oscillation. This disables some transition frequencies (in 2018 the transition $|1\rangle \rightarrow |4\rangle$ was not possible to induce).
The SIOS laser interferometers measure the properties of the induced oscillations. In principle, the capacitive sensors could also measure this signal but this feature is not yet implemented in the RAMSEY^{TR}-setup (see section 3.5.3). Further, the OROS sensors measure the spreading of the driven oscillations to other components (gantry, granite, ...) and can detect parasitic vibrations from the outside (turbo pumps, crane movement, ...).

3.6.1. AFG - arbitrary function generator

The AFG provides the voltage signal for the mirror oscillations. It is placed in the left rack outside the vacuum chamber. The sine like signals are transmitted via the PI-table controllers of region II and region IV to the piezoelectric crystals of these regions. The voltage amplitude induces a mechanical oscillation with the same frequency and a strongly frequency-dependent mechanical amplitude.
Since 2010, the AFG has been a Tektronix[90] *AFG3102C*. It can produce signals with frequencies between 1 µHz and 100 MHz (for sine waves[91]) with a resolution of 1 µHz or 12 digits. The internal frequency reference can relatively change approximately $\pm 10^{-6}$ per year due to aging or thermal changes. The amplitude V_{pp} can be set between 20 mV and 10 V with a resolution of 1 mV. Typical settings for GRS measurements are frequencies from 100 Hz to 1000 Hz and amplitudes from 0.1 V to 5 V (the main limit for higher values are the PI-tables). This AFG has two outputs (one for each region). The phase between these signals can be fixed between −180° to 180° with a resolution of 0.01° (for sine waves). After changing the frequencies, the phase between the outputs has to be adjusted again, otherwise an arbitrary phase between the signals will be added. The LabView-controller has done this automatically since spring 2017. During the beam time 181-17/1 (3-14-358-II), previously to the program fix, this problem corrupted the data unnoticed due to broken laser interferometer measurements [136](p.11-14).
The LabView measurement program controls the AFG remotely. The settings are changed either manually on the PC or automatically via the measurement queue. Furthermore, a real arbitrary mode has already been implemented since 2017 [136]. Any given list of amplitude values will be played with a chosen repetition rate. This is the first step for state preparation with chirped frequencies [185].

[90] Tektronix Inc., 14150 SW Karl Braun Drive, Beaverton, OR 97077, United States, www.tek.com (21.4.2021)
[91] Other wave forms have smaller ranges.

As backup we bought a second Tektronix *AFG3102C* in May 2017. It can either be used for systematic checks (clock comparison) or at a second experiment (*q*BOUNCINO).

At the beginning of one measurement the corresponding LabView program changes the settings of the AFG (frequency, amplitudes of each region and phase). Only during the *veto* time of the PF2 turbine control, the outputs are turned on. The piezoelectric crystals of the PI-tables rest during the background measurement. During one cycle, a characteristic pattern of job commands and setting data is stored. In the data analysis this pattern is reassembled and the timing of the found cycle determined. The length of such cycles determines the type of the measurement. Neutron measurement cycles have a typical length of 200 s. The other detected cycles are mainly vibration tests in order to find the correct voltage amplitude and phase for a given frequency and mechanical amplitude. The cycles are counted within one neutron measurement and compared to the counted cycles of the detector and the PF2-control. For frequency measurements these numbers have to match. Zero rates have no AFG cycles but matching detector and PF2 cycles. All neutron measurements with different cycle counts between the three components are primarily excluded for further evaluation. They could be partly zero rate and frequency measurements. Similarly, within one measurement ID the settings are compared and all those with various settings are also excluded. If the LabView program crashes, no data are stored. The detector still runs further until the reboot of the LabView software (these measurements have many more detector cycles than the other two). If the last command to the AFG was turning it on, the measurement continues normally with always oscillating mirrors. Otherwise, it is a zero rate and therefore also excluded. All excluded measurements can only be incorporated again in the analysis if a time-dependent evaluation of the detector is carried out and the different parts are separated in different IDs. Especially for LabView crashes during the night, it is worth the effort because many neutrons are detected and reduce the statistical error.

3.6.2. SIOS - laser interferometer

Up to three laser interferometers from SIOS[92] measure the oscillations of the mirrors (frequency, mechanical amplitude and the phase between the regions [178](p.66-70), [114](p.21-24))[93]. Each one consists of a controller, a laser head, fragile glass fibers and data cables for the connection. The controller has a built-in HeNe laser (632.8 nm and 2 mW [65](p.31-35)). A glass fiber guides the light to the laser head. Each laser head splits the incoming laser into three independent partial beams. The laser head consists of three Michelson interferometers. One arm is reflected internally on a movable mirror (a so-called *schwinger* which can oscillate to stabilize the laser feedback). The second arm is guided with small mirrors and pentaprisms on the mirrors of the regions which reflect it back to the laser head. Small photo diodes read out the interference and send the data to the controller via special multi-strand cables. Either a LabView program or special programs from the manufacturer calculate the relative distance, velocity and acceleration of the mirrors with very high accuracy[94]. If the triggers of the controllers are connected with BNC-cables to an external trigger source, multiple interferometers act as a single one with fixed phase relations between all beams [136](p.19-21). The sampling rate and block length also have an influence on the accuracy and can induce shifts. The used sample rate was 2517 Hz with a block length of 29000 points [114](p.27-30,48-49), [254](p.90-91).
Due to the operation within the vacuum chambers, feedthroughs split the glass fibers and the data connections. This is quite critical and can be a source of losses.

The performance of the laser interferometer is measured with two parameters: the light output of the single beams and the feedback. A wavemeter from Thorlabs[95] measures the light output which should be between 20 µW to 80 µW at each beam. This is only possible if the vacuum chamber is open. High light output also yields a high possible feedback. A laser power below 5 µW makes it impossible to have a feedback at all. The loss in laser power appeared after some time during the beam times and led to complete loss of beams. The reason were either damages of the fiber done by students, slow misadjusting or smutching of the optics. In order to undo such losses, we send the interferometers back to the manufacture SIOS for repairs and calibration between the beam times. Afterwards, they perform as if they would be new.

[92] SIOS Meßtechnik GmbH, Am Vogelherd 46, 98693 Ilmenau, Germany, www.sios-precision.com (13.11.2023)
[93] During the first use in 2010, the interferometer was also used for height measurements. Moving prisms, temperature changes,.. induce corrections which complicate the measurements. Steps are not measurable due to the loss of the phase [178](p.31-60).
[94] This is done via a Fourier filter and fitting a cosine to the reduced data [183](p.14-21).
[95] Thorlabs Inc., 56 Sparta Road, Newton, NJ 07860, United States, www.thorlabs.com (21.4.2021)

The feedback mainly depends on the adjustment of the beam optics. Only if the beam reaches the laser head again, it is possible to have a feedback. For fine tuning (maximizing) the feedback has to be observed live (e.g. the *Infas* software or an oscilloscope). Slow misadjustment within the evacuated vacuum chamber leads to a decreasing feedback over time. If it is too low (below 5 %), the chamber has to be vented and the optics readjusted. If the reason is a decreased laser beam power, the feedback will not be completely restored.
In the future, the three piezoelectric driven mirrors could speed up the adjustment process and make it also possible at vacuum conditions. The mirrors were bought 2014 from Radiant Dyes. Two mirrors are already built into the scanning laser beams. Already 2014, Tamara Putz started programming the automation. Unfortunately, the needed DAC *USB 3105* has been missing since then. In 2018, a new one was bought waiting for installment.

The names of the three interferometers are *main/internal*, *reference/external* and *exeternal*.
The main interferometer is a SIOS *SP 15000 TR* and is situated at the end of the granite behind the detector [114](p.21-24). Large movable pentaprisms attached to the gantry and movable mirrors enable scanning the mirror surface and detecting the motion of them (vertical and/or rotational) [136](p.21-23), [48](p.10-12). One beam scans region II and is called *scanV*, the other region IV and is called *scanH*[96]. The third beam is fixed to one point of region II via three small pentaprisms and is called *r2ref*. Joining the three beams together enables measuring the phase between the two oscillating regions. In figure 3.24 you can see the positioning of the laser beams on the mirrors.

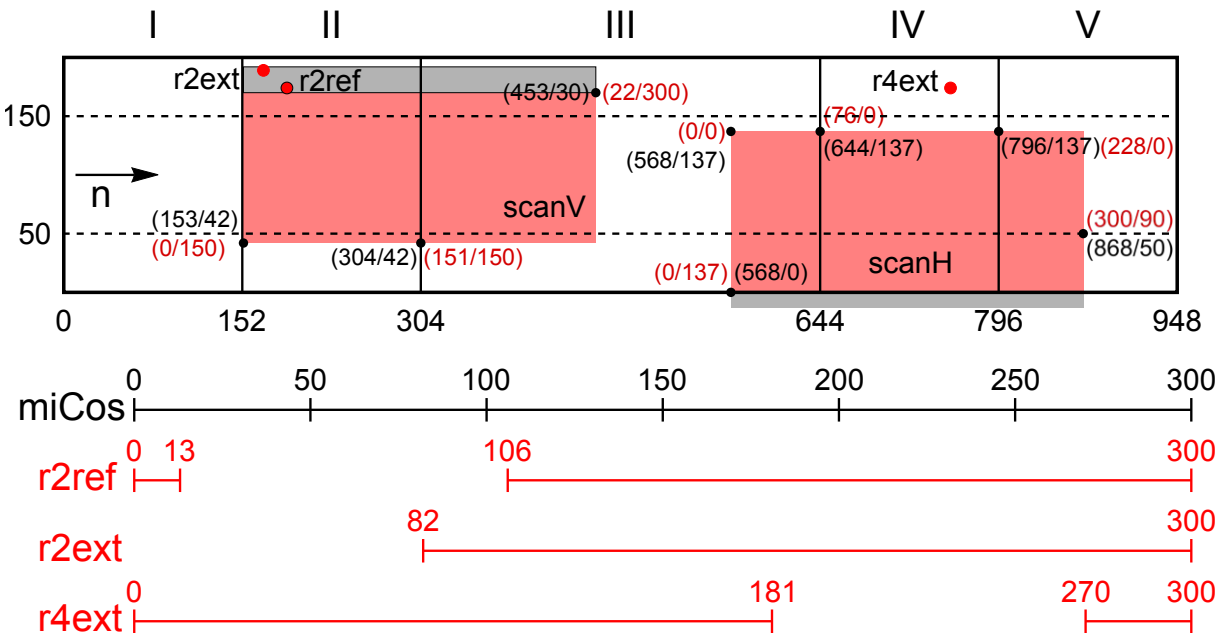

Figure 3.24.: Positioning of all laser beams on the mirrors during the beam time 183-18/2 (3-14-358-IV) including when the fixed beams are not blocked. In the region (106-147)/(22-137) in miCos coordinates all laser beams are on the oscillating regions.

Unfortunately, the strong oscillations of the mirrors induce a strongly frequency-dependent feedback of the laser optics attached to the gantry and on the small stage below the interferometer [137], [254](p.90), [48]. This distorts the measurements of the amplitude and the phase of each beam [114](p.30-47). The strength of these distortions depends strongly on the frequency and is constant as long as the system stays mechanically constant. Loosening screws of some mirrors or placing weights changes these distortions. It is possible to reduce these effects for a certain frequency. In order to suppress the effect entirely either the oscillating regions or the gantry and the main SIOS laser interferometer have to be isolated from the granite. At the moment, the induced sound waves easily propagate through the granite and the massive support structures to the unfirm ends where the small optic's mirrors are mounted. You can feel the oscillations by touching these spots.
To cope with these problems the two old SIOS *SP 2000 TR* were reactivated [139](p.72). Both were used completely decoupled from the granite. One is placed on an ITEM-frame attached to the vacuum chamber

[96] *V* and *H* stands for the German words *Vorne* and *Hinten*.

itself. This is called the *external* or *reference interferometer*. One beam is guided via a small pentaprism to region II (*r2fix* or *r2ext*) and a second to region IV (*r4fix* or *r4ext*). All optics are also attached to the ITEM frame. This configuration makes it possible to measure the phase and amplitudes on one spot of each oscillating region. These values have always been taken for the analysis. A disadvantage is the comparably much higher vibrational noise due to the surrounding and the missing damping of the granite [136](p.24-25), which can be suppressed with FFT filters.
In order to check if the oscillations of the piezo stages disturb the *external interferometer*, there are two possibilities. First if only one region is oscillating, the *internal* laser will measure an amplitude on the second region due to vibrating optics, the *external* one should not measure anything except the real motion of the resting stage. A second possibility is the use of an *exexternal laser*. In principle, it is a setup similar to the *external* interferometer (it is completely decoupled from the granite) [254](p.97-98). The only difference is its position. It is placed temporarily on long aluminum profiles attached to the PF2/UCN platform above the open vacuum chamber. The laser beams are adjusted close to the *r2fix* and *r4fix* beams. In 2017 and in February 2018, we measured a good congruence between both external interferometers.
The SIOS *SP 2000 TR* were bought 2010 and 2012 therefore they are called SIOS-2010 [90, 178] and SIOS-2012 respectively to distinguish them. Both were used as reference laser one after each other. The exchange normally was necessary because the used one needed recalibration and the second already came back from SIOS. There is only one difference between the two interferometers: The SIOS-2012 has an adjustment plate underneath the laser head, which makes it much easier to adjust the beams.
During the beam times in 2018, the SIOS-2012 interferometer was used.

3.6.3. OROS - vibration measurements

From the beginning of *q*BOUNCE, shielding the experiment from external vibrational disturbance was important [287](p.47-48). These potentially strong oscillations can induce state transitions. The main external sources are neighboring experiments (pumps, especially turbo pumps with their high rotational speed (e.g. 450 Hz to 820 Hz)) or maintenances of the reactor (e.g. crane movements or driving forklifts). The RAMSEY^{TR}-setup itself is passively shielded via the massive granite block against external disturbances. At the beginning, the smaller setups also had an active damping plate below the granite block. With the start of the GRS experiments and the implementation of the SIOS laser interferometer interference due to vibrations occurred. The oscillations from the piezoelectric stages have been able to vibrate the laser optics and tamper the amplitude and phase measurements which led to the introduction of the decoupled *external* SIOS laser interferometer. In 2013, David Jelem did the first systematic studies of the propagation of the internal disturbance on to the SIOS laser interferometer with the OROS setup [137]. In 2017, Nico Einsidler further studied the internal and external vibrational noise with this system [79].

An OROS[97] four channel analyzer *OR34* can actively monitor vibrations within and surrounding the experiment. Up to four *Dytran 3055B2* acceleration sensors are placed on different spots (granite, gantry, external SIOS laser interferometer, PF2/UCN platform). The recorded spectra can be analyzed via *OROS NVGate*, *Audacity* or *Mathematica*. More information can be found in Nico Einsidler's Bachelor thesis [79](p.10-11).

[97] OROS S.A.S.U.. 23 chemin des Pres, 38240 Meylan, France, www.oros.com (21.4.2021)

3.7. Auxiliary systems

3.7.1. Linear gauges

The linear gauges (LG) from Mitutoyo[98] measure the height of a surface relatively [139](p.70), [159](p.11-13), [96](p.13-14). They consist of a controller, a cable and the gauge itself. The linear gauge has a small round tip. A spring pushes it outwards with a small force. A small pressure can move it up to 10 mm inwards (e.g. placing it on a surface). A laser-hologram measurement system within the gauge records the movement and calculates the current position relative to an arbitrarily chosen fixed point. Rapid movement of the tip or reaching the ends of the range can result in a random offset. The tip needs special care. Forces perpendicular to the vertical direction (direction of movement) can damage the system permanently by inducing a non-linearity.
For measurements either the gauge is fixed to a holder and the surface moves vertically (e.g. a mirror on a piezoelectric stage) or the linear gauge is manually moved from one surface to another. In a fixed position the accuracy is only limited by the linear gauge itself (0.2 µm), the movement of the surface (active PI-tables vibrate slightly in order to stay at a constant height) and the mechanical stability of the holder. The holders can slowly induce a drift, therefore they are set up and real measurements are taken after many hours of slowly settling to a stable position (e.g. after one night).
To move linear gauges they are fixed to holders with a small granite block as a foot. The flatness of this granite and the surface below additionally increase the uncertainty. If the surface is also a granite block which has a flatness below 1 µm, the effect is neglected. If the surface is metal (e.g. the aluminum bottom of the *q*BOUNCINO vacuum chamber), the measurement is not reliable anymore due to the large uncertainty. A second additional source of uncertainty is the cable between the gauge and its controller. Changing mechanical stress due to the movement changes the measurement and induces drifts up to few µm. Especially force on the connection point of the cable and the gauge can easily change the measured value up to 4 µm. To reduce all these effects the cable is first fixed with Kapton tape to the holder as a strain relief and also to the path from the controller to the gauge to have the cable hanging with the least stress possible in all positions during the movement. The biggest influence is the operator moving the gauges because every snatchy movement adds an offset to the measurement. Skilled and patient students can reach a repeatability of below 0.2 µm for small distances (10 mm) and only slightly more for much longer distances [159](p.18).
Linear gauges are used to measure the relative step height between two mirrors by moving back and forth between both sides of the gap. Comparing the measurements on both ends of the gap results in a relative tilt between both mirrors. Carina Killian describes in her project thesis [159](p.13-15) how to calculate step height and tilt and their measurement errors with multiple repeated measurements. The results can be compared to the measurements of the capacitive sensors, particularly to check the correctness of the step calculation algorithms including the gantry movement corrections (see section 3.5.4).
Absolute measurements of a surface height are also possible. To complete this task the starting point is a height gauge block standing on the flat granite block surface. An accuracy below 1 µm is possible.
Three fixed linear gauges positioned on three different corners can monitor the movement of a surface. For an absolute measurement they need a reference point. This method applies to various aligning processes: clamping absorbers, electrodes [122] or the complete mirror setup. In order to clamp an absorber, they are gently placed on the mirror and the linear gauges use this position as reference plane. After placing spacers between the glass plates and clamping them, the gauges display the gap and also their slow drift to a final value. For electrodes, a position on glass spacers is used as reference, which induces an additional uncertainty due to the thickness of the spacers. To align the mirror setup three linear gauges are placed absolutely referenced to a 100.000 mm gauge block on to the corners of the first region. The coarse adjustment positions the mirror surface approximately to a height of 105.00 mm (±10 µm) with the PI-table actively regulated to its range center[99]. After waiting to stabilize the drift of the coarse adjustment, the PI-table sets the exact surface height which is displayed by the gauges. All further regions are adjusted in the following way: the next region is placed as close as possible to the previous one (distance ⩾30 µm). Two linear gauges are referenced via the gap and the third one absolutely on the other side. The adjustment procedure is similar to the previous procedure. In the end, the correct height position is checked again with the gauges and if necessary, the procedure has to be repeated.

[98] Mitutoyo Corporation, 20-1, Sakado 1-Chome, Takatsu-ku, Kawasaki-shi, Kanagawa 213-8533, Japan, www.mitutoyo.com (24.4.2021)
[99] If the PI-table is turned off, it rests at the bottom of its range. The adjustments goal has to be set half the PI-table's range lower than the targeted mirror surface height.

The final settings of the PI-tables are used the entire beam time and checked again afterwards. This method was used in 2017 and 2018 to align the mirrors because the capacitive sensor step control did not compute trustworthy results which withstand a comparison measurement with the linear gauges. In 2019, Jakob Micko implemented some changes in the step control (polynomial instead of linear fitting of the mirror surface). The adjusted steps were conclusive with the linear gauge measurements. Since then, this method has been used as it was originally intended.

All used linear gauges have a range of 10 mm and an accuracy of 0.2 µm. The resolution and the measuring force depend on the model. In Grenoble, we have three *LGH-110C Laser Hologages* with a resolution of 0.01 µm and a force of 0.12 N. In Vienna, there are one *LGH-1010C Laser Hologage* and two *LGH-1010 Laser Hologages* with a resolution of only 0.1 µm each [225](p.17). The applied force is 0.1 N and 0.45 N respectively.
The controllers at the ILL are three *EH-102S*. At the ATI, we have an *EH-102P* and an *EF-12PRH* controller. It is possible to connect them with a special RS-Link cable only to read out one controller.

3.8. Data acquisition

The main data acquisition is done by a server. Most of the device controllers are connected either via Ethernet or via USB to the server. Due to the number of devices three USB hubs with 8 sockets each and two Ethernet switches with 24 sockets each bundle the inputs. Some devices have only an analog input and output (tilt sensors, PF2-turbine signals, B-field sensors,...). For the communication with them so-called *logic boxes* or DAQs are installed [285]. Nearly all described controllers, devices and electronics (including the detector fridge) are concentrated in two racks. After the contamination in 2017, various cables were unplugged during the clean up. In winter 2018, we used the opportunity during the reassembly of the organically grown wiring to establish again an efficient and structured cabling. Especially, the cable length was reduced as much as possible. This is very crucial for the USB network which therefore increased its performance (more maximal operable devices).
The servers themselves consist of two identical customized computers called *Pinea* and *Neron*[100]. One is operating the complete RAMSEY^{TR}-setup via a complex LabView program (since the beginning of the RAMSEY^{TR}-setup *Neron* has been used for this task), the other is a backup. In the meantime it can independently operate a second setup (e.g. *q*BOUNCINO) or different devices from the same setup.
For data storage a Synology[101] Network Accessed Storage (NAS) with 4 hard drives (RAID 10 cluster) is also connected to the servers. In 2014, Jörg Herzinger configured the hardware and installed a *syslog* system during his master thesis [115]. All servers send their data to the NAS which gives the data a universal timestamp[102], stores it by date and device and each night compresses all data from the previous day. Additionally, three backups are made (external hard drive, ILL - data server, ATI - network drives). With the Herzinger's *Mathematica* package *Syslog reader* the data can be used for the data analysis [115]. In 2019, Julius Piso developed a database based on *mongoDB* during his Bachelor's thesis [241](p.13-16) which once filled with the data provides a better and faster access to them. I used both methods for the data evaluation. The appendix section A.2 presents a detailed description of this analysis.

3.8.1. Jörg's box

The so-called *Jörg's box* is a combination of a power supply and a ADC/DAC card. The power supply provides ±12 V. The ADC/DAC card is a *NI USB-6229 OEM* with 12 analog inputs and 12 outputs (16-bit) [115](p.32-33,45-). The electronic workshop of the ATI built a housing for the *Jörg's box*. All inputs and outputs are BNC sockets. This logic box is used for the tilt sensors and the PF2 control.

[100] Two summits in the Chartreuse visible from Grenoble.
[101] Synology Inc., 9F., No.1, Yuandong Rd., Banqiao Dist., New Taipei City 220632, Taiwan, www.synology.com (24.4.2021)
[102] Therefore, all data are synchronized but this does not mean that they are synchronous to the real time. The difference can be up to 8 min depending on the clock of the NAS.

3.8.2. LabView

LabView is a visual programming language from National Instruments[103] (NI) which enables a very modular architecture. Many manufacturers of the devices (e.g. controllers, sensors) provide libraries for LabView in order to remotely control them. These subprograms or also called *subVIs* can be easily integrated into complex measurement control systems. Due to this advantage nearly all components within the RAMSEY^{TR}-setup are controlled by a single LabView project.
Tobias Lins [178](p.63-66) wrote one of the first parts which were able to control the SIOS laser interferometer, AFG, PI-tables, miCos, and some ADC (for e.g. the PF2 signals) and DAC with a central data storage of all these components. Over the next few years multiple different programs on various PC's were used to operate all components of the *q*BOUNCE-setup.
Since 2014, Jörg Herzinger rewrote and unified the LabView project during his master thesis [115]. It has a modular architecture which makes it easy to add new components. In addition, he implemented the *syslog* system for the data acquisition which also provides an easy and structured access to the data. A version control system (*git*) is in place to save the changes in the programming. With LabView it is only possible to handle the files. Mergers within one file, as possible for texts, would result in errors.
Each implementation of new devices and features developed the main program further. In particular during beam times, necessities often increased the development at the expense of good style. Changes of the program during preparation times are better documented (e.g. SIOS laser interferometer [136]). Paul Klieber presents a short introduction of LabView and the implementation of a new device in his Bachelor's thesis [162](p.12-15&28-33).

The LabView project is operated with a *main* window and a *visualization*. In the *main* program all devices and additional measurement programs can be turned on or off and this program starts or terminates the corresponding subVIs. There, the configuration of the devices is loaded too (after changing the proper config file) and an ID is assigned to each measurement. Via the *visualization* most devices display their measurements and can be operated (depending on the programming status of the device). The devices and their assigned subprograms are running in the background and only for very specific tasks or tests have to be displayed.
For measurement routine of various devices (e.g. miCos movement and CapSens measurements) a script mode is available. This script contains simple job commands to operate specific devices and basic codes (if-cases, loops, variables).

3.9. B-field and polarized measurements

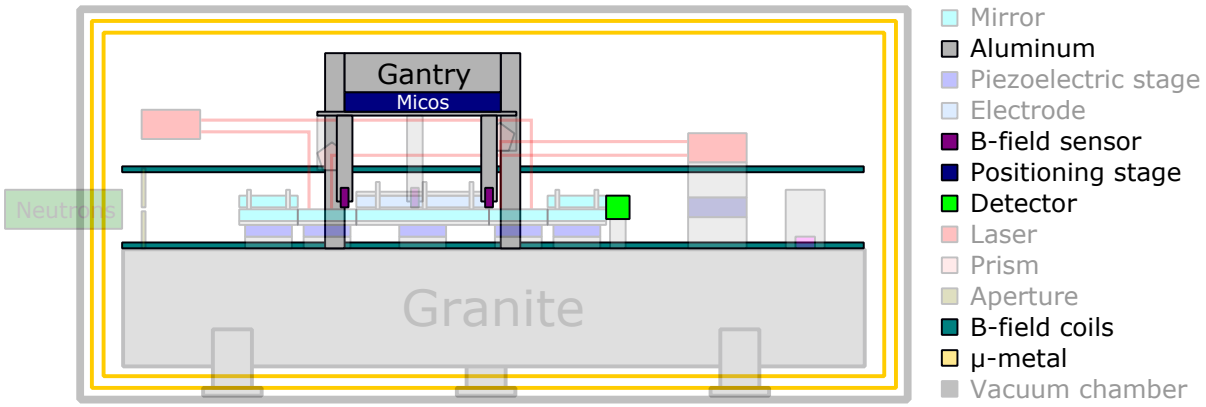

Figure 3.25.: A schematic view of the components to produce, shield and measure magnetic fields within the RAMSEY^{TR}-setup

[103] National Instruments Corporation, 11500 N. Mopac Expressway, Austin, TX 78759-3504, United States, www.ni.com (13.11.2023)

3.9.1. µ-metal shielding

Neutrons are expected to have no electric charge, a very small electric dipole moment and are very hard to polarize. These properties reduce disturbances of the electric field to almost zero. On the contrary, the magnetic dipole moment of the neutron due to its spin interacts strongly with any surrounding magnetic field ($\vec{m} = -60.3077\,\mathrm{neV/T}$ [300]). Not only such fields can rotate the spin, they can also change the energy of the neutron, especially within strong gradients. This can lead to disturbance of the gravitationally bound states even so strongly that they could induce state transitions. Therefore, the magnetic field around the setup should be reduced to a minimum to be able to ignore this systematic effect.
Within the reactor hall the homogeneous Earth's magnetic field is expected with a field strength of 50 µT to 100 µT. Additionally, there are stray gradient fields from the structure itself, the huge rotatable hall crane and neighboring experiments with similar strengths [44](p.30-37).
A reduction to rest field gradients of around 1 µT/m would reduce possible effects to $-0.060\,307\,7\,\mathrm{peV/m}$. There are two possible ways: either to use an active coil system which produces a field opposite to the remaining field or a passive shielding, which is realized with µ-metal. After a special thermal treating, this nickel-iron alloy can have a relative magnetic permeability up to 100 000 [318](p.10). This pushes the surrounding magnetic field lines within the metal. If the µ-metal forms a box, the contained volume has a strongly reduced field. Mechanical stress on the µ-metal changes its properties strongly by reducing the permeability by orders of magnitudes.
Modern nEDM experiments have to use both methods in order to achieve their measurement goals. In GRS the requirements are much more relaxed. It is sufficient to use a µ-metal shielding and take care which materials are used within the field free region. Only non-magnetic metals or vacuum compatible isolators should be used (aluminum, copper, brass, glass, granite, ...). Stainless steel usage is critical. Only *V4A* steel (*316L*) should be non magnetic. This has to be checked for every piece because mechanical stress can induce magnetization. Glowing these parts can reduce this to an acceptably low level. In addition, electric motors within the shielding are a strong source of stray fields. They have to be shielded if they are necessary for the setup (miCos table of the gantry).
The RAMSEY$^{\mathrm{TR}}$-setup has a double walled µ-metal shielding on the inner surface of the vacuum chamber surrounding the granite and all devices on top of it [254](p.73-77). Magnetic Shields Limited[104] designed, manufactured and helped to assemble the shielding. Additionally, they provided a third layer which could be placed outside the chamber in case the shielding does not reach the needed strength.

3.9.2. Magnetic field sensors

Two *FLC3-70* flux gates[105] from Stefan Mayer Instruments[106] (SMI) measure the residual magnetic field within the vacuum chamber [262](p.4), [318](p.12), [40](p.5-6). Their assigned places are on the moving parts of the gantry close to the *B* and *B2* capacitive sensor positions (see figure 3.21). Their vertical position is 89.5 mm above the granite measured from the lowest part of the cylindrical sensor. The time resolution is from DC to 1 kHz in three axes (the ADC can limit it at lower frequencies). The maximum measurement range is ±200 µT for all three axes with an accuracy of ±1 % ± 0.5 µT [42](p39-40).
The power supply can provide a voltage from 4.8 V to 12 V. The conversion factor between voltage and magnetic field is ±35 µT/V independent of the power supply. This enables a range between ±84 µT to ±210 µT depending on the supplied voltage: During the measurements (2017-2019), a power supply from the ATI electronic workshop provided 5.001(1) V. Polarized measurements need a higher voltage supply (up to 12 V to have the broadest range or only 9.9 V to use a suitable ADC range with the higher resolution) to be able to measure the produced magnetic field from the coils.
The voltage signal is symmetric around the OUT- signal $\left(V_{\mathrm{OUT\text{-}}} = \frac{V_{power} - V_{\mathrm{GND}}}{2}\right)$. This voltage is equal to a zero surrounding B-field. The maximum field is displayed with a voltage equal to GND or the power supply depending on direction. The correct conversion between the signal and the magnetic field is:

$$B_{axis}[\mu\mathrm{T}] = f_{conversion}[\mu\mathrm{T\,V^{-1}}] \times (V_{axis}[\mathrm{V}] - V_{\mathrm{OUT\text{-}}}) \tag{3.63}$$

[104] Magnetic Shields Limited, Headcorn Road, Staplehurst, Tonbridge, Kent, TN12 0DS, United Kingdom; www.magneticshields.co.uk (1.6.2021)
[105] Due to their shape they are called *Tonnen*.
[106] Stefan Mayer Instruments, Wallstraße 7, 46535 Dinslaken, Germany; www.stefan-mayer.com (13.11.2023)

Six cables are attached to the *Tonnen* sensors and are bundled into a 3x2 pin *Molex*-socket connector (3 mm grid). These six cables have a color assignment:

- 1 Black: V- = GND
- 2 Yellow: X
- 3 Red: V+ = power supply (5 V)
- 4 Green: OUT- = $(V_+ - V_-)/2 \pm 1\%$
- 5 White: Y
- 6 Blue: Z

A 15 stranded cable (one side a sub-D plug, the other side unbundled to suitable *Molex* connectors) can connect up to three flux gates to the read-out electronics. Since autumn 2017, the cabling and the electronics have been completely replaced due to many flaws of the predecessor (broken wires, not vacuum safe, broken LabView controller,..). Matthias Winder used it for the first time for the characterizations of the new coils [318].

MFS-3A flux gates "le Bleu"

There exist also *MFS-3A* magnetic field sensors from Ametes for measuring higher fields up to ±7.3 mT [42](p.39-44). They are used to measure the fields within the detectors during the polarization measurements with fields up to ±6 mT during polarizing the soft iron foil. One is built into the M-detector [32](p.13). The sensor needs a 5 V power supply and has an analog output signal for each direction with zero at half the supplied voltage. The sensitivity is 280 mV/mT. The resolution is ±10 µT and the accuracy ±3 %.

DAQ for sensors

Since autumn 2017, a new *USB 2408* ADC from Measurement Computing[107] has been the read-out electronics for the flux gates [318](p.11,13). Beside others the main reason was the increased resolution from previously 16-bit to 24-bit. A 5 V power supply and therefore a range of the sensors of ±87.5 µT results in a theoretical resolution of 5.215 pT instead of 1.335 nT for 16-bit. Measurement ranges of the *USB 2408* are ± 10/5/2.5/1.25 V. The absolute accuracies of 300 µV (at ±5 V) and 200 µV (at ±2.5 V) correspond to ≈ 10.5 nT and ≈ 7 nT respectively.
There exist two possibilities to connect the magnetic field sensors to the ADC *USB 2408*. Either the GND of the power supply or the OUT- signal of the sensors is connected to the AGND (analog ground) of the *USB 2408*. For the first option, the range is set to ±5 V for a signal range of 0 V to 5 V, which reduces the achievable resolution. The second possibility is the more optimal way. There, the signal is symmetric around zero and an optimal range of ±2.5 V can be set with a higher resolution. Both options are already implemented into the corresponding new written LabView VI. No matter which possibility is chosen, all AGND (analog ground) of the *USB 2408* have to be wired to each other because some are not internally connected.
In December 2017, during the test of the new large guide-field coils (see section 3.9.4), Mathias Winder [318](p.24-28) and I used the first possibility. This setting was further used during the beam times in Grenoble. The new LabView VI for the readout of the *USB 2408* is working and storing to the syslog but was not fully integrated into the *main.vi* of the *q*BOUNCE-LabView.

Cabling sensor-ADC

The cabling consists of three parts (all bought and assembled in January, 2018): a grid connector to bundle the power supply and all wires from the *USB 2408* to a conventional 15-pin D-sub cable, a long D-sub cable to connect the grid to a vacuum feedthrough, and a vacuum safe cable within the vacuum chamber to connect the sensors.

[107] Measurement Computing Corporation, 10 Commerce Way, Norton, MA 02766, United States, www.mccdaq.com (28.4.2021)

The cable grid connects the ADC and the power supply with a female D-sub plug. Two different versions of this grid represent the connection possibilities. One grid consists of the female half of a standard 15-pin D-sub cable. At the other end the strands are separated and bundled to four 6 pin *Molex* connectors. Each connector represents one sensor (with each X, Y, Z, and OUT- signal). The forth connector represents the power supply. The additional pins on these connectors are to connect the analog ground (AGND) of the *USB 2408*. All four connectors are plugged into pin connectors screwed into the ADC. This makes it easier to change the grid. The vacuum cable from the sensor connector to the vacuum flange (male 15-pin D-sub socket) is a Teflon coated 15 stranded flat band cable. It has one female D-sub end and the other side is split into three parts with *Molex* connectors at the end to connect it to the sensors. Additionally, wires distribute the power supply and the GND to all three connectors[108]. A dummy connector is also available for use outside the vacuum chamber instead of the expensive vacuum clean cable.

The D-sub pin assignment outside the vacuum is:

- 1 - brown: sensor 1 X-Dir
- 2 - red: sensor 1 Y-Dir
- 3 - orange: sensor 1 Z-Dir
- 4 - pink (pale): sensor 1 OUT- min
- 5 - yellow: sensor 2 X-Dir
- 6 - dark green: sensor 2 Y-Dir
- 7 - cyan: sensor 2 Z-Dir
- 8 - dark blue: sensor 2 OUT- min
- 9 - pale blue: sensor 3 X-Dir
- 10 - violet (dark): sensor 3 Y-Dir
- 11 - gray: sensor 3 Z-Dir
- 12 - white: sensor 3 OUT- min
- 13 - black: GND
- 14 - brown-black: power supply
- 15 - red-black: empty

3.9.3. Measurement principle

Space-time torsion models, axions and other *New Physics* models predict a spin-dependent transition of the gravitational state [8, 132, 133, 165]. A beam of polarized neutrons can test these models and set limits on them [139](p.86-89). Within *q*BOUNCE this is realized in the following way [267](p.29-30): a pair of large Helmholtz coils (guide field) quantizes the spin of the UCN beam during the flight through the setup. At the end, a polarization-sensitive detector measures the neutron count rate for only one spin polarization. The other spin component is absorbed in a soft iron coating on the detector entrance window [139](p.89-90). These measurements need a very high count rate (>30 mcps). More than half of the neutrons are lost due to polarization. Additionally, the polarized foil has only a high polarization for very slow neutrons (<7.5 m/s). The remaining count rate is 30 % of the unpolarized beam. Gunther Cronenberg et al. characterized the velocity dependence of the utilized foil in 2012 during TEST-2034 [65](p.73-77). In spring of 2021, Hugo Wetter remeasured the same spin polarization foil built into the M-detector as his master thesis at the PF2/TEST beam in the beam time 189-21/1 [315].
Additionally, a power supply, relays, magnetic field sensors and ADC are necessary. The power supply provides the current for the magnetic coils. The relays can switch the direction of the produced magnetic field and the polarization selection of the detector independently. The magnetic field sensors together with the ADC either measure the rest magnetic field in the chamber or a LabView controlled feedback loop stabilizes the produced and measured magnetic field by adjusting the power supply. In the future, additional spin flippers in the oscillating regions could enable to change the spin and the gravitational states simultaneous which is interesting for some BSM theories.

[108] Take care the wire assignment is mirrored within the vacuum chamber due to the vacuum feedthrough.

3.9.4. Magnetic field coils

Beside the polarizing detector, the magnetic coil pair is the most important part of a polarized measurement. It also displays the development of the *q*BOUNCE-setup and its increase in size and complexity. There exist three generations of coils for each setup generation (GRS^{TJ}-setup, RABI^{GC}-setup and RAMSEY^{TR}-setup) adapted to their vacuum chamber size at the time (see figure 3.26).
The smallest coil pair has the dimensions of only 360 mm × 360 mm and only covers one region. Measurements in 2011 led to limits for hypothetical spin-dependent particles [139](p.89-92). Tobias Rechberger prepared measurements with the Rabi coils but they were discarded in favor of longer and more successful measurements of the quantum bouncing ball of Martin Thalhammer [299] and the development of the RAMSEY^{TR}-setup. He also kept free space within this setup for a new larger coil pair.
Patrick Schmidt first calculated the coils' parameters [267]. He estimated the field of the coils with a superposition of fields of round wires in *Mathematica*. Mathias Winder simulated a 3D model in the finite elements program *CST Studio Suite*. Further, he characterized the newly wound coils in 2017 in his project thesis [318]. The winding team were Mathias Windner, Anselm Balthasar, Paul Feichtinger and Christoph Mühlmann under my supervision. In May 2018, the coils were shipped to Grenoble and in 2019 Jakob Micko finally built them into the RAMSEY^{TR}-setup.

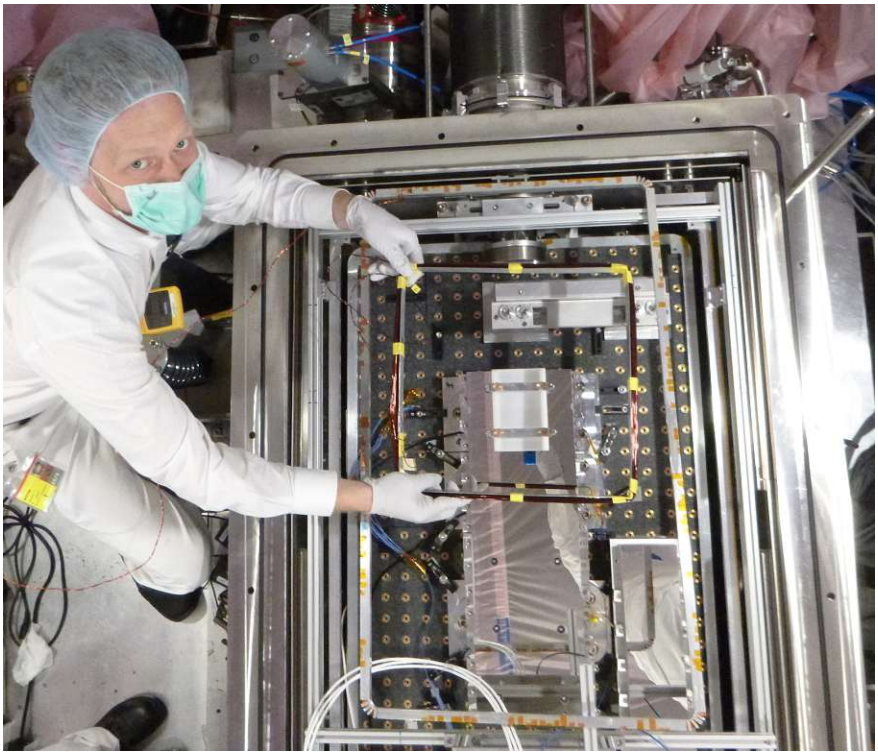

Figure 3.26.: Reunion of all three coil generations in June 2019 at the PF2. The largest coils are already built into the RAMSEY^{TR}-setup and only partially visible.

Ramsey magnetic field coils

The coils can only be placed close to the edge of the granite which has a surface area of 1900 mm × 700 mm. This also defines the outer dimensions of the coil and the length of one winding L to ≈ 5.2 m. The mid distance between the pair of coils has to be at mirror surface height, at 105 mm above the granite surface. The lower coil lies on the granite plate and the upper coil is fixed with aluminum clamps to the ITEM frame of the external SIOS laser interferometer.
The designed field strength B_z should be between 100 and 200 µT and should have as small as possible gradients. Due to constrained geometry only the winding number N and the current I set the field strength ($B_z \propto NI$). The proposed values are 150 windings and a current of approximately 330 mA. Simulations and preliminary measurements show that this current corresponds to a magnetic field of 130 µT at the coil center [318](p.14,29).

The installation within the vacuum chamber reduces the heat transfer of the coils. As an approximation, only thermal radiation can cool the coils which heat up due to the wire resistance. Therefore, the wire diameter d is a very important parameter of the coil design. However, geometric constraints provide upper limits of the wire diameter. The final temperature of the coils is defined by the balance between the heat production and the radiation cooling [267](p.35) [318](p.8-9):

$$P = UI = I^2R = \epsilon\sigma A_{coil}(T_{coil}^4 - T_{chamber}^4) \tag{3.64}$$

$$P = I^2\frac{LN\rho_{\mathrm{Cu}}}{A_{wire}} = \epsilon\sigma A_{coil}(T_{coil}^4 - T_{chamber}^4)$$

$$P = I^2\frac{4LN\rho_{\mathrm{Cu}}}{d^2\pi} = \epsilon\sigma L(N_{layer} + N/N_{layer})d(T_{coil}^4 - T_{chamber}^4)$$

$$\frac{4I^2N\rho_{\mathrm{Cu}}}{d^3\pi\epsilon\sigma(N_{layer} + N/N_{layer})} + T_{chamber}^4 = T_{coil}^4 \tag{3.65}$$

The radiation cooling is described by the Stefan-Boltzmann law with its corresponding constant $\sigma = \frac{2\pi^5 {k_\mathrm{B}}^4}{15h^3{c_0}^2}$. ϵ is the degree of emission, A is either the surface of the coil or the cross section of the wire.
The built Ramsey coils consist of an aluminum profile, edges carved out of aluminum and a copper wire [318](p.11,21-23).
Aluminum has only an ϵ of 3 % (painting the coil profile black could increase the emission). The profile itself is u-shaped with a width of 15 mm, a height of 20 mm and a wall thickness of 2 mm. The edges have the same gap and wall dimensions and a curvature of 22 mm. The profile and the edges are welded together and form the frame of the coil. The outer dimensions of the frame matches the size of the granite surface.
The copper wire is a *Damid PE Gr2* from Dahréntråd[109] (Reel: 250 No 62, Batch No.: 75628-01) with a diameter $d = 1$ mm and coating of Kapton lacquer. In a test winding Mühlmann and Winder were able to fit ten windings in the 11 mm gap as one layer. However, during the real winding only nine windings per layer were possible due to a not optimal tension of the wire (with higher stress the wire ripped apart). In total, the winding number N is 153 which corresponds to a layer number N_{layer} of 17.
Assuming a specific resistance ρ_{Cu} of $1.709 \times 10^{-8}\,\Omega\,\mathrm{m}$ and a temperature $T_{chamber}$ of the surrounding vacuum chamber of 25 °C the temperature of the coil T_{coil} will rise up to approximately 58 °C (eq. 3.65). The actual temperature will be lower because there will also be heat exchange via the material in contact with the coils and the reflectivity could be improved. In contrast, a wire diameter of 0.5 mm could reach temperatures higher than 150 °C.
At some points vacuum tight epoxy raisin (*Loctite Hysol 9492*) covers the coil in order to keep the wire from unwinding. On both end faces of each coil, temperature sensors[110] are glued in the raisin to monitor the heating of the coils.
For the winding process itself Günther Kratky from the ATI cut a wooden board for fixing the coil frame onto a rotating chair in the reactor hall[111]. The wooden support also secured the coils during their transport to Grenoble. During the winding, two students rotated the board and counted the turns, two cleaned the wire and kept tension on the wire and one guided the wire in the correct position on the coil. Both coils are slightly different and therefore differentiable. Their names are *S* and *H* standing for *Sous* and *Haute* (French for lower and upper coil). The lower coil was first wound counterclockwise and the upper one afterwards clockwise. The visible differences are: the lower one has an additional welding in one of the long profiles (in total nine instead of eight) and it has three beautifully wound corners. In contrast, the upper one has only one nice corner and additionally there is a layer error (the 3^{rd} layer has only eight windings), which made an additional winding necessary.
In Vienna, Mathias Winder manually measured the wire resistance (16.9(1) Ω each coil) and the ratio between the current and B-field of 0.19 µT/mA with a *Hameg 4040* power supply (borrowed from the MONOPOL) and the *Tonne* B-field sensors [318](p.24-28). As simulations suggest the µ-metal within the chamber walls will enhance the produced magnetic field by nearly a factor of 2 [318](p.14-20). More detailed measurements of the resistance under real conditions are necessary to better monitor the coil operation (register coil failures). Magnetic field maps within the chamber with open and closed vacuum chamber top cover will unveil the real relation between applied current and produced B-field. In winter 2021, Christoph Grüner conducted these experiments with a new fully operational *Hameg 4040* power supply in Grenoble as a preparation of the polarized measurements.

[109] AB Dahréntråd Jonslund SE, 465 80 Nossebro, Sweden, www.lww.se/dahrentrad/ (28.4.2021)
[110] PT100 from RS Pro (RS: 611-7788) with an active length of 5 mm and a temperature range of −50 °C to 500 °C.
[111] this chair was already used for winding the guide field of the MONOPOL [107](p.155).

3.9.5. Power supply and operation

Jakob Micko installed the coils within the RAMSEY^{TR}-setup and attached the cabling. Since summer 2020, a new power supply (*Hameg 4040* from Rohde & Schwarz[112]) has been available and operable. It was first used for the characterization of the electrode test setup at the ATI [247] and then shipped to Grenoble in the beginning of 2021.
Its output power is up to 32 V and 10 A at four independent channels. One channel can power up the coils to produce a magnetic field up to 700 µT, all four channels could produce a field up to 2.5 mT. At normal operations one channel with 0.33 A and 5 V is sufficient to produce 130 µT. Another channel provides the current for the detector coil.
The next step of the preparation for a polarized measurement is to program a LabView VI which uses the data of the magnetic field sensors to actively regulate the B-field by controlling the power supply output. This also reduces the influence from time dependencies of the surrounding field. This was already observed in a similar setup at the PF2/VCN-beam with the MONOPOL resonator [44].
Christoph Grüner realized additional controllable relays to switch between the possible spin states. This enables the experimental control to switch between the three possible states (up - down - off) without changing the wiring.

3.10. *q*BOUNCINO

*q*BOUNCINO is a second small scale *q*BOUNCE assembly beside the currently running RAMSEY^{TR}-setup. Its main task is to house systematic tests of new equipment and detectors before they are used in the main setup. *q*BOUNCINO's favored beam side is the platform PF2/TEST with the PF2/EDM as an alternative. This enables parallel experiments to the RAMSEY^{TR}-setup which can measure continuously fully assembled at PF2/UCN beam site. *q*BOUNCINO consists of spare parts and old setup parts. The vacuum chamber is from the RABI^{GC}-setup. In order to reduce weight, the substructure was replaced with an aluminum floor and frame instead of a granite and a complete leveling. The mirrors and their supply are spare ones or from the qBB^{MT}-setup. Various detectors are possible (counter tubes, CR-39,..). The main counter tube detector is the repaired M-detector. A completely independent electronic system (2^{nd} detector sensor card, 2^{nd} quadADC, *Pinea*) provides strict separation from the RAMSEY^{TR}-setup. The lower neutron flux at the PF2/TEST beam prolongates the CR-39 measurements. The missing beam sharing slightly compensates for it.

Magdalena Pieler and Valentin Czamler first assembled the setup between June and October 2018 during the cycles 183-18/2 and 184-18/3 (3-14-385) [236]. They successfully implemented *q*BOUNCINO including the newly repaired M-detector with a new assembled detector sensor card [32] and developed a shielding against the stray neutrons from the neighboring PF2/VCN beam. The first major test was the proof of neutron reflections on a vertical mirror. For this purpose, they used the main mirror of a neutron Llyode interferometer including its holder [89]. One reflection increased the count rate by 16 % [236](p.37). A final CR-39 measurement to determine if the neutron state changes during the reflection failed due to a faulty detector coating. This was the first step to reduce losses due to beam divergence [48]. In the future, more tests with channel-like structure on top of the mirrors are planned in order to completely reduce the losses of the divergence. After testing such prepared mirrors, they could be immediately introduced into the large RAMSEY^{TR}-setup and potentially increase the count rate up to a factor 10. This will lead the way to a *high luminosity* RAMSEY^{TR}-setup and a future storage setup.

In 2019, a Japanese group used *q*BOUNCINO to test their newly developed photo emulsion detectors [206]. These detectors can have a spatial resolution in the order of 100 nm. With the help of the PF2 staff and Jakob Micko, they could also compare it to CR-39 detectors after a state selector. This measurements were repeated in 2021 [155, 302]. In the future, this collaboration will further develop these detectors which can increase the sensitivity of any quantum bouncing ball measurement.

In principle, any tests are possible within the setup up to a polarized Rabi measurement with three spare PI-tables, the spare AFG and many parts from the RABI^{GC}-setup (gantry,...). To simplify the interchangeability between the setup it is important to take care of a modular mirror supply system (coarse adjustments, base plates, PI-table dummies,...) which meets the different mirror surface height specifications.

[112] Rohde & Schwarz GmbH & Co. KG, Mühldorfstraße 15, 81671 München, Germany, www.rohde-schwarz.com (25.6.2021)

4. Measurements

The following chapter contains the results of the measurements conducted during this thesis. The first section gives a short chronological overview. The following two sections describe all auxiliary measurements without and with neutrons. The last three sections conclude with the three GRS-measurement campaigns: RABI-GRS-18, RAMSEY-GRS-18 and the neutron's electric charge measurement Rams$\vec{E}$y.

4.1. Chronological overview of the measurements

In fall 2016, Tobias Rechberger together with students (Rudolf Golubich [101], Jakob Micko [193] and Peter Salajka [262]), his supervisor Prof. Hartmut Abele and the PF2-Team (Thomas Brenner, Peter Geltenbort and Tobias Jenke) started assembling the RAMSEY^{TR}-setup during the first beam time (cycle 180-16/3) of the proposal *3-14-358* [254]. In winter 2017, I joined for the second beam time (cycle 181-17/1, *3-14-358-II*) together with the new bachelor student Nico Einsidler [79] and the experienced master student Jakob Micko [193]. Problems with the laser interferometers (see section 3.6.2) and the step control (see section 3.5.4) obstructed a proper measurement with the full Ramsey-type GRS setup. In the subsequent months Tobias Rechberger, Tobias Jenke (PF2 responsible) and I tried to solve the occurred problems with the students Alice Jardel (oscillations [136]), Anselm Balthasar (detector [32]) and Paul Feichtinger (step control [84]). Delays due to small nuclear incidents and pending approvals prevented a restart of the reactor at the ILL in 2017. Therefore, I completely took over the further developments of the RAMSEY^{TR}-setup as Tobias Rechberger finished his thesis [254]. I used the gained time to prepare future experiments: electric charge measurement - Christoph Mühlmann [208] and Florian Honz [119], polarized-beam measurements - Mathias Winder [318].

In 2018, all major measurements of this thesis were performed in three beam times at the PF2 with the help of its team (Thomas Brenner, Peter Geltenbort, Tobias Jenke and Stephanie Roccia). The following sections will concentrated on this year. The table below presents an overview of the activities at PF2 during this year:

Table 4.1.: Overview of the beam times in 2018

Cycle (proposal)	Dates	Measurement campaign	Students
182-18/1 (*3-14-358-III*)	01.03.-24.04.2018	CR-39, aperture, RABI-GRS-18	LA [14], DS [274]
183-18/2 (*3-14-358-IV*)	22.05.-12.07.2018	RAMSEY-GRS-18, shutter	MP & VC [236]
184-18/3 (*3-14-384*)	03.09.-25.10.2018	Rams$\vec{E}$y	EK [169], CK [159], VP [233]
183-18/2 (*3-14-385-I*)	03.07.-12.07.2018	*q*BOUNCINO	MP & VC [236]
184-18/3 (*3-14-385-II*)	03.09.-01.10.2018	*q*BOUNCINO	MP & VC [236]

During the second half of 2017, it was not possible to access the experiment due to a minor radioactive contamination. Therefore, Tobias Rechberger, Lukas Achatz, Florian Honz and I performed many upgrades and repairs of the setup in the weeks before the first reactor cycle in the year 2018 (e.g. new miCos tables, new cabling due to damages, CapSens linearity tests [254](p.101-106)).
The first cycle (182-18/1, *3-14-358-III*) was dominated by rebuilding the Ramsey setup. Lukas Achatz [14] and Daniel Schuh [274] were the supporting students of this beam time. At the beginning, we disassembled the already completed 5-region setup (Ramsey-2017) in order to newly clamp the absorber regions (see section 3.1.5). The goal was to improve the state selection and we measured it with CR-39 detectors. The results are in section 4.3.2 and in more detail in the master thesis of Lukas Achatz [14]. We also repeated the aperture measurement of 2016 in order to better understand its results (see more in section 4.3.1). In the last weeks, we successfully completed a Rabi-type GRS setup for the first time since 2012 (RABI-GRS-18, see more in section 4.4)[1]. Beside the known transitions $|2\rangle \rightarrow |4\rangle$ and $|1\rangle \rightarrow |3\rangle$, we

[1]The new post-doc René Sedmik joined the experimental team for the second part of this measurement.

measured the transition $|2\rangle \rightarrow |5\rangle$ for the first time. Additionally, we probed the multi-state regime (100-300 Hz) with high amplitudes which enables to test more accurate multi-state theories in the future. I also implemented the so-called *measurement queue* to automatically change measurements. This reduced the changing time from more than 10 minutes down to below 12 seconds exactly between two detector cycles. This also enables to change measurements at any time without needing a student being awake.

The beginning of the second beam time (cycle 183-18/2, *3-14-358-IV*) was dedicated to finalize a 5-region Ramsey-type GRS setup (RAMSEY-GRS-18, see section 4.5). I tested and selected the third region mirror and together with René Sedmik we cleaned and adjusted the complete setup as precisely as possible. After closing the chamber, the finalized RAMSEY^{TR}-setup ran automatically with some minor troubles until the end of the cycle. It proved for the first time that a Ramsey-type GRS setup is possible to realize. The main focus was on the transitions $|2\rangle \rightarrow |4\rangle$ and $|1\rangle \rightarrow |3\rangle$. Also during this time, I started to optimize the LabView measurement control whenever there were no bugs to fix in this software project. At the end of the reactor cycle, Magdalena Pieler, Valentin Czamler and I with the PF2 team built up the *q*BOUNCINO setup (*3-14-385-I*, see section 3.10) at the PF2/TEST beam [236].

In the last cycle of 2018 (184-18/3), the *q*BOUNCINO measurements continued (*3-14-385-II*). After useless exhausting efforts in the beginning, Magdalena Pieler and Valentin Czamler succeeded to show that a vertical mirror as a wall can improve the neutron count rate, which was the first step to store UCNs within *q*BOUNCE. Unfortunately the long CR-39 measurement at the end failed due to a malfunction of its coating. All results of this test campaign are summarized in their project thesis [236].
The main setup at the PF2/UCN beam continued to run the complete cycle (*3-14-384*) with the help of the new PhD student Jakob Micko [194], the project students Elisabeth Kreuzgruber [169], Carina Killian [159] and Vito Pecile [233] and in the beginning also René Sedmik. Due to many efforts for *q*BOUNCINO in the beginning, the RAMSEY^{TR}-setup continued to measure in the same configuration as during the RAMSEY-GRS-18 period before summer. With the full workforce, the setup was changed for the electric charge measurement (built-in of the Rams$\vec{E}$y electrode and assembly of the *electrode test setup* in Grenoble). After cleaning and manual adjusting of the setup, the vacuum chamber was closed again and continued to measure as a Ramsey-type GRS setup with no applied electric field. Before applying a high voltage to the electrodes, we had to integrate the LabView control of the electrode test setup and to provisionally repair severe damages of the setup due to undocumented safety upgrades. During the last two weeks of the cycle, the Rams$\vec{E}$y setup was able to successfully measure with applied electric fields and set a limit on the neutron's electric charge q_n within a GRS setup for the first time ever. The results of the Rams$\vec{E}$y experiment are displayed in section 4.6.

Before the first beam time in 2019, Jakob Micko took over and successfully improved the running RAMSEY^{TR}-setup in the course of the following three years [194]. I only helped him during the preparation and the start of his first beam time as the responsible PhD. Back in Vienna, six bachelor students and I studied the used large Rams$\vec{E}$y electrode in detail and tested possible electrode materials (see section 3.3). An in-depth description of the measurement results can be found in the Bachelor's theses of the involved students: Anika Gassner [96], Julius Piso [241], Jasmin Juroszek [151], Nicole Pruggmayer [247], Paul Klieber [162] and Luca Neubacher [225].

4.2. Stability of environment

For a GRS measurement it is always important that the environmental parameters (vacuum pressure, magnetic field strength, detector performance,...) stay as stable as possible. The exact values play an important role for setting limits to *New Physics* models. In the following sections, I will summarize the results for each parameter and display opportunities to further investigate the influences on its stability. Additional information and measurement results are presented in the appendix A.3.

4.2.1. Vacuum pressure

The main vacuum chamber (as described in section 3.4) is always closed for neutron measurements. Therefore, the vacuum pressure is also a good indicator when the setup was running and how efficient we used the assigned beam time. For multiple changes and adjustments of the setup, we had to vent the chamber. In the future, a higher degree of automation (aperture, state selector, laser optics,...) and optimization of each component (in order to prevent failures) would reduce the reasons to break the

vacuum. This also reduces the efforts for cleaning the chamber and the mirrors which is always necessary before closing and evacuating the chamber.
The Pfeiffer PBR260 sensors typically measured a reached vacuum pressures between 3×10^{-5} mbar and 1×10^{-4} mbar. This is at the lower limit of the other sensor (PCR280). Therefore, it observed always higher values with a lower resolution. The pressure in the prevacuum circuit stabilized around 2×10^{-2} mbar. The beam tube was always evacuated in the beginning or before the reactor cycles and stayed evacuated the complete beam time at a value around 5×10^{-5} mbar.
The following table summarizes the average pressure for each GRS measurement. Within, averages without an error are the median of 10 000 randomly selected data points to avoid biases of the measured high values during the evacuation in the beginning. The appendix A.3.1 displays more detailed information and corresponding figures.

Table 4.2.: Summary of the vacuum pressure for all GRS measurements

GRS measurement	Vacuum chamber PCR280		Vacuum chamber PBR260		Pre vacuum PCR280		Beam tube PBR260	
	Max-Min 10^{-5} mbar	Average 10^{-5} mbar	Max-Min 10^{-5} mbar	Average 10^{-5} mbar	Max-Min 10^{-2} mbar	Average 10^{-2} mbar	Max-Min 10^{-5} mbar	Average 10^{-5} mbar
RABI-GRS-18-I	12.7 - 7.06	9.8(13)	7.12 - 5.57	6.28(44)	2.15 - 1.83	1.97(9)	4.89 - 3.89	4.03(8)
RABI-GRS-18-II	275 - 8.01	12.6	191 - 5.72	6.86	15.4 - 1.77	2.1	5.94 - 4.31	4.60(20)
RAMSEY-GRS-18	62 - 5.01	9.6(20)	10.8 - 2.46	2.9(1)	3.86 - 1.28	1.4(3)	7.36 - 4.72	5.9(6)
RAMSEY-GRS-18-Fall	1 bar - 14.60	18.1	1 bar - 6.24	9.8	3.42 - 0.87	2.0(7)	60.5 - 6.50	7.1(22)
Rams$\vec{E}$y-0 V I	995 - 13.50	16.8	667 - 6.06	9.13	27.8 - 1.83	2.2	6.43 - 4.72	5.36(31)
Rams$\vec{E}$y-0 V II	1 bar - 8.01	12	1 bar - 3.34	4.43	1 bar - 1.12	1.6	5.55 - 4.68	4.98(11)
Rams$\vec{E}$y-HV	9.07 - 5.01	7.0(10)	3.31 - 2.29	2.73(27)	1.46 - 1.18	1.32(6)	5.27 - 3.92	4.54(22)

Studying the vacuum pressure and its characteristics (e.g. evacuation speed, final pressure) enables to learn more about the vacuum setup (e.g. pump performance, outgasing of new components). Daniel Schuh did such an analysis for the test measurement during the cycle 182-18/1 (3-14-358-III) as his project thesis [274]. Robin Havlik continued his works [112]. Jasmin Juroszek also tried to fit functions to the evacuation curves to learn more about the processes involved in the evacuation (e.g. outgasing or geometries) for the *electrode test setup* in Vienna and the two used *q*BOUNCINO chambers [151]. Such analyses are good starting points for further developments. One goal would be to implement the analysis directly in the LabView measurement control system. Checking the parameters already during the evacuation can display possible changes of the setup: e.g. introduction of new parts with different vacuum compatibilities, general cleanliness, vacuum pump performances, detection of vacuum valve leaks.

4.2.2. Leveling

As described in section 3.5.1, the active leveling keeps the granite surface horizontal and with it the mirror surfaces. As an important preparation, we performed a relative and an absolute calibration by turning the tilt sensor in 90° steps and using a mechanical high precision bubble level between the RABI-GRS-18 and RAMSEY-GRS-18 measurement. I used similar evaluation techniques as previous works [287](p.42-43) and [86](p.16-18) for this evaluation performed after the beam times. It results in a tilt sensor's offset of $(x, y) = (6.5(2)\,\mu\text{rad}, 100.9(2)\,\mu\text{rad})$ using all 22 data points[2]. During the beam times, we used the fast evaluated values of $6(11)\,\mu\text{rad}$ and $108(8)\,\mu\text{rad}$ for the tilt angle targets in x and y direction respectively. The difference in the offset is still below the absolute accuracy of 25 µrad of the bubble level. As a direct comparison, we measured a slightly tilted surface with both devices. The results were $(48(12)\,\mu\text{rad}, -303(2)\,\mu\text{rad})$ and $(50(25)\,\mu\text{rad}, -350(25)\,\mu\text{rad})$ respectively which agree well. In the worst case of a not corrected tilt of 50 µrad, the gravitational acceleration would shift by a factor of $\Delta g/g = 1.25 \times 10^{-9}$ which is not measurable at the moment with GRS and therefore it is negligible.
Jakob Micko repeated this calibration with an upgraded tilt sensor bearing (three legs for a defined contact to the granite surface) and a better water level [194](p.30-31) in order to reduce the absolute errors below 10 µrad. This calibration should be redone annually and there are possibilities to improve its software implementation and its documentation (e.g. evaluation already within LabView).

The leveling itself is only active during vacuum conditions. During venting, the heavy granite block moves between 100 µrad and 250 µrad in both tilt directions due to changed mechanical stress of the air pressure. These tilt values are more than the piezoelectric stages underneath the granite can counteract.

[2]Using only a subset (e.g. only using a consecutive set of 5 points) changes the fitted values up to 5 µrad.

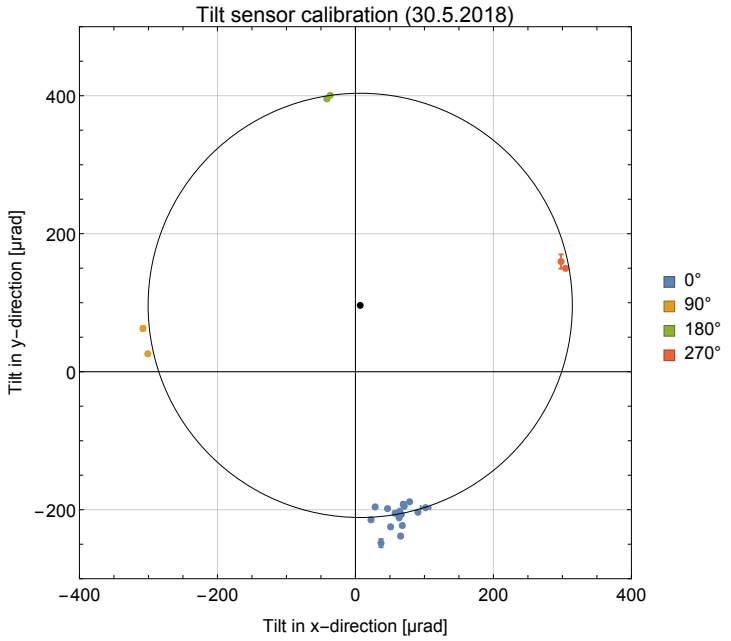

Figure 4.1.: The calibration of the tilt sensor before the RAMSEY-GRS-18 measurements. The fitted circle (radius and rotation angle) represents the alignment of the granite surface compared to the sensor. The circle's midpoint displays the offset of the tilt sensor.

Therefore, we adjusted the coarse alignment of the vacuum chamber always after the evacuation. During vacuum conditions, the granite surfaces tilts back to its aligned position and active leveling is possible again. The PID feedback loop stabilizes the granite surface aligned to the target position, which is set to the offset of the tilt sensor. Movements of the cranes (niveau C or niveau D) or heavy forklifts, cause strong disturbances. These are visible as spikes in an overview plot when the PID is too slow to counteract these external forces. The movement of the 35 kg gantry stirs the few tonnes of granite stone. Due to the slow movement the active leveling is able to compensate it and this effect is only visible in the voltage setting of the piezoelectric stages. As an example figure 4.2 displays the tilt measurement during the beam time 184-18/3 where all the described phenomena are visible. The appendix section A.3.3 contains all overview plots of the other reactor cycles.

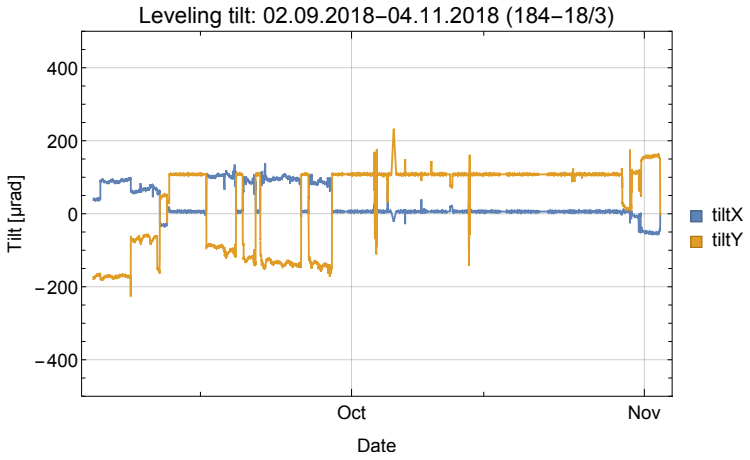

Figure 4.2.: The horizontal alignment of the granite surface during the Rams$\vec{E}$y measurements. In the beginning of the cycle, it is recognizable when we measured and activated the leveling and when the vacuum chamber was vented and the surface slowly drifted. For the most part of the second part of the cycle, the chamber was closed and the granite surface was aligned except for two ventings and some disturbances (spike-shaped artifacts). During vacuum conditions, the active leveling kept the granite surface aligned to (6 µrad, 108 µrad).

Already in 2008, the leveling reached a relative precision of 0.67 µrad [287](p.41-47). Similarly, the RABI^{GC}-setup reached an uncertainty of 0.5 µrad [86]. The RAMSEY^{TR}-setup reached a value of 0.1 µrad in the quiet surrounding of the ATI in Vienna during the first tests in 2016 [189](p.17-27). Tobias Rechberger reported a similar relative adjustment precision of the full setup in Grenoble in 2017 [254](p.70-72). In the following, I present the evaluation of the leveling during the measurements in 2018. As seen in figure A.23, the relative precision is worse than the previously measured ones. The main cause are the long intervals used for the statistical analysis which contain multiple external disturbances. The table 4.3 summarizes the average values for all GRS measurements in 2018.

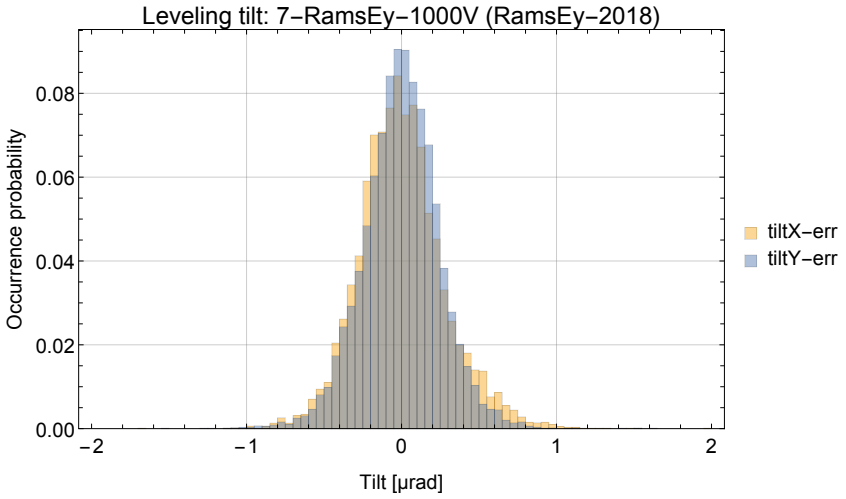

Figure 4.3.: Histogram of the offsets to the target position during the beam time 184-18/3.

Table 4.3.: Summary of the tilt sensor's readings for all GRS measurements in 2018

GRS measurement	Temperature [°C]		Tilt X [µrad]		Tilt Y [µrad]	
	Min-Max	Average	Min-Max	Average	Min-Max	Average
RABI-GRS-18-I	23.29 - 26.97	26.38(49)	-73.5 - 104.6	0.4(52)	-26.7 - 181	0.1(222)
RABI-GRS-18-II	22.22 - 27.71	27.10(59)	-12.8 - 15.7	-0.1(18)	-13.9 - 36.6	0.1(40)
RAMSEY-GRS-18-I	26.74 - 28.33	27.62(42)	-42.8 - 18.9	6.03(77)	12.6 - 183.9	118(24)
RAMSEY-GRS-18-II	28.34 - 29.15	28.41(29)	-11.0 - 42.3	6.00(51)	45.7 - 191.0	108.0(24)
RAMSEY-GRS-18-III	29.46 - 32.06	31.16(68)	-21.8 - 36.6	6.01(46)	46.5 - 219.8	108.0(32)
RAMSEY-GRS-18-Fall	28.43 - 31.20	29.76(97)	1.1 - 124	6.2(470)	28.0 - 176	108(15)
Rams$\vec{E}$y-0 V I	28.97 - 31.09	30.25(80)	-24.6 - 34.7	6.01(77)	54.7 - 143	108.0(11)
Rams$\vec{E}$y-0 V II	29.52 - 31.38	31.11(31)	-31.3 - 84.2	6.0(82)	1.7 - 233	108.0(86)
Rams$\vec{E}$y-HV	29.68 - 31.13	31.03(11)	-13.5 - 19.2	6.01(57)	71.0 - 148	108.0(15)

4.2.3. Oscillations

Comparing the voltage signal input of the AFG (see section 3.6.1) with the measured mirror oscillations determined by the SIOS laser interferometers (see section 3.6.2) gives a good insight into the mechanical properties of the RAMSEY^{TR}-setup. The RABI-GRS-18 measurement provides the best data set for such an analysis due to its wide frequency range which is presented in the following.

Figure 4.4 displays the ratio between the voltage amplitude and the measured oscillation strength a_v. The ratio drop corresponds roughly to the function $A \cdot \nu^{-1.47}$. Therefore, for higher frequencies a higher voltage signal is needed in order to induce the same mechanical amplitude. However, at low frequencies, a very low AFG signal already creates a large movement of the mirror surfaces.
Within the ratio also small spikes are visible which are mechanical resonances. The external laser beam *r2fix* has only one measured resonance around 300 Hz which originated from the piezoelectric tables. The internal laser beams *r2ref* and *scanV* show additional resonances and more noise. These mainly arose from the movements of the optics which are fixed on the granite too. This fact prevents to use

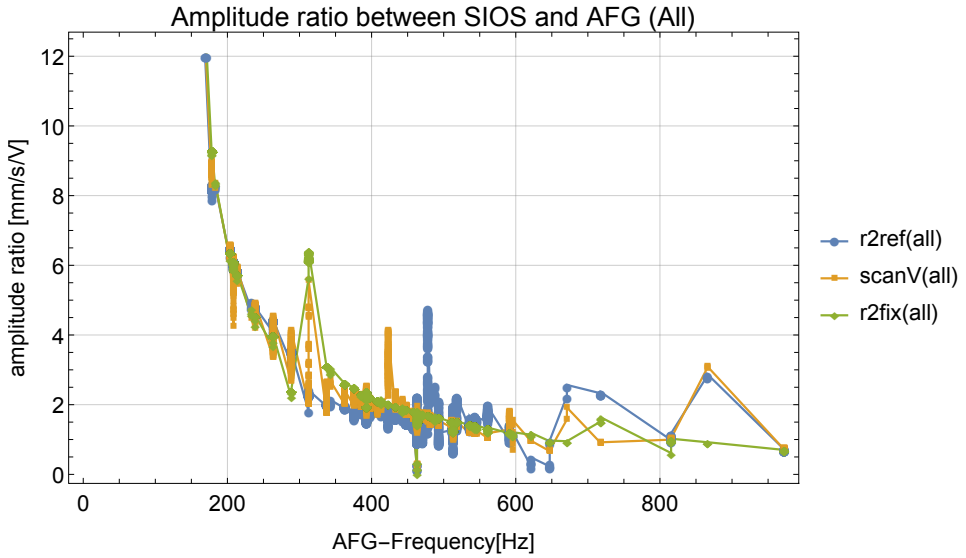

Figure 4.4.: Rabi-grs-18: ratio between applied voltage [V] and induced mechanical oscillation strength a_v [mm/s] with a strong frequency dependency and mechanic resonances (e.g. 300 Hz).

the internal laser interferometer for determining the oscillation strength a_v and phase difference $\Delta\phi$ between the regions. This will be possible if dampers are built into the feet of the gantry and the internal interferometer or it is completely decoupled from the granite as the external interferometer. Additional scanning with a small step size before a beam time could reveal more information about the mechanical resonances within the current setup. In particular, studying the strong resonance regions is important, as it was done in 2019 [167] and led to improvements of the coarse adjustment plates underneath the piezoelectric stages. During all cycles in 2018, such a region was around the transition $|1\rangle \rightarrow |4\rangle$ (647 Hz) and we avoided this unstable regions.

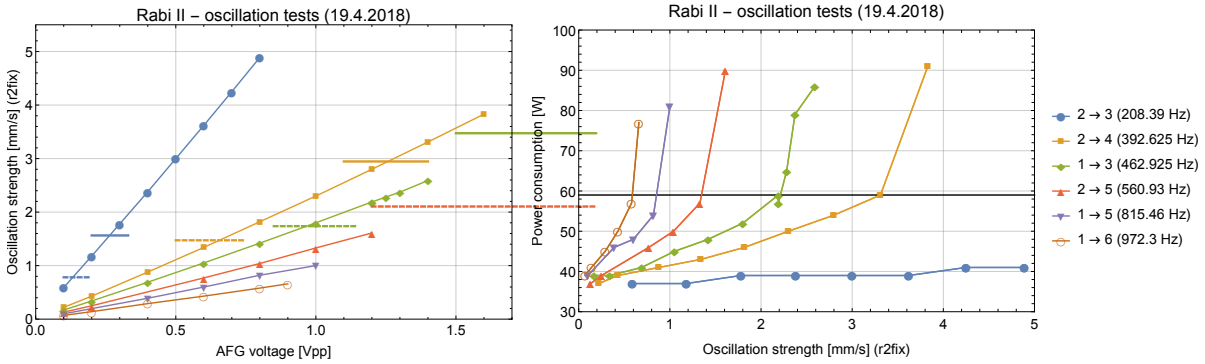

(a) Ratio between applied voltage and resulting mechanical oscillation for different state transitions. The dashed lines are the needed oscillation strengths a_v to induce Ramsey transitions, the horizontal and continuous lines show a single Rabi setup.

(b) Power consumption of different mechanical oscillation strengths. The black line is the previously observed maximal stable available power (compare to [178](fig. 5.7)).

Figure 4.5.: Oscillation tests of different transitions with the Rabi-grs-18 II setup

Similar to fig. 4.4, figure 4.5 displays the relation of the driving voltage signal to the resulting mechanical movement for all possible transitions of the Rabi-grs-18 setup ($|1\rangle \rightarrow |4\rangle$ and $|2\rangle \rightarrow |6\rangle$ were not stable enough to test them). The ability to induce an oscillation is strongly depended on the frequency and drops with higher frequencies. In contrast, the needed oscillation strength a_v rises linearly with higher transition frequencies (see eq. (2.103)). The Rabi-grs-18 setup was only able to fully drive the transitions $|2\rangle \rightarrow |3\rangle$ and $|2\rangle \rightarrow |4\rangle$. The Ramsey-grs-18 setup was additionally able to address a full state reversal for $|1\rangle \rightarrow |3\rangle$. All other tested available state transitions were only partly responsive (depending on

the frequency and the GRS type). This manifests in a reduced contrast of the transmission peak in the measured spectrum.
The power consumption of the piezoelectric stages below the mirrors increased linearly with higher induced voltage signals until a certain point (60 W-70 W). Above, the power consumption rose much faster and the piezoelectric stages were unstable. They started to overheat and randomly shut down for minutes. A similar behavior was already observed in 2011 [178](p.70-73) with a maximal usable power of 59 W. Since then, all piezoelectric stage controllers received new amplifiers. Therefore, it is possible to drive them with a slightly higher power consumption. However, reducing the cycle length (190 s) at this high amplitudes is highly recommended to prevent overheating.
The power consumption also increases faster for higher frequencies. Therefore, the power consumption limit is reached earlier. This is the main limiting factor which prevents us to use state transitions with high frequencies. One possibility is to increase the mirror lengths of the oscillating regions, which is only limited possible in the current RAMSEY^{TR}-setup. Reducing the mirror weight by reducing its thickness would be another option. However, this could lead to losses in the rigidity and allow more bending of the surface. In the end, Jakob Micko [194](p.41) changed the piezoelectric stages from *PI-518* to *PI-558* due to their better transmission ratio after testing this with his student Veronika Kraus [167] and the help of Stefan Ballok and Tobias Jenke. In addition, he replaced the table controller *E-712* with a new type which provided a higher power to drive oscillations. These actions enabled him to observe the transition $|1\rangle \rightarrow |6\rangle$ within the full RAMSEY^{TR}-setup.
As already mentioned, more detailed studies are necessary to better understand the mechanical properties. An online power meter for all oscillating piezoelectric stages would help to automatize such studies and could stop the oscillations if the power consumption is too high. However, a full automation for such tests is not possible. Mechanical eigenfrequencies can destroy the piezoelectric stages and the mounted mirrors on top of them. Such frequency regions have to be excluded manually in advance.

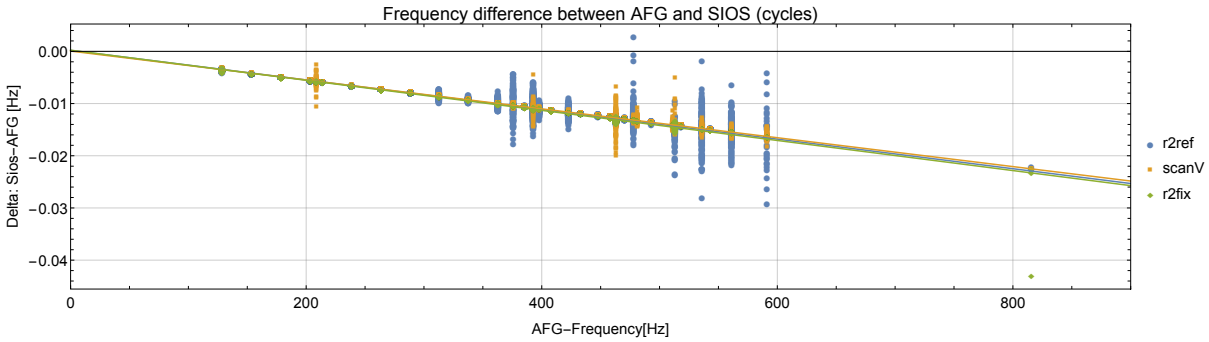

Figure 4.6.: RABI-GRS-18: Frequency difference between SIOS laser interferometer and AFG due to not synchronized clocks.

Figure 4.6 shows the frequency difference between the AFG and the SIOS laser interferometers. The reasons for the linear increase are the different time bases of both devices. For all measurements of this thesis, the offset is too small to be noticeable. Jakob Micko improved the sensitivity to be able to observe systematic shifts. To avoid them, he implemented a rubidium clock to provide the same time base for all devices and make the frequency uncertainty unnoticeable again [194](p.45-46). Additionally, the noise due to mechanical disturbances of the internal interferometer is clearly visible.

4.2.4. Alignment of the mirror's surfaces

For the RAMSEY^{TR}-setup, the capacitive sensor system (see section 3.5.3) was extended in order to be able to measure all five mirrors [267]. The additionally necessary pitch angle correction complicated too much the step control used for the mirror alignment. The used linear approximation of the mirror surfaces failed to describe them and the calculated steps could not be confirmed by linear gauge measurements during the beam time in 2017 [254](p.98-106). In the end, we manually adjusted all steps with the linear gauges for the first Ramsey assembly in 2017 (see section 3.7.1).
After this beam time, Paul Feichtinger [84] investigated together with Tobias Rechberger and me the reasons for the failure of the step control and the inconclusive measurements of the capacitive sensors. We concluded that the system itself is quite stable and consistent, the observed waviness of the mirror

surfaces is real but more sensors are needed in the center to be able to match all sensors to each other. Shortly before the first beam time in 2018, we exchanged the miCos-stage with the better vacuum-suitable one, which changed the mechanical behavior of the measurement system (different correction profiles). In addition, we added three sensors (*B1*, *PB1*, *PA2*) in the center and moved sensor *p* to *p2*. I also completely reworked the LabView programming for the capacitive sensors in order to handle the higher sensor number and to enable different correction modes. The testing of the programming took until the middle of the RAMSEY-GRS-18 measurements. The step control implementation was not improved during this time. In 2020, Jakob Micko finally implemented an upgraded automatic step control which consistently adjusted the steps below the accuracy of the linear gauges [194](p.41-45).
Due to this delay, we manually adjusted the mirror alignment with linear gauges for all measurements with more than one mirror in 2018. Carina Killian evaluated these adjustments for the Ramsey measurements in her project thesis [159]. The obtained optimal piezoelectric stage settings were applied for the entire measurement period until we changed the mirror configuration which required new linear gauge measurements. The following histogram (fig. 4.7) displays the precision of the active stabilization of the piezoelectric stages.

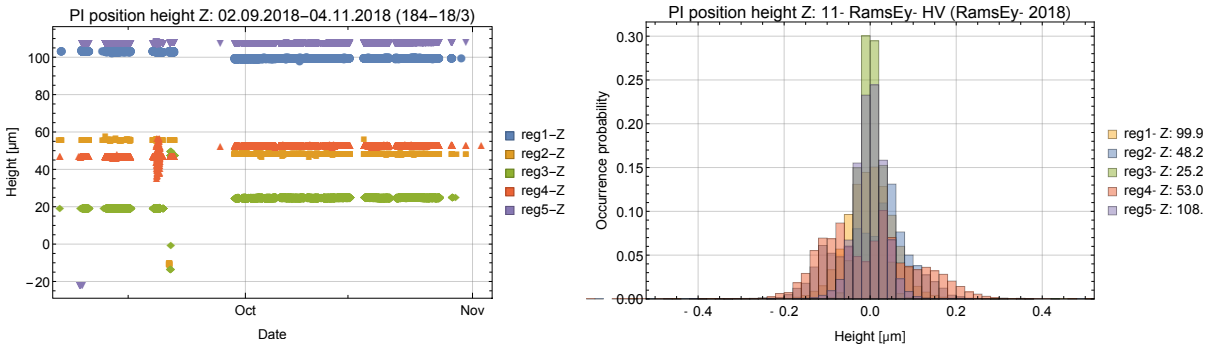

(a) Piezoelectric stage heights during the beam time 184-18/3. Different settings were applied for the RAMSEY-GRS-18-fall measurements in the beginning and the Rams$\vec{E}$y measurements in the second half.

(b) Height stability during the high voltage measurements of Rams$\vec{E}$y. The main instabilities of region II and region IV are due to the applied oscillations and the different stabilizing method. The legend includes the mean heights.

Figure 4.7.: Piezoelectric stage height stability during the beam time 184-18/3

The piezoelectric stages kept their position with a precision below 0.1 µm. However, thermal expansions during the oscillations or a new calibration (auto zero) after a system crash could change the absolute position. Therefore, the capacitve sensors system continuously measured the mirror alignment without readjustments by the step control. The measurements of the reference sensors on the fixed reference mirror are a good test for the long term stability of the complete system.

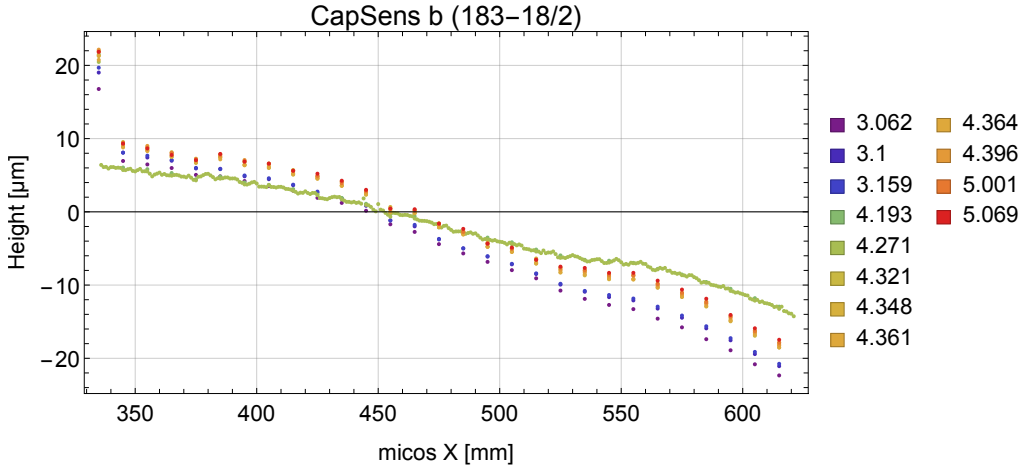

Figure 4.8.: Measurements of sensor *b* (raw data) during the RAMSEY-GRS-18 measurements. The color represents the time within this beam time and the number the measurement ID.

Figure 4.8 displays as an example the reference sensor b over the course of a month during the RAMSEY-GRS-18 measurements. The measured distance between the sensor and the mirror surface changed up to 5 µm nearly constant over the full range of the miCos stage. An exception is the measurement 4.271 which used a different step size. This influenced also the measurement (different overall pitch). Thermal expansion of the gantry and other parts of the setup can explain the different measured values in the setup. 3D simulations of these parts at different temperatures and gantry positions could help to quantify these effects better and visualize differences in the deformations due to varied loads.

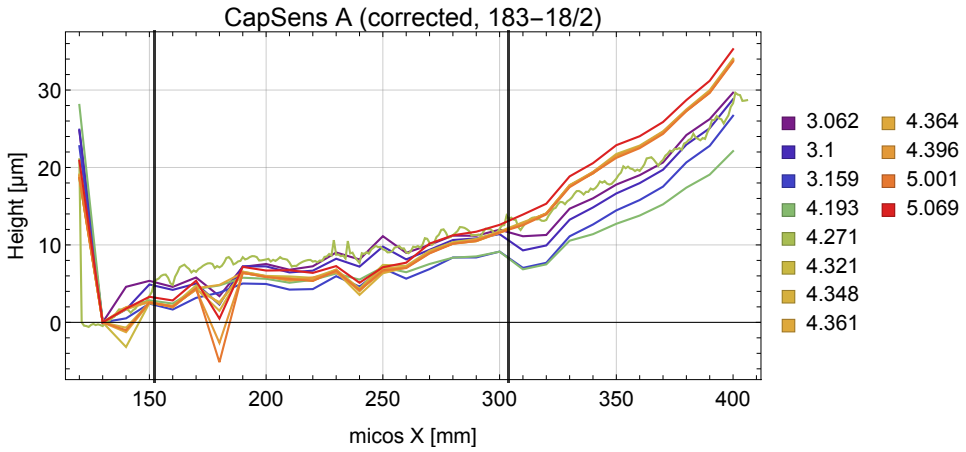

Figure 4.9.: Measurements of sensor A (corrected data) during the RAMSEY-GRS-18 measurements. The color represents the time within this beam time and the numbers the measurement ID. The black vertical lines mark the gaps between the mirrors.

Figure 4.9 presents the corrected values of sensor A. There is no visible step between region I and region II. Within region II the observed deviations are artifacts from the correction and the mirror waviness. Overall, the measurements are reproduced within a ± 2 µm band. The values in region III can be separated in lower earlier measurements (violet-blue) and later higher ones (orange-red). A major system crash in the middle of the cycle was the reason for this difference. All piezoelectric stages had to be restarted and calibrated again. To compensate changes, I used the capacitive sensor maps to manually reset the height of some piezo stages by a few µm. By chance, the mirror alignment was better after the incident (see step between region II and region III) and therefore the neutron's zero rate increased.

The method of manually aligning the mirror surfaces worked sufficiently well to measure for the first time with a full Ramsey-type GRS setup and probe the electric charge of the neutron. However, using an automatized step control drastically minimizes the work needed to align the setup and can compensate the long term changes of the setup due to thermal expansions or new calibrations.
Reevaluating the old measurements with the new methods developed by Jakob Micko would help to understand the mechanical and capacitive setup better and further improve the programming (LabView). The capacitive measurement during the Rams$\vec{E}$y charge determination will be tricky because we had to measure without a ground connection of region III and we shifted region IV to the side by few cm. Both circumstances introduced additional offsets in all sensor readings which makes it harder to evaluate the step heights with the capacitive sensor measurements.
To be able to use all 14 sensor positions is very beneficial. In 2018, we used 11 due to restrictions in the available sensor holders. In the following years this number reduced down to 9 due to broken sensors, even though Jakob Micko reused the sensors of the old RABI^{GC}-setup. To increase the number, the current capacitive sensor setup has to be upgraded to operate up to 15 sensors and enough operational sensors have to be available[3]. An alternative or supplementary approach would be to use a different measuring system based on a different physical method (e.g. laser Fabry-Pérot cavities - *DeltaSens* [289]). Comparing a different method with the existing capacitive sensors can clarify if the conductivity distribution of the mirror surface disturbs the measurements and mimics a surface waviness. The more accurate and precise method should be used in the future. However, the correction algorithms are quite similar for different physical methods. For this, the influence of the mirror surfaces itself on the corrections has to be studied in more detail than before [233].

[3]Five new holders lift the other restriction

Additional GRS measurements with induced steps or tilts are necessary to quantitatively determine the systematic influence of the misalignment on the transmission rates, the transition frequencies and their contrasts. Together with theoretical considerations these help to better define the needed accuracy for the alignment system. Already the RAMSEY-GRS-18 measurements showed that small steps can reduce the zero rate by 10 %. Jakob Micko presented in his PhD-thesis a conducted measurement series with introduced steps (±1 µm) [194](p.86-88). He observed a significant reduction in the transmission rate but the changes in the transition frequency were insignificant.

4.2.5. B-field

The magnetic field gradients can potentially induce state transitions. Therefore, a double layer of µ-metal (see section 3.9.1) within the vacuum chamber shields the experiment against external fields (e.g. Earth's magnetic field, stray fields from neighboring experiments or the huge hall crane). In addition, two sensors monitor the field inside the vacuum chamber (see section 3.9.2). In 2018, we used a new data acquisition system for the field probes, which we first tested in Vienna for the new large magnetic field coils [318] (see section 3.9.4). The new developed LabView control was not fully implemented into the main measurement control system during the beam times in 2018. Therefore, it was only partly running and was a source of some system crashes.

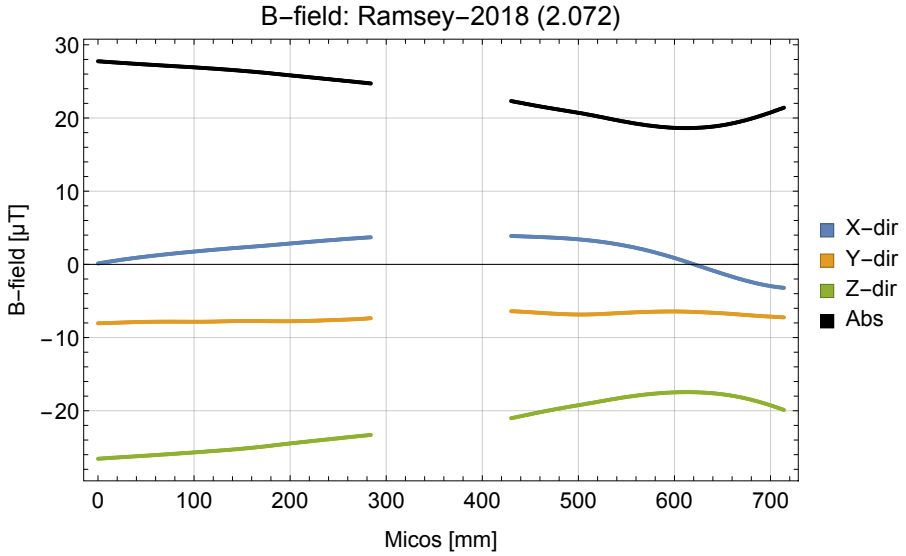

Figure 4.10.: The magnetic field with an open vacuum chamber measured with two sensors 430 mm apart

Figure 4.10 displays a typical scan of the magnetic field sensors within an open vacuum chamber. The average field is around 25 µT which is comparable or already lower as previously measured (2008: 165 µT[287](p.49-51), 2016: 50 µT on the empty platform [262](p.7-12), [254](p.74-77)).

Figure 4.11 presents a combined magnetic field map of multiple measurements many weeks apart. This proofs that the field within the chamber is constant over long times and that the data acquisition has a very small noise level well below 0.1 µT for long (weeks) and below 1 nT for short time periods (minutes). This is low enough that in 2019 the experiment status of the neighboring neutron lifetime experiment was visible by observing changes in the residual magnetic field, which were in the order of 2 nT [40](p.9-17). Closing the chamber (and with it the magnetic shielding) lowers the overall field strength significantly. In the front part of the experiment, the field strength is around 1 µT comparable to previously observed values in older setups [287](p.49-51), [65](p.41-43). The benchmark for the empty large vacuum chamber of the RAMSEY^{TR}-setup is 0.4 µT [262](p.7-12), [254](p.73-77).
However, at the end of the setup, there was a strong increase of the absolute field strength. After a preliminary evaluation in 2019, we found its reason. The electric motor of the large linear stage (miCos) of the gantry produced strong permanent stray fields (up to 4 mT on its surface). In the following experimental campaigns, the motor was additionally shielded with its own small µ-metal cap which resolved the problem [40](p.7-8), [194](p.34-35) and reduced the magnetic field at all accessible sensor positions below 1 µT.

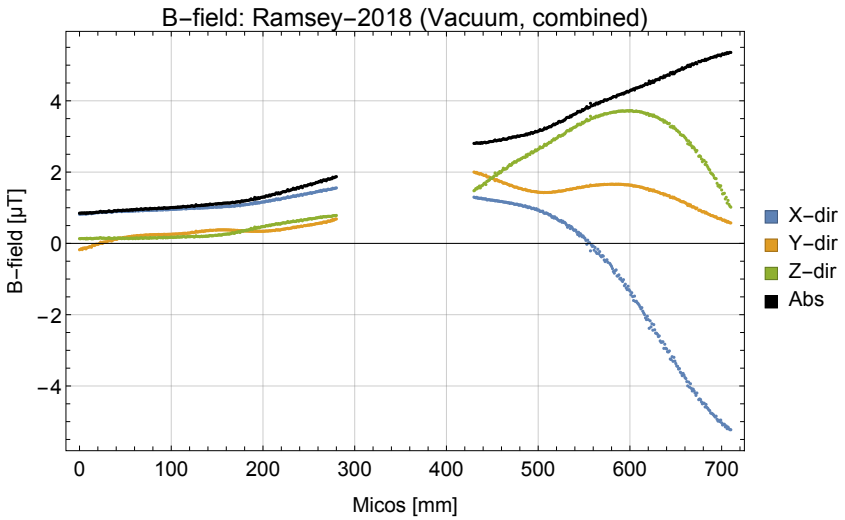

Figure 4.11.: Magnetic field in a closed vacuum chamber.

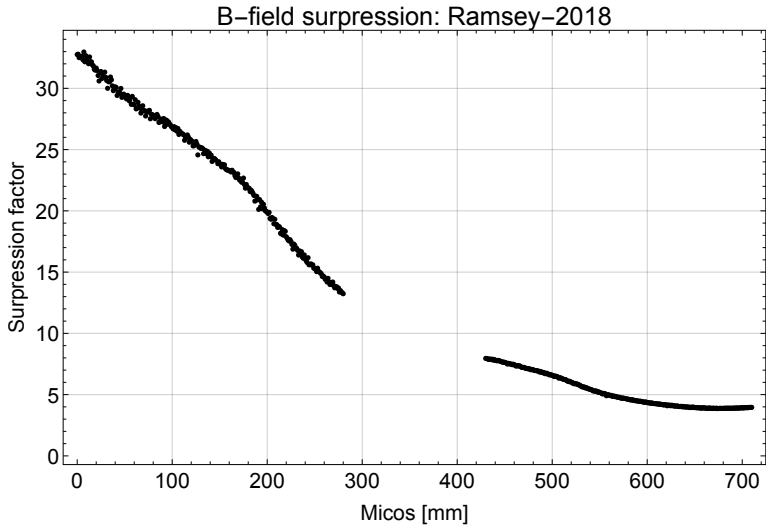

Figure 4.12.: Ratio between open and closed vacuum chamber as depicted in fig. 4.10 and fig. 4.11.

Figure 4.12 depicts the shielding factor during the measurements in 2018. This factor is the ratio between the magnetic field with an open and a closed top cover of the vacuum chamber. The factor drops from nearly 35 down to 5 due to the stray magnetic fields of the miCos motor. The aimed and already measured shielding factor is around 100 in the empty chamber [254](p.73-77). Therefore, a reevaluation is necessary to quantify the improvements due to the additional shielding.

As presented here, the sensors are important tools in order to find magnetized elements within the magnetic shielding and to monitor the residual fields. Therefore, more sensors at different positions are helpful to gain a more refined field map within the experiment (e.g. connecting the field sensor already built into the detectors). In addition, simulations of the RAMSEY^{TR}-setup (e.g. with *CST-Studio*) can complement the measurements, because they can depict the field strengths and orientations in regions which are inaccessible for sensors. For the design of the large coils, Mathias Winder already created a first version with a simplified geometry [318](p.14-20).
For the polarized measurements, the sensors will play an even more important role. They can be used to stabilize the introduced guiding field (reducing the influence from external stray fields). In addition, producing magnetic field gradients in region III enable to study the influence of them on the gravitationally bound states and their systematic effects. One goal is to even drive transitions between states with magnetic fields as it was already proposed by the GRANIT collaboration [212] in order to have an additional method besides oscillating mirrors and steps. All these possibilities require a better knowledge of the magnetic fields within the vacuum chamber and therefore more accurate measurements.

4.3. Neutron measurements

All measurements using neutrons which are not GRS measurements are summarized in this section. They are important systematic examinations of the setup and the results are crucial ingredients for the theoretical description.

4.3.1. Aperture - velocity spectrum

As described in section 3.1.3, different settings of the aperture enable to measure the velocity spectrum inside the setup. During the beam time *3-14-358-III* (cycle 182-18/1), Lukas Achatz, Daniel Schuh and I performed such a differential aperture measurement between 28th and 31st March 2018.
The aperture blade positions were the same as for the velocity measurement in 2016 (beam time *3-14-358-I*, cycle 179-16/3, compare to Micko's diploma thesis [193] p.21, tab.4) because the positions of the aperture and the first region were kept the same. This time we measured two data sets with different velocity intervals (1 m/s and 2 m/s). The neutron detector measured the transmission rate after region I already with the final mounted absorber in place (gap size of ≈22 µm). This is the second major difference to the measurement in 2016 where a gap size of ≈100 µm increased the transmission rate significantly.
Table 4.4 summarizes the most important measurement parameters. To simplify the aperture adjustment procedure only one aperture blade was moved between measurements. Therefore, consecutive measurements probe the spectrum with a different velocity interval width (e.g. 6-7 m/s, 6-8 m/s, 7-8 m/s). The average adjustment break between two measurements was 50 min (including venting and evacuation of the vacuum chamber). With this method we were able to measure up to five measurement points per day. During the long nights, we adjusted the setup to measure the edges of the velocity spectrum where we expected to have the lowest neutron rate. Note that due to the accuracy of the height gauge (0.02 mm) there is also an uncertainty of the set velocity interval which increases relatively for higher velocity settings.

Table 4.4.: Parameters of the aperture measurement

Velocity [m/s]		Blade position [mm]		ID	Start time	Cycles
Low	High	Lower	Higher			190 s
4	6	96.70	101.30	4.002	21:08 - 28.03.2018	200
6	7	101.30	102.28	4.003	10:14 - 29.03.2018	29
6	8	101.30	102.92	4.004	12:52 - 29.03.2018	24
7	8	102.29	102.92	4.005	15:13 - 29.03.2018	38
7	9	102.29	103.35	4.006	18:28 - 29.03.2018	28
8	9	102.93	103.35	4.008	10:14 - 30.03.2018	44
8	10	102.93	103.67	4.001	18:48 - 28.03.2018	17
9	10	103.36	103.67	4.009	14:08 - 30.03.2018	22
9	11	103.36	103.90	4.010	16:10 - 30.03.2018	19
10	11	103.67	103.90	4.013	11:34 - 31.03.2018	26
10	12	103.67	104.07	4.011	18:41 - 30.03.2018	17
11	12	103.90	104.07	4.012	20:20 - 30.03.2018	233
11	13	103.90	104.21	4.007	20:59 - 29.03.2018	206

Table 4.5 displays the neutron rate measurements including different correction methods according to section 3.2.3.

As displayed in figure 4.13, the measurements agree well with the fitted Maxwell-Boltzmann distribution only at the edges. In the central region an additional structure disturbs the spectrum. This could be interpreted that the geometrical combination of the beam guides, the aperture and the first region suppresses neutrons with a velocity around 8.5 m/s. Similar disturbances are found at the differential aperture measurements 2016 [193](p.19-22), [254](p.109-110) and 2019 [160](p.27-29). However, the TOF measurement done at the same time within the beam guides represents nearly perfect Maxwell-Boltzmann distributions [254](p.107-109), [160](p.25-27).
The fitted curve for the 1 m/s measurements deviates strongly from the other velocity interval and the combined fit. The reasons for this are missing data points at the far edges of the spectrum which were not probed due to time constraints.

Table 4.5.: Parameters of the aperture measurement

Velocity [m/s] Low	High	Detector rate [mcps]	Monitor rate [cps]	Complete corr. [mcps]	Background corr. [mcps]
6	7	21.05 ± 1.95	18.147 ± 0.057	19.20 ± 1.90	20.00 ± 1.97
7	8	28.53 ± 1.99	17.665 ± 0.049	27.12 ± 1.98	27.48 ± 2.01
8	9	22.73 ± 1.65	16.012 ± 0.044	23.67 ± 1.83	21.68 ± 1.67
9	10	35.89 ± 2.93	13.961 ± 0.058	43.84 ± 3.71	34.84 ± 2.94
10	11	28.54 ± 2.40	15.505 ± 0.056	31.04 ± 2.73	27.49 ± 2.42
11	12	24.01 ± 0.74	16.115 ± 0.019	24.91 ± 0.86	22.96 ± 0.79
4	6	16.24 ± 0.65	17.749 ± 0.022	14.91 ± 0.70	15.19 ± 0.71
6	8	48.46 ± 3.26	18.015 ± 0.063	45.85 ± 3.17	47.42 ± 3.27
7	9	55.08 ± 3.22	17.323 ± 0.057	54.39 ± 3.26	54.03 ± 3.23
8	10	75.23 ± 4.83	17.168 ± 0.073	75.38 ± 4.92	74.18 ± 4.83
9	11	57.34 ± 3.99	14.054 ± 0.062	70.36 ± 5.00	56.29 ± 4.00
10	12	61.30 ± 4.36	15.687 ± 0.070	67.20 ± 4.88	60.25 ± 4.37
11	13	39.14 ± 1.00	17.457 ± 0.021	38.05 ± 1.04	38.09 ± 1.04

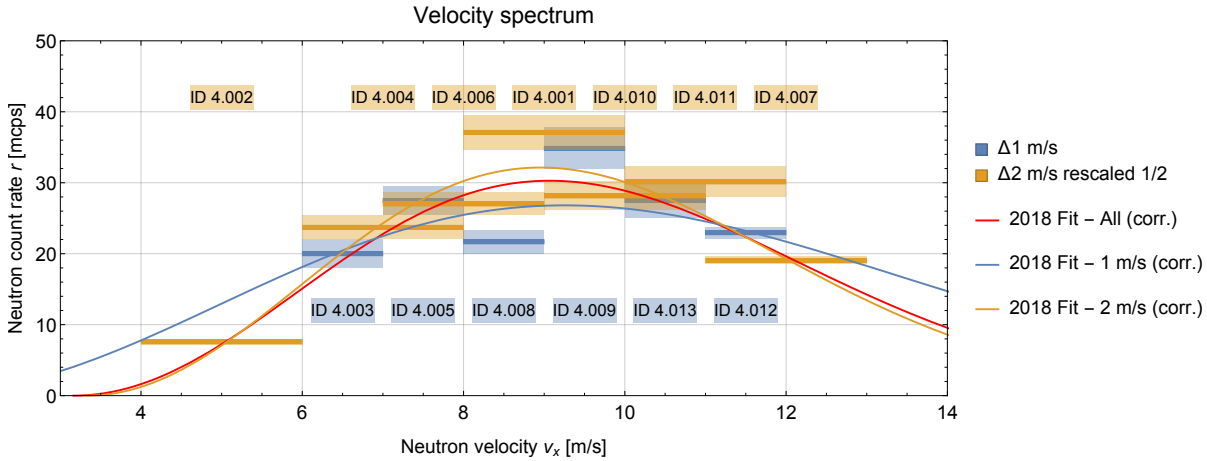

Figure 4.13.: Aperture measurement 2018: the measured rates including the fitted theoretical curves, for a better comparison the count rates of the 2 m/s measurements were rescaled by a factor of two.

The most important fit parameters can be found in table 4.6 and additional tests in the appendix A.4.1 (different detector corrections and tests of different exponents b and c). For all further calculations of the GRS-measurement, the following parameters for a simple Maxwell-Boltzmann distribution (eq. (2.148)) are used, ignoring all additional disturbances:

- $n_{2018} = 215.3$
- $v_{02018} = 3.163\,\mathrm{m/s}$
- $a_{2018} = 4.176\,\mathrm{m/s}$: Corresponding neutron spectrum temperature $T = 2.1\,\mathrm{mK}$

Table 4.6.: Aperture velocity measurement fits 2018

Data	Correction	Parameter	χ^2	red-χ^2_{red}	p-value
2018 - All (13)	Background only	$n = 215.4(33)$ $v_0 = 3.16(10)$ $a = 4.176(98)$	44.308	4.431	2.90×10^{-6}
2018 - 1 m/s (6)	Background only	$n = 259(36)$ $v_0 = 1.2(14)$ $a = 5.7(10)$	18.72	6.24	3.12×10^{-4}
2018 - 2 m/s (7)	Background only	$n = 217.7(33)$ $v_0 = 3.32(10)$ $a = 3.98(10)$	14.04	3.51	7.17×10^{-3}

In order to learn more about the velocity distribution within the setup, an aperture measurement with the complete setup would be preferable which includes also the velocity hardening of the mirror row due to divergence. However, in order to have enough statistics, this needs a significant increase in the zero count rate r_0 or much longer measurement times, especially if the disturbances at the center are studied in more detail.
Before the next measurement, I recommend to automatize the aperture blade adjustment. This reduces the time between two different blade settings below one minute and the vacuum can be kept during this period. This is also important for future studies of the relation between contrast and neutron velocity (velocity-depending state damping within the absorber regions). Furthermore, an automation eliminates some systematic effects: In the first hour, the vacuum pressure especially inside the absorber gap is not stable and therefore the rates are potentially increasing [194]. This introduces an uncertainty to the counted neutrons in the beginning, which can have a significant influence on the final transmission rate, because most measurements last only for some hours. Second, each time venting and opening the chamber brings dust and dirt into the chamber and on the mirrors. Even after a fast cleaning this means different residual staining in the setup and therefore different initial conditions for each measurement.
An alternative to differential velocity measurements with a small velocity interval are integral velocity measurements. Here only one aperture blade is moved. The other one is kept constant at the edge of the spectrum. This measurement type can exclude the effects of a very narrow gap between the aperture blades. Also a higher count rate can reduce the measurement times of some points. However, in the central spectrum the differences of the measured rates are important which increase the measurement times significantly in order to reduce the statistical error enough. The total measurement times are comparable between both methods. As a revision this can be done with both blades and should lead to the same conclusion. An important parameter for the integral measurement is the selection of the aperture blade's settings. A rash choice could decrease the significance of the fitted spectrum drastically. More about this measurement type can be found in the following comparison to older measurements.

Comparison to previous velocity measurements

Since the first measurement of gravitationally bound quantum states, one of the most important preparatory measurements has been the determination of the velocity spectrum. The qBB measurements and the first GRS measurements needed a very small velocity spread to increase the contrast. The knowledge of the velocity distribution helped to adjust the used velocity interval close to the mean neutron velocity of the UCN beam. Ramsey-type GRS measurements are able to use a wider velocity interval (up to the entire available spectrum). Therefore, the knowledge of the shape of the spectrum is very important because this determines the degree of washout effects of the side peaks due to the velocity spreading (see more in the theory section 2.2.3).

Two different types of velocity determination have been used. Time-of-flight measurements (TOF) and aperture measurement. A TOF spectrum is generated by a chopper inserted into the beam guide. A detector at a certain distance detects the pulses. The velocity information is encoded within the arrival time of the neutrons of the pulse. However, the chopper opening function is also convoluted into this signal. Aperture measurements consist of multiple aperture blade settings limiting the velocity spectrum to different intervals as already described previously in details (see section 3.1.3). In the following I summarize all previous measurements using these two methods and compare them with the one from this thesis.

The first velocity measurement was a TOF spectrum for the discovery of the quantized states of UCNs in 1999 at the PF2 [258](p.17). The PhD thesis of Martin Klein contains a detailed description of their used setup including a two-disk chopper [161](p.12-17). The fitted velocity distribution was the following empirically determined analytic function:

$$\frac{\mathrm{d}N}{\mathrm{d}t}(t) = t^{-n} \cdot \left(\mathrm{e}^{-\frac{t-t_1}{a_1}} + 1\right)^{-1} \cdot \left(\mathrm{e}^{-\frac{t-t_2}{a_2}} + 1\right)^{-2} \cdot T_{Alu}(d) \tag{4.1}$$

For determining the fit parameters a complex chopper opening function was convoluted to the fit function in order to find the best description of the measured data. The final parameters are: $n = 4.596(9)$, $t_1 = 10.84(3)$, $a_1 = 56.69(13)$, $t_2 = 2.36(2)$ and $a_2 = 26.88(2)$. The transmission $T_{Alu}(d)$ was calculated for the aluminum entrance window ($d = 300\,\mu\mathrm{m}$). The results are not comparable to the current measurements.

David Stadler describes the first integral aperture measurement for the campaigns *3-14-237* & *3-14-245* [287](p.30-32). He used an integral fit function for the data and expressed the results in a velocity spectrum which has similarities to a Maxwell-Boltzmann distributions:

$$F(z) = c\,\mathrm{erf}\left(-a \cdot z + k\right) + b \qquad f(v_\mathrm{n}) = \frac{d^2}{{v_\mathrm{n}}^3} \cdot c\frac{2a}{\sqrt{\pi}} \mathrm{e}^{-\left(k - ag\frac{d}{2{v_\mathrm{n}}^2}\right)^2} \tag{4.2}$$

The adjustment of the upper and the lower blade were evaluated separately: $a = 0.593$ & 0.546, $k = 28.921\,\mathrm{mm}$ & $15.741\,\mathrm{mm}$, $b = 3.500\,\mathrm{s}^{-1}$ & $3.749\,\mathrm{s}^{-1}$ at a distance of $d = 150\,\mathrm{mm}$. The comparison displays an averaged curve called *Stadler-Aperture-2008*.

Graphs and descriptions of the corresponding TOF measurement of the campaign *3-14-237* can be found in [264](p.33), [138](p.92-96) and [139](p.39-42).

In his PhD thesis, Tobias Jenke evaluated two integral aperture measurements: The first during the measurement cycle *3-14-253* [139](p.43-45). This resulted in the parameters $N = 1.606$, $c = 1.588(83)$, $b = 0.719(23)$, $v_0 = 3.24\,\mathrm{m/s}$ [4]. The second measurement was at the end of *3-14-283* in 2010 [264](p.26), [139](p.77-78). The fitted values are $N = 0.306$, $c = 4.993(48) * b - 1 \approx 3.164(47)$, $b = 0.834(5)$, $v_0 = 3.24\,\mathrm{m/s}$. They are marked *Jenke-Aperture-253* and *Jenke-Aperture-283* for the comparison. Both measurements have different results. Also the distance between the aperture and the first region was different (150 mm and 180 mm). However, they are evaluated with the same underlying integral function derived from the generalized Maxwell-Boltzmann distribution (without the corresponding factor a):

$$F(z) = N \cdot \Gamma\left(\frac{1+c}{b}, \left(z(v_\mathrm{n}) - v_0\right)^b\right) + N_0 \tag{4.3}$$

Gregor Wautischer similarly analyzed an integral aperture measurement in 2011 [310](p.67-70). His final values were: $N = 7.598(4524)$, $c = 5.666(358)$ and $b = 1.644(56)$ with a background fixation of $N_0 = 0.641\,\mathrm{mcps}$ and a fixed cutoff velocity of $v_0 = 3.24\,\mathrm{m/s}$. Compared to previous measurements the fitted errors are rather large and the velocity spectrum is much slower than all other measurements. For the later comparison, we call it *Wautischer-Aperture-2011*.

Gunther Cronenberg presented also an integral aperture measurement as a systematic test for his RABI$^{\mathrm{GC}}$-setup (*3-14-305*) [65](p.20-21). He concluded that the velocity spread for the narrow used velocity interval does not change the theoretical transition curve strongly. Therefore, he only used the mean velocity. In his thesis only a graph of the measurements is displayed. However, Tobias Jenke crosschecked the evaluations and his final parameters are $\tilde{a} = 1/(2a^2) = 0.850339 \rightarrow a \approx 0.766812$, $c = 4.716\,69$, $b = 1$ (fixed) and $v_0 = 3.24\,\mathrm{m/s}$ (fixed) using the function displayed in eq. (4.4). In the comparison, graph 4.14, the function is denoted as *Cronenberg-Aperture-TJ*. This measurement also is the first measurement with the new aperture [42] which has been used in a different modification in the RAMSEY$^{\mathrm{TR}}$-setup and therefore for this thesis.

In 2014, Martin Thalhammer with his colleagues (Tobias Rechberger and Tobias Jenke) and his students (Tamara Putz and Martin Stöger) measured the velocity spectrum with the aperture as a preparation for his qBB$^{\mathrm{MT}}$-setup. They used two different absorber height settings (30 µm and 100 µm) for a comparison. A detailed description of these measurements will be in Thalhammer's PhD thesis [299]. Here, I will present the results of the measurement with the wider absorber gap due to its higher statistics. Tobias Jenke provided the values of the following fit parameters according to eq. (4.4): $\tilde{a} = 1/(2a^2) = 1 \rightarrow a \approx 0.707\,107$ (fixed), $c = 2.951\,75$, $b = 0.806\,712$ and $v_0 = 3.24\,\mathrm{m/s}$ (fixed). For comparison, the measurement is denoted as *Thalhammer-Aperture-TJ*.

For Ramsey-type GRS setups the determination of the velocity distribution and its shape is very important. The multiple side peaks (fringes) are strongly velocity depending in contrary to the single main peak of Rabi-type setups. A broad velocity interval, which is used to increase the statistical significance, washes out the side pattern of the theoretical Ramsey transition curves and helps to separate close-by state transitions (see figure 2.12).
Beside the differential aperture measurement of this thesis, multiple measurements were performed with the current RAMSEY$^{\mathrm{TR}}$-setup. The comparison between them is very important to gain more information of the influence on the neutron velocity selection of single components (PF2-turbine, beam-line, aperture, mirror regions).

[4] This value was fixed due to neutron optical potential of the aluminum entrance window

Already during the assembly of the beam line, Tobias Rechberger and the team of students (Peter Salajka [262], Rudolf Golubich [101] and Jakob Micko [193]) performed a TOF measurement during the beam time 179-16/3 (*3-14-358-I*) [101], [254](p.107-109). He used a modified differential version of the previously used fit function introducing the Maxwell-Boltzmann factor a as $\tilde{a} = 1/(2a^2)$:

$$f(v_\mathrm{n}) = (v_\mathrm{n} - v_0)^c \mathrm{e}^{-\tilde{a}(v_\mathrm{n}-v_0)^b} \tag{4.4}$$

The normalized spectrum of the measurements in 2016 has the following parameters: $\tilde{a} = 1/(2a^2) = 11.7793 \rightarrow a \approx 0.20603$, $c = 14.2208$, $b = 0.474\,257$ and $v_0 = 0.772\,086\,\mathrm{m/s}$. This measured spectrum is named *Rechberger-TOF-2016*.

During the further progress of the assembly, a differential aperture measurement was recorded for the first time [254](p.109-110). The measured rates of each data point can be found in the master thesis of Jakob Micko [193](p.19-22). This enables to analyze the measurement of 2016 similar to the measurement of 2018. Table 4.7 displays a detailed analysis. Therefore, both measurements are directly comparable to each other except the different gap size of region I. It was also the starting point for the measurement in 2018 to further investigate the structure in the center of the spectrum as it can be seen in figure 4.15. This measurement is denoted *Rechberger-Aperture-2016*.

Table 4.7.: Aperture velocity measurements 2016

Data	Correction	Parameter	χ^2	red-χ^2_{red}	p-value
2016 - All(9)	uncorrected	$n = 2415(25)$ $v_0 = 3.488(55)$ $a = 3.827(52)$	131.9	21.99	5.1×10^{-26}

Already 2019, the beam line was disassembled due to repairs of the large gate valve shutters and the alignment of the guides close to the turbine. As a quality control most beam lines of PF2 were characterized with a TOF-measurement by PF2-responsible Tobias Jenke. The results can be found in the master thesis of Carina Killian [160](p.25-27). She used the generalized Maxwell-Boltzmann distribution (eq. (2.150)) with equal exponents ($c = b$) for her analysis:

$$f(v_\mathrm{n}) = n\sqrt{\frac{2}{\pi}}\frac{(v_\mathrm{n} - v_0)^b}{a^3}\mathrm{e}^{-\frac{(v_\mathrm{n}-v_0)^b}{2a^2}}\Theta(v_\mathrm{n} - v_0) \tag{4.5}$$

The fitted parameter were $n = 0.710(1)$, $a = 2.900(6)$ $b = 1.770(1)$ and $v_0 = 3.160(3)\,\mathrm{m/s}$, which are called *Killian-TOF-2019*. She evaluated also an aperture measurement which was measured by her, Jakob Micko [194] and me in June 2019 [160](p.27-29). In her thesis she only presents a plot of the measurement and comparison with central moments to the corresponding TOF measurement. Therefore, this cannot be used for a further comparison.
In 2020, Jakob Micko, the students (Andrej Brandalik [48] and Hugo Wetter [315]) and the PF2-team (Tobias Jenke) performed an integral aperture measurement after the change of the beam guides from glass to stainless steel. He presents a detailed description and analysis of this data set in his thesis [194]. In the future, newer measurements are expected to be conducted. These should also be compared to all the other measurements (which should partly be reevaluated) in order to gain more insight into the influences on the velocity spectrum of the neutrons.

As seen in figure 4.14, the TOF and the aperture measurements of the RAMSEY$^{\mathrm{TR}}$-setup are quite similar within their own method. Between the measurement methods, there is a velocity offset of around 1 m/s. Older measurements are quite different to each other and to the measurements of the current setup (except the RABI$^{\mathrm{GC}}$-setup measurement which is similar to the aperture measurements within the RAMSEY$^{\mathrm{TR}}$-setup). Reasons for this can be the different beam line geometries, different used apertures or different evaluation methods. Only reevaluations of the complete measurements could bring more insights to the causes.
Figure 4.15 displays in more details the aperture measurement of 2016 [193](p.19-22) including the same evaluation as done for the measurement of 2018 (this thesis, rescaled to the same normalization). From the fitted spectrum it is visible that the newer measurement is slightly harder. This is mainly due to the smaller slit of region I. Slower neutrons interact more often with the absorber as the slits get narrower. Therefore, higher states are stronger suppressed. Faster neutrons can pass the absorber even with higher states. Similarly, the TOF spectra are softer due to the absence of the velocity depending damping of

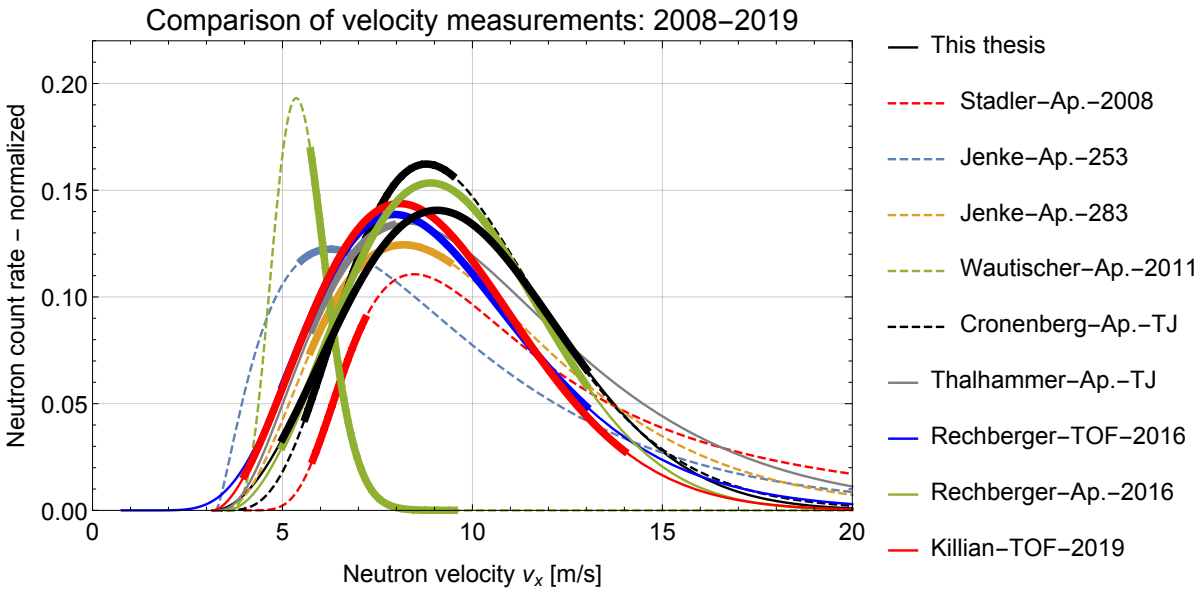

Figure 4.14.: Comparison of all available velocity measurements for different setups from 2008 to 2019. The dashed measurements have different beam line setups (different heights) and are integral aperture measurements. Continuous lines are measured at the state-of-the-art RAMSEY^{TR}-setup. The thicker parts of each line represent the used velocity interval for the measurements of the same beam time.

the first region. The direct comparison of the 1 m/s interval measurements reveals the same structure in the center of the spectrum. For both data sets the measurements of the interval 8-9 m/s is significantly lower than their neighboring rates. This cannot be described within a Maxwell-Boltzmann spectrum and suggests that this velocity is suppressed by the beam-line geometry. The neutron path should be back traced starting from the parabola set by the velocity, absorber slit and gap of the first region. This can reveal problematic zones within the beam guides (e.g. obstacles, steps) where this track is not traceable back to the turbine. The remeasuring in 2019 was a result of this structure. The center of the spectrum was resolved even with smaller velocity intervals and similar structures were visible.
In the beginning of 2020, the beam guides were exchanged and the shutter removed. The aperture measurements of 2020 suggested that the effect was reduced to almost the level of statistical fluctuations. Jakob Micko presents a detailed analysis of this measurement in his thesis [194]. However, these results are still statistical compatible with the old aperture measurements within the RAMSEY^{TR}-setup.

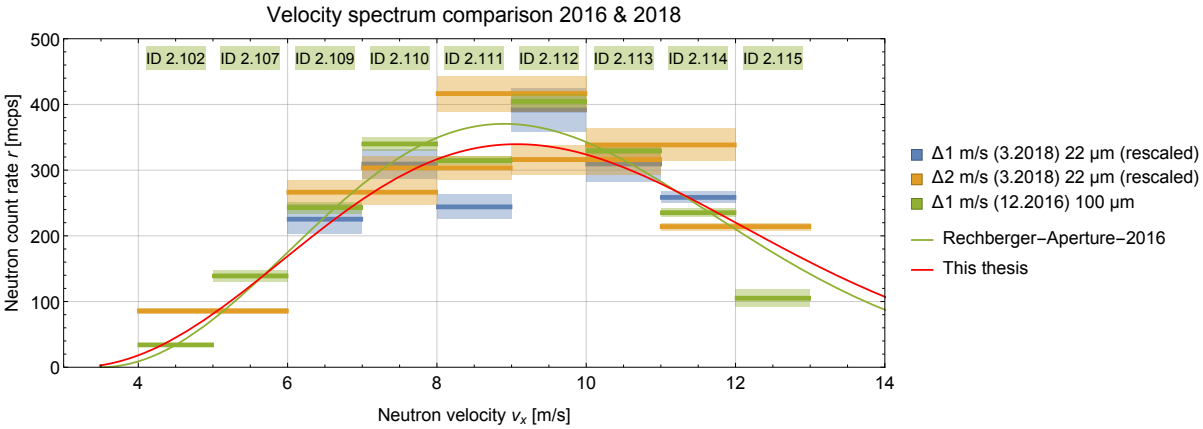

Figure 4.15.: Comparison of the aperture measurements 2016 and 2018 (this thesis)

4.3.2. CR-39 results

Beside the determination of the velocity spectrum, the measurement of the state occupation with CR-39 is one of the most important preparatory measurements. Using this technique also enables to measure the neutron beam distribution or systematically test the method itself.

For this thesis, most CR-39 measurements were performed during the cycle 182-18/1 (*3-14-358-III*). The main focus was to determine the state occupation of the newly clamped absorbers. At first it was intended to clamp the absorbers multiple times until the first state was populated around 70 % and not only 50 % as it has been before (see [254](p.110-112)). We abandoned this goal due to many retakes of the same measurements. Additionally, we tested the beam profile between the beam guide end cap and the aperture. Due to the high count rate, we used these measurements to test different etching times and their changes in the pattern recognition. Nearly all measurements are displayed within the master thesis of Lukas Achatz [14]. In autumn of 2018, Magdalena Pieler and Valentin Czamler also performed some CR-39 measurements within the *q*BOUNCINO setup [236]. Elisabeth Kreuzgruber and Jakob Micko were helping to develop and read out the detectors. Unfortunately either the detectors were underexposed or the coating was too noisy. The table 4.8 gives an overview of all CR-39 measurements during this thesis.

Table 4.8.: Overview of CR-39 measurements during the beam times in 2018

ID	Irradiation Cycles, ID	Chemistry	Purpose	Expected Detected	Details Students, Labbook
102	14.3.2018 256, 3.008	15-16.3.2018 13.4.2018(+1.5 h)	Region V (801+804)	2600 n none	[14](p.48-52), 67-70,73
128	16.3.2018 320, 3.010	18-19.3.2018 13.4.2018(+1.5 h)	Region I (802+805)	3900 n none	[14](p.36-48), 71-73
T35	18.3.2018 1, 3.011	18-19.3.2018	End cap	$>2 \times 10^6$ 32391 (line)	[14](p.26-36), 73-74
016	18.3.2018 1, 3.011	18-19.3.2018	Before aperture	$>2 \times 10^6$ 44533 (line)	[14](p.26-36), 73-74
L11	18.3.2018 574, 3.013	21-22.3.2018	Region V (801+804)	7000 n 2905 n	[14](p.48-52), 75-77
116	23.3.2018 1063, 3.016	26-27.3.2018 13.4.2018(+1.5 h)	Region I (802+805)	13650 n none	[14](p.36-48), 79-80
003	31.3.2018 1129, 4.014	06-07.4.2018	Region I (802+805)	13800 n 14111 n	[14](p.36-48), 92-94
E03	03.4.2018 1, 4.015	06-13.4.2018 sequence	End cap EDM	$>2 \times 10^6$ >4400(5x5)	[14](p.26-36), 93-95
103	03.4.2018 1, 4.015	06-13.4.2018 sequence	End cap MAM	$>2 \times 10^6$ >5000(5x5)	[14](p.26-36), 93-95
070	05.4.2018 1295, 4.070	12-13.4.2018	Region I + Region V	3800 n 5285 n	[14](p.52-60), 101-104
062	05.4.2018 1295, 4.070	12-13.4.2018	Region I + Region V	3800 n 10278 n	[14](p.52-60), 101-104
039	09.9.2018 16 h, 11.029	11.9.2018	*q*BOUNCINO	0 n none	[236](p.38), 115-116
145	10.9.2018 39 h, 11.031	11-12.9.2018	*q*BOUNCINO	1100 n none	[236](p.38-39), 118-119
141	22.9.2018 207 h, 11.056	4-5.10.2018	*q*BOUNCINO	8000 n $>10^5$	[236](p.39-40), 127-130

State population

Lukas Achatz fully evaluated only the detectors 003, L11, 062 and 070. He was not able to find any line shaped neutron track pattern on the other irradiated detectors (102, 116, 128). His results are shown in the following table (taken from [14](tab. 4.08, 4.10, 4.12 and 4.14)) which are the measured state populations for all measurements of this thesis:

Not only he fitted the track pattern to the first three gravitational states (see table 4.9) but also separately to the first four states. Table 4.10 summarizes these results. Comparing both evaluation results two differences are visible: Taking more states into account reduces the calculated population of the lowest states and also increases the error of all states. This was already expected from earlier detector evaluations.

Table 4.9.: CR-39 state occupation measurements 2018 taken from [14]

	region I	region V	region I + region V calculated	region I + region V measured
CR-39 ID	003	L11	-	062&070
neutrons	14111	2905	-	10599
χ^2_{red}	0.82	1.06	-	0.93
DOF	41	33	-	53
$\|b_1\|^2$ [%]	$47.5^{+1.2}_{-1.4}$	$43.2^{+4.7}_{-6.0}$	53.8	$60.7^{+2.2}_{-6.1}$
$\|b_2\|^2$ [%]	$38.3^{+2.6}_{-2.2}$	$39.5^{+6.9}_{-6.1}$	39.8	$39.3^{+6.8}_{-2.0}$
$\|b_3\|^2$ [%]	$14.2^{+3.1}_{-3.1}$	$17.3^{+2.0}_{-12.7}$	6.4	$0.0^{+4.0}_{-0.0}$
Spatial resolution [µm]	$3.65^{+0.08}_{-0.10}$	$3.60^{+0.25}_{-0.36}$	-	$2.53^{+0.15}_{-0.17}$
Absorber height [µm]	$31.00^{+0.75}_{-0.53}$	$27.38^{+2.44}_{-1.21}$	-	$34.25^{+17.82}_{-1.86}$

Table 4.10.: CR-39 state occupation tests in 2018 [14](tab. 4.09, 4.11, 4.13 and 4.15)

	region I	region V	region I + region V calculated	region I + region V measured
CR-39 ID	003	L11	-	062&070
neutrons	14111	2905	-	10599
χ^2_{red}	0.83	1.09	-	0.95
DOF	40	32	-	52
$\|b_1\|^2$ [%]	$43.9^{+6.2}_{-3.7}$	$42.4^{+11.1}_{-14.3}$	54.6	$55.7^{+2.1}_{-2.2}$
$\|b_2\|^2$ [%]	$34.6^{+9.0}_{-5.5}$	$40.6^{+6.9}_{-9.5}$	41.2	$43.7^{+5.7}_{-2.2}$
$\|b_3\|^2$ [%]	$8.3^{+6.4}_{-5.3}$	$17.0^{+2.4}_{-11.6}$	4.1	$0.0^{+3.9}_{-0.0}$
$\|b_4\|^2$ [%]	$13.2^{+21.4}_{-10.5}$	$0.0^{+11.2}_{-0.0}$	0.0	$0.7^{+11.6}_{-0.7}$
Spatial resolution [µm]	$3.50^{+0.22}_{-0.10}$	$3.35^{+0.35}_{-0.34}$	-	$2.53^{+0.14}_{-0.20}$
Absorber height [µm]	$29.96^{+1.28}_{-0.56}$	$27.75^{+2.68}_{-1.68}$	-	$34.10^{+0.0}_{-2.60}$

The results of the state population evaluations after one absorber region is approximately 45 % - 40 % - 15 %. This means the contrasts of the transitions starting from the first or the second state are expected to be similar. The high content of the third state will reduce the contrast of the transition $|1\rangle \rightarrow |3\rangle$ to a comparable contrast of its neighboring transitions $|2\rangle \rightarrow |4\rangle$ and $|2\rangle \rightarrow |5\rangle$.
Combining two absorbers in a row reduces the third state more than expected to a negligible level. This shows using longer absorber regions could increase the contrast for the first states if we use the same wide-ranged velocity interval.

The spatial resolution is worse than expected (compared to previous evaluations as seen in the next subsection). Also the fitted absorber height is much larger than the set height of approximately 22 µm. The main reason could be the different neutron detection method used in the evaluation of Lukas Achatz (see more in section 3.2.4). A detailed analysis is needed to check that the newly used method (track recognition with machine learning) will find the same center coordinates for a single neutron track as the earlier used method (detection directly by the microscope software). A difference can blur the height distribution of the neutrons above the mirror[5].

Comparison to older state population measurements

CR-39 state occupation measurements were performed for all previous GRS setups (GRS^{TJ}-setup [139](p.78-79), RABI^{GC}-setup [65](p.24-27) and RAMSEY^{TR}-setup [254](p.110-112)). In the following I will quote these measurements and compare them to the measurements of 2018. This is not entirely possible because each CR-39 detector was evaluated completely differently, even though the irradiation and chemical treatment was quite similar. However, the detectors themselves were sometimes from the same patches which enables better to compare the evaluation processes (H. Filter Patch #8: 003, 129, T37 & D. Seiler: L06, L09, L11).

The experimental team of the first RAMSEY^{TR}-setup assembly beam time (3-14-358-I, cycle 180-16/3) measured the state distribution in winter 2016-2017 [254](p.110-112). Martin Thalhammer [299] and Nadine Freistetter [93] performed the microscopy read out and evaluation in Vienna.

[5] Setting the correct center is discussed in [199](p.16-19)

Table 4.11.: CR-39 state occupation tests in 2016-2017 [254](p.112, tab. 9.2)

	region I	region V	region I + region V	
			calculated	measured
CR-39 ID	T37	L06	-	129
neutrons	2265	12232	-	7147
χ^2_{red}	1.15	1.61	-	0.99
$\|b_1\|^2$ [%]	$52.1^{+2.2}_{-2.2}$	$45.9^{+0.9}_{-1.0}$	58.5	$59.2^{+1.2}_{-1.0}$
$\|b_2\|^2$ [%]	$36.6^{+3.4}_{-3.6}$	$43.1^{+1.6}_{-1.7}$	38.6	$37.9^{+1.8}_{-2.3}$
$\|b_3\|^2$ [%]	$10.7^{+2.3}_{-3.3}$	$11.1^{+1.1}_{-0.9}$	2.9	$3.0^{+1.4}_{-1.2}$
$\|b_4\|^2$ [%]	$0.7^{+4.7}_{-0.7}$	$0.0^{+0.5}_{-0.0}$	-	-
Absorber height set	25 µm	26 µm	-	-

The original absorbers had a wider gap but were used with the same setup with the same velocity spreading. As a result of this measurement, the absorber gap was lowered in 2018 in order to increase the population of the lowest state. The measured results proved the opposite. The state population stayed nearly the same or decreased for the lowest state. However, the total neutron count rate decreased as expected[6].
All detectors were from similar patches as 2018. However, the evaluation was done differently. Also in between the microscope was brought to Grenoble and had to be readjusted. These two facts are expected to be the reason of the significantly lower errors of the older measurements.

Table 4.12.: CR-39 state occupation tests in 2012 [65](p.24-27 tab. 3.2)

	region I
CR-39 ID	L09
neutrons	5051
χ^2_{red}	0.86
Parameters	7
$\|b_1\|^2$ [%]	$59.70^{+1.59}_{-1.48}$
$\|b_2\|^2$ [%]	$34.03^{+2.17}_{-2.15}$
$\|b_3\|^2$ [%]	$6.27^{+2.61}_{-2.68}$
Spatial resolution [µm]	$1.36^{+0.13}_{-0.14}$
Absorber height [µm]	$28.45^{+0.62}_{-0.49}$
Absorber height set	30 µm

As seen in table 4.12, Gunther Cronenberg only shows one CR-39 measurement of his RABI^{GC}-setup. He irradiated the L09 detector for 59 h in a flux of 70.9(31) mcps. The state preparation after the measured first region is better than all the succeeding measurements. One explanation of the better state preparation is the lower used velocity interval (5.6 m/s to 9.5 m/s [65](p.20)). Faster neutrons interact less often with the absorber therefore higher states are able to pass through the absorber gap and enter the setup. In addition, the resolution is much better than the evaluation of 2018. Similarly, the fitted absorber height is lower than the set height. This is the opposite to the findings of L. Achatz.

Table 4.13.: CR-39 state occupation tests in 2009-11 [139](p.48 eq. 2.34-2.35, p.78 tab. 3.3)

	3-14-253 & TEST1692	3-14-283 & DIR94
CR-39 ID	HA01	HB07
χ^2	42.1	
Parameters	38 - 6	
$\|b_1\|^2$ [%]	$53.5^{+2.3}_{-2.0}$	$69.64^{+2.14}_{-1.70}$
$\|b_2\|^2$ [%]	$39.1^{+3.4}_{-3.4}$	$30.36^{+1.86}_{-1.70}$
$\|b_3\|^2$ [%]	$7.5^{+3.2}_{-3.1}$	$0.00^{+1.67}_{-0.00}$
Spatial resolution [µm]	$2.04^{+0.22}_{-0.17}$	
Absorber length	150 mm (& 100 mm)	150 mm
Absorber height set	25.5 µm (& 27.1 µm)	22.3(1) µm
Absorber height [µm]	$33.7^{+2.8}_{-1.4}$	
Velocity interval	5.7 m/s - 7 m/s [147]	5.74 m/s - 9.52 m/s

[6]See measurements in table A.5 and in section A.4.3.

Table 4.13 displays the results of two CR-39 measurements for the GRS^{TJ}-setup. Tobias Jenke described both iterations of this setup in his thesis [139](p.45-48, 78-86) and in [147]. The first state occupation measurement has more details due to the fact that it was also important for the qBB measurements of 2009. The main difference between both iterations is the absorber gap height and the different velocity distribution. The higher proportion of the lowest state (nearly 70 %) can be explained with the lower absorber gap height. Similar to the findings of Gunther Cronenberg, the overall better state preparations compared to the RAMSEY^{TR}-setup can be reasoned with the lower velocity interval.

More detailed studies of the relation between velocity and state preparation are very important for future statistical optimizations (count rate vs. contrast). Only with an automatized aperture this could be systematically explored.
Equipping the absorber with piezo motors similar to the electrodes (see subsection 3.3.6 [162, 225]) enables to study in detail the influence of the absorber gap height to the state distribution. This could be also used to built an absorber test bench which can compare the influence of the different surface roughness.
Implementing new detector systems and replacing the CR-39 detectors can increase the resolutions (Japanese emulsion detectors [206]) or especially online detectors speed up the read-out process.
In order to be able to better use the already existing measurements (and not wasting expensive beam times for redoing measurements), the complete CR-39 evaluation process has to be standardized and the different techniques compared to each other. Only if all detectors are evaluated with the same carefully-tested technique, then the results like the gap height or the resolution can be really compared.

4.3.3. Shutter characterization

On the 13.6.2018 the monitor count rate rose suddenly by more than 25 % which was not observed in the zero rate of the main detector or the reactor power itself. In the following days, Tobias Jenke and I searched for a possible explanation. During this time, we discovered a misalignment of the shutter (15.6.2018). The opening position was around 22.5° and the closing position at −92°. Quite fast we determined with the help of Thomas Brenner that only the limit stop of the closing position was loose and therefore the shutter reel over turned by 24.5°. In this position the shutter was again slightly open and the monitor background rate was increased by incoming neutrons.

On the 19.6.2018 we conducted a series of monitor rate measurements at different shutter positions to determine the best shutter *open* and *closed* positions (IDs 4.218-4.244, see data points in the appendix A.4.4). The measurements are presented in figure 4.16. The new shutter positions were set with the mechanic limit stops and tested with neutrons: *open* = 24° and *closed* = −65°.

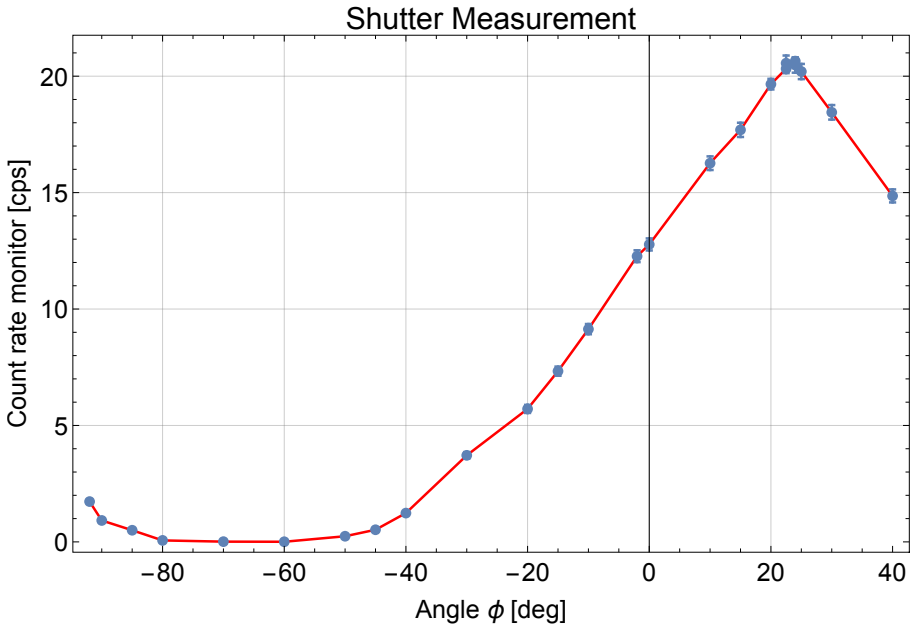

Figure 4.16.: The monitor rate for different shutter real positions measured on the 19.6.2018.

This measurement also reveals how UCNs pass through such a rotatable shutter. Two different geometrical approaches are presented in the subsection 3.1.2. For comparison, the measured rates were divided by the highest rate in order to have relative transmissions similar to the theoretical predictions. Also the angles were shifted by the angle of the highest count rate (24°). All angles outside ±90° were shifted by 180° in order to account for the π symmetry of the shutter reel. Figure 4.17 reveals that the UCN beam is only reduced once at the shutter entrance and the *single guide approach* with the parameters $r_b = 40\,\text{mm}$ and $r_s = 65\,\text{mm}$ perfectly describes the behavior of this rotatable shutter.

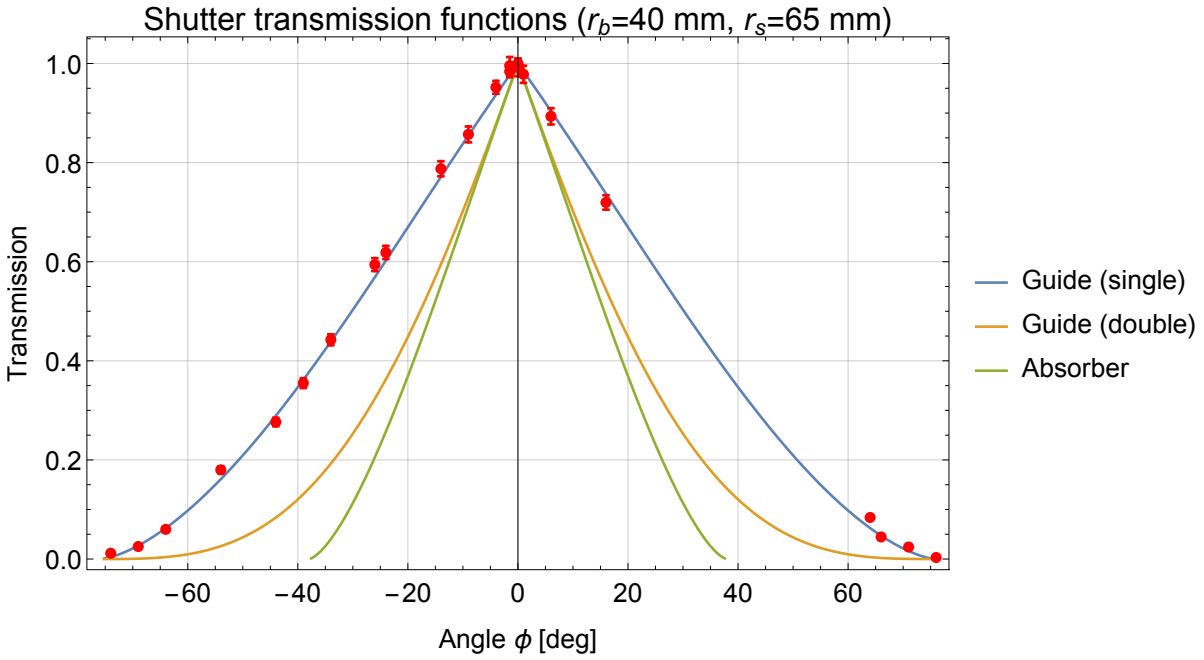

Figure 4.17.: The relative transmission of the shutter measurements compared to different shutter transmission functions as proposed in section 3.1.2.

4.4. RABI-GRS-18

Similar to 2017 [193], a three-region Rabi-type setup should test GRS within the RAMSEY^{TR}-setup prior to the assembly of the five-region Ramsey-type GRS setup. After the testing of the newly clamped state selectors [14] and the aperture measurements, we assembled the so-called RABI-GRS-18 setup. It was operable in the last two weeks of the cycle 182-18/1 (*3-14-358-III*) [274].
This measurement is split in two independent runs: RABI-GRS-18 I was the first assembly of three regions in 2018 starting on the 12.4.2018 and lasting to the 17.4.2018. The primary goal was to measure within multiple resonances and far away from any transitions with high statistics to proof that the GRS works. In between, multiple zero rate measurements additionally showed its stability (see fig. A.40 in the appendix). Both goals were not achieved in 2017 [193] and were only reached 2018 with a better mirror alignment [84] and exchanges of vacuum compatible components (e.g. miCos stages and mirror-GND cables). After this successful run, we vented and opened the chamber in order to prepare the final preparation measurements for the Ramsey assembly (installation of the long region III). An unplanned reactor shut down in the evening of the 17.4.2018 changed this plan. In the following two days, the Rabi setup was reassembled and adjusted. The second so called RABI-GRS-18 II run started with the restart of the reactor on the 20.4.2018 and ended with the final shut down of the beam time 182-18/1 in the morning of the 26.4.2018. The aim of these measurements was to map as many as possible different resonances with the high count rate of the RABI-GRS-18 setup (50 mcps) which could be used as comparison to the later assembled Ramsey-setups and the previous measured RABI^{GC}-setup [65].

4.4.1. Statistical overview of RABI-GRS-18 measurements

The table 4.14 reveals the key parameters of both RABI-GRS-18 measurements. The major difference is the different reactor power level which also manifests as a higher monitor rate (after the reactor restart the operators increased the reactor power in order to fully burn the fuel element after skipping two days of beam time). However due to a new mirror alignment, the zero rate stayed the same. A second difference was the average number of neutrons per measurement point.
RABI-GRS-18 I consists of only a few measurements with many neutrons per data point. In contrast RABI-GRS-18 II has nearly seven times more measurement points in only twice the measurement time. Many measurements consist of below 400 neutrons which represents an error above ±5 %. Longer and fewer measurements would have increased the readability of the final graphs (see fig. 4.18). Similarly, RABI-GRS-18 II has only half the neutron counts during the zero rate measurements. However, it has more measurement points at different frequency settings. For more readable graphs a measurement plan between the ones from both runs is favorable. Points with a low number of counts (< 400 neutrons) have a too large error for the expected low contrast (30 %).
For all RABI-GRS-18 measurements, the detector backgrounds were stable and sufficiently low. Also the zero rate and monitor rate were stable which enabled to fully correct all measurement points and rescale them to relative transmissions. I corrected both measurement runs independently, joined them afterwards and applied together the fits. All measured points can be found in the appendix A.5.

Table 4.14.: RABI-GRS-18 Statistics

Property	RABI-GRS-18 I	RABI-GRS-18 II
Reactor power	49.6(1) MW	58(1) MW
Time period	12-17.4.2018	20-26.4.2018
Measurement points	5 (794.7 cycles)	34 (1612 cycles)
Zero rates points	5 (730 cycles)	8 (321 cycles)
Dropped measurements points	2 (3.8 cycles)	5 (5 cycles)
Measurement counts	5991 n / 150 986 s	12043 n / 306 281 s
Zero rate (corrected)	52.35(62) mcps	51.99(94) mcps
Zero counts	7444 n / 138 700.1 s	3170 n / 60 990.1 s
Monitor rate	18.0072(79) cps	23.7137(80) cps
Monitor neutron counts	5229497 n / 290 412.0 s	8731036 n / 368 185.9 s
Detector background rate	0.830(112) mcps	0.707(94) mcps
Detector background counts	55 cts / 66 242.4 s	57 cts / 80 655.5 s
Monitor background rate	0.12404(137) cps	0.14453(134) cps
Monitor background counts	8217 cts / 66 242.4 s	11657 cts / 80 656.8 s

4.4.2. RABI-GRS-18 - results

The 29 data points above 300 Hz are in good agreement with a multi two-level approach using the measured velocity distribution (see section 4.3.1). The fitted local gravitational acceleration is $g_{fit} = 9.781(80)\,\mathrm{m\,s^{-2}}$ with a p-value of 6.61 %. These results can be seen in figure 4.18 and details of the fits are displayed in the appendix A.5.3.

In total three transitions are detected within the high frequency data points (>300 Hz). These are namely $|2 \to 4\rangle$, $|1 \to 3\rangle$, $|2 \to 5\rangle$. Their frequencies are $\nu_{24} = 391.9(21)$ Hz, $\nu_{13} = 462.2(25)$ Hz and $\nu_{25} = 560.0(31)$ Hz respectively.
The RABI^{GC}-setup revealed a slightly higher transition frequency of $\nu_{13} = 464.1(12)$ Hz at $g_{GC} = 9.844(37)\,\mathrm{m\,s^{-2}}$ which is still within their error bars [65]. The statistical error of the new measurement is twice as high as the Rabi measurement of 2012, even though 3 to 4 times more neutrons were observed. The main reason is the much higher contrast observed for $|1 \to 4\rangle$ ($c_{14}^{GC} = 78.0(1)$ %) which increases the sensitivity significantly. The contrast for $|1 \to 3\rangle$ is quite comparable ($c_{13}^{2018} = 43.1(21)$ % vs $c_{13}^{GC} = 43.6(1)$ %). The low amplitudes of the measurements were a second reason. Most measurements had an oscillation strength a_v of $1.5\,\mathrm{mm\,s^{-1}}$ or $1.7\,\mathrm{mm\,s^{-1}}$ due to mechanical limits at the highest applied frequencies (600 Hz, constant amplitude scans). We would have been able to address higher amplitudes at lower frequencies. This would have been necessary to deploy the maximal available contrast

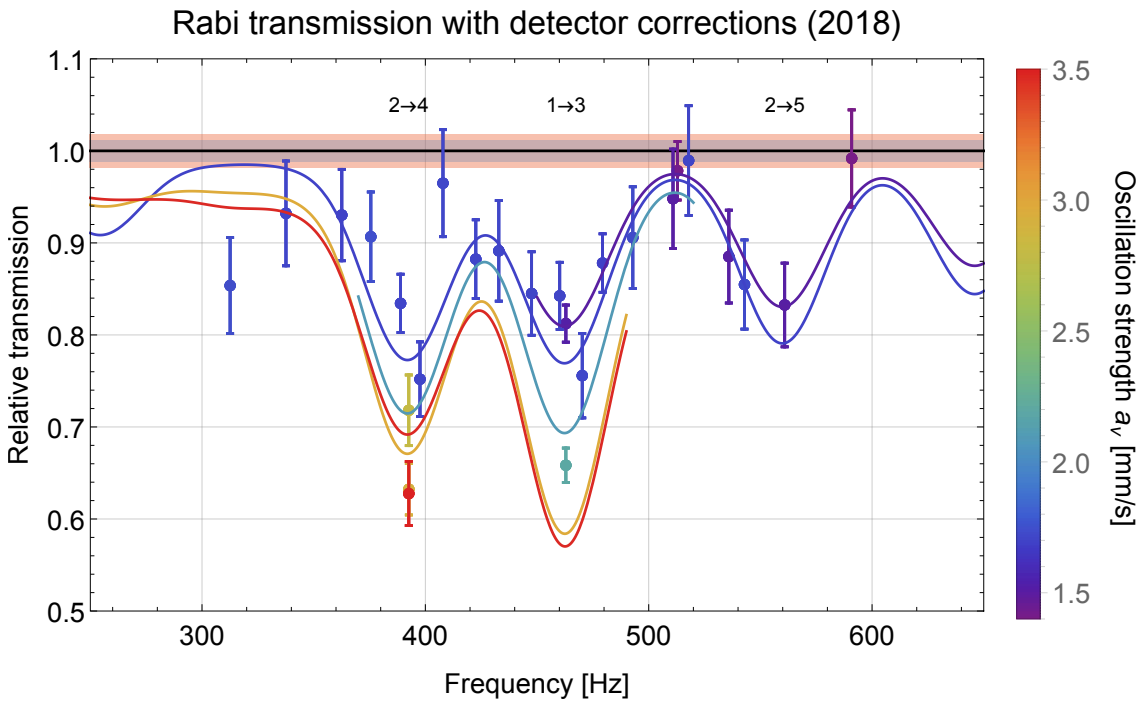

Figure 4.18.: RABI-GRS-18 high frequency transitions with a 10 Hz binning for similar oscillations strengths a_v

(2.6 mm s^{-1} for $|2 \rightarrow 4\rangle$ and 3.1 mm s^{-1} for $|1 \rightarrow 3\rangle$). In similar cases future experiments should use frequency-depending amplitudes to match the resonance conditions as close as possible (see eq. (2.103)) and still stay within the mechanical limit of the piezoelectric stages at all frequencies.
The transition $|2 \rightarrow 4\rangle$ was only measured in the GRS^{TJ}-setup before. The results are not comparable due to the squeezed states in the first GRS setup of Tobias Jenke [139]. The transition $|2 \rightarrow 5\rangle$ was observed for the first time. More details on the robustness of the fit are in the appendix A.5.3.

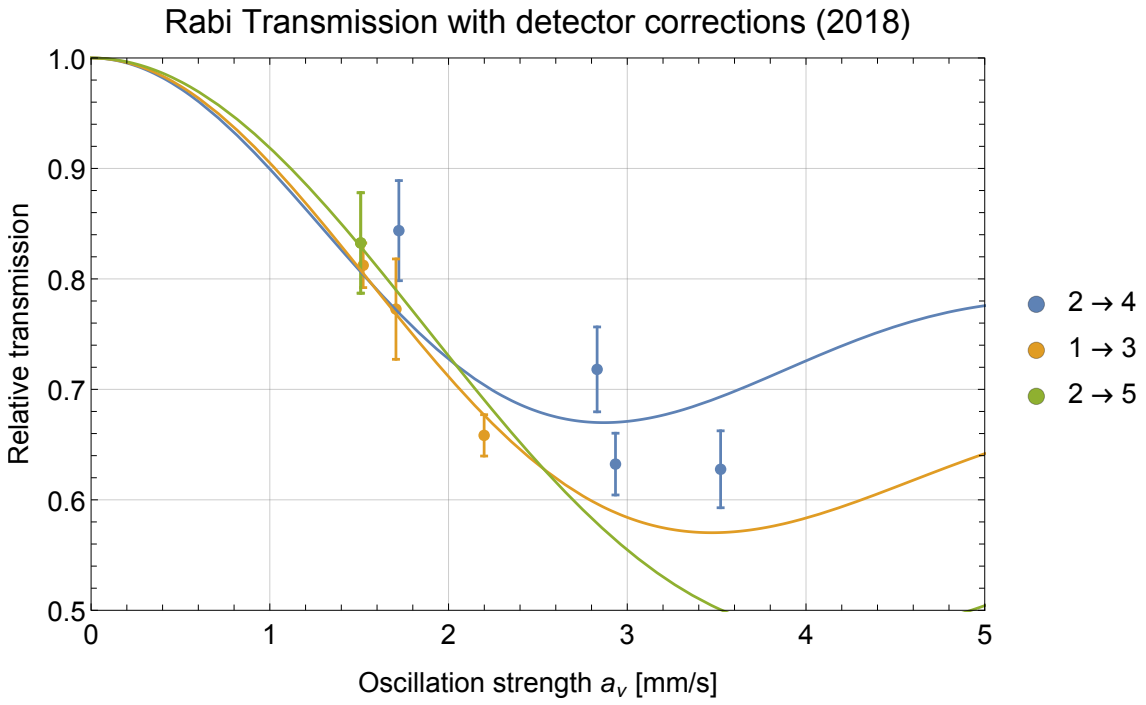

Figure 4.19.: RABI-GRS-18 all measured transitions

Compared to the Ramsey measurements shown later (see fig. 4.23 in section 4.5), we measured only a few data points with different amplitudes within the resonances. Still, a revival of the initial state at high amplitudes as predicted by the theory is not observed.

The ten measurement points at low frequencies (<300 Hz) and high amplitudes (3-5 mm s^{-1}) cannot be described with a two-level approach with an acceptable significance level and physical fit parameters (the best attempt is visualized in fig. 4.20). In this region multiple transitions overlap. In these crossover areas a neutron in one state has two or more different states available to transit into. This makes multilevel calculations necessary. Especially, the high amplitude also enables multiple transitions within the flight time through the single oscillating region (region II). This setting space opens an opportunity to test new numeric approaches for multilevel calculations. Additionally, at low frequencies the mechanical amplitude increases and starts to periodically, mechanically block the neutron beam significantly with the mirrors. Further investigations with the Ramsey setup are strongly advised.
A second feature is visible at 300 Hz. The two closest data points are well below the theoretical prediction. Remeasuring this region could distinguish between a statistical fluctuation or the necessity to improve the corresponding theories.

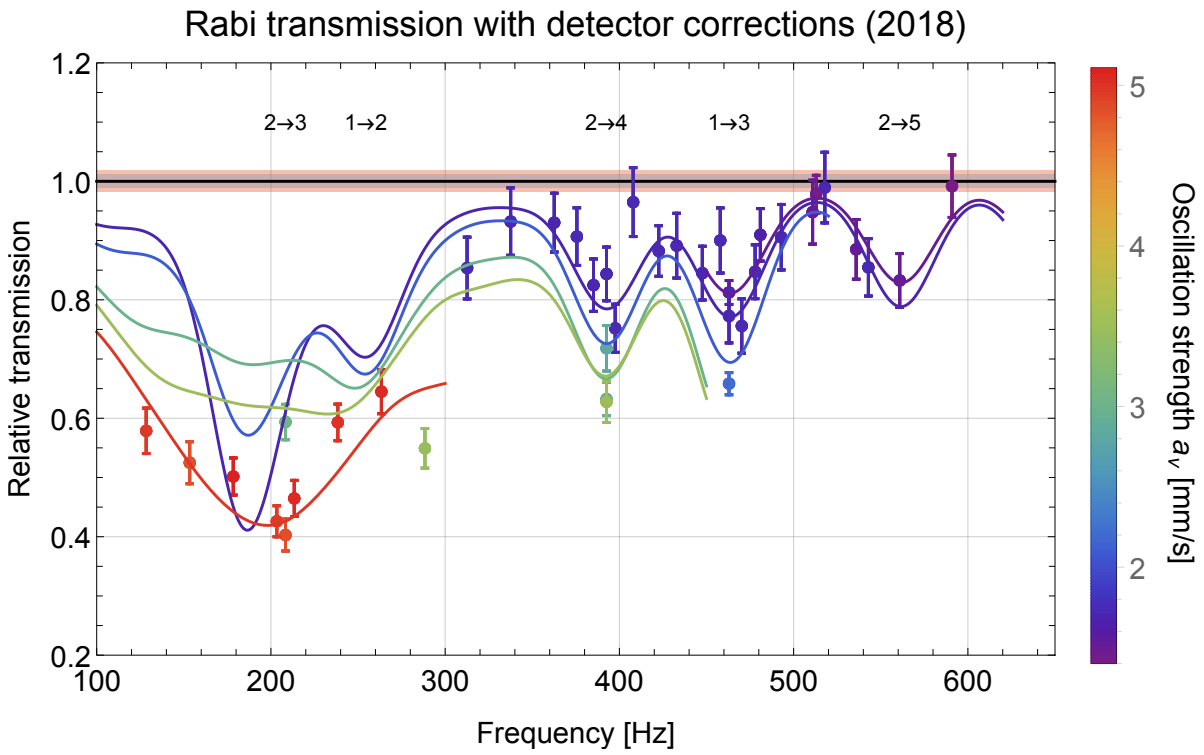

Figure 4.20.: RABI-GRS-18 all measured points

4.5. RAMSEY-GRS-18

In the beginning of the beam time 183-18/2, I tested two different region III mirrors (as described in A.4.3). I decided to use the newer electrode mirror #811 because it had a measured surface topology, even though it had some visible scratches from the conducted tests in the beginning of the year. All mirrors were aligned by hand with the linear gauges (see section 3.7.1). The capacitive sensors were only used to measure the step heights and not to readjust them. At the time, this automatized step control was not ready for usage (Jakob Micko enabled and verified this feature in the following years [194]).
After carefully aligning all parts and cleaning the chamber and the mirrors, the chamber was finally closed on the 1st of June 2018 and the first zero rate measurement started in the evening of this day. Until the reactor shut down on the 5th of July, the chamber stayed closed and evacuated. Instabilities of LabView control system and of the monitor detector interrupted this long measurement time twice and separated the data in three subsets (independent measurement periods, see table 4.15). I constantly

worked on the LabView issues to improve the stability and fix some bugs while the setup was running fully automatized. The monitor detector showed some instabilities. From time to time the monitor rate increased by a factor of 50 % without changing the spectral shape or any other statistical related parameters (except the average rate). At the start of the next beam time glass shards were found close to the detector gap. The most plausible explanation is movements of these shards and consequently the changing of the opening area of the monitor detector. Therefore, we omitted the monitor correction for all the data points of this beam time.
In the beginning, the focus of the Ramsey studies was the transitions $|1\rangle \rightarrow |3\rangle$ and $|2\rangle \rightarrow |4\rangle$ (which were also studied with the RABI-GRS-18 setup). Later it shifted to the transition $|2\rangle \rightarrow |4\rangle$ only. This transition was studied with frequency, amplitude and phase sweeps. Each point was measured with at least 400 neutrons. This was an improvement compared to the RABI-GRS-18 measurement but still not optimal in order to determine the transition frequency and to generate visible convincing graphs.
At the end of the beam time, Magdalena Pieler and Valentin Czamler helped during the deactivation of the full setup, with manual remeasuring of the step heights and preparing for the next cycle. Even though, they had to set up the *q*BOUNCINO setup for the first time [236], there was enough time for us to do all these works due to the one week earlier shut down of the reactor.

Table 4.15.: Statistical overview of the RAMSEY-GRS-18 GRS measurement periods

Setting	RAMSEY-GRS-18-I	RAMSEY-GRS-18-II	RAMSEY-GRS-18-III	RAMSEY-GRS-18-Fall
Time period	3 - 19.6.2018	19 - 26.6.2018	26.6. - 4.7.2018	11 - 15.9.2018
Reactor power	52.5 MW	52.5 MW	52.5 MW	51.5 MW
Monitor rates	19.637(4) cps	25.083(7) cps	20.762(6) cps	113.92(2) cps
Zero rates	17.33(36) mcps	19.43(44) mcps	19.38(44) mcps	22.35(101) mcps
Zero rates data points	10	8	5	2
Neutrons of the zero rates	2547 n	2762 n	2028 n	507 n
Phase data points	7	3	6	0
Amplitude data points	16	0	0	0
Frequency data points	16	1	13	8
Neutrons of all data points	13759 n	1232 n	7469 n	2702 n

4.5.1. Phase variations between the oscillating regions

In the beginning it was not clear how we are able to see a Ramsey-type GRS transition in the fastest way because it was never done before. The first attempt was to sweep the amplitude in different resonances (fig. 4.23). There we did not observe a revival of the lower state at high amplitudes due to the broad velocity distribution. Due to the low contrast, the not yet fully measured frequency sweeps (2nd attempt, fig. A.42) did not show a clear signature of quantum mechanics. Therefore, I started to measure different phases at resonance of the transition $|2\rangle \rightarrow |4\rangle$. Soon we saw an effect that not only proves that the quantum mechanics is the main effect of the new GRS setup but also that it is a Ramsey-type setup and not two independent Rabi-type GRS setups. As seen in figure 4.21, variations of the phase between the two oscillating regions influence the transition probability due to the coherent superposition of states in region III. At a π phase difference, the lower state is populated again instead of the higher excited state. After this basic proof of principle (the first proof of a working Ramsey-type GRS setup ever done), we measured further at different frequencies, amplitudes and phases to map the transition with more data points.

As figure 4.21 displays, the inverted phases did not completely increase the rate back to the zero rate. This is due to different systematic effects: e.g. the measurement could be slightly off resonance or the mechanical amplitudes of both regions could be not equal. Jakob Micko later used this effect as a stability test of the setup and to precisely measure the transition frequency [194](p.25-27, & 89-93). In order to account for this effect, I not only fitted the full Ramsey theory (eq. (2.124)) to the measurements at different phases but also different sine functions (as seen in table 4.16). As a comparison, a classical approach (see [254](p.54-58)) or a double Rabi-type setup would predict a linear behavior of the relative transmission for different phases.

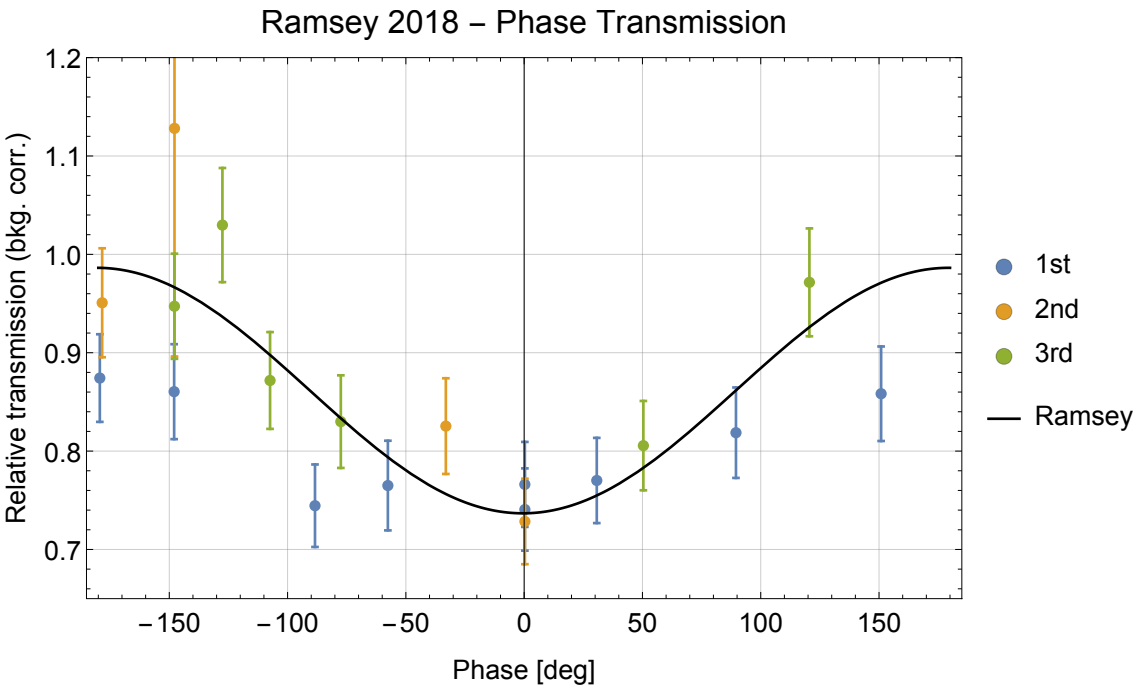

Figure 4.21.: RAMSEY-GRS-18 phase: measured data points at 392.625 Hz

The phase sweep also reveals interesting mechanical details. As seen in the comparison between the applied voltage and the induced mechanical oscillations (see table A.27 in appendix A.6), the AFG signal is around 30.8° shifted to the measured phase of the SIOS laser interferometers[7]. At a closer look this difference varies with the phase difference between the regions, because the mechanical oscillations influence each other by transmitting these vibrations via the granite below to each other. Similarly, the mechanical amplitude a_x varies slightly, even though the voltage amplitude of the function generator was kept the same for both regions during all measurement points.

Table 4.16.: Fit routines comparison Ramsey phase sweep (Discrete velocity spectrum 2018, transition $|2\rangle \rightarrow |4\rangle$ at $\nu_{24} = 392.625\,\text{Hz}$, $a_v = 1.44(3)\,\text{mm}\,\text{s}^{-1}$)

Data	Parameter	χ^2	red-χ^2_{red}	p-value	Formular
19 SIOS Phase	$d = 0.828(11)$	52.86	2.937	2.75×10^{-5}	Flat: $r = d$
19 SIOS Phase	$k = 0.00025(12)$ $d = 0.820(12)$	48.368	2.845	7.54×10^{-5}	Linear: $r = k \times \phi + d$
19 SIOS Phase	$a = 0.083(14)$ $d = 0.836(11)$	21.173	1.245	0.2186	Sine: $r = a \times \sin\left(\phi\frac{\pi}{180} - \pi/2\right) + d$
19 SIOS Phase	$a = 0.084(15)$ $\Delta\phi = -\pi/2 - 4.9(119)°$ $d = 0.837(11)$	21.004	1.313	0.1784	Shifted: $r = a \times \sin\left(\phi\frac{\pi}{180} + \Delta\phi\right) + d$
19 SIOS Phase	$a = 0.082(14)$ $s = 1.19(18)$ $\Delta\phi = -\pi/2 - 11.9(135)°$ $d = 0.827(13)$	20.294	1.353	0.1609	Scaled: $r = a \times \sin\left(s\phi\frac{\pi}{180} + \Delta\phi\right) + d$
19 SIOS Phase	$c_{24} = 28.6(19)$	32.917	1.829	0.0171	Ramsey: eq. (2.124)

[7] The phase difference can origin from the piezoelectric stage mechanics or their controllers which transmit the voltage signal. A second reason is probably the interplay between the AFG and the laser interferometer. At the time (2018), they were not synchronized by a commonly used rubidium clock [194](p.46-48). In addition, firmware updates of the interferometers reduced the noise of their raw data which sometimes was misinterpreted by LabView evaluation as a phase offset.

The table 4.16 shows that the linear fits are statistically excluded and therefore the Ramsey-like behavior is proven. However, the sine like fits describe the data very well and all of them are equally likely. The Ramsey fit is by one order of magnitude less likely than the sine fits due to the systematic effects. By reducing these effects and decreasing the statistical uncertainty (higher counted neutron number and higher contrast), the Ramsey theory should describe the data better than the sine fits. However, the sine fits also tested if the measured phase is shifted compared to the real phase experience by the wave function. The current uncertainty of approximately 12° is larger than the detected shift of around 5°.

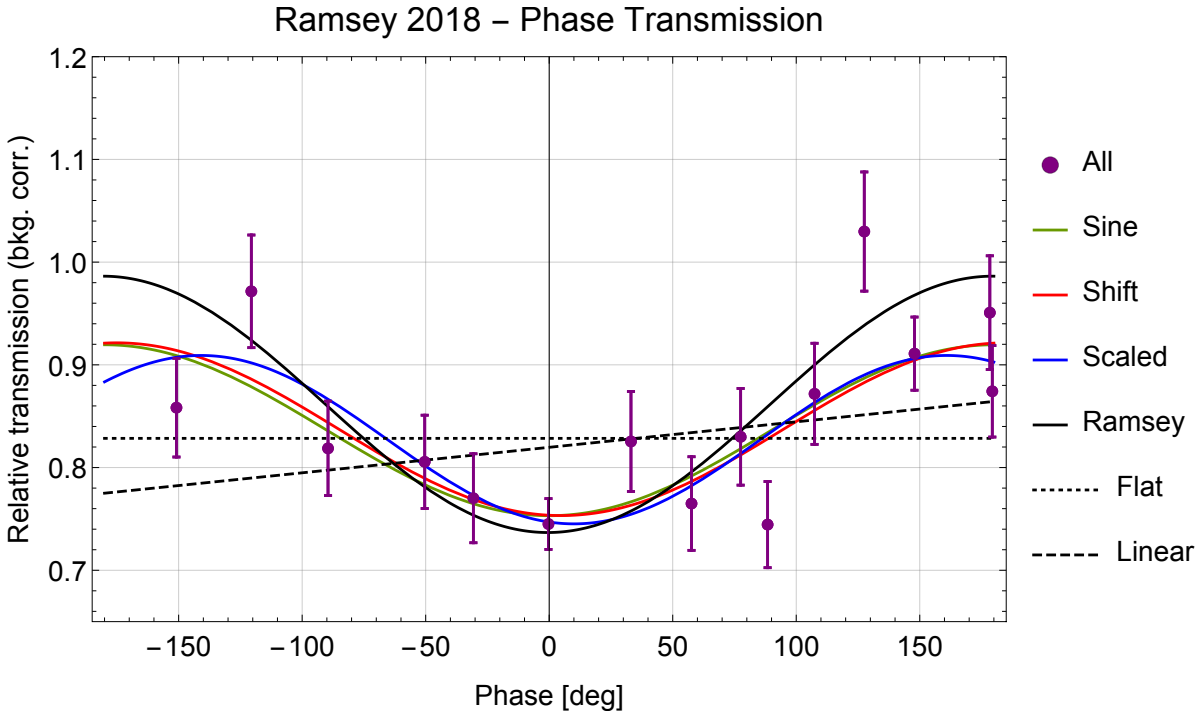

Figure 4.22.: RAMSEY-GRS-18 combined phase measured points - different fitting functions

Already Tobias Rechberger made a preliminary analysis of this data set to finalize his thesis [254](p.116-119). The fitted results are quite similar to the full evaluation. All other published proof-of-principle evaluations contain faulty graphs due to mistakes in the preliminary data evaluation [276]. This can easily be spotted by observing shifted zero degree measurements in data plots.

4.5.2. Frequency and amplitude variations

In contrast to the phase plot, the amplitude plot and the frequency plots are not so conclusive. However, they are the first of their kind for a Ramsey-type GRS measurement.

As displayed in figure 4.23, higher amplitudes do not induce a state reversal as theoretical expected (see fig. 2.9). Even including a strong velocity spreading cannot reduce the theoretical prediction (2-level approach) enough to describe the measurements[8]. Real multi-state effects could explain the low rates at higher amplitudes. The excited 4th state could be further excited (e.g. $|4\rangle \rightarrow |6\rangle$ at 325.28 Hz or $|4\rangle \rightarrow |7\rangle$ at 473.31 Hz) and therefore also not be able to pass the second absorber region. Similarly, a close transition for the 3rd state is the transition $|3\rangle \rightarrow |7\rangle$ at 509.48 Hz for example. A detailed theoretical analysis is necessary to quantify this effect. Systematic effects are a second cause (e.g. unequal amplitudes of the oscillating regions, mechanical resonances). Jakob Micko tested this by reversing the phase of the second oscillating mirror [194](p.90). Without systematic influences and in the two state case, the reversed rate should be stable at the zero rate for all different oscillation strengths.

[8] The only point at high amplitudes (around 2.8 mm/s) which is in favor of the theoretical prediction was measured during a LabView crash and therefore afterwards the measurement was repeated resulting in a lower rate. However, it passed all systematic tests (AFG status, time resolved detector evaluation, SIOS laser interferometer measurements,..) and therefore it was not excluded.

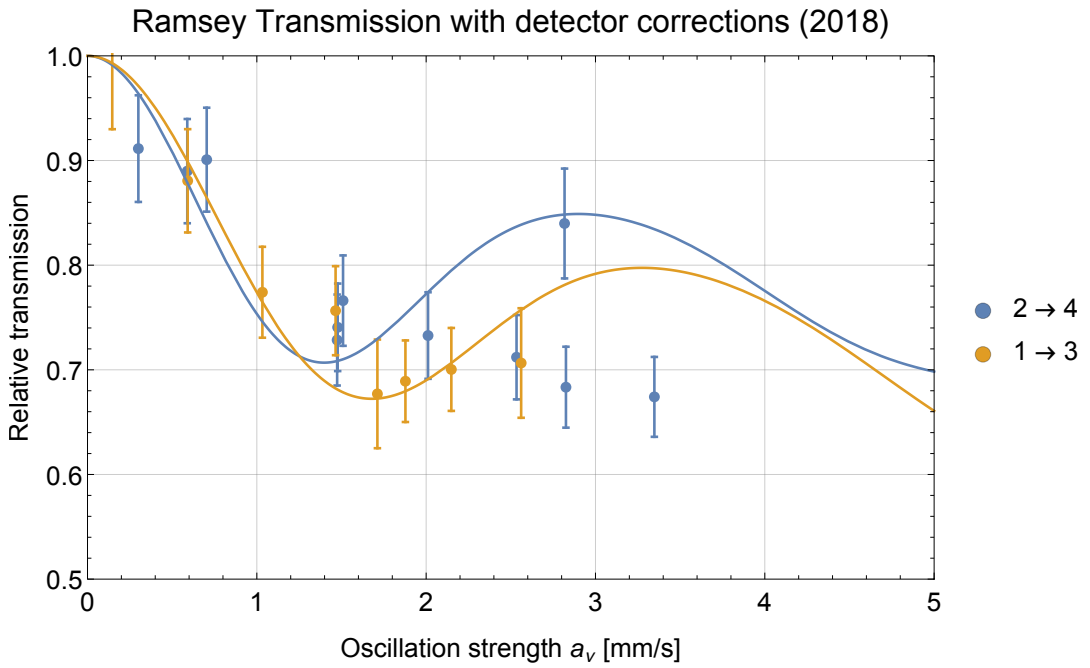

Figure 4.23.: RAMSEY-GRS-18 measured points with different amplitudes at resonance

Remarkable is the fact that the amplitudes for both transitions are quite similar (30 %) which is due to the high content of the second state after the first state selectors. Therefore, it is statistically the same which transition is studied in more detail. The transition with the lower frequency has the advantage to need less mechanical energy applied to the piezoelectric stages and therefore goes easier on its piezoelectric crystals. This is one of the reasons why mainly the transition $|2\rangle \rightarrow |4\rangle$ was examined. Figure 4.24 displays the measured data points around this transition by excluding measurements with high oscillation based on the previously displayed observation. This data set follows the theory predictions quite well within the statistical fluctuations.

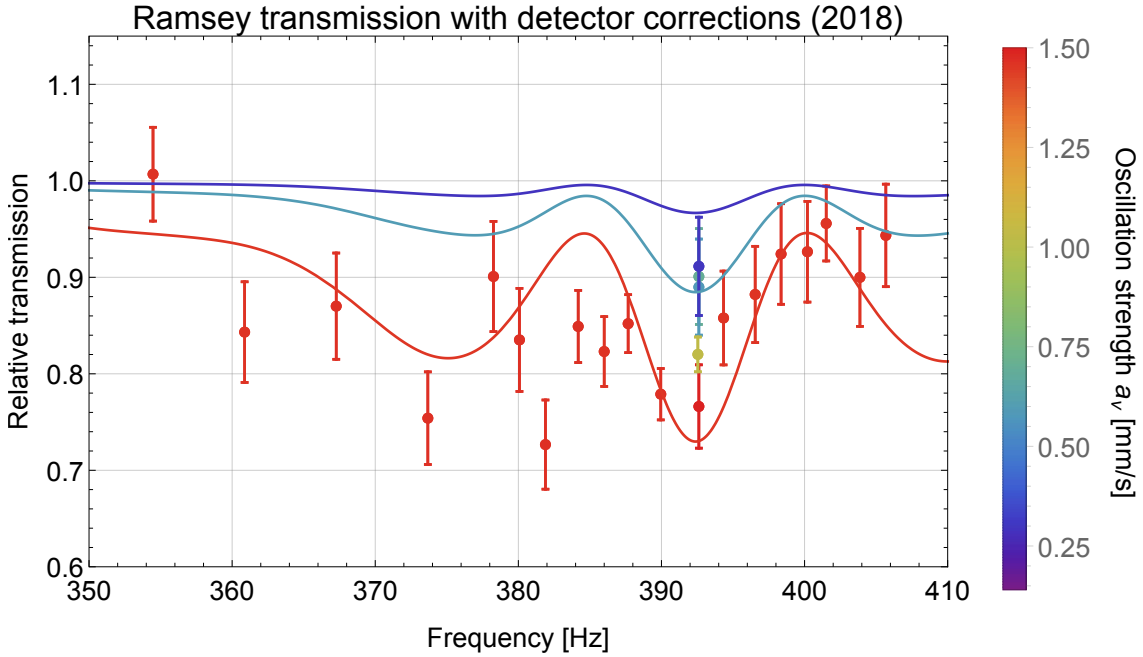

Figure 4.24.: RAMSEY-GRS-18 frequency measured points with low amplitudes (<1.6 mm/s) around the transition $|2\rangle \rightarrow |4\rangle$. For readability the data points were joined with a binning of 2 Hz in this plot.

4.5.3. RAMSEY-GRS-18 combined results

The evaluation to determine the transition contrasts (c_{24}, c_{13}) and the local gravitational acceleration g uses all available data points (amplitude, frequencies or phase sweeps of different transitions). The fitted routine uses a multi 2-level state Ramsey-type GRS theory (eq. (2.124), see more in theory section 2.2.2) with a velocity convolution (see section 2.2.3) of the measured spectrum (see section 4.3.1). The following table 4.17 provides the fitted results of all data points or a subset of them.

Table 4.17.: RAMSEY-GRS-18 fitted values: discrete velocity spectrum 2018 ($\Delta 0.01\,\mathrm{m/s}$), SIOS data, multi 2-level Ramsey theory ($c_{12} = 10\,\%$, $c_{25} = 54\,\%$, values taken from RABI-GRS-18)

Data	Parameter	χ^2	red-χ^2_{red}	p-value
All (62)	$c_{24} = 32.2(14)\,\%$ $c_{13} = 34.7(23)\,\%$ $g = 9.8014(89)\,\mathrm{m\,s^{-2}}$	156.35	2.650	9.55×10^{-11}
a_v<1.6 mm s^{-1} (53)	$c_{24} = 29.8(14)\,\%$ $c_{13} = 30.6(39)\,\%$ $g = 9.7982(96)\,\mathrm{m\,s^{-2}}$	104.47	2.089	1.02×10^{-5}
Only zero phase + a_v<1.6 mm s^{-1} (37)	$c_{24} = 29.2(17)\,\%$ $c_{13} = 33.4(47)\,\%$ $g = 9.752(13)\,\mathrm{m\,s^{-2}}$	63.76	1.875	0.00148
3rd measurement period (19)	$c_{24} = 24.3(26)\,\%$ $c_{13} = 30\,\%(fixed)$ $g = 9.802(17)\,\mathrm{m\,s^{-2}}$	16.43	0.967	0.4935

Converting the globally fitted gravitational acceleration g leads to the transition frequencies of $\nu_{24} = 392.47(24)\,\mathrm{Hz}$ and $\nu_{13} = 462.81(28)\,\mathrm{Hz}$. This main result of fitting all data points is statistically not well supported. Excluding the values of high oscillation amplitudes significantly increases the likelihood while only reducing slightly the contrast and the gravitational acceleration g ($\nu_{24} = 392.38(26)\,\mathrm{Hz}$ and $\nu_{13} = 462.71(30)\,\mathrm{Hz}$). Omitting the measurements with different phases only slightly increases the probability but shifts small g to nonphysical values. This emphasizes the importance of not only measuring at different frequencies but also at different phases in order to accurately determine the transition frequency. Measuring at different oscillation strengths is only necessary to have an as high as possible contrast.
The data is split in single measurement periods[9]. The 3rd measurement period by itself shows a clear signature of a Ramsey-GRS curve as seen in figure 4.25. The evaluation of other subsets is displayed in the appendix A.6.1.

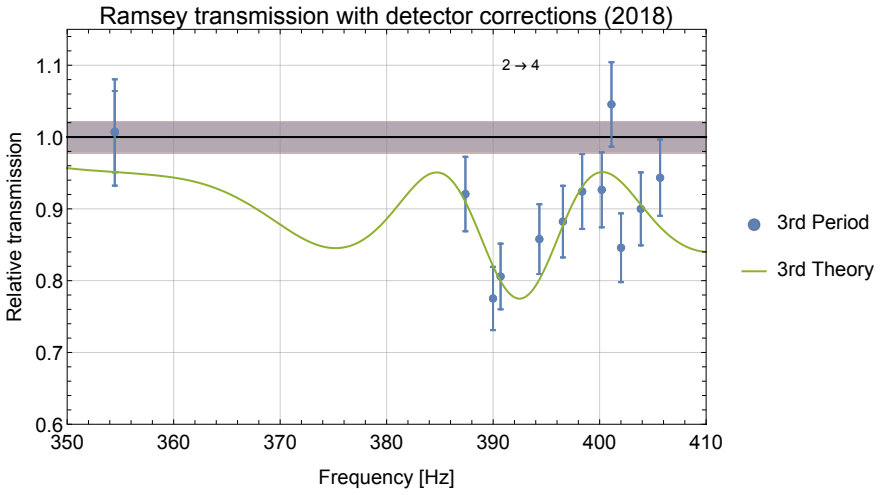

Figure 4.25.: RAMSEY-GRS-18: data points form 3rd measurement period and its theory function

[9]During one measurement period, all parameters are the same. Therefore, all data points are evaluated with the same common mean zero rate. Between different periods, some settings could have changed significantly (e.g. step height or venting of the vacuum chamber).

Overall, the results have not yet reached high levels of confidences. However, improvements after this first Ramsey-type GRS measurement during the commissioning time of the RAMSEY^{TR}-setup revealed the true potential of the new apparatus with nearly perfect fitted χ^2-values [194]. The most important changes were the working automatic mirror alignment system, introduction of a rubidium clock for accurate synchronization of all systems and optimized measurement schemes.

4.5.4. Rabi tests within a complete Ramsey-type setup

As a test during the proof of principle time of the full Ramsey-type setup, we induced single Rabi transitions with both oscillating mirrors (region II & region IV) separately. For the two different oscillation strengths a_v which are matching either a $\pi/2$-flip or a full π-flip, the 2-level Rabi theory predicts transmission probabilities of 83 % or 70 % respectively (using the results of the full Ramsey measurements as input parameters).

The measurements are presented in the table 4.18. Their transmission rates are compatible with the predictions. They are within or in the vicinity of the error bars. In addition, we can observe that the resting mirror region slightly oscillates. This is by a factor 8 stronger for region II. Still, it is more than by a factor 50 lower than a real transition amplitude. However, detailed measurements of all resting mirrors should be done in future setup alignments in order to exclude parasitic oscillations on other mirrors.

Table 4.18.: Rabi rates of the cycle Ramsey-2018 (3-14-358-IV)

ID	Start	Livetime[s]	UCN	Transmission	ν(SIOS)	a_v(reg2)	a_v(reg4)	Type
4.246	16:47 19.06.2018	57 139.5 s	847 n	0.717(33)	392.614(1) Hz	1.452(1) mm s^{-1}	0.0041(2) mm s^{-1}	region II $\pi/2$
4.288	17:30 21.06.2018	21 280.0 s	401 n	0.924(55)	392.614(1) Hz	1.444(1) mm s^{-1}	0.0033(2) mm s^{-1}	region II $\pi/2$
4.294	00:06 22.06.2018	28 120.0 s	401 n	0.688(41)	392.614(1) Hz	3.057(3) mm s^{-1}	0.0075(5) mm s^{-1}	region II π
4.308	14:43 22.06.2018	24 320.0 s	403 n	0.807(48)	392.614(1) Hz	0.0269(10) mm s^{-1}	1.465(4) mm s^{-1}	region IV $\pi/2$
4.315	22:18 22.06.2018	29 640.0 s	402 n	0.652(39)	392.614(1) Hz	0.0552(25) mm s^{-1}	3.071(9) mm s^{-1}	region IV π

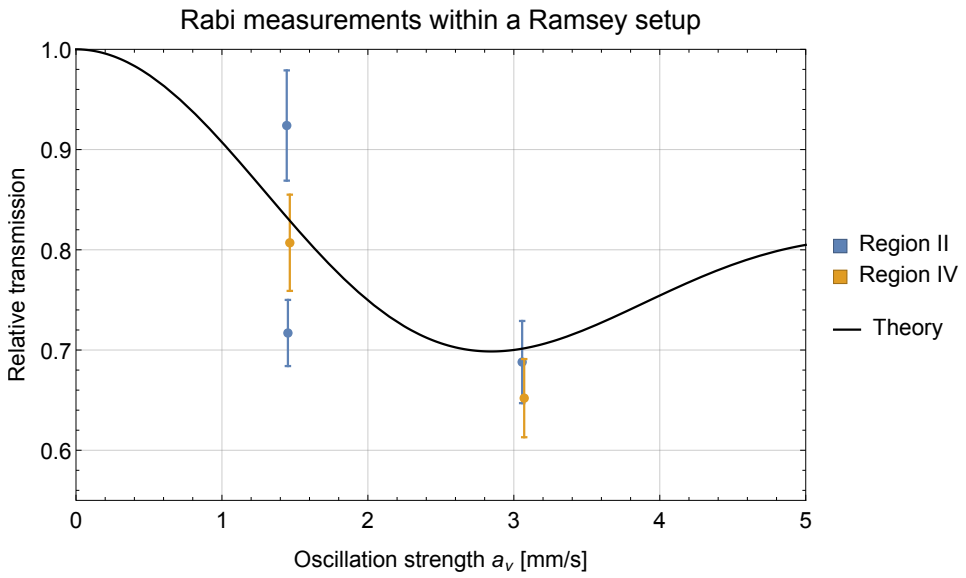

Figure 4.26.: Visualization of table 4.18

4.6. Rams$\vec{E}$y - the electric charge measurements using GRS

The beam time 184-18/3 (3-14-384, autumn 2018) was dedicated to the electric charge measurement of the neutron as proposed in [77] and described in the theory section 2.3. For the measurement itself, we brought the electrode test setup (described in section 3.3) to Grenoble and integrated it into the RAMSEY^{TR}-setup during the beam time.

In her project thesis [169], Elisabeth Kreuzgruber describes the complete electrode setup as it was implemented during the electric charge measurement and all auxiliary measurements needed to operate the high electric field. In the following subsection I present these measurements on the bases of her evaluations before I display the neutron measurements and the final value of the measured neutron's electric charge.

4.6.1. Rams$\vec{E}$y-measurement timeline

The GRS measurement started already during this implementation time after we had finished to adjust and clean everything within the vacuum chamber and we had closed and evacuated the chamber on 28.9.2018. This measurement period is denoted as the 0 V measurements (28.9-13.10.2018). Only on 3.10.2018 we opened the chamber briefly to readjust the laser beams. Severe damages due to undocumented changes in the clamping circuit of the ammeter delayed the start of the real high voltage measurements. After an unnecessary opening of the vacuum chamber in the morning of 13.10.2018, Jakob Micko and I found the damage of the electrode setup during this Saturday evening. The next day (14.10.2018), we were able to repair provisionally these flaws and start up the high voltage to 1000 V. Unfortunately, the reactor shut down in the evening of the same day and restarted three days later (17.10.2018) with only 34.5 MW power (only 67 % of the nominal reactor power of this cycle). In the remaining two weeks, we were able to measure at 1000 V a complete transition ($|2\rangle \rightarrow |4\rangle$, 5 points + some points remeasuring due to LabView crashes, each point with at least 400 counted neutrons). On 23.10.2018, I increased the voltage to 1750 V. I was not able to reach the intended 2000 V because of an undocumented change of the hardware limit of the power supply. Until the reactor shut down on 28.10.2018, we remeasured the 5 different frequency points at this higher electric field setting. After this beam time, Jakob Micko and the PF2 team sent the electrode test setup back to Vienna for the final tests with the used Rams$\vec{E}$y electrode (described in section 3.3 and in the theses [96, 151, 241, 247]).

4.6.2. Rams$\vec{E}$y-electrode alignment

As described in subsection 3.3.6, the large Rams$\vec{E}$y electrode had to be aligned parallel and to a known distance in order to be able to determine the electric field strength at a certain applied voltage. The electrode itself was designed and built only shortly before the measurement campaign. Therefore, the first alignment was already for the charge measurement with no experience of its mechanics. To spare the titanium surfaces the absolute reference to glass spacers was discarded and we had to align the upper electrode from an arbitrary position.

For the pitch angle α with its long leverage, the alignment worked very well as it was from the beginning already close to flat (around 0.1 mrad off). The roll angle β was similarly adjusted but was extremely large at the beginning (approx. 4 mrad). During the alignment process, we used a fast fit routine in an excel spreadsheet to calculate the needed alignment angle. A detailed evaluation of Elisabeth Kreuzgruber [169](p.21-25) revealed after the beam time that the final pitch angle α was 0.28(5) µrad and the roll angle β was 110(25) µrad. These tilt angles translate into an opposite height adjustment of both ends of <0.1 µm and 5.2 µm respectively. The first value is below the possible adjustment precision (0.1 µm) for the pitch angle α. The second value representing the roll angle β is quite large which stayed for the complete charge measurement due to the lack of precise evaluations at the time. Later measurements in Vienna revealed that more measurement points, especially far away from parallel alignment, increase the precision of the determined zero tilt angle significantly [96]. Due to the time pressure during the first alignment this was not done.

During the alignment process, the goal was to reach a distance between the electrodes of approximately 200 µm which corresponds to a capacitance of around 1.5 nF. The distance itself is much larger than the size of the neutron wave functions (20 µm - 50 µm) and still small enough that the applied voltage is

reasonable low to reach high electric fields. The exact value is only important for the evaluation of the electric charge measurement. During the alignment, we only measured eight points in a distance interval of 60 µm as we lowered the upper electrode after we tried to remove the strong roll angle tilt. This low number of data points made it very hard for Elisabeth Kreuzgruber to determine the exact height [169](p.25-27). Additionally, the error due to the precision of the capacitance measurement was overestimated by nearly a factor of 10 due to the manual reading from the display. Only after the ability to remote control the multimeter, the readout with higher resolution revealed the true measurement precision [151, 162, 225, 241]. She tested different models to describe the behavior during the height setting changes. All models were statistically not distinguishable. The models with multiple fit parameters had also strong problems with overfitting. Only trying to rule out models due to nonphysical fitted parameters reduced its numbers. She favored the most simple model with only fitting an offset to the guessed height due to the problem with overfitting (only eight data points). The calculated height of this model is 206.9(8) µm which corresponds to electric field strengths of 4.83(5) MV/m and 8.45(9) MV/m at an applied voltage of 1000 V and 1750 V respectively.
Later studies with orders of magnitudes more data points enabled not only to fit the electrode area and the error of the capacitance measurements, but also the expected parallel parasitic capacitance which was similar to the measured capacitance with an open ground connection [96, 151, 162, 225]. This behavior can also be observed to the fitted model of the first alignment. The fitted parasitic capacitance was 0.12(3) nF and the measured capacitance with an open ground connection was 0.118 nF. The corresponding height of this model is 228.2(58) µm. For an applied voltage of 1000 V and 1750 V, this translates to an electric field strength of 4.38(11) MV/m and 7.67(20) MV/m respectively. I used these values for the final analysis of the electric charge measurement. The following table 4.19 displays a summary of all important values:

Table 4.19.: Rams$\vec{E}$y electrode alignment during the charge measurement (values taken from [169])

Property	Value
Electrode distance d	228.2(58) µm
Pitch angle α	0.28(5) µrad
Roll angle β	110(25) µrad
Electric field at 1000 V	4.38(11) MV/m
Electric field at 1750 V	7.67(20) MV/m

All described values from above are taken from the project thesis of Elisabeth Kreuzgruber [169](p.22-27). She also listed all measurement points in its appendix [169](p.49-51).

4.6.3. Rams$\vec{E}$y electronic settings

Similar to the alignment, Elisabeth Kreuzgruber evaluated all important parameters of the electronic settings (e.g. voltage, dark current, stability and charging behavior) [169](p.28-44). In general, the setup reached the addressed voltage and was quite stable. The only concern was the high dark current due to the wrong cabling after the provisional repairs[10] (which was still better than after the undocumented change when six reversed Si diodes blocked the current going from the electrode to the ammeter). Fortunately no electrode breakthrough occurred because the safety diode strands to the ground were not attached as they should be. A spark would have damaged the ammeter. Back in Vienna Julius Piso restored the correct cabling with the help of Anika Gassner and the electronic workshop [241]. This reduced the dark current significantly[11].
I tried to only slowly charge and discharge the Rams$\vec{E}$y electrode (3.6 V s^{-1}). However after each LabView crash, the power supply lost the remote connection. During reconnecting, the measurement program set the voltage outputs to zero. In order not to discharge the electrodes I ramped up as fast as possible the voltage to the used value. The table 4.20 displays all important electric settings.

During the electric charge measurement, we did not reach the maximal possible voltage of the Rams$\vec{E}$y electrode. During the first tests in Vienna after the beam time, Anika Gassner, Julius Piso and I applied

[10] The resistor line was correctly attached to the ammeter but the parallel connection to the ground via a 100 MΩ resistor was missing. Additional the Return-AI connection was cabled to the reversed Si diode strand instead of the floating shielding of the signal coaxial cable.
[11] Jasmin Juroszek [151] and Nicole Pruggmayer [247] completely reduced the dark current to zero by introducing eight HV-diodes into the reversed diode strand which contained before only six Si diodes.

Table 4.20.: Rams$\vec{E}$y electric parameters during the charge measurement (values taken from [169])

Setting	0 V	1000 V	1750 V
Applied voltage	1.35(32) V	1000.39(2) V	1750.44(10) V
FuG current I	−21.8(49) nA	13.5(86) nA	32.3(94) nA
Ammeter measurement	0.119(9) a u	4.727(31) a u	8.07(11) a u

more than 2000 V at an electrode gap size of 99.6(13) µm. We did not observe destructive breakthroughs but a high dark current (a detailed evaluation is displayed in [96]). In the following year, Jasmin Juroszek, Nicole Pruggmayer and I repeated the experiment with an upgraded clamping circuit which eliminated the dark current completely. We observed destructive breakthroughs with the slightly deteriorated surface of the Rams$\vec{E}$y electrode at field strengths around 10 MV/m (see more in [151]). All electrode tests conducted in Vienna (see section 3.3.1) suggest that we could have doubled the applied voltage for the charge measurement. However, much higher fields would have definitely destroyed the used electrode.

4.6.4. Rams$\vec{E}$y GRS measurements and the determination of the neutron's electric charge

The GRS measurements for the electric charge measurement took place in the second half of the beam time. The first GRS period in the beginning of the beam time[12] was attributed to the RAMSEY-GRS-18 measurements (see section 4.5) as *Ramsey-2018 Fall* because they used the same mirror configuration which was different to the Rams$\vec{E}$y setup. Table 4.21 presents an overview of the measurement periods of the charge measurement (Rams$\vec{E}$y). Detailed summaries of all used zero rates and frequency measurements are listed in the tables A.29, A.30, A.31 and A.32 in the appendix A.7.

Table 4.21.: Statistical overview of the Rams$\vec{E}$y GRS measurements

Setting	0 V	1000 V	1750 V
Time period	28.9 - 3.10 - 13.10.2018	17. - 23.10.2018	23. - 27.10.2018
Reactor power	51.5 MW	34.5 MW	34.5 MW
Monitor rates	115.87(3) cps + 117.35(2) cps	82.79(2) cps	82.80(2) cps
Zero rates	20.00(45) mcps + 19.08(31) mcps	12.84(57) mcps	12.42(59) mcps
Zero rates data points	16 = 4 + 12	2	1
Neutrons of the zero rates	5679 n = 1984 n + 3695 n	505 n	446 n
Frequency data points	21 = 3 + 18	9	5
Different frequency settings	9	5	5
Neutrons during frequency rates	6486 n = 1026 n + 5460 n	2926 n	1554 n

Figure 4.27 displays the measured GRS rates already separated by the voltage setting. The amplitude strength a_v was approximately 1.47 mm/s for all measurement points which corresponds to the expected π-flip at a neutron velocity of 9 m/s (see eq. (2.126)). The phase between the oscillating regions was adjusted to 0° seen by the SIOS laser interferometer. With the usage of *Mathematica*, I fitted for each setting and their combinations a multi 2-level Ramsey theory curve (eq. (2.125)) with a variable g. The contrast was only a free parameter for the measured transition $|2\rangle \rightarrow |4\rangle$. For the neighboring transitions, the contrast values were taken from previous measurements (RABI-GRS-18, see section 4.4). Similar to the other GRS measurements of this thesis, the fit included the spreading due to the measured velocity spectrum (see measurement section 4.3.1). The final curves are plotted together with their data points in the same color. The table 4.22 presents the fit results of the different data sets.

The fitted results of the different measurement periods (voltage settings) are statistically not distinguishable from the combined fit results. The contrast of the transition c_{24} is always approximately 35 % and the gravitational acceleration of each fit is slightly lower than the classically measured value in Grenoble ($g_{q\text{BOUNCE}} = 9.805\,\text{m}\,\text{s}^{-2}$, see section 2.1.3) but within the range of their corresponding fitted uncertainties.

[12] 10.-15.9.2018

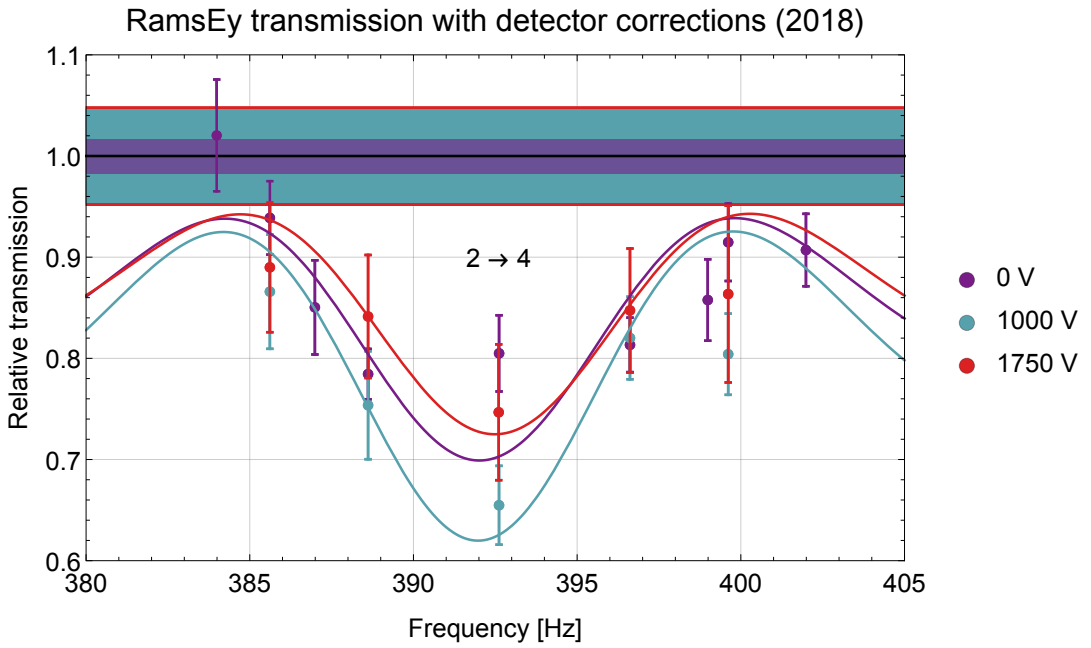

Figure 4.27.: Rams$\vec{E}$y frequency data points with their corresponding fitted theory curves (multi 2-level Ramsey with velocity spreading)

Table 4.22.: Rams$\vec{E}$y fitted values: discrete velocity spectrum 2018 ($\Delta 0.01\,\mathrm{m/s}$), SIOS data, multi 2-level Ramsey theory ($c_{12} = 10\,\%$, $c_{13} = 43\,\%$, $c_{25} = 54\,\%$, values taken from RABI-GRS-18)

Data	Parameter	χ^2	red-χ^2_{red}	p-value
All (35)	$c_{24} = 35.4(21)\,\%$ $g = 9.791(10)\,\mathrm{m\,s^{-2}}$	49.21	1.491	0.0346
0 V (21)	$c_{24} = 33.0(28)\,\%$ $g = 9.784(13)\,\mathrm{m\,s^{-2}}$	31.96	1.682	0.0316
1000 V (9)	$c_{24} = 42.0(38)\,\%$ $g = 9.783(19)\,\mathrm{m\,s^{-2}}$	11.12	1.588	0.1335
1750 V (5)	$c_{24} = 30.0(59)\,\%$ $g = 9.802(36)\,\mathrm{m\,s^{-2}}$	1.401	0.4670	0.2947
HV combined (14)	$c_{24} = 38.1(29)\,\%$ $g = 9.797(15)\,\mathrm{m\,s^{-2}}$	18.54	1.545	0.1002
All (35)	$c_{24} = 35.2(21)\,\%$ $g = 9.784\,\mathrm{m\,s^{-2}}(fix)$ $q_\mathrm{n} = 2.7(33) \times 10^{-17}\,e$	49.08	1.487	0.0354
All (35)	$c_{24} = 35.5(21)\,\%$ $g_{q\mathrm{BOUNCE}} = 9.805\,\mathrm{m\,s^{-2}}(fix)$ $q_\mathrm{n} = -0.8(33) \times 10^{-17}\,e$	50.42	1.528	0.0267

Figure 4.28 shows the fitted transition frequency ν_{24} for the three different electric field strengths E_z. Fitting a linear function ($\nu_{fi}{}^{\vec{E}} = k \cdot E_z + d$) to the three values gives the following values:

- $d = \nu_{fi}{}^{g} = \nu_{24} = 391.99(34)\,\mathrm{Hz}$
- $k = \Delta_{\nu_{fi}}/\nu_{fi}{}^{g} = 0.030(106)\,\mathrm{Hz\,m\,MV^{-1}}$
- $\chi^2 = \chi^2_{red} = 0.1623$
- p-value = 0.313

With the formula (2.180) this can be translated into $g = 9.783(13)\,\mathrm{m/s^2}$ and a neutron's electric charge of $q_\mathrm{n} = 1.2(43) \times 10^{-17}\,e$.

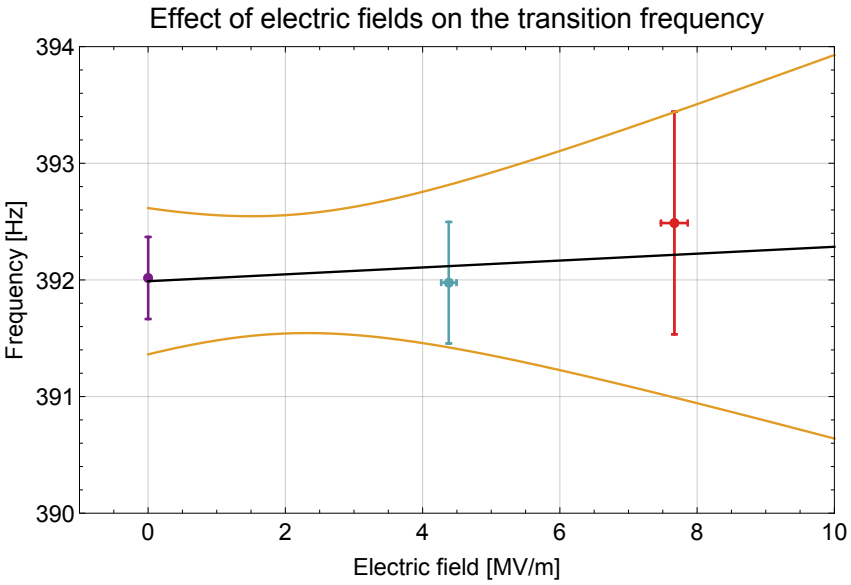

Figure 4.28.: Rams$\vec{E}$y fitted transition frequency for different electric field strengths (color according to the voltage setting) including a linear regression (black) and its 68 % confidence bands (orange)

A more elegant way is to fit both parameters (g, q_n) already with all data points at once (as already described in the theory section 2.3.3). Due to their similar behavior, one of them has to be kept fixed while the other one together with the contrast c_{24} is fitted. The best fitted value for the hypothetical charge is $q_\mathrm{n} = 2.7(33) \times 10^{-17}\,e$ (at a fixed local gravitational acceleration of $g = 9.784\,\mathrm{m\,s^{-2}}$ taken from the zero voltage measurement). This is quite similar to the expected sensitivity of $2.8 \times 10^{-17}\,e$ for this measurement[13]. Due to a lower zero rate and some software crashes the data taking took more than 8.2 d. Both extracted values are *in agreement with the commonly accepted neutrality of the free neutron*[14] similar to the much better measurement of Baumann et al. [36]. The limit on any hypothetical neutron's electric charge of this thesis is $|q_\mathrm{n}| < 9.2 \times 10^{-17}\,e$ (95 % confidence level). The following figure 4.29 displays a detailed map of the χ^2 values for different sets of fixed values for the neutron charge q_n and the gravitational acceleration g (the contrast parameter c_{24} is fitted to the data accordingly).

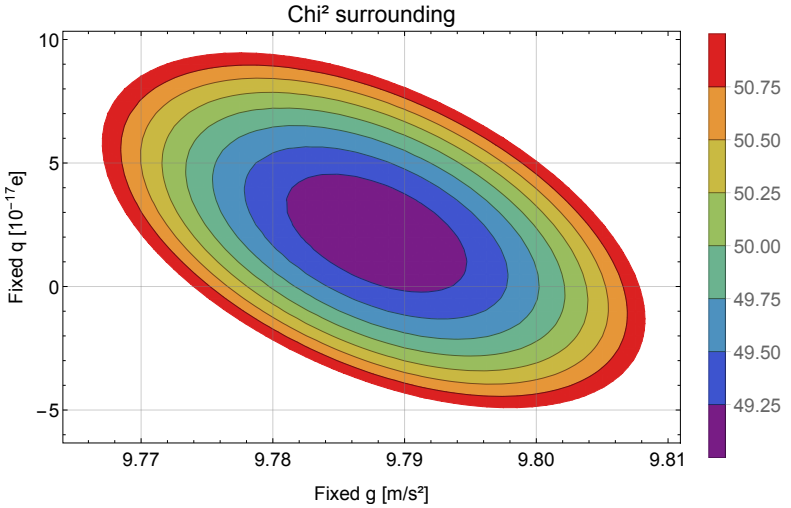

Figure 4.29.: χ^2 surrounding of the evaluated neutron charge value (Rams$\vec{E}$y)

[13] The measured sensitivity is slightly lower than expected, even though more neutrons are counted. The reason is the additional uncertainty of $\nu_{fit}{}^{g}$. Future measurements will profit from all GRS measurements in between and the cumulative low error of this transition frequency measurement.

[14] quote [36]

4.7. Summary of results

Here, I display an overview of the results of the measurements conducted at the PF2 UCN facility together with other members of the *q*BOUNCE collaboration and many students [14, 159, 169, 233, 236, 274] during three reactor cycles of the ILL high flux reactor in 2018 and at the ATI in Vienna between 2017 and 2022:

- State distribution with CR-39 (L11, 003, 070, 062) [14]
  - Approximately $|1\rangle = 45(5)\,\%$ $|1\rangle = 40(5)\,\%$ and $|1\rangle = 15(5)\,\%$
  - Additional beam divergence test and sequential etching (T35, 016, E03, 103)
- Aperture velocity spectrum (differential, $\Delta 1\,\mathrm{m/s}$ and $\Delta 2\,\mathrm{m/s}$)
  - $n_{2018} = 215.3$, $v_{02018} = 3.163\,\mathrm{m/s}$ and $b = c = 2(fixed)$
  - $a_{2018} = 4.176\,\mathrm{m/s}$: Corresponding neutron spectrum temperature $T = 2.1\,\mathrm{mK}$
- RABI-GRS-18 (3-14-358-III, 182-18/1) [14, 274]
  - $\nu_{24} = 391.9(21)\,\mathrm{Hz}$ and $\nu_{13} = 462.2(25)\,\mathrm{Hz}$
  - $\nu_{25} = 560.0(31)\,\mathrm{Hz}$ (new observed transition)
  - $g = 9.781(80)\,\mathrm{m/s^2}$ (29 data points, $\chi^2_{red} = 1.455$, $p = 0.066$)
  - Excluding high oscillation strengths: $a_v < 2\,\mathrm{mm/s}$ (25 data points, $\chi^2_{red} = 1.099$, $p = 0.34$)
  - Additional data below 300 Hz and higher amplitudes (up to 5 mm/s): multi-state theory testing ground
- RAMSEY-GRS-18 (3-14-358-IV, 183-18/2)
  - Rotable shutter characterization
  - Amplitude variations: $|2\rangle \rightarrow |4\rangle$ and $|1\rangle \rightarrow |3\rangle$
  - Phase and frequency studies: $|2\rangle \rightarrow |4\rangle$
  - $\nu_{24} = 392.47(24)\,\mathrm{Hz}$ and $\nu_{13} = 462.81(28)\,\mathrm{Hz}$
  - $g = 9.8014(89)\,\mathrm{m/s^2}$ (62 data points, $\chi^2_{red} = 2.65$)
  - Deviations at high amplitudes: $a_v < 1.6\,\mathrm{mm/s} \rightarrow g = 9.7982(96)\,\mathrm{m/s^2}$ ($n = 53$, $\chi^2_{red} = 2.09$)
- Rams$\vec{E}$y (3-14-384, 184-18/3) [159, 169, 233]
  - 0 V, 1000 V and 1750 V at 228.2(58) µm (evaluated by Elisabeth Kreuzgruber [169])
  - 0.00(1) MV/m, 4.38(11) MV/m and 7.67(20) MV/m
  - >5 points each in transitions $|2\rangle \rightarrow |4\rangle$ [46]
  - $g = 9.791(10)\,\mathrm{m/s^2} \rightarrow \nu_{24} = 392.19(27)\,\mathrm{Hz}$ (35 data points, $\chi^2_{red} = 1.491$, $p = 0.035$)
  - $q_\mathrm{n} = 2.7(33) \times 10^{-17}\,e$ ($g = 9.784\,\mathrm{m/s^2}$, 35 data points, $\chi^2_{red} = 1.487$, $p = 0.035$)
- Implementation of the *q*BOUNCINO test setup [236]
- Electrode tests at the ATI in Vienna [96, 119, 151, 162, 225, 241, 247]
  - 2017/18, Ti-Ti small electrodes + glass spacers: 19 MV/m [119]
  - 2019/20, Cu-Cu small electrodes + glass spacers: >10 MV/m [241]
  - 2019/20, Rams$\vec{E}$y electrode without spacers: >20 MV/m [96]
  - 2020/21, Cu-Cu small electrodes + glass spacers: 7.6 MV/m [247]
  - 2020/21, Rams$\vec{E}$y electrode without spacers: 10.8 MV/m [151]
  - 2021/22, Ti-Ti small electrodes without spacers: 4.1 MV/m [225]
  - 2021/22, small mirror electrodes without spacers: 11.4 MV/m [162]

5. Conclusion and outlook

In this thesis, I presented the final commissioning and the first measurements of the RAMSEY^{TR}-setup which is the first operational Ramsey-type GRS and which enables the qBOUNCE collaboration to more precisely study gravitationally bound quantum states of UCN and set lower limits on BSM theories [254]. This commissioning included a full characterization of the setup, a preceding Rabi-type GRS measurement (RABI-GRS-18), a first full Ramsey-type GRS measurement (RAMSEY-GRS-18) and the full evaluation of these including the stability of the entire setup during three beam times. The RABI-GRS-18 was the first successful GRS measurement using the new RAMSEY^{TR}-setup. The following RAMSEY-GRS-18 proved its superiority by lowering the statistical uncertainty by a factor of more than four compared to RABI^{GC}-setup in its first reactor cycle. With a similar number of counted neutrons and similar contrasts (approx. 20000 n, 30 %), it surpassed the RABI-GRS-18 measurements by a factor of nine which is more than the theoretically expected value of 5.5. Based on this work, Jakob Micko [194] exploited the full potential of the current setup which led to a gain factor of 42 in the statistical uncertainty between his results and the findings of Gunther Cronenberg [65] nearly 10 years earlier with the RABI^{GC}-setup.

The measurements during this thesis agreed with the multi 2-level theory for amplitudes up to the resonance conditions and frequencies above 300 Hz. A reevaluation and remeasuring at higher oscillation strengths and in the multi-state region below 300 Hz are good testing grounds for the numerical multi-state algorithm in order to be able to explore these observable regions of the current RAMSEY^{TR}-setup. In addition to the presented GRS measurements, Jakob Micko probed the region around the transition $|1\rangle \rightarrow |6\rangle$. For better constraints of BSM models, all other available transitions below 1000 Hz should be measured with similar precision, which also enables to calculate the exact energy levels and to search for state-dependent energy shifts. Such on-going measurements with the current experiment need further improvements of each component to promote a higher degree of automation and to speed up the evaluation process. This progress is part of the qBOUNCE-experiments since the beginning and supported by many students over the last decade. I presented within this thesis and in the internal documentation [1, 45] many possibilities and ideas for improvements. Additionally, many components of the RAMSEY^{TR}-setup will be part of a future generation qBOUNCE experiment which increases the importance of this on-going upgrades.

One of the next measurements will be with polarized neutrons in order to set limits to hypothetical spin-dependent gravitational models. I participated in the hardware preparations (e.g. winding of the coils) and Jakob Micko already demonstrated a first polarized measurement within the RAMSEY^{TR}-setup [194](p.94). One of the most important developments is to increase the count rate as much as possible to compensate for the losses of the beam polarization. One path is to optimize the UCN transport from the PF2 turbine to the experiment. The highest losses occur due to the velocity selection of the aperture. Monte Carlo simulations and corresponding measurements of different beam guide geometries could lead to a higher count rate and should be studied in detail. Within the setup, the UCNs are mainly lost due to the horizontal beam divergence. Reducing these losses by having reflecting walls similar to neutron guides could increase the count rate significantly and would enable to faster measure through the parameter space (frequency, amplitude, phase). Within the qBOUNCINO setup (a small test platform assembled in 2018 [236]), we were already able to show a neutron rate increase due to a mirror wall. Further investigations are currently running to also prove that reflection on a wall preserves the gravitational quantum state of the UCN.

The second main part of this thesis was the integration of an electric field in the system. This enabled to test the neutron's neutrality within the RAMSEY^{TR}-setup in order to demonstrate its capabilities to test BSM theories. In 2018, the Rams$\vec{E}$y measurement probed the electric charge q_n to $2.7(33) \times 10^{-17}\, e$. This was the first quantum mechanical determination of this quantity and the first within a Ramsey-type spectrometer. Investigations and improvement of the setup [194] by the qBOUNCE collaboration during the last years revealed that the sensitivity of this measurement could be increased by a factor of 75 within the current setup. Reaching the current best limit of the neutron charge ($-2(8) \times 10^{-22}\, e$ [319]) is only possible by storing enough UCNs in their bound quantum states within their propagation time. A storage

time around 100 s would even enable to set new limits on the neutron's electric charge.

Storing UCNs in their quantum states increases the propagation time by orders of magnitude and consequently the sensitivity. This requires multiple new developments in order to build the next generation of GRS experiments. Two approaches are possible: One is to start from a very simple configuration, similar to the first tests in *q*BOUNCINO in 2018 [236]. There, one adjustable vertical mirror as a wall and a detector with a very good spatial resolution (e.g. CR-39) can quantify the requirements of the vertical alignment and the losses due to the gap between the horizontal and the vertical mirror. In the next steps, this experiment can be repeated with a similar wall-like mirror on the other side, different coatings and materials of the walls and an extended setup's length. Such experiments can additionally trigger new detector developments and can be beneficial for the current RAMSEY^{TR}-setup by reducing beam divergence losses.
Another approach, which can be done simultaneously, is to build a storage bottle for UCNs and to probe the gravitational state evolution within due to wall interactions, applied oscillations and other disturbances. Some possible ideas have been developed by the *q*BOUNCE collaboration already over the last years and are waiting to be built soon.

The research of the *q*BOUNCE collaboration over the past years, especially the commissioning of the RAMSEY^{TR}-setup, increased the capabilities to probe BSM theories with gravitationally bound states. This thesis displays the search for an electric charge of the neutron as an example for such a test. This will provide a valuable basis for future research with the next generation of spectrometers. Going forward many generations of students will have the opportunity to contribute to the improvements of all different aspects of GRS.

A. Appendix

A.1. Theory

A.1.1. Statistics

Mean of n measurement:

$$\bar{x} = \sum_{i=1}^{n} \frac{x_i}{n} \tag{A.1}$$

Mean of m measurements mean values (of n measurement each):

$$\bar{x}_j = \sum_{i=1}^{n} \frac{x_i}{n}$$

$$\bar{x} = \sum_{j=1}^{m} \frac{\bar{x}_j}{m} = \sum_{j=1}^{m} \frac{\sum_{i=1}^{n} \frac{x_i}{n}}{m} = \frac{1}{n \cdot m} \sum_{j=1}^{m} \sum_{i=1}^{n} x_i = \sum_{k=1}^{m \cdot n} \frac{x_k}{m \cdot n}$$

$$\bar{x} = \sum_{j=1}^{m} \frac{\bar{x}_j}{m} = \sum_{k=1}^{m \cdot n} \frac{x_k}{m \cdot n} \tag{A.2}$$

The mean value of mean values is equal to a global mean value of all single measurements. This result is important if only mean values of measurements (incl. standard deviation) are stored.

Standard deviation of a sample:

$$\sigma_x = \sqrt{\frac{\sum_{i=1}^{n} (x_i - \bar{x})^2}{n-1}} \tag{A.3}$$

Standard deviation of an ensemble:

$$\sigma_x = \sqrt{\frac{\sum_{i=1}^{n} (x_i - \bar{x})^2}{n}} \tag{A.4}$$

$$\sigma_x^2 = \frac{\sum_{i=1}^{n} (x_i - \bar{x})^2}{n} = \sum_{i=1}^{n} \frac{1}{n} (x_i - \bar{x})^2 = \sum_{i=1}^{n} \frac{1}{n} \left(x_i^2 - 2 x_i \bar{x} + \bar{x}^2 \right) = \left(\sum_{i=1}^{n} \frac{1}{n} x_i^2 \right) - \bar{x}^2$$

$$\sigma_{x_j}^2 + \bar{x}_j^2 = \left(\sum_{i=1}^{n} \frac{1}{n} x_i^2 \right)$$

Standard deviation of an ensemble of m mean values including their standard deviations

$$\sigma_{\bar{x}} = \sqrt{\frac{\sum_{k=1}^{n \cdot m} (x_k - \bar{x})^2}{n \cdot m}} = \sqrt{\sum_{j=1}^{m} \frac{1}{m} \sum_{i=1}^{n} \frac{1}{n} (x_{i,j} - \bar{x})^2} = \sqrt{\sum_{j=1}^{m} \frac{1}{m} \sum_{i=1}^{n} \frac{1}{n} \left(x_{i,j}^2 - 2 x_{i,j} \bar{x} + \bar{x}^2 \right)}$$

$$\sigma_{\bar{x}} = \sqrt{\sum_{j=1}^{m} \frac{1}{m} \left(\sum_{i=1}^{n} \frac{1}{n} x_{i,j}^2 - 2 \bar{x} \sum_{i=1}^{n} \frac{1}{n} x_{i,j} + \sum_{i=1}^{n} \frac{1}{n} \bar{x}^2 \right)} = \sqrt{\sum_{j=1}^{m} \frac{1}{m} \left(\sum_{i=1}^{n} \frac{1}{n} x_{i,j}^2 - 2 x_j \bar{x} + \frac{n}{n} \bar{x}^2 \right)}$$

$$\sigma_{\bar{x}} = \sqrt{\sum_{j=1}^{m} \frac{1}{m} \left(\sigma_{x_j}^2 + \bar{x}_j^2 - 2x_j\bar{x} + \bar{x}^2 \right)}$$

$$\sigma_{\bar{x}} = \sqrt{\sum_{j=1}^{m} \frac{\sigma_{x_j}^2}{m} + \sum_{j=1}^{m} \frac{(\bar{x}_j - \bar{x})^2}{m}} \tag{A.5}$$

The main result is that the variance of the mean of mean values ($\sigma_{\bar{x}}^2$) is the variances of the averaging of the means plus the mean of the variances of the single mean values ($\sigma_{x_j}^2$).

A.2. Data analysis

The LabView experimental control stores all measurement data directly into the *syslog* data structure (see section 3.8.2). Already within the LabView project, the first data evaluations are preformed and also stored in the *syslog* folders beside the original raw data [115]. Before the final data evaluation, a *python* script feeds all data into a *mongoDB* database [241]. This speeds up later the data extraction for the evaluation.

I preformed all evaluations with *Mathematica* (version 11.1 and 11.3) in order to be able to use notebooks from previous students which mainly used this program. In the future, a *python* evaluation could improve the accessibility (no license fees) and speed up the evaluations of large amounts of data.
The evaluation is split up into multiple notebooks and commonly used packages. All needed files are in version controlled folders (*git*). At the start, only the cycle has to be chosen. Afterwards, the notebooks are executed in numerical order. Within each notebook, all beam time specific values are set in the beginning. A *keyData* file stores all properties which are used in multiple notebooks. The results of each notebook (summaries - *.txt* files, plots - *.pdf* files) are stored in designated folders where the proceeding notebooks can read them in and use them for further evaluations. The headers of each *.txt* file will provide all the information needed. The analysis splits into an evaluation grid as seen in figure A.1. This has the advantage that only the effected part of the evaluation has to rerun after a bug-fix or an improvement implementation. It also enables to use different programming languages for single tasks. In the following subsections, I will shortly describe each evaluation step.

In the future, more parts of the evaluation can be integrated into the measurement control system and the existing evaluation only checks the results. Also problems during the analysis can be reduced if the measurements are preformed flawless (less LabView crashes, clean measurement starts and ends,...). Therefore, the experience of the analysis should be used to improve the data acquisition. The final goal is to have complete real-time data evaluation including an automatized measurement report writing in order to reduce the time until the publication of the final results.

A.2.1. syslog data structure

Jörg Herzinger introduced the so-called *syslog*[1] [115]. Before each measurement campaign the main folder location is designated (either locally or remote via a created port on a NAS). Each device has an assigned tag as a label. If the device is operated the first time during the beam time, it will create a folder with the tag as its name where all its data are stored[2]. If a device has more than one output (e.g. multiple sensor readings, jobs, raw data, evaluated data, ...), so-called *subtags* are used to differentiate between the different data outputs.

The data structure is always the same for all files and devices. The first column is the time of the used server (the same for all devices). The second denotes the PC name where the LabView is running. Therefore, multiple PCs can be used to operate one experiment and still all data are synchronized (if the remote option is chosen). It is also possible to run multiple experiments simultaneously without interference by using different ports of the remote storage. The third column is the corresponding *syslog*

[1] It is based on the Unix-like *syslog* system logging protocol.
[2] Only the detector is an exception. The corresponding folder (*InterWinner*) has to be created manually and the assignment additionally changed.

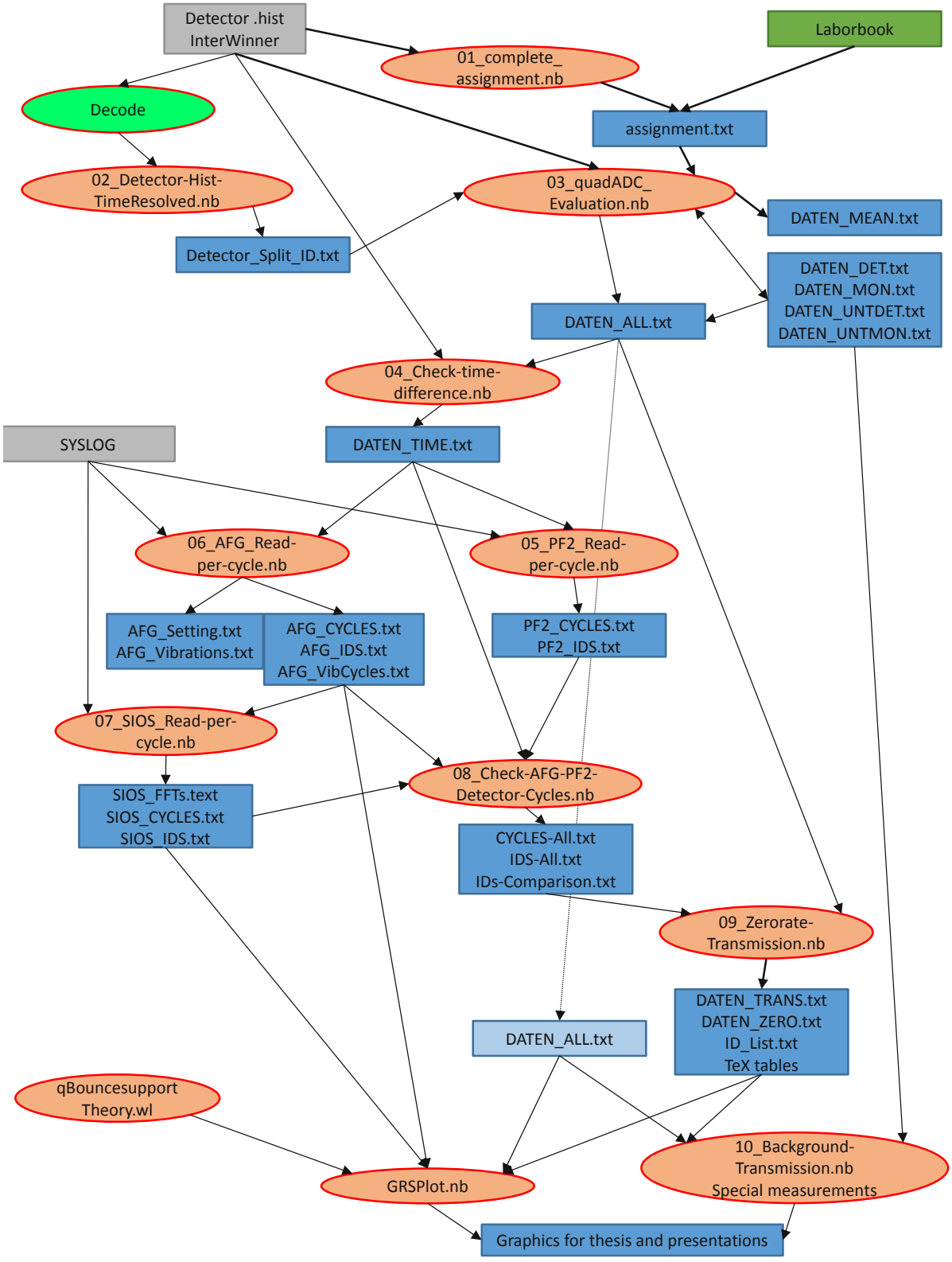

Figure A.1.: A schematic view of all components and their connections used for the data analysis.

tag and subtag. All following columns are the data stored by the device. The column assignment should be stated in a device-specific *notice* file in the main folder[3].

[3]This is hard coded within the corresponding *job.vi*. This was and is not always up-to-date but should be in the future.

The *syslog* server produces for each subtag a new file for each day. An optional script running on the NAS compresses all files from the previous days to a *.gz* file daily. The *Mathematica* package *SyslogReader.m* can extract the data and import it into a notebook [115](p.69-81).

A.2.2. MongoDB database

Julius Piso introduced this database to host all measurement data [241]. At the moment, each beam time has to be manually imported once into it with a dedicated *python* file. For each device, a model for the columns is applied which can also include *dictionaries*. With changes of the corresponding LabView .vi, the model has to be adapted too. During the import also the measurement ID and beam time (cycle) name are assigned and indexed.

The major advantage of this additional step is the data extraction. There is no restriction for the method. The database can be inspected with *MongoDB Compass*. Julius Piso already implemented a *Mathematica* extraction as the package *qBounceDB.wl*[4]. This indirect method is much faster than the direct access, mainly because the data are stored and imported as numbers or boolean and not as strings. Additional to import via measurement IDs or time ranges as with the slower *SyslogReader.m* package, it is also possible to only extract a small random sample. This is very useful if a plot over a long time range is needed (e.g. vacuum pressure). A second major advantage is that the database is hosted on a Linux server at the ATI. All students are able to access their data very easily and it is not necessary that they receive a complete copy of their data. For long-term studies, it is also possible to extract a data set belonging to multiple cycles without any additional effort.

A.2.3. *Mathematica* packages

qBounceSupportTheory.wl: Here I packed all theory functions for all calculations especially the GRS calculations of a Rabi or Ramsey-type setup. The notebook *Theory-qBounce.nb* describes all functions and displays the theoretical results in further detail. It is also the origin of this package.

qBounceSupportParameters.wl: This package hosts all important parameters (e.g. for plotting, setup geometries, beam characteristics).

qBounceSupportAnalysis.wl: All important functions and parameters for the data analysis are packed into this package.

list2D.m, quadADCdefV05 and statistikV2.m: These packages originate from Tobias Jenke and are used for the detector evaluation [139].

CR39Analysis Hanno Filter created this bundle of packages for the analysis of CR-39 detectors and we used it without large changes (see section 3.2.4) [89].

A.2.4. Evaluation grid

This bundle of *Mathematica* notebooks was used for the data evaluation of this thesis.

00_Create-CycleKeyDataFile.nb

This notebook creates the so-called *cycleKeyData.txt* file which contains all information and general parameters needed for the evaluation of the chosen beam time.

[4]The *Mathematica* version has to be at least 11.3 or higher.

01_complete_assignment.nb

The assignment file or originally called *Zuordnung* contains a list of all measurement IDs used for neutron measurements and their purposes. Tobias Jenke already implemented this file usage [139]. The newer notebook automatically creates the assignment file by reading in the names of all detector files. The purpose and the success of the rate measurement has to be added/changed manually by consulting the corresponding Labbook. Measurement IDs with broken detector files can either be manually analyzed again with *decode* or have to be removed at this stage from all further analysis.

02_Detector-Hist-TimeResolved.nb

Some detector measurements are corrupted. Either the LabView crashed or something else changed the setup parameters (AFG, Shutters, PI-tables,...) during one measurement. Therefore, if there is a doubt that one rate measurement is not self-consisting, they have to be analyzed time-resolved. This is possible with the software *decodeGui* written by Martin Thalhammer [298, 299]. I used a time resolution of 1 s for both detectors (input 1 - detector, input 2 - monitor) and two time windows (gate 01 - measurement, gate 10 - background). It is important to store the original *hist* files in a different folder during this process for an important later evaluation step. The notebook reads the results and merges the time intervals back together to cycles and background windows. A summary of each cycle is stored in a text file. Also the complete ID and parts of it can be stored for the later evaluations. Separating the ID also proves if the measurement conditions were stable or not (e.g. the AFG stopped after a LabView crash. The first part is a frequency measurement and the second a zero rate.).

03_quadADC_Evaluation.nb

This notebook originates from Tobias Jenke [139]. It uses the assignment to read in the *hist* files of the detector and makes the complete evaluation including the detector corrections (see section 3.2.3). Corrupted IDs can be replaced by trustworthy parts of it.

04_Check-time-difference.nb

Not all timestamps are synchronous. Again the exception is the detector. The *InterWinner* software operates directly the detector's readout. At the end of a measurement, LabView starts *decode* locally on the measurement PC (*Neron*) to evaluate the measurement and create the corresponding *hist* file. The timestamps within the *hist* file originate from InterWinner and therefore the local PC. All other data receive their timestamps from *syslog* which is running on the NAS. The time difference between these two computers can be up to 8 min and shifting more than 1 s per day. This is much more than the 12 s which the *measurement queue* needs to change measurements between two cycles. Without correction complete cycles would be wrongly assigned during the later evaluations. This notebook corrects the time difference for each detector measurement ID by comparing the time extracted by the detector evaluation with the actual creation time of the *hist* file. Therefore, it is important to store the original *hist* files in a sub-folder if *decode* reevaluates a certain ID.

05_PF2_Read-per-cycle.nb

The stored logic signals of PF2 turbine control (see section 3.1.1) hold all the timing information of each cycle. This notebook reconstructs each cycle and assigns them to detector IDs. It is problematic if measurements start or end in the middle of a turbine cycle. Better is to use the *measurement queue* to have clean starts and ends of important rate measurements.

06_AFG_Read-per-cycle.nb

The AFG outputs are turned on and off for the measurement window of each cycle in order to reduce the stress on the piezoelectric crystals within the PI tables (turned off and resting during the background window). 3 s after these commands the settings of each channel are also requested and stored. With this information the notebook reconstructs all the cycles where the mirrors oscillate and assigns them

to detector IDs. For each ID it also checks if only one setting (frequency, amplitude,...) is applied. Additionally, the oscillation tests are evaluated which gives insight to the mechanical properties of the setup.

07_SIOS_Read-per-cycle.nb

The SIOS interferometers frequently measure the oscillations of the regions and analyze them with a fast Fourier analysis (FFT). This notebook loads all stored FFT results and assigns them to cycles and IDs from detector measurements or oscillation tests. Additionally, it removes all FFTs from further analysis which were measured (partly) outside the measurement window, where the signal quality was too low or the laser beam was mechanically blocked. The results can proof that the AFG worked probably during the complete measurement duration. The measured and averaged phase, amplitude and frequencies will be important parameters for the final evaluation of the GRS measurements.

08_Check-AFG-PF2-Detector-Cycles.nb

At this point of the evaluation, all information of the cycles (detector timing, PF2-signals, AFG and SIOS) were brought together ID-wise and cycle-wise. At first, the number of cycles counted with the detector, PF2 and AFG are compared for each ID together with the starting and end times. Useful IDs have the same number of cycles for the detector and the PF2. The number of AFG-cycles should be either the same (frequency measurement) or zero (zero rate). Everything between will be excluded as *mixed*. Similarly, the overall timing comparison is needed to match in order to further use these data points. The SIOS evaluation results check the status of the AFG (matching frequency, real mechanical amplitude). Frequency measurements are excluded if they where not measured with the SIOS. A summary of the IDs and a decided purpose for each ID are stored. In addition, this is done on the level of cycles and summarized again over each ID.

09_Zerorate-Transmission.nb

The different methods to find the purpose of each ID are compared. The notebook checks each ID and categorizes them with some manual input (frequency measurement, zero rate, background, excluded). All IDs with mixed AFG states or no SIOS measurement confirming the frequency are excluded. Mixed IDs could be reevaluated with a time resolved detector evaluation and splitting the ID in multiple parts (see subsection A.2.4). This is necessary frequently for IDs containing a LabView software crash.
In the second part, the IDs are assigned to different measurement periods. For each period, the common averaged zero rate is calculated and with it the relative transmission (incl. detector corrections) of all detector rates. The notebook also summarizes the final used data points as LaTeX-tables for the usage in a thesis.
At the end, a standardized summary table is created. This can be used as an input for completely independent GRS-analyses which are necessary for cross checking the results by different persons.

10_Background-Transmission.nb

This notebook summarizes the specialized background measurements and the common detector background. In addition, it displays the transmission rates of various non-GRS measurements (e.g. aperture measurements, transmission through various mirror configurations, shutter tests,...) and prepares them for specialized evaluations if needed.

Specialized measurements

For all major measurement types exist their unique evaluation notebooks in order to fully evaluate them individually according to their underlying theoretical predictions (e.g. RABI-GRS-18, RAMSEY-GRS-18, Rams$\vec{E}$y, aperture, shutter tests,...).

A.3. Measurements

A.3.1. Vacuum pressure

As referred in the measurement section 4.2.1, the following figures give an overview over the three reactor cycles of 2018 by displaying the pressure of the main vacuum chamber of the RAMSEY^{TR}-setup:

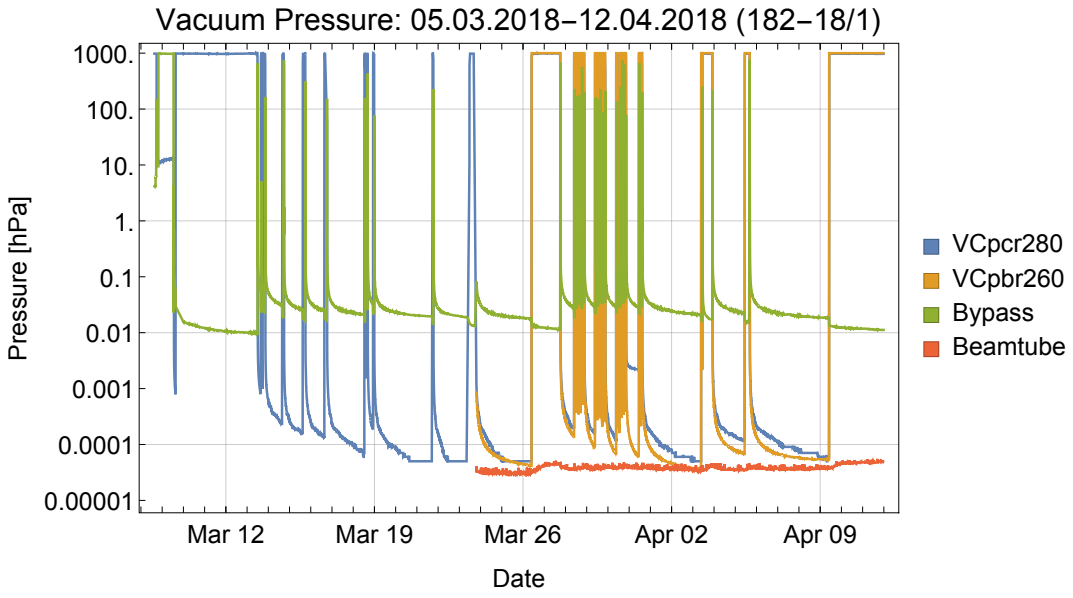

Figure A.2.: Overview of the first part of the cycle 182-18/1 (*3-14-358-III*): For each rate measurement and CR-39 measurement, the chamber was closed only for some hours up to some days. In between, the vacuum chamber had to be opened for changes of the setup. In the middle of the cycle (28-31.3.2018), the aperture measurements are visible, where we opened the chamber up to 5 times a day. We connected the second DualGauge to the PC on 24 March. Therefore, there are no measurement values for the beam tube sensor and the high vacuum sensor *PBR260* before this day (see fig. 3.15).

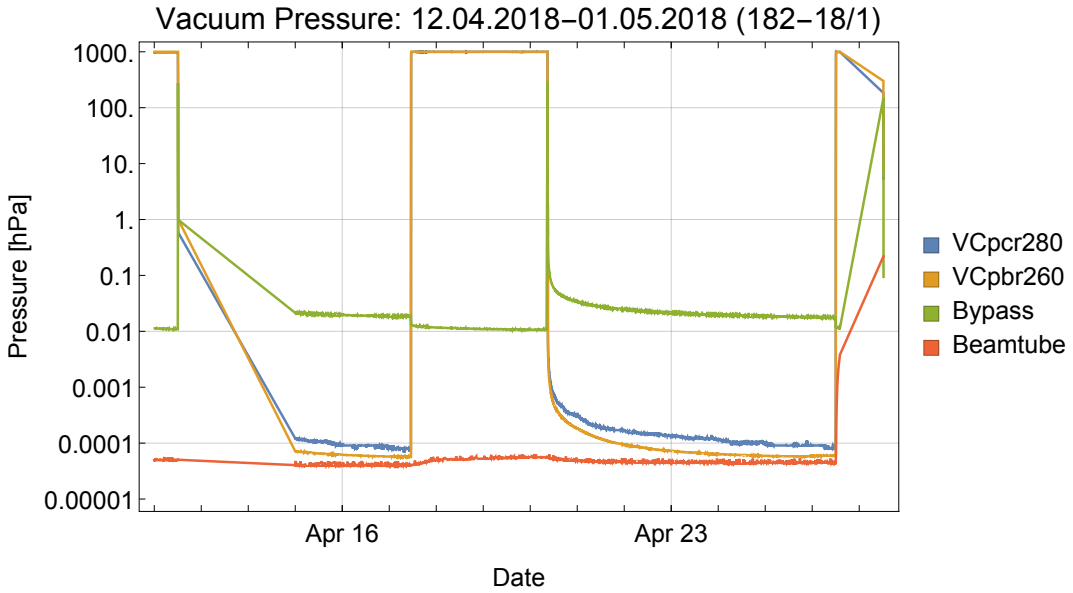

Figure A.3.: Overview of the end of the cycle 182-18/1 (*3-14-358-III*): Only the two parts of the RABI-GRS-18 measurements are visible. After the first day of evacuating, the pressure decreased very slowly which can be taken as constant.

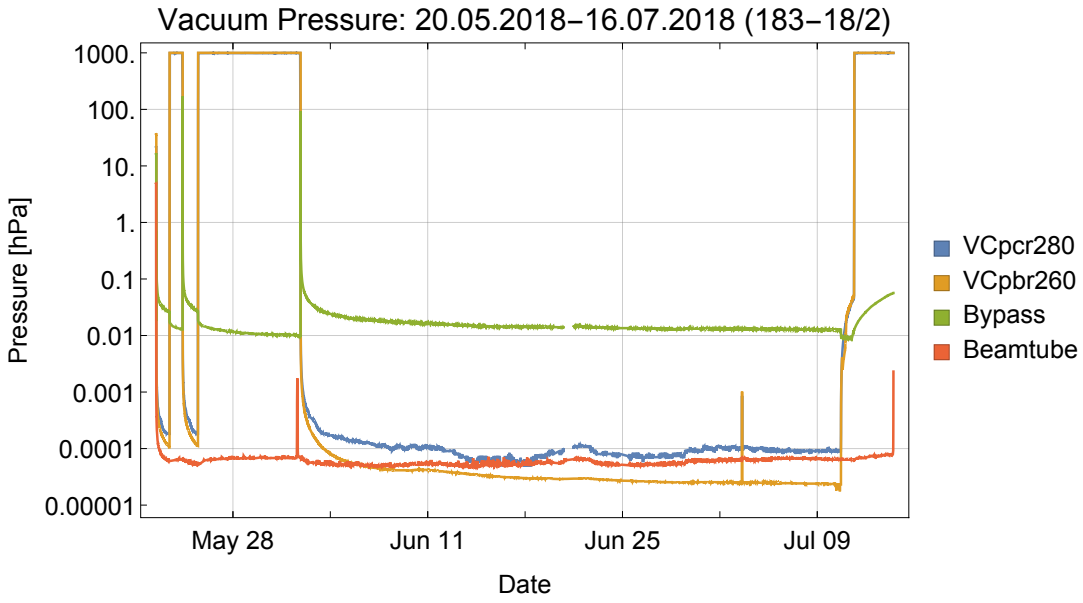

Figure A.4.: Overview of the cycle 183-18/2 (*3-14-358-IV*): After two transmission measurements of region III, the chamber stayed closed the entire beam time for the RAMSEY-GRS-18 measurements. During this time, the vacuum pressure nearly stabilized to a constant value.

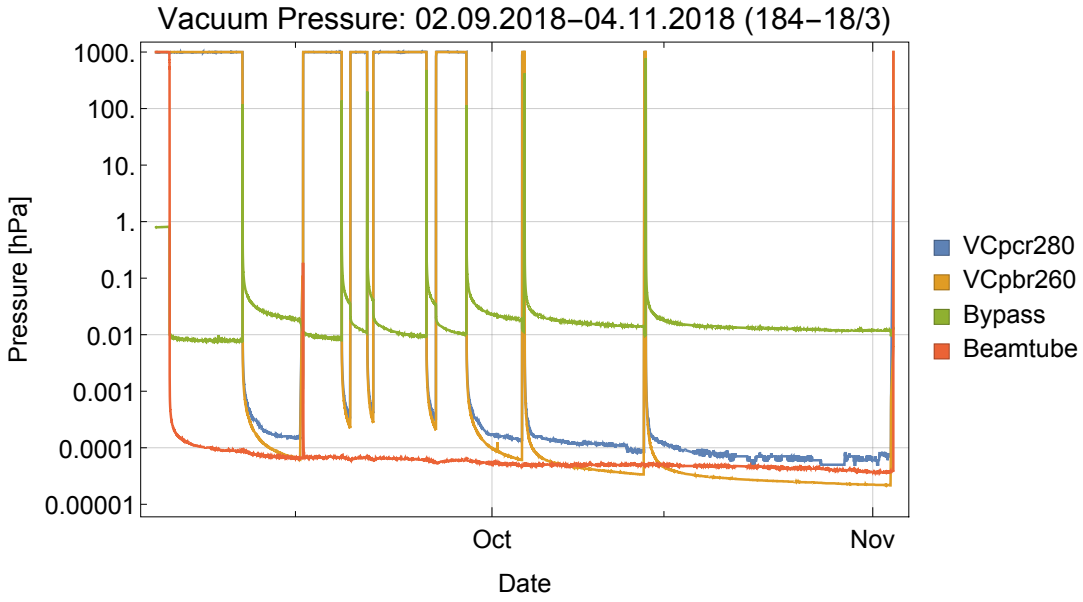

Figure A.5.: Overview of the cycle 184-18/3 (*3-14-384*): The first half of the cycle was mainly used for adjustments of the RAMSEY^{TR}-setup and the implementation of the large Rams$\vec{E}$y electrode. Only the RAMSEY-GRS-18-fall measurements and some region III transmission rate determinations suspended these works. The second half was used for the Rams$\vec{E}$y GRS measurements and was only interrupted twice for readjustments and tests of the setup.

In all cycles, the prevacuum pressure is lower when the vacuum chamber is vented than if it is evacuated due to the smaller volume the prevacuum pump has to evacuate. In addition, the different inaccuracies of both used vacuum sensor models are clearly visible. At ambient conditions only the sensors *PCR280* display correct values and can be used as a barometer. On the contrary, the turbo pump creates a vacuum pressure on the lower range limit of these sensors (5×10^{-5} mbar). The other sensor type (*PBR260*) is more accurate and precise measuring these "high vacuum" conditions which prevail during neutron measurements.

The following histogram (fig. A.6) displays the difference between the two sensor types installed in the main vacuum chamber:

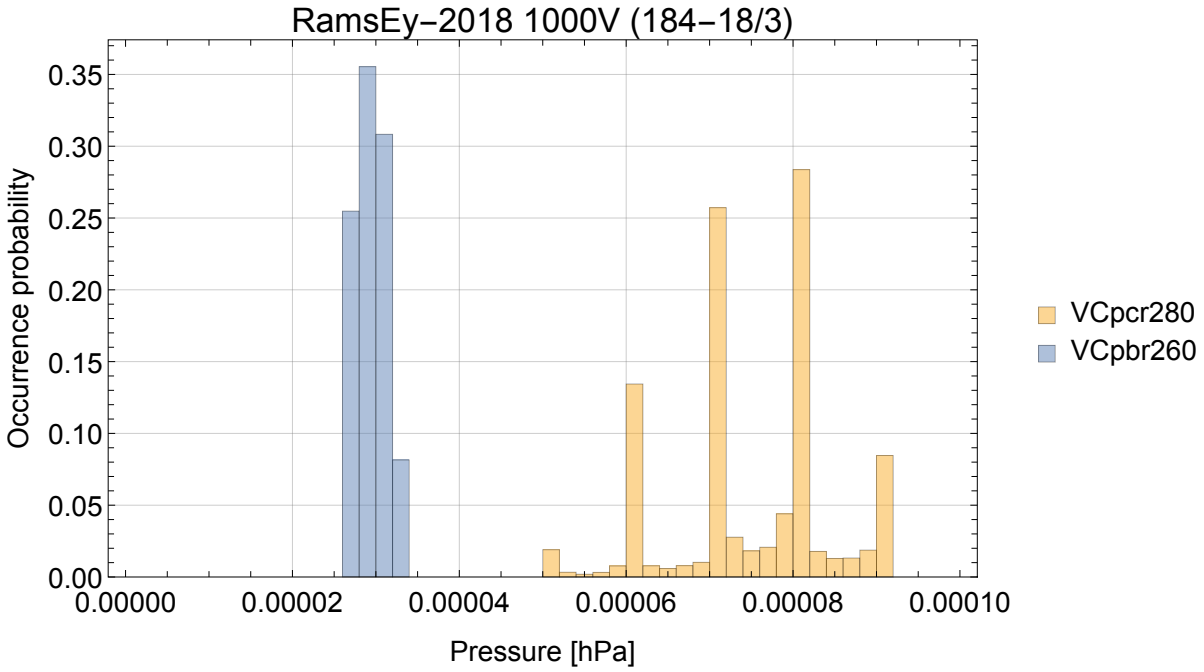

Figure A.6.: Histogram of the different vacuum gauges within the main vacuum chamber: The sensors *PBR260* are more precise and have a higher resolution at the measurement conditions.

Small pressure changes within the beam tube are visible during the evacuation and venting process. This can be explained with the mechanical stress changes on the trunk and the neutron window separating both vacua.
In a detailed view (fig. A.7), a second effect is visible. A small pressure rise can be seen approximately every 200 s. This correlates with the neutron measurement cycles (see section 3.1.1). In each cycle the pneumatic shutter opens and closes. This also slightly moves the beam tubes and small gas leakages occur.

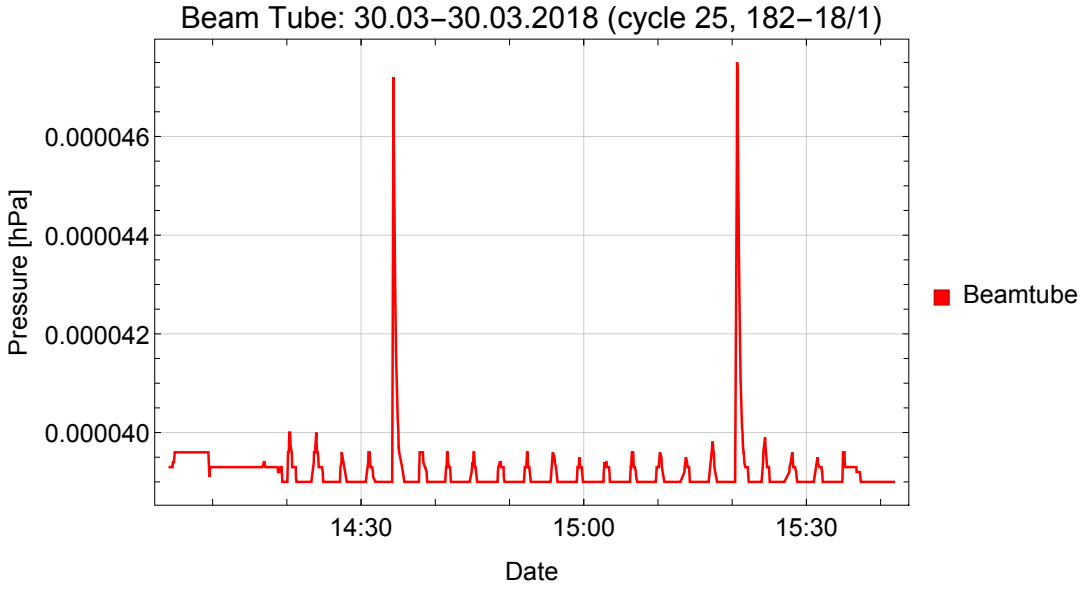

Figure A.7.: A detailed view of the beam tube pressure during an aperture measurement (ID 4.009, see section A.3). All 22 cycles of this rate determination are visible.

Beside these small measurable effects, the beam tube pressure is always constant around 6×10^{-5} mbar as figure A.8 displays it.

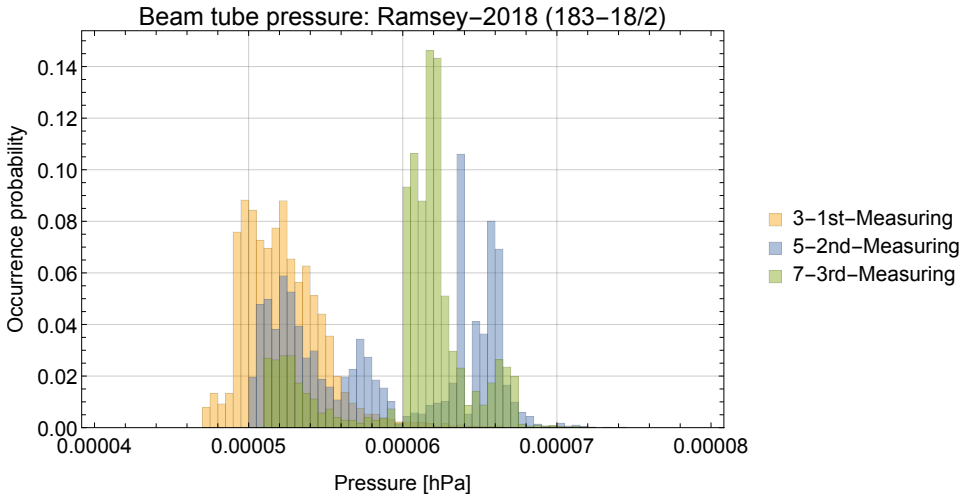

Figure A.8.: Histograms of beam tube pressures during the RAMSEY-GRS-18 measurements for the different measurement periods (see more in section 4.5).

A.3.2. Detector and its sensors

The performance of the detector depends on its amplification factors (within the gas and the electronics) and the ability to discriminate between the neutron signal and noise. The additional sensors are necessary to constantly monitor this (see more in section 3.2.1).

As seen in fig. A.9 and fig. A.10, the neutrons are detected differently in both detectors (see details in section 3.2). The main detector has a boron converter foil as an entrance window. Either the released lithium nucleus (peak at channel 320) or the α particle (peak at channel 720) enters the detector. An additional third peak is visible around the channel 920. This is a second helium peak when the boron splits in two parts without emitting a gamma ray after the neutron capture (branching ratio of 6 %).
On the other hand, the monitor detector captures neutrons within its gas filling which contains He-3. Therefore, all released kinetic energies are detected (peak at channel 700) except the capture happens too close to the wall and one particle (proton or tritium nucleus) escapes the detector volume without transferring all its kinetic energy to the detector gas.

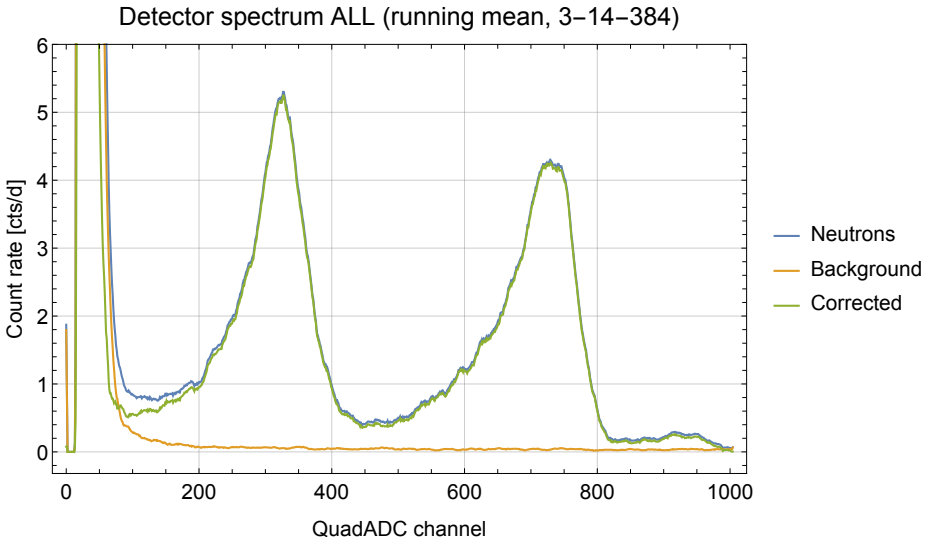

Figure A.9.: Combined main detector energy spectrum of the beam time 184-18/3

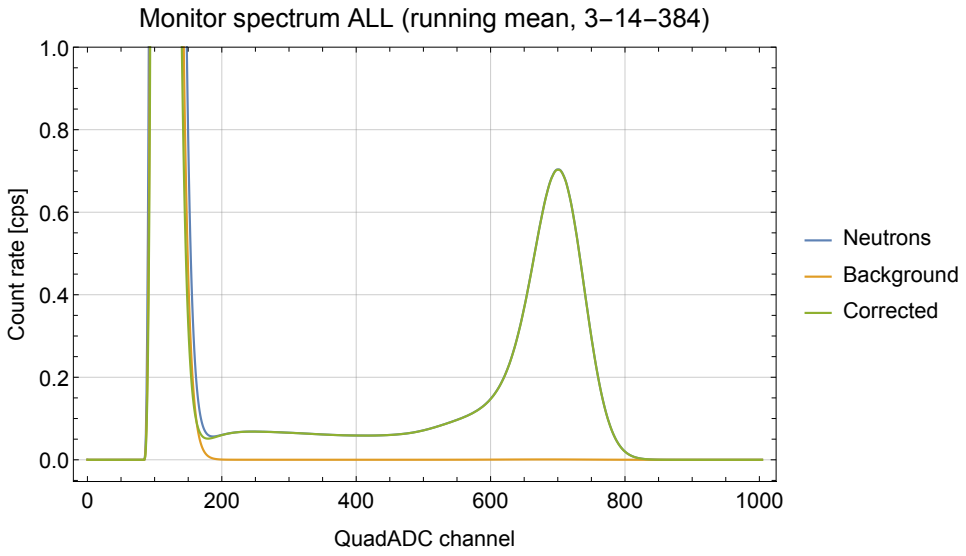

Figure A.10.: Combined monitor detector energy spectrum of the beam time 184-18/3

Both detectors have in common that electronic noise dominates the measured signal at low energies. Therefore, we used a *region-of-interest* (ROI) for the evaluation. The ROI of the detector was set to the channels from 100 to 1023 and the one of the monitor to 200-1023. These settings were already used during optimization of the gas amplification and the additional electronic amplification.

Beside the high voltage (fixed in the beginning, see appendix A.4.6), the gas amplification is also influenced by the gas flow, gas mixture, pressure and temperature. Within the main detector, these values are continuously measured with dedicated sensors except the gas mixture which is taken as constant after one day of flushing the detector with $ArCO_2$. We adjusted the valves to set the overpressure and the flow only in the beginning of the first beam time (10-12.3.2018). This setting was kept the complete year[5]. Between the beam times, we closed only the main valve of the gas bottle. Over the course of the year, the bottle pressure decreased from 165 bar to 125 bar. Daniel Schuh evaluated all sensor data of the beginning of the beam time 182-18/1 [274]. Robin Havlik continued his work [112] including a detailed description of the valve adjustment time. Already Magdalena Pieler and Valentin Czamler used these developments for their *q*BOUNCINO evaluations [236](p.32-34). In the following, I will present the evaluation of the complete beam time 184-18/3 based on the previous works (the other reactor cycles are displayed at the end of the appendix A.3.2) and I will discuss the observed phenomena.

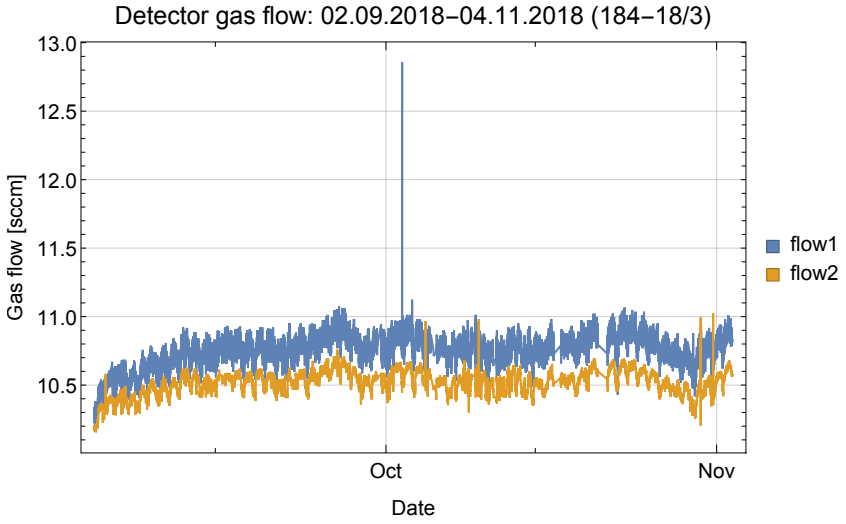

Figure A.11.: Gas flow of $ArCO_2$ through the detector during the Rams$\vec{E}$y measurements.

[5]Except the one incident when one student turned the throttling valve of the gas bottle instead of looking on the readings.

As figure A.11 displays, the gas flow is quite constant around 10.5 sccm (standard cubic centimeters per second, one bubble per second). There has been a slight offset between the two flow sensors since 16 March 2018 [112](p.13-14). Temperature changes and therefore pressure changes induce a daily oscillation of the flow. All sensors should be recalibrated soon (especially the flow sensor #3, which was used for *q*BOUNCINO, has a large offset compared to the other two).

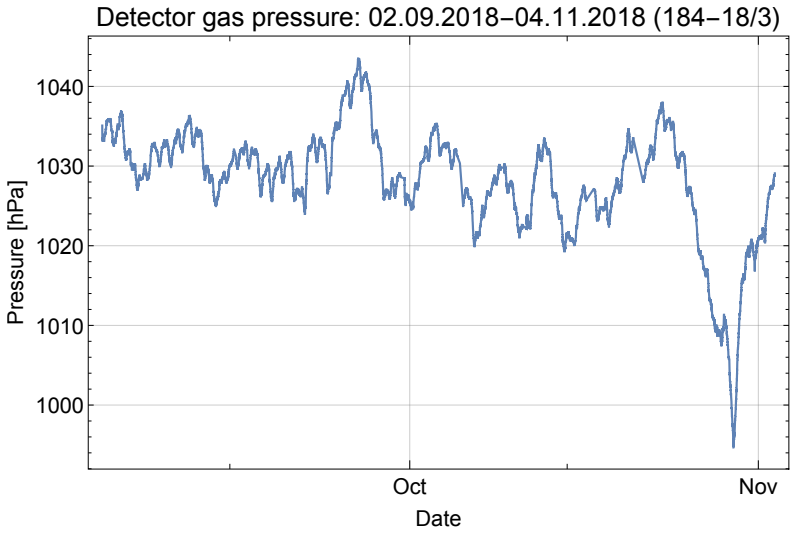

Figure A.12.: The pressure within the detector gas volume during the Rams$\vec{E}$y measurements.

Figure A.12 displays the overpressure within the detector (30 mbar to 40 mbar). Beside the daily pressure changes due to the day/night cycle, the weather and its local air pressure (low and high pressure areas) strongly influence the detector pressure because the underpressure in the reactor hall and the overpressure in the counter tube are only relative to each other and the atmosphere. Daniel Schuh found a way to nearly eliminate these influences by subtracting the air pressure measured at the airport Grenoble (35 km away from the reactor, available within the *Mathematica* database) [274]. This enables to see a slow pressure drop in the detector volume due to the slow emptying of the gas bottle. A weather station closer to the experiment (best within the reactor hall) would increase the accuracy of this method. This also helps if the gas amplification has to be corrected due to the pressure changes within the detector volume. If the vacuum chamber is vented, the vacuum gauge *PCR280* can be used as a coarse barometer to cross check the overpressure. Also an active pressure control would stabilize it and therefore stabilize further the gas amplification.

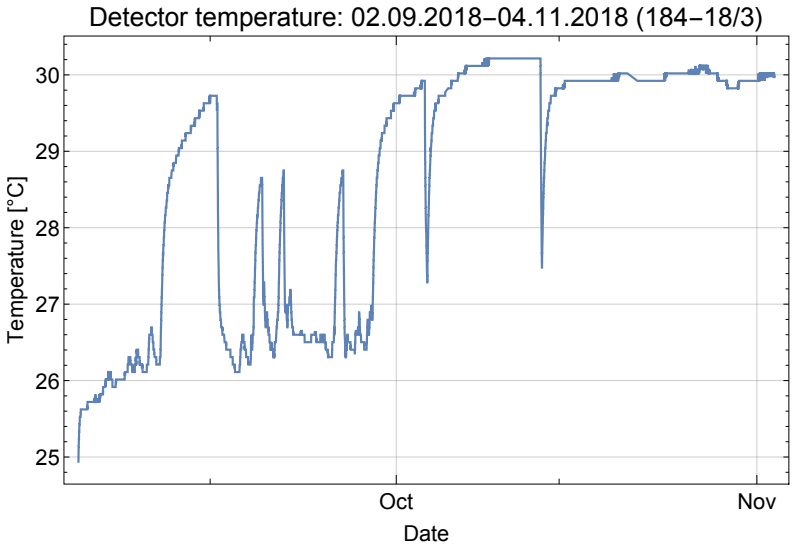

Figure A.13.: The temperature of the detector electronics during the Rams$\vec{E}$y measurements.

The temperature of the main detector correlates strongly with the vacuum conditions as depicted in figure A.13. After the evacuation start, the temperature within the detector slowly increases according to the Newton's law of cooling for a few days [274](p.15-18). During venting, the temperature quickly decreases again to the ambient conditions. The main reason is the lack of convection cooling within the vacuum. Further investigations are necessary to determine if the complete detector heats up or only the temperature sensor due to a too high measuring current. Four additional temperature sensors are situated in the large magnetic coils (see section 3.9.4). However, until now they are not connected, which disables to use them as a comparison. In the future, these sensors could record the temperature in the complete volume of the vacuum chamber. The only second active digital thermometer is placed within the tilt sensor (see comparison in section 4.2.2). A thermometer as part of a weather station, which is connected to the PC, would simplify the evaluation significantly[6].

The following table summarizes the values during the main GRS measurement sets:

Table A.1.: Summary of the detector sensor readings for all GRS measurements

GRS measurement	Pressure [mbar]		Temperature [°C]		Flow 1 [sccm]		Flow 2 [sccm]	
	Min-Max	Average	Min-Max	Average	Min-Max	Average	Min-Max	Average
RABI-GRS-18-I	1010.1 - 1034.1	1023.3(53)	22.89 - 26.31	25.61(62)	10.06 - 10.50	10.29(8)	9.85 - 10.23	10.04(7)
RABI-GRS-18-II	1023.1 - 1034.9	1027.9(23)	23.77 - 27.43	26.66(67)	10.09 - 10.55	10.31(7)	9.93 - 10.27	10.09(7)
RAMSEY-GRS-18-I	1015.7 - 1032.3	1022.1(35)	26.21 - 28.16	27.54(53)	10.17 - 10.72	10.46(7)	9.99 - 10.36	10.20(7)
RAMSEY-GRS-18-II	1022.5 - 1030.5	1026.6(17)	28.26 - 29.73	29.39(46)	10.01 - 10.65	10.35(10)	9.72 - 10.26	10.07(10)
RAMSEY-GRS-18-III	1015.4 - 1026.6	1020.9(25)	29.63 - 31.09	30.19(53)	9.81 - 10.75	10.25(11)	9.74 - 10.23	9.97(5)
RAMSEY-GRS-18-Fall	1024.9 - 1035.7	1030.4(24)	26.11 - 29.72	28.29(140)	9.54 - 10.96	10.74(8)	10.36 - 10.64	10.53(5)
Rams$\vec{E}$y-0 V I	1024.4 - 1035.7	1028.9(30)	26.70 - 29.92	29.42(58)	10.40 - 12.59	10.81(9)	10.34 - 10.69	10.56(6)
Rams$\vec{E}$y-0 V II	1019.9 - 1035.1	1027.6(38)	27.28 - 30.21	29.97(48)	9.06 - 11.38	10.77(8)	9.70 - 10.99	10.52(7)
Rams$\vec{E}$y-HV	1002.3 - 1038.1	1025.2(87)	29.82 - 30.12	29.97(6)	10.30 - 11.07	10.81(9)	10.34 - 10.71	10.55(7)

In addition to an online weather station, a simple mass spectrometer attached to the gas circuit could also measure the gas mixture. The flow could be adjusted depending to its reading. This could further reduce the usage of the detector gas.

Detector sensors: graphs of other cycles

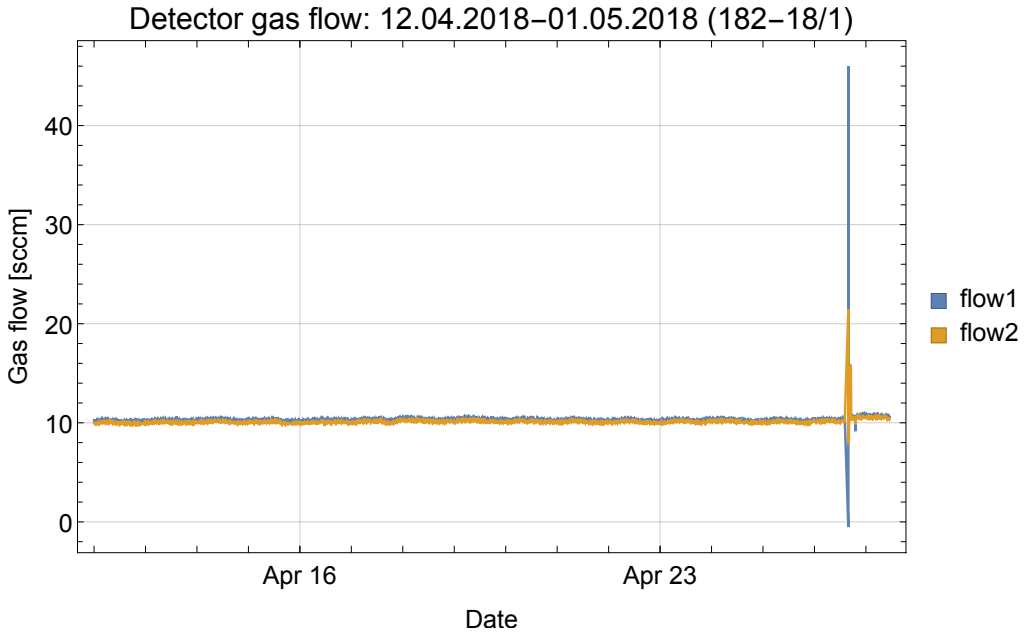

Figure A.14.: Gas flow of $ArCO_2$ through the detector during the RABI-GRS-18 measurements. The strong flow fluctuations on 26 April are due to the hose exchange of the detector.

[6] At the moment the weather station readings are only noted in the Labbook.

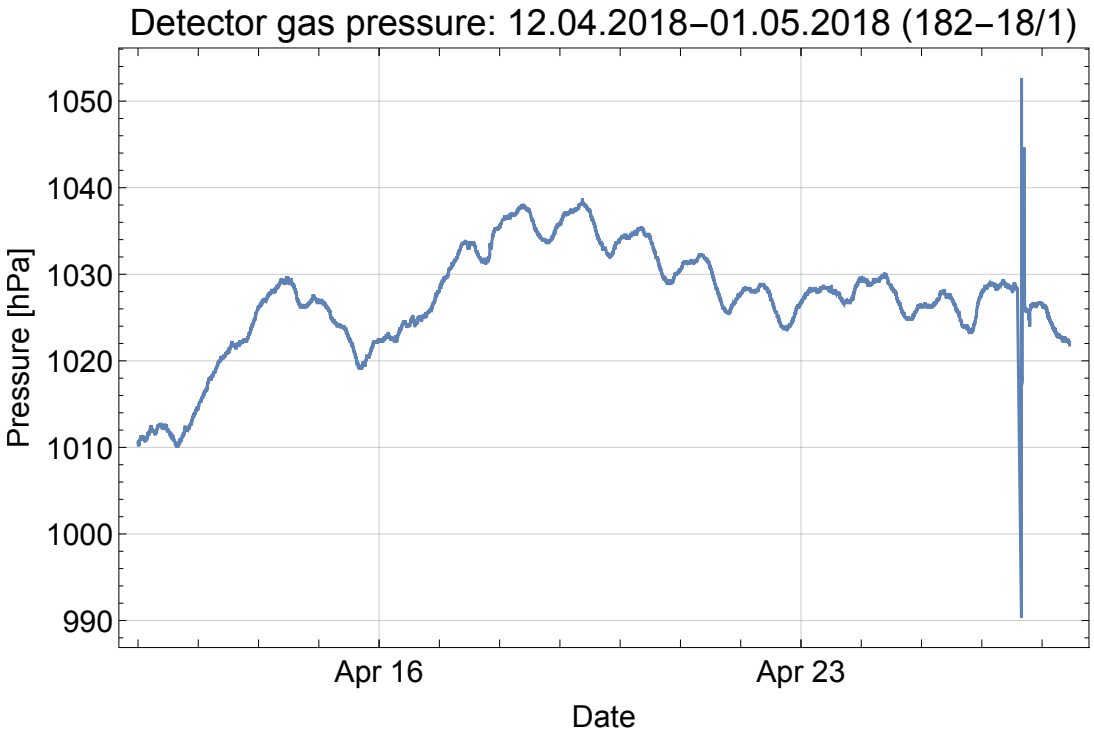

Figure A.15.: The pressure within the detector gas volume during the RABI-GRS-18 measurements.

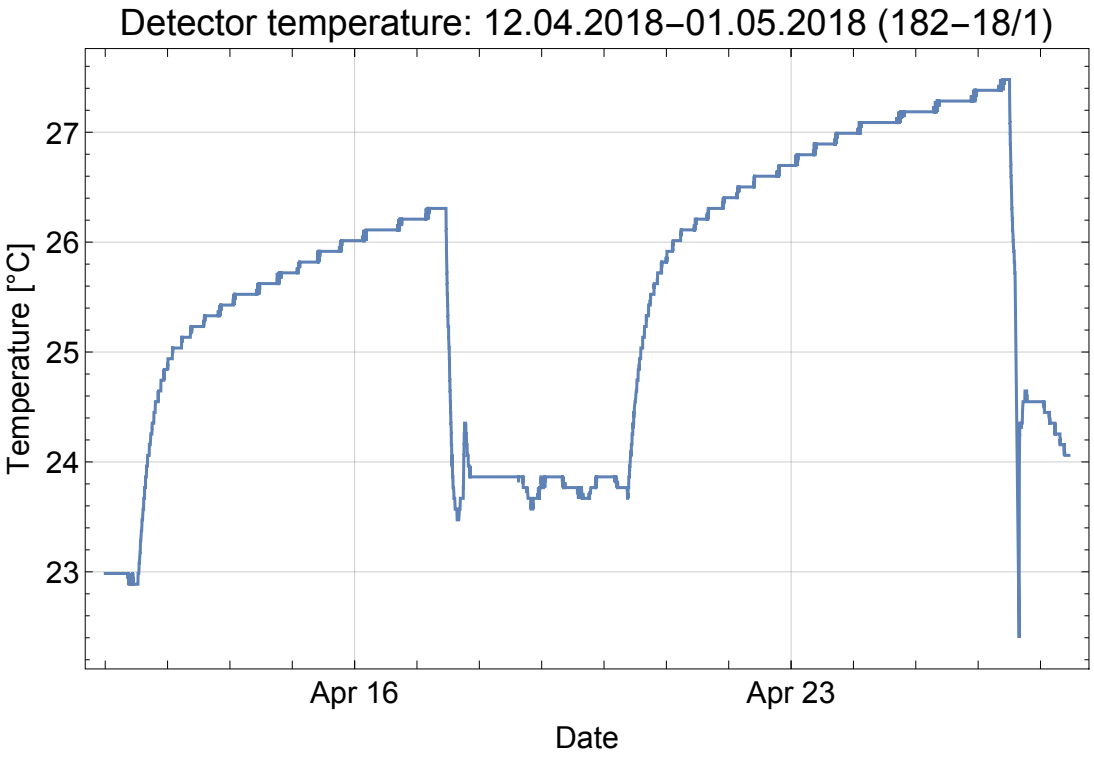

Figure A.16.: The temperature of the detector electronics during the RABI-GRS-18 measurements. The two measurement periods are clearly visible. The reactor hall temperature also increased during this period.

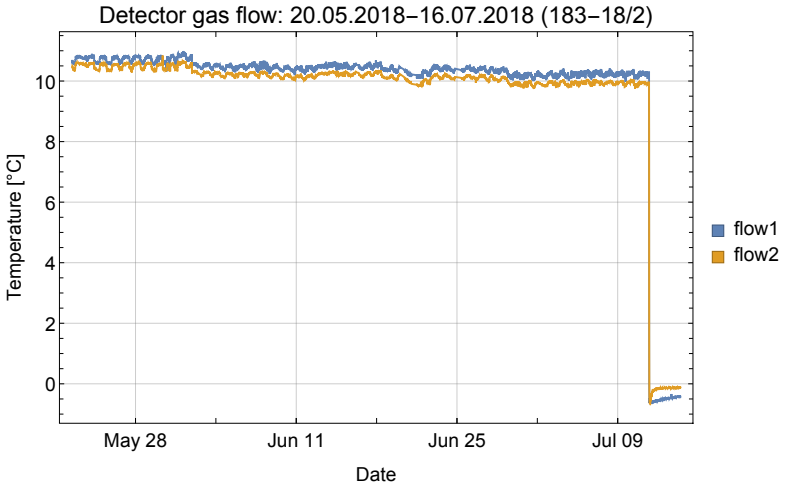

Figure A.17.: Gas flow of $ArCO_2$ through the detector during the RAMSEY-GRS-18 measurements. *Flow 1* is situated before the detector and *flow 2* after. On 12.7.2018 we closed the main valve of the gas bottle. The flow measured values returned to the zero values (incl. an offset from an old calibration).

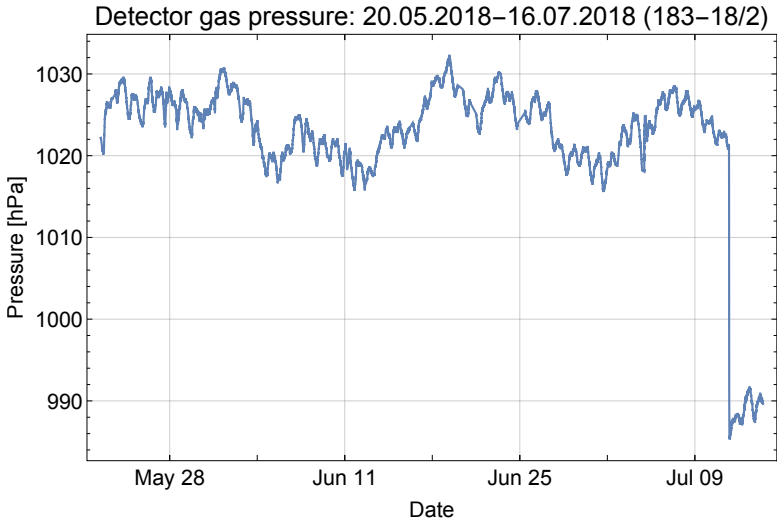

Figure A.18.: The pressure within the detector gas volume during the RAMSEY-GRS-18 measurements. After closing the main valve, the overpressure decreased to the ambient value. The difference could be estimated as 36 mbar.

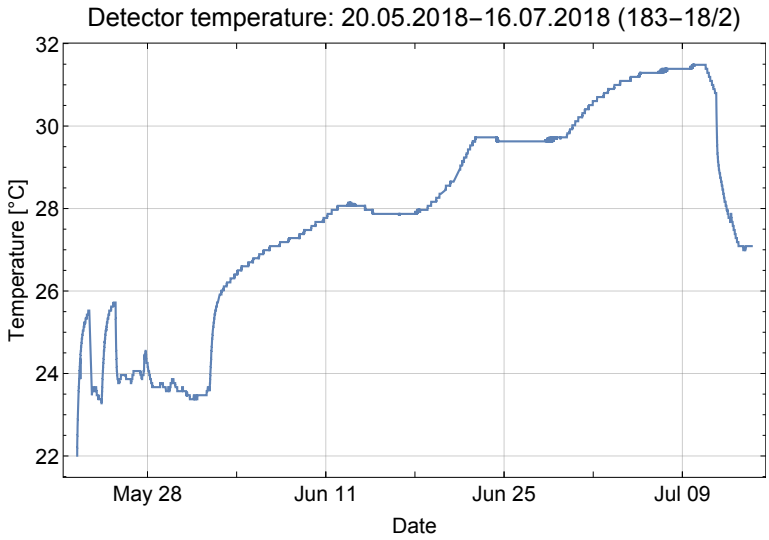

Figure A.19.: The temperature of the detector electronics during the RAMSEY-GRS-18 measurements. After the heat up period of the sensor, the temperature further increased due to the hot weather in the beginning of summer.

A.3.3. Leveling: additional plots

Here are displayed additional plots for the leveling/tilt sensor's evaluations which are described in section 4.2.2.

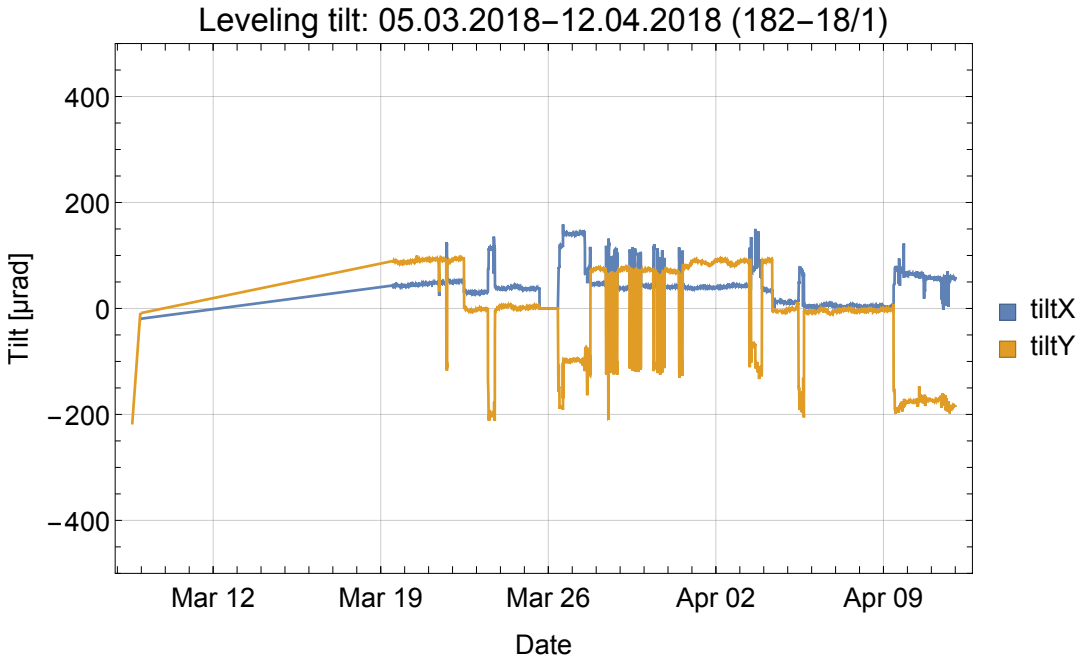

Figure A.20.: The horizontal alignment of the granite surface during the test phase of the first beam time of 2018. The active leveling was rarely used.

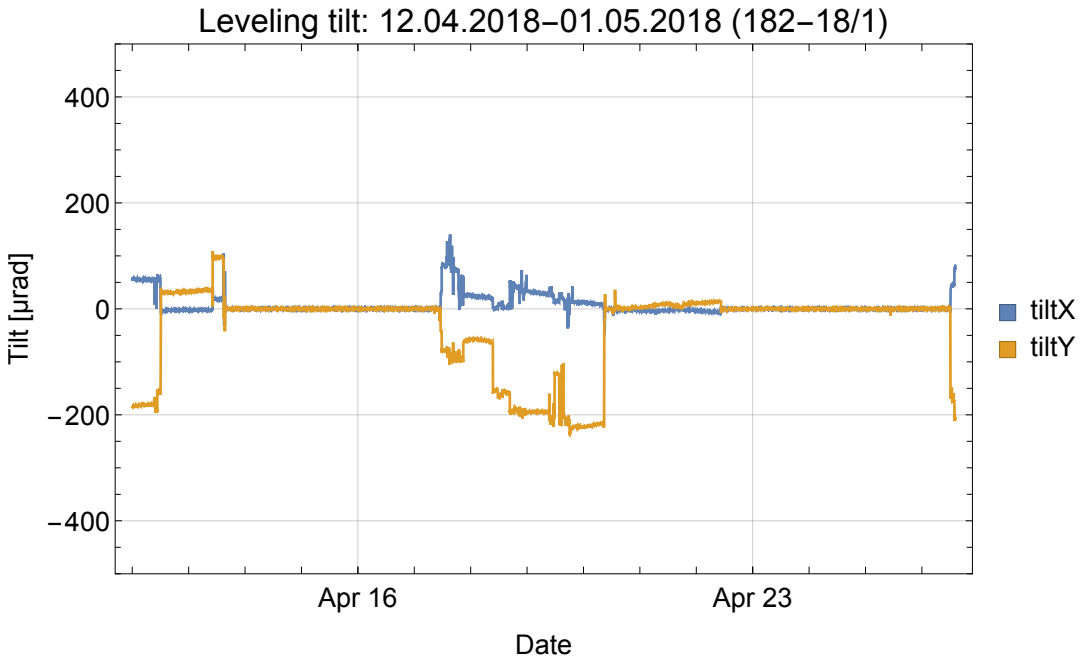

Figure A.21.: The horizontal alignment of the granite surface during the RABI-GRS-18 measurements. In the beginning of each measurement phase there were some troubles with the active leveling. For the most parts, the surfaces was aligned to (0, 0) of the tilt sensor readings due to the lack of a calibration.

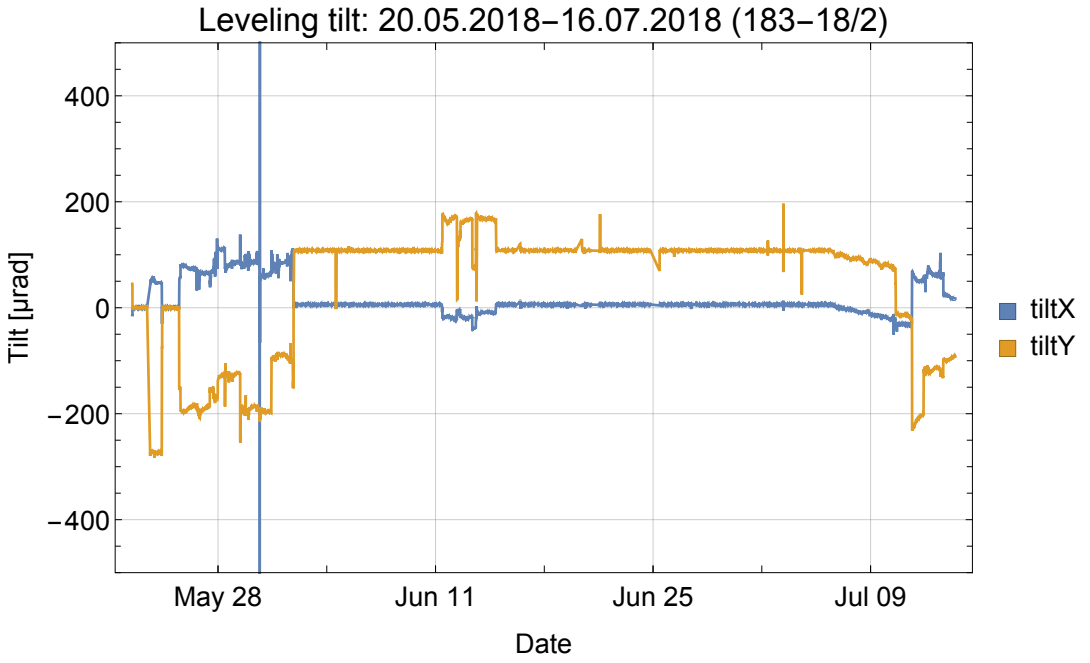

Figure A.22.: The horizontal alignment of the granite surface during the RAMSEY-GRS-18 measurements. In the beginning of the cycle, the granite surface was twice aligned to a measured zero value. This was during the two region III transmission measurements with vacuum conditions. Due to a deactivated leveling, the setup period with an open vacuum chamber is clearly visible in the beginning (25.5-1.6.2018) and the end (>11.7.2018). During the main GRS measurements, the active leveling kept the granite aligned to (6 µrad, 108 µrad). Between 11.6.2018 and 14.6.2018 the active leveling was not working due to some programming issues in the LabView control system which I had to fix during this break. From the 6.7.2018 onward, the leveling was turned off after the reactor shut down. The surface alignment slowly drifted away from its target position.

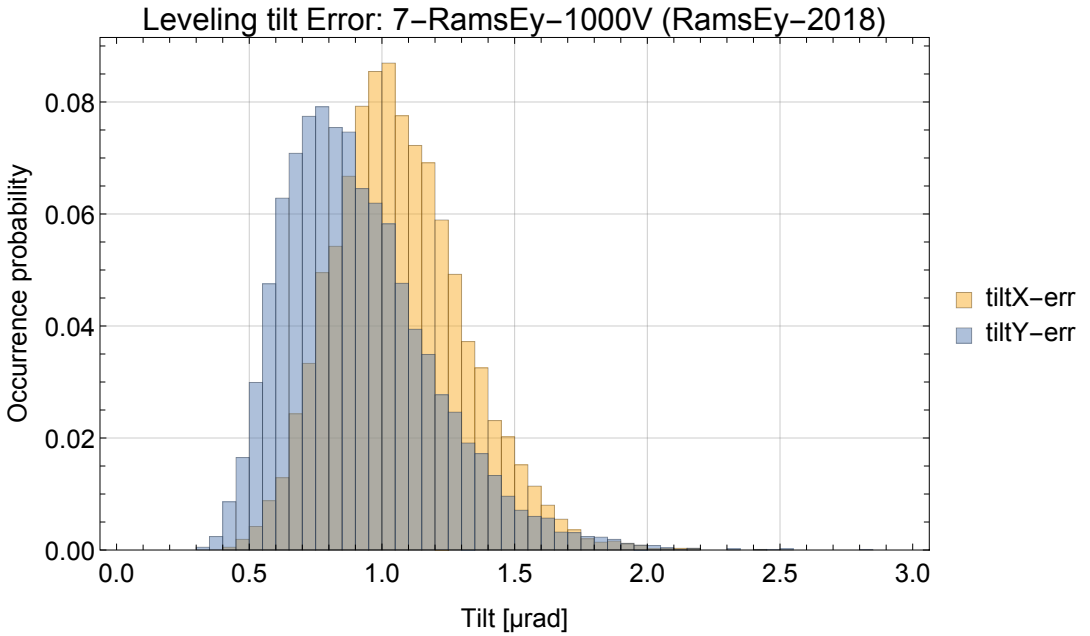

Figure A.23.: Histogram of the standard deviations of each single measurement point during the beam time 184-18/3.

Similar to the detector sensors (see section A.3.2), the tilt sensor measures the temperature in air inside the vacuum chamber. As seen in figure A.27, the temperature increases around 2 K during evacuations. This is not so pronounced as for the detector sensors (>4 K). However, the origin should be further investigated. In addition, the noise of the measurement values should be reduced. The main causes are the low resolution of the sensor (0.1 K) and the fact that the stored values are already averaged.

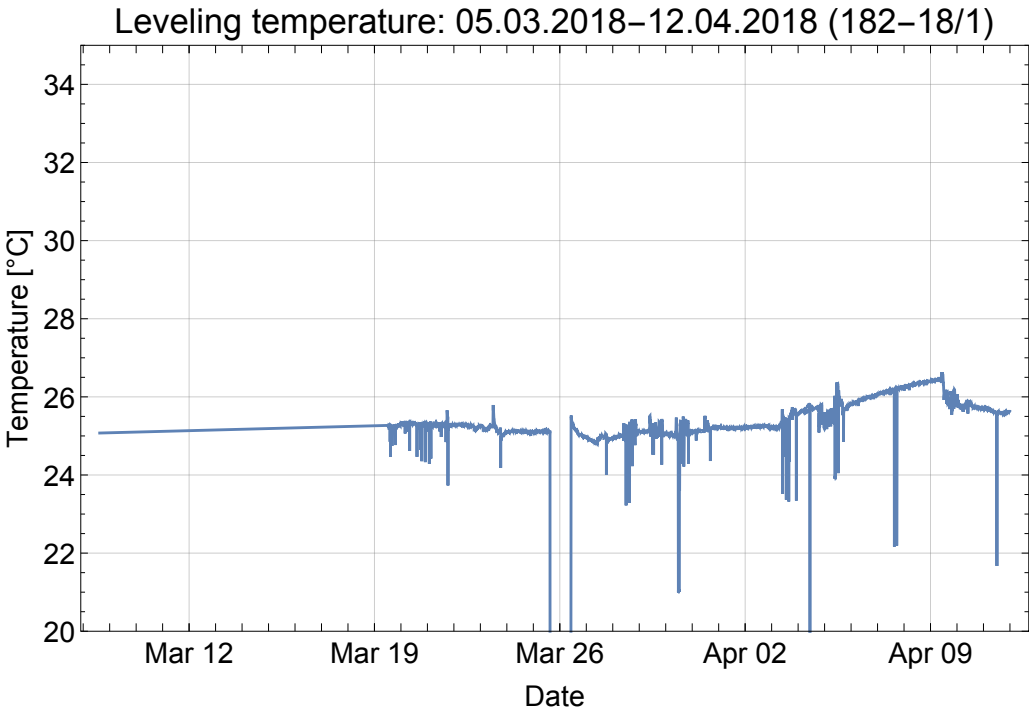

Figure A.24.: The temperature of the tilt sensor during the first half of the beam time 182-18/1. Due to the short evacuation periods the influence due to the vacuum conditions is negligible.

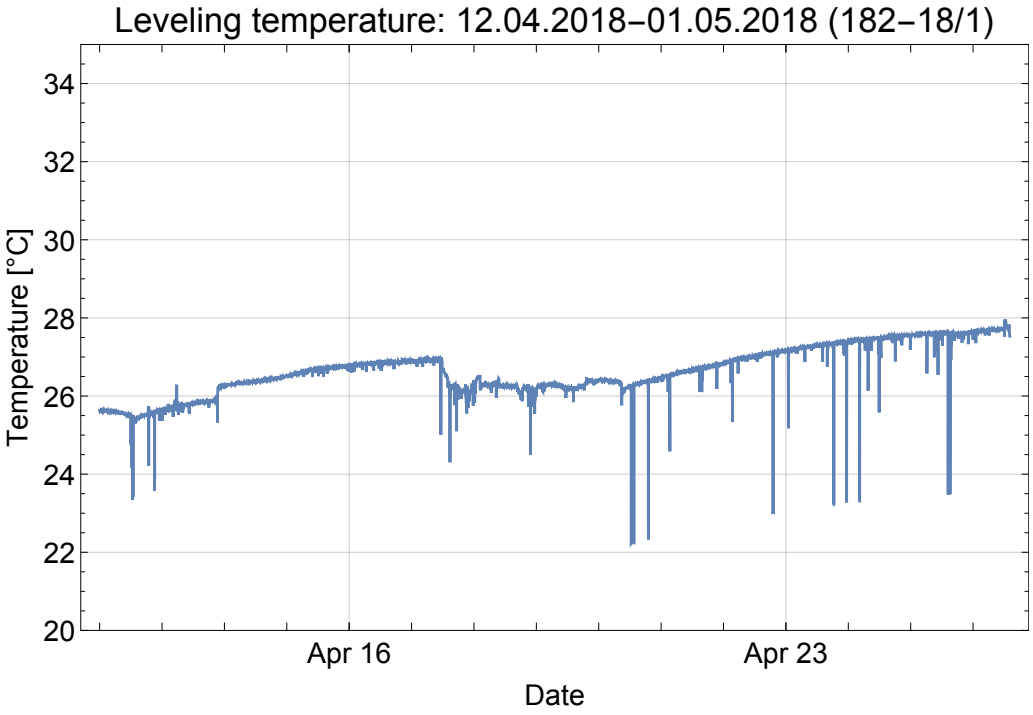

Figure A.25.: The temperature of the tilt sensor during the RABI-GRS-18 measurements. The slow rise of the temperature during the evacuation is clearly visible.

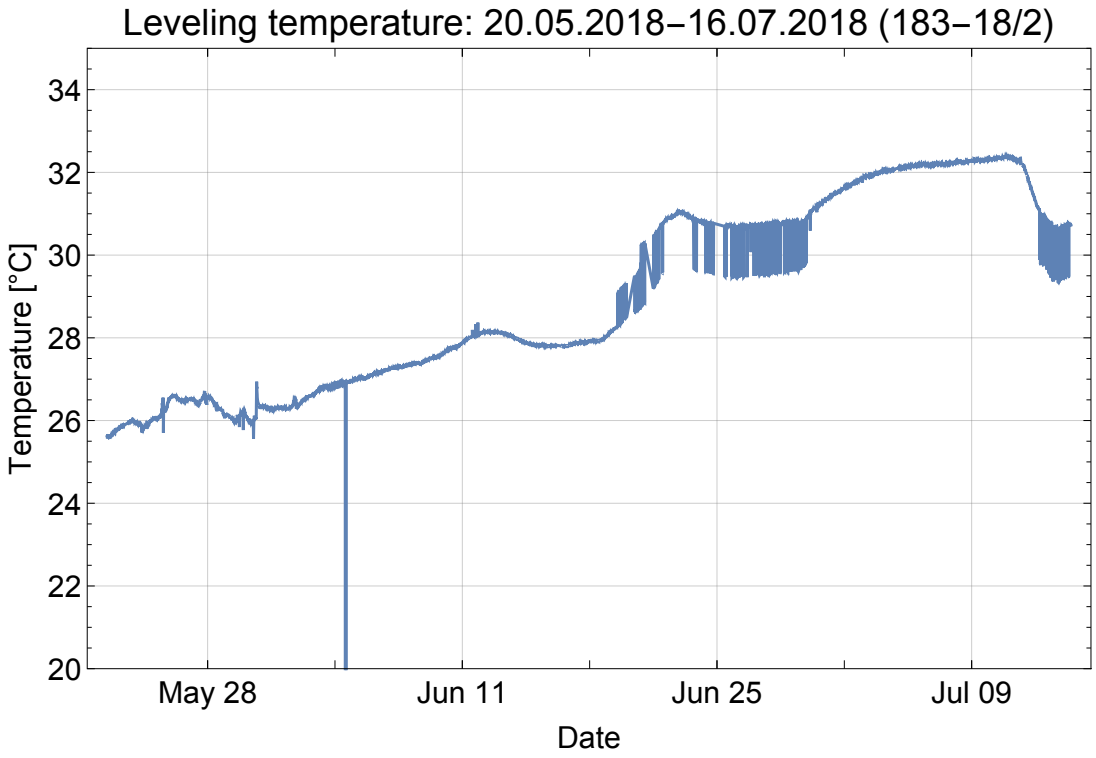

Figure A.26.: The temperature of the tilt sensor during the RAMSEY-GRS-18 measurements. Similar to the reactor hall and the air above Grenoble, the temperature rose slowly upwards.

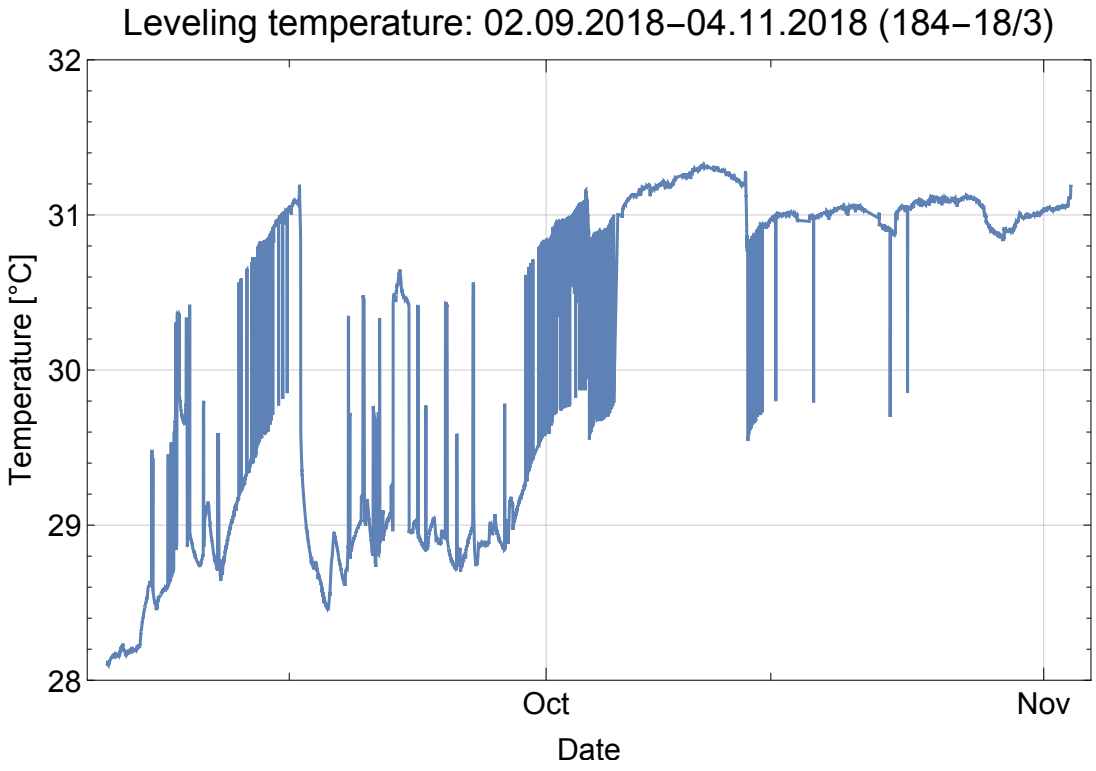

Figure A.27.: The temperature of the tilt sensor during the Rams$\vec{E}$y measurements.

A.4. Additional data of the neutron measurements

A.4.1. Aperture

The detector count rates are only corrected with their subtracted background. As seen in table A.2, the uncorrected values have a very similar result not only in the parameters but also in the statistical significance. As expected, the scaling factor n is slightly larger due to a higher count rate of the raw measurements.
The monitor correction was discarded due to its significantly higher χ^2 value. Also the monitor rate itself is not stable enough for such a correction (variation above 20 %). As seen later during the first Ramsey measurements (see section 4.5), glass shards above the monitor detector and movement of beam guide itself changed the monitor rate significantly and abruptly, independently of the zero rate r_0 and the reactor power. The aperture measurement is very prone for such influences on the monitor rate. Each venting and evacuation apply large mechanical stress changes on the beam guide end inside the vacuum chamber which can result in small movement of the beam guides.

Table A.2.: Aperture velocity measurement fits: comparison of different corrections

Data	Correction	Parameter	χ^2	red-χ^2_{red}	p-value
2018 - All (13)	Complete	n = 221.7(34) v_0 = 3.329(92) a = 4.052(89)	61.399	6.1399	1.97×10^{-9}
2018 - All (13)	uncorrected	n = 223.4(32) v_0 = 3.098(96) a = 4.217(95)	45.214	4.521	1.99×10^{-6}
2018 - 1 m/s (6)	uncorrected	n = 276(39) v_0 = 1.0(15) a = 5.8(10)	19.07	6.36	2.64×10^{-4}
2018 - 2 m/s (7)	uncorrected	n = 224.0(40) v_0 = 3.25(10) a = 4.03(10)	14.19	3.55	6.72×10^{-3}

Generalized Maxwell-Boltzmann distribution

As already described in section 2.2.3, not only the Maxwell-Boltzmann distribution for ideal gases (eq. (2.148)) but also its generalized form (eq. (2.150)) can be used to describe the measured velocity spectrum beside many other possible functions. Summarized in table A.3, the results are inconclusive. Eliminating the velocity cutoff ($v_0 = 0$), as it would be expected for an ideal gas, is statistical excluded by the measurement. Increasing the number of fit parameters (including b and c) reduces the χ^2 significantly but the reduced χ^2_{red} stays nearly constant due to the low number of measurement points. As shown in figure A.29, the lowest χ^2 is close to $b = 4$ and $c = 1$. However, corresponding neutron temperature is too high for UCNs (T = 223 mK). As seen in figure A.28, all tested fit functions are quite similar within the chosen velocity interval for the GRS measurements (5-13 m/s). Using a physically not so well motivated generalized Maxwell-Boltzmann distribution will not change the state transition probability significantly. Therefore, using the simpler Maxwell-Boltzmann distribution for the ideal gas is sufficient.

Table A.3.: Aperture velocity measurement fits: comparison of different fit functions

Data	Correction	Parameter	χ^2	red-χ^2_{red}	p-value
2018 - All(13)	Background only	$n = 289.5(83)$ $v_0 = 0$ (fixed) $a = 7.72(15)$ $b = c = 2$ (fixed)	256.0	23.27	1.5×10^{-48}
2018 - All(13)	Background only	$n = 38(169)$ $v_0 = 2.2(22)$ $a = 4.04(25)$ $b = 2$ (fixed) $c = 2.9(23)$	44.12	4.902	1.34×10^{-6}
2018 - All(13)	Background only	$n = 33.12(83)$ $v_0 = 2.15(13)$ $a = 4.035(95)$ $b = 2$ (fixed) $c = 3$ (fixed)	44.120	4.4012	3.13×10^{-6}
2018 - All(13)	Background only	$n = 401(264)$ $v_0 = 2.34(88)$ $a = 7.6(49)$ $b = c = 2.46(48)$	43.39	4.822	1.82×10^{-6}
2018 - All(13)	Background only	$n = 768 \times 10^3$ $v_0 = 4.0$ $a = 42.8(23)$ $b = 3.98(9)$ $c = 0.96(11)$	39.61	4.951	3.79×10^{-6}
2018 - All(13)	Background only	$n = 754(53) \times 10^3$ $v_0 = 3.935(74)$ $a = 43.7(15)$ $b = 4$ (fixed) $c = 1$ (fixed)	40.118	4.0118	1.62×10^{-5}

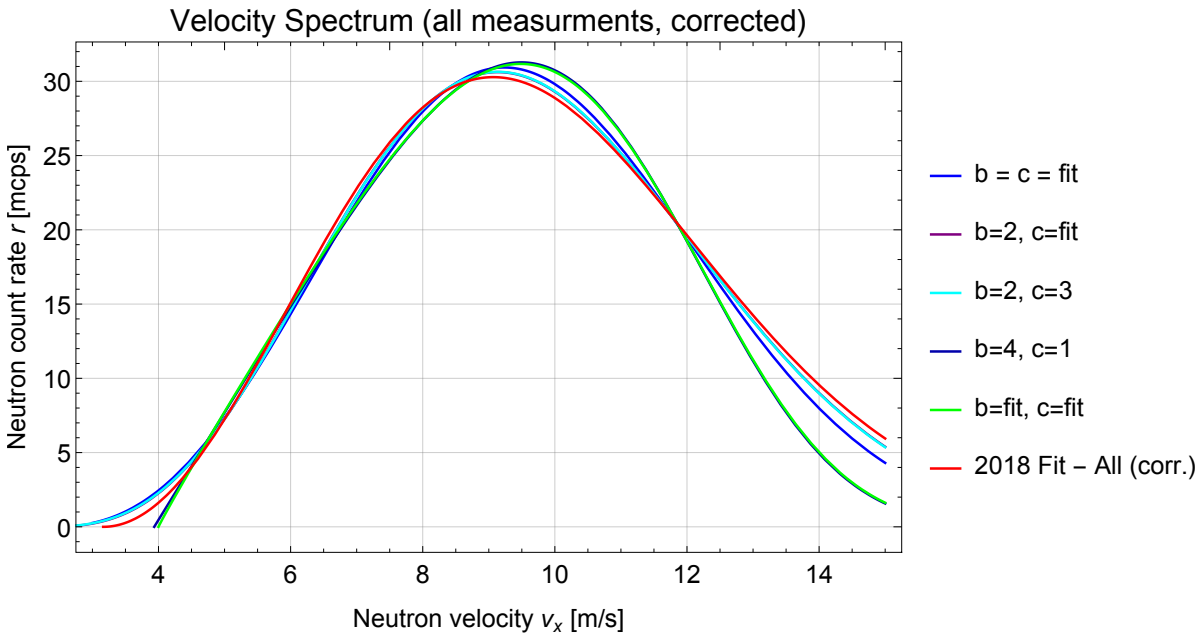

Figure A.28.: Aperture measurement 2018: comparison of different fit functions

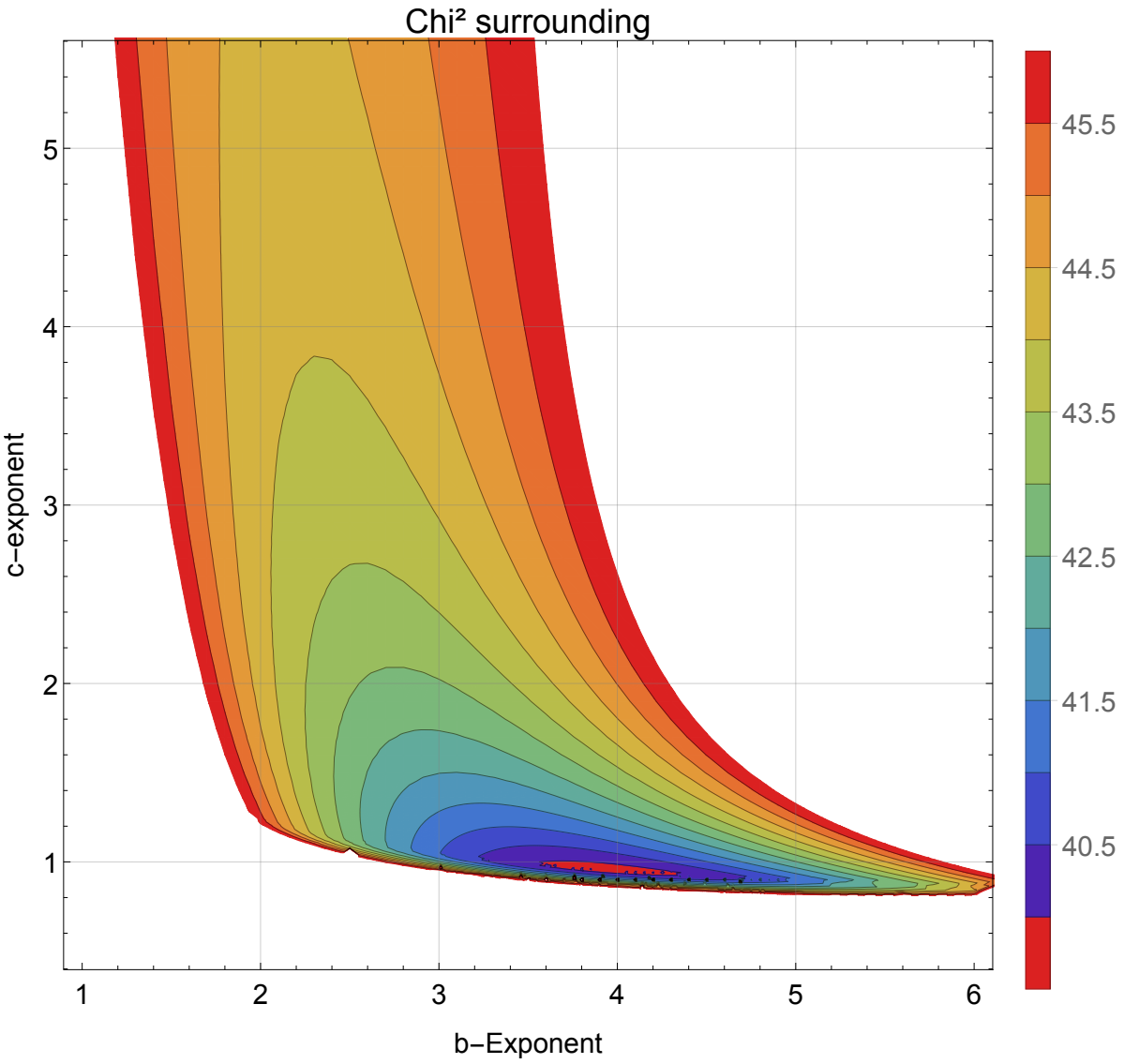

Figure A.29.: Aperture measurement 2018: χ^2 surrounding

A.4.2. CR-39

Additional measurements corresponding to section 4.3.2.

Coating performance

As described in the subsection 3.2.4, it is quite difficult to produce homogeneous boron coatings with the correct thickness on the plastic CR-39. Therefore, the available CR-39 detectors during a beam time have a large variety of qualities. Optical inspections (number of cracks, color changes,...) determine the possible usage of each individual detector. The best are used for the state occupation determination, the worst during measurements in very intense beams. However, only the full evaluation can determine the real performance (detector efficiency).

ID 070 and ID 062 were older detectors. Both had a strong color deviation between their two halves (green/purple). One half of the coating was severely damaged/cracked. Therefore, both were used together with the better halves in the center because we used all other available detectors with better qualities before. Both detectors performed better than expected for the conditions of their coating.

Another rather old detector was ID L11. It had an inconspicuous coating. During chemical treatment, one side of the coating resisted multiple attempts to be solved by a sulfuric acid and hydrogen peroxide mixture. Only after the etching with a lye, the last pieces peeled off. The detection with the microscope showed a strong gradient in the efficiency [14](p.49). However on one side the neutron track was clearly visible and enough to extract a state population. Further etching of the poor half could increase the number of detected neutrons to the expected one.

ID 016 and ID T35 originated from Hanno Filter's coating patch 7 [89]. Both had multiple scratches in the coating and therefore were good candidates to study the beam divergence after the end cap. Both detectors showed a high number of neutron counts in the center of the beam (up to 570 n per picture or 100 n per 100 µm × 100 µm, respectively 800 n and 135 n).

ID 003 was from the well performing patch 8 from Hanno Filter which he produced in autumn 2016 [89]. Tobias Rechberger used its siblings with the IDs 036, 122, 129, T37 for his state population measurements within the RAMSEY^{TR}-setup [254]. As similar detectors from this patch, ID 003 showed a good neutron detection efficiency. Together with the long exposure time this enabled to choose fewer classifications (only the one with mostly neutrons and less background) and still have a very high statistics for a state population determination.

The IDs E03, 102, 103, 116, 128, 141, 145 are part of the coating patch 13 which Hanno Filter produced in January 2017. Only the ones used at the end caps (E03, 103) showed a neutron pattern. Their neutron density was approximately 200 neutrons per microscope picture[7]. We used the other CR-39 detectors to study the state populations. We did not find neutron track patterns (lines) at any of them. Some of them were under-irradiated (102, 128, 145). Others showed to much noise (141). A detailed study of the complete detector area was discarded during the evaluation process due to time constraints. However, this could be done to better understand the properties of this coating patch and finding the neutron track would increase the statistics of the state population studies. An additional problem for this patch and all later produced ones is the change of the CR-39 manufacturer. It is not clear what is the used material for each individual detector. A different material needs a different etching time and temperature which could explain the found under-irradiation of some detectors of this patch.

The ID 039 was the only one from the coating test patch 3 (Hanno Filter). It had only around 50 nm of natural boron covering it. This is too thin to be able to detect something. However, it ended up in Grenoble and was used in the experiment (qBOUNCINO) until I checked its origin. Therefore, we discarded its measurement.

In the future, each new coated patch of CR-39 detectors should be tested in order to implement a quality control. One detector of the patch could be irradiated in Vienna at the PuBe neutron source, which is always available. Using the same irradiation geometry, irradiation duration, chemical treatment, microscope technique and data evaluation would enable to compare different patches, especially their detection efficiencies. This also prevents surprises in Grenoble after long irradiation times when nothing

[7] This is 3-4 time less than observed in similar measurements (ID 016 & T35). However, the detectors were only scanned in one small area which was probably not the one with the highest density. A full scan is recommended in order to be able to compare the detector efficiencies more accurately.

is found on the developed detector surfaces and narrows down the sources of errors due to gained trust into the efficiency of the coating.

Vertical beam divergence

The primary idea of the beam divergence measurements was to determine if the neutron window slit in the beam guide's end cap is wide enough to completely illuminate the aperture slit with UCNs. A second reason for these measurements was to test the efficiency of CR-39 coatings. At this position the irradiation time is only one PF2 switcher cycle long (190 s) instead of hundreds for measurements after one absorber region (multiple days). We used detectors with visible damages in the coating which excluded them for long state occupation determinations. The used detectors and their position can be found in the following table:

Table A.4.: CR-39 beam divergence tests in 2018

CR-39 ID	T35	016	103	E03
x: Position	0 mm	16 mm	0 mm	0 mm
Place	end cap	aperture	end cap	end cap
y: Center position	−17.5 mm	27.5 mm	−27.5 mm	27.5 mm
Central edge	EDM	MAM	EDM	MAM
Displacement of central edge	10 mm → MAM	20 mm → EDM	20 mm → MAM	20 mm → EDM
z: Height above granite	40.2 mm	41.5 mm	40.2 mm+bending	40.2 mm+bending
Label position	upper edge	upper edge	upper edge	upper edge
Edging time	5 h	5 h	2.5 h+1.5 h+1 h+3x0.5 h+1 h+4.5 h	
Highest n density	800 per picture	570 per picture	250 per picture	200 per picture
Per 100 µm × 100 µm	135 n	97 n	-	-

Within the 16 mm between the detectors, the neutron falls down approximately 20 µm. Compared to the accuracy of the measured vertical position of the CR-39 detectors, this is negligible.
Lukas Achatz scanned one line through the complete detectors (429 pictures) for the first two detectors [14](p.26-36). The beam heights can be correlated by their centers as the scans did not start at the edges. As seen in figure A.30 the beam profile changes. Close to the end cap the beam has a quite trapezoidal shape ($a = 24.1$ mm, $c = 15.4$ mm). This proofs that the UCNs only fly through the neutron window (see paragraph 3.1.2) and not through the NiMo coated aluminum flange. In front of the aperture, the beam has already a strong vertical divergence. This can be described with a Gaussian function ($\sigma = 9.3$ mm) or still a trapezoidal shape ($a = 8.4$ mm, $c = 37.2$ mm).

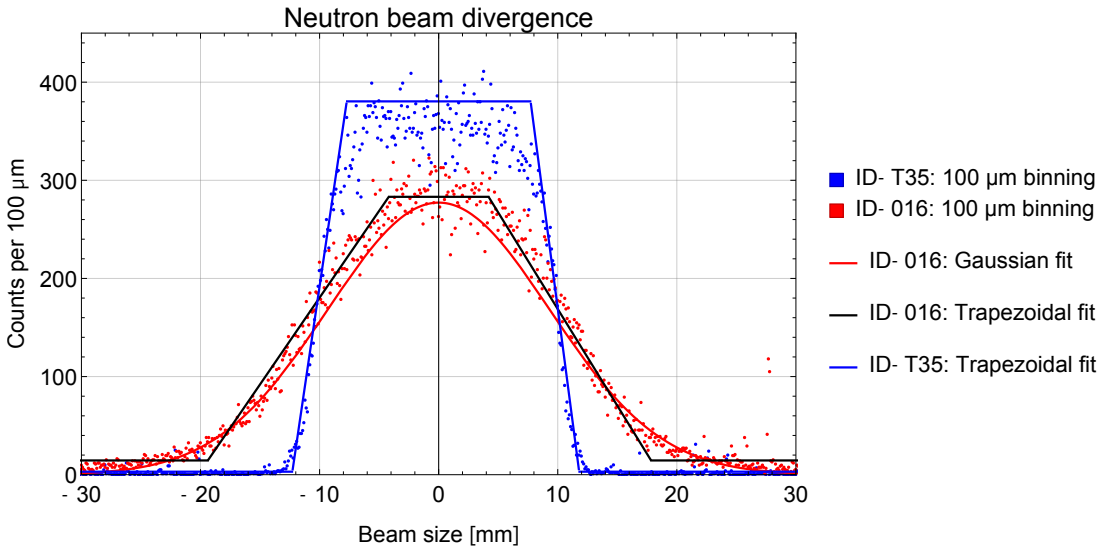

Figure A.30.: Beam profile behind the end cap (blue) and before the aperture (red, scaled to same total counts).

An even higher statistic could be achieved by scanning the complete detectors. This huge data set of detected neutrons is exceptionally well-suited to test and compare different neutron detection algorithms described in section 3.2.4. Also for the exact determination of the end-cap neutron window (height and gap size) a re-scan starting from the edge is necessary.
The detectors E03 and 103 can also be used to resolve the neutron window by scanning their complete surfaces. A major drawback is their large neutron tracks due to the longer etching times (12 h in total). These tracks will overlap in the most dense regions.

The vertical divergence itself reduces the usable neutron beam for any GRS setup tremendously. Changes of the beam guide shape and especially the end cap could increase the neutron flux entering the first absorber. However, this has to be simulated with Monte Carlo algorithms very detailed in advance. Additional measurements with spatial resolution detectors (e.g. CR-39) in the region around the aperture will show a more detailed picture of the beam divergence in horizontal and vertical direction. Any studies trying to reduce the neutron losses are highly recommended. Any possible increase in flux decreases the statistical uncertainty of any measurement within the RAMSEY^{TR}-setup.

A.4.3. Beam divergence

During the three beam times, multiple different mirror configurations were installed for various measurements: from a single absorber region for state population measurements (see section 4.3.2) or aperture measurements (see section 4.3.1) to a full five region Ramsey-type GRS setup (see section 4.5). The highest variation of short setups was assembled in the first beam time (182-18/1) (tab. A.6 & tab. A.5). The two following beam times (183-18/2 & 184-18/3) consisted mainly of full Ramsey assemblies (tab. A.7) or test of region III mirrors (tab. A.6). Comparing these different setups reveals the beam divergence, losses inside the neutron absorbers (region I & region V) and general absorption on the different mirror surfaces (see table A.8). Two factors can obstruct these comparisons: The step heights have to be set to zero and the mirrors have to be clean. If one of these requirements is not fulfilled, additional neutron losses occur. In the following tables, different configurations are first compared with similar measurements and in the end the generalized rates are compared between different setups in the table A.8. Andrej Brandalik analyzed a similar collection of different assemblies from a beam time in 2020 for his bachelor's thesis [48](p.22-30).

Table A.5.: Rate measurements with different short mirror configurations

Beam time	Mirrors	Measurement	Detector	Monitor	Cycles
182-18/1	I (603+709)	ID 2.675 (p.63)	193.7(64) mcps	22.60(7) cps	250
182-18/1	I (603, 105 mm)	ID 3.003 (p.64)	27.00(17) cps	22.62(15) cps	5
182-18/1	I (603, 104.9 mm)	ID 3.004 (p.64)	33.90(30) cps	22.40(24) cps	2
182-18/1	I (603, 105.1 mm)	ID 3.005 (p.64)	21.52(19) cps	22.39(20) cps	3
182-18/1	V (801+804)	ID 3.007 (p.65)	177.7(24) mcps	21.85(3) cps	160
182-18/1	I (802+805)	ID 3.009 (p.70-71)	162.1(20) mcps	23.71(2) cps	224
182-18/1	V (801+804)	ID 3.012 (p.74-75)	160.5(40) mcps	18.67(4) cps	52
182-18/1	I (802+805)	ID 3.014 (p.77)	169.1(11) mcps	24.16(1) cps	672
182-18/1	I (802+805) - ≈100 mm Mam	ID 3.010 (p.72)	95.3(13) mcps	20.81(2) cps	317
182-18/1	I (802+805) EDM only	ID 3.021 (p.82)	92.2(14) mcps	18.35(2) cps	257
182-18/1	I (802+805) MAM only	ID 3.022 (p.82)	84.2(45) mcps	18.04(7) cps	22
182-18/1	V (801+804) MAM only	ID 3.023 (p.83)	82.5(38) mcps	17.17(5) cps	30
182-18/1	V (801+804) EDM only	ID 3.024 (p.84)	95.2(46) mcps	17.31(6) cps	24
182-18/1	I (802+805), V (801+804)	ID 4.037 (p.98)	78.0(36) mcps	20.68(6) cps	31.6
182-18/1	I (802+805), V (801+804)	ID 4.041 (p.99-101)	77.6(29) mcps	22.57(5) cps	49

Comparing the old absorber region from 2016-2017 directly with the newly clamped absorber regions reveals a reduction in the transmission of 5 % to 20 %. This can be explained by the reduction of the gap size from 25 µm to 22 µm or approximately 12 %.
The measurements without absorbers show a strong height dependency, which either can be explained that the beam guide is too low or the lower mirror exposes the detector to more parts of the beam. To distinguish both effects, a similar measurement with an absorber is necessary. The absorber itself is reducing the beam intensity by a factor of 140(5).
Comparing the newly clamped absorbers to each other suggests a slightly better transmission for the

new region V. Tests with half blocked beams (ID 3.021-3.024) support this observation. Additionally, this set of measurements shows a small but significant difference between the sides of the beams (MAM/EDM: region I 91.3(51) %, region V - 86.7(58) %). Either both absorbers are clamped similar tilted, the neutron beam has an asymmetric y-dependence or the detector has an inhomogeneous efficiency (differences in the boron coating thickness).
The measurement of ID 3.010 (182-18/1) is different to all other measurements. A CR-39 detector was at the position of the main detector. The counter tube was situated beside the CR-39 holder irradiated by neutron beam passing beside the absorber on the mambo side. Already after the first region, the same amount of UCNs flies past the absorber on both sides as the counted neutrons in the detector.
Combining both absorber regions reduces the total beam intensity by a factor of 2.5. This is due to a stronger suppression of higher states and the beam divergence.

Table A.6.: Rate measurements with different region III mirrors (I (802+805), II (702))

Beam time	Region III mirrors	Measurement	Det. rate	Monitor	Cycles	Reactor
182-18/1	V (801+804)	RABI-GRS-18 I	52.35(62) mcps	18.007(8) cps	730	49.6 MW
182-18/1	V (801+804)	RABI-GRS-18 II	51.99(94) mcps	23.714(8) cps	321	58 MW
183-18/2	III (707)	1.016	54.23(101) mcps	21.17(2) cps	286.8	52.5 MW
183-18/2	III (811)	1.067	45.07(150) mcps	24.70(3) cps	108	52.5 MW
183-18/2	III (811)	1.079	56.57(96) mcps	24.86(2) cps	328	52.5 MW
184-18/3	III (811)	2.055	57.5(29) mcps	116.1(1) cps	37	51.5 MW
184-18/3	III (811)	2.058	49.8(25) mcps	114.2(1) cps	43	51.5 MW
184-18/3	III (831)	2.094	46.0(16) mcps	116.9(1) cps	92	51.5 MW
184-18/3	III (831)+Electrode	2.475	71.5(17) mcps	117.8(1) cps	125	51.5 MW

The strong variations between similar measurements with the same mirrors are due to different piezoelectric stage settings resulting in different step heights. Therefore, it is impossible to really compare the transmission property differences between the mirror surfaces.

Table A.7.: Rate measurements with a Ramsey mirror configurations, combined and corrected zero rates

Beam time	Measurement	Det. rate	Monitor	Cycles	Reactor
183-18/2	RAMSEY-GRS-18-0	15.1(57) mcps	18.55(1) cps	374.8	52.5 MW
183-18/2	RAMSEY-GRS-18-I	17.33(36) mcps	19.64(1) cps	747.4	52.5 MW
183-18/2	RAMSEY-GRS-18-II	19.43(44) mcps	25.08(1) cps	715.4	52.5 MW
183-18/2	RAMSEY-GRS-18-III	19.38(44) mcps	20.77(1) cps	536	52.5 MW
184-18/3	RAMSEY-GRS-18-Fall	22.4(10) mcps	116.74(4) cps	115	51.5 MW
184-18/3	Rams$\vec{E}$y-I	19.43(45) mcps	115.87(3) cps	522	51.5 MW
184-18/3	Rams$\vec{E}$y-II	18.49(32) mcps	117.35(1) cps	1019	51.5 MW
184-18/3	Rams$\vec{E}$y-HV	15.71(47) mcps	117.83(4) cps	386	51.5 MW
184-18/3	Rams$\vec{E}$y-HV	11.72(37) mcps	82.80(2) cps	491	34.5 MW

The zero rate increase for the RAMSEY-GRS-18 measurements is due to better mirror position settings which coincidentally reduce the step sizes. This resetting was necessary after a full crash of the data acquisition system. As seen during the Rams$\vec{E}$y - measurements, opening and closing the chamber even for only a short period reduces the zero rate (even though the step settings were kept constant). The strong rate drop for the final high voltage measurements is due to a different reactor power level.

Table A.8.: Rate measurements with different mirror numbers for beam divergence tests

Mirrors	Method	Det. rate	Monitor	Cycles	Reactor
I (802+805)	best	169.1(11) mcps	24.16(1) cps	672	49.6 MW
V (801+804)	best	177.7(24) mcps	21.85(3) cps	160	49.6 MW
I (802+805), V (801+804)	mean	77.7(23) mcps	21.83(4) cps	80.6	49.6 MW
I (802+805), II (702), V (801+804)	RABI-GRS-18-I	52.35(62) mcps	18.007(8) cps	730	49.6 MW
I (802+805), II (702), III (811)	best	56.57(96) mcps	24.86(2) cps	328	52.5 MW
I (802+805), II (702), III (831)	best	71.5(17) mcps	117.8(1) cps	125	51.5 MW
RAMSEY-GRS-18	best	19.38(44) mcps	20.762(6) cps	536	52.5 MW
Rams$\vec{E}$y	best	19.43(45) mcps	115.87(3) cps	522	51.5 MW

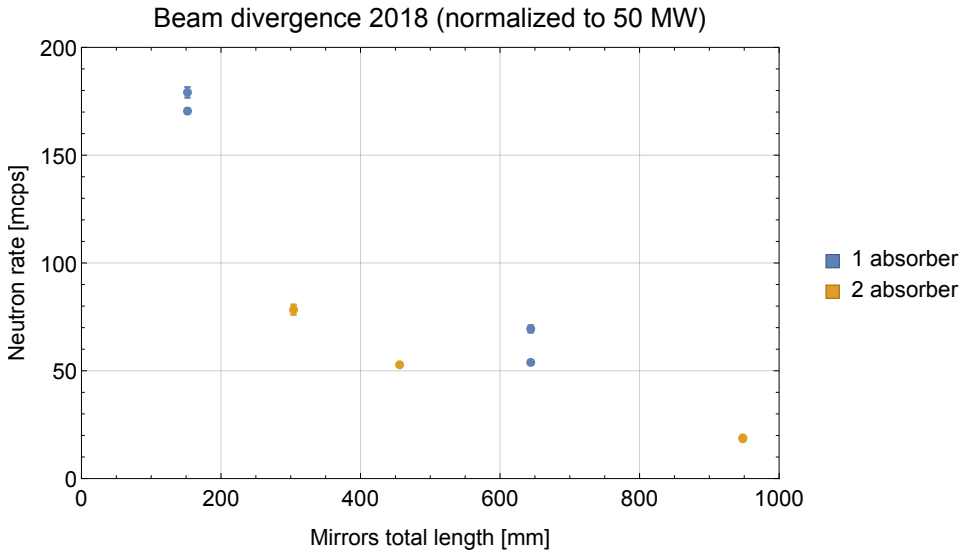

Figure A.31.: Displayed values of table A.8

A.4.4. Shutter test rates

Table A.9.: Shutter position test rates of the cycle Ramsey-2018 (3-14-358-IV) - (IDs) are not used for the evaluation

ID	Start	Cycles	Livetime[s]	UCN(MON)	Rate(MON)	Measurement
4.218	11:07 19.06.2018	1.	190.0 s	329	1.732(95) cps	−92°
4.219	11:16 19.06.2018	1.	190.0 s	3906	20.558(329) cps	22.5°
(4.220)	11:21 19.06.2018	0.369	70.1 s	530	7.562(328) cps	20°
4.221	11:27 19.06.2018	2.	380.0 s	7470	19.658(227) cps	20°
4.222	11:35 19.06.2018	1.	190.0 s	3362	17.695(305) cps	15°
4.223	11:40 19.06.2018	1.	190.0 s	2331	12.268(254) cps	−2°
4.224	11:44 19.06.2018	27.	5130.0 s	54	0.011(1) cps	−70°
4.225	13:22 19.06.2018	1.	190.0 s	1393	7.332(196) cps	−15°
4.226	13:31 19.06.2018	1.	190.0 s	706	3.716(140) cps	−30°
4.227	13:36 19.06.2018	1.	190.0 s	99	0.521(52) cps	−45°
4.228	13:42 19.06.2018	1.	190.0 s	1	0.005(5) cps	−60°
4.229	13:53 19.06.2018	1.	190.0 s	12	0.063(18) cps	−80°
4.230	13:59 19.06.2018	4.	760.0 s	699	0.920(35) cps	−90°
4.231	14:23 19.06.2018	1.	190.0 s	95	0.500(51) cps	−85°
4.232	14:27 19.06.2018	1.	190.0 s	46	0.242(36) cps	−50°
4.233	14:33 19.06.2018	1.	190.0 s	235	1.237(81) cps	−40°
4.234	14:39 19.06.2018	1.	190.0 s	1085	5.711(173) cps	−20°
4.235	14:44 19.06.2018	1.	190.0 s	1736	9.137(219) cps	−10°
4.236	14:50 19.06.2018	1.	190.0 s	2427	12.774(259) cps	0°
4.237	14:56 19.06.2018	1.	190.0 s	3090	16.263(293) cps	10°
4.238	15:02 19.06.2018	3.	570.0 s	11582	20.319(189) cps	23°
4.239	15:22 19.06.2018	1.	190.0 s	3505	18.447(312) cps	30°
4.240	15:40 19.06.2018	1.	190.0 s	2823	14.858(280) cps	40°
4.241	15:44 19.06.2018	1.	190.0 s	3838	20.200(326) cps	25°
4.242	15:52 19.06.2018	5.	950.0 s	19616	20.648(147) cps	24°
4.243	16:14 19.06.2018	1.	190.0 s	3891	20.479(328) cps	24°
(4.244)	16:33 19.06.2018	0.	0.0 s	7	0.016(6) cps	−65°

Figure A.32 displays the influence of shutter reel diameter r_s in the context of the *single guide approach*.

A comparison with the measured data reveals the most likely radius of 65 mm.

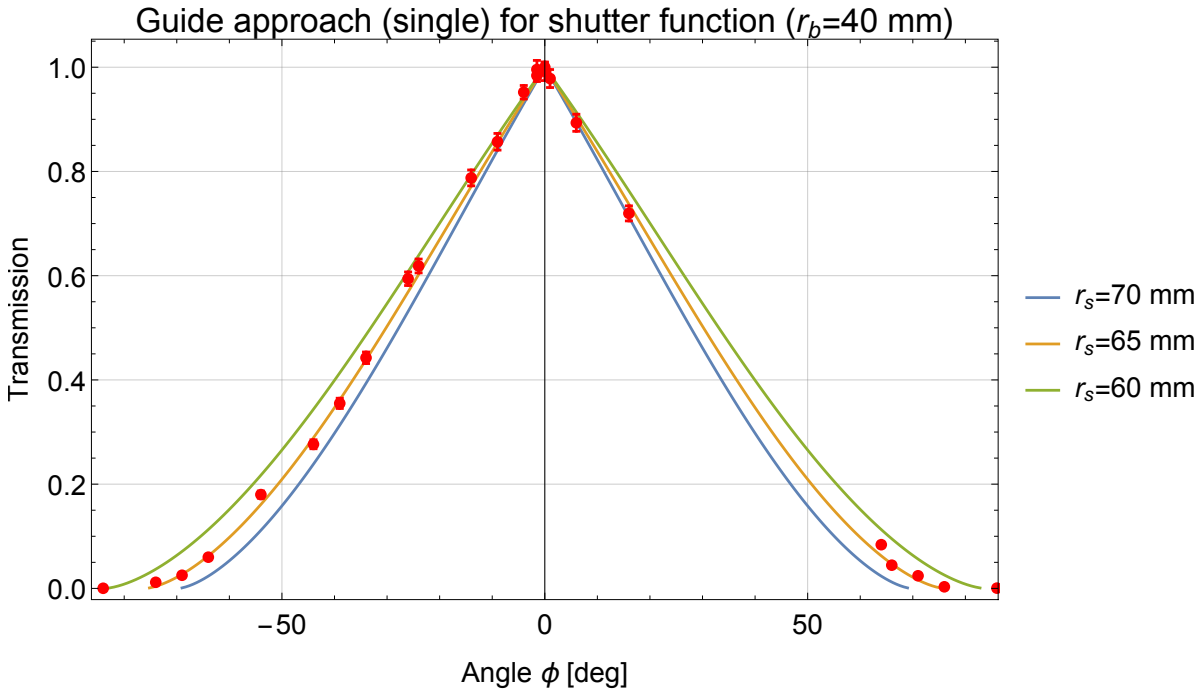

Figure A.32.: The relative transmission of the shutter measurements compared to the single guide approach with different shutter reel radii r_s.

A.4.5. Detector background

As described in the section 3.2.1, a very low background is necessary for GRS measurements. All rate measurements have to be corrected with the background count rate (see subsection 3.2.3). The active rotational shutter blocks the neutron beam during the background measurement window, which enables to measure these rates continuously in parallel to all other neutron count rates (see table A.10). Additionally, we measured background rates during works on the setup and also when the reactor was shut down (see tables at the end of this section).

Table A.10.: Cumulative background determination during rate measurements

Beamtime	Measurement	Time [s]	Detector rate [mcps]	Detector counts	Monitor rate [mcps]	Monitor counts	Comments
182-18/1	Test[18] I	691 267.5 s	0.845(35) mcps	584 cts	98.97(39) mcps	68415 cts	CR-39 incl.
182-18/1	RABI-GRS-18 I	66 242.4 s	0.830(112) mcps	55 cts	124.04(137) mcps	8217 cts	
182-18/1	RABI-GRS-18 II	80 655.5 s	0.707(94) mcps	57 cts	144.53(134) mcps	11657 cts	
183-18/2	Prepartion	533 864.0 s	0.88(4) mcps	470 cts	16.44(18) mcps	8775 cts	
183-18/2	RAMSEY-GRS-18-I	129 193.0 s	0.61(7) mcps	79 cts	233.3(13) mcps	30139 cts	Shutter problem
183-18/2	RAMSEY-GRS-18-II	18 000.3 s	0.89(22) mcps	16 cts	97.44(233) mcps	1754 cts	
183-18/2	RAMSEY-GRS-18-III	74 676.1 s	0.54(8) mcps	40 cts	56.18(87) mcps	4195 cts	
183-18/2	End	109 061.0 s	0.63(8) mcps	69 cts	4.00(19) mcps	436 cts	Reactor down
183-18/2	Total	874 698 s	0.813(30) mcps	711 cts	257.57(87) mcps	87051 cts	Excl. some IDs
184-18/3	Preparation	330 752.0 s	0.73(5) mcps	240 cts	825.70(158) mcps	273090 cts	Monitor tests
184-18/3	RAMSEY-GRS-18 Fall	220 745.0 s	0.33(4) mcps	73 cts	158.60(85) mcps	35008 cts	
184-18/3	Test region III	154 322.0 s	0.63(6) mcps	97 cts	78.84(71) mcps	12167 cts	
184-18/3	Rams$\vec{E}$y-0 V I	183 799.0 s	0.73(6) mcps	134 cts	151.40(91) mcps	27826 cts	
184-18/3	Rams$\vec{E}$y-0 V II	159 773.0 s	0.61(6) mcps	97 cts	145.50(95) mcps	23251 cts	
184-18/3	Rams$\vec{E}$y-HV Start	189 507.0 s	0.68(6) mcps	129 cts	16.07(29) mcps	3045 cts	Reactor down
184-18/3	Rams$\vec{E}$y-HV	368 804.0 s	0.62(4) mcps	228 cts	42.09(34) mcps	15522 cts	
184-18/3	End	341 567.0 s	0.62(4) mcps	212 cts	3.66(10) mcps	1249 cts	Reactor down
184-18/3	Total	1 839 335 s	0.657(19) mcps	1209 cts	66.78(19) mcps	129547 cts	Excl. some IDs

The initial measured detector background rates of 0.41(4) mcps [113] and 0.47(4) mcps [93] (in ideal conditions at the ATI, Vienna) are the benchmarks for the main detector (P-detector). As already previously observed (0.45(2) mcps [254](p.116)), more disturbances occur in Grenoble. Therefore, the measured averaged backgrounds between 0.66(2) mcps and 0.85(4) mcps were slightly higher during the cycles in 2018. However, this is still enough to have a signal to noise ratio between 15 and 75 depending on the measurement. In addition, Figure A.33 proofs that the background rate of the main detector is independent of the reactor. Figure A.34 shows that the neutron contribution to the background of the main detector is negligible.

The repaired M-detector has also an undisturbed background rate of 0.49(5) mcps [32](p.28-29). During the usage within the *q*BOUNCINO experiment (2018), the background rate was between 2.8(2) mcps and 3.5(2) mcps [236](p.34). This high rate was measured with and without an active reactor. The missing shielding against external electromagnetic disturbances (Faraday cage) is suspected to be the main cause. In addition, the detector had to be strongly shielded against the neighboring VCN beam to even be able to reach this still high background level. For future uses of the detector at different beam sites, the shielding should be implemented as already for the RAMSEY^{TR}-setup [298].

The background rate of the monitor detector is strongly influenced by the efficiency of the shielding against the stray neutrons of the reactor and the tightness of the shutter[8] (as seen in the figure A.33, the monitor background rate depends on the reactor power level). Only during a reactor shut down, the true electronic background noise is measurable. As seen in table A.10, the purely electronic noise of the monitor detector was around 3 mcps to 4 mcps (for both used monitor detectors). Due to neutrons passing through the shielding the monitor's average background levels could reach up to 150 mcps which still provide a signal to noise ratio of approximately 750. Therefore, a high monitor count rate relaxes the requirements of the background suppression (mainly shielding against fast/thermal neutrons from the reactor).

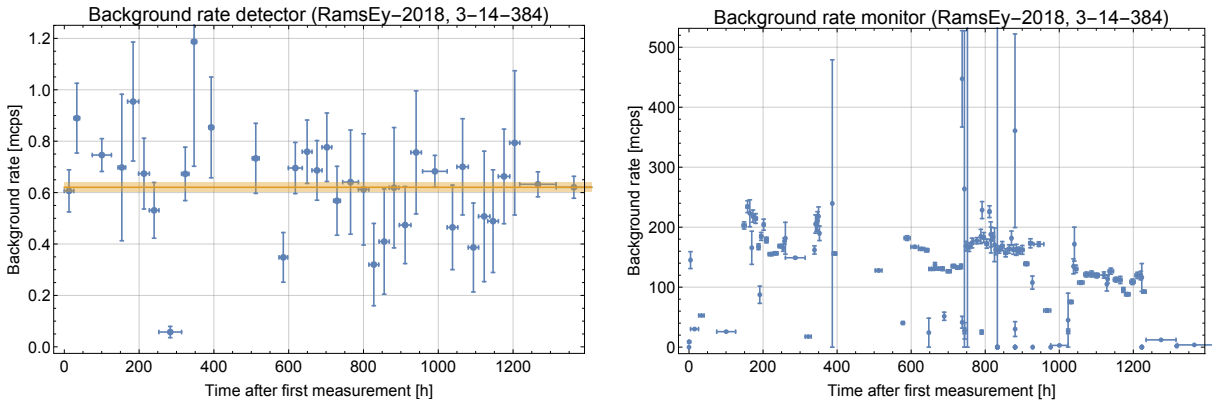

(a) Detector background rate

(b) Monitor background rate

Figure A.33.: Stability of the background rates. The horizontal error bars represents the measurement duration.

[8] Due to a loose screw, the rotatable shutter overturned during the cycle 183-18/2. In the closed position, the shutter was slightly opened again which resulted in high background rates between 200 mcps and 2 cps depending on the turbine switcher position. A detailed description of the phenomenon is described in section 4.3.3 and displayed in the appendix A.4.5.

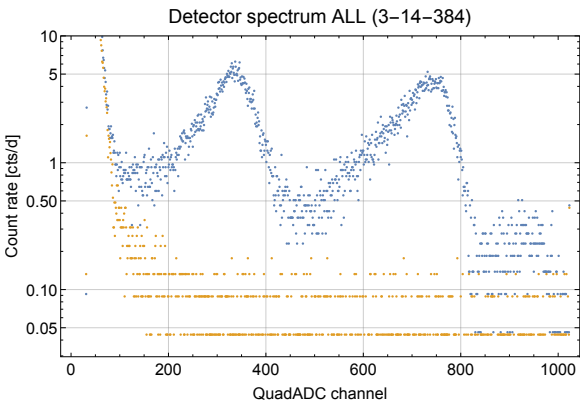

(a) Detector spectrum: neutrons (blue), background (orange)

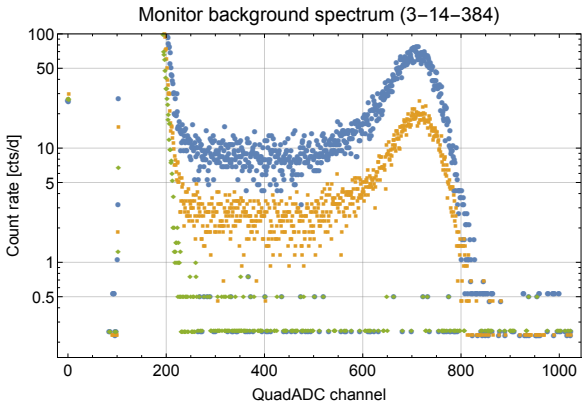

(b) Monitor background spectrum: 51.5 MW(blue), 34.5 MW(orange), shut down (green)

Figure A.34.: Detector pulse height spectra

Background rate measurements

Table A.11.: All long background rates (>12 h) of all cycle

Beamtime cycle	ID	Start	Bkgtime [s]	Detector Rate	Counts	Monitor Rate	Counts	Comments
182-18/1	2.674	22:05 12.03.2018	46267.2	0.97(14) mcps	45	16.36(59) mcps	757	Open chamber
182-18/1	3.013	22:43 18.03.2018	115968.	1.07(10) mcps	124	59.58(72) mcps	6909	CR-39
182-18/1	4.101	22:36 09.04.2018	211842.	0.66(6) mcps	139	8.94(21) mcps	1894	Open chamber
183-18/2	1.166	19:55 26.05.2018	76533.2	1.32(13) mcps	101	8.51(33) mcps	651	Open chamber
183-18/2	1.180	22:52 27.05.2018	417480.	0.75(4) mcps	314	4.05(10) mcps	1692	Open chamber
183-18/2	3.109	12:34 06.06.2018	59215.4	0.61(10) mcps	36	323.0(23) mcps	19129	Short cycles
183-18/2	5.086	14:21 03.07.2018	20140.	0.84(20) mcps	17	11.17(74) mcps	225	Closed shutter
183-18/2	6.006	16:57 10.07.2018	81764.1	0.66(9) mcps	54	0.84(10) mcps	69	Reactor down
184-18/3	1.015	21:32 04.09.2018	77069.4	0.64(9) mcps	49	30.18(63) mcps	2326	
184-18/3	1.016	19:28 05.09.2018	48335.7	0.89(14) mcps	43	52.74(104) mcps	2549	
184-18/3	1.021	20:09 07.09.2018	183628.	0.75(6) mcps	137	25.80(37) mcps	4737	
184-18/3	2.003	19:00 17.09.2018	58955.2	0.61(10) mcps	36	17.59(55) mcps	1037	
184-18/3	4.033	10:14 15.10.2018	168878.	0.69(6) mcps	116	2.89(13) mcps	488	Reactor down
184-18/3	5.120	03:52 26.10.2018	249487.	0.63(5) mcps	156	12.11(22) mcps	3022	
184-18/3	6.002	16:28 29.10.2018	327548.	0.61(4) mcps	201	3.73(11) mcps	1222	Reactor down

Table A.12.: Dedicated active background measurements

Beamtime	Measurement ID	Time [s]	Detector rate	counts	Monitor rate	counts	Comments
184-18/3	2.002	73 340.1 s	0.00(00) mcps	0 cts	109.10(4) cps	7999911 n	open chamber
184-18/3	3.271	14 906.3 s	0.34(15) mcps	5 cts	118.20(9) cps	1761403 n	Dead region V

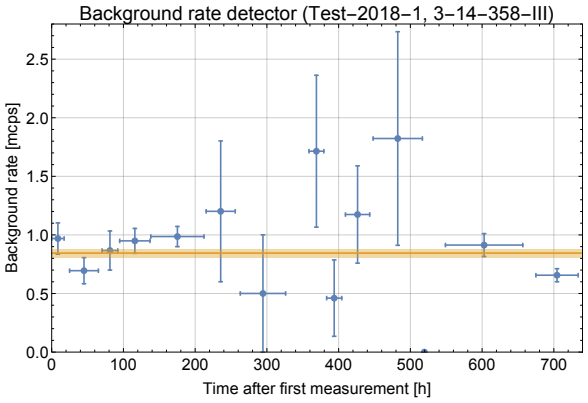

(a) Detector background rate

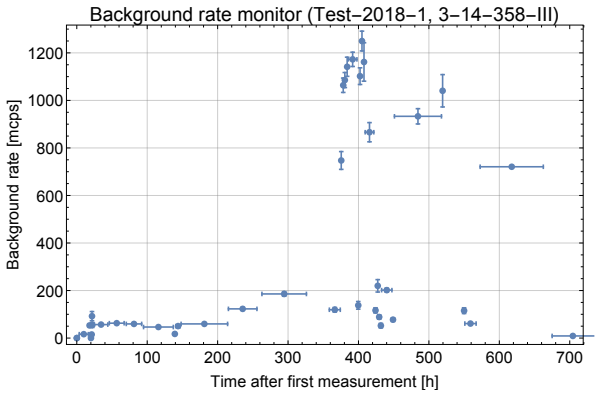

(b) Monitor background rate

Figure A.35.: Stability of the background rates: Test-2018 I

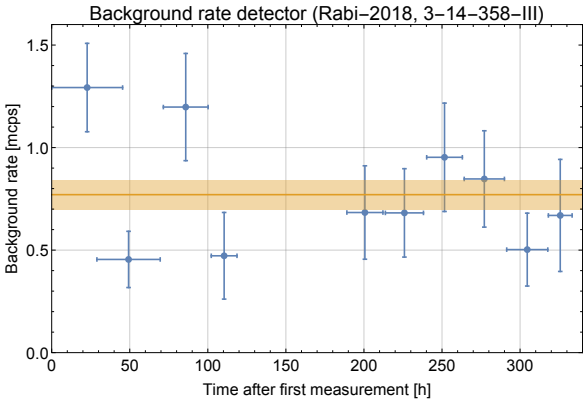

(a) Detector background rate

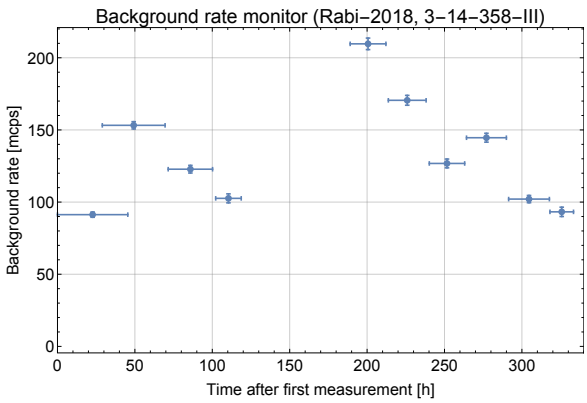

(b) Monitor background rate

Figure A.36.: Stability of the background rates: Rabi-grs-18

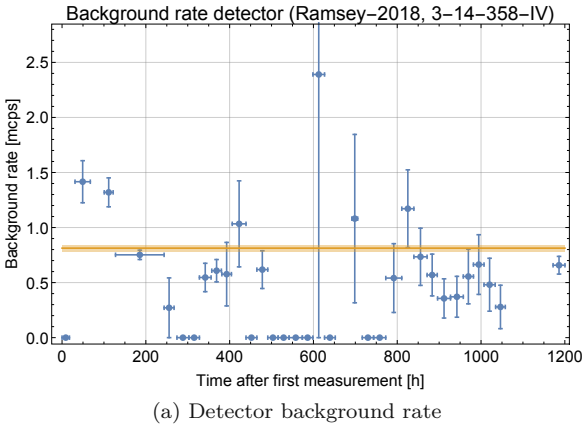

(a) Detector background rate

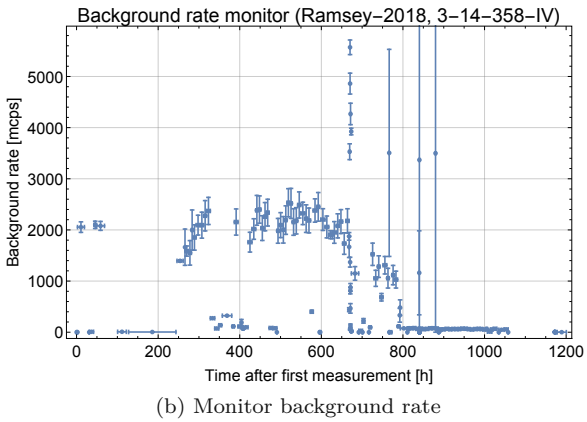

(b) Monitor background rate

Figure A.37.: Stability of the background rates: Ramsey-grs-18

A.4.6. Monitor amplification measurement

In the beginning of the beam time 184-18/3 (3-14-384) we replaced the monitor detector. In order to optimize the signal to noise ratio, we varied the gain of the amplifier which shifted the spectrum within the quadADC measurement window. The goal was to have a good separation between the signal peak and the noise and to have additionally an as high as possible neutron count rate within the ROI (200-1023). The following figure displays this measurement in the beginning of September 2018.

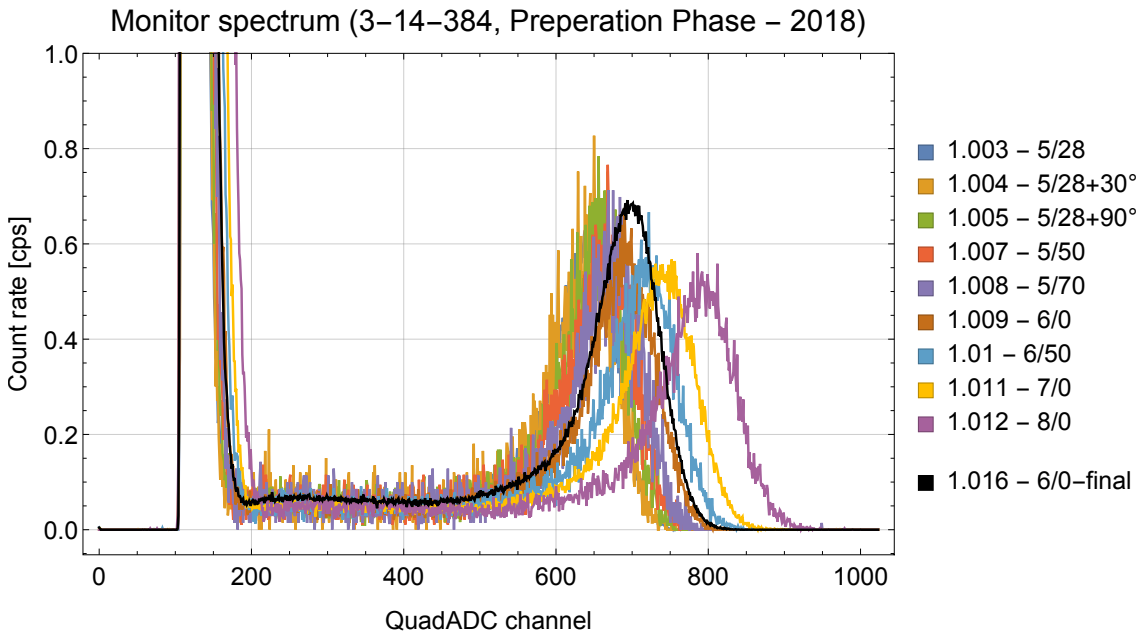

Figure A.38.: Different monitor signal amplification - measurements 4-6.9.2018

We did also a similar measurement during the cycle 183-18/2 where we additionally varied the voltage of the detector. Decreasing the voltage decreases also the separation between the background and the signal peak.

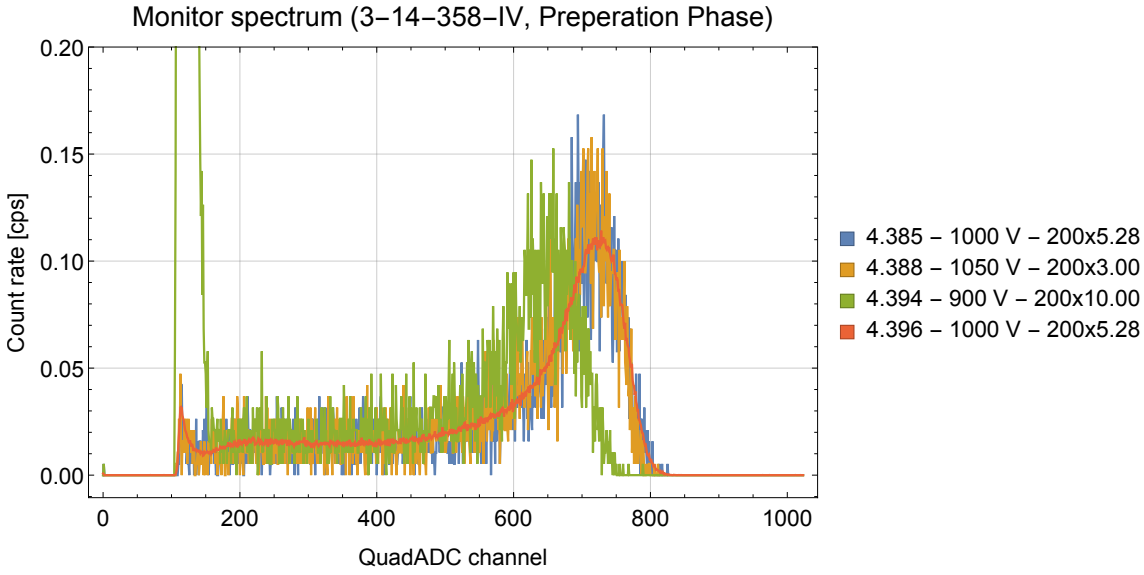

Figure A.39.: Different monitor signal amplification - measurements 26.6.2018

A.5. RABI-GRS-18 data points

The following presented data points are evaluated in the section 4.4.

Table A.13.: Mean zero rates of the cycle Rabi-2018 (3-14-358-III)

ID-Start	ID-End	Livetime[s]	UCN(DET)	Rate[mcps](unCorr)	Rate[mcps](CorrBack)	Rate[mcps](CorrTotal)
5.001	5.259	138700.0	7444	53.67±0.62	52.84±0.63	52.35±0.62
6.001	6.359	60990.1	3170	51.98±0.92	51.27±0.92	51.99±0.94
6.245	6.359	20900.0	1056	50.53±1.55	49.82±1.55	52.71±1.65

A.5.1. Rabi-2018 I

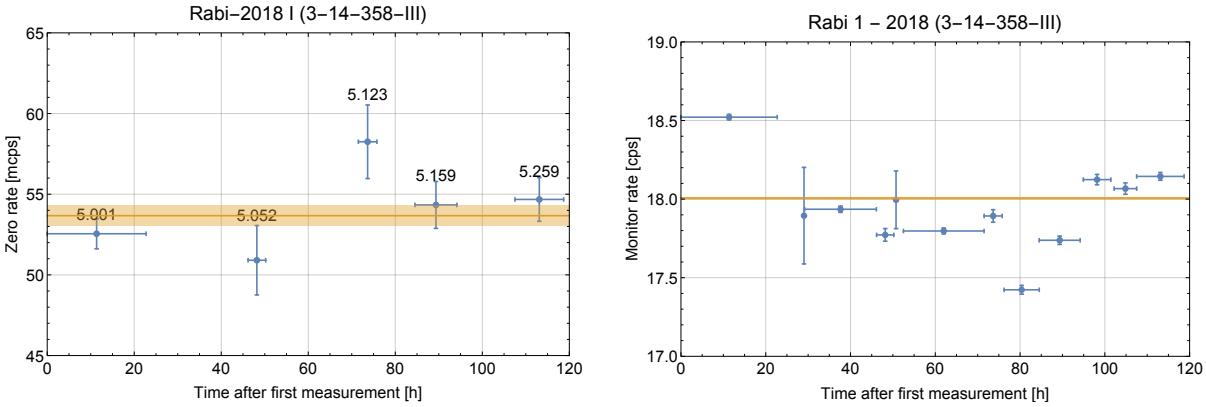

(a) Zero rate (b) Monitor rate

Figure A.40.: Stability of Rabi-2018-I

Table A.14.: All zero rates of the cycle Rabi-2018-I (3-14-358-III)

ID	Start	Livetime[s]	UCN(DET)	UCN(MON)	Bkg[s]	Bkg(DET)	Bkg(MON)
5.001	12:11 12.04.2018	60800.1	3195	1126102	13923.2	18	1271
5.052	10:21 14.04.2018	11020.0	561	195852	2291.9	1	219
5.123	11:43 15.04.2018	11210.0	653	200580	2774.3	6	496
5.159	00:43 16.04.2018	25840.0	1404	458357	5885.7	6	506
5.259	23:42 16.04.2018	29830.0	1631	541253	6979.1	4	555

Table A.15.: All frequency rates of the cycle Rabi-2018-I (3-14-358-III)

ID	Start	Livetime[s]	UCN(DET)	UCN(MON)	Bkg[s]	Bkg(DET)	Bkg(MON)
5.048	17:23 13.04.2018	45535.9	1601	816713	10043.6	4	1074
5.073	16:40 14.04.2018	51870.1	2223	923145	10636.5	6	1462
5.151	16:25 15.04.2018	22610.0	1139	393936	4640.8	5	577
5.214	11:07 16.04.2018	17100.0	584	309925	4233.4	4	574
5.256	18:24 16.04.2018	13870.0	444	250589	3607.3	1	531

The IDs 5.047 and 5.067 are excluded from further analysis due to a none continuous AFG or an unstable PI-table.

Table A.16.: All frequency settings of the cycle Rabi-2018-I (3-14-358-III)

ID	ν [Hz]-AFG	a_{x1}[V]	a_{x2}[V]	$\Delta\phi$ [deg]-AFG	FFTs(SIOS)	ν(r2fix)	a_v(r2fix)
5.048	462.925	1.4	0.02	0.	1815	462.912	2.1991(105)
5.073	462.925	1.0	0.02	0.	1779	462.912	1.5224(108)
5.151	512.925	1.1	0.02	0.	845	512.911	1.4105(213)
5.214	392.625	1.5	0.02	0.	621	392.614	2.9341(66)
5.256	208.390	0.5	0.02	0.	460	208.384	3.0582(21)

A.5.2. Rabi-2018 II

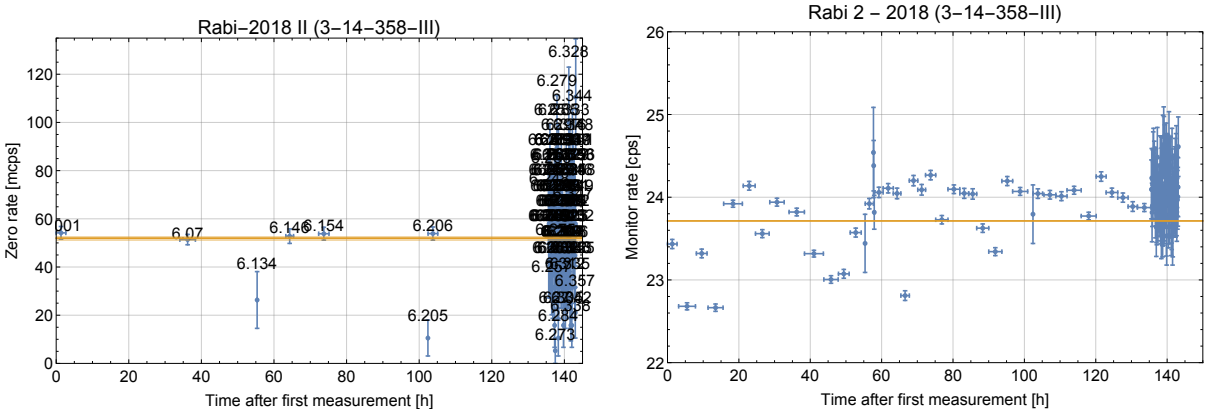

(a) Zero rate

(b) Monitor rate

Figure A.41.: Stability of Rabi-2018-II

Table A.17.: All zero rates of the cycle Rabi-2018-II (3-14-358-III)

ID	Start	Livetime[s]	UCN(DET)	UCN(MON)	Bkg[s]	Bkg(DET)	Bkg(MON)
6.001	09:14 20.04.2018	7790.0	422	182554	883.3	1	352
6.070	19:18 21.04.2018	11210.0	576	267033	2894.9	1	485
6.134	16:34 22.04.2018	190.0	5	4454	11.1	0	0
6.146	00:30 23.04.2018	5890.0	311	141629	1096.3	0	109
6.154	09:33 23.04.2018	7600.0	409	184430	1750.1	1	208
6.205	15:36 24.04.2018	190.0	2	4521	70.1	0	4
6.206	15:41 24.04.2018	7220.0	389	173597	1532.77	1	155
6.245-6.359	00:48 26.04.2018	20900.0	1056	490119	3947.0	2	408

Due to a misuse of the newly implemented queue, the last zero rate before the reactor shut down was separated into multiple measurement IDs with only one cycle each (ID 6.245-6.359). For the analysis these were joined together as one zero rate.

The IDs 6.138, 6.139, 6.140 were excluded from the analysis due to a mixture of active AFG and zero rates and zero rates and the IDs 6.089 and 6.134 due to problems with the detector *decode*.

Table A.18.: All frequency rates of the cycle Rabi-2018-II (3-14-358-III)

ID	Start	Livetime	UCN		Background		
		[s]	Det.	Mon.	[s]	Det.	Mon.
6.011	12:21 20.04.2018	12540.7	260	284437	2925.87	1	711
6.016	17:20 20.04.2018	8550.0	259	199389	1174.81	1	451
6.026	20:36 20.04.2018	11590.0	297	262683	2192.91	3	350
6.030	00:58 21.04.2018	13490.0	311	322694	3779.30	1	424
6.034	06:28 21.04.2018	8740.0	249	210967	2213.37	2	473
6.042	09:54 21.04.2018	10260.0	349	241723	2290.61	1	286
6.050	13:53 21.04.2018	10640.0	267	254722	2623.92	1	315
6.073	23:37 21.04.2018	14250.0	442	332278	3114.75	1	716
6.078	05:03 22.04.2018	11020.0	313	253520	2119.63	3	420
6.082	09:09 22.04.2018	8170.0	359	188512	1623.38	3	279
6.090	12:27 22.04.2018	8170.0	332	192587	1923.24	1	491
6.136	16:39 22.04.2018	6080.0	312	145445	1444.43	2	138
6.142	19:17 22.04.2018	6270.0	304	150847	1535.52	0	159
6.144	21:39 22.04.2018	7600.0	309	183224	1737.85	3	176
6.148	02:37 23.04.2018	6650.0	304	151691	1105.12	2	133
6.150	05:00 23.04.2018	6270.0	301	151738	1521.34	4	168
6.152	07:21 23.04.2018	5890.0	312	141889	1303.43	0	123
6.156	12:23 23.04.2018	9310.0	406	220906	1987.63	1	184
6.159	15:49 23.04.2018	8930.0	405	215182	1976.90	1	204
6.162	19:09 23.04.2018	6650.0	304	159909	1531.34	1	150
6.164	21:38 23.04.2018	6080.0	303	146159	1301.69	0	123
6.166	23:52 23.04.2018	9120.0	405	215469	1981.33	0	192
6.168	03:15 24.04.2018	10260.0	402	239490	1791.57	1	200
6.171	06:56 24.04.2018	8170.0	409	197677	1750.48	5	186
6.173	09:57 24.04.2018	10830.0	512	260678	3025.72	4	980
6.222	18:44 24.04.2018	8930.0	405	214582	2008.28	2	216
6.225	22:03 24.04.2018	8360.0	405	200747	1947.35	1	192
6.227	01:11 25.04.2018	10640.0	411	256253	2413.61	1	247
6.230	05:09 25.04.2018	11400.0	381	271006	2414.15	0	242
6.233	09:21 25.04.2018	7410.0	354	179693	1756.11	2	184
6.235	12:09 25.04.2018	8740.0	390	210260	1950.28	1	191
6.238	15:24 25.04.2018	7790.0	412	186923	1752.15	0	183
6.240	18:18 25.04.2018	7030.0	354	167928	1536.64	0	175
6.242	20:54 25.04.2018	10450.0	505	249494	2396.17	2	234

Table A.19.: All frequency settings of the cycle Rabi-2018-II (3-14-358-III)

ID	ν [Hz]-AFG	a_{x1}[V]	a_{x2}[V]	$\Delta\phi$ [deg]-AFG	FFTs(SIOS)	ν(r2fix)	a_v(r2fix)
6.011	208.39	0.8	0.02	0.	393	208.384	4.8478(48)
6.016	128.4	0.073	0.02	0.	284	128.396	4.9794(438)
6.026	178.39	0.55	0.02	0.	379	178.385	5.1065(42)
6.030	203.39	0.78	0.02	0.	454	203.384	4.9642(50)
6.034	153.4	0.25	0.02	0.	279	153.396	4.8434(43)
6.042	263.4	1.27	0.02	0.	348	263.393	5.0665(48)
6.050	213.4	0.88	0.02	0.	355	213.394	5.0544(59)
6.073	238.4	1.1	0.02	0.	477	238.393	5.0046(38)
6.078	288.4	1.45	0.02	0.	371	288.392	3.4749(25)
6.082	542.9	1.2	0.02	0.	273	542.885	1.7321(8)
6.090	462.925	0.95	0.02	0.	259	462.912	1.7057(11)
6.136	407.9	0.81	0.6	0.	179	407.889	1.7249(19)
6.142	492.9	1.05	0.6	0.	206	492.886	1.7332(76)
6.144	470.25	0.98	0.6	0.	253	470.237	1.7249(9)
6.148	457.9	0.94	0.6	0.	228	457.887	1.7134(9)
6.150	432.9	0.87	0.6	0.	206	432.888	1.7203(8)
6.152	517.9	1.11	0.6	0.	198	517.886	1.7095(15)
6.156	385.15	0.74	0.6	0.	307	385.139	1.7063(24)
6.159	447.6	0.91	0.6	0.	296	447.588	1.7097(9)
6.162	312.6	0.28	0.6	0.	229	312.591	1.7388(249)
6.164	337.6	0.55	0.6	0.	199	337.591	1.7112(18)
6.166	392.6	0.76	0.6	0.	306	392.589	1.7220(12)
6.168	397.6	0.77	0.6	0.	341	397.589	1.7134(19)
6.171	362.6	0.65	0.6	0.	267	362.59	1.6976(15)
6.173	422.6	0.84	0.6	0.	366	422.588	1.7131(17)
6.222	477.9	1.007	0.6	0.	293	477.887	1.7272(32)
6.225	375.6	0.7	0.6	0.	266	375.59	1.7453(32)
6.227	392.6	1.21	0.6	0.	361	392.589	2.8312(29)
6.230	392.6	1.48	0.6	0.	371	392.589	3.5223(39)
6.233	535.9	1.035	0.6	0.	236	535.885	1.5090(15)
6.235	560.9	1.11	0.6	0.	292	560.884	1.5087(7)
6.238	590.9	1.12	0.6	0.	261	590.884	1.4022(9)
6.240	510.9	0.975	0.6	0.	229	510.886	1.5128(19)
6.242	480.9	0.98	0.6	0.	348	480.887	1.6625(34)

A.5.3. Fitted values for RABI-GRS-18

Table A.20 displays different additions to the main fit routine (changing the mirror length l_{II}, rescaling the amplitude a_v, shifting the velocity spectrum and reducing the set of points). All have the potential to reduce the χ^2 significantly. The gravitational acceleration g is only slightly changed by either of these methods (within the error bars only).
Decreasing the mirror length from 152 mm to 130 mm, rescaling the amplitude by a factor of 0.77(8) or shifting the complete velocity to higher velocities as different fits suggest can be interpreted as the same underlying causes: One explanation is that the velocity spectrum is harder at the end of the three mirror setup as measured with only one region due to the stronger divergence of slower neutrons. For Ramsey measurements this effect should be even more important. Other reasons could be a wrong measurement of the mechanical amplitude by the SIOS laser interferometer or the theory has problems describing high amplitudes (as seen in fig. 4.19). Ignoring the higher oscillation amplitude measurements completely (see table A.21) abolishes these found effects and gives more spotlight to an other effect: The additional parameters highly correlate with the contrast of each transition due to the small variety of the oscillation amplitudes.
The best result is generated by dropping the five measurements with amplitudes above $2\,\mathrm{mm\,s^{-1}}$. The p-value is than 34.0 %. This supports the assumption that the theory has problems to describe higher amplitudes. It expects an increase in the count rate but a further drop is measured (see fig. 2.7).

Table A.20.: Fit routines comparison (All used a discrete velocity spectrum 2018 ($\Delta 0.01\,\mathrm{m/s}$), SIOS data, multi 2-level Rabi theory ($c_{12} = 10\,\%$, $c_{14} = 50\,\%$)

Data	Parameter	red-χ^2_{red}	p-value
29 SIOS ($> 300\,\mathrm{Hz}$)	$c_{24} = 34.6(19)\,\%$ $c_{13} = 43.1(21)\,\%$ $c_{25} = 52.7(113)\,\%$ $g = 9.781(80)\,\mathrm{m\,s^{-2}}$	1.455	0.06608
29 SIOS ($> 300\,\mathrm{Hz}$)	$c_{24} = 35.5(20)\,\%$ $c_{13} = 52.5(59)\,\%$ $c_{25} = 61.8(144)\,\%$ $g = 9.778(109)\,\mathrm{m\,s^{-2}}$ $length = 130.2(96)\,\mathrm{mm}$	1.3047	0.1450
29 SIOS ($> 300\,\mathrm{Hz}$)	$c_{24} = 38.7(35)\,\%$ $c_{13} = 63.0(112)\,\%$ $c_{25} = 83.3(240)\,\%$ $g = 9.773(83)\,\mathrm{m\,s^{-2}}$ $scale = 0.773(83)\,\mathrm{mm}$	1.1197	0.3104
29 SIOS ($> 300\,\mathrm{Hz}$)	$c_{24} = 34.6(19)\,\%$ $c_{13} = 50.9(53)\,\%$ $c_{25} = 60.4(139)\,\%$ $g = 9.778(107)\,\mathrm{m\,s^{-2}}$ $\Delta v_\mathrm{n} = 1.22(64)\,\mathrm{m\,s^{-1}}$	1.3030	0.1461
25 SIOS ($> 300\,\mathrm{Hz}$ & $< 2\,\mathrm{mm\,s^{-1}}$)	$c_{24} = 27.8(36)\,\%$ $c_{13} = 39.4(33)\,\%$ $c_{25} = 52.6(114)\,\%$ $g = 9.785(89)\,\mathrm{m\,s^{-2}}$	1.099	0.3395
39 SIOS (all)	$c_{12} = 24(33)\,\%$ $c_{23} = 11(53)\,\%$ $c_{34} = 71(33)\,\%$ $c_{24} = 30.4(20)\,\%$ $c_{13} = 41.2(21)\,\%$ $c_{25} = 52.2(115)\,\%$ $g = 9.828(84)\,\mathrm{m\,s^{-2}}$	3.128	6.1×10^{-9}

Adding an offset to the frequency rates would indicate that the mirror alignment changes between the zero rate and the frequency measurement which was not observed. Using only a single mean neutron velocity $\overline{v}_\mathrm{n}$ gives similar results with a slightly lower g. For Rabi measurements this simplification can be applied as Gunther Cronenberg already performed it for his RABI^{GC}-setup [65].

For the main results (high frequencies) the neighboring transitions ($|1 \rightarrow 2\rangle$ and $|1 \rightarrow 4\rangle$) are taken

into account in order to increase slightly the p-value.
By omitting transitions, they can be tested against the null hypothesis that they are not existing at all. The first two transition are significant without doubt. The weakest significance level has the first ever measured $|2 \rightarrow 5\rangle$ transition with a false-positive probability of only 3.8 sigmas due to the only 3 points probing the transition. Table A.23 displays a detailed list of the comparison.

Table A.21.: Fit routines comparison (All used a discrete velocity spectrum 2018 ($\Delta 0.01\,\mathrm{m/s}$), SIOS data, multi 2-level Rabi theory ($c_{12} = 10\,\%$, $c_{14} = 50\,\%$)

Data	Parameter	red-χ^2_{red}	p-value
29 SIOS ($> 300\,\mathrm{Hz}$)	$c_{24} = 34.6(19)\,\%$ $c_{13} = 43.1(21)\,\%$ $c_{25} = 52.7(113)\,\%$ $g = 9.781(80)\,\mathrm{m\,s^{-2}}$	1.455	0.06608
29 SIOS ($> 300\,\mathrm{Hz}$)	$c_{24} = 35.2(29)\,\%$ $c_{13} = 43.9(35)\,\%$ $c_{25} = 54.8(133)\,\%$ $g = 9.781(78)\,\mathrm{m\,s^{-2}}$ $offset = -0.0049(167)$	1.5121	0.05144
25 SIOS ($> 300\,\mathrm{Hz}$ & $< 2\,\mathrm{mm\,s^{-1}}$)	$c_{24} = 27.3(43)\,\%$ $c_{13} = 38.4(62)\,\%$ $c_{25} = 51.4(127)\,\%$ $g = 9.785(86)\,\mathrm{m\,s^{-2}}$ $length = 155(17)\,\mathrm{mm}$	1.153	0.2860
25 SIOS ($> 300\,\mathrm{Hz}$ & $< 2\,\mathrm{mm\,s^{-1}}$)	$c_{24} = 27.1(39)\,\%$ $c_{13} = 37.6(56)\,\%$ $c_{25} = 50.4(122)\,\%$ $g = 9.787(84)\,\mathrm{m\,s^{-2}}$ $\Delta v_\mathrm{n} = -0.33(87)\,\mathrm{m\,s^{-1}}$	1.150	0.2891
25 SIOS ($> 300\,\mathrm{Hz}$ (only RABI-GRS-18-II)	$c_{24} = 32.6(24)\,\%$ $c_{13} = 37.5(45)\,\%$ $c_{25} = 53.4(114)\,\%$ $g = 9.795(88)\,\mathrm{m\,s^{-2}}$	1.469	0.0761
29 SIOS ($> 300\,\mathrm{Hz}$) + Single velocity	$c_{24} = 31.0(22)\,\%$ $c_{13} = 45.0(48)\,\%$ $c_{25} = 53.3(122)\,\%$ $g = 9.762(92)\,\mathrm{m\,s^{-2}}$ $v_\mathrm{n} = 9.29(59)\,\mathrm{m\,s^{-1}}$	1.275	0.1655
25 SIOS ($> 300\,\mathrm{Hz}$ & $< 2\,\mathrm{mm\,s^{-1}}$) + Single velocity	$c_{24} = 25.4(41)\,\%$ $c_{13} = 37.0(54)\,\%$ $c_{25} = 48.5(111)\,\%$ $g = 9.762(85)\,\mathrm{m\,s^{-2}}$ $v_\mathrm{n} = 8.49(78)\,\mathrm{m\,s^{-1}}$	1.193	0.2487

Table A.22.: Fit routines comparison (All used a discrete velocity spectrum 2018 ($\Delta 0.01\,\mathrm{m/s}$), SIOS data, multi 2-level Rabi theory

Data	Parameter	red-χ^2_{red}	p-value
39 SIOS (all)	$c_{12} = -39(15)\,\%$ $c_{23} = 122(10)\,\%$ $c_{24} = 31.2(19)\,\%$ $c_{13} = 41.9(21)\,\%$ $c_{25} = 51.5(111)\,\%$ $g = 9.782(82)\,\mathrm{m\,s^{-2}}$	3.164	2.4×10^{-9}
39 SIOS (all)	$c_{12} = 132(3)\,\%$ $c_{24} = 29.8(22)\,\%$ $c_{13} = 45.1(32)\,\%$ $c_{25} = 44.8(96)\,\%$ $g = 9.551(74)\,\mathrm{m\,s^{-2}}$	7.165	1.6×10^{-33}
39 SIOS (all)	$c_{23} = 95.6(21)\,\%$ $c_{24} = 30.5(19)\,\%$ $c_{13} = 42.0(22)\,\%$ $c_{25} = 50.6(108)\,\%$ $g = 9.746(80)\,\mathrm{m\,s^{-2}}$	3.277	3.6×10^{-10}

Table A.23.: Fit routines comparison with different transition number (discrete velocity spectrum 2018 ($\Delta 0.01\,\mathrm{m/s}$), SIOS data, multi 2-level Rabi theory)

Data	Parameter	χ^2	red-χ^2_{red}	p-value
29 SIOS ($> 300\,\mathrm{Hz}$)	$c_{12} = 10.0\,\%(fixed)$ $c_{24} = 34.6(19)\,\%$ $c_{13} = 43.1(21)\,\%$ $c_{25} = 52.7(113)\,\%$ $c_{14} = 50.0\,\%(fixed)$ $g = 9.781(80)\,\mathrm{m\,s^{-2}}$	36.38	1.455	0.06608
29 SIOS ($> 300\,\mathrm{Hz}$)	$c_{24} = 35.2(19)\,\%$ $c_{13} = 43.5(22)\,\%$ $c_{25} = 54.0(111)\,\%$ $g = 9.779(79)\,\mathrm{m\,s^{-2}}$	37.60	1.504	0.05063
29 SIOS ($> 300\,\mathrm{Hz}$)	$c_{12} = 10.0\,\%(fixed)$ $c_{24} = 34.7(19)\,\%$ $c_{13} = 43.3(21)\,\%$ $c_{25} = 52.9(111)\,\%$ $g = 9.781(79)\,\mathrm{m\,s^{-2}}$	36.47	1.459	0.06478
29 SIOS ($> 300\,\mathrm{Hz}$)	$c_{24} = 35.1(19)\,\%$ $c_{13} = 43.3(22)\,\%$ $c_{25} = 52.8(113)\,\%$ $c_{14} = 50.0\,\%(fixed)$ $g = 9.780(80)\,\mathrm{m\,s^{-2}}$	37.50	1.500	0.05175
29 SIOS ($> 300\,\mathrm{Hz}$)	$c_{24} = 35.7(19)\,\%$ $c_{13} = 44.4(21)\,\%$ $g = 9.812(87)\,\mathrm{m\,s^{-2}}$	62.50	2.404	0.000077
29 SIOS ($> 300\,\mathrm{Hz}$)	$c_{24} = 39.2(19)\,\%$ $c_{25} = 82.9(123)\,\%$ $g = 9.850(83)\,\mathrm{m\,s^{-2}}$	473.7	18.22	9.6×10^{-84}
29 SIOS ($> 300\,\mathrm{Hz}$)	$c_{13} = 58.3(41)\,\%$ $c_{25} = 50.1(91)\,\%$ $g = 9.408(59)\,\mathrm{m\,s^{-2}}$	374.1	14.39	2.4×10^{-63}

A.6. RAMSEY-GRS-18 data points

The analysis of these data points can be found in section 4.5.

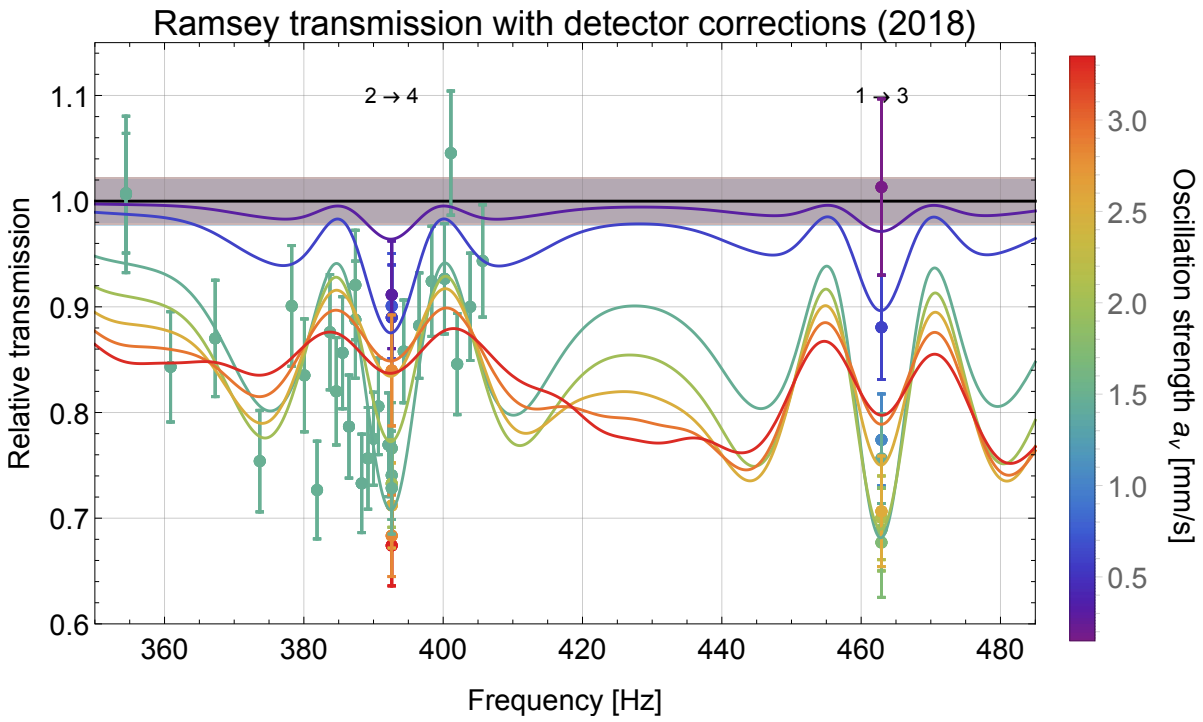

Figure A.42.: All RAMSEY-GRS-18 frequency measured points

Figure A.42 shows the problems of the theory to describe high amplitudes similar to the amplitude sweep (4.23). The Ramsey pattern in the frequency domain is not clearly visible due to the numerous points with low statistics. However, the main transition dip and its width (approx. 10 Hz) are visible and are comparable to theoretical predictions of 7.5 Hz (eq. (2.140)).

The following IDs were separated in multiple parts during the detector evaluation: 3.232, 4.160, 4.178, 4.326, 4.327, 4.341, 5.085

Due to multiple reasons I eliminated several measurements from the final analysis: ID 3.232, 4.159, 4.179 (no SIOS FFTs) - 4.245, 4.261, 4.270, 4.280, 4.326, 4.431 (too short and problematic) - 4.262 (mirror deadjustment) - 4.327, 4.328, 4.331, 4.336, 4.341, 4.342, 4.347 (region IV problems) - 5.104, 5.112, 5.115 (problems with quadADC).

Table A.24.: All zero rates of the cycle Ramsey-2018 (3-14-358-IV)

ID	Start	Livetime	UCN		Background			Measurement
		[s]	Det.	Mon.	[s]	Det.	Mon.	
1.079	16:14 24.05.2018	62320.1	3580	1549343	277.07	1	576	1-Prepartion
3.001	21:18 01.06.2018	47850.1	702	871479	2807.70	1	3915	2-Start
3.058	01:23 03.06.2018	23370.0	403	442790	27.07	0	42	2-Start
3.062	08:39 03.06.2018	11400.0	217	215253	13.013	0	26	3-1st-Measuring
3.080	14:46 04.06.2018	22800.0	402	431791	25.91	0	59	3-1st-Measuring
3.100	03:42 06.06.2018	11590.0	210	223155	12652.00	5	1725	3-1st-Measuring
3.159	12:34 07.06.2018	12730.0	242	245950	4733.75	2	537	3-1st-Measuring
3.233	15:07 08.06.2018	950.0	21	18522	824.21	1	58	3-1st-Measuring
4.001	15:39 08.06.2018	828.8	18	16065	1014.72	0	72	3-1st-Measuring
4.026	22:13 09.06.2018	18620.0	345	363973	28.12	0	67	3-1st-Measuring
4.069	02:06 12.06.2018	18238.1	345	361088	33.80	0	67	3-1st-Measuring
4.126	22:44 14.06.2018	20140.0	344	388943	30.62	0	68	3-1st-Measuring
4.193	03:27 18.06.2018	24700.0	403	486245	37.51	0	78	3-1st-Measuring
4.243	16:14 19.06.2018	190.0	5	3891	930.00	5	3649	4-Shutter
4.271	20:03 20.06.2018	15178.2	285	315307	112.57	0	25	5-2nd-Measuring
4.281	11:45 21.06.2018	17860.0	334	460878	733.23	0	70	5-2nd-Measuring
4.300	08:49 22.06.2018	19000.0	437	558797	28.84	0	37	5-2nd-Measuring
4.321	07:30 23.06.2018	18810.0	403	514649	28.40	0	30	5-2nd-Measuring
4.348	16:39 24.06.2018	51608.8	1016	1268813	4759.21	3	362	5-2nd-Measuring
4.360	09:58 25.06.2018	48.1	1	1242	0.00	0	0	5-2nd-Measuring
4.361	10:01 25.06.2018	9628.1	203	238635	1121.52	0	84	5-2nd-Measuring
4.364	13:19 25.06.2018	3800.0	83	95276	440.71	1	29	5-2nd-Measuring
4.385	15:13 26.06.2018	190.0	0	3927	219.57	0	15	6-Monitor
4.396	15:42 26.06.2018	21280.0	402	436589	2670.92	4	186	7-3rd-Measuring
4.401	23:02 26.06.2018	21090.0	401	427232	2246.97	1	135	7-3rd-Measuring
5.001	16:56 28.06.2018	18620.0	403	383116	2493.80	1	138	7-3rd-Measuring
5.034	14:04 30.06.2018	19760.0	401	427959	2426.45	0	150	7-3rd-Measuring
5.069	12:59 02.07.2018	21090.0	421	455546	2645.22	0	172	7-3rd-Measuring

Table A.25.: Mean zero rates of the cycle Ramsey-2018 (3-14-358-IV)

ID		Livetime	UCN	Rate[mcps]			Measurement
Start	End	[s]	Det.	unCorr	CorrBack	CorrTotal	
1.079	1.079	62320.1	3580	57.45±0.96	56.56±0.95	53.18±0.93	1-Prepartion
3.001	3.058	71220.1	1105	15.52±0.47	15.18±0.57	15.25±0.53	2-Start
3.062	4.193	141997.0	2547	17.94±0.36	17.33±0.36	17.57±0.35	3-1st-Measuring
4.243	4.243	190.0	5	26.32±11.77	20.76±10.49	-2.23±3.43	4-Shutter
4.271	4.364	135933.0	2762	20.32±0.39	19.43±0.44	19.25±0.39	5-2nd-Measuring
4.385	4.385	190.0	0	0.00±0.03	0.00±0.03	0.00±0.03	6-Monitor
4.396	5.069	101840.0	2028	19.91±0.44	19.38±0.44	19.25±0.44	7-3rd-Measuring

Table A.26.: All frequency rates of the cycle Ramsey-2018 (3-14-358-IV)

ID	Start	Livetime[s]	UCN(DET)	UCN(MON)	Bkg[s]	Bkg(DET)	Bkg(MON)	Measurement
3.069	20:01 03.06.2018	31540.0	402	601459	55.88	0	117	3-1st-Measuring
3.075	05:49 04.06.2018	28880.0	405	552750	32.49	0	68	3-1st-Measuring
3.084	21:51 04.06.2018	29450.0	404	563421	33.74	0	80	3-1st-Measuring
3.089	06:59 05.06.2018	32110.0	403	607738	2883.04	2	788	3-1st-Measuring
3.095	17:44 05.06.2018	16530.0	204	318003	17407.80	11	1275	3-1st-Measuring
3.109	12:28 06.06.2018	17040.0	219	327559	59215.40	36	19129	3-1st-Measuring
3.164	17:50 07.06.2018	28880.0	401	560383	32.96	0	71	3-1st-Measuring
3.171	02:47 08.06.2018	25650.0	416	497459	2118.66	2	237	3-1st-Measuring
4.002	16:12 08.06.2018	32787.2	403	634270	3576.10	6	348	3-1st-Measuring
4.011	03:21 09.06.2018	30970.0	401	601754	47.15	0	83	3-1st-Measuring
4.018	12:58 09.06.2018	29830.0	401	578110	50.06	0	101	3-1st-Measuring
4.031	04:00 10.06.2018	22230.0	305	436508	33.77	0	81	3-1st-Measuring
4.036	10:54 10.06.2018	22990.0	306	449327	34.88	0	71	3-1st-Measuring
4.042	18:02 10.06.2018	19570.0	313	383593	29.66	0	67	3-1st-Measuring
4.047	00:06 11.06.2018	22610.0	322	448504	34.22	0	80	3-1st-Measuring
4.053	07:07 11.06.2018	20710.0	320	419745	9353.58	8	772	3-1st-Measuring
4.060	16:08 11.06.2018	21660.0	321	428024	11653.60	5	908	3-1st-Measuring
4.074	07:45 12.06.2018	23180.0	306	486356	35.34	0	74	3-1st-Measuring
4.080	14:57 12.06.2018	19760.0	298	391337	29.98	0	60	3-1st-Measuring
4.085	21:05 12.06.2018	18620.0	302	368019	28.28	0	62	3-1st-Measuring
4.090	02:52 13.06.2018	22230.0	304	463731	33.57	0	85	3-1st-Measuring
4.096	09:46 13.06.2018	19380.0	304	490280	29.38	0	74	3-1st-Measuring
4.101	15:47 13.06.2018	21090.0	321	410177	32.02	0	69	3-1st-Measuring
4.106	22:19 13.06.2018	21660.0	302	419142	33.06	0	72	3-1st-Measuring
4.112	05:03 14.06.2018	25080.0	402	481777	38.19	0	95	3-1st-Measuring
4.118	12:50 14.06.2018	31920.0	503	613984	48.64	0	113	3-1st-Measuring
4.131	04:59 15.06.2018	24510.0	402	475594	37.07	0	81	3-1st-Measuring
4.138	12:36 15.06.2018	19950.0	315	386840	532.07	0	213	3-1st-Measuring
4.143	18:55 15.06.2018	30210.0	402	584675	45.81	0	109	3-1st-Measuring
4.151	04:18 16.06.2018	20710.0	314	402724	31.41	0	77	3-1st-Measuring
4.160	10:58 16.06.2018	9302.1	169	180681	2.00	0	0	3-1st-Measuring
4.162	13:53 16.06.2018	32364.7	403	628041	49.04	0	108	3-1st-Measuring
4.170	23:56 16.06.2018	29830.0	403	585767	45.20	1	93	3-1st-Measuring
4.178	09:12 17.06.2018	27170.0	402	535021	324.11	0	618	3-1st-Measuring
4.186	18:29 17.06.2018	28880.0	403	571707	43.58	0	85	3-1st-Measuring
4.199	11:07 18.06.2018	26030.0	403	519041	39.76	0	86	3-1st-Measuring
4.205	19:12 18.06.2018	25840.0	401	523225	39.22	0	68	3-1st-Measuring
4.211	03:13 19.06.2018	25460.0	353	524538	38.58	0	84	3-1st-Measuring
4.366	14:37 25.06.2018	26790.0	403	660125	2924.43	5	227	5-2nd-Measuring
4.372	23:44 25.06.2018	20710.0	401	508856	2032.01	3	163	5-2nd-Measuring
4.377	06:43 26.06.2018	23750.0	402	514918	2874.46	2	187	5-2nd-Measuring
4.383	14:52 26.06.2018	1140.0	26	23042	1.72	0	2	5-2nd-Measuring
4.396	15:42 26.06.2018	21280.0	402	436589	2670.92	4	186	7-3rd-Measuring
4.407	06:12 27.06.2018	23180.0	404	520343	3090.33	2	200	7-3rd-Measuring
4.413	14:14 27.06.2018	24130.0	401	551137	2472.24	1	191	7-3rd-Measuring
4.419	22:24 27.06.2018	25270.0	408	578415	2705.14	1	211	7-3rd-Measuring
4.426	06:59 28.06.2018	19570.0	401	455902	2415.69	1	175	7-3rd-Measuring
5.006	23:24 28.06.2018	20710.0	401	423523	2438.35	1	137	7-3rd-Measuring
5.018	15:18 29.06.2018	21850.0	404	445727	2642.77	0	153	7-3rd-Measuring
5.023	22:49 29.06.2018	21470.0	404	455842	2843.02	3	179	7-3rd-Measuring
5.029	06:15 30.06.2018	22800.0	402	486366	2654.63	1	163	7-3rd-Measuring
5.040	20:52 30.06.2018	23750.0	402	521629	3267.77	1	228	7-3rd-Measuring
5.046	05:08 01.07.2018	22420.0	403	489284	2431.07	2	164	7-3rd-Measuring
5.051	12:45 01.07.2018	21850.0	403	478419	2861.64	2	174	7-3rd-Measuring
5.057	20:19 01.07.2018	23370.0	401	512365	3066.69	0	164	7-3rd-Measuring
5.063	04:25 02.07.2018	24890.0	402	543196	3072.87	3	191	7-3rd-Measuring
5.074	20:15 02.07.2018	19380.0	403	413720	2234.36	3	139	7-3rd-Measuring
5.079	02:53 03.07.2018	22040.0	405	484176	2634.96	2	140	7-3rd-Measuring
5.085	10:27 03.07.2018	10830.0	217	233719	1525.51	1	98	7-3rd-Measuring
5.092	21:24 03.07.2018	20140.0	404	437734	2628.66	0	143	7-3rd-Measuring
5.098	04:22 04.07.2018	25840.0	402	557609	3086.97	2	208	7-3rd-Measuring

Table A.27.: All frequency settings of the cycle Ramsey-2018 (3-14-358-IV)

ID	ν [Hz]-AFG	a_{x1}[V]	a_{x2}[V]	$\Delta\phi$ [deg]-AFG	FFTs(SIOS)	ν(SIOS)	a_v(reg2)	a_v(reg4)	$\Delta\phi$(reg2-reg4)[deg]
3.065	462.925	0.4	0.386	-36.7	825	462.912	0.5916(7)	0.5566(32)	0.23±0.09
3.069	462.925	1.36	1.4	-36.7	1034	462.912	2.1487(65)	2.1589(55)	0.08±0.09
3.075	462.925	0.682	0.7	-36.7	937	462.912	1.0328(20)	1.0358(25)	0.26±0.07
3.084	462.925	0.951	0.982	-36.7	954	462.912	1.4651(35)	1.4775(47)	0.12±0.05
3.089	462.925	1.2	1.24	-36.7	1043	462.912	1.8776(66)	1.8928(59)	0.07±0.08
3.095	462.925	1.1	1.135	-36.7	547	462.912	1.7120(68)	1.7231(58)	0.11±0.09
3.109	462.925	1.600	1.652	-36.7	321	462.912	2.5610(101)	2.5915(99)	0.37±0.21
3.164	392.625	0.769	0.802	-30.8	923	392.614	1.5092(17)	1.5032(65)	-0.29±0.06
3.171	392.625	0.371	0.385	-30.8	824	392.614	0.7040(10)	0.6991(15)	-0.28±0.06
4.002	392.625	1.6	1.677	-30.8	1033	392.614	3.3478(55)	3.3248(35)	-0.35±0.05
4.011	392.625	1.241	1.294	-30.8	964	392.614	2.5338(53)	2.5086(39)	-0.29±0.03
4.018	392.625	0.752	0.781	-30.8	940	392.614	1.4775(17)	1.4608(30)	-0.30±0.06
4.031	389.218	0.748	0.78	-30.0	703	389.207	1.4763(16)	1.4697(35)	0.12±0.06
4.036	388.319	0.748	0.777	-30.0	725	388.308	1.4636(13)	1.4701(29)	-0.20±0.08
4.042	387.407	0.747	0.774	-30.2	610	387.396	1.4768(10)	1.4728(28)	-0.10±0.05
4.047	386.488	0.746	0.772	-30.2	700	386.477	1.4703(10)	1.4721(23)	0.00±0.08
4.053	385.57	0.749	0.77	-30.4	658	385.56	1.4619(42)	1.4683(38)	-0.38±0.21
4.060	384.658	0.749	0.77	-31.2	685	384.648	1.4857(64)	1.4734(38)	-0.27±0.16
4.074	381.904	0.727	0.76	-31.9	733	381.894	1.4738(29)	1.4712(28)	-0.31±0.14
4.080	380.087	0.703	0.751	-32.5	635	380.077	1.4837(32)	1.4699(27)	0.05±0.08
4.085	378.27	0.67	0.747	-30.0	584	378.26	1.4827(47)	1.4704(24)	-0.61±0.11
4.090	373.685	0.701	0.736	-26.0	703	373.675	1.4799(68)	1.4692(28)	0.26±0.23
4.096	367.284	0.705	0.725	-28.5	619	367.274	1.4800(24)	1.4709(16)	0.04±0.08
4.101	360.882	0.675	0.709	-28.5	685	360.872	1.4683(10)	1.4720(7)	-0.18±0.04
4.106	392.159	0.742	0.781	-30.8	703	392.148	1.4575(9)	1.4627(32)	-0.31±0.07
4.112	392.625	0.311	0.326	-30.8	799	392.614	0.5892(7)	0.5899(15)	-0.42±0.09
4.118	392.625	0.752	0.781	149.2	1014	392.614	1.4247(9)	1.4569(19)	179.40±0.06
4.131	392.625	0.161	0.168	-30.8	784	392.614	0.3003(3)	0.3009(15)	-0.43±0.14
4.138	383.759	0.743	0.766	-31.2	639	383.748	1.4764(19)	1.4737(40)	-0.14±0.12
4.143	392.625	1.008	1.05	-30.8	950	392.614	2.0111(17)	2.0002(28)	-0.35±0.04
4.151	392.625	1.378	1.437	-30.8	63	392.614	2.8174(29)	2.8017(32)	-0.41±0.02
4.160	462.925	0.1	0.1	-30.8	146	462.912	0.1461(2)	0.1433(9)	-5.68±0.26
4.162	392.625	1.378	1.437	-30.8	1020	392.614	2.8256(41)	2.8072(35)	-0.44±0.03
4.170	392.625	0.752	0.781	-120.8	947	392.614	1.4575(18)	1.4597(32)	88.41±0.08
4.178	392.625	0.752	0.781	59.2	589	392.614	1.4453(3)	1.4601(23)	-89.53±0.06
4.186	392.625	0.752	0.781	0.0	892	392.614	1.4668(7)	1.4601(27)	-30.69±0.07
4.199	392.625	0.752	0.781	120.0	807	392.614	1.4265(11)	1.4580(75)	-150.90±0.07
4.205	392.625	0.752	0.781	180.0	789	392.614	1.4294(4)	1.4561(26)	147.90±0.08
4.211	392.625	0.752	0.781	-90.0	784	392.614	1.4669(10)	1.4587(25)	57.61±0.07
4.366	392.625	0.752	0.781	-30.8	768	392.614	1.4743(11)	1.4618(5)	-0.31±0.00
4.372	392.625	0.752	0.781	150.0	580	392.614	1.4218(6)	1.4549(27)	178.40±0.16
4.377	392.625	0.752	0.781	-65.0	667	392.614	1.4739(11)	1.4591(10)	33.10±0.03
4.383	392.625	0.752	0.781	-180.0	32	392.614	1.4294(2)	1.4546(5)	147.80±0.03
4.396	392.625	0.752	0.781	-180.0	599	392.614	1.4293(4)	1.4543(6)	147.80±0.04
4.407	392.625	0.752	0.781	-140.0	657	392.614	1.4461(12)	1.4541(6)	107.40±0.04
4.413	392.625	0.752	0.781	-110.0	679	392.614	1.4609(11)	1.4551(7)	77.49±0.05
4.419	392.625	0.752	0.781	20.0	713	392.614	1.4587(6)	1.4602(11)	-50.39±0.05
4.426	392.625	0.752	0.781	-160.0	548	392.614	1.4380(5)	1.4535(7)	127.50±0.05
5.006	392.625	0.752	0.781	90.0	587	392.614	1.4269(7)	1.4564(9)	-120.60±0.03
5.018	400.21	0.775	0.805	-32.0	601	400.199	1.4708(10)	1.4703(9)	-0.11±0.03
5.023	405.69	0.789	0.822	-31.6	606	405.679	1.4762(14)	1.4718(9)	0.02±0.09
5.029	396.56	0.765	0.799	-31.6	629	396.549	1.4715(8)	1.4711(8)	-0.17±0.02
5.040	402.02	0.783	0.811	-32.1	685	402.009	1.4726(14)	1.4707(10)	-0.07±0.03
5.046	403.88	0.787	0.818	-32.0	618	403.869	1.4688(8)	1.4747(8)	0.10±0.02
5.051	398.37	0.773	0.803	-31.8	614	398.359	1.4774(9)	1.4731(8)	-0.23±0.03
5.057	394.35	0.759	0.792	-31.3	656	394.34	1.4723(9)	1.4715(8)	-0.00±0.04
5.063	390.71	0.748	0.785	-31.0	697	390.7	1.4720(9)	1.4742(10)	-0.04±0.05
5.074	401.12	0.778	0.808	-32.1	537	401.109	1.4700(9)	1.4711(10)	0.11±0.03
5.079	387.407	0.747	0.774	-30.2	621	387.397	1.4838(15)	1.4763(11)	-0.34±0.04
5.085	354.48	0.668	0.687	-27.1	290	354.471	1.4679(22)	1.4756(15)	-0.14±0.10
5.092	354.48	0.668	0.687	-27.1	563	354.471	1.4673(19)	1.4754(13)	-0.18±0.07
5.098	390.	0.747	0.784	-30.8	723	389.99	1.4743(12)	1.4751(9)	-0.07±0.05

A.6.1. RAMSEY-GRS-18 - additional fits

Table A.28.: RAMSEY-GRS-18 fitted values: discrete velocity spectrum 2018 ($\Delta 0.01\,\mathrm{m/s}$), SIOS data, multi 2-level Ramsey theory ($c_{12} = 10\,\%$, $c_{25} = 54\,\%$, values taken from RABI-GRS-18)

Data	Parameter	χ^2	red-χ^2_{red}	p-value
1st measurement set (39)	$c_{24} = 39.7(20)\,\%$ $c_{13} = 44.7(41)\,\%$ $g = 9.887(10)\,\mathrm{m\,s^{-2}}$	112.95	3.138	7.16×10^{-10}
1st measurement set + a_v<1.6 mm s^{-1} (30)	$c_{24} = 35.6(21)\,\%$ $c_{13} = 36.5(51)\,\%$ $g = 9.871(12)\,\mathrm{m\,s^{-2}}$	75.22	2.786	1.96×10^{-6}
3rd measurement set (19)	$c_{24} = 24.3(26)\,\%$ $c_{13} = 30\,\%(fixed)$ $g = 9.802(17)\,\mathrm{m\,s^{-2}}$	16.43	0.967	0.4935
Fall (8)	$c_{24} = 37.5(54)\,\%$ $g = 9.837(31)\,\mathrm{m\,s^{-2}}$	13.45	2.241	0.0365
Only zero phase (46)	$c_{24} = 32.5(16)\,\%$ $c_{13} = 36.9(29)\,\%$ $g = 9.763(12)\,\mathrm{m\,s^{-2}}$	117.40	2.730	7.95×10^{-9}
Only zero phase + a_v<1.6 mm s^{-1} (37)	$c_{24} = 29.2(17)\,\%$ $c_{13} = 33.4(47)\,\%$ $g = 9.752(13)\,\mathrm{m\,s^{-2}}$	63.76	1.875	0.00148

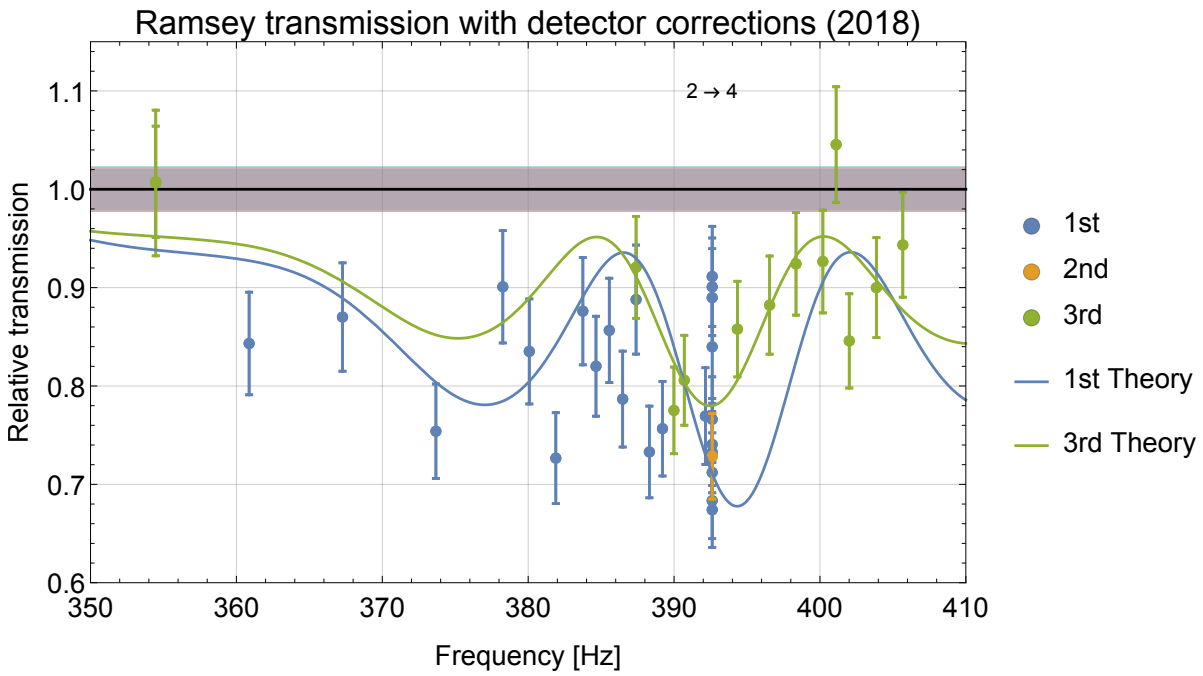

Figure A.43.: RAMSEY-GRS-18: all data points for different measurement periods (1st, 2nd, 3rd)

A.7. Rams$\vec{E}$y-2018 data points

The evaluation of these data points are presented in section 4.6.4.

Table A.29.: All zero rates of the cycle Rams$\vec{E}$y-2018 (3-14-384)

ID	Start	Livetime	UCN		Background			Measurement
		[s]	Det.	Mon.	[s]	Det.	Mon.	
1.060	16:56 10.09.2018	28500.0	172	3270147	5747.75	5	1166	1-Preparation
1.061	03:24 11.09.2018	23940.0	143	2767295	2407.90	0	564	1-Preparation
1.080	12:46 11.09.2018	4842.3	105	558626	443.53	1	99	2-Ramsey-2018
1.157	23:55 12.09.2018	17100.0	402	1988639	2424.17	1	495	2-Ramsey-2018
2.094	20:16 20.09.2018	17480.0	816	2043393	22252.80	19	3470	3-Transmission-Reg3
3.001	22:23 28.09.2018	40090.0	818	4633232	12307.40	12	2238	4-1st-Measuring-0V
3.035	16:22 29.09.2018	31730.0	649	3551121	38674.00	31	6466	4-1st-Measuring-0V
3.061	16:52 01.10.2018	21280.0	403	2521027	28384.90	22	3699	4-1st-Measuring-0V
3.071	07:30 02.10.2018	6080.0	114	704341	7660.09	8	1048	4-1st-Measuring-0V
3.093	16:00 03.10.2018	19760.0	404	2347777	25687.10	22	3250	5-2nd-Measuring-0V
3.111	05:21 05.10.2018	9088.1	174	1071828	9506.39	4	1280	5-2nd-Measuring-0V
3.133	17:41 05.10.2018	21470.0	409	2503202	2732.08	1	460	5-2nd-Measuring-0V
3.152	17:23 06.10.2018	51870.0	1016	6038932	6791.22	1	1205	5-2nd-Measuring-0V
3.188	15:54 07.10.2018	4940.0	102	572064	1146.57	1	262	5-2nd-Measuring-0V
3.215	02:31 09.10.2018	20710.0	391	2432199	2576.78	0	418	5-2nd-Measuring-0V
3.216	09:48 09.10.2018	66.3	0	7773	0.20	0	0	5-2nd-Measuring-0V
3.218	09:54 09.10.2018	105.8	1	12380	0.00	0	0	5-2nd-Measuring-0V
3.219	09:57 09.10.2018	75.0	0	8891	0.00	0	0	5-2nd-Measuring-0V
3.231	10:52 09.10.2018	21706.5	401	2522006	4701.68	1	764	5-2nd-Measuring-0V
3.263	02:10 11.10.2018	20900.0	395	2470026	2556.68	4	416	5-2nd-Measuring-0V
3.280	16:28 11.10.2018	22990.0	402	2718016	5296.92	2	853	5-2nd-Measuring-0V
4.001	12:42 13.10.2018	73340.1	1202	8641790	12272.70	8	2107	6-HV-Start
5.003	09:35 17.10.2018	30780.0	401	2578520	10893.90	7	821	7-RamsEy-1000V
5.051	18:07 21.10.2018	8544.5	104	704728	2524.59	0	286	7-RamsEy-1000V
5.074	10:27 23.10.2018	18050.0	202	1488055	6059.15	5	578	8-HV-Trans
5.120	03:48 26.10.2018	35910.0	446	2974330	249487.00	156	3022	9-RamsEy-1750V

The following IDs were separated in multiple parts during the detector evaluation: 1.060, 1.061, 3.111, 3.215, 3.263, 5.120

Table A.30.: Mean zero rates of the cycle Rams$\vec{E}$y-2018 (3-14-384)

ID		Livetime	UCN	Rate[mcps]			Measurement
Start	End	[s]	Det.	unCorr	CorrBack	CorrTotal	
1.060	1.061	52440.0	315	6.01±0.34	5.28±0.32	5.24±0.32	1-Preparation
1.080	1.157	21942.3	507	23.11±1.03	22.78±1.02	22.35±1.01	2-Ramsey-2018
2.094	2.094	17480.0	816	46.68±1.63	46.05±1.62	45.99±1.62	3-Transmission-Reg3
3.001	3.071	99180.1	1984	20.00±0.45	19.27±0.45	19.43±0.45	4-1st-Measuring-0V
3.093	3.280	193682.0	3695	19.08±0.31	18.47±0.31	18.49±0.32	5-2nd-Measuring-0V
4.001	4.001	73340.1	1202	16.39±0.47	15.71±0.47	10.72±0.38	6-HV-Start
5.003	5.051	39324.5	505	12.84±0.57	12.32±0.57	12.21±0.56	7-RamsEy-1000V
5.074	5.074	18050.0	202	11.19±0.79	10.55±0.81	10.51±0.81	8-HV-Trans
5.120	5.120	35910.0	446	12.42±0.59	11.78±0.57	11.78±0.57	9-RamsEy-1750V
5.003	5.120	93284.5	1153	12.36±0.36	11.77±0.37	11.72±0.37	Rams$\vec{E}$y-HV

The following IDs were separated in multiple parts during the detector evaluation: 1.147, 1.194, 3.110, 3.203, 3.204, 3.214, 3.262, 5.041, 5.103.

Table A.31.: All frequency rates of the cycle Rams$\vec{E}$y-2018 (3-14-384)

ID	Start	Livetime	UCN		Background			Measurement
		[s]	Det.	Mon.	[s]	Det.	Mon.	
1.141	00:51 12.09.2018	25460.0	401	2943152	3310.83	3	710	2-Ramsey-2018
1.147	09:39 12.09.2018	15200.0	209	1763239	7382.66	7	1236	2-Ramsey-2018
1.152	16:26 12.09.2018	20298.4	401	2333272	4311.27	4	796	2-Ramsey-2018
1.162	05:54 13.09.2018	22230.0	407	2585096	8074.69	6	1442	2-Ramsey-2018
1.168	15:02 13.09.2018	21470.0	404	2497012	25117.50	17	3894	2-Ramsey-2018
1.177	04:39 14.09.2018	21090.0	405	2434946	22830.40	8	3571	2-Ramsey-2018
1.186	17:32 14.09.2018	20710.0	405	2374166	22370.50	16	3769	2-Ramsey-2018
1.194	06:10 15.09.2018	3990.0	70	466055	5019.96	3	831	2-Ramsey-2018
3.044	12:57 30.09.2018	25080.0	406	2925348	31762.80	18	5201	4-1st-Measuring-0V
3.074	11:33 02.10.2018	21280.0	401	2492031	26820.90	17	3507	4-1st-Measuring-0V
3.084	01:45 03.10.2018	12540.0	219	1499940	16514.10	10	2157	4-1st-Measuring-0V
3.090	10:20 03.10.2018	190.0	4	22507	1126.56	1	58	5-2nd-Measuring-0V
3.102	05:24 04.10.2018	23370.0	402	2759510	16977.00	11	2293	5-2nd-Measuring-0V
3.110	17:32 04.10.2018	19000.0	321	2247826	20411.30	13	2706	5-2nd-Measuring-0V
3.140	01:16 06.10.2018	24700.0	401	2880646	3256.68	4	543	5-2nd-Measuring-0V
3.147	10:00 06.10.2018	20900.0	405	2440044	2678.84	4	465	5-2nd-Measuring-0V
3.164	11:43 07.10.2018	9880.0	154	1144103	1332.81	0	246	5-2nd-Measuring-0V
3.191	17:47 07.10.2018	20900.0	401	2425696	2703.29	2	494	5-2nd-Measuring-0V
3.196	01:10 08.10.2018	24700.0	403	2855752	3060.17	3	528	5-2nd-Measuring-0V
3.203	09:51 08.10.2018	15960.0	247	1872143	2382.03	1	538	5-2nd-Measuring-0V
3.204	15:46 08.10.2018	2006.1	37	234482	430.95	0	81	5-2nd-Measuring-0V
3.209	17:34 08.10.2018	23560.0	401	2759027	4188.17	3	771	5-2nd-Measuring-0V
3.214	02:12 09.10.2018	760.0	15	88898	216.76	0	37	5-2nd-Measuring-0V
3.241	19:03 09.10.2018	24130.0	402	2852020	3031.67	1	511	5-2nd-Measuring-0V
3.248	03:33 10.10.2018	27740.0	401	3280820	3477.06	1	547	5-2nd-Measuring-0V
3.255	13:19 10.10.2018	25080.0	401	2961210	3257.83	2	533	5-2nd-Measuring-0V
3.262	22:11 10.10.2018	11210.0	197	1326911	1288.31	0	234	5-2nd-Measuring-0V
3.286	01:14 12.10.2018	24130.0	403	2854364	3015.91	0	489	5-2nd-Measuring-0V
3.287	09:44 12.10.2018	27930.0	403	3276063	15044.60	10	2091	5-2nd-Measuring-0V
3.291	22:46 12.10.2018	26410.0	402	3095905	3049.28	0	528	5-2nd-Measuring-0V
3.299	08:00 13.10.2018	3230.0	67	381621	910.81	2	98	5-2nd-Measuring-0V
5.010	22:23 17.10.2018	7030.0	79	585930	860.79	0	116	7-RamsEy-1000V
5.012	00:59 18.10.2018	28880.0	321	2398210	3425.76	1	447	7-RamsEy-1000V
5.017	11:06 18.10.2018	41420.0	401	3411607	12657.60	8	1363	7-RamsEy-1000V
5.026	03:45 19.10.2018	36860.0	402	3053181	7334.05	6	888	7-RamsEy-1000V
5.033	17:29 19.10.2018	38950.0	401	3227072	4991.86	2	609	7-RamsEy-1000V
5.041	07:14 20.10.2018	36290.0	300	3010222	7942.30	3	949	7-RamsEy-1000V
5.054	21:32 21.10.2018	39710.0	404	3284752	5004.53	3	634	7-RamsEy-1000V
5.062	11:31 22.10.2018	38950.0	401	3190076	7266.90	3	818	7-RamsEy-1000V
5.069	01:54 23.10.2018	24130.0	217	1978151	3250.73	1	364	7-RamsEy-1000V
5.081	17:52 23.10.2018	36290.0	403	3000449	10298.70	7	907	9-RamsEy-1750V
5.089	08:14 24.10.2018	38000.0	402	3156234	5509.44	3	600	9-RamsEy-1750V
5.096	21:49 24.10.2018	37810.0	402	3134963	4572.23	5	547	9-RamsEy-1750V
5.103	11:05 25.10.2018	13300.0	144	1103149	2320.45	1	277	9-RamsEy-1750V
5.113	16:15 25.10.2018	21660.0	203	1781050	16798.50	12	1554	9-RamsEy-1750V

The IDs 3.090 and 3.286 were excluded for the final analysis because the SIOS was inactive. For the IDs 3.102 and from 5.010 to 5.113 the internal laser beam measurements were used to determine the amplitude due to signal loss of the external fixed beams.

Table A.32.: All frequency settings of the cycle Rams$\vec{E}$y-2018 (3-14-384)

ID	ν [Hz]-AFG	a_{x1}[V]	a_{x2}[V]	$\Delta\phi$ [deg]-AFG	FFTs(SIOS)	ν(SIOS)	a_v(reg2)	a_v(reg4)	$\Delta\phi$(reg2-reg4)[deg]
1.141	394.	0.766	0.792	-31.6	716	393.989	1.4892(12)	1.4748(12)	0.21±0.03
1.147	394.857	0.768	0.794	-31.5	438	394.846	1.4882(12)	-	-
1.152	395.714	0.769	0.796	-31.4	562	395.703	1.4876(11)	-	-
1.162	396.571	0.772	0.8	-31.5	616	396.56	1.4891(13)	-	-
1.168	397.429	0.773	0.803	-31.5	592	397.418	1.4892(13)	-	-
1.177	398.286	0.774	0.805	-31.7	587	398.275	1.4902(14)	-	-
1.186	399.143	0.777	0.806	-31.9	561	399.132	1.4910(13)	-	-
1.194	400.	0.752	0.781	-32.	108	399.989	1.4330(12)	-	-
3.044	392.625	0.678	0.746	-31.9	703	392.616	1.4708(33)	1.4409(1362)	0.36±28.07
3.074	402.	0.705	0.772	-32.2	622	401.989	1.4651(0)	1.4664(11)	-
3.084	399.	0.696	0.763	-32.	352	398.989	1.4645(0)	1.4668(10)	0.12±0.00
3.090	396.	0.69	0.754	-32.	0	-	-	-	-
3.102	402.	0.705	0.772	-32.2	604	401.989	1.4616(14)	1.4629(12)	-0.00±0.04
3.110	399.	0.696	0.763	-32.	479	398.989	1.4608(14)	1.4612(11)	0.28±0.07
3.140	387.	0.669	0.726	-29.9	712	386.989	1.4757(8)	1.4590(12)	-0.65±0.06
3.147	384.	0.663	0.714	-30.9	609	383.989	1.4835(8)	1.4572(11)	0.40±0.05
3.164	392.625	0.678	0.746	-31.9	285	392.614	1.4673(11)	1.4405(17)	0.09±0.06
3.191	385.625	0.662	0.727	-30.4	601	385.614	1.4701(10)	1.4723(11)	-0.10±0.06
3.196	388.625	0.672	0.737	-30.5	715	388.614	1.4711(8)	1.4722(10)	-0.20±0.12
3.203	396.625	0.697	0.762	-31.8	463	396.614	1.4721(7)	1.4711(13)	-0.17±0.06
3.204	396.625	0.697	0.762	-31.8	49	396.614	1.4709(5)	1.4720(10)	-0.11±0.04
3.209	399.625	0.701	0.773	-31.9	577	399.614	1.4684(7)	1.4737(10)	0.04±0.04
3.214	392.625	0.68	0.761	-31.8	19	392.614	1.4737(7)	1.4746(5)	0.00±0.04
3.241	385.625	0.662	0.727	-30.4	650	385.614	1.4710(11)	1.4783(12)	-0.11±0.07
3.248	388.625	0.672	0.737	-30.5	794	388.614	1.4706(12)	1.4771(10)	-0.17±0.09
3.255	396.625	0.697	0.762	-31.8	709	396.614	1.4706(4)	1.4747(11)	-0.27±0.05
3.262	399.625	0.701	0.773	-31.9	325	399.614	1.4659(9)	1.4793(12)	0.12±0.06
3.286	385.625	0.662	0.727	-30.4	0	-	-	-	-
3.287	388.625	0.672	0.737	-30.5	305	388.614	1.4691(10)	1.4806(12)	-0.31±0.05
3.291	396.625	0.697	0.762	-31.8	945	396.614	1.4727(8)	1.4785(18)	-0.24±0.08
3.299	399.625	0.701	0.773	-31.9	116	399.614	1.4668(8)	1.4842(14)	0.16±0.07
5.010	385.625	0.662	0.727	-30.4	261	385.614	1.4492(0)	1.4955(0)	-
5.012	385.625	0.662	0.727	-30.4	1082	385.614	1.4492(0)	1.4955(0)	-
5.017	388.625	0.672	0.737	-30.5	1597	388.614	1.4670(0)	1.5082(0)	-
5.026	396.625	0.697	0.762	-31.8	1414	396.614	1.4651(0)	1.4659(0)	-
5.033	399.625	0.701	0.773	-31.9	1507	399.614	1.4630(0)	1.4883(0)	-
5.041	392.625	0.68	0.761	-31.8	1371	392.614	1.4735(0)	1.4590(0)	-
5.054	396.625	0.697	0.762	-31.8	1529	396.614	1.4651(0)	1.4577(0)	-
5.062	399.625	0.701	0.773	-31.9	1506	399.614	1.4616(0)	1.4835(2)	-
5.069	392.625	0.68	0.761	-31.8	928	392.614	1.4739(0)	1.4550(0)	-
5.081	385.625	0.662	0.727	-30.4	1396	385.614	1.4603(0)	1.4832(9)	-
5.089	388.625	0.672	0.737	-30.5	1471	388.614	1.4655(0)	1.4790(11)	-
5.096	396.625	0.697	0.762	-31.8	1451	396.614	1.4668(0)	1.4807(12)	-
5.103	399.625	0.701	0.773	-31.9	508	399.614	1.4593(0)	1.4825(7)	-
5.113	392.615	0.68	0.761	-31.8	811	392.604	1.4726(0)	1.4826(9)	-

Table A.33.: Linear fit routines comparison Rams$\vec{E}$y frequency (neutron charge)

Data	Parameter	χ^2	red-χ^2_{red}	p-value	Formular
35 SIOS Frequ All	$k = -0.000\,01(172)$ $d = 0.83(68)$	74.95	2.271	0.000042	Linear
21 SIOS Frequ 0 V	$k = 0.000\,37(200)$ $d = 0.70(79)$	44.47	2.34	0.00081	Linear
9 SIOS Frequ 1000 V	$k = 0.0013(42)$ $d = 0.25(164)$	15.18	2.168	0.0338	Linear
5 SIOS Frequ 1750 V	$k = -0.0022(62)$ $d = 1.72(241)$	2.485	0.8283	0.478	Linear

A.8. Supervised theses

- Anselm Balthasar
  - Bachelor's thesis [32], *Minimierung des Untergrundes eines Neutronendetektors*, 2018
- Paul Feichtinger
  - Bachelor's thesis [84], *Analyse der Stufenkontrolle des* qBounce *Experiments*, 2018
- Christoph Mühlmann
  - Project Thesis [208], *Simulation of different capacitor designs for* qBounce, 2018
- Mathias Winder
  - Project Thesis [318], qBounce: *Magnetic field for spin measurement*, 2018
- Florian Honz
  - Project Thesis [119], *qBounc$\vec{E}$: Measurement of titanium electrodes at the ATI*, 2018
- Daniel Schuh
  - Project Thesis [274], *Analysis of detector sensor data and vacuum sensor data in the vacuum chamber of a qBounce Experiment*, 2018
- Lukas Achatz
  - Diploma Thesis [14], *Systematic tests for Gravitational Resonance Spectroscopy*, 2018
- Elisabeth Kreuzgruber
  - Project Thesis [169], *Characterization of the* qBounc$\vec{E}$ *electrode setup used in ILL cycle 184-18/3*, 2019
- Magdalena Pieler & Valentin Czamler
  - Project Thesis [236], qBouncino *a small scale* qBounce *setup*, 2019
- Carina Killian
  - Project Thesis [159], *Analysis and correction of the* qBounce *step control system*, 2019
- Vito Pecile
  - Project Thesis [233], *Analysis and correction of the* qBounce *step control system*, 2019
- Anika Gassner
  - Bachelor's thesis [96], *Search for the voltage limits of the* qBounc$\vec{E}$ *electrode*, 2020
- Julius Piso
  - Bachelor's thesis [241], *Electrical characterization of the* qBounc$\vec{E}$ *electrode measurement setup*, 2020
- Jasmin Jurosek
  - Bachelor's Thesis [151], *Continuing the search for the voltage limits of the* qBounc$\vec{E}$ *electrode*, 2021
- Nicole Pruggmayer
  - Bachelor's Thesis [247], *Continued electrical characterization of the* qBounce *electrode measurement setup*, 2022
- Paul Klieber
  - Bachelor's thesis [162], *Refinement of the qBounce electrode setup - the integration process of piezomotors in the electrode bracket*, 2022
- Luca Neubacher
  - Bachelor's thesis [225], *qBounc$\vec{E}$: Measurement of a titanium electrode with improved alignment control*, 2022

- Robin Havlic
  - Bachelor's thesis [112], *Analysis of the detector sensors environment from the qBounce-experiment during beam time 182-18/1*, 2023

List of Figures

List of Tables

Bibliography

[1] *Redmine-Wiki: Internal online qBouncepedia.*

[2] C. Abel, S. Afach, N. Ayres, C. Baker, G. Ban, G. Bison, K. Bodek et al.: *Measurement of the permanent electric dipole moment of the neutron*, Phys. Rev. Lett. 124, no. 8, 2020, doi:10.1103/physrevlett.124.081803.

[3] H. Abele: *The neutron. Its properties and basic interactions*, Prog. Part. Nucl. Phys. 60, no. 1, pp. 1–81, 2008, ISSN 0146-6410, doi:10.1016/j.ppnp.2007.05.002.

[4] H. Abele: *The neutron alphabet: Exploring the properties of fundamental interactions*, Nucl. Instrum. Methods Phys. Res., Sect. A 611, no. 2009, pp. 193–197, 2009, ISSN 0168-9002, doi:10.1016/j.nima.2009.07.100.

[5] H. Abele: *Precision experiments with cold and ultra-cold neutrons*, Hyperfine Interactions 237, no. 1, 2016, doi:10.1007/s10751-016-1352-z.

[6] H. Abele, S. Baessler and A. Westphal: *Quantum states of neutrons in the gravitational field and limits for non-Newtonian interaction in the range between 1 micron and 10 microns*, Lect. Notes Phys. 631, pp. 355–366, 2003, doi:10.1007/978-3-540-45230-0_10.

[7] H. Abele, G. Cronenberg, P. Geltenbort, T. Jenke, T. Lins and H. Saul: *qBounce, the quantum Bouncing Ball experiment*, Phys. Procedia 17, pp. 4–9, 2011, doi:10.1016/j.phpro.2011.06.011.

[8] H. Abele, A. Ivanov, T. Jenke, M. Pitschmann and P. Geltenbort: *Gravity Resonance Spectroscopy and Einstein-Cartan Gravity*, arXiv 2015, doi:10.48550/arxiv.1510.03063.

[9] H. Abele, T. Jenke and G. Konrad: *Spectroscopy with cold and ultra-cold neutrons*, EPJ Web of Conf. 93, 05002, 2015, doi:10.1051/epjconf/20159305002.

[10] H. Abele, T. Jenke, H. Leeb and J. Schmiedmayer: *Ramsey's method of separated oscillating fields and its application to gravitationally induced quantum phase shifts*, Phys. Rev. D 81, no. 6, p. 065019, 2010, doi:10.1103/physrevd.81.065019.

[11] H. Abele, T. Jenke and H. Lemmel: *Happy Birthday, Ultra-Cold Neutron!*, EPJ Web of Conf. 219, no. 4554655, pp. 1–9, 2019, doi:10.1051/epjconf/201921901001.

[12] H. Abele, T. Jenke, D. Stadler and P. Geltenbort: *QuBounce: the dynamics of ultra-cold neutrons falling in the gravity potential of the Earth*, Nucl. Phys. A 827, no. 1-4, pp. 593c–595c, 2009, doi:10.1016/j.nuclphysa.2009.05.131.

[13] H. Abele and H. Leeb: *Gravitation and quantum interference experiments with neutrons*, New J. Phys. 14, no. 5, p. 055010, 2012, doi:10.1088/1367-2630/14/5/055010.

[14] L. Achatz: *Systematic tests for gravitational resonance spectroscopy*, Diploma thesis, TU Wien, Wien, 2018, doi:10.34726/HSS.2018.61622.

[15] R. Adhikari, Y. Cheng, A. E. Meyerovich and V. V. Nesvizhevsky: *Quantum size effect and biased diffusion of gravitationally bound neutrons in a rough waveguide*, Phys. Rev. A 75, no. 6, p. 063613, 2007, doi:10.1103/physreva.75.063613.

[16] J. R. Albright: *Integrals of products of Airy functions*, J. Phys. A: Math. Gen. 10, no. 4, pp. 485–490, 1977, doi:10.1088/0305-4470/10/4/011.

[17] C. G. Aminoff, A. M. Steane, P. Bouyer, P. Desbiolles, J. Dalibard and C. Cohen-Tannoudji: *Cesium atoms bouncing in a stable gravitational cavity*, Phys. Rev. Lett. 71, no. 19, pp. 3083–3086, 1993, doi:10.1103/physrevlett.71.3083.

[18] A. Anghel, F. Atchison, B. Blau, B. van den Brandt, M. Daum, R. Doelling, M. Dubs et al.: *The PSI ultra-cold neutron source*, Nucl. Instrum. Methods Phys. Res., Sect. A 611, no. 2-3, pp. 272–275, 2009, doi:10.1016/j.nima.2009.07.077.

[19] A. Anghel, G. Bison, B. Blau, M. Daum, N. Hild, K. Kirch, B. Lauss et al.: *The ultracold neutron source at the Paul Scherrer Institute – Performance and status*, Journal of Neutron Research 20, no. 4, pp. 83–86, 2019, ISSN 14772655, 10238166, doi:10.3233/JNR-180086.

[20] I. Antoniadis, S. Baessler, M. Büchner, V. V. Fedorov, S. Hoedl, A. Lambrecht, V. V. Nesvizhevsky et al.: *Short-range fundamental forces*, C. R. Phys. 12, no. 8, pp. 755–778, 2011, doi:10.1016/j.crhy.2011.05.004.

[21] H. Atac, M. Constantinou, Z.-E. Meziani, M. Paolone and N. Sparveris: *Measurement of the neutron charge radius and the role of its constituents*, Nat. Commun. 12, no. 1, 2021, doi:10.1038/s41467-021-22028-z.

[22] F. Atchison, B. Blau, K. Bodek, T. Bryś, F. Chapuis, M. Daum, G. Heidenreich et al.: *The PSI UCN Source*, in *ICANS-XVII*, 2005.

[23] F. Atchison, B. Blau, A. Bollhalder, M. Daum, P. Fierlinger, P. Geltenbort, G. Hampel et al.: *Transmission of very slow neutrons through material foils and its influence on the design of ultracold neutron sources*, Nucl. Instrum. Methods Phys. Res., Sect. A 608, no. 1, pp. 144–151, 2009, doi:10.1016/j.nima.2009.06.047.

[24] F. Atchison, B. Blau, M. Daum, P. Fierlinger, P. Geltenbort, M. Gupta, R. Henneck et al.: *Measurement of the Fermi potential of diamond-like carbon and other materials*, Nucl. Instrum. Methods Phys. Res. Sect. B Beam Interact. Mater. At. 260, no. 2, pp. 647–656, 2007, doi:10.1016/j.nimb.2007.04.253.

[25] N. J. Ayres, G. Ban, L. Bienstman, G. Bison, K. Bodek, V. Bondar, T. Bouillaud et al.: *The design of the n2EDM experiment*, Eur. Phys. J. C 81, no. 6, 2021, doi:10.1140/epjc/s10052-021-09298-z.

[26] S. Baessler: *Gravitationally bound quantum states of ultracold neutrons and their applications*, J. Phys. G: Nucl. Part. Phys. 36, no. 10, p. 104005, 2009, doi:10.1088/0954-3899/36/10/104005.

[27] S. Baessler, M. Beau, M. Kreuz, V. N. Kurlov, V. V. Nesvizhevsky, G. Pignol, K. V. Protasov, F. Vezzu and A. Y. Voronin: *The GRANIT spectrometer*, C. R. Phys. 12, no. 8, pp. 707–728, 2011, doi:10.1016/j.crhy.2011.04.010.

[28] S. Baessler, A. M. Gagarski, E. V. Lychagin, A. Mietke, A. Y. Muzychka, V. V. Nesvizhevsky, G. Pignol, A. V. Strelkov, B. P. Toperverg and K. Zhernenkov: *New methodical developments for GRANIT*, C. R. Phys. 12, no. 8, pp. 729–754, 2011, doi:10.1016/j.crhy.2011.04.014.

[29] S. Baessler, V. V. Nesvizhevsky, K. V. Protasov and A. Y. Voronin: *Constraint on the coupling of axionlike particles to matter via an ultracold neutron gravitational experiment*, Phys. Rev. D 75, no. 7, p. 075006, 2007, doi:10.1103/physrevd.75.075006.

[30] S. Baessler, V. V. Nesvizhevsky, G. Pignol, K. V. Protasov and A. Y. Voronin: *Constraints on spin-dependent short-range interactions using gravitational quantum levels of ultracold neutrons*, Nucl. Instrum. Methods Phys. Res., Sect. A 611, no. 2-3, pp. 149–152, 2009, doi:10.1016/j.nima.2009.07.048.

[31] S. Ballok: *Shielding of the detectors and exchange of beam tubes*, Project thesis, TU Wien, 2023.

[32] A. Balthasar: *Minimirung des Untergrundes eines Neutronendetektors*, Bachelor's thesis, TU Wien, Wien, 2018.

[33] J. Baumann: *Experimentelle Grenzen für die elektrische Ladung des freien Neutrons*, Phd thesis, Universität Bayreuth, 1988.

[34] J. Baumann, R. Gahler, J. Kalus and W. Mampe: *A neutron optical imaging system for the search for a neutron charge*, J. Phys. E: Sci. Instrum. 20, no. 4, pp. 448–450, 1987, doi:10.1088/0022-3735/20/4/023.

[35] J. Baumann, R. Gähler, A. I. Ioffe, J. Kalus and W. Mampe: *Measurement of the charge of the neutron*, Nucl. Instrum. Methods Phys. Res., Sect. A 284, no. 1, pp. 130–133, 1989, doi: 10.1016/0168-9002(89)90265-9.

[36] J. Baumann, R. Gähler, J. Kalus and W. Mampe: *Experimental limit for the charge of the free neutron*, Phys. Rev. D 37, no. 11, pp. 3107–3112, 1988, doi:10.1103/physrevd.37.3107.

[37] J. Baumann, R. Gähler, J. Kalus and W. Mampe: *Measurement of the charge of the free neutron*, Mater. Sci. Forum 27-28, pp. 307–310, 1988, doi:10.4028/www.scientific.net/msf.27-28.307.

[38] J. Baumann, J. Kalus, R. Gähler, W. Mampe and B. Alefeld: *A neutron optical imaging system for the determination of an upper limit of the neutron charge*, Physica B+C 151, no. 1-2, pp. 130–134, 1988, doi:10.1016/0378-4363(88)90156-8.

[39] H. Becquerel: *Sur les radiations invisibles émises par les sels d'uranium*, C. R. hebd. Séanc. Acad. Sci. Paris 122, pp. 420–421;501–503;559–564;689–694;, 1896.

[40] R. C. Bergmayr: *Characterisation of the magnetic field at the qBounce setup measured during cycle 185/19-1*, Project thesis, TU Wien, 2020.

[41] BIPM: *Le Système international d'unités / The International System of Units ('The SI Brochure')*, Bureau international des poids et mesures, ninth ed., 2019, ISBN 978-92-822-2272-0.

[42] T. Bittner: *Entwicklung eines Blendensystems zur Geschwindigkeitsselektion für das qBounce Experiment*, Diploma thesis, TU Wien, 2013.

[43] Y. V. Borisov, N. V. Borovikova, L. A. Grigoreva, A. V. Vasil'ev, S. N. Ivanov, V. V. Nesvizhevskii, N. T. Kashukeev, A. P. Serebrov and P. S. Yaidzhiev: *Study of potential application of ultracold neutrons for measuring the neutron electric charge*, Zhurnal Tekhnicheskoi Fiziki 58, no. 5, pp. 951–958, 1988.

[44] J. Bosina: *Charakterisierung eines 'Badurek'-Resonators für sehr kalte Neutronen*, Diploma thesis, TU Wien, 2015, doi:10.34726/HSS.2015.25544.

[45] J. Bosina: *qBounce-Manual*, 2023.

[46] J. Bosina, H. Filter, J. Micko, T. Jenke, M. Pitschmann, S. Roccia, R. I. P. Sedmik and H. Abele: *qBounce: first measurement of the neutron electric charge with a Ramsey-type GRS experiment*, in *Proceedings of the 56th Rencontres de Moriond - Gravitation 2022*, pp. 137–142, arXiv, 2023, doi:10.48550/arxiv.2301.05984.

[47] O. Bourrion, B. Clement, D. Tourres, G. Pignol, Y. Xi, D. Rebreyend and V. V. Nesvizhevsky: *C2D8: An eight channel CCD readout electronics dedicated to low energy neutron detection*, Nucl. Instrum. Methods Phys. Res., Sect. A 880, pp. 28–34, 2018, doi:10.1016/j.nima.2017.10.072.

[48] A. Brandalik: *Neutron beam divergence and mirror vibrations of the qBounce experiment*, Bachelor's thesis, TU Wien, 2020.

[49] P. Brax, H. Fischer, C. Käding and M. Pitschmann: *The environment dependent dilaton in the laboratory and the solar system*, Eur. Phys. J. C 82, no. 934, 2022, doi:10.1140/epjc/s10052-022-10905-w.

[50] P. Brax and G. Pignol: *Strongly coupled chameleons and the neutronic quantum bouncer*, Phys. Rev. Lett. 107, no. 11, p. 111301, 2011, doi:10.1103/physrevlett.107.111301.

[51] P. Brax and M. Pitschmann: *Exact solutions to nonlinear symmetron theory: One- and two-mirror systems*, Phys. Rev. D 97, no. 6, p. 064015, 2018, doi:10.1103/physrevd.97.064015.

[52] G. Breit: *The propagation of Schroedinger waves in a uniform field of force*, Phys. Rev. 32, no. 2, pp. 273–276, 1928, doi:10.1103/physrev.32.273.

[53] G. Bressi, G. Carugno, F. D. Valle, G. Galeazzi, G. Ruoso and G. Sartori: *Testing the neutrality of matter by acoustic means in a spherical resonator*, Phys. Rev. A 83, no. 5, p. 052101, 2011, doi:10.1103/physreva.83.052101.

[54] L. de Broglie: *Recherches sur la théorie des Quanta*, Phd thesis, Migration - université en cours d'affectation, 1924.

[55] Bureau international des poids et mesures: *Comptes Rendus des Séances de la 17e Conférence Générale des Poids et Mesures*, 1983.

[56] Bureau international des poids et mesures: *Conférence généraledes poids et mesures - Comptes rendus de la 26e réunion de la CGPM (13-16 novembre 2018)*, 2018, ISBN 978-92-822-2276-8.

[57] J. A. Cañas, J. Bernal and A. Martín-Ruiz: *Exact classical limit of the quantum bouncer*, arXiv 2022, doi:10.48550/arxiv.2208.13277.

[58] J. Chadwick: *Possible existence of a neutron*, Nature 129, no. 3252, pp. 312–312, 1932, doi:10.1038/129312a0.

[59] J. Chadwick and M. Goldhaber: *A nuclear photo-effect: disintegration of the diplon by -rays*, Nature 134, no. 3381, pp. 237–238, 1934, doi:10.1038/134237a0.

[60] E. Chanel, S. Baudoin, M.-H. Baurand, N. Belkhier, E. Bourgeat-Lami, S. Degenkolb, M. van der Grinten et al.: *Concept and strategy of SuperSUN: A new ultracold neutron converter*, Journal of Neutron Research 24, no. 2, pp. 111–121, 2023, doi:10.3233/jnr-220013.

[61] L. A. Chizhova, S. Rotter, T. Jenke, G. Cronenberg, P. Geltenbort, G. Wautischer, H. Filter, H. Abele and J. Burgdörfer: *Vectorial velocity filter for ultracold neutrons based on a surface-disordered mirror system*, Phys. Rev. E 89, no. 3, p. 032907, 2014, doi:10.1103/physreve.89.032907.

[62] B. Clement, A. Bes, A. Lacoste, R. Combe, V. V. Nesvizhevsky, G. Pignol, D. Rebreyend and Y. Xi: *Boron-10 conversion layer for ultra-cold neutron detection*, J. Instrum. 14, no. 09, pp. P09003–P09003, 2019, doi:10.1088/1748-0221/14/09/p09003.

[63] B. Clément, S. Baessler, V. V. Nesvizhevsky, E. Perry, G. Pignol, J. A. Pioquinto, K. V. Protasov et al.: *Manipulation of gravitational quantum states of a bouncing neutron with the GRANIT spectrometer*, arXiv 2022, doi:10.48550/arxiv.2205.11130.

[64] B. Clément, L. Gesson, T. Jenke, V. V. Nesvizhevsky, G. Pignol, S. Roccia and J. P. Scordillis: *Spatial resolution determination of a position sensitive ultra-cold neutron detector*, Nucl. Instrum. Methods Phys. Res., Sect. A 1040, p. 167212, 2022, ISSN 0168-9002, doi:10.1016/j.nima.2022.167212.

[65] G. Cronenberg: *Frequency measurments testing Newton's gravity law with the Rabi-qBounce experiment*, Phd thesis, TU Wien, Wien, 2016, doi:10.34726/HSS.2015.21420.

[66] G. Cronenberg, P. Brax, H. Filter, P. Geltenbort, T. Jenke, G. Pignol, M. Pitschmann, M. Thalhammer and H. Abele: *Acoustic Rabi oscillations between gravitational quantum states and impact on symmetron dark energy*, Nature Physics 14, no. 10, pp. 1022–1026, 2018, doi:10.1038/s41567-018-0205-x.

[67] G. Cronenberg, K. Durstberger-Rennhofer, P. Geltenbort, T. Jenke, H. Lemmel and H. Abele: *Methods and applications of gravity resonance spectroscopy within the qBounce experiment*, J. Phys: Conf. Ser. 340, p. 012045, 2012, doi:10.1088/1742-6596/340/1/012045.

[68] G. Cronenberg, H. Filter, M. Thalhammer, T. Jenke, H. Abele and P. Geltenbort: *A gravity of Earth measurement with a qBounce experiment*, in *Proceedings of The European Physical Society Conference on High Energy Physics (EPS-HEP2015)*, Sissa Medialab, 2016, doi:10.22323/1.234.0408.

[69] M. Daum, B. Franke, P. Geltenbort, E. Gutsmiedl, S. Ivanov, J. Karch, M. Kasprzak et al.: *Transmission of ultra-cold neutrons through guides coated with materials of high optical potential*, Nucl. Instrum. Methods Phys. Res., Sect. A 741, pp. 71–77, 2014, doi:10.1016/j.nima.2013.12.050.

[70] P. I. Dee: *Attempts to detect the interaction of neutrons with electrons*, Proceedings of the Royal Society of London. Series A, Containing Papers of a Mathematical and Physical Character 136, no. 830, pp. 727–734, 1932, doi:10.1098/rspa.1932.0114.

[71] S. Degenkolb, M. Kreuz and O. Zimmer: *A tapered transition guide with irregular octagonal cross-section*, Journal of Neutron Research 20, no. 4, pp. 117–122, 2019, doi:10.3233/jnr-180100.

[72] S. M. Degenkolb: *Optical magnetometry using multiphoton transitions*, Phd thesis, 2016.

[73] S. T. Dembiński, A. J. Makowski and P. Pepłowski: *Quantum bouncer with chaos*, Phys. Rev. Lett. 70, no. 8, pp. 1093–1096, 1993, doi:10.1103/physrevlett.70.1093.

[74] S. T. Dembinski and L. Wolniewicz: *Remarks on solving the one-dimensional time-dependent Schrödinger equation on the interval : the case of a quantum bouncer*, J. Phys. A: Math. Gen. 29, no. 2, pp. 349–355, 1996, doi:10.1088/0305-4470/29/2/015.

[75] R. D. Desko and D. J. Bord: *The quantum bouncer revisited*, Amer. J. Phys. 51, no. 1, pp. 82–84, 1983, doi:10.1119/1.13400.

[76] D. Dubbers: *The present status of particle physics with slow neutrons*, Phys. Procedia 51, pp. 13–18, 2014, ISSN 1875-3892, doi:10.1016/j.phpro.2013.12.005.

[77] K. Durstberger-Rennhofer, T. Jenke and H. Abele: *Probing the neutron's electric neutrality with Ramsey spectroscopy of gravitational quantum states of ultracold neutrons*, Phys. Rev. D 84, no. 3, p. 036004, 2011, doi:10.1103/physrevd.84.036004.

[78] S. Döge: *Scattering of ultracold neutrons in condensed deuterium and on material surfaces*, Phd thesis, TU München, 2019, doi:10.14459/2019MD1464401.

[79] N. Einsidler: *Vibration studies for the qBounce experimental platform*, Bachelor's thesis, TU Wien, 2017.

[80] J. Engel, M. J. Ramsey-Musolf and U. van Kolck: *Electric dipole moments of nucleons, nuclei, and atoms: The Standard Model and beyond*, Prog. Part. Nucl. Phys. 71, pp. 21–74, 2013, doi:10.1016/j.ppnp.2013.03.003.

[81] A. Ernst: *Simulation of a quantum bouncingball in k-space*, Bachelor's thesis, TU Wien, 2023.

[82] M. Escobar, F. Lamy, A. E. Meyerovich and V. V. Nesvizhevsky: *Rough mirror as a quantum state selector: analysis and design*, Adv. High Energy Phys. 2014, pp. 1–11, 2014, doi:10.1155/2014/764182.

[83] M. Escobar and A. E. Meyerovich: *Beams of gravitationally bound ultracold neutrons in rough waveguides*, Phys. Rev. A 83, no. 3, p. 033618, 2011, doi:10.1103/physreva.83.033618.

[84] P. Feichtinger: *Analyse der Stufenkontrolle des qBounce Experiments*, Bachelor's thesis, TU Wien, 2018.

[85] G. Feinberg and M. Goldhaber: *Microscopic tests of symmetry principles*, Proceedings of the National Academy of Sciences 45, no. 8, pp. 1301–1312, 1959, doi:10.1073/pnas.45.8.1301.

[86] J. Fellinger: *Einrichten der Experimentieroberfläche des q-Bounce Experiments senkrecht zum Erdmittelpunkt*, Bachelor's thesis, TU Wien, 2012.

[87] E. Fermi: *The development of the first chain reacting pile*, Proceedings of the American Philosophical Society 90, no. 1, pp. 20–24, 1946, ISSN 0003049X.

[88] H. Filter: *Miniforschung: Neutronendetektor auf CR-39 Basis*, Project thesis, Ruprecht-Karls-Universität Heidelberg, 2009.

[89] H. M. Filter: *Interference experiment with slow neutrons : a feasibility study of Lloyd's mirror at the Institut Laue-Langevin*, Phd thesis, TU Wien, Wien, 2018, doi:10.34726/HSS.2018.37910.

[90] M. Fink: *Reflexion von Neutronen im Zuge des Quantum Bouncing Ball Experiments*, Bachelor's thesis, TU Wien, 2010.

[91] R. Foot, H. Lew and R. R. Volkas: *Electric-charge quantization*, J. Phys. G: Nucl. Part. Phys. 19, no. 3, pp. 361–372, 1993, doi:10.1088/0954-3899/19/3/005.

[92] A. I. Frank: *Fundamental properties of the neutron: Fifty years of research*, Soviet Physics Uspekhi 25, no. 5, pp. 280–297, 1982, doi:10.1070/pu1982v025n05abeh004548.

[93] N. Freistetter: *Extension of the neutron detector within the qBounce experiments*, Bachelor's thesis, TU Wien, 2017.

[94] R. Gaehler, J. Kalus and W. Mampe: *Experimental limit for the charge of the free neutron*, in B. N. Taylor and W. D. Phillips (editors), *Precision Measurement and Fundamental Constants II*, *NBS special publication*, vol. 617, pp. 257–261, National Bureau of Standards, Washington, DC, 1984.

[95] R. Gahler, J. Kalus and W. Mampe: *An optical instrument for the search of a neutron charge*, J. Phys. E: Sci. Instrum. 13, no. 5, pp. 546–548, 1980, doi:10.1088/0022-3735/13/5/019.

[96] A. Gassner: *Search for the voltage limits of the qBounc$\vec{E}$ electrode*, Bachelor's thesis, TU Wien, 2020.

[97] J. Gea-Banacloche: *A quantum bouncing ball*, Amer. J. Phys. 67, no. 9, pp. 776–782, 1999, doi:10.1119/1.19124.

[98] R. L. Gibbs: *The quantum bouncer*, Amer. J. Phys. 43, no. 1, pp. 25–28, 1975, doi:10.1119/1.10024.

[99] R. H. Goeckermann and I. Perlman: *Characteristics of bismuth fission with high energy particles*, Phys. Rev. 73, no. 9, pp. 1127–1128, 1948, doi:10.1103/physrev.73.1127.

[100] R. Golub, D. Richardson and S. K. Lamoreaux: *Ultra-cold neutrons*, CRC press, S.l, 2019, ISBN 9780367403041.

[101] R. Golubich: *Analysis of the velocity spectra at the PF2 located at the Insititute Laue Langevin*, Project thesis, TU Wien, 2017.

[102] F. M. Gonzalez, E. M. Fries, C. Cude-Woods, T. Bailey, M. Blatnik, L. J. Broussard, N. B. Callahan et al.: *Improved neutron lifetime measurement with UCNτ*, Phys. Rev. Lett. 127, no. 16, p. 162501, 2021, ISSN 1079-7114, doi:10.1103/physrevlett.127.162501.

[103] D. A. Goodings and T. Szeredi: *The quantum bouncer by the path integral method*, Amer. J. Phys. 59, no. 10, pp. 924–930, 1991, doi:10.1119/1.16673.

[104] A. Gruber: *Automation of the qBounce experiment's vacuum system*, Bachelor's thesis, TU Wien, 2016.

[105] R. Gähler: *Experimentelle Grenzen für die elektrische Ladung des Neutrons*, Phd thesis, 1980.

[106] R. Gähler, J. Kalus and W. Mampe: *Experimental limit for the charge of the free neutron*, Phys. Rev. D 25, no. 11, pp. 2887–2894, 1982, doi:10.1103/physrevd.25.2887.

[107] C. Gösselsberger: *Entwicklung eines Wanderwellen-Neutronenspinresonators*, Phd thesis, TU Wien, 2012.

[108] O. Hahn and F. Strassmann: *Über den Nachweis und das Verhalten der bei der Bestrahlung des Urans mittels Neutronen entstehenden Erdalkalimetalle*, Die Naturwissenschaften 27, no. 1, pp. 11–15, 1939, doi:10.1007/bf01488241.

[109] J. Hansson, D. Olevik, C. Türk and H. Wiklund: *Comment on "Measurement of quantum states of neutrons in the Earth's gravitational field"*, Phys. Rev. D 68, no. 10, p. 108701, 2003, doi:10.1103/physrevd.68.108701.

[110] V. Hardel, P.-A. Hervieux and G. Manfredi: *Relaxation to quantum equilibrium and the Born rule in Nelson's stochastic dynamics*, Found. Phys. 53, no. 6, 2023, doi:10.1007/s10701-023-00730-w.

[111] N. Haverkamp: *Entwicklung von Detektoren für einen Wasserstoff-Atomstrahl und für ultra-kalte Neutronen*, Diploma thesis, Ruprecht-Karls-Universität Heidelberg, 2000.

[112] R. Havlik: *Analysis of the detector sensors environmentfrom the qBounce-experiment during beamtime 182-18/1*, Bachelor's thesis, TU Wien, 2023.

[113] P. T. Heistracher: *Extension and characterisation of neutron detector within the qBounce experiment*, Bachelor's thesis, TU Wien, 2015.

[114] M. Heiss: *Vorbereitung von Gravitationsexperimenten im Rahmen des qBounce-Experiments*, Diploma thesis, TU Wien, 2017, doi:10.34726/HSS.2017.28223.

[115] J. Herzinger: *Entwicklung einer Instrumentansteuerung für das qBounce Experiment*, Diploma thesis, TU Wien, Wien, 2014, doi:10.34726/HSS.2014.23828.

[116] J. Hingerl: *A versatile device for studying ultracold neutrons and testing cryogenic storage volumes*, Diploma thesis, TU München, 2019.

[117] K. Hirota, T. Ariga, M. Hino, G. Ichikawa, S. Kawasaki, M. Kitaguchi, K. Mishima, N. Muto, N. Naganawa and H. M. Shimizu: *Neutron imaging using a fine-grained nuclear emulsion*, Journal of Imaging 7, no. 1, p. 4, 2021, doi:10.3390/jimaging7010004.

[118] B. Holzmann: *Vergleich der verwendeten Zählsysteme des qBounce Experiments am Institut Laue-Langevin*, Bachelor's thesis, TU Wien, 2012.

[119] F. Honz: *qBounc$\vec{E}$: Measurement of titanium electrodes at the ATI*, Project thesis, TU Wien, 2018.

[120] N. Huber: *Extending the software environment of the qBounce platform*, Bachelor's thesis, TU Wien, 2017.

[121] G. Ichikawa, S. Komamiya, Y. Kamiya, Y. Minami, M. Tani, P. Geltenbort, K. Yamamura et al.: *Observation of the spatial distribution of gravitationally bound quantum states of ultracold neutrons and its derivation using the Wigner function*, Phys. Rev. Lett. 112, no. 7, p. 071101, 2014, doi:10.1103/PhysRevLett.112.071101.

[122] M. P. Iro: *Construction of an apparatus to generate strong electric fields at small distances and low pressure for the qBounce-experiment*, Bachelor's thesis, TU Wien, 2013.

[123] T. M. Ito, E. R. Adamek, N. B. Callahan, J. H. Choi, S. M. Clayton, C. Cude-Woods, S. Currie et al.: *Performance of the upgraded ultracold neutron source at Los Alamos National Laboratory and its implication for a possible neutron electric dipole moment experiment*, Phys. Rev. C 97, no. 1, p. 012501, 2018, doi:10.1103/physrevc.97.012501.

[124] A. Ivanov, M. Pitschmann and M. Wellenzohn: *Effective low-energy gravitational potential for slow fermions coupled to linearized massive gravity*, Phys. Rev. D 92, no. 10, p. 105034, 2015, doi:10.1103/physrevd.92.105034.

[125] A. Ivanov, M. Pitschmann and M. Wellenzohn: *Erratum: Effective low-energy gravitational potential for slow fermions coupled to linearized massive gravity [Phys. Rev. D 92, 105034 (2015)]*, Phys. Rev. D 95, no. 2, p. 029901, 2017, doi:10.1103/physrevd.95.029901.

[126] A. N. Ivanov, G. Cronenberg, R. Höllwieser, T. Jenke, M. Pitschmann, M. Wellenzohn and H. Abele: *Exact solution for chameleon field, self-coupled through the Ratra-Peebles potential with n=1 and confined between two parallel plates*, Phys. Rev. D 94, no. 8, p. 085005, 2016, doi:10.1103/physrevd.94.085005.

[127] A. N. Ivanov, R. Höllwieser, T. Jenke, M. Wellenzohn and H. Abele: *Influence of the chameleon field potential on transition frequencies of gravitationally bound quantum states of ultracold neutrons*, Phys. Rev. D 87, no. 10, p. 105013, 2013, doi:10.1103/physrevd.87.105013.

[128] A. N. Ivanov and M. Pitschmann: *Nonrelativistic approximation of the Dirac equation for slow fermions in static metric spacetimes*, Phys. Rev. D 90, no. 4, p. 045040, 2014, doi:10.1103/physrevd.90.045040.

[129] A. N. Ivanov and M. Wellenzohn: *Effective low-energy potential for slow Dirac fermions in Einstein-Cartan gravity with torsion and chameleon field*, Phys. Rev. D 92, no. 12, p. 125004, 2015, doi:10.1103/physrevd.92.125004.

[130] A. N. Ivanov and M. Wellenzohn: *Nonrelativistic approximation of the Dirac equation for slow fermions coupled to the chameleon and torsion fields in the gravitational field of the Earth*, Phys. Rev. D 92, no. 6, p. 065006, 2015, doi:10.1103/physrevd.92.065006.

[131] A. N. Ivanov and M. Wellenzohn: *Standard electroweak interactions in gravitational theory with chameleon field and torsion*, Phys. Rev. D 91, no. 8, p. 085025, 2015, doi:10.1103/physrevd.91.085025.

[132] A. N. Ivanov and M. Wellenzohn: *Einstein-Cartan gravity with torsion field serving as an origin for the cosmological constant or dark energy density*, The Astrophysical Journal 829, no. 1, p. 47, 2016, doi:10.3847/0004-637x/829/1/47.

[133] A. N. Ivanov and M. Wellenzohn: *Spin precession of slow neutrons in Einstein-Cartan gravity with torsion, chameleon and magnetic field*, Phys. Rev. D 93, no. 4, p. 045031, 2016, doi:10.1103/PhysRevD.93.045031.

[134] A. N. Ivanov, M. Wellenzohn and H. Abele: *Probing of violation of Lorentz invariance by ultracold neutrons in the Standard Model Extension*, Phys. Lett. B 797, p. 134819, 2019, doi:10.1016/j.physletb.2019.134819.

[135] A. N. Ivanov, M. Wellenzohn and H. Abele: *Quantum gravitational states of ultracold neutrons as a tool for probing of beyond-Riemann gravity*, Phys. Lett. B 822, p. 136640, 2021, doi:10.1016/j.physletb.2021.136640.

[136] A. Jardel: *Study of the mechanical oscillations of a quantum bouncer*, Project thesis, Institut Laue Langevin, 2017.

[137] D. Jelem: *Vibrationstests am Aufbau des qBounce Experiments*, Bachelor's thesis, TU Wien, 2013.

[138] T. Jenke: *Weiterentwicklung eines Experiments zur Realisierung eines Quantum Bouncing Balls und Suche nach Extradimensionen der Raumzeit*, Diploma thesis, Ruprecht-Karls-Universität Heidelberg, 2008.

[139] T. Jenke: *qBounce - vom Quantum Bouncer zur Gravitationsresonanzspektroskopie*, Phd thesis, TU Wien, 2011.

[140] T. Jenke and H. Abele: *Eperiments with gravitationally-bound ultracold neutrons at the European Spallation Source ESS*, Phys. Procedia 51, pp. 67–72, 2014, doi:10.1016/j.phpro.2013.12.016.

[141] T. Jenke, J. Bosina, G. Cronenberg, H. Filter, P. Geltenbort, A. N. Ivanov, J. Micko et al.: *Testing gravity at short distances: Gravity Resonance Spectroscopy with qBounce*, EPJ Web of Conf. 219, p. 05003, 2019, doi:10.1051/epjconf/201921905003.

[142] T. Jenke, J. Bosina, J. Micko, M. Pitschmann, R. Sedmik and H. Abele: *Gravity resonance spectroscopy and dark energy symmetron fields*, Eur. Phys. J. Special Topics 230, no. 4, pp. 1131–1136, 2021, doi:10.1140/epjs/s11734-021-00088-y.

[143] T. Jenke, G. Cronenberg, J. Burgdörfer, L. Chizhova, P. Geltenbort, A. Ivanov, T. Lauer et al.: *Gravity Resonance Spectroscopy constrains dark energy and dark matter scenarios*, Phys. Rev. Lett. 112, no. 15, p. 151105, 2014, doi:10.1103/physrevlett.112.151105.

[144] T. Jenke, G. Cronenberg, H. Filter, P. Geltenbort, M. Klein, T. Lauer, K. Mitsch et al.: *Ultracold neutron detectors based on B-10 converters used in the qBounce experiments*, Nucl. Instrum. Methods Phys. Res., Sect. A 732, pp. 1–8, 2013, doi:10.1016/j.nima.2013.06.024.

[145] T. Jenke, G. Cronenberg, P. Geltenbort, A. N. Ivanov, T. Lauer, T. Lins, U. Schmidt, H. Saul and H. Abele: *A quantized frequency reference in the short-ranged gravity potential and its application for dark matter and dark energy searches*, arXiv 2012, doi:10.48550/arxiv.1208.3875.

[146] T. Jenke, G. Cronenberg, M. Thalhammer, T. Rechberger, P. Geltenbort and H. Abele: *Gravity experiments with ultracold neutrons and the qBounce experiment*, in *Proceedings of 50th Rencontres de Moriond on Gravitation: 100 years after GR*, arXiv, 2015, doi:10.48550/arxiv.1510.03078, aRSIF.

[147] T. Jenke, P. Geltenbort, H. Lemmel and H. Abele: *Realization of a gravity-resonance-spectroscopy technique*, Nature Physics 7, no. 6, pp. 468–472, 2011, doi:10.1038/nphys1970.

[148] T. Jenke, D. Stadler, H. Abele and P. Geltenbort: *Q-BOUNCE—Experiments with quantum bouncing ultracold neutrons*, Nucl. Instrum. Methods Phys. Res., Sect. A 611, no. 2-3, pp. 318–321, 2009, doi:10.1016/j.nima.2009.07.073.

[149] M. Jugl: *Theoretische Betrachtung von Mehr-Niveau-Systemen bei der GRS anhand von vier simulierten Übergangsreihenfolgen*, Bachelor's thesis, TU Wien, 2023.

[150] J. Jung: *Aufbau und Betreuung des qBounce-Versuchsaufbaus während der Experimentierzeit 3-14-305 am Institut Laue-Langevin in Grenoble/Frankreich*, Project thesis, TU Wien, 2013.

[151] J. Juroszek: *Continuing the search for the voltagelimits of the qBounce electrode*, Bachelor's thesis, TU Wien, 2021.

[152] J. Kalus and R. Gähler: *An improved method to search for the neutron charge*, Le Journal de Physique Colloques 45, no. C3, pp. 17–20, 1984, doi:10.1051/jphyscol:1984304.

[153] Y. Kamiya, G. Ichikawa and S. Komamiya: *Precision measurement of the position-space wave functions of gravitationally bound ultracold neutrons*, Adv. High Energy Phys. 2014, pp. 1–7, 2014, doi:10.1155/2014/859241.

[154] K. C. Kao: *Electric polarization and relaxation*, in *Dielectric Phenomena in Solids*, pp. 41–114, Elsevier, 2004, doi:10.1016/b978-012396561-5/50012-8.

[155] M. Kaplan: *Analysis of CR39 track detectors*, Bachelor's thesis, TU Wien, 2022.

[156] S. Kawasaki, G. Ichikawa, M. Hino, Y. Kamiya, M. Kitaguchi, S. Komamiya, T. Sanuki and S. Sonoda: *Development of a pixel detector for ultra-cold neutrons*, Nucl. Instrum. Methods Phys. Res., Sect. A 615, no. 1, pp. 42–47, 2010, doi:10.1016/j.nima.2010.01.011.

[157] S. Keerl: *Systematische Tests des Vakuumsystems des qBounce Experiments*, Bachelor's thesis, TU Wien, 2012.

[158] E. H. Kennard: *Zur Quantenmechanik einfacher Bewegungstypen*, Zeitschrift für Physik 44, no. 4-5, pp. 326–352, 1927, doi:10.1007/bf01391200.

[159] C. Killian: *Analysis and correction of the qBounce step control system*, Project thesis, TU Wien, 2019.

[160] C. Killian: *qBounce: Systematic analysis of the Ramsey setup*, Diploma thesis, TU Wien, 2020, doi:10.34726/HSS.2020.71161.

[161] M. O. Klein: *Experimente zur Quantenmechanik mit ultrakalten Neutronen und Entwicklung eines neuen Detektors zum ortsaufgelösten Nachweis von thermischen Neutronen auf großen Flächen*, Phd thesis, Ruprecht-Karls-Universität Heidelberg, 2000.

[162] P. Klieber: *Refinement of the qBounce electrode setup - the integration process of piezomotors in the electrode bracket*, Bachelor's thesis, TU Wien, 2022.

[163] E. Klinkby, K. Batkov, F. Mezei, E. Pitcher, T. Schönfeldt, A. Takibayev and L. Zanini: *In-pile ^{4}He source for UCN production at the ESS*, Adv. High Energy Phys. 2014, pp. 1–4, 2014, doi:10.1155/2014/241639.

[164] F. Kono, K. Kurihara and T. Tamada: *Current status of neutron crystallography in structural biology*, Biophysics and Physicobiology 19, no. 0, 2022, doi:10.2142/biophysico.bppb-v19.0009.

[165] V. A. Kostelecký and Z. Li: *Seaches for beyond-Riemann gravity*, Physical Review D 104, no. 4, p. 044054, 2021, ISSN 2470-0029, doi:10.1103/physrevd.104.044054.

[166] C. Krantz: *Quantum states of neutrons in the gravitational field*, Diploma thesis, Ruprecht-Karls-Universität Heidelberg, 2006.

[167] V. Kraus: *Systematic testings of the oscillating region's mechanical resonances for the Ramsey-qBounce experiment*, Bachelor's thesis, TU Wien, 2020.

[168] M. Kreuz, V. V. Nesvizhevsky, P. Schmidt-Wellenburg, T. Soldner, M. Thomas, H. G. Boerner, F. Naraghi et al.: *A method to measure the resonance transitions between the gravitationally bound quantum states of neutrons in the GRANIT spectrometer*, Nucl. Instrum. Methods Phys. Res., Sect. A 611, no. 2-3, pp. 326–330, 2009, doi:10.1016/j.nima.2009.07.059.

[169] E. Kreuzgruber: *Characterisation of the qBounce$\vec{E}$ electrode setup used in ILL cycle 184-18/3*, Project thesis, TU Wien, 2019.

[170] C. Käding, M. Pitschmann and C. Voith: *Dilaton-induced open quantum dynamics*, Eur. Phys. J. C 83, no. 8, 2023, doi:10.1140/epjc/s10052-023-11939-4.

[171] L. D. Landau and E. M. Lifshitz: *Kvantovaia mekhanika. english*, 1958, by L.D. Landau and E.M. Lifshitz. Translated from the Russian by J.B. Sykes and J.S. Bell., Addison-Wesley series in advanced physics.

[172] P. W. Langhoff: *Schrödinger particle in a gravitational well*, Amer. J. Phys. 39, no. 8, pp. 954–957, 1971, doi:10.1119/1.1986333.

[173] R. V. Latham: *High voltage vacuum insulation: basic concepts and technological practice*, Academic Press, London San Diego, 1995, ISBN 9780124371750.

[174] B. Lauss and B. Blau: *UCN, the ultracold neutron source – neutrons for particle physics*, SciPost Physics Proceedings 5, p. 004, 2021, doi:10.21468/scipostphysproc.5.004.

[175] F. G. Lemoine, S. C. Kenyon, J. K. Factor, R. G. Trimmer, N. K. Pavlis, D. S. Chinn, C. M. Cox et al.: *The development of the joint NASA, GSFC and NIMA geopotential model EGM96*, Tech. Rep. NASA/TP-1998-206861, NASA Goddard Space Flight Center, Maryland, 20771 USA, 1998.

[176] A. Leopold: *Homogeneity considerations for the production of spatially resolving neutron detectors for the qBounce experiment on the µm-scale via a Physical Vapour Deposition unit*, Project thesis, TU Wien, 2014.

[177] K. K. H. Leung, M. Ahmed, R. Alarcon, A. Aleksandrova, S. Baessler, L. Barrón-Palos, L. Bartoszek et al.: *The neutron electric dipole moment experiment at the Spallation Neutron Source*, EPJ Web of Conf. 219, p. 02005, 2019, doi:10.1051/epjconf/201921902005.

[178] T. Lins: *Quantenzustände im Gravitationsfeld der Erde*, Diploma thesis, TU München, 2011.

[179] G. Locher: *Biological effects and therapeutic possibilities of neutrons*, Am. J. Roentgenol. Radium Ther. 36, no. 1, pp. 1–13, 1936.

[180] V. I. Luschikov and A. I. Frank: *Quantum effects occurring when ultracold neutrons are stored on a plane*, JETP Lett. 28, no. 9, pp. 559–561, 1978.

[181] V. I. Lushchikov, Y. N. Pokotilovskii, A. V. Strelkov and F. L. Shapiro: *Observation of Ultracold Neutrons*, JETP Lett. 9, no. 1, pp. 23–26, 1969.

[182] B. Luzum, N. Capitaine, A. Fienga, W. Folkner, T. Fukushima, J. Hilton, C. Hohenkerk et al.: *The IAU 2009 system of astronomical constants: the report of the IAU working group on numerical standards for Fundamental Astronomy*, Celestial Mechanics and Dynamical Astronomy 110, no. 4, pp. 293–304, 2011, doi:10.1007/s10569-011-9352-4.

[183] S. Lüftenegger: *Vibrationstest eines mehrteiligen Setups für ein qBounce Experiment und Methoden zur Amplitudenauswertung*, Project thesis, TU Wien, 2011.

[184] T. D. Malouff, D. S. Seneviratne, D. K. Ebner, W. C. Stross, M. R. Waddle, D. M. Trifiletti and S. Krishnan: *Boron neutron capture therapy: a review of clinical applications*, Frontiers in Oncology 11, 2021, doi:10.3389/fonc.2021.601820.

[185] G. Manfredi, O. Morandi, L. Friedland, T. Jenke and H. Abele: *Chirped-frequency excitation of gravitationally bound ultracold neutrons*, Phys. Rev. D 95, no. 2, p. 025016, 2017, doi:10.1103/physrevd.95.025016.

[186] I. Marson and J. E. Faller: *g-the acceleration of gravity: its measurement and its importance*, J. Phys. E: Sci. Instrum. 19, no. 1, pp. 22–32, 1986, doi:10.1088/0022-3735/19/1/002.

[187] J. Martin, J. Birchall, D. Bowman, L. Buchmann, L. Clarke, C. Davis, B. Filippone et al.: *Canadian Spallation Ultracold Neutron Source* 2008.

[188] R. Matsumiya, H. Akatsuka, C. P. Bidinosti, C. A. Davis, B. Franke, D. Fujimoto, M. T. W. Gericke et al.: *The precision nEDM measurement with UltraCold neutrons at TRIUMF*, in *Proceedings of the 24th International Spin Symposium (SPIN2021)*, Journal of the Physical Society of Japan, 2022, doi:10.7566/jpscp.37.020701.

[189] S. Mayr: *Nivellierung des qBounce-Experimentes*, Project thesis, TU Wien, 2016.

[190] L. Meitner and O. R. Frisch: *Disintegration of uranium by neutrons: a new type of nuclear reaction*, Nature 143, no. 3615, pp. 239–240, 1939, doi:10.1038/143239a0.

[191] A. E. Meyerovich and V. V. Nesvizhevsky: *Gravitational quantum states of neutrons in a rough waveguide*, Phys. Rev. A 73, no. 6, p. 063616, 2006, doi:10.1103/physreva.73.063616.

[192] J. Micko: *Electric field studies of a square electrode configuration for qBounce*, Project thesis, TU Wien, 2017.

[193] J. Micko: *qBounce - gravity resonance and Ramsey spectroscopy*, Diploma thesis, TU Wien, 2018, doi:10.34726/HSS.2018.40408.

[194] J. Micko: *qBounce: Ramsey spectroscopy using gravitationally bound quantum states of neutrons*, Phd thesis, TU Wien, 2023, doi:10.34726/HSS.2023.105602.

[195] J. Micko, J. Bosina, S. S. Cranganore, T. Jenke, M. Pitschmann, S. Roccia, R. I. P. Sedmik and H. Abele: *qBounce: Systematic shifts of transition frequencies of gravitational states of ultra-cold neutrons using Ramsey gravity resonance spectroscopy*, in *Proceedings of the 56th RENCONTRES DE MORIOND - Gravitation 2022*, pp. 143–148, arXiv, 2023, doi:10.58027/1e1n-7973.

[196] J. Micko, J. Bosina and T. Jenke: *Considerations for the migration from Rabi- to Ramsey spectroscopy of the qBounce experiment*, in *Proceedings of the 54th Rencontres de Moriond - Gravitation*, pp. 121–126, 2019, ISSN 979-10-96879-10-6.

[197] G. A. Miller: *Charge densities of the neutron and proton*, Phys. Rev. Lett. 99, no. 11, p. 112001, 2007, doi:10.1103/physrevlett.99.112001.

[198] D. P. Mitchell and P. N. Powers: *Bragg reflection of slow neutrons*, Phys. Rev. 50, no. 5, pp. 486–487, 1936, doi:10.1103/physrev.50.486.2.

[199] K. Mitsch: *Spurdetektoranalyse der qBounce-Experimente 2009*, Bachelor's thesis, TU Wien, 2010.

[200] M. Mock: *Aufbau und Erweiterung eines Vakuumsystems zur Erzeugung hoher elektrischer Felder für das q-Bounce Experiment*, Bachelor's thesis, TU Wien, 2016.

[201] P. J. Mohr, D. B. Newell and B. N. Taylor: *CODATA recommended values of the fundamental physical constants: : 2014* 2015, doi:10.5281/ZENODO.22826.

[202] P. J. Mohr, D. B. Newell, B. N. Taylor and E. Tiesinga: *Data and analysis for the CODATA 2017 special fundamental constants adjustment*, Metrologia 55, no. 1, pp. 125–146, 2018, doi:10.1088/1681-7575/aa99bc.

[203] P. J. Mohr, B. N. Taylor and D. B. Newell: *CODATA recommended values of the fundamental physical constants: 2010*, Rev. Mod. Phys. 84, no. 4, pp. 1527–1605, 2012, doi:10.1103/revmodphys.84.1527.

[204] D. E. Morrissey and M. J. Ramsey-Musolf: *Electroweak baryogenesis*, New J. Phys. 14, no. 12, p. 125003, 2012, doi:10.1088/1367-2630/14/12/125003.

[205] A. Muneem, J. Yoshida, H. Ekawa, M. Hino, K. Hirota, G. Ichikawa, A. Kasagi et al.: *Investigation of neutron imaging applications using fine-grained nuclear emulsion*, J. Appl. Phys. 133, no. 5, p. 054902, 2023, doi:10.1063/5.0131098.

[206] N. Muto, H. Abele, T. Ariga, J. Bosina, M. Hino, K. Hirota, G. Ichikawa et al.: *A novel nuclear emulsion detector for measurement of quantum states of ultracold neutrons in the Earth's gravitational field*, J. Instrum. 17, no. 07, p. P07014, 2022, doi:10.1088/1748-0221/17/07/p07014.

[207] B. Märkisch, H. Mest, H. Saul, X. Wang, H. Abele, D. Dubbers, M. Klopf et al.: *Measurement of the weak axial-vector coupling constant in the decay of free neutrons using a pulsed cold neutron beam*, Phys. Rev. Lett. 122, no. 24, p. 242501, 2019, doi:10.1103/physrevlett.122.242501.

[208] C. Mühlmann: *Simulation of different capacitor designs for qbounce*, Project thesis, Atominstitut, TU Wien, 2018.

[209] N. Naganawa, S. Awano, M. Hino, M. Hirose, K. Hirota, H. Kawahara, M. Kitaguchi et al.: *A neutron detector with submicron spatial resolution using fine-grained nuclear emulsion*, Phys. Procedia 88, pp. 224–230, 2017, doi:10.1016/j.phpro.2017.06.031.

[210] S. L. Nahrwold: *Developement of a detector for bound quantum states of neutrons in the Earth's gravitational field*, Diploma thesis, Ruprecht-Karls-Universität Heidelberg, 2004.

[211] V. V. Nesvizhevsky: *Investigation of quantum neutron states in the terrestrial gravitational field above a mirror*, Physics-Uspekhi 47, no. 5, pp. 515–521, 2004, doi:10.1070/pu2004v047n05abeh001754.

[212] V. V. Nesvizhevsky: *Near-surface quantum states of neutrons in the gravitational and centrifugal potentials*, Physics-Uspekhi 53, no. 7, pp. 645–675, 2010, doi:10.3367/ufne.0180.201007a.0673.

[213] V. V. Nesvizhevsky, H. Börner, A. M. Gagarski, G. A. Petrov, A. K. Petukhov, H. Abele, S. Bässler, T. Stöferle and S. M. Soloviev: *Search for quantum states of the neutron in a gravitational field: gravitational levels*, Nucl. Instrum. Methods Phys. Res., Sect. A 440, no. 3, pp. 754–759, 2000, doi:10.1016/s0168-9002(99)01077-3.

[214] V. V. Nesvizhevsky, H. G. Börner, A. M. Gagarski, A. K. Petoukhov, G. A. Petrov, H. Abele, S. Baessler et al.: *Measurement of quantum states of neutrons in the Earth's gravitational field*, Phys. Rev. D 67, no. 10, p. 102002, 2003, doi:10.1103/PhysRevD.67.102002.

[215] V. V. Nesvizhevsky, H. G. Börner, A. K. Petukhov, H. Abele, S. Baessler, F. J. Ruess, T. Stöferle et al.: *Quantum states of neutrons in the Earth's gravitational field*, Nature 415, no. 6869, pp. 297–299, 2002, doi:10.1038/415297a.

[216] V. V. Nesvizhevsky and GRANIT-collaboration: *Gravitational quantum states of neutrons and the new GRANIT spectrometer*, Mod. Phys. Lett. A 27, no. 05, p. 1230006, 2012, doi:10.1142/s0217732312300066.

[217] V. V. Nesvizhevsky, A. K. Petoukhov, H. G. Börner, K. V. Protasov, A. Y. Voronin, A. Westphal, S. Baessler, H. Abele and A. M. Gagarski: *Reply to "Comment on 'Measurement of quantum states of neutrons in the Earth's gravitational field' "*, Phys. Rev. D 68, no. 10, p. 108702, 2003, doi:10.1103/physrevd.68.108702.

[218] V. V. Nesvizhevsky, A. K. Petukhov, H. G. Boerner, T. A. Baranova, A. M. Gagarski, G. A. Petrov, K. V. Protasov et al.: *Study of the neutron quantum states in the gravity field*, Eur. Phys. J. C 40, no. 4, pp. 479–491, 2005, doi:10.1140/epjc/s2005-02135-y.

[219] V. V. Nesvizhevsky, A. K. Petukhov, H. G. Borner, T. A. Baranova, A. M. Gagarski, G. A. Petrov, K. V. Protasov et al.: *Investigation of the neutron quantum states in the Earth's gravitational field*, J. Res. Natl. Inst. Stand. Technol. 110, no. 3, p. 263, 2005, doi:10.6028/jres.110.036.

[220] V. V. Nesvizhevsky, A. K. Petukhov, K. V. Protasov and A. Y. Voronin: *Centrifugal quantum states of neutrons*, Phys. Rev. A 78, no. 3, p. 033616, 2008, doi:10.1103/physreva.78.033616.

[221] V. V. Nesvizhevsky, G. Pignol and K. V. Protasov: *Neutron scattering and extra-short-range interactions*, Phys. Rev. D 77, no. 3, p. 034020, 2008, doi:10.1103/physrevd.77.034020.

[222] V. V. Nesvizhevsky and K. V. Protasov: *Constrains on non-Newtonian gravity from the experiment on neutron quantum states in the Earth's gravitational field*, Classical and Quantum Gravity 21, no. 19, pp. 4557–4566, 2004, doi:10.1088/0264-9381/21/19/005.

[223] V. V. Nesvizhevsky and A. Y. Voronin: *Centrifugal quantum states of neutrons*, C. R. Phys. 12, no. 8, pp. 791–795, 2011, doi:10.1016/j.crhy.2011.07.001.

[224] V. V. Nesvizhevsky, A. Y. Voronin, R. Cubitt and K. V. Protasov: *Neutron whispering gallery*, Nature Physics 6, no. 2, pp. 114–117, 2009, doi:10.1038/nphys1478.

[225] L. Neubacher: *qBouncE⃗: Measurement of a titanium electrode with improved alignment control*, Bachelor's thesis, TU Wien, 2022.

[226] R. Neubacher: *Movie of a quantum bouncing ball*, Bachelor's thesis, TU Wien, 2023.

[227] P. Neuhuber: *Improvement of the displacement regulation program for the neutron mirrors of the qBounce experiment series*, Bachelor's thesis, TU Wien, 2017.

[228] NIMA: *World Geodetic System 1984: technical report 8350.2 third edition*, Tech. rep., National Imagery and Mapping Agency, Department of Defense, 2000.

[229] P. R. O'Connor and G. T. Seaborg: *High energy spallation and fission products of uranium*, Phys. Rev. 74, no. 9, pp. 1189–1190, 1948, doi:10.1103/physrev.74.1189.

[230] H. Paetz: *Key nuclear reaction experiments*, Institute of Physics Publishing, 2015, ISBN 9780750311731.

[231] R. Patsch: *Space charge phenomena in polyethylene at high electric fields*, J. Phys. D: Appl. Phys. 23, no. 12, pp. 1497–1505, 1990, doi:10.1088/0022-3727/23/12/005.

[232] N. K. Pavlis, S. A. Holmes, S. C. Kenyon and J. K. Factor: *The development and evaluation of the Earth Gravitational Model 2008 (EGM2008)*, J. Geophys. Res. 117, no. B4, pp. 1–38, 2012, doi:10.1029/2011jb008916.

[233] V. F. Pecile: *Analysis and correction of the qBounce step control system*, Project thesis, TU Wien, 2019.

[234] F. M. Piegsa: *Novel concept for a neutron electric charge measurement using a Talbot-Lau interferometer at a pulsed source*, Phys. Rev. C 98, no. 4, p. 045503, 2018, doi:10.1103/physrevc.98.045503.

[235] F. M. Piegsa, M. Fertl, S. N. Ivanov, M. Kreuz, K. K. H. Leung, P. Schmidt-Wellenburg, T. Soldner and O. Zimmer: *New source for ultracold neutrons at the Institut Laue-Langevin*, Phys. Rev. C 90, no. 1, p. 015501, 2014, doi:10.1103/physrevc.90.015501.

[236] M. Pieler and V. Czamler: *qBouncino: a small scale qBounce setup*, Project thesis, TU Wien, 2019.

[237] G. Pignol: *réparation de l'expérience GRANIT et recherche de nouvelles interactions avec lesneutrons.*, Phd thesis, Université Joseph-Fourier - Grenoble, 2009.

[238] G. Pignol, S. Baessler, V. V. Nesvizhevsky, K. Protasov, D. Rebreyend and A. Voronin: *Gravitational Resonance Spectroscopy with an oscillating magnetic field gradient in the GRANIT flow through arrangement*, Adv. High Energy Phys. 2014, pp. 1–7, 2014, doi:10.1155/2014/628125.

[239] G. Pignol, K. V. Protasov, D. Rebreyend, F. Vezzu, V. V. Nesvizhevsky, A. K. Petukhov, H. G. Börner et al.: *GRANIT project: a trap for gravitational quantum states of UCN*, arXiv 2007, doi:10.48550/arxiv.0708.2541.

[240] G. Pignol, K. V. Ptotasov and V. V. Nesvizhevsky: *A note on spontaneous emission of gravitons by a quantum bouncer*, Classical and Quantum Gravity 24, no. 9, pp. 2439–2441, 2007, doi:10.1088/0264-9381/24/9/n02.

[241] J. Piso: *Electrical characterization of the qBounc$\vec{E}$ electrode measurement setup*, Bachelor's thesis, TU Wien, 2020.

[242] M. Pitschmann: *Exact solutions to nonlinear symmetron theory: One- and two-mirror systems. II.*, Phys. Rev. D 103, no. 8, p. 084013, 2021, doi:10.1103/physrevd.103.084013.

[243] M. Pitschmann: *Erratum: Exact solutions to nonlinear symmetron theory: One- and two-mirror systems. II. [Phys. Rev. D 103, 084013 (2021)]*, Phys. Rev. D 106, no. 10, p. 109902, 2022, doi:10.1103/physrevd.106.109902.

[244] M. Pitschmann and H. Abele: *Schrödinger equation for a non-relativistic particle in a gravitational field confined by two vibrating mirrors*, arXiv 2019, doi:10.48550/arxiv.1912.12236.

[245] C. Plonka-Spehr, A. Kraft, P. Iaydjiev, J. Klepp, V. V. Nesvizhevsky, P. Geltenbort and T. Lauer: *An optical device for ultra-cold neutrons - Investigation of systematic effects and applications*, Nucl. Instrum. Methods Phys. Res., Sect. A 618, no. 1-3, pp. 239–247, 2010, doi:10.1016/j.nima.2010.02.110.

[246] Y. N. Pokotilovski, M. I. Novopoltsev, P. Geltenbort and T. Brenner: *A differential time-of-flight spectrometer of very slow neutrons*, Instruments and Exper. Techn. 54, pp. 16–22, 2011, doi:10.48550/arxiv.1102.2851.

[247] N. Pruggmayer: *Continued electrical characterization of the qBounce electrode measurement setup*, Bachelor's thesis, TU Wien, 2022.

[248] I. I. Rabi, S. Millman, P. Kusch and J. R. Zacharias: *The molecular beam resonance method for measuring nuclear magnetic moments. the magnetic moments of Li-6, Li-7 and F-19*, Phys. Rev. 55, no. 6, pp. 526–535, 1939, doi:10.1103/physrev.55.526.

[249] P. Radvanyi and J. Villain: *The discovery of radioactivity*, C. R. Phys. 18, no. 9-10, pp. 544–550, 2017, doi:10.1016/j.crhy.2017.10.008.

[250] N. F. Ramsey: *A molecular beam resonance method with separated oscillating fields*, Phys. Rev. 78, no. 6, pp. 695–699, 1950, doi:10.1103/physrev.78.695.

[251] N. F. Ramsey: *Resonance transitions induced by perturbations at two or more different frequencies*, Phys. Rev. 100, no. 4, pp. 1191–1194, 1955, doi:10.1103/physrev.100.1191.

[252] D. Rath: *Weiterentwicklung des Blendensystems für das qBounce Experiment*, Bachelor's thesis, TU Wien, 2016.

[253] H. Rauch, W. Treimer and U. Bonse: *Test of a single crystal neutron interferometer*, Phys. Lett. A 47, no. 5, pp. 369–371, 1974, doi:10.1016/0375-9601(74)90132-7.

[254] T. Rechberger: *Ramsey spectroscopy of gravitationally bound quantum states of ultracold neutrons*, Phd thesis, TU Wien, Wien, 2018, doi:10.34726/HSS.2018.37909.

[255] R. Reiter, B. Schlederer and D. Seppi: *Quantenmechanisches Verhalten eines ultrakalten Neutrons im Gravitationsfeld*, Project thesis, TU Wien, 2009.

[256] T. M. Roach, H. Abele, M. G. Boshier, H. L. Grossman, K. P. Zetie and E. A. Hinds: *Realization of a magnetic mirror for cold atoms*, Phys. Rev. Lett. 75, no. 4, pp. 629–632, 1995, doi:10.1103/physrevlett.75.629.

[257] D. Roulier, F. Vezzu, S. Baessler, B. Clément, D. Morton, V. V. Nesvizhevsky, G. Pignol and D. Rebreyend: *Status of the GRANIT facility*, Adv. High Energy Phys. 2015, pp. 1–10, 2015, doi:10.1155/2015/730437.

[258] F. Ruess: *Quantum states in the gravitational field*, Diploma thesis, University of Heidelberg, 2000.

[259] E. Rutherford: *LXXIX. The scattering of α and β particles by matter and the structure of the atom*, The London, Edinburgh, and Dublin Philosophical Magazine and Journal of Science 21, no. 125, pp. 669–688, 1911, doi:10.1080/14786440508637080.

[260] E. Rutherford: *The scattering of α and β particles by matter and the structure of the atom*, Memoirs and proceedings of the Manchester Literary and Philosophical Society 55, pp. 380–382, 1911.

[261] J. J. Sakurai: *Modern quantum mechanics - 2. edición*, Addison Wesley, 2011, ISBN 9780805382914.

[262] P. Salajka: *Measurement of the magnetic shielding of the qBounce eExperiment*, Project thesis, TU Wien, 2018.

[263] T. Sanuki, S. Komamiya, S. Kawasaki and S. Sonoda: *Proposal for measuring the quantum states of neutrons in the gravitational field with a CCD-based pixel sensor*, Nucl. Instrum. Methods Phys. Res., Sect. A 600, no. 3, pp. 657–660, 2009, doi:10.1016/j.nima.2008.12.187.

[264] H. Saul: *Weiterentwicklung des Detektor- und Auslesekonzepts für das Gravitationsexperiment qBounce*, Diploma thesis, TU Wien, TU München, 2011.

[265] J. Schilberg: *qBounce: Simulation der Wahrscheinlichkeitsstromdichte*, Project thesis, TU Wien, 2023.

[266] A. J. Schimmoller, G. McCaul, H. Abele and D. I. Bondar: *Decoherence-free entropic gravity: Model and experimental tests*, Phys. Rev. Research 3, no. 3, p. 033065, 2021, doi:10.1103/physrevresearch.3.033065.

[267] P. Schmidt: *Studien zur Ramsey-Spektroskopie ultrakalter Neutronen im Rahmen des qBounce Experiments*, Diploma thesis, TU Wien, 2017.

[268] P. Schmidt-Wellenburg, K. H. Andersen, P. Courtois, M. Kreuz, S. Mironov, V. V. Nesvizhevsky, G. Pignol et al.: *Ultracold-neutron infrastructure for the gravitational spectrometer GRANIT*, Nucl. Instrum. Methods Phys. Res., Sect. A 611, no. 2-3, pp. 267–271, 2009, doi:10.1016/j.nima.2009.07.096.

[269] J. Schmiedmayer, P. Riehs, J. A. Harvey and N. W. Hill: *Measurement of the electric polarizability of the neutron*, Phys. Rev. Lett. 66, no. 8, pp. 1015–1018, 1991, doi:10.1103/physrevlett.66.1015.

[270] J. M. Schnee: *Experimentelle Weiterentwicklungen zum qBounce Experiment*, Bachelor's thesis, TU Wien, 2022.

[271] L. Schrangl: *Systematische Untersuchung hoher elektrischer Felder zwischen Neutronenspiegeln für das qBounce-Experiment*, Project thesis, TU Wien, 2012.

[272] E. Schrödinger: *Quantisierung als Eigenwertproblem*, Annalen der Physik 385, no. 13, pp. 437–490, 1926, doi:10.1002/andp.19263851302.

[273] D. Schuh: *On finite size effects and applicability of perturbation theory in the qBOUNCE experiment*, Project thesis, TU Wien, 2018.

[274] D. Schuh: *Analysis of detector sensor data and vacuum sensor data in the vacuum chamber of a qBounce experiment*, Project thesis, TU Wien, 2019.

[275] P. Schwerdtfeger and J. K. Nagle: *2018 Table of static dipole polarizabilities of the neutral elements in the periodic table*, Molecular Physics 117, no. 9-12, pp. 1200–1225, 2018, doi:10.1080/00268976.2018.1535143.

[276] R. I. P. Sedmik, J. Bosina, L. Achatz, P. Geltenbort, M. Heiss, A. N. Ivanov, T. Jenke et al.: *Proof of principle for Ramsey-type gravity resonance spectroscopy with qBounce*, in T. Jenke, S. Degenkolb, P. Geltenbort, M. Jentschel, V. V. Nesvizhevsky, D. Rebreyend, S. Roccia, T. Soldner, A. Stutz and O. Zimmer (editors), *EPJ Web of Conf.*, vol. 219, p. 05004, EDP Sciences, 2019, doi:10.1051/epjconf/201921905004.

[277] A. P. Serebrov, E. A. Kolomensky, A. K. Fomin, I. A. Krasnoshchekova, A. V. Vassiljev, D. M. Prudnikov, I. V. Shoka et al.: *Neutron lifetime measurements with a large gravitational trap for ultracold neutrons*, Phys. Rev. C 97, no. 5, 2018, doi:10.1103/physrevc.97.055503.

[278] I. S. Shapiro and I. V. Estulin: *Concerning the electric charge of the neutron*, JETP 3, pp. 626–628, 1956.

[279] C. G. Shull, K. W. Billman and F. A. Wedgwood: *Experimental limit for the neutron charge*, Phys. Rev. 153, no. 5, pp. 1415–1422, 1967, doi:10.1103/physrev.153.1415.

[280] C. Siemensen: *Untersuchung der Ladung des Neutrons*, Phd thesis, Johannes Gutenberg-Universität Mainz, 2015, doi:10.25358/openscience-1260.

[281] C. Siemensen, D. Brose, L. Böhmer, P. Geltenbort and C. Plonka-Spehr: *Improved instrument for the determination of the neutron electric charge*, Nucl. Instrum. Methods Phys. Res., Sect. A 778, pp. 26–30, 2015, doi:10.1016/j.nima.2015.01.015.

[282] C. Siemensen, C. Düsing, P. Geltenbort, C. Giebel, T. Reich and C. Plonka: *Search for an electric charge of the neutron*, Phys. Rev. D 97, no. 5, p. 052004, 2018, doi:10.1103/physrevd.97.052004.

[283] L. Sihver, M. Giacomelli, S. Ota, J. Skvarc, N. Yasuda, R. Ilic and S. Kodaira: *Projectile fragment emission angles in fragmentation reactions of light heavy ions in the energy region < 200 MeV/nucleon: Experimental study*, Radiat. Meas. 48, pp. 73–81, 2013, doi:10.1016/j.radmeas.2012.08.006.

[284] R. L. Sime: *Marietta Blau in the history of cosmic rays*, Physics Today 65, no. 10, pp. 8–8, 2012, doi:10.1063/pt.3.1728.

[285] M. Spanring: *Kalibrierung der analogen Eingänge sowie der digitalen Ausgänge des Steuerungs- und Datenerfassungssystems "Logic Box"*, Project thesis, TU Wien, 2013.

[286] M. Spanring: *Untersuchung des Überschlagsverhalten zwischen planparallelen Platten bei bekannten Abstand und in Abhängigkeit vom Durck*, Bachelor's thesis, TU Wien, 2013.

[287] D. Stadler: *Dynamik ultrakalter Neutronen im Gravitationsfeld der Erde*, Diploma thesis, Ruprecht-Karls-Universität Heidelberg, 2009.

[288] H.-G. Stangl: *Characterisation of the vacuum system of the qBounce experiment*, Bachelor's thesis, TU Wien, 2015.

[289] H.-G. Stangl: *Development of a laser-guided large scale surface metrology device*, Diploma thesis, TU Wien, 2021, doi:10.34726/HSS.2021.93464.

[290] A. Steyerl: *Measurements of total cross sections for very slow neutrons with velocities from 100 m/sec to 5 m/sec*, Phys. Lett. B 29, no. 1, pp. 33–35, 1969, doi:10.1016/0370-2693(69)90127-0.

[291] A. Steyerl: *A "neutron turbine" as an efficient source of ultracold neutrons*, Nuclear Instruments and Methods 125, no. 3, pp. 461–469, 1975, doi:10.1016/0029-554x(75)90265-7.

[292] A. Steyerl: *Ultracold Neutrons*, World Scientific Publishing Co Pte Ltd, 2020, ISBN 9789811212703.

[293] A. Steyerl, B. Gmal, K. A. Steinhauser, N. Achiwa and D. Richter: *Features and performance of a gravity spectrometer for ultracold neutrons*, Zeitschrift für Physik B Condensed Matter 50, no. 4, pp. 281–288, 1983, doi:10.1007/bf01470039.

[294] A. Steyerl, H. Nagel, F.-X. Schreiber, K.-A. Steinhauser, R. Gähler, W. Gläser, P. Ageron et al.: *A new source of cold and ultracold neutrons*, Phys. Lett. A 116, no. 7, pp. 347–352, 1986, doi:10.1016/0375-9601(86)90587-6.

[295] M. Suda, M. Faber, J. Bosina, T. Jenke, C. Käding, J. Micko, M. Pitschmann and H. Abele: *Spectra of neutron wave functions in Earth's gravitational field*, Zeitschrift für Naturforschung A 77, no. 9, pp. 875–898, 2022, doi:10.1515/zna-2022-0050.

[296] N. Suga: *Metrology handbook: the science of measurement*, Mitutoyo (UK) Ltd, Andover, 2007, ISBN 9780955613302.

[297] E. Takasugi and M. Tanaka: *Charge nonconservation and charges of neutrinos, neutron, and atoms*, Phys. Rev. D 44, no. 11, pp. 3706–3708, 1991, doi:10.1103/physrevd.44.3706.

[298] M. Thalhammer: *Optimierung der Detektorsignalverarbeitung des Gravitatonsexperiments qBounce*, Diploma thesis, TU Wien, 2013.

[299] M. Thalhammer: *tba*, Phd thesis, TU Wien, 2024.

[300] E. Tiesinga, P. J. Mohr, D. B. Newell and B. N. Taylor: *CODATA recommended values of the fundamental physical constants: 2018*, Rev. Mod. Phys. 93, no. 2, p. 025010, 2021, doi: 10.1103/revmodphys.93.025010.

[301] L. Timmen: *Absolute und relative gravity measurements at ILL Grenoble with the Hannover absolute gravity meter FG5X-220 (Oct. 2021) and the relative meters Scintrex CG-3-4493 and CG-6-171 (Aug. and Oct. 2021)*, techreport, Institut für Erdmessung (IfE), Leibniz Universität Hannover, Schneiderberg 50, 30167 Hannover, Germany, 2022.

[302] J. Trauner: *Development of a step measurement and control system based on absolute distanceinterferometry for qBounce*, Bachelor's thesis, TU Wien, 2022.

[303] S. Vanbergen, W. Schreyer, S. Ahmed, T. Andalib, M. Barnes, B. Bell, J. Chak et al.: *A spallation target at TRIUMF for fundamental neutron physics*, EPJ Web of Conf. 285, p. 07004, 2023, doi:10.1051/epjconf/202328507004.

[304] A. A. Vankov: *Quantum bouncer: theory and experiment*, arXiv 2009, doi:10.48550/arxiv.0906.5138.

[305] C. Voith: *Single-particle state of an open quantum dynamical system in a dilaton environment*, Diploma thesis, TU Wien, 2023, doi:10.34726/HSS.2023.112390.

[306] A. Y. Voronin, H. Abele, S. Baessler, V. V. Nesvizhevsky, A. K. Petukhov, K. V. Protasov and A. Westphal: *Quantum motion of a neutron in a waveguide in the gravitational field*, Phys. Rev. D 73, no. 4, p. 044029, 2006, doi:10.1103/physrevd.73.044029.

[307] V. V. Voronin, L. A. Akselrod, V. N. Zabenkin and I. A. Kuznetsov: *New approach to test a neutron electroneutrality by the spin interferometry technique*, Phys. Procedia 42, pp. 25–30, 2013, doi:10.1016/j.phpro.2013.03.171.

[308] H. Wallis, J. Dalibard and C. Cohen-Tannoudji: *Trapping atoms in a gravitational cavity*, Appl. Phys. B: Photophysics and Laser Chemistry 54, no. 5, pp. 407–419, 1992, doi: 10.1007/bf00325387.

[309] X. Wang, G. Konrad and H. Abele: *RxB drift momentum spectrometer with high resolution and large phase space acceptance*, Nucl. Instrum. Methods Phys. Res., Sect. A 701, pp. 254–261, 2013, ISSN 0168-9002, doi:10.1016/j.nima.2012.10.071.

[310] G. Wautischer: *Realisation of quantum transport measurements with UCN within the qBounce project*, Diploma thesis, TU Wien, 2015.

[311] M. S. Weber: *Gravitation in der Interferometrie mit kalten Neutronen*, Phd thesis, Universität Innsbruck, 1998.

[312] A. Westphal: *Quantum Mechanics and Gravitation*, Diploma thesis, Ruprecht-Karls-Universität Heidelberg, 2001, doi:10.48550/ARXIV.GR-QC/0208062.

[313] A. Westphal, H. Abele and S. Baessler: *Analytically derived limits on short-range fifth forces from quantum states of neutrons in the Earth's gravitational field*, arXiv 2007, doi:10.48550/arxiv.hep-ph/0703108.

[314] A. Westphal, H. Abele, S. Baessler, V. V. Nesvizhevsky, K. V. Protasov and A. Y. Voronin: *A quantum mechanical description of the experiment on the observation of gravitationally bound states*, Eur. Phys. J. C 51, no. 2, pp. 367–375, 2007, doi:10.1140/epjc/s10052-007-0283-x.

[315] H. Wetter: *Characterisation of the spin-dependent detector for the Ramsey GRS*, Diploma thesis, TU Wien, 2022, doi:10.34726/HSS.2022.82727.

[316] N. Wheeler: *Classical/quantum dynamics in a uniform gravitational field: B. bouncing ball*, Lecture notes, Reed College Physics Department, 2002.

[317] S. Whineray: *An energy representation approach to the quantum bouncer*, Amer. J. Phys. 60, no. 10, pp. 948–950, 1992, doi:10.1119/1.17024.

[318] M. Winder: *qBounce: magnetic field for spin measurement*, Project thesis, TU Wien, 2018.

[319] R. L. Workman, V. D. Burkert, V. Crede, E. Klempt, U. Thoma, L. Tiator, K. Agashe et al.: *Review of Particle Physics*, Progress of Theoretical and Experimental Physics 2022, no. 8, 2022, doi:10.1093/ptep/ptac097.

[320] D. Wurm, D. H. Beck, T. Chupp, S. Degenkolb, K. Fierlinger, P. Fierlinger, H. Filter et al.: *The PanEDM neutron electric dipole moment experiment at the ILL*, in T. Jenke, S. Degenkolb, P. Geltenbort, M. Jentschel, V. V. Nesvizhevsky, D. Rebreyend, S. Roccia, T. Soldner, A. Stutz and O. Zimmer (editors), *EPJ Web of Conf.*, vol. 219, p. 02006, EDP Sciences, 2019, doi:10.1051/epjconf/201921902006.

[321] Y. B. Zel'dovich: *Storage of cold neutrons*, JETP 9, no. 6, pp. 1389–1390, 1959, j. Exptl. Theoret. Phys. (U.S.S.R.) 36, 1952-1953(June, 1959).

[322] O. Zimmer, F. M. Piegsa and S. N. Ivanov: *Superthermal source of ultracold neutrons for fundamental physics experiments*, Phys. Rev. Lett. 107, no. 13, p. 134801, 2011, doi:10.1103/physrevlett.107.134801.

[323] R. Zimmermann: *Vibrationsmessungen im Rahmen des Quantum Bouncing Ball Experimentes*, Bachelor's thesis, TU Wien, 2010.

[324] G. van der Zouw: *Gravitational and Aharonov-Bohm phases in neutron interferometry*, Phd thesis, Universität Wien, 2000.

[325] G. van der Zouw, M. Weber, J. Felber, R. Gähler, P. Geltenbort and A. Zeilinger: *Aharonov–Bohm and gravity experiments with the very-cold-neutron interferometer*, Nucl. Instrum. Methods Phys. Res., Sect. A 440, no. 3, pp. 568–574, 2000, doi:10.1016/s0168-9002(99)01038-4.

Glossary

ADC - An *analog digital converter* converts analog measurement signals to digital signals which the PC can interprete: 98, 110, 113, 123, 136–140

AFG - An *arbitrary function generator* produces a voltage signal with a tunable amplitude and frequency. Preset function shapes are typical sine, rectangular, triangular. However any arbitrary signal can be generated: 10, 77, 93, 131, 132, 137, 143, 149, 151, 171, 172, 189, 190, 217, 218, 220, 227, 231, 238

ATI - The *Atominstitut* is one of the four institutes of the faculty of physics at the TU Wien. Since Hartmut Abele started his professorship there in 2011, the ATI also hosts the *q*BOUNCE group: 5, 18, 22, 27, 28, 40, 75, 88, 98, 102, 106, 108, 111, 112, 121, 136, 138, 142, 143, 149, 181, 188, 213, 261–264

BNC - *Bayonet Neill Concelman* (BNC) are standardized connectors for coaxial cables. They are specified for 4 GHz, 500 V and maximal 1 A. They commonly have a resistance of 50 Ω or 75 Ω and sometimes 93 Ω. They are frequently used for signal transmission: 96, 112, 113, 132, 136, 263

CERN - It stands for the French name *Conseil Européen pour la Recherche Nucléaire*. It is a large European particle physics organisation hosting the largest and most powerfull particle accelerators at their laboratories in Geneva, Switzerland: 104

CODATA - The *Committee on Data of the International Science Council* is an international collaboration founded by the International Science Council to increase global collobaration in science and availabilty of open data. Its *Task Group on Fundamental Physical Constants* regularly publishes a summary of fundamental physical constants with their commonly accepted values every four years. The most recent set of values is the CODATA 2018 [300] which is used in this thesis: 35–37, 261, 265, 266, 268

CR-39 - *Columbia Resin #39* is a plastic polymer consisting of allyl diglycol carbonate which is commonly used for eyeglass lenses. *q*BOUNCE uses it as neutron detector with a boron coating: 11, 20, 22–24, 27–29, 77, 82, 83, 94, 95, 101–105, 143, 145, 146, 162–165, 181, 184, 188, 191, 207–210, 212, 214, 238, 241

DAC - A *digital analog converter* converts digital signals from the PC into analog input signals for adjustable devices like piezoelectric actuators: 106, 123, 133, 136, 137

DAQ - *Data acquisition devices* are used to communicate with sensors, especially if the peripheral devices only produce signals which a computer cannot handle directly: 136

ESS - The *European Synchrotron Source* will be the strongest spallation source for neutrons. It is under construction in Lund, Sweden: 15, 18, 39, 40

FFT - The *Fast Fourier Transformation* is an algorithm for discrete Fourier transformations: 134, 190, 224

FRM2 - The *Forschungs Reaktor München 2* is located in Garching near Munich (Germany). Similar to the ILL it is a high flux reactor and it is the succesor of the FRM (the atomic egg): 40

GND - *Ground* is the direct connection between a device and the earth (zero potential): 138–140, 166

GRANIT - A collaboration between the ILL, LPSC and LMA in order to study the properties of gravitational bound UCN: 21

GRS - *Gravitational Resonance Spectroscopy* is a method developed and first realized by the *q*BOUNCE-collaboration in order to measure transition frequencies between gravitational bound states: 5, 7, 10, 11, 13, 15, 16, 21–29, 31, 36, 37, 39–41, 44, 51, 55–60, 64, 65, 67, 68, 71, 75, 86, 90, 91, 95, 100, 105, 109, 116, 117, 123, 124, 127, 131, 134, 138, 141, 145–154, 156–159, 163, 165–181, 183, 184, 188, 190–192, 194, 197–204, 209, 210, 212, 215, 217, 219, 221–225, 227, 228, 235–242, 262, 263, 266

GRS^{TJ}-setup - Tobias Jenke completed the first GRS setup during his PhD under supervision of Hartmut Abele [139]. It took data between 2008 and 2011 at the ILL in Grenoble: 22, 24, 25, 60, 86, 116, 123, 124, 141, 163, 165, 168, 235

I^{2}C - The *Inter-Integrated-Circuit* is a serial data bus: 96

ILL - The *Institut Laue-Langevin* is a large reasearch facility in Grenoble with the most powerful research reactor in the world (www.ill.eu): 5, 7, 14, 15, 17–22, 28, 39, 40, 75, 77, 99, 106, 112, 114, 136, 145, 181, 261–264

ITEM - is a company mainly known to their produced aluminum profile which is also called ITEM: 87, 133, 134, 141, 262

JINR - The *Joint Institute for Nuclear Research* is located in Dubna near Moscow (Russia): 15, 20, 40

LANL - The *Los Alamos National Laboratory* is located in New Mexico (United States) (www.lanl.gov). It was founded 1943 as part of the Manhatten project: 39, 40

LMA - The *Laboratoire des Matériaux Avancés* is material science center in Lyon, France (lma.in2p3.fr): 21, 261

LPSC - The *Laboratoire de Physique Subatomique & Cosmologie* is research center in Grenoble, France (lpsc.in2p3.fr, 1.12.2023): 21, 261

LabView - A *software for instrument control* developed and distributed by National Instruments: 10, 25, 27, 77, 93, 96, 106, 110, 111, 113, 123, 126, 127, 131, 132, 136, 137, 139, 140, 143, 146, 147, 152–154, 169–172, 176, 177, 186, 188–190, 201, 239

Mathematica - A *symbolic mathematics software* developed and distributed by Wolfram Research: 10, 36, 37, 39, 40, 43, 49, 55, 101, 104, 113, 134, 136, 141, 178, 186, 188, 196

miCos - A German company specialized in producing positioning stages. Physik Instrumente (PI) acquired it in 2011: 124–127, 133, 137, 138, 145, 152–155, 166, 237

Monopol - A Badurek-type neutron resonator for beam preparation and analysis. It origins from the russian Drabkin resonator. Until now three generations of resonators were built and tested at the ATI. MONOPOL stands for monochromatic polarized neutron pulses which the device can produce in nearly any shape [44]: 142

NAS - The *network accessed storage* stores the measurement data centralized on its hard drives: 136, 186, 188, 189

NIM - The *Nuclear Instrumentation Modules* are electronic modules commonly used in experimental physics. These standardized modules fit in special crates which provide 12 V and 24 V at the backplane: 96

OROS - It is a French company (www.oros.com) specialized in building sensors for measuring noise and vibrations: 10, 131, 134

PF2 - The instrument PF2 (*Physique Fondamentale 2*) is one of the strongest sources of UCNs and VCNs. Since 1986, it is situated at the niveau D of the ILL reactor: 5, 7, 15, 19, 21, 22, 24, 25, 27, 28, 39, 40, 71, 75–78, 81–83, 87, 93, 96, 98–102, 116–118, 120, 123, 125–127, 132, 134, 136, 137, 140, 141, 143, 145, 146, 158–160, 176, 181, 183, 189, 190, 208, 237

PI - Physik Instrumente (PI) is a German company (www.physikinstrumente.de) producing devices for Nanopositioning: 72, 88, 89, 91–93, 106, 113, 124, 125, 127, 131, 132, 135–137, 143, 189, 217, 237, 262

PNPI - The *St. Petersburg Nuclear Physics Institute* is located in Gatchina near St. Petersburg (Russia). During the Soviet area it was called *Leningrad Nuclear Physics Institute*: 15, 20, 39, 40

POG - Präzisionsoptik Gera GmbH (www.pog.eu) is a German company producing optical glass plates: 89–91, 107–109

PSI - The *Paul Scherrer Institut* near Villigen in Switzerland is a large research facility famous for its highly specialized particle accelerators (www.psi.ch, 1.12.2023): 17, 19, 39, 40

PVD - *Physical vapor deposition* is a method to produce thin film or coatings on surfaces: 27, 102

RAID - The *Redundant Array of Independent Disks* is a storage architecture which allows to cluster

multiple hard drives into one virtual storage with a certain degree of resilience: 136

ROI - The *Region Of Interest* is a section of a measured spectrum where the wanted signal is expected. It excludes regions with high background and therefore increases the signal to background ratio: 99, 195, 215

RABI-GRS-18 - A Rabi-type GRS measurements within RAMSEY^{TR}-setup during the beam time 182-18/1 (3-14-358-III) in spring 2018: 10, 11, 26, 28, 51, 56, 90, 127, 145, 147, 149–151, 166–170, 174, 178, 179, 181, 183, 190, 191, 197, 198, 200, 202, 210, 212, 215, 217, 219, 221–223, 228, 236–242

RABI^{GC}-setup - Gunther Cronenberg with the *q*BOUNCE-collobration and many students developed and built this Rabi-type GRS setup with three regions as his PhD thesis [65]. It took data at the ILL in Grenoble in 2012 (3-14-305: cycles 167-12/2 and 168-12/3): 22–27, 29, 51, 81, 85, 86, 98, 100, 105, 116, 120, 124, 125, 141, 143, 149, 153, 159, 160, 163, 164, 166, 167, 183, 221, 235, 264, 266

Rams$\vec{E}$y - The neutron charge measurement with a Ramsey-type GRS setup done at the ILL in autumn 2018 during the beam time 184-18/3 (3-14-384) [169]: 9–11, 28, 51, 64, 90, 91, 105–107, 109, 111, 114, 116, 117, 119, 127, 145–149, 152, 153, 176–181, 183, 190, 192, 195–197, 203, 210, 212, 229–231, 237–239, 241, 242

RAMSEY-GRS-18 - A Ramsey-type GRS measurements within RAMSEY^{TR}-setup during the beam time 183-18/2 (3-14-358-IV) in spring 2018: 10, 11, 28, 51, 90, 100, 105, 109, 117, 127, 145–150, 152–154, 169–175, 178, 181, 183, 190, 192, 194, 197, 199, 201, 203, 210, 212, 215, 224, 225, 227, 228, 237–242

RAMSEY^{TR}-setup - Tobias Rechberger with the *q*BOUNCE-collobration and many students developed and built this Ramsey-type GRS setup as his PhD thesis [254]. It is situated since 2016 at the ILL in Grenoble (3-14-358): 5, 22, 26–29, 39, 53, 59, 60, 64, 68, 71, 72, 75, 76, 82, 85–87, 90, 93, 94, 96, 98–100, 105, 106, 111, 115–118, 120–125, 131, 134, 136–138, 141, 143, 145, 146, 149, 151, 154, 155, 159–161, 163, 165, 166, 175, 176, 183, 184, 191, 192, 207, 209, 213, 235–239, 263, 266, 267

SHV - The *safe high voltage connectors* are very similar to BNC connectors. The major difference is the thicker dielectric which enables a higher voltage up to 5 kV and currents up to 5 A. Therefore, we use them as high voltage supply cables for the detectors: 96, 105

SIOS - Messtechnik GmbH (www.sios.de) is a German company specialized on laser interferometers: 10, 87, 90, 107, 113, 124, 125, 127, 131–134, 137, 141, 149, 151, 171, 172, 174, 175, 178, 179, 190, 218, 220–224, 227, 228, 230, 231, 238, 241, 242

BSM - the term *Beyond the Standard Model* summmaryizes all extensions of the Standard Model and new theortical approaches which try to describe observations which are not predictable by the SM (e.g. neutrino mass): 13, 17, 140, 183, 184

SM - the *Standard Model of particle physics* is the most precise description of elementary particles and their interactions: 13, 16, 17, 263, 264, 266

SNS - The *Spallation Neutron Source* at the Oak Ridge National Laboratory in Tennesse (US) is the most powerfull spallation neutron source in the world since 2007 (neutrons.ornl.gov/sns, 1.12.2023): 17, 18

TOF - *Time of flight* is a measurement setup with a pulsed beam and a detector with a good time resolution. Due to the different velocities, different neutrons arrive at different times: 18, 19, 59, 60, 88, 156, 158–160

TRIGA - The TRIGA reactor is a widely used reseracher reactor type. Since 1962, a TRIGA Mark 2 reactor is operated at the Atominstitut (ATI) in Vienna. The name itself is an acronym for *Training, Research, Isotopes, General Atomics*: 18, 99, 102, 263

TRIUMF - The *Tri University Meson Facility* in Vancouver is the most important particle physics research facility in Canada. It hosts a 520 MeV cyclotron and the connected neutron spallation source TUCAN producing UCNs (www.triumf.ca, 1.12.2023): 17, 39

TTL - The *transistor-transistor logic* (TTL) consists of bipolar junction transistors. Signals are transmitted as voltage levels: 77

USB - The *universal serial bus* is a computer bus standard which is mainly used to connect peripheral devices with a computer: 136

UCN - *Ultra-cold neutrons* have energies below the pseudo fermi potential V_F of a specific material. The

exact value is material dependent (≈ 100 neV): 5, 13–23, 28, 29, 31, 32, 39, 59, 61, 62, 77–79, 87, 88, 95, 100, 101, 109, 111, 115, 140, 146, 158, 166, 175, 181, 183, 184, 204, 208, 210, 211, 219, 225, 229, 230, 235–237, 261–264, 267, 268

VCN - *Very cold neutrons* have a wavelength from 20 Å to 100 Å: 213, 262

WEP - The *weak equivalence principle* states that the inertial mass m_i of a particle is the same as its gravitational mass m_g: 31

μ-metal - "A nickel-iron soft ferromagnetic alloy with very high permeability" (en.wikipedia.org/wiki/Mu-metal, 7.9.2020): 10, 117, 124, 138, 142, 154

nEDM - The *neutron's electric dipole moment* is predicted below $10^{-30}\,e\,\mathrm{cm}$ within the Standard Model of particle physics (SM). The currently best measurement set the limit to $0.0(13) \times 10^{-26}\,e\,\mathrm{cm}$ [2, 319]: 17, 138

qBB - *quantum bouncing ball* is the quantum mechanical analogue of a hopping ball described by the gravitational quantum states of the *quantum bouncer*: 21–24, 27, 86, 95, 104, 105, 116, 120, 121, 123, 143, 158, 159, 165, 235, 264

qBB$^{\mathrm{MT}}$-setup - Martin Thalhammer developed and measured with the *q*BOUNCE-collobration and many students the *quantum Bouncing Ball* at the ILL in Grenoble in 2014 during the cycles 171-14/1 and 172-14/2 (3-14-331) [299]. This was the first, best and most successfull measurement of this kind: 23, 27, 86, 95, 104, 105, 116, 120, 121, 123, 143, 159

***q*BOUNCE** - A collaboration between the Atominsitut (ATI) and the ILL in order to study the properties of gravitational bound UCN: 1, 5, 7, 9, 16, 19, 21–25, 27–29, 31, 35, 37, 39–41, 45, 55, 64, 75, 77, 86, 88, 95, 97, 107, 109, 116, 117, 121, 134, 137, 139–141, 143, 146, 178, 179, 181, 183, 184, 232, 241, 261, 263, 264

***q*BOUNCINO** - A small scale test setup consisting of spare and old parts of different *q*BOUNCE setups. The main part is the RABI$^{\mathrm{GC}}$-setup-vacuum chamber [236]: 24, 25, 27–29, 75, 85, 87, 96, 99, 101, 105, 106, 111, 116–121, 123, 132, 135, 136, 143, 145–147, 162, 170, 181, 183, 184, 195, 196, 207, 213, 232, 237

a - The *dimensionless Maxwell-Boltzmann distribution parameter* ($1/\sqrt{2a}$ [254] p.109, b [160] p.26). For the real Maxwell-Boltzmann distribution for a velocity distribution of gas particles $a = \sqrt{k_\mathrm{B}T/m}$. The temperature T can be expressed as $T = a^2 m/k_\mathrm{B}$: 59, 60, 157, 159, 160, 181, 204, 205, 264

$a_\oplus$ - The *equatorial semi axis* of the Earth (6378.137 km) [228]: 38, 39

a_E - The *electrode length* in x-direction: 69, 110, 113, 114

Ai - The *Airy function* Ai: 33, 34, 43

AiZ - The *Root of the Airy function* Ai: 33, 34, 40, 41, 43, 65

a_v - The *mechanical oscillation strength* [mm/s] of the mirrors ($= \omega a_x$): 44–57, 59, 60, 63, 73, 149, 150, 167, 168, 171, 174, 175, 178, 181, 218, 220, 221, 227, 228, 231, 235–238, 241, 264, 269

$a_v V_{fi}$ - The *Rabi frequency* ($= a_x \omega V_{fi}$ [s^{-1}]): 44, 46–51, 53–55, 57, 63, 269

a_x - The *mechanical oscillation amplitude* of the mirrors [μm]: 41, 44, 45, 48, 49, 63, 171, 218, 220, 227, 231, 264

b - The *exponent of the velocity* within the exponential function of Maxwell-Boltzmann distribution (b [139] p.44, b [254] p.109, a [160] p.26). In the simple case this is set to 2: 60, 157, 159, 160, 181, 204, 205

b - The *time-dependent state population* of the quantum bouncer: 34, 41, 42, 44, 48–51, 53–55, 63, 163, 164, 265, 267, 269

$b_\oplus$ - The *equatorial semi axis* of the Earth (6356.752 km) [228]: 38, 39

b_E - The *electrode width* (y-direction): 69, 110, 113, 114

Bi - The *Airy function* Bi: 33

c - The *exponent of the velocity* in the linear term of Maxwell-Boltzmann distribution (c [139] p.44, c

[254] p.109, *a* [160] p.26). In the simple case this is set to 2: 60, 157, 159, 160, 181, 204, 205

c - It describes the *visible contrast* of a state transition: 50, 51, 59, 71, 73, 91, 167, 171, 174, 178–180, 221–223, 228, 241, 242, 265

$c_{\boldsymbol{fi}}$ - It describes the *visible contrast* of a state transition between state i and f: 50, 59

c - The *time-dependent state population* after the transformation $b(\tilde{t}) = c(\tilde{t}) \times u(\tilde{t})$: 44–49, 63, 265, 267

c_0 - The *speed of light* in vacuum is $299\,792\,458\,\mathrm{m\,s^{-1}}$ (SI-defintion since 1983 [55]): 36, 142, 268

C - The *capacity* of the electrodes commonly measured in [pF]: 69, 265

C_P - The *parasitic capacity* due to the measurement circuit for the determination of the electrode's capacity C [pF]: 69

C_n - The *normalization coefficient* of the wavefunction $\varphi_n(z)$ ($\langle {C_n}^* \varphi_n(z) | C_n \varphi_n(z) \rangle = 1$): 33, 265

d - The *distance* between two surfaces (e.g. electrodes, mirror-absorber,..): 14, 68, 69, 110, 113, 114, 177

d - The *time-dependent state population* after transforming the differential equation into a matrix eigenvalue problem ($c\left(\tilde{t}\right) = \left(\mathrm{e}^{\frac{\mathrm{i}}{2}\left(\Delta\omega\tilde{t}+\phi\right)}, \mathrm{e}^{-\frac{\mathrm{i}}{2}\left(\Delta\omega\tilde{t}+\phi\right)}\right) d\left(\tilde{t}\right)$): 45–49, 63, 265

$\tilde{d}$ - The *final time-dependent state population* including the phase information ($c\left(\tilde{t}\right) = \left(\mathrm{e}^{\frac{\mathrm{i}}{2}\Delta\omega\tilde{t}}, \mathrm{e}^{-\frac{\mathrm{i}}{2}\Delta\omega\tilde{t}}\right) \tilde{d}\left(\tilde{t}\right)$): 47–49, 265

e - The *elementary charge* (charge of a proton) is exactly defined to $1.602\,176\,634 \times 10^{-19}\,\mathrm{C}$ (SI-defintion since 5.2019 [41]): 36, 265, 268

$\vec{E}$ - The *electric field* [$\mathrm{MV\,m^{-1}}$]: 14, 41, 64–67, 73, 179, 236, 265, 267–269

E_z - The *electric field strength* in the vertical direction is the according component of the electric field $|\vec{E}|_z$: 14, 64–68, 70, 71, 73, 179

e^- - The *electron* is a lepton and an elementary particle with a negative electric charge of -e: 16, 268

E - The *energy*: 18, 20, 24, 31, 32, 34–38, 40–42, 44, 49, 64, 235, 265, 269

$\tilde{E}$ - The *dimensionless energy* is calculated via E/E_0: 32, 35, 64

E_0 - The *characteristic energy scale* of the gravitational bound states: 32, 34–38, 40, 41, 64, 235, 265

$\boldsymbol{f}$ - The *final state* of the gravitational bound neutron: 33–37, 40–51, 53–55, 57–59, 63, 65–73, 91, 179, 180, 241, 264–269

$f(t)$ - The *time-dependent disturbance* (vibration/ oscillation) in the lab frame: 41, 42, 63

$f(\tilde{t})$ - The *time-dependent disturbance* (vibration/ oscillation) in the oscillation frame: 42, 44

$\dot{f}(\tilde{t})$ - The *derivation of the time-dependent disturbance* (vibration/ oscillation) in the oscillation frame: 42, 44, 45

$f(v_\mathrm{n})$ - The *arbitrary velocity distribution*. Neutron physicists commonly use the Maxwell-Boltzmann distribution: 59, 60, 159, 160, 265

$f(v_{\mathrm{n}i})$ - This is a *discrete velocity distribution*: 59

$F(v_\mathrm{n})$ - This is the *integrated velocity distribution* $\int f(v_\mathrm{n})\,\mathrm{d}v_\mathrm{n}$: 59, 60

G - The *gravitational constant* is measured only to $6.674\,30(15) \times 10^{-11}\,\mathrm{m^3\,kg^{-1}\,s^{-2}}$ (CODATA 2018 [300]) which makes it to a fundamental constant with one of the highest uncertainties: 31, 38

g - is the *local gravitational acceleration* on Earth. The exact value depends on the latitude (Earth's rotation), altitude and local mass distribution: 5, 7, 19, 20, 22, 26, 31, 32, 35, 36, 38–41, 49–51, 64–68, 70, 73, 84, 85, 122, 147, 159, 167, 174, 178–181, 221–223, 228, 241, 268, 269

g_e - The local gravitational acceleration on the equator is defined to $9.780\,325\,335\,9\,\mathrm{m/s^2}$ [228]: 38–40

g_p - The local gravitational acceleration on the poles is $9.832\,184\,937\,8\,\mathrm{m/s^2}$ [228]: 39, 40

g_0 - The *standard gravitational acceleration* on Earth is fixed to $9.806\,65\,\mathrm{m\,s^{-2}}$ since 1901. Due to its universality it is used in the theory chapter: 35, 39, 40, 43, 64

$\hat{H}_0$ - The *Hamiltonian of the unperturbed system* of the quantum bouncer on a flat surface - $\hat{H}_0 = -\frac{\hbar^2}{2m_i}\frac{\partial^2}{\partial\tilde{z}^2} + m_g g\tilde{z} + V_F\Theta\left(-\tilde{z}\right)$: 41, 42, 63, 266

h - The *Planck's constant* is now defined to $6.626\,070\,15 \times 10^{-34}\,\mathrm{J\,s}$ (SI-defintion since 5.2019 [41]) 18, 24, 31, 34, 36, 37, 40, 41, 43, 50, 65, 142, 268, 269

$\boldsymbol{i}$ - The *initial state* of the gravitational bound neutron: 20, 33–37, 40–51, 53–55, 57–59, 63, 65–73, 91, 179, 180, 241, 264–269

k_B - The *Boltzmann constant* is defined to $1.380\,649 \times 10^{-23}\,\mathrm{J\,K^{-1}}$ (SI-defintion since 5.2019 [41]): 18, 36, 59, 142, 264

l_{II} - The *mirror length* of region I, II, IV, V (x-direction). Within RAMSEY$^{\mathrm{TR}}$-setup this length is 152 mm (slightly longer than the 150 mm lengths within in the RABI$^{\mathrm{GC}}$-setup): 50, 55, 56, 58, 59, 71, 221, 236, 269

l_{III} - The *mirror length* of region III (x-direction) within a Ramsey-type GRS setup (e.g. for RAMSEY$^{\mathrm{TR}}$-setup = 340 mm): 56, 58, 59, 236, 267

$M_\oplus$ - The *mass of the Earth* $(5.9722(6) \times 10^{24}\,\mathrm{kg})$ [182]: 31

m_g - The *gravitational mass* of a particle is proportional to interaction strength with an external gravitational field: 31, 32, 35–37, 64, 264

m_i - The *inertial mass* of a particle is its resistance to momentum changes due to external forces: 31, 32, 35–37, 42, 64, 264

m_n - The *mass of a neutron* has been measured as $1.674\,927\,498\,04(95) \times 10^{-27}\,\mathrm{kg}$ (CODATA 2018 [300]): 14, 17–20, 31, 35–37, 40, 41, 43, 50, 59, 64–68, 70, 73

M - This *matrix* describes the free propagation in multiple states: 53

N - The *number of measured neutrons* in one measurement point: 70, 71

n - This *scaling factor* rescales the Maxwell-Boltzmann like distribution from a probability distribution (normalized) to the actual measured velocity spectrum (N [139] p.44, n [160] p.26): 59, 60, 157, 160, 181, 204, 205

n - The *neutron* is a hadron consiting of two down quarks and one up quark. 13–20, 24, 31, 32, 35–37, 40, 41, 43, 50, 55, 56, 58–62, 64–68, 70, 71, 73, 84, 94, 146, 159, 160, 170, 175, 178–181, 183, 207, 208, 214, 221, 222, 236, 265–269

N_A - The *Avogadro constant* is defined to $6.022\,140\,76 \times 10^{23}\,\mathrm{mol^{-1}}$ (SI-defintion since 5.2019 [41]): 36

P - The *transition probability* of a given inital state i to a final state f: 49–51, 55, 57–59, 63

p^+ - The *proton* is a hadron consiting of two up quarks and one down quark: 16, 94

q_n - The *charge of a neutron* is zero within the Standard Model of particle physics (SM). The best charge measurement with neutrons is $-0.4(11) \times 10^{-21}\,e$ [36]: 13–17, 32, 41, 58, 64–68, 70, 73, 146, 179–181, 183, 236

$R_\oplus$ - The *mean radius of the Earth* (6371 km) [228]: 31, 39

$\langle r_B \rangle$ - The *averaged detector background count rate* [mcps]: 100, 101

r_D - The *detector count rate* [mcps]: 100, 101

r_{D_c} - The *corrected detector count rate* [mcps]: 100, 101

r_M - The *monitor count rate* [cps]: 100, 101

$\langle r_{MB} \rangle$ - The *averaged monitor background count rate* [cps]: 100, 101

$\langle r_M \rangle$ - The averaged monitor count rate [cps]: 100, 101

r_{fi} - The *transition rate* is the measured transmission rate through the full spectrometer exactly at a state transition: 70, 71

r_0 - The *zero rate* is the measured transmission rate through the full spectrometer without any oscillations applied: 56, 70, 71, 73, 158, 204, 236

r_b - The *radius* of the beam guides which is around 40 mm in the RAMSEY^{TR}-setup: 79, 80, 166

region I - The *first region* in the setup. It is a 152 mm long absorber/scatterer region to select only the lowest bound states: 23, 51, 83, 84, 91, 105, 153, 156, 160, 162–164, 209, 210, 235, 266, 267

region II - The *second region* in the setup. It is a 152 mm long mirror which can oscillate in order to drive transitions: 23, 27, 53, 55, 110, 131, 133, 134, 152, 153, 169, 175, 235, 267–269

region III - The *third region* in the setup and it is only used for the RAMSEY^{TR}-setup. It is a 340 mm long region where the state super position can propagate: 27, 53, 105, 106, 109, 124, 126, 127, 153, 155, 166, 169, 170, 192, 201, 209, 210, 212, 235, 238, 239, 241, 266, 267

region IV - Is the *fourth region* in the setup. It is a 152 mm long mirror which finishes the induced transition of region II by similar mechanical oscillations: 27, 53, 110, 131, 133, 134, 152, 153, 175, 224, 235, 268, 269

region V - Is the *last region* in the setup. It is a 152 mm long absorber/scatterer region similar to region I: 91, 105, 162–164, 209, 210, 214

r_s - The *radius* of the shutter real which is approximately 65 mm in the RAMSEY^{TR}-setup: 79, 80, 166, 211, 212, 240

T - The *temperature* is a collective thermodynamic parameter associated to kinetic energy distribution of the single particles. For neutrons the velocity spectrum is used to extract the *neutron temperature* similar to gases: 18, 59, 264

t_f - The *flight time* = traveling time of a neutron from the aperture to the region I = distance between aperture and region I / neutron velocity (d/v_n): 84

t - The *time* in general: 14, 31, 41, 42, 44–51, 53, 63, 70, 84, 158, 265, 267–269

t - The *time* t in the lab frame: 41, 42, 63, 265, 269

$\tilde{t}$ - The *time* t in the oscillation frame: 42, 44–51, 53, 63, 265, 267, 269

t_p - The *propagation time* = traveling time of a neutron through the region III of a Ramsey setup, where no oscillation is applied = mirror length of region III / neutron velocity (l_{III}/v_n): 53–55, 57–59, 63, 70, 71

T - The *transmission probability* displays the percentage of neutrons which are able to reach the detector: 50, 51, 55, 57–59, 63, 69, 70, 267

T_{0V} - The *transmission probability* T of a zero Volt measurement: 69, 70

T_+ - The *transmission probability* T of a high voltage measurement: 69, 70

u - The *arbitrary function* which transforms the state population coefficient as $b_f(\tilde{t}) = c_f(\tilde{t}) \times u(\tilde{t})$: 44, 265, 267

U - This *matrix* describes a Rabi excitation in multiple states: 45, 47–49, 53

U - The applied *voltage* on the electrodes in units of [V]: 68

v_0 - The *lower cut off* of the velocity spectrum (v_0 [139] p.44, v_0 [254] p.109, v_0 [160] p.26). For UCNs this appears if they pass through a filter as an aluminium foil (v_0=3.24 m/s [139] p.44): 59, 60, 157, 159, 160, 181, 204, 205, 267

$V_{\vec{E}}$ - The *electric potential*: 41, 64

V_F - The *Fermi pseudo potential* summarizes the averaged interaction of a neutron with matter: 17, 18, 32, 42, 63, 263, 266

$V_{\mathbf{fi}}$ - The *matrix element* of the transition ($= \langle f|\frac{\partial}{\partial \tilde{z}}|i\rangle$): 33, 41, 43–51, 53–55, 57, 58, 63, 69, 70, 241, 264, 269

V_g - The *linear Newtonian gravitational potential*: 31, 35, 41

$\vec{v}_\Lambda$ - The *eigenvector* of a matrix: 46, 47

v_n - The *neutron velocity* is for UCN typically around 10 m/s or below: 14, 18, 50, 55, 56, 59–62, 71, 84, 159, 160, 221, 222, 236, 265, 267, 269

$\overline{v}_\mathrm{n}$ - The *mean neutron velocity* is one characteristic parameter of the velocity distribution. It is often used to caclulate the transition amplitudes: 18, 59, 221

$V(z)$ - The *vertical potential* which only depends on the height z: 31, 32

V_z - The *vertical linear potential* in Lab Frame. It is a fixed value for the quantum bouncer calculations: 32, 41, 42, 44, 48, 49

z_0 - The *characteristic length scale* of the gravitational bound states: 21, 32–38, 40, 41, 43, 64, 235, 268

z - The *height* above a flat surface on the surface of Earth: 19, 20, 31–35, 39, 40, 42–44, 49, 63, 64, 159, 265, 266, 268, 269

$\tilde{z}$ - The *dimensionless height* is equal to z/z_0: 32, 35, 64

z - The *height* z in the lab frame: 42, 63, 269

$\tilde{z}$ - The *height* z in the oscillation frame: 42–44, 49, 63, 266, 268, 269

∞ - *Infinity*: Ramsey has no limits (TR $\to \infty$): 32, 268

α - The *fine-structure constant* or also called the Sommerfeld's constant expresses the strength of the electromagnetic force $\frac{e^2}{2\epsilon_0 h c_0} \approx \frac{1}{137}$: 268

α - The *pitch angle* is a rotation around the y-axis which is horizontially and perpendicular to the direction of travel: 69, 113, 114, 128, 130, 176, 177

β - The *roll angle* is a rotation around the x-axis which is equal to the direction of travel (= neutron flight direction): 69, 113, 114, 128, 130, 176, 177

γ - The *yaw angle* is a rotation around the z-axis which is vertical upwards (perpendicular to the mirror surface): 130

$\Delta_{\nu_{\mathbf{fi}}}$ - The *shift of the transition frequency* ν_{fi} due to an applied electric field $\vec{E}$ expressed as a difference ($= {\nu_{fi}}^g - {\nu_{fi}}^{\vec{E}}$): 65–70, 179

$\Delta\nu_m := \nu - \nu_{fi}$ - The *detuned frequency* from resonance [Hz] at the maximal slope: 58, 69

$\Delta\phi$ - The *mechanical phase difference* between the oscillations of region IV and region II ($= \phi_{IV} - \phi_{II}$): 53–55, 150, 218, 220, 227, 231

$\Delta\omega$ - The *detuned angular frequency* from the resonance angular frequency ($:= \omega - \omega_{fi}$ [s^{-1}]): 45–50, 53–55, 57, 58, 63, 69, 70, 265, 269

$\Delta\omega_m$ - The *detuned angular frequency* from the resonance [s^{-1}] at the maximal slope ($:= \omega_m - \omega_{fi}$): 58, 69, 70, 268

δ_m - The *distance of the measured points* from the maximal slopes of detuned angular frequency ($\Delta\omega_m \pm \delta_m$): 58, 69, 70, 268

$\Delta\tilde{t}$ - The *time offset* in the oscillation frame: 48

ϵ_0 - The *vacuum permittivity* or also called the absolute dielectric permittivity in vacuum was before 2019 exactly defined within the SI system. It is measured as $\epsilon_0 = \frac{e^2}{2\alpha h c_0}\, 8.854\,187\,812\,8(13) \times 10^{-12}\,\mathrm{F\,m^{-1}}$ (CODATA 2018 [300]) since then: 69, 110, 113, 268

Θ - The *Heaviside step function*: 32, 42, 60, 63, 160, 266

λ_B - The *De Broglie wavelenght* of a particle depends on its kinetic energy [54]: 18

Λ - The *eigenvalue* of a matrix: 46, 47, 268

$\bar{\nu}_{\mathrm{e}^-}$ - The *anti electron neutrino*: 16

ν - The *oscillation frequency* [Hz]: 5, 7, 24, 25, 34, 36, 37, 40, 41, 50, 56, 58, 59, 63, 65–70, 72, 73, 149, 167, 171, 174, 175, 179–181, 218, 220, 227, 231, 236, 241, 268, 269

$\nu_{\mathbf{fi}}$ - The *transition frequency* between state i and f ($= |(E_i - (E_f)|/h$ [Hz]): 34, 36, 37, 40, 41, 50, 58, 59, 63, 65–70, 72, 73, 179, 180, 268, 269

$\nu_{\mathbf{fi}}^{\vec{E}}$ - The *state transition frequency* with taking an applied electric field $\vec{E}$ into account: 65, 66, 73, 179, 268

$\nu_{\mathbf{fi}}^{-\vec{E}}$ - The *state transition frequency* with taking an anti-parallel electric field $\vec{E}$ into account: 65, 66

$\nu_{\mathbf{fi}}^{+\vec{E}}$ - The *state transition frequency* with taking a parallel electric field $\vec{E}$ into account: 65, 66

$\nu_{\mathbf{fi}}^{g}$ - The *state transition frequency* with only taking a linearized Newtonian gravitational potential into account: 65–68, 70, 73, 179, 180, 268

σ - The symbol for the *statistical error* of a measured quantity. The symbol of this quantity is denoted in the index: 15, 36, 37, 40, 41, 65–68, 70, 100, 101

τ - The *interaction time* = traveling time of a neutron through an oscillating region(II or IV) = mirror length of oscillating region / neutron velocity (l_{II}/v_{n}): 24, 51, 53–59, 63, 69–71, 236

τ_{II} - The *interaction time 2* = traveling time of a neutron through oscillating region II = mirror length of oscillating region / neutron velocity (l_{II}/v_{n}): 53, 54

τ_{IV} - The *interaction time 4* = traveling time of a neutron through oscillating region IV = mirror length of oscillating region / neutron velocity: 53, 54

$\phi_{\oplus}$ - The *latitude* on the Earth: 38, 39

ϕ - The *initial phase* of the incoming neutron: 41, 44–51, 53–55, 63, 150, 218, 220, 227, 231, 265, 268, 269

ϕ_{II} - The *initial phase* between the incoming neutron and the mechanical oscillation of region II: 53, 54, 268

ϕ_{IV} - The *initial phase* between the incoming neutron and the mechanical oscillation of region IV: 53–55, 268

$\varphi_n(z)$ - The *wave eigenfunctions* describe the wavefunction $\psi = \sum b\varphi_n(z)$: 33, 34, 265, 269

Ψ - The *time-dependent wavefunction* $\Psi(\vec{r},t)$ or $\Psi(z,t)$: 42, 49, 63, 269

$\Psi(z,t)$ - The *time-dependent wavefuntion* Ψ in the lab frame: 42, 63

$\tilde{\Psi}\left(\tilde{z},\tilde{t}\right)$ - The *time-dependent wavefuntion* in the oscillation frame: 42, 49, 63

ψ - The *time-independent wavefunction* $\psi(\vec{r})$ or $\psi(z)$: 32–34, 42–44, 49, 63, 269

$\tilde{\psi}$ - The *time-independent wavefuntion* of the unperturbed system in the oscillation frame: 42–44, 49, 63

ω - The *angular frequency* ($= 2\pi\nu$) [s^{-1}]: 41, 44, 45, 48, 49, 53, 63, 264, 268, 269

$\omega_{\mathbf{fi}}$ - The *transition angular frequency* ($= |(E_i - E_f)|/\hbar$ [s^{-1}]): 44, 45, 53, 63, 268

Ω_R - The *(general) Rabi frequency* ($= \sqrt{\Delta\omega^2 + a_v {V_{fi}}^2}$ [s^{-1}]): 46–51, 53–55, 63